



# Mechanisms and Methods in Redox and Redox-Mediated Reactions Involving Open-Shell Intermediates

## Citation

Sun, Rui. 2022. Mechanisms and Methods in Redox and Redox-Mediated Reactions Involving Open-Shell Intermediates. Doctoral dissertation, Harvard University Graduate School of Arts and Sciences.

## Permanent link

<https://nrs.harvard.edu/URN-3:HUL.INSTREPOS:37371917>

## Terms of Use

This article was downloaded from Harvard University's DASH repository, and is made available under the terms and conditions applicable to Other Posted Material, as set forth at <http://nrs.harvard.edu/urn-3:HUL.InstRepos:dash.current.terms-of-use#LAA>

## Share Your Story

The Harvard community has made this article openly available.  
Please share how this access benefits you. [Submit a story](#).

[Accessibility](#)

HARVARD UNIVERSITY  
Graduate School of Arts and Sciences



DISSERTATION ACCEPTANCE CERTIFICATE

The undersigned, appointed by the  
Department of Chemistry & Chemical Biology  
have examined a dissertation entitled:

Mechanisms and Methods in Redox and Redox-Mediated Reactions Involving Open-Shell Intermediates

presented by: Rui Sun

candidate for the degree of Doctor of Philosophy and hereby  
certify that it is worthy of acceptance.

Signature Daniel G. Nocera  
Typed name: Professor Daniel G. Nocera

Signature Eric N. Jacobsen  
Typed name: Professor Eric N. Jacobsen

Signature Theodore A. Betley  
Typed name: Professor Theodore A. Betley

Date: 21 January 2022



**Mechanisms and Methods in Redox and Redox-Mediated Reactions  
Involving Open-Shell Intermediates**

A dissertation presented

by

Rui Sun

to

The Department of Chemistry and Chemical Biology

in partial fulfillment of the requirements

for the degree of

Doctor of Philosophy

in the subject of

Chemistry

Harvard University

Cambridge, Massachusetts

January 2022



© 2022 Rui Sun

All rights reserved.

## **Mechanisms and Methods in Redox and Redox-Mediated Reactions Involving Open-Shell Intermediates**

### **Abstract**

The application and implication of redox reactions in transition metal chemistry and biological processes have long been established. There has been a resurgence of interest in the application of redox reactions in organic chemistry due to the development of photoredox catalysis, where the combination of a photocatalyst and light is used to generate highly energetic open-shell species that are inaccessible under thermal conditions. Despite the breadth of transformations that have been realized, the transience of the reaction intermediates has resulted in mechanistic ambiguity, precluding rational reaction optimization and development.

Chapters 2 to 4 of this dissertation explore the mechanisms of photoredox-mediated nickel-catalyzed carbon-heteroatom cross-coupling reactions. Chapter 2 establishes a thermally-sustained Ni(I/III) cycle as a potential productive mechanism for cross-coupling between aryl bromides and alcohols. A deleterious bi-metallic comproportionation, which results in the formation of inactive Ni(II) species, was identified. Chapter 3 shows that a similar Ni(I/III) mechanism is operative in the cross-coupling between aryl iodides and thiols. Guided by these mechanistic insights, we developed light-free analogues of photoredox cross-coupling reactions. Chapter 4 demonstrates that cross-coupling of aryl bromides with amines, alcohols, and carboxylic acids can be realized under strictly thermal conditions when photocatalyst and light are replaced with a substoichiometric amount of Zn metal. Chapter 5 reports the finding that triplet states of ketones selectively abstract amidyl N-H bonds over weaker C-H bonds. This chemoselectivity is due to an asynchronous concerted proton-coupled electron transfer (CPET) reaction, whereby substrates with lower ionization energies preferentially undergo hydrogen atom transfer (HAT). To highlight the utility of this discovery, we show that camphorquinone, a

1,2-diketone, can catalyze the intramolecular hydroamidation of alkenes. Chapters 6 and 7 shift to redox reactions of tetrapyrroles to deliver unusual intermediates of biological significance, arising from redox non-innocence of the macrocycle. In Chapter 6, we demonstrate that cobalt and nickel complexes of a *B,C*-tetrahydrocorrins, whose state of hydrogenation occupies a seldom-explored chemical space halfway between corrole and corrins, undergoes primarily ligand-centered redox chemistry. Chapter 7 presents the synthesis and characterization of a chlorinphlorin — an elusive dearomatized tetrapyrrole formed through the proton-coupled electron transfer reduction of a chlorin.

## Table of Contents

Title Page .....	i
Copyright .....	ii
Abstract.....	iii
Table of Contents .....	v
List of Figures .....	ix
List of Tables .....	xxvii
Acknowledgements .....	xxviii
<b>Chapter 1. Introduction.....</b>	<b>1</b>
1.1 Principles of Photoredox Catalysis .....	2
1.2 Metallaphotoredox Ni-Catalyzed Cross-Coupling Reactions.....	3
1.3 Mechanistic Uncertainty in Photoredox Reactions .....	5
1.4 Tetrapyrrole Compounds and Their Redox Chemistry .....	7
1.5 Summaries of Chapters .....	9
1.6 References .....	14
<b>Chapter 2. Mechanistic Studies on the Ni-Catalyzed Redox-Mediated Cross-Coupling Between Aryl Bromides and Alcohols.....</b>	<b>21</b>
2.1 Introduction .....	22
2.2 Quantum and Faradaic Yields .....	23
2.3 Transient Absorption and Electrochemical Studies on the Reaction Solution.....	24
2.4 Identification and Characterization of a Paramagnetic Ni Intermediate .....	29
2.5 Reactivity of the Paramagnetic Ni Intermediate <b>1</b> .....	34

2.6	Proposed Reaction Pathway and Optimization for Energy Efficiency .....	36
2.7	Conclusions .....	38
2.8	Materials and Methods .....	38
2.9	Acknowledgements .....	50
2.10	References .....	51
<b>Chapter 3. Mechanism, Optimization, and Generalization of the Photoredox Cross-Coupling Between Thiols and Aryl Halides .....</b>		<b>55</b>
3.1	Introduction .....	56
3.2	Quenching Studies .....	58
3.3	Effect of Thiolate and pyHI on (dtbbpy)NiCl <sub>2</sub> .....	63
3.4	Reaction Progress and Quantum Yield Measurements .....	63
3.5	Transient Intermediates and Reaction Kinetics .....	65
3.6	Reaction Optimization and Generalization .....	78
3.7	Discussion .....	80
3.8	Conclusions .....	82
3.9	Materials and Methods .....	83
3.10	Acknowledgements .....	93
3.11	References .....	94
<b>Chapter 4. Mechanism-Informed, Light-Free Access to Photoredox-Like Reactivity in Ni-Catalyzed Carbon-Heteroatom Cross-Coupling Reactions .....</b>		<b>99</b>
4.1	Introduction .....	100

4.2	Development of Light-Free Analogues of Photoredox-Mediated Cross-Coupling Reactions .....	103
4.3	Control Experiments and Mechanistic Insights.....	107
4.4	Generality of the Light-Free Reactions .....	109
4.5	Conclusions.....	112
4.6	Materials and Methods .....	113
4.7	Product Characterization.....	116
4.8	NMR Spectra.....	134
4.9	Acknowledgements .....	180
4.10	References .....	181
 <b>Chapter 5. Selective Activation of N-H Bonds by Photoexcited Ketones through Unidirectional Proton-Coupled Electron Transfer .....</b>		<b>187</b>
5.1	Introduction.....	188
5.2	Transient Absorption Studies of Amidyl Radical Formation.....	190
5.3	Mechanism of the PCET Process.....	193
5.4	Intramolecular Hydroamidation with Camphorquinone.....	197
5.5	Conclusions.....	201
5.6	Materials and Methods .....	201
5.7	Acknowledgements .....	203
5.8	References .....	204
 <b>Chapter 6. Properties and Reactivity of Tetradehydrocorrins .....</b>		<b>209</b>
6.1	Introduction.....	210

6.2	Syntheses of [M-TDC] <sup>+</sup> Complexes and Crystal Structure of [Ni-TDC] <sup>+</sup> .....	212
6.3	Oxidation-Reduction Chemistry of [M-TDC] <sup>+</sup> Complexes .....	214
6.4	Computational Studies of Ni-TDC Derivatives .....	222
6.5	Femtosecond Transient Absorption Spectroscopy of Ni-TDC Compounds.....	225
6.6	Conclusions.....	229
6.7	Materials and Methods .....	229
6.8	NMR Spectra.....	235
6.9	Acknowledgements .....	236
6.10	References .....	237
<b>Chapter 7. Synthesis of an Elusive Dearomatized Tetrapyrrole: The Chlorinphlorin .....</b>		<b>243</b>
7.1	Introduction.....	244
7.2	Synthesis and Structure of <i>meso</i> -Tetraphenylchlorinphlorin.....	245
7.3	Conclusions.....	247
7.4	Materials and Methods .....	247
7.5	NMR Spectra.....	250
7.6	Acknowledgements .....	251
7.7	References .....	252

## List of Figures

<b>Figure 1.1.</b>	Simplified diagram illustrating the possible productive pathways in a photochemical reaction. Chr = chromophore. Sub = substrate. Prdt = product. ....	2
<b>Figure 1.2.</b>	Scheme showing the general mechanism for an idealized ET-based photoredox reaction. The green arrows indicate productive pathways and red arrows indicate nonproductive pathways. ....	3
<b>Figure 1.3.</b>	Overview of the cross-coupling reactions that have been realized under dual Ir/Ni photoredox catalysis.....	4
<b>Figure 1.4.</b>	Idealized mechanism for thermal cross-coupling (A) and proposed mechanism for metallaphotoredox cross-coupling (B). ....	5
<b>Figure 1.5.</b>	Examples of photoredox reactions which operate through 'dark' mechanisms with their respective quantum yields ( $\Phi$ ). ....	7
<b>Figure 1.6.</b>	Porphyrin and corrole (top), along with some of their hydrogenated derivatives (bottom). ....	8
<b>Figure 1.7.</b>	Summary of Chapter 2 showing the elucidated mechanism for redox-mediated cross-coupling between alcohols and aryl bromides, along with the identification of an <i>in situ</i> generated dimeric Ni(I)-Ni(II) intermediate. ....	9
<b>Figure 1.8.</b>	Summary of Chapter 3 highlighting the critical role of pyridinium as a redox shuttle, as well as the operative Ni(I/III) dark cycle responsible for C-S cross-coupling reactivity.....	10
<b>Figure 1.9.</b>	Summary of Chapter 4 demonstrating the amination, esterification, and etherification of aryl bromides under light-free conditions using a combination of Ni cross-coupling catalyst activated by a substoichiometric amount of Zn metal as a reductant. ....	11
<b>Figure 1.10.</b>	Summary of Chapter 5 showing that intramolecular cycloamidation of an alkene can be effected using a simple diketone photocatalyst through selective N-H bond activation. ....	12



- Figure 1.11.** Summary of Chapter 6 showing the structure of the tetrahydrocorrins (TDC) core (top left), the crystal structure of Ni-TDC (bottom left), and the calculated frontier orbitals of Ni-TDC that highlight the ligand involvement (right). ..... 13
- Figure 1.12.** Summary of Chapter 7 showing the proton-coupled electron transfer (PCET) reduction of a chlorin to form a chlorinophlorin, along with the crystal structure of the latter. .... 13
- Figure 2.1.** Conditions for photoredox-catalyzed aryl etherification. dF-CF<sub>3</sub>-ppy = 2-(2,4-difluorophenyl)-5-(trifluoromethyl)pyridine. dtbbpy = 4,4'-di-*tert*-butyl-2,2'-dipyridyl. dme = 1,2-dimethoxyethane. .... 23
- Figure 2.2.** Quantum and faradaic yields for the redox-mediated cross-coupling reaction... 24
- Figure 2.3.** Transient absorption (TA) spectra of the initial reaction solution. (A) Spectrum obtained after exciting ( $\lambda_{\text{exc}} = 425 \text{ nm}$ ) a solution of 0.2 mM [Ir(dF-CF<sub>3</sub>-ppy)<sub>2</sub>-(dtbbpy)]PF<sub>6</sub>, 5 mM NiCl<sub>2</sub>(dme), 5 mM dtbbpy, and 50 mM quinuclidine in MeCN. (B) Single-wavelength kinetic trace monitored at 670 nm of the same solution as in A with the addition of 25 mM (— grey) and 100 mM (— orange) 4'-bromoacetophenone. Solid lines show mono-exponential fits and inset show the fitted lifetime in the presence of different concentrations of aryl bromide. .... 25
- Figure 2.4.** Dynamic Stern-Volmer quenching plots. (A) Dynamic Stern-Volmer quenching plot for the Ir(III) excited state under different concentrations of quinuclidine (— pink) and (dtbbpy)NiCl<sub>2</sub> (— blue). (B) Dynamic Stern-Volmer quenching plot for the Ir(III) excited state under different concentrations of (dtbbpy)Ni(2,4-bis(CF<sub>3</sub>)phenyl)(OCH<sub>2</sub>CF<sub>3</sub>).  $\tau$  and  $\tau_0$  represent the measured fluorophore lifetime in a solution with and without quencher, respectively. .... 25
- Figure 2.5.** Crystal structure of quinuclidine-bound (dtbbpy)NiCl<sub>2</sub> as a dimeric cation. Data were collected at 100 K. Thermal ellipsoids are drawn at 50% probability and hydrogen atoms are omitted for clarity. .... 26
- Figure 2.6.** Computational studies of the quinuclidine dimer radical cation. (A) Simulated absorption line spectrum of the quinuclidine dimer radical cation (blue lines, right y-axis). The line spectrum has been Gaussian-broadened to 0.35 eV at half-width half height. The optimized molecular structure shows a N-N bond length of 2.308 Å and is displayed for reference. We note that the associated absorption line (435 nm) is extremely sensitive to the N-N distance, which is underestimated in our

- calculations by comparison to the experiment. (B) Frontier molecular orbitals associated with the lowest-energy transition..... 26
- Figure 2.7.** Spectroelectrochemistry in MeCN of  $[\text{Ir}(\text{dF-CF}_3\text{-ppy})_2(\text{dtbbpy})][\text{PF}_6]$  under a cathodic potential of  $-1.8$  V vs  $\text{Fc}^+/\text{Fc}$  showing a transition from the Ir(III) state (— black) to an Ir(II) state (— pink). The difference in extinction coefficients between the Ir(II) and Ir(III),  $\Delta\varepsilon$  (— blue), is shown against the right axis..... 27
- Figure 2.8.** Deconvolution of the TA spectrum at 30 ns after photoexciting ( $\lambda_{\text{exc}} = 425$  nm) a solution of 0.2 mM  $[\text{Ir}(\text{dF-CF}_3\text{-ppy})_2(\text{dtbbpy})][\text{PF}_6]$ , 5 mM  $\text{NiCl}_2(\text{dme})$ , 5 mM dtbbpy, and 50 mM quinuclidine in MeCN. The Ir(II) spectrum (— blue) was obtained by spectroelectrochemistry. The quinuclidine dimer radical cation spectrum (— green) was obtained by subtracting the Ir(II) contribution from the TA spectrum at 30 ns with minimization of the first derivative of the resultant spectrum with respect to wavelength. .... 27
- Figure 2.9.** CV of a 1.0 mM solution in MeCN of the Ir(III) photocatalyst  $[\text{Ir}(\text{dF-CF}_3\text{-ppy})_2(\text{dtbbpy})][\text{PF}_6]$  taken with a 3.0 mm glassy carbon (GC) working electrode at  $\nu = 0.1$  V  $\text{s}^{-1}$ .  $E_{1/2} = -1.74$  V..... 28
- Figure 2.10.** CVs of a MeCN solution containing 12.5 mM  $\text{NiCl}_2(\text{dme})$ , 12.5 mM dtbbpy, 275 mM quinuclidine (left) in the presence of 375 mM methanol (corresponding to initial concentrations in the photoredox reaction) and (right) in the absence of methanol. The working electrode was 3.0 mm GC and the scan rate was  $\nu = 0.1$  V  $\text{s}^{-1}$ ..... 28
- Figure 2.11.** Single-wavelength kinetic traces ( $\lambda_{\text{exc}} = 425$  nm) monitored at 670 nm. (A) Kinetic trace of a solution containing 0.2 mM  $[\text{Ir}(\text{dF-CF}_3\text{-ppy})_2(\text{dtbbpy})][\text{PF}_6]$ , 5 mM (dtbbpy) $\text{NiCl}_2$ , and 100 mM 4'-bromoacetophenone with 25 mM (— grey) and 100 mM (— orange) quinuclidine. (B) Kinetic trace of a solution containing 0.2 mM  $[\text{Ir}(\text{dF-CF}_3\text{-ppy})_2(\text{dtbbpy})][\text{PF}_6]$ , 100 mM 4'-bromoacetophenone, and 50 mM quinuclidine with 2.5 mM (— grey) and 10 mM (— orange) (dtbbpy) $\text{NiCl}_2$ . Solid lines show mono-exponential fits and insets show the fitted lifetime in the presence of different concentrations of the additive under study..... 29
- Figure 2.12.** Apparatus used for *in situ* monitoring of the photochemical reaction..... 30
- Figure 2.13.** Characterization of a paramagnetic Ni intermediate. (A) Crystal structure of **1** collected at 100 K with thermal ellipsoids drawn at 50% probability and hydrogen atoms omitted for clarity. (B) Difference spectra observed from *in situ* monitoring

of the photoredox reaction solution containing 4'-bromoacetophenone, MeOH, quinuclidine, NiCl<sub>2</sub>(dme), dtbbpy, and [Ir(dF-CF<sub>3</sub>-ppy)<sub>2</sub>(dtbbpy)]PF<sub>6</sub> (top), from spectroelectrochemistry on a solution of NiCl<sub>2</sub>(dme), dtbbpy, and quinuclidine at -1.74 V vs Fc<sup>+</sup>/Fc (middle), and from the comproportionation of Ni(dtbbpy)(cod) with NiCl<sub>2</sub>(dme) in the presence of dtbbpy and quinuclidine (bottom). (C) X-band EPR spectrum collected at 77 K on a frozen MeCN solution of **1** prepared *via* comproportionation..... 31

**Figure 2.14.** Spectroelectrochemistry of a MeCN solution containing 12.5 mM NiCl<sub>2</sub>(dme), 12.5 mM dtbbpy, and 275 mM quinuclidine under a cathodic potential of -1.74 V vs Fc<sup>+</sup>/Fc showing a transition from the initial Ni(II) state (— black) to a state with spectroscopic features consistent with complex **1** (— red). ..... 32

**Figure 2.15.** Computational studies of complex **1**. (A) Simulated absorption line spectrum of **1** (blue lines, right y-axis). The line spectrum has been Gaussian-broadened to 0.2 eV at half-width half height (blue shaded, left y-axis). (B) Frontier molecular orbitals associated with the strongest low-energy transition at 732 nm. The β-HOMO (bottom) is characterized predominantly as a σ orbital between the dz<sub>2</sub> orbitals of the involved Ni atoms. The β-LUMO (top) features π\* orbitals of the dtbbpy ligands, classifying the excited state as a MLCT state. Hydrogen atoms are omitted for clarity. .... 32

**Figure 2.16.** Spectroscopic study of the comproportionation reaction performed in the presence of quinuclidine. In the absence of quinuclidine, no discernible spectrum is observed. .... 33

**Figure 2.17.** Stability of **1** towards dilution. (A) Dilution of Ni(I) in the presence of quinuclidine (— blue) and both (dtbbpy)NiCl<sub>2</sub> and quinuclidine (— red), demonstrating the decomposition of Ni(I) upon dilution in the absence of excess (dtbbpy)NiCl<sub>2</sub>. (B) Difference spectrum of the sample diluted in the presence of (dtbbpy)NiCl<sub>2</sub> and quinuclidine after air exposure shows that the characteristic spectroscopic features of **1** were retained under these conditions..... 33

**Figure 2.18.** TON for **1** increases with decreasing concentration, implicating a potential bimetallic pathway for catalyst deactivation..... 34

**Figure 2.19.** Spectroscopic studies of oxidative addition. (A) Absorption spectrum of the oxidative addition product. (B) Absorption spectrum of a 1 mM solution of

	(dtbbpy)Ni( <i>o</i> -tolyl)(Br) under similar conditions. Both spectra are background-corrected for (dtbbpy)NiCl <sub>2</sub> . .....	35
<b>Figure 2.20.</b>	DFT study demonstrating that comproportionation between a monomeric Ni(I) species and the expected Ni(III) intermediate formed after oxidative addition is highly exergonic.....	35
<b>Figure 2.21.</b>	Proposed cycle for the redox-mediated cross-coupling reaction between alcohols and aryl bromides. ....	36
<b>Figure 2.22.</b>	Energy optimization of the cross-coupling reaction. Left: power-dependence of the quantum yield for the photoredox reaction ( $\lambda_{exc} = 435$ nm). Inset shows an enlarged view of the high-power regime. Right: Current-dependence of the faradaic yield under cathodic galvanostatic electrolysis with a GC working electrode in a divided H-cell. Product yields were determined by <sup>1</sup> H NMR relative to 1,3-benzodioxole. Error bars denote SD ( $n = 3$ ).....	37
<b>Figure 3.1.</b>	Mechanisms for C-S cross-coupling. (A) Proposed mechanisms for photoredox-mediated nickel-catalyzed aryl thiolation. (B) Self-sustained mechanism driven by a redox mediator as deduced from this work.....	57
<b>Figure 3.2.</b>	Emission decay and spectra of *Ir(III). Emission decay monitored at 500 nm for samples containing 50 $\mu$ M Ir(III) in the absence and presence of 200 mM pyridine ( $\lambda_{exc} = 355$ nm). The inset shows the corresponding steady-state emission spectra while exciting at 370 nm. The overlapped emission decays and steady-state emission spectra suggest that pyridine does not quench *Ir(III). ....	60
<b>Figure 3.3.</b>	Stern-Volmer quenching of *Ir(III) by Ni(II). (A) UV-vis absorption spectra of solutions containing 50 $\mu$ M Ir(III); 50 $\mu$ M Ir(III) and 200 mM pyridine; and 50 $\mu$ M Ir(III), 200 mM pyridine with various concentrations of Ni(II). The strong absorption spectrum of Ni(II) overlaps with the absorption spectrum of Ir(III), causing a significant inner filter effect. (B) Steady-state Stern-Volmer quenching plot (black) based on the corrected quenching ratio ( $I_0/I_{corr}$ ) (see Materials and Methods), and dynamic Stern-Volmer quenching plot based on the emission lifetime $\tau$ . The dynamic quenching plot was linearly fitted to extract the quenching rate constants.....	60
<b>Figure 3.4.</b>	Stern-Volmer quenching of *Ir(III) by (A) 4-iodotoluene ( <b>1a</b> ), (B) 4-methoxybenzyl mercaptan ( <b>2</b> ) in the absence (top) and presence (bottom) of 200 mM pyridine, (C)	

pyridinium iodide and (D) tetrabutylammonium iodide. Steady-state (black) and dynamic (red) quenching plots match well, suggesting the absence of static quenching. Linear fitting was used to extract the quenching rate constants. The presence of pyridine in **B** (bottom) increases the quenching, possibly due to proton-coupled electron transfer..... 61

**Figure 3.5.** Spectroscopic studies on the reaction solution. (A) Time-resolved emission decay of the excited photocatalyst  $^*Ir(III)$  in a fresh and illuminated sample, the latter of which was subjected to 20 min blue light irradiation under standard reaction conditions (Table 3.2, top panel). The scatter plots and solid lines show the raw data and single-exponential fittings, respectively. The fitted lifetime  $\tau$  is significantly lower for an illuminated sample when compared to a fresh one. This change in  $^*Ir(III)$  lifetime is accompanied by a change in the color of the reaction solution, as shown in the inset. (B) UV-vis absorption spectra of solution **S1** (Table 3.1), **S1** with an additional 100 mM pyHI at 0 h and 18 h in the dark, and a solution containing Ni(II) with  $RS^-$  (potassium (4-methoxyphenyl)methanethiolate), the spectrum for which is normalized with that of **S1** at 500 nm. .... 62

**Figure 3.6.** Chemical and quantum yields of the aryl thiolation reaction. (A) Aryl thiolation progress for a standard reaction solution with the addition of 50 mM pyHI, exposure to air, or both. (B) Power dependence of the quantum yield for aryl thiolation between 4-methoxybenzyl mercaptan and 4-iodotoluene (**1a**) or 4'-iodoacetophenone with and without additional 50 mM pyHI ( $\lambda_{exc} = 435$  nm). Lines are included to highlight the trend. .... 64

**Figure 3.7.** Transient absorption studies on the quenching of  $^*Ir(III)$ . (A) TA spectra of a solution containing 150  $\mu M$  **Ir(III)** and 25 mM TBAI or pyHI ( $\lambda_{exc} = 430$  nm). The inset shows that the corresponding TA spectrum at 30 ns can be deconvolved into contributions from **Ir(II)** (red) and  $I_2 \cdot^-$  (blue). The delay times listed in the bottom panel also apply to the top panel. (B) The TA kinetic traces probed at 525 nm and 700 nm predominantly show the decay of **Ir(II)** and  $I_2 \cdot^-$ , respectively. The scatter plots and the solid lines show the raw data and model fittings, respectively (see Materials and Methods for details). .... 65

**Figure 3.8.** Reaction between **Ir(II)** and 1-methylpyridinium iodide. TA kinetic trace measured at 525 nm for a MeCN solution containing 150  $\mu M$  **Ir(III)** and 25 mM 1-methylpyridinium iodide. The fast decay with a time constant of  $\tau = 0.200(4)$   $\mu s$  is

due to the reaction between **Ir(II)** and 1-methylpyridinium, and the rate constant is extracted to be  $k = 2.00(4) \times 10^8 \text{ M}^{-1} \text{ s}^{-1}$  based on a single exponential fit (solid line)..... 68

**Figure 3.9.** Reaction between **Ir(II)** and pyHI. TA kinetic trace measured at 525 nm for a MeCN solution containing 150  $\mu\text{M}$  **Ir(III)**, 25 mM pyHI and 150 mM thiophenol in the absence (black plots) or presence (red plots) of 200 mM pyridine. The initial fast decays are due to the reaction between **Ir(II)** and  $\text{pyH}^+$ , for which the rate constant was extracted based on single-exponential fitting. In the absence of pyridine, the decay time is 0.35(1)  $\mu\text{s}$  corresponding to  $k_{\text{ET1}} = 1.14(3) \times 10^8 \text{ M}^{-1} \text{ s}^{-1}$ . In the presence of 200 mM pyridine, the decay time is 0.46(1)  $\mu\text{s}$  corresponding to  $k_{\text{ET1}} = 8.7(2) \times 10^7 \text{ M}^{-1} \text{ s}^{-1}$ . ..... 68

**Figure 3.10.** Formation of thiyl radical. TA spectra of MeCN solutions containing 150  $\mu\text{M}$  **Ir(III)**, 25 mM pyHI and 150 mM thiophenol in the absence (**A**) or presence (**B**) of 200 mM py ( $\lambda_{\text{exc}} = 430 \text{ nm}$ ). (**C**) The TA spectra at 6.3  $\mu\text{s}$  for solutions in **A** and **B** were aligned at 700 nm to show a difference due to the thiophenoxy radical. The inset shows the difference TA spectrum (grey), which matches the absorption spectrum of thiophenoxy radical (red) obtained independently by photo-exciting a diphenyl disulfide solution (6 mM) in MeCN at  $\lambda_{\text{exc}} = 355 \text{ nm}$ . ..... 69

**Figure 3.11.** TA kinetic trace probed at 700 nm for solution **S2** (150  $\mu\text{M}$  **Ir(III)** and 25 mM pyHI) with 150 mM thiophenol, 150 mM thiophenol in the presence of 200 mM pyridine, and 150 mM 4-methoxybenzyl mercaptan in the presence of 200 mM pyridine ( $\lambda_{\text{exc}} = 430 \text{ nm}$ ). The faster decay for solutions containing pyridine is due to PCET between  $\text{I}_2 \cdot^-$  and thiol with pyridine as a base. The scatter plots and solid lines show the raw data and model fittings, respectively (see Materials and Methods for details). The inset shows the difference TA spectrum at 6.3  $\mu\text{s}$  (grey) for solutions of **S2** with 150 mM thiophenol in the absence and presence of 200 mM pyridine; this difference spectrum matches the TA spectrum of thiophenoxy radical (red) obtained independently from directly exciting diphenyl disulfide at  $\lambda_{\text{exc}} = 355 \text{ nm}$ . ..... 70

**Figure 3.12.** TA spectra of reaction solutions with the inclusion of Ni. (**A**) TA spectra ( $\lambda_{\text{exc}} = 430 \text{ nm}$ ) of solution **S4** (150  $\mu\text{M}$  **Ir(III)**, 25 mM pyHI, 200 mM pyridine, 150 mM 4-methoxybenzyl mercaptan, and 10 mM **Ni(II)**). (**B**) The difference TA spectrum at 7.5  $\mu\text{s}$  for solution **S3** and **S4** (parent spectra shown in the inset), revealing the

presence of a putative **Ni(I)** intermediate. (C) TA kinetic trace measured at 600 nm for solution **S3** (black) and **S4** (red). The additional rising feature on the red curve suggests the formation of **Ni(I)** with a time constant of 1.56  $\mu\text{s}$ . (D) TA kinetic trace measured at 600 nm for solution **S4** with 0.1 and 0.5 M 4-iodotoluene, **1a**. The faster decay for solutions with higher concentrations of aryl iodide implies the oxidative addition of aryl iodide to the **Ni(I)**. The scatter plots and solid lines show the raw data and model fittings, respectively (see Materials and Methods for details). The inset shows the linear fit to extract the oxidative addition rate constant  $k_{\text{OA}}$  of 4-iodotoluene, **1a**..... 71

**Figure 3.13.** **Ni(I)** made from comproportionation between **Ni(0)** and **Ni(II)**. (A) The EPR spectrum (black curve) for a comproportionation solution in the presence of 200 mM py (see Materials and Methods). The simulated EPR spectrum was obtained using  $g_1 = 2.20$ ,  $g_2 = 2.15$ ,  $g_3 = 2.05$  and  $S = 1/2$ . (B) The UV-vis absorption spectrum of a comproportionation solution in the presence of 200 mM pyridine (see Materials and Methods). The spectrum of the same solution after exposure to air shows diminished absorption. (C) The UV-vis absorption spectrum of **Ni(II)** and **Ni(0)** in the presence of 200 mM pyridine (see Materials and Methods). (D) The difference spectrum of the two raw spectra shown in **B**..... 72

**Figure 3.14.** Decay of **Ir(II)** and formation of **Ni(I)** mediated by pyHI. TA kinetic traces at 525 nm for MeCN solutions containing 150  $\mu\text{M}$  **Ir(III)** and 25 mM pyHI or TBAI in the absence (A) or presence (B) of 10 mM **Ni(II)** and 200 mM py. TA kinetic traces at 600 nm for MeCN solutions containing 150  $\mu\text{M}$  **Ir(III)** and 25 mM pyHI or TBAI in the absence (C) or presence (D) of 10 mM **Ni(II)** and 200 mM py. Model fitting (black line in D) suggests a rate constant of  $k_{\text{BET2}} = 8.5(4) \times 10^9 \text{ M}^{-1} \text{ s}^{-1}$  for the back reaction between **Ni(I)** and  $\text{I}_2 \cdot^-$  (see Materials and Methods). The fitting details for the red line in D are provided in Figure 3.15. .... 74

**Figure 3.15.** Direct reduction of **Ni(II)** by **Ir(II)** in the presence of pyridine. The TA signal at 600 nm for a solution containing 150  $\mu\text{M}$  **Ir(III)**, 25 mM TBAI, 10 mM **Ni(II)** and 200 mM py was fitted with a custom model (red trace, see Materials and Methods for fitting details). The signal consists of two components including a back reaction component (blue trace) due to the reaction between **Ir(II)** and  $\text{I}_2 \cdot^-$  with a known rate constant of  $k_{\text{BET1}} = 9.4 \times 10^9 \text{ M}^{-1} \text{ s}^{-1}$ , and fitted component **Ni(I)** (dark cyan trace) showing a formation time of 41(8)  $\mu\text{s}$  with a corresponding rate constant of  $k_{\text{ET3}} = 2.5(5) \times 10^6 \text{ M}^{-1} \text{ s}^{-1}$ ..... 75

- Figure 3.16.** Direct reduction of **Ni(II)** by **Ir(III)** in the absence of pyridine. The TA signal at 600 nm for a solution containing 150  $\mu\text{M}$  **Ir(III)**, 25 mM TBAI and 10 mM **Ni(II)** was fitted with a custom model (red trace, see Materials and Methods for fitting details). The fitted formation of **Ni(I)** shows a formation time of 3.3(4)  $\mu\text{s}$  and a rate constant of  $k_{\text{ET4}} = 3.0(4) \times 10^7 \text{ M}^{-1} \text{ s}^{-1}$ . ..... 76
- Figure 3.17.** **Ni(II)** interaction with pyridine. (A) The UV-vis absorption spectra for **Ni(II)** in the absence (black curve) and presence (red curve) of 200 mM pyridine. (B) The CV for 10 mM **Ni(II)** in the absence (black curve) and presence (red curve) of 200 mM py (See Materials and Methods). The onset of reduction shifted cathodically by  $\sim 200$  mV for the solution with pyridine when compared to that without. .... 77
- Figure 3.18.** Complete reaction mechanism and key rate constants for photoredox mediated nickel-catalyzed aryl thiolation. <sup>a</sup> PCET reaction between  $\text{I}_2 \cdot^-$  and compound **2**. <sup>b</sup> PCET reaction between  $\text{I}_2 \cdot^-$  and thiophenol. <sup>c</sup> Rate was reported by ref 53. <sup>d</sup> For the reaction with 200 mM pyridine. <sup>e</sup> Oxidative addition of 4-iodotoluene.  $\text{Ni}^{\text{II}} = \text{L}_n\text{Ni}^{\text{II}}\text{X}_2$ ;  $\text{Ni}^{\text{I}} = \text{L}_n\text{Ni}^{\text{I}}\text{X}$ . ET = electron transfer; PT = proton transfer. .... 81
- Figure 3.19.** Blue-light-driven photoredox setups. (A) Reactions running in 20-mL glass vials were excited with a Kessil lamp (A160WE). (B) Reactions running in J. Young NMR tubes were excited with a blue LED strip light arranged in a cylindrical configuration. .... 84
- Figure 4.1.** Strategies for carbon-heteroatom cross-coupling: (A) traditional thermal catalysis, ligand-controlled reactivity; (B) redox catalysis, oxidation state-controlled reactivity; (C) this work, light-free access to photoredox-like oxidation state-controlled reactivity. .... 101
- Figure 4.2.** Mechanisms invoked in photoredox Ni-catalyzed cross-coupling: (A) energy transfer-mediated catalysis; (B) oxidation state modulation; (C) thermally-sustained Ni(I/III) cycle. PC = photocatalyst. EnT = energy transfer. ET = electron transfer. .... 102
- Figure 4.3.** Effects of nickel source on yields for the three cross-coupling reactions. Yields were determined by  $^{19}\text{F}$  NMR for amination and  $^1\text{H}$  NMR for etherification and esterification. COD = 1,5-cyclooctadiene. .... 108



<b>Figure 4.4.</b>	Absorption spectrum of a MeCN solution containing 12.5 mM (dtbbpy)NiCl <sub>2</sub> and 250 mM quinuclidine (— green, left axis), 12.5 mM (dtbbpy)NiCl <sub>2</sub> and 250 mM quinuclidine stirred with Zn(0) (— blue, left axis), and the difference spectrum between the two samples (— orange, right axis). Note the peaks <i>circa</i> 670 and 840 nm corresponding to the Ni(I)-Ni(II) dimer in the difference spectrum. ....	108
<b>Figure 4.5.</b>	Reaction yield as a function of nickel loading. Catalyst loading was calculated with respect to aryl bromide. Error bars denote SD ( <i>n</i> = 3). ....	109
<b>Figure 4.6.</b>	Demonstration of the generality of light-free reactivity. [a] DABCO used as the base. [b] Quinuclidine used as the base and DMSO used as the solvent. [c] Quinuclidine used as the base. [d] DBU used as the base. [e] MTBD used as the base. [f] See Materials and Methods for details. [g] Reaction performed at 40 °C. [h] Reaction performed at 60 °C. <i>Boc</i> = <i>tert</i> -butyloxycarbonyl.....	110
<b>Figure 4.7.</b>	<sup>1</sup> H NMR spectrum of (1).....	134
<b>Figure 4.8.</b>	<sup>13</sup> C NMR spectrum of (1).....	134
<b>Figure 4.9.</b>	<sup>19</sup> F NMR spectrum of (1). ....	135
<b>Figure 4.10.</b>	<sup>1</sup> H NMR spectrum of (2).....	135
<b>Figure 4.11.</b>	<sup>13</sup> C NMR spectrum of (2).....	136
<b>Figure 4.12.</b>	<sup>19</sup> F NMR spectrum of (2). ....	136
<b>Figure 4.13.</b>	<sup>1</sup> H NMR spectrum of (3).....	137
<b>Figure 4.14.</b>	<sup>13</sup> C NMR spectrum of (3).....	137
<b>Figure 4.15.</b>	<sup>19</sup> F NMR spectrum of (3). ....	138
<b>Figure 4.16.</b>	<sup>1</sup> H NMR spectrum of (4). ....	138
<b>Figure 4.17.</b>	<sup>13</sup> C NMR spectrum of (4).....	139
<b>Figure 4.18.</b>	<sup>19</sup> F NMR spectrum of (4). ....	139
<b>Figure 4.19.</b>	<sup>1</sup> H NMR spectrum of (5). ....	140
<b>Figure 4.20.</b>	<sup>13</sup> C NMR spectrum of (5).....	140

<b>Figure 4.21.</b>	$^{19}\text{F}$ NMR spectrum of (5).	141
<b>Figure 4.22.</b>	$^1\text{H}$ NMR spectrum of (6).	141
<b>Figure 4.23.</b>	$^{13}\text{C}$ NMR spectrum of (6).	142
<b>Figure 4.24.</b>	$^{19}\text{F}$ NMR spectrum of (6).	142
<b>Figure 4.25.</b>	$^1\text{H}$ NMR spectrum of (7).	143
<b>Figure 4.26.</b>	$^{13}\text{C}$ NMR spectrum of (7).	143
<b>Figure 4.27.</b>	$^{19}\text{F}$ NMR spectrum of (7).	144
<b>Figure 4.28.</b>	$^1\text{H}$ NMR spectrum of (8).	144
<b>Figure 4.29.</b>	$^{13}\text{C}$ NMR spectrum of (8).	145
<b>Figure 4.30.</b>	$^{19}\text{F}$ NMR spectrum of (8).	145
<b>Figure 4.31.</b>	$^1\text{H}$ NMR spectrum of (9).	146
<b>Figure 4.32.</b>	$^{13}\text{C}$ NMR spectrum of (9).	146
<b>Figure 4.33.</b>	$^{19}\text{F}$ NMR spectrum of (9).	147
<b>Figure 4.34.</b>	$^1\text{H}$ NMR spectrum of (10).	147
<b>Figure 4.35.</b>	$^{13}\text{C}$ NMR spectrum of (10).	148
<b>Figure 4.36.</b>	$^{19}\text{F}$ NMR spectrum of (10).	148
<b>Figure 4.37.</b>	$^1\text{H}$ NMR spectrum of (11).	149
<b>Figure 4.38.</b>	$^{13}\text{C}$ NMR spectrum of (11).	149
<b>Figure 4.39.</b>	$^1\text{H}$ NMR spectrum of (12).	150
<b>Figure 4.40.</b>	$^{13}\text{C}$ NMR spectrum of (12).	150
<b>Figure 4.41.</b>	$^1\text{H}$ NMR spectrum of (13).	151
<b>Figure 4.42.</b>	$^{13}\text{C}$ NMR spectrum of (13).	151

<b>Figure 4.43.</b>	$^1\text{H}$ NMR spectrum of (14).	152
<b>Figure 4.44.</b>	$^{13}\text{C}$ NMR spectrum of (14).	152
<b>Figure 4.45.</b>	$^1\text{H}$ NMR spectrum of (15).	153
<b>Figure 4.46.</b>	$^{13}\text{C}$ NMR spectrum of (15).	153
<b>Figure 4.47.</b>	$^1\text{H}$ NMR spectrum of (16).	154
<b>Figure 4.48.</b>	$^{13}\text{C}$ NMR spectrum of (16).	154
<b>Figure 4.49.</b>	$^1\text{H}$ NMR spectrum of (17).	155
<b>Figure 4.50.</b>	$^{13}\text{C}$ NMR spectrum of (17).	155
<b>Figure 4.51.</b>	$^1\text{H}$ NMR spectrum of (18).	156
<b>Figure 4.52.</b>	$^{13}\text{C}$ NMR spectrum of (18).	156
<b>Figure 4.53.</b>	$^1\text{H}$ NMR spectrum of (19).	157
<b>Figure 4.54.</b>	$^{13}\text{C}$ NMR spectrum of (19).	157
<b>Figure 4.55.</b>	$^1\text{H}$ NMR spectrum of (20).	158
<b>Figure 4.56.</b>	$^{13}\text{C}$ NMR spectrum of (20).	158
<b>Figure 4.57.</b>	$^{19}\text{F}$ NMR spectrum of (20).	159
<b>Figure 4.58.</b>	$^1\text{H}$ NMR spectrum of (21).	159
<b>Figure 4.59.</b>	$^{13}\text{C}$ NMR spectrum of (21).	160
<b>Figure 4.60.</b>	$^1\text{H}$ NMR spectrum of (22).	160
<b>Figure 4.61.</b>	$^{13}\text{C}$ NMR spectrum of (22).	161
<b>Figure 4.62.</b>	$^{19}\text{F}$ NMR spectrum of (22).	161
<b>Figure 4.63.</b>	$^1\text{H}$ NMR spectrum of (23).	162
<b>Figure 4.64.</b>	$^{13}\text{C}$ NMR spectrum of (23).	162

<b>Figure 4.65.</b>	$^1\text{H}$ NMR spectrum of (24).	163
<b>Figure 4.66.</b>	$^{13}\text{C}$ NMR spectrum of (24).	163
<b>Figure 4.67.</b>	$^1\text{H}$ NMR spectrum of (25).	164
<b>Figure 4.68.</b>	$^{13}\text{C}$ NMR spectrum of (25).	164
<b>Figure 4.69.</b>	$^1\text{H}$ NMR spectrum of (26).	165
<b>Figure 4.70.</b>	$^{13}\text{C}$ NMR spectrum of (26).	165
<b>Figure 4.71.</b>	$^1\text{H}$ NMR spectrum of (27).	166
<b>Figure 4.72.</b>	$^{13}\text{C}$ NMR spectrum of (27).	166
<b>Figure 4.73.</b>	$^1\text{H}$ NMR spectrum of (28).	167
<b>Figure 4.74.</b>	$^{13}\text{C}$ NMR spectrum of (28).	167
<b>Figure 4.75.</b>	$^1\text{H}$ NMR spectrum of (29).	168
<b>Figure 4.76.</b>	$^{13}\text{C}$ NMR spectrum of (29).	168
<b>Figure 4.77.</b>	$^1\text{H}$ NMR spectrum of (30).	169
<b>Figure 4.78.</b>	$^{13}\text{C}$ NMR spectrum of (30).	169
<b>Figure 4.79.</b>	$^1\text{H}$ NMR spectrum of (31).	170
<b>Figure 4.80.</b>	$^{13}\text{C}$ NMR spectrum of (31).	170
<b>Figure 4.81.</b>	$^1\text{H}$ NMR spectrum of (32).	171
<b>Figure 4.82.</b>	$^{13}\text{C}$ NMR spectrum of (32).	171
<b>Figure 4.83.</b>	$^1\text{H}$ NMR spectrum of (33).	172
<b>Figure 4.84.</b>	$^{13}\text{C}$ NMR spectrum of (33).	172
<b>Figure 4.85.</b>	$^1\text{H}$ NMR spectrum of (34).	173
<b>Figure 4.86.</b>	$^{13}\text{C}$ NMR spectrum of (34).	173

<b>Figure 4.87.</b>	$^1\text{H}$ NMR spectrum of (35). .....	174
<b>Figure 4.88.</b>	$^{13}\text{C}$ NMR spectrum of (35). .....	174
<b>Figure 4.89.</b>	$^1\text{H}$ NMR spectrum of (36). .....	175
<b>Figure 4.90.</b>	$^{13}\text{C}$ NMR spectrum of (36). .....	175
<b>Figure 4.91.</b>	$^{19}\text{F}$ NMR spectrum of (36). .....	176
<b>Figure 4.92.</b>	$^1\text{H}$ NMR spectrum of (37). .....	176
<b>Figure 4.93.</b>	$^{13}\text{C}$ NMR spectrum of (37). .....	177
<b>Figure 4.94.</b>	$^1\text{H}$ NMR spectrum of (38). .....	177
<b>Figure 4.95.</b>	$^{13}\text{C}$ NMR spectrum of (38). .....	178
<b>Figure 4.96.</b>	$^1\text{H}$ NMR spectrum of (39). .....	178
<b>Figure 4.97.</b>	$^{13}\text{C}$ NMR spectrum of (39). .....	179
<b>Figure 4.98.</b>	$^1\text{H}$ NMR spectrum of (40). .....	179
<b>Figure 4.99.</b>	$^{13}\text{C}$ NMR spectrum of (40). .....	180
<b>Figure 5.1.</b>	Photoredox intramolecular hydroamidation reaction promoted by bidirectional and unidirectional PCET. The bidirectional PCET occurs by an outer-sphere electron transfer to a photoexcited acceptor (PC*) followed by proton transfer to an exogenous base. Unidirectional PCET occurs when the photoredox reagent, $\text{PC}_\beta^*$ , is the electron and proton acceptor such as the triplet excited state of ketones (this work). .....	190
<b>Figure 5.2.</b>	TA spectra of DCM solutions containing CQ (5 mM) and amide substrates (10 mM) in DCM. <b>A:</b> for a solution of CQ alone. <b>B:</b> for a solution of CQ with amide 5 as the substrate. <b>C:</b> for a solution of CQ with amide 1 as the substrate. $\lambda_{\text{exc}} = 460 \text{ nm}$ . .....	191
<b>Figure 5.3.</b>	Electrochemical studies on CQ. <b>(A)</b> Cyclic voltammogram of 2 mM CQ in DCM with 0.1 M [TBA][PF <sub>6</sub> ] as the supporting electrolyte. <b>(B)</b> Spectroelectrochemistry on 2 mM CQ in DCM with 0.1 M [TBA][PF <sub>6</sub> ] as the supporting electrolyte in a 0.5 mm pathlength cell using a Pt mesh working electrode. ....	192

<b>Figure 5.4.</b>	Kinetic trace monitored at 430 nm of a DCM solution containing 5 mM CQ, and 10 mM amide substrate <b>5</b> in the presence (— blue) and absence (— black) of 2 mM [NBu <sub>4</sub> ][OP(O)(OBu) <sub>2</sub> ] as base. Insets show a magnified view at shorter timescales along with extracted rate constants. $\lambda_{\text{exc}} = 460$ nm. ....	192
<b>Figure 5.5.</b>	Mechanisms of amidyl radical generation. <b>Left:</b> A square scheme illustrating the possible pathways for PCET. <b>Right:</b> Stern-Volmer plot for the quenching of CQ (1 mM) by acetanilide (— black) and <i>N</i> -methylacetanilide (— red) in DCM. ....	194
<b>Figure 5.6.</b>	Stern-Volmer plots for different quenchers reacting with 1 mM CQ in DCM. $\lambda_{\text{exc}} = 450$ nm. ....	196
<b>Figure 5.7.</b>	TA spectra of a DCM solution containing CQ (10 mM) and phenol (20 mM) showing the evolution from an initial spectrum dominated by *CQ (— orange trace) to one dominated by PhO· (— blue trace). $\lambda_{\text{exc}} = 460$ nm. ....	197
<b>Figure 5.8.</b>	Time traces for the yield of cyclized product <b>4</b> (dashed lines) and % remaining of CQ (solid lines). Black traces are for the reaction performed with PhSSPh and red traces are with (TRIPS) <sub>2</sub> . The conditions for the reactions were as described in the Materials and Methods section. ....	199
<b>Figure 5.9.</b>	Photoredox intramolecular cycloamidation using various ketones as the photocatalyst. Yields as determined by <sup>1</sup> H NMR spectroscopy are denoted in parentheses. *For ketones which absorbed poorly in the visible region, a 370 nm LED light source (Kessil) was used in place of the standard blue LEDs. ....	200
<b>Figure 5.10.</b>	Scope of the CQ-mediated intramolecular alkene hydroamidation reaction. <sup>a</sup> PhSSPh used as the disulfide. <sup>b</sup> (TripS) <sub>2</sub> used as the disulfide. Yields determined by <sup>1</sup> H NMR spectroscopy using 1,4-bis(trifluoromethyl)benzene or 1,3,5-tris(trifluoromethyl)benzene as an internal standard. ....	201
<b>Figure 6.1.</b>	Structures of various tetrapyrrolic macrocycles. ....	210
<b>Figure 6.2.</b>	Corrole and its derivatives in various states of hydrogenation. ....	211
<b>Figure 6.3.</b>	Synthetic scheme for the preparation of metallated TDCs. ....	213
<b>Figure 6.4.</b>	Refined routes to <i>p</i> Tol-DHDP-Me ( <b>1</b> ). The prior route is shown in blue, the new route in red. ....	213

- Figure 6.5.** Crystal structure of  $[\text{Ni-TDC}]^+$  with hydrogen atoms, counter-ion, and solvent molecules omitted for clarity..... 214
- Figure 6.6.** UV-vis spectra of  $[\text{Co-TDC}]^+$  as the acetate salt in MeCN before (— blue) and after (— red) treatment with excess  $\text{KO}_2$  and 18-crown-6. No appreciable spectroscopic changes were observed in the sample treated with 18-crown-6 and  $\text{KO}_2$  upon air exposure. .... 215
- Figure 6.7.** CVs of  $[\text{Co-TDC}]^+$  (A) and  $[\text{Ni-TDC}]^+$  (B) using a glassy carbon working electrode in MeCN with 0.1 M  $n\text{-Bu}_4\text{NPF}_6$  as the supporting electrolyte.  $\nu = 0.1$  V/s.  $E_{1/2}[\text{Co(II/I)}] = -0.46$  V,  $E_{1/2}[\text{Co(I/O)}] = -1.56$  V.  $E_{1/2}[\text{Ni(II/I)}] = -0.70$  V,  $E_{1/2}[\text{Ni(I/O)}] = -1.43$  V.... 216
- Figure 6.8.** EPR spectrum of  $[\text{Ni-TDC}]$  collected at 3 K. Simulated with an isotropic signal at  $g = 2.02$ ..... 216
- Figure 6.9.** Reductive spectroelectrochemistry of  $[\text{M-TDC}]^+$  complexes in MeCN containing 0.1 M  $n\text{-Bu}_4\text{NPF}_6$ . (A) UV-vis-NIR spectra of  $[\text{Co-TDC}]^+$  showing the cationic (— black), singly reduced (— blue,  $E_{\text{appl}} = -0.7$  V), and doubly reduced (— red,  $E_{\text{appl}} = -1.7$  V) redox states. (B) UV-vis-NIR spectra of  $[\text{Ni-TDC}]^+$  showing the cationic (— black), singly reduced (— blue,  $E_{\text{appl}} = -1.0$  V), and doubly reduced (— red,  $E_{\text{appl}} = -1.7$  V) redox states. .... 217
- Figure 6.10.** CVs of 1 mM  $[\text{Ni-TDC}]^+$  in the presence of acid using a glassy carbon working electrode in MeCN with 0.1 M  $n\text{-Bu}_4\text{NPF}_6$  as the supporting electrolyte.  $\nu = 0.1$  V/s. (A) With added benzoic acid (BzOH). (B) with added trifluoroacetic acid (TFA). 218
- Figure 6.11.** Chemical reduction of  $[\text{Ni-TDC}]^+$  with  $\text{LiBH}_4$ . (A) Initial spectrum of  $[\text{Ni-TDC}]^+$  (— orange), immediately after addition of excess  $\text{LiBH}_4$  (— blue), 10 min after addition of  $\text{LiBH}_4$  (— red). (B) Treatment of the  $\text{LiBH}_4$ -derived intermediate with excess trifluoroacetic acid (TFA) showing the initial (— blue) and final (— green) spectra. .... 219
- Figure 6.12.** HRMS (ESI, positive mode) of the putative  $[\text{Ni-TDC-H}]$  intermediate after treatment with TFA. The peak at 715.3330 is consistent with the formation of  $[\text{Ni-TDC-H}_2]^+$ . .... 219
- Figure 6.13.** Reductive spectroelectrochemistry of 1mM  $[\text{Ni-TDC}]^+$  in MeCN containing 0.1 M  $n\text{-Bu}_4\text{NPF}_6$  (— orange) and final spectra under an applied potential ( $E_{\text{appl}}$ ) of (A)  $-1.5$  V

	with excess benzoic acid (BzOH) (— blue) and (B) -0.8 V with excess trifluoroacetic acid (TFA) (— green).....	220
<b>Figure 6.14.</b>	Reductive spectroelectrochemistry of 1 mM [Ni-TDC] <sup>+</sup> with excess BzOH in MeCN containing 0.1 M <i>n</i> -Bu <sub>4</sub> PF <sub>6</sub> showing the initial (— orange) and final (— blue) spectra under an applied potential of -0.8 V vs Fc <sup>+</sup> /Fc. ....	220
<b>Figure 6.15.</b>	A mechanism for the chemical reduction of [Ni-TDC] <sup>+</sup> by LiBH <sub>4</sub> and subsequent reaction with acid. Note that only one of the possible isomers is shown for [Ni-TDC-H] and [Ni-TDC-H <sub>2</sub> ] <sup>+</sup> . ....	221
<b>Figure 6.16.</b>	Comparison of crystallographic and computed structure of [Ni-TDC] <sup>+</sup> . Crystal structure is cropped to be more directly comparable to the calculated structure. Hydrogen atoms are omitted for clarity.....	223
<b>Figure 6.17.</b>	Frontier orbitals and relative energies of [Ni-TDC] <sup>+</sup> . ....	224
<b>Figure 6.18.</b>	Frontier orbital evolution along the reduction series of [Ni-TDC] <sup>+</sup> . Energies are not to scale. ....	224
<b>Figure 6.19.</b>	TA spectra and dynamic traces of Ni-TDC compounds in THF. The TA spectral evolution and dynamic traces are shown for [Ni-TDC] <sup>+</sup> (A and B), [Ni-TDC] (C and D), and [Ni-TDC] <sup>-</sup> (E and F). λ <sub>exc</sub> = 400 nm. ....	226
<b>Figure 6.20.</b>	Ultrafast TA spectral evolution for [Ni-TDC] <sup>+</sup> (A), [Ni-TDC] (B) and [Ni-TDC] <sup>-</sup> (C). ....	228
<b>Figure 6.21.</b>	<sup>1</sup> H NMR spectrum of [Ni-TDC] <sup>+</sup> taken in CDCl <sub>3</sub> . ....	235
<b>Figure 7.1.</b>	Reduction of tetrapyrrole macrocyclic rings to produce phlorins. ....	245
<b>Figure 7.2.</b>	UV-vis characterization of chlorinphlorin. (A) Thin-layer UV-vis spectroelectrochemistry in a N <sub>2</sub> -filled glovebox on a solution of 15 mM <i>meso</i> -tetraphenylchlorin and 100 mM benzoic acid in CD <sub>2</sub> Cl <sub>2</sub> with <i>n</i> -Bu <sub>4</sub> NPF <sub>6</sub> (0.1 M) as an electrolyte under an applied potential of -1.78 V vs Fc <sup>+</sup> /Fc. The black and red traces show the initial and final spectra, respectively. (B) UV-vis spectrum of the isolated <i>meso</i> -tetraphenylchlorinphlorin product from chemical reduction in DCM. ....	246



<b>Figure 7.3.</b>	Crystal structure of the synthesized chlorinphlorin. A hydrogen-bonded pyridine molecule and all non-oxidizable hydrogen atoms bound to carbon have been omitted for clarity. Thermal ellipsoids are drawn at 50% probability.....	247
<b>Figure 7.4.</b>	Crystal structure with the difference-Fourier map (green) used to locate hydrogen atoms bound to pyrrolic nitrogen atoms. ....	250
<b>Figure 7.5.</b>	$^1\text{H}$ NMR (400 MHz, $\text{CD}_2\text{Cl}_2$ ) of <i>meso</i> -tetraphenylchlorinphlorin.....	250
<b>Figure 7.6.</b>	$^{13}\text{C}$ NMR (101 MHz, $\text{CD}_2\text{Cl}_2$ ) of <i>meso</i> -tetraphenylchlorinphlorin.....	251

## List of Tables

<b>Table 2.1.</b>	Quantum and faradaic yields.....	37
<b>Table 2.2.</b>	Crystal data for the quinuclidine-bound (dtbbpy)NiCl <sub>2</sub> dimer. ....	49
<b>Table 2.3.</b>	Crystal data for 1.....	50
<b>Table 3.1.</b>	Composition of key solutions used in kinetics studies. ....	58
<b>Table 3.2.</b>	Photoredox mediated nickel-catalyzed aryl thiolation and Stern-Volmer quenching studies.....	59
<b>Table 3.3.</b>	Optimization for the cross-coupling between thiol and aryl bromide. ....	78
<b>Table 3.4.</b>	Photoredox mediated nickel-catalyzed aryl thiolation using aryl bromide. Top panel shows the reaction used in photochemical kinetics studies with the bromo analogue of <b>1a</b> ; bottom panel shows generalization to a range of substrates. ....	79
<b>Table 4.1.</b>	Optimization of light-free amination.....	104
<b>Table 4.2.</b>	Optimization of light-free etherification.....	105
<b>Table 4.3.</b>	Optimization of light-free esterification. ....	106
<b>Table 4.4.</b>	Summary of control reactions without Ni or Zn.....	116
<b>Table 5.1.</b>	Correlation of the quenching rate ( $k_q$ ) of *CQ in DCM with different thermodynamic parameters of the quenchers.....	195
<b>Table 5.2.</b>	Optimization of the CQ-mediated intramolecular cycloamidation of alkenes...	198
<b>Table 6.1.</b>	Fitting parameters for TA kinetic traces. ....	227
<b>Table 6.2.</b>	Crystal data and structure refinement for [Ni-TDC] <sup>+</sup> .....	234
<b>Table 7.1.</b>	Crystal data and structure refinement for <i>meso</i> -tetraphenylchlorinphlorin. ....	249

## Acknowledgements

This dissertation is the culmination of many different experiences over the past few years: days spent fumbling in the lab, long hours of frustration mulling over obstinately inexplicable data punctuated by rare and precious moments of insight, and, most importantly, all the encouragement, advice, and help from the many people whom I have had the privilege of knowing. Foremost among these people is my advisor, Dan Nocera. I thank Dan for his mentorship, support, and faith in me — for trusting me with the independence to pursue my own ideas while still offering invaluable guidance and encouragement whenever I needed him. He has been instrumental in my development as a scientist, and I could not have asked for a better mentor. I would also like to thank the members of my committee, Prof. Eric Jacobsen and Prof. Ted Betley. Their advice and insights during GAC meetings have greatly helped to give me direction in my research projects. Additionally, I am grateful for having had the opportunity to attend their lectures in CHEM 105 and CHEM 155. The fundamentals I learned in those classes have helped me throughout my time as a graduate student. Thank you as well to my undergraduate mentors: Prof. Jeremy Rawson, Prof. Tomislav Friščić, and Prof. Bruce Arndtsen. I would not have made it this far into graduate school if not for the experience that I gained from working in their labs.

I am deeply indebted to my colleagues and friends in the Nocera Group. I would like to thank Yangzhong Qin for being my most valuable mentor (apart from Dan) and helping to shape many of the projects that we worked on. He set an example with his meticulous experimental habits. His consistent optimism and encouragement were also very appreciated during those times when we were ostensibly making very little progress in our research. Another one of my postdoctoral collaborators, Mengran Liu, helped to introduce me to the colorful world of porphyrin chemistry. I would not have had the opportunity to participate in the work described in Chapters 6 and of 7 this dissertation were it not for her. I also wish to thank my first officemate, Serge Rucolo, for his help during my first year of graduate school. Additionally, I am grateful for having had the chance to work with some wonderful undergraduate students: Nathaniel Hibbert, Shelby Elder, and all the members of CHEM 145. Their infectious enthusiasm was a

source of inspiration for me during the past few years. I also wish to thank Dilek Dogutan, Lindsay Shepard, and Hannah Kelley for keeping the lab running; Matt Nava, Miguel Gonzalez, and Adam Rieth for their insights and suggestions during my group meetings; Qilei Zhu and Zhifei Yan for many interesting and fruitful conversations — we now have a huge backlog of '10-minute ideas' to test out; Nick Ayoub, Dan Loh, and Tom Keane for all those interesting and random discussions we had in my office that kept me up to date on various aspects of popular culture; and all the other members of the Nocera Group that I have had the pleasure of knowing for making the lab such a wonderful and fun place to work.

Among the staff in CCB, I would like to especially thank Shao-Liang Zheng for his help with crystallography — it was truly a humbling experience every time I saw him solving and refining a crystal structure that I had thought was hopeless. I am also grateful for all the help Dongtao Cui, Tony Lowe, Shaw Huang, and Bill Collins have provided with NMR and EPR experiments. The instruments in the Laukien-Purcell Instrumentation Center were the ones that I relied on the most outside of those in the Nocera Group, and much of the work I did would not have been possible were it not for the aforementioned people.

Outside of CCB, I wish to thank all my friends from the Cronkhite Graduate Center who made my life outside of lab much more memorable. I will miss all the fun and eclectic conversations we had over dinner in the dining hall. I also wish to thank Ryan Chown for his steadfast friendship. He has been one of the first people to whom I turned to for advice ever since high school, and I hope we remain close friends for years to come. Thank you as well to my parents, who always believed in me even when I doubted myself, for their unconditional support.

Lastly, I wish to thank Shinan Wang for her friendship; for giving me something to look forward to on weekends; for introducing me to Doraemon; for making the tough times less difficult and the happy ones more meaningful; for being a constant source of happiness and motivation. I am truly grateful to have found someone so wonderful, interesting, and unique.

*Page intentionally left blank*

# Chapter 1

## Introduction

## 1.1 Principles of Photoredox Catalysis

Photochemistry involves light absorption and utilization as an energetic impetus to drive chemical transformations. The photochemical paradigm lies at the heart of many biological processes,<sup>1-3</sup> photodynamic therapy,<sup>4-6</sup> astrochemistry<sup>7</sup> and solar energy conversion,<sup>8-10</sup> which stores light in chemical products that are endergonic to ground state reactant. In all of these processes, the photo-excited state of a light-absorbing molecule (chromophore) undergoes an intramolecular reaction (e.g., isomerization or fragmentation) or is quenched via an intermolecular reaction with a substrate. This quenching typically occurs by either electron transfer (ET) or energy transfer (EnT), where the former leads to reduction or oxidation of the substrate and the latter leads to promotion of the substrate into an electronically excited state (Figure 1.1). In both cases, the substrate is activated towards further reactions through the quenching process.

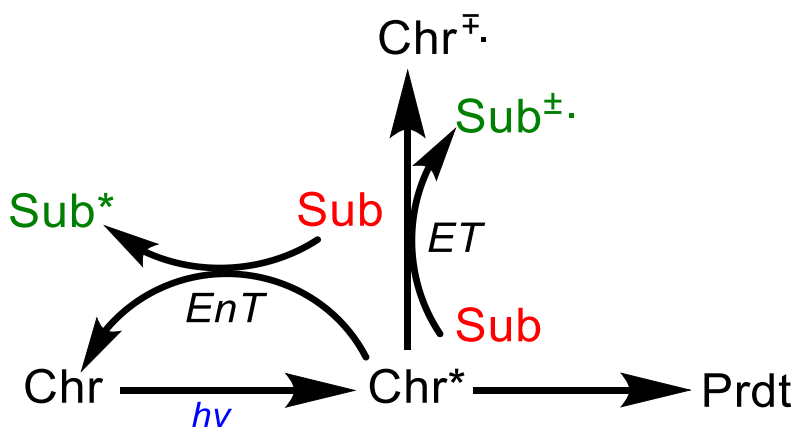


**Figure 1.1.** Simplified diagram illustrating the possible productive pathways in a photochemical reaction. Chr = chromophore. Sub = substrate. Prdt = product.

With the emergence of photoredox chemistry, photochemistry has also been placed at the forefront of methodology development in organic chemistry.<sup>11</sup> In these reactions, a photocatalyst [typically a cyclometallated complex of Ir(III) or Ru(II)] serves as the chromophore. In the excited state, these compounds then interact with substrates through the quenching processes described above, allowing for selective access to reaction intermediates and pathways that typically are

inaccessible under thermal conditions.<sup>12-15</sup> This powerful strategy has led to the development of numerous reactions for the hydrofunctionalization of alkenes, cycloadditions, C-H functionalization, and cross-coupling reactions, among many others.<sup>16-21</sup>

The general mechanism for an idealized photoredox reaction based on quenching of the photocatalyst through ET is shown in Figure 1.2. The photocatalyst (**PC**) first absorbs a photon and enters the excited state (Step I), **\*PC**, which can then undergo nonproductive relaxation (Step II) or engage in a productive ET reaction with substrate (**Sub**) to form **PC<sup>±•</sup>** and **Sub<sup>±•</sup>** (Step III). Since the direct redox reaction between **PC** and **Sub** is endergonic in the ground state, **PC<sup>±•</sup>** and **Sub<sup>±•</sup>** can engage in an exergonic but non-productive back electron transfer (BET) reaction to reform **PC** and **Sub** (Step IV). Alternatively, **Sub<sup>±•</sup>** can undergo subsequent chemical steps to form a product radical (Step V), **Prdt<sup>±•</sup>**, which reacts with **PC<sup>±•</sup>** to form the final product molecule and regenerate the photocatalyst (Step VI). The redox processes between **PC** and **Sub** can also be facilitated by redox mediators in many cases.

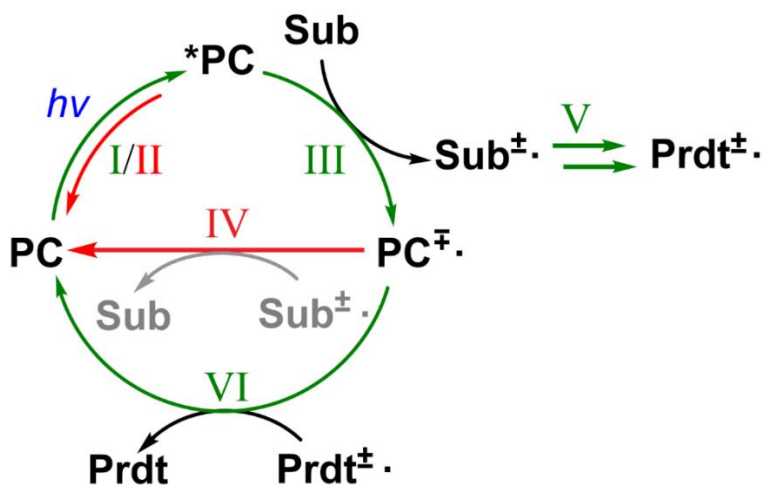


**Figure 1.2.** Scheme showing the general mechanism for an idealized ET-based photoredox reaction. The green arrows indicate productive pathways and red arrows indicate nonproductive pathways.

## 1.2 Metallaphotoredox Ni-Catalyzed Cross-Coupling Reactions

Cross-coupling reactions, where selective bond formation is achieved between a nucleophile and carbon-based electrophile by means of a transition metal catalyst, constitute one



of the most synthetically important classes of reactions in medicinal chemistry.<sup>22-25</sup> Although these methods have traditionally relied on Pd-based catalysts, the development of sustainable base metal alternatives is a highly active area of research.<sup>26-29</sup> In particular, Ni, the first-row congener of Pd, has emerged at the forefront of this search of new metal catalysts. Despite being more sustainable, the replacement of Pd with Ni leads to significant differences in catalyst reactivity. In comparison to Pd, oxidative addition is typically more facile and reductive elimination more difficult for Ni complexes.<sup>30</sup> This is especially pertinent to carbon-heteroatom cross-coupling reactions, where the reductive elimination at Ni(II) is, in many cases, endothermic.<sup>31-34</sup> Although the development of elaborate and specialized ligands has led to Ni catalysts capable of thermal carbon-heteroatom cross-coupling reactions,<sup>35-37</sup> an alternative approach relies on the application of photoredox catalysis to facilitate Ni cross-coupling. In this metallaphotoredox strategy, a photocatalyst is introduced to the reaction that is proposed to generate open-shell Ni-species, such as Ni(III) complexes, *in situ* upon illumination.<sup>12, 31</sup> These open-shell species are more amenable towards reductive elimination compared to ground-state Ni(II) complexes, thereby effecting carbon-heteroatom cross-coupling under mild conditions. Through this approach, the etherification,<sup>32</sup> amination,<sup>38</sup> sulfonamidation,<sup>39</sup> thiolation,<sup>40</sup> and esterification<sup>41</sup> of aryl halides have all been realized under mild conditions with Ni catalysis (Figure 1.3).

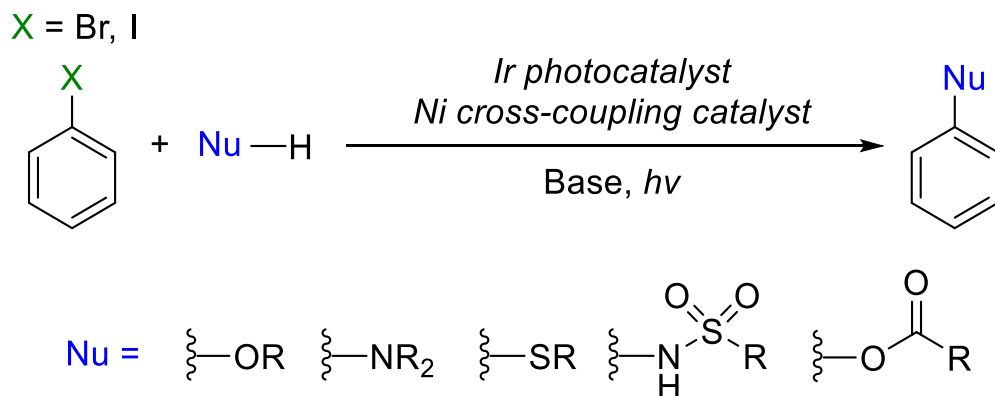


**Figure 1.3.** Overview of the cross-coupling reactions that have been realized under dual Ir/Ni photoredox catalysis.

The general mechanisms for a thermal cross-coupling reaction and the proposed mechanism for a metallaphotoredox cross-coupling reaction are shown in Figure 1.4A and 1.4B, respectively. Under thermal conditions, oxidative addition of an electrophile, such as an aryl halide ( $\text{Ar-X}$ ), occurs on the Ni center,  $\text{Ni}^n$ . Next, a transmetalation or ligand substitution occurs, whereby the  $\text{X}$  leaving group is exchanged for a nucleophile,  $\text{Nu}$ . Finally, the cycle is closed by reductive elimination of the cross-coupled product with concomitant regeneration of the  $\text{Ni}^n$  catalyst. Conversely, in a metallaphotoredox reaction, the Ni complex formed after transmetalation is intercepted by an excited state photocatalyst,  $^*\text{PC}$ , and is thereby oxidized. After reductive elimination from this high-valent intermediate, the resulting metal species is then reduced by the reduced photocatalyst,  $\text{PC}^{\cdot-}$ , to turn over the cycle and regenerate the photocatalyst. A key feature of these proposed mechanisms is the necessity of photon absorption for every turnover of the cycle, thus limiting the quantum yield ( $\Phi = \text{mols product/mols photons absorbed}$ ) to a theoretical maximum of  $\Phi \leq 1$ .

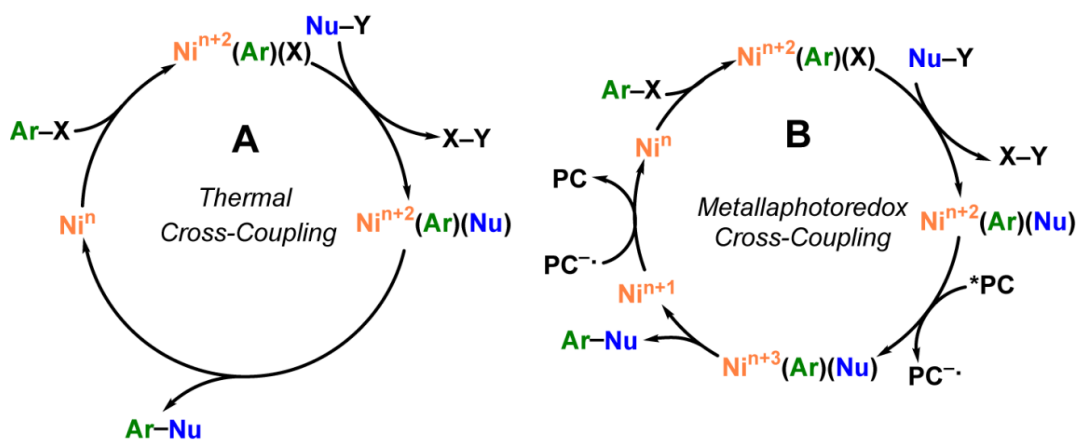


**Figure 1.4.** Idealized mechanism for thermal cross-coupling (A) and proposed mechanism for metallaphotoredox cross-coupling (B).

### 1.3 Mechanistic Uncertainty in Photoredox Reactions

Despite the impressive breadth of chemical transformations that can be realized under photoredox conditions, the highly energetic excited states of the photocatalysts lead to a multitude of potential reaction pathways with short-lived reaction intermediates that are

intractable by traditional methods, thereby obfuscating the operative reaction mechanisms in many cases. This difficulty of mechanistic elucidation is especially pronounced in metallaphotoredox systems, where the introduction of a transition metal catalyst, which can exist in multiple oxidation states and coordination environments, adds further complexity. This is exacerbated by the fact that the majority of metallaphotoredox methods to date use first row transition metals, such as Ni or Cu,<sup>17, 38-39, 42-48</sup> which tend to have labile ligands and undergo both one- and two-electron chemistry with ease. The challenge of elucidating metallaphotoredox mechanisms is exemplified by the Ni-catalyzed, photoredox-mediated, cross-coupling between aryl iodides and thiols,<sup>40</sup> for which three distinct mechanisms have been proposed involving different oxidation states of the Ni catalyst and Ir photocatalyst, with two of these putative mechanisms having been investigated in-depth computationally.<sup>49</sup> As shown in Chapter 3 of this dissertation, none of these three proposed mechanisms is likely to be the dominant pathway for product formation.

As a consequence of the ostensible mechanistic intractability in many photoredox systems, reaction optimization (and even development)<sup>50-53</sup> is often done quasi-randomly through a labor-intensive sampling of reaction space with extensive screening of multiple parameters; hypotheses for why a certain set of conditions are most efficient are then given *post hoc*. Although such an approach has resulted in numerous reactions with high chemical yields, it is fundamentally limited by the throughput of the screening process and the chemical intuition of the researcher in choosing which conditions to test in the absence of mechanistic insight that would allow for a more rational process. Moreover, the assumption of an erroneous reaction mechanism can even mislead reaction optimization by diverting attention away from critical reaction parameters. In this regard, dark cycles (i.e., productive self-sustained pathways which do not require a photon for turnover) in photoredox reactions have profound implications for optimization; their existence not only implies that the necessity for high-energy photons and precious metal photocatalysts can be entirely obviated but dictates whether emphasis during reaction optimization should be placed on photophysical properties and electron transfer pathways or on propagating these dark processes. Seminal work by Yoon and coworkers has

confirmed self-sustained reactivity in the photoredox Diels-Alder cycloaddition, [2+2] cycloaddition of enones, and  $\alpha$ -aldehyde alkylation (Figure 1.5).<sup>54</sup> This conclusion was reached primarily through quantum yield ( $\Phi$ ) measurements, where values of  $\Phi \gg 1$  have been obtained for the aforementioned reactions.<sup>54</sup> However, the extent to which such self-sustained processes contribute to other photoredox systems, and specifically metallaphotoredox cross-coupling reactions, was not known at the onset of our studies.

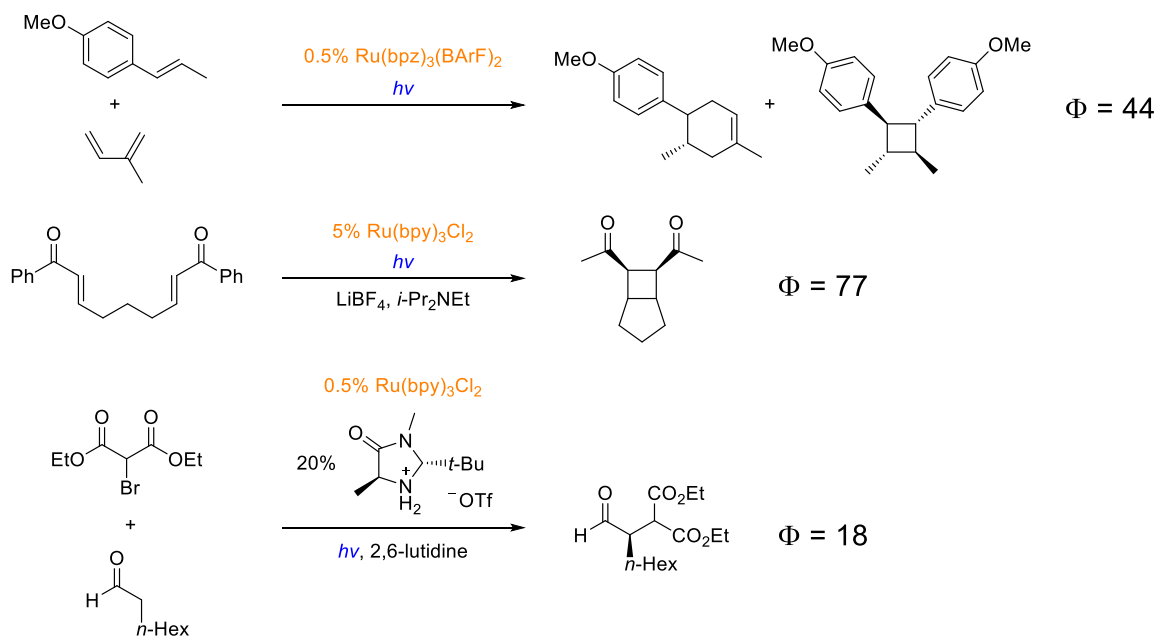


**Figure 1.5.** Examples of photoredox reactions which operate through 'dark' mechanisms with their respective quantum yields ( $\Phi$ ).<sup>54</sup>

#### 1.4 Tetrapyrrole Compounds and Their Redox Chemistry

In biological systems, the energetic impetus for redox transformations is typically provided by adenosine triphosphate (ATP) rather than light. Many of the enzymes that catalyze redox reactions require tetrapyrrole complexes as cofactors. The tetrapyrrole motif, which refers to macrocyclic molecules featuring pyrroles bridged by methine carbons, is ubiquitous in biological systems. The prototypical tetrapyrrole, porphyrin, and its hydrogenated derivatives (Figure 1.6), chlorin and bacteriochlorin, are essential components in biological processes such as photosynthesis, oxygen transport, and biosynthetic enzymes.<sup>55-58</sup> Corrin, a ring-contracted

congener of porphyrin, is the core macrocycle in vitamin B<sub>12</sub>.<sup>59</sup> In addition to their critical biological functions, synthetic tetrapyrroles and their metallated derivatives have found applications in catalysis, medicine, information storage, and energy conversion.<sup>4, 60-67</sup> Many of these applications rely on the exceptional redox non-innocence of the tetrapyrrole ligand, which is capable of accommodating multiple electrons and holes in its  $\pi$ -manifold.<sup>68-70</sup> However, this redox-innocence also leads to ligand-centered reactivity and resulting functionalization of the tetrapyrrole, with the products often having properties distinct from those of the parent macrocycles. For instance, ring hydrogenation of Co and Ni porphyrins to form phlorins and isobacteriochlorins has been implicated under conditions for hydrogen evolution reaction (HER) catalysis.<sup>71-73</sup> Ligand non-innocence has also been proposed to play a crucial role in the electrochemical reduction of CO<sub>2</sub> to CO in aqueous solvent catalyzed by an Fe porphyrin.<sup>74</sup> Furthermore, in the application of porphyrins and chlorins as photodynamic therapy agents, photobleaching, whereby the porphyrins undergo photoinduced modifications or decomposition leading to loss of absorption, has been proposed to be primarily due to redox reactions undergone by the macrocycle.<sup>75</sup> Thus, an understanding of the redox reactivity of tetrapyrroles is critical as it constitutes a ubiquitous reaction paradigm with this widely-used class of molecules.

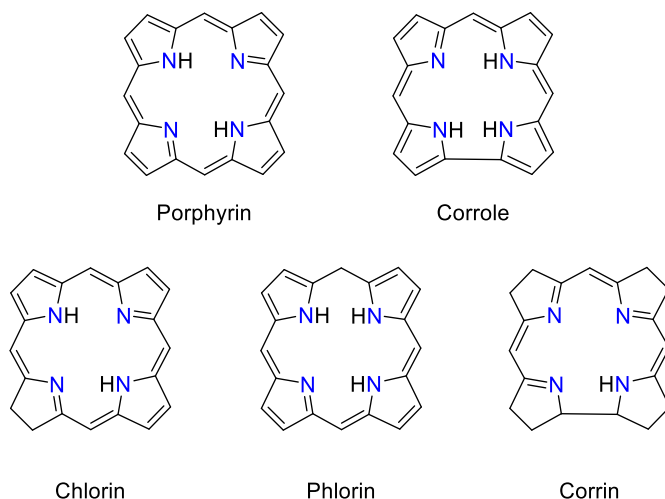


**Figure 1.6.** Porphyrin and corrole (top), along with some of their hydrogenated derivatives (bottom).

## 1.5 Summaries of Chapters

Chapters 2 through 5 describe detailed mechanistic studies of several photoredox reactions, leading to their optimization for energy efficiency or the development of light-free analogues. Chapter 2 describes a mechanistic investigation and optimization of a redox-mediated aryl etherification cross-coupling reaction (Figure 1.7). A reaction cycle for Ni-catalyzed aryl etherification is proposed under both photoredox and electrochemically-mediated conditions. We demonstrate that a self-sustained Ni(I/III) cycle is operative in both cases by chemically synthesizing and characterizing a common paramagnetic Ni intermediate and establishing its catalytic activity. Furthermore, deleterious pathways leading to off-cycle Ni(II) species have been identified, allowing us to discover optimized conditions for achieving self-sustained reactivity at a ~15-fold increase in the quantum yield and a ~3-fold increase in the faradaic yield. These results highlight the importance of leveraging insight of complete reaction cycles for increasing the efficiency of redox-mediated reactions.

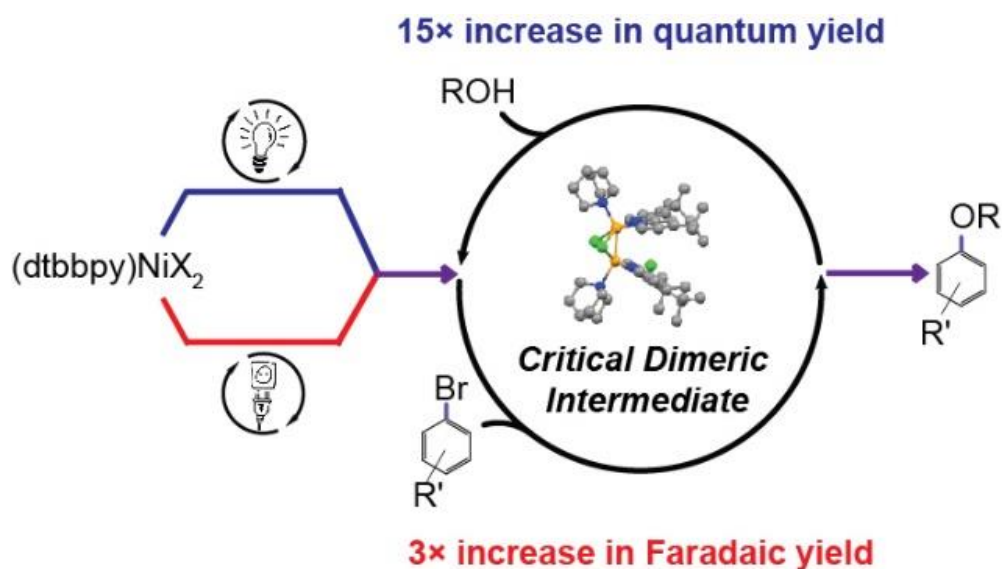


**Figure 1.7.** Summary of Chapter 2 showing the elucidated mechanism for redox-mediated cross-coupling between alcohols and aryl bromides, along with the identification of an *in situ* generated dimeric Ni(I)-Ni(II) intermediate.

Chapter 3 describes the mechanism and optimization of an aryl thiolation cross-coupling reaction (Figure 1.8). Photoredox-mediated nickel-catalyzed cross-couplings have evolved as a

new effective strategy to forge carbon-heteroatom bonds that are difficult to access with traditional methods. Experimental mechanistic studies are challenging because these reactions involve multiple highly reactive intermediates and perplexing reaction pathways, engendering competing, but unverified, proposals for substrate conversions. We report a comprehensive mechanistic study of photoredox nickel-catalyzed C-S cross-coupling based on time-resolved transient absorption spectroscopy, Stern-Volmer quenching, and quantum yield measurements. We have (i) discovered a self-sustained productive Ni(I/III) cycle leading to a quantum yield  $\Phi > 1$ ; (ii) found that pyridinium iodide, formed *in situ*, serves as the dominant quencher for the excited state photocatalyst and a critical redox mediator to facilitate the formation of the active Ni(I) catalyst; and (iii) observed critical intermediates and determined the rate constants associated with their reactivity. Not only do the findings reveal a complete reaction cycle for C-S cross-coupling, but the mechanistic insights have also allowed for the reaction efficiency to be optimized and the substrate scope to be expanded from aryl iodides to include aryl bromides, thus broadening the applicability of photoredox C-S cross-coupling chemistry.

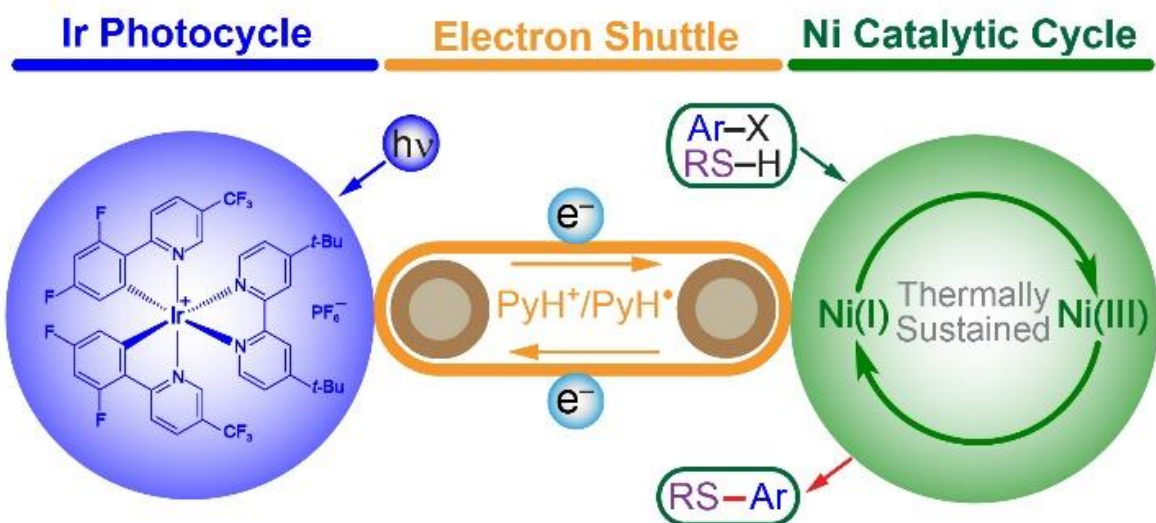


**Figure 1.8.** Summary of Chapter 3 highlighting the critical role of pyridinium as a redox shuttle, as well as the operative Ni(I/III) dark cycle responsible for C-S cross-coupling reactivity.

Chapter 4 presents our development of light-free protocols for cross-coupling based on mechanistic studies in Chapters 2 and 3 (Figure 1.9). We establish self-sustained Ni(I/III) cycles

as a potentially general paradigm in photoredox Ni-catalyzed carbon-heteroatom cross-coupling reactions by presenting a strategy that allows us to recapitulate photoredox-like reactivity in the absence of light across a wide range of substrates in the amination, etherification, and esterification of aryl bromides, the latter of which has remained, hitherto, elusive under thermal Ni catalysis. Moreover, the accessibility of esterification in the absence of light is especially notable since previous mechanistic studies on this transformation under photoredox conditions have unanimously invoked energy transfer-mediated pathways.

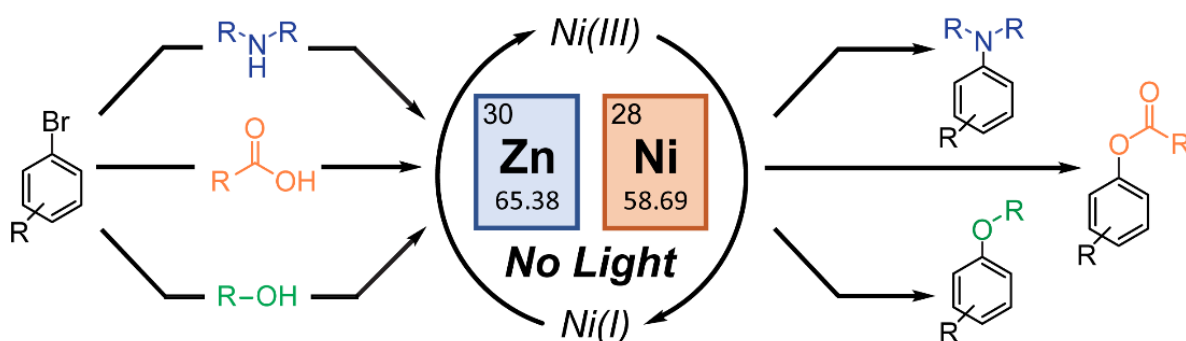


**Figure 1.9.** Summary of Chapter 4 demonstrating the amination, esterification, and etherification of aryl bromides under light-free conditions using a combination of Ni cross-coupling catalyst activated by a substoichiometric amount of Zn metal as a reductant.

Chapter 5 reports the surprising discovery that the selective abstraction of hydrogen atoms from strong amide N-H bonds in the presence of weaker C-H bonds through proton-coupled electron transfer (PCET), which was previously accomplished using a combination of Ir photocatalyst and base,<sup>76</sup> could be effected using the triplet excited state of ketones (Figure 1.10). This was demonstrated by showing that the intramolecular anti-Markovnikov hydroamidation of alkenes could be achieved under blue LED illumination using a diketone, camphorquinone (CQ), in the absence of base. Mechanistic studies suggest that this selectivity results from a concerted asynchronous PCET from <sup>\*</sup>CQ, with the quenching rate for the excited state being primarily dictated by the ionization energy (and hence, redox potential) of the substrate. These results show that hydroamidation can be achieved using a non-toxic and inexpensive homogeneous organo-photocatalyst in place of the Ir-based photocatalysts previously employed.



✓ **Base-free**    ✓ **Non-toxic**  
 ✓ **Inexpensive**   ✓ **Biocompatible**

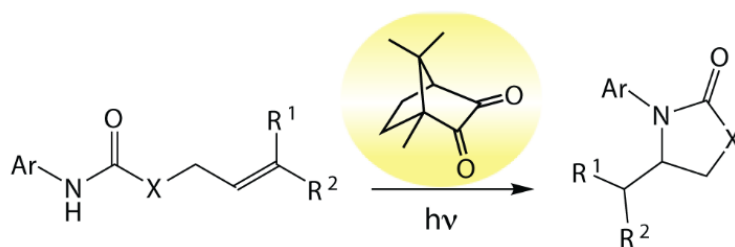


**Figure 1.10.** Summary of Chapter 5 showing that intramolecular cycloamidation of an alkene can be effected using a simple diketone photocatalyst through selective N-H bond activation.

Chapters 6 and 7 are dedicated to investigating the redox properties of two underexplored tetrapyrrole macrocycles. Chapter 6 presents the preparation and characterization of metallated derivatives of a monoanionic tetrapyrrole: *B,C*-tetrahydrocorrin (TDC, Figure 1.11). TDC resides chemically between corroles and corrins. This chemical space remains largely unexplored due to a lack of reliable synthetic strategies. We report the preparation and characterization of Co(II)- and Ni(II)-metallated TDC derivatives ( $[\text{Co-TDC}]^+$  and  $[\text{Ni-TDC}]^+$ , respectively) with a combination of crystallographic, electrochemical, computational, and spectroscopic techniques.  $[\text{Ni-TDC}]^+$  was found to undergo primarily ligand-centered electrochemical reduction, leading to hydrogenation of the macrocycle under cathodic electrolysis in the presence of acid. Transient absorption (TA) spectroscopy reveals that  $[\text{Ni-TDC}]^+$  and the two-electron-reduced  $[\text{Ni-TDC}]^-$  possess long-lived excited states whereas the excited state of singly reduced  $[\text{Ni-TDC}]$  exhibits picosecond dynamics. The Co(I) compound,  $[\text{Co-TDC}]$ , is air stable, highlighting the notable property of the TDC ligand in stabilizing low-valent metal centers in contradistinction to other tetrapyrroles such as corroles, which are distinguished by their ability to stabilize metals in higher oxidation states.

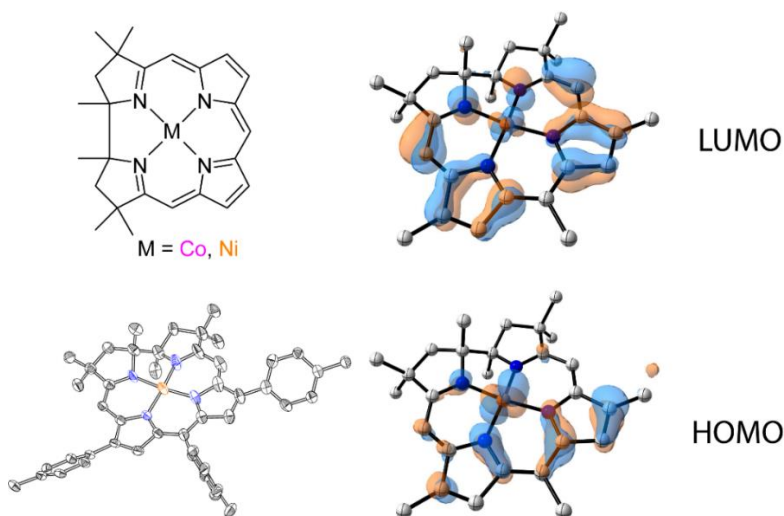


**Figure 1.11.** Summary of Chapter 6 showing the structure of the tetradehydrocorrins (TDC) core (top left), the crystal structure of Ni-TDC (bottom left), and the calculated frontier orbitals of Ni-TDC that highlight the ligand involvement (right).

Chapter 7 describes the synthesis and structural characterization of a chlorinphlorin (Figure 1.12). Redox non-innocence of pyrrole macrocycles allows for their hydrogenation by proton-coupled electron transfer (PCET). The initial reduction of porphyrins by PCET occurs at a bridging methine carbon, yielding a phlorin. In macrocyclic cores that are reduced beyond porphyrins, the phlorin is unusual. The chlorinphlorin is an especially rare compound and consequently its formation and chemistry have eluded characterization. We report the chemical preparation of a chlorinphlorin including its X-ray crystal structure, which is distinguished by a tetrahedral geometry about the methine carbon of the macrocycle, resulting in the formal reduction of an olefin bond.

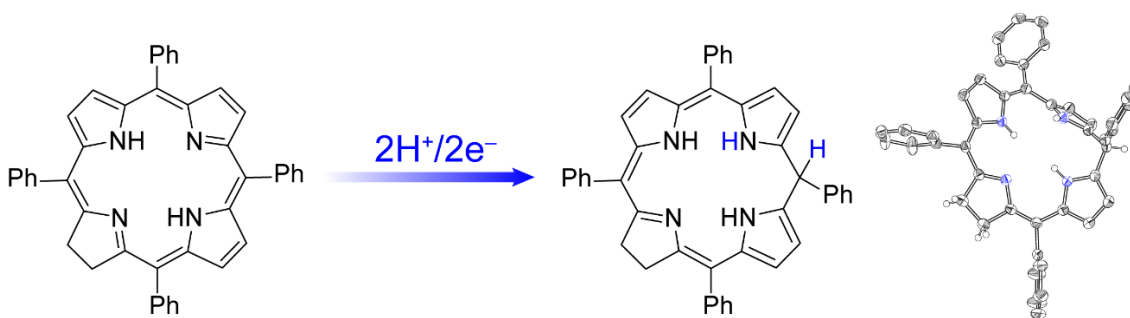


**Figure 1.12.** Summary of Chapter 7 showing the proton-coupled electron transfer (PCET) reduction of a chlorin to form a chlorinphlorin, along with the crystal structure of the latter.

## 1.6 References

1. McEvoy, J. P.; Brudvig, G. W., Water-Splitting Chemistry of Photosystem II. *Chem. Rev.* **2006**, *106*, 4455-4483.
2. Tremezaygues, L. E. A.; Sticherling, M.; Pföhler, C.; Friedrich, M.; Meineke, V.; Seifert, M.; Tilgen, W.; Reichrath, J., Cutaneous Photosynthesis of Vitamin D: An Evolutionary Highly-Conserved Endocrine System that Protects against Environmental Hazards Including UV-radiation and Microbial Infections. *Anticancer Res.* **2006**, *26*, 2743.
3. Kandori, H., Retinal Proteins: Photochemistry and Optogenetics. *Bull. Chem. Soc. Jpn.* **2019**, *93*, 76-85.
4. Dolmans, D. E. J. G. J.; Fukumura, D.; Jain, R. K., Photodynamic Therapy for Cancer. *Nat. Rev. Cancer* **2003**, *3*, 380-387.
5. Gunaydin, G.; Gedik, M. E.; Ayan, S., Photodynamic Therapy for the Treatment and Diagnosis of Cancer—A Review of the Current Clinical Status. *Front. Chem.* **2021**, *9*, 608.
6. Moore, C. M.; Pendse, D.; Emberton, M., Photodynamic Therapy for Prostate Cancer—A Review of Current Status and Future Promise. *Nat. Clin. Pract. Urol.* **2009**, *6*, 18-30.
7. Öberg, K. I., Photochemistry and Astrochemistry: Photochemical Pathways to Interstellar Complex Organic Molecules. *Chem. Rev.* **2016**, *116*, 9631-9663.
8. Nocera, D. G., The Artificial Leaf. *Acc. Chem. Res.* **2012**, *45*, 767-776.
9. He, J.; Janáky, C., Recent Advances in Solar-Driven Carbon Dioxide Conversion: Expectations versus Reality. *ACS Energy Lett.* **2020**, *5*, 1996-2014.
10. Chen, Y.; Jia, G.; Hu, Y.; Fan, G.; Tsang, Y. H.; Li, Z.; Zou, Z., Two-Dimensional Nanomaterials for Photocatalytic CO<sub>2</sub> Reduction to Solar Fuels. *Sustain. Energy Fuels* **2017**, *1*, 1875-1898.
11. Romero, N. A.; Nicewicz, D. A., Organic Photoredox Catalysis. *Chem. Rev.* **2016**, *116*, 10075-10166.
12. Chan, A. Y.; Perry, I. B.; Bissonnette, N. B.; Buksh, B. F.; Edwards, G. A.; Frye, L. I.; Garry, O. L.; Lavagnino, M. N.; Li, B. X.; Liang, Y.; Mao, E.; Millet, A.; Oakley, J. V.; Reed, N. L.; Sakai, H. A.; Seath, C. P.; MacMillan, D. W. C., Metallaphotoredox: The Merger of Photoredox and Transition Metal Catalysis. *Chem. Rev.* **2021**.
13. Kwon, K.; Simons, R. T.; Nandakumar, M.; Roizen, J. L., Strategies to Generate Nitrogen-Centered Radicals That May Rely on Photoredox Catalysis: Development in Reaction Methodology and Applications in Organic Synthesis. *Chem. Rev.* **2021**.
14. Pitre, S. P.; Overman, L. E., Strategic Use of Visible-Light Photoredox Catalysis in Natural Product Synthesis. *Chem. Rev.* **2021**.
15. Zhou, Q.-Q.; Zou, Y.-Q.; Lu, L.-Q.; Xiao, W.-J., Visible-Light-Induced Organic Photochemical Reactions through Energy-Transfer Pathways. *Angew. Chem. Int. Ed.* **2019**, *58*, 1586-1604.
16. Prier, C. K.; Rankic, D. A.; MacMillan, D. W. C., Visible Light Photoredox Catalysis with Transition Metal Complexes: Applications in Organic Synthesis. *Chem. Rev.* **2013**, *113*, 5322-5363.

17. Ackerman, L. K. G.; Alvarado, J. I. M.; Doyle, A. G., Direct C-C Bond Formation from Alkanes Using Ni-Photoredox Catalysis. *J. Am. Chem. Soc.* **2018**, *140*, 14059-14063.
18. Lim, C.-H.; Kudisch, M.; Liu, B.; Miyake, G. M., C-N Cross-Coupling via Photoexcitation of Nickel–Amine Complexes. *J. Am. Chem. Soc.* **2018**, *140*, 7667-7673.
19. Lu, J.; Pattengale, B.; Liu, Q.; Yang, S.; Shi, W.; Li, S.; Huang, J.; Zhang, J., Donor–Acceptor Fluorophores for Energy-Transfer-Mediated Photocatalysis. *J. Am. Chem. Soc.* **2018**, *140*, 13719-13725.
20. Murray, P. R. D.; Bussink, W. M. M.; Davies, G. H. M.; van der Mei, F. W.; Antropow, A. H.; Edwards, J. T.; D’Agostino, L. A.; Ellis, J. M.; Hamann, L. G.; Romanov-Michailidis, F.; Knowles, R. R., Intermolecular Crossed [2 + 2] Cycloaddition Promoted by Visible-Light Triplet Photosensitization: Expedient Access to Polysubstituted 2-Oxaspiro[3.3]heptanes. *J. Am. Chem. Soc.* **2021**, *143*, 4055-4063.
21. Amador, A. G.; Scholz, S. O.; Skubi, K. L.; Yoon, T. P., *Science of Synthesis: Photocatalysis in Organic Synthesis*. Thieme Chemistry: 2018; Vol. 1, p 467.
22. Brown, D. G.; Boström, J., Analysis of Past and Present Synthetic Methodologies on Medicinal Chemistry: Where Have All the New Reactions Gone? *J. Med. Chem.* **2016**, *59*, 4443-4458.
23. Campeau, L.-C.; Hazari, N., Cross-Coupling and Related Reactions: Connecting Past Success to the Development of New Reactions for the Future. *Organometallics* **2019**, *38*, 3-35.
24. Gildner, P. G.; Colacot, T. J., Reactions of the 21st Century: Two Decades of Innovative Catalyst Design for Palladium-Catalyzed Cross-Couplings. *Organometallics* **2015**, *34*, 5497-5508.
25. Ruiz-Castillo, P.; Buchwald, S. L., Applications of Palladium-Catalyzed C-N Cross-Coupling Reactions. *Chem. Rev.* **2016**, *116*, 12564-12649.
26. Han, F.-S., Transition-Metal-Catalyzed Suzuki–Miyaura Cross-Coupling Reactions: A Remarkable Advance from Palladium to Nickel Catalysts. *Chem. Soc. Rev.* **2013**, *42*, 5270-5298.
27. Lee, C.-C.; Ke, W.-C.; Chan, K.-T.; Lai, C.-L.; Hu, C.-H.; Lee, H. M., Nickel(II) Complexes of Bidentate N-Heterocyclic Carbene/Phosphine Ligands: Efficient Catalysts for Suzuki Coupling of Aryl Chlorides. *Chem. Eur. J.* **2007**, *13*, 582-591.
28. Gurung, S. K.; Thapa, S.; Kafle, A.; Dickie, D. A.; Giri, R., Copper-Catalyzed Suzuki–Miyaura Coupling of Arylboronate Esters: Transmetalation with (PN)CuF and Identification of Intermediates. *Org. Lett.* **2014**, *16*, 1264-1267.
29. Mesganaw, T.; Garg, N. K., Ni- and Fe-Catalyzed Cross-Coupling Reactions of Phenol Derivatives. *Org. Process Res. Dev.* **2013**, *17*, 29-39.
30. Tasker, S. Z.; Standley, E. A.; Jamison, T. F., Recent Advances in Homogeneous Nickel Catalysis. *Nature* **2014**, *509*, 299.
31. Zhu, C.; Yue, H.; Jia, J.; Rueping, M., Nickel-Catalyzed C-Heteroatom Cross-Coupling Reactions under Mild Conditions via Facilitated Reductive Elimination. *Angew. Chem. Int. Ed.* **2021**, *60*, 17810-17831.

32. Terrett, J. A.; Cuthbertson, J. D.; Shurtleff, V. W.; MacMillan, D. W. C., Switching on Elusive Organometallic Mechanisms with Photoredox Catalysis. *Nature* **2015**, *524*, 330-334.
33. Shields, B. J.; Kudisch, B.; Scholes, G. D.; Doyle, A. G., Long-Lived Charge-Transfer States of Nickel(II) Aryl Halide Complexes Facilitate Bimolecular Photoinduced Electron Transfer. *J. Am. Chem. Soc.* **2018**, *140*, 3035-3039.
34. Han, R.; Hillhouse, G. L., Carbon–Oxygen Reductive-Elimination from Nickel(II) Oxametallacycles and Factors that Control Formation of Ether, Aldehyde, Alcohol, or Ester Products. *J. Am. Chem. Soc.* **1997**, *119*, 8135-8136.
35. Tassone, J. P.; England, E. V.; MacQueen, P. M.; Ferguson, M. J.; Stradiotto, M., PhPAd-DalPhos: Ligand-Enabled, Nickel-Catalyzed Cross-Coupling of (Hetero)aryl Electrophiles with Bulky Primary Alkylamines. *Angew. Chem. Int. Ed.* **2019**, *58*, 2485-2489.
36. Clark, J. S. K.; Ferguson, M. J.; McDonald, R.; Stradiotto, M., PAd2-DalPhos Enables the Nickel-Catalyzed C–N Cross-Coupling of Primary Heteroaryl amines and (Hetero)aryl Chlorides. *Angew. Chem. Int. Ed.* **2019**, *58*, 6391-6395.
37. MacQueen, P. M.; Tassone, J. P.; Diaz, C.; Stradiotto, M., Exploiting Ancillary Ligation To Enable Nickel-Catalyzed C–O Cross-Couplings of Aryl Electrophiles with Aliphatic Alcohols. *J. Am. Chem. Soc.* **2018**, *140*, 5023-5027.
38. Corcoran, E. B.; Pirnot, M. T.; Lin, S. S.; Dreher, S. D.; DiRocco, D. A.; Davies, I. W.; Buchwald, S. L.; MacMillan, D. W. C., Aryl Amination Using Ligand-Free Ni(II) Salts and Photoredox Catalysis. *Science* **2016**, *353*, 279-283.
39. Kim, T.; McCarver, S. J.; Lee, C.; MacMillan, D. W. C., Sulfonamidation of Aryl and Heteroaryl Halides through Photosensitized Nickel Catalysis. *Angew. Chem. Int. Ed.* **2018**, *57*, 3488-3492.
40. Oderinde, M. S.; Frenette, M.; Robbins, D. W.; Aquila, B.; Johannes, J. W., Photoredox Mediated Nickel Catalyzed Cross-Coupling of Thiols with Aryl and Heteroaryl Iodides via Thiyl Radicals. *J. Am. Chem. Soc.* **2016**, *138*, 1760-1763.
41. Welin, E. R.; Le, C.; Arias-Rotondo, D. M.; McCusker, J. K.; MacMillan, D. W. C., Photosensitized, Energy Transfer-Mediated Organometallic Catalysis through Electronically Excited Nickel(II). *Science* **2017**, *355*, 380-385.
42. Terrett, J. A.; Cuthbertson, J. D.; Shurtleff, V. W.; MacMillan, D. W. C., Switching on elusive organometallic mechanisms with photoredox catalysis. *Nature* **2015**, *524*, 330-334.
43. Kariofillis, S. K.; Shields, B. J.; Tekle-Smith, M. A.; Zacuto, M. J.; Doyle, A. G., Nickel/Photoredox-Catalyzed Methylation of (Hetero)aryl Chlorides Using Trimethyl Orthoformate as a Methyl Radical Source. *J. Am. Chem. Soc.* **2020**, *142*, 7683-7689.
44. Barzanò, G.; Mao, R.; Garreau, M.; Waser, J.; Hu, X., Tandem Photoredox and Copper-Catalyzed Decarboxylative C(sp<sup>3</sup>)-N Coupling of Anilines and Imines Using an Organic Photocatalyst. *Org. Lett.* **2020**, *22*, 5412-5416.
45. Hossain, A.; Bhattacharyya, A.; Reiser, O., Copper's Rapid Ascent in Visible-Light Photoredox Catalysis. *Science* **2019**, *364*, eaav9713.

46. McLean, E. B.; Lee, A.-L., Dual Copper- and Photoredox-Catalysed Reactions. *Tetrahedron* **2018**, *74*, 4881-4902.
47. Tao, C.; Wang, B.; Sun, L.; Liu, Z.; Zhai, Y.; Zhang, X.; Wang, J., Merging Visible-Light Photoredox and Copper Catalysis in Catalytic Aerobic Oxidation of Amines to Nitriles. *Org. Biomol. Chem.* **2017**, *15*, 328-332.
48. McLean, E. B.; Gauchot, V.; Brunen, S.; Burns, D. J.; Lee, A.-L., Dual copper- and Photoredox-Catalysed C(sp<sup>2</sup>)-C(sp<sup>3</sup>) coupling. *Chem. Commun.* **2019**, *55*, 4238-4241.
49. Ren, H.; Li, G.-F.; Zhu, B.; Lv, X.-D.; Yao, L.-S.; Wang, X.-L.; Su, Z.-M.; Guan, W., How Does Iridium(III) Photocatalyst Regulate Nickel(II) Catalyst in Metallaphotoredox-Catalyzed C-S Cross-Coupling? Theoretical and Experimental Insights. *ACS Catal.* **2019**, *9*, 3858-3865.
50. McNally, A.; Prier Christopher, K.; MacMillan David, W. C., Discovery of an  $\alpha$ -Amino C - H Arylation Reaction Using the Strategy of Accelerated Serendipity. *Science* **2011**, *334*, 1114-1117.
51. Strieth-Kalthoff, F.; Henkel, C.; Teders, M.; Kahnt, A.; Knolle, W.; Gómez-Suárez, A.; Dirian, K.; Alex, W.; Bergander, K.; Daniliuc, C. G.; Abel, B.; Guldi, D. M.; Glorius, F., Discovery of Unforeseen Energy-Transfer-Based Transformations Using a Combined Screening Approach. *Chem* **2019**, *5*, 2183-2194.
52. Hopkinson, M. N.; Gómez-Suárez, A.; Teders, M.; Sahoo, B.; Glorius, F., Accelerated Discovery in Photocatalysis Using a Mechanism-Based Screening Method. *Angew. Chem. Int. Ed.* **2016**, *55*, 4361-4366.
53. Teders, M.; Gómez-Suárez, A.; Pitzer, L.; Hopkinson, M. N.; Glorius, F., Diverse Visible-Light-Promoted Functionalizations of Benzotriazoles Inspired by Mechanism-Based Luminescence Screening. *Angew. Chem. Int. Ed.* **2017**, *56*, 902-906.
54. Cismesia, M. A.; Yoon, T. P., Characterizing Chain Processes in Visible Light Photoredox Catalysis. *Chem. Sci.* **2015**, *6*, 5426-5434.
55. Frydman, R. B.; Frydman, B.; Valasinas, A., 1 - Protoporphyrin: Synthesis and Biosynthesis of Its Metabolic Intermediates. In *The Porphyrins*, Dolphin, D., Ed. Academic Press: 1979; pp 1-123.
56. Ragsdale, S. W., 67 - Biochemistry of Methyl-CoM Reductase and Coenzyme F<sub>430</sub>. In *The Porphyrin Handbook*, Kadish, K. M.; Smith, K. M.; Guillard, R., Eds. Academic Press: Amsterdam, 2003; pp 205-228.
57. Eyck, L. F. T., 10 - Hemoglobin and Myoglobin. In *The Porphyrins*, Dolphin, D., Ed. Academic Press: 1979; pp 445-472.
58. Fenna, R. E.; Matthews, B. W., 11 - Bacteriochlorophyll-Proteins from Green Photosynthetic Bacteria. In *The Porphyrins*, Dolphin, D., Ed. Academic Press: 1979; pp 473-494.
59. Burnham, B. F.; Plane, R. A., Studies on the Biosynthesis of the Corrin Ring of Vitamin B<sub>12</sub>. *Biochem. J* **1966**, *98*, 13C-15C.
60. Costa e Silva, R.; Oliveira da Silva, L.; de Andrade Bartolomeu, A.; Brocksom, T. J.; de Oliveira, K. T., Recent Applications of Porphyrins as Photocatalysts in Organic Synthesis: Batch and Continuous Flow Approaches. *Beilstein J. Org. Chem.* **2020**, *16*, 917-955.

61. Barona-Castaño, J. C.; Carmona-Vargas, C. C.; Brocksom, T. J.; De Oliveira, K. T., Porphyrins as Catalysts in Scalable Organic Reactions. *Molecules* **2016**, *21*.
62. Teo, R. D.; Hwang, J. Y.; Termini, J.; Gross, Z.; Gray, H. B., Fighting Cancer with Corroles. *Chem. Rev.* **2017**, *117*, 2711-2729.
63. Imran, M.; Ramzan, M.; Qureshi, A. K.; Khan, M. A.; Tariq, M., Emerging Applications of Porphyrins and Metalloporphyrins in Biomedicine and Diagnostic Magnetic Resonance Imaging. *Biosensors* **2018**, *8*.
64. Longevial, J-F.; Clément, S.; Wytko, J. A.; Ruppert, R.; Weiss, J.; Richeter, S., Peripherally Metalated Porphyrins with Applications in Catalysis, Molecular Electronics and Biomedicine. *Chem. Eur. J.* **2018**, *24*, 15442-15460.
65. Jurow, M.; Schuckman, A. E.; Batteas, J. D.; Drain, C. M., Porphyrins as Molecular Electronic Components of Functional Devices. *Coord. Chem. Rev.* **2010**, *254*, 2297-2310.
66. Gust, D.; Moore, T. A.; Moore, A. L., Solar Fuels via Artificial Photosynthesis. *Acc. Chem. Res.* **2009**, *42*, 1890-1898.
67. Costentin, C.; Robert, M.; Savéant, J.-M., Current Issues in Molecular Catalysis Illustrated by Iron Porphyrins as Catalysts of the CO<sub>2</sub>-to-CO Electrochemical Conversion. *Acc. Chem. Res.* **2015**, *48*, 2996-3006.
68. Kaim, W.; Schwederski, B., Non-Innocent Ligands in Bioinorganic Chemistry—An Overview. *Coord. Chem. Rev.* **2010**, *254*, 1580-1588.
69. Fuhrhop, J.-H., The Reactivity of the Porphyrin Ligand. *Angew. Chem. Int. Ed. Engl.* **1974**, *13*, 321-335.
70. Kadish, K. M., The Electrochemistry of Metalloporphyrins in Nonaqueous Media. In *Prog. Inorg. Chem.*, 1986; pp 435-605.
71. Solis, B. H.; Maher, A. G.; Dogutan, D. K.; Nocera, D. G.; Hammes-Schiffer, S., Nickel Phlorin Intermediate Formed by Proton-Coupled Electron Transfer in Hydrogen Evolution Mechanism. *Proc. Natl. Acad. Sci. U.S.A.* **2016**, *113*, 485-492.
72. Maher, A. G.; Liu, M.; Nocera, D. G., Ligand Noninnocence in Nickel Porphyrins: Nickel Isobacteriochlorin Formation under Hydrogen Evolution Conditions. *Inorg. Chem.* **2019**, *58*, 7958-7968.
73. Solis, B. H.; Maher, A. G.; Honda, T.; Powers, D. C.; Nocera, D. G.; Hammes-Schiffer, S., Theoretical Analysis of Cobalt Hangman Porphyrins: Ligand Dearomatization and Mechanistic Implications for Hydrogen Evolution. *ACS Catal.* **2014**, *4*, 4516-4526.
74. Zhang, Y.-Q.; Chen, J.-Y.; Siegbahn, P. E. M.; Liao, R.-Z., Harnessing Noninnocent Porphyrin Ligand to Circumvent Fe-Hydride Formation in the Selective Fe-Catalyzed CO<sub>2</sub> Reduction in Aqueous Solution. *ACS Catal.* **2020**, *10*, 6332-6345.
75. Bonnett, R.; Djelal, B. D.; Hamilton, P. A.; Martinez, G.; Wierrani, F., Photobleaching of 5,10,15,20-Tetrakis(m-hydroxyphenyl)porphyrin (m-THPP) and the Corresponding Chlorin (m-THPC) and Bacteriochlorin(m-THPBC). A Comparative Study. *J. Photochem. Photobiol. B: Biol.* **1999**, *53*, 136-143.

76. Miller, D. C.; Choi, G. J.; Orbe, H. S.; Knowles, R. R., Catalytic Olefin Hydroamidation Enabled by Proton-Coupled Electron Transfer. *J. Am. Chem. Soc.* **2015**, *137*, 13492-13495.



*Page intentionally left blank*

## Chapter 2

# Mechanistic Studies on the Ni-Catalyzed Redox-Mediated Cross-Coupling Between Aryl Bromides and Alcohols

*Parts of this chapter have been published:*

Sun, R.; Qin, Y.; Ruccolo, S.; Schnedermann, C.; Costentin, C.; Nocera, D. G., Elucidation of a Redox-Mediated Reaction Cycle for Nickel-Catalyzed Cross Coupling. *J. Am. Chem. Soc.* **2019**, *141*, 89-93.

## 2.1 Introduction

Synthetic methods that furnish challenging bonds under mild conditions with high specificity are crucial in the preparation of fine chemicals.<sup>1,2</sup> In recent years, two powerful strategies<sup>3-5</sup> have emerged that rely on energetic electron redox processes to facilitate thermally inaccessible transformations: photoredox catalysis, where a combination of photon energy and redox-active chromophores provides the necessary thermodynamic impetus to initiate electron transfer, and electrochemically-mediated synthesis, where an electrical potential is imposed on the reaction medium through an electrode.

Despite the impressive chemical yields and selectivity achieved in many redox-mediated systems, comparably little attention has been given to optimizing their energy efficiency, which is an important metric in determining the economic feasibility and environmental sustainability of the synthetic methodology.<sup>6-9</sup> Moreover, the mechanisms in many cases remain poorly understood, thus hampering reaction reproducibility and rational optimization.<sup>6,10,11</sup> Some work implicates sustained chain processes to drive photoredox catalytic reactions.<sup>12,13</sup> However, it has not been verified whether these chain reactions constitute the dominant productive pathway in redox-mediated systems. The presence of these channels has profound implications for reaction optimization, since it determines whether photophysical and electron transfer pathways should be targeted as opposed to self-sustained pathways.<sup>6</sup> The elucidation of these pathways requires studies that identify catalytic intermediates and deleterious side reactions.

Redox-mediated Ni-catalyzed cross coupling, which represents one of the most ubiquitous classes of redox-mediated methodologies, is commonly proposed to operate *via* closed catalytic cycles where a photon or electron, respectively, is required for every turnover.<sup>14</sup> Conversely, work by Doyle and co-workers have implicated a potential self-sustained Ni(I/III) cycle for such Ni-catalyzed reactions,<sup>15</sup> though the proposed paramagnetic intermediates have not been directly observed and the reaction pathway through which they are accessed remains unclear. We report detailed studies of Ni-catalyzed aryl etherification (Figure 2.1)<sup>16</sup> relying on a combination of photophysical, electrochemical, and synthetic approaches to identify productive and deleterious reaction pathways and intermediates. Based on these insights, the photo- and

electro-redox methodologies have been optimized, leading to 15- and 3-fold increases in quantum and faradaic yields, respectively.

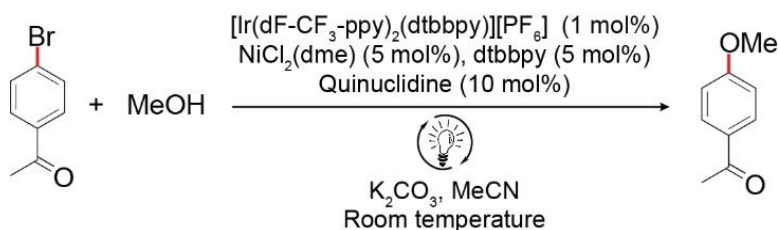


**Figure 2.1.** Conditions for photoredox-catalyzed aryl etherification. dF-CF<sub>3</sub>-ppy = 2-(2,4-difluorophenyl)-5-(trifluoromethyl)pyridine. dtbbpy = 4,4'-di-*tert*-butyl-2,2'-dipyridyl. dme = 1,2-dimethoxyethane.

## 2.2 Quantum and Faradaic Yields

The photoredox quantum yield ( $\phi$ ) for the reaction in Figure 2.1 was determined. We modified the published methodology<sup>16</sup> by replacing the combination of K<sub>2</sub>CO<sub>3</sub> and catalytic quinuclidine with a stoichiometric amount of the latter to arrive at a homogeneous reaction, which was needed for spectroscopic studies. Under our conditions, we observe by <sup>1</sup>H NMR the same result as that obtained in previous synthetic studies—namely, the quantitative conversion of 4'-bromoacetophenone to the corresponding ether. Light, Ir(III) photocatalyst and quinuclidine are needed for efficient reaction. As opposed to >95% conversion after 2 h of irradiation, no product formation was observed in the absence of light. Furthermore, we observe a greatly diminished conversion in the absence of Ir(III) photocatalyst (48% after 24 h) or when quinuclidine was replaced with K<sub>2</sub>CO<sub>3</sub> (37% after 24 h). With light excitation of  $\lambda_{\text{exc}} = 435$  nm and  $P = 11.0$  mW, a quantum yield of  $\phi = 1.63 \pm 0.08$  was determined (see Figure 2.2, top). Values of  $\phi > 1$  indicate multiple turnovers per incident photon, supporting the presence of a productive self-sustained channel. Next, we turned our attention to the electrochemical reaction to confirm if similar reactivity is present. Whereas the Ni-catalyzed aryl etherification can be achieved under electrochemical conditions,<sup>17</sup> we discovered that the faradaic yield was  $5.6 \pm 0.8$  (see Figure 2.2, bottom) when a galvanostatic electrolysis was performed in a divided H-cell with a cathodic current of 1 mA, again implicating productive self-sustained catalytic activity.

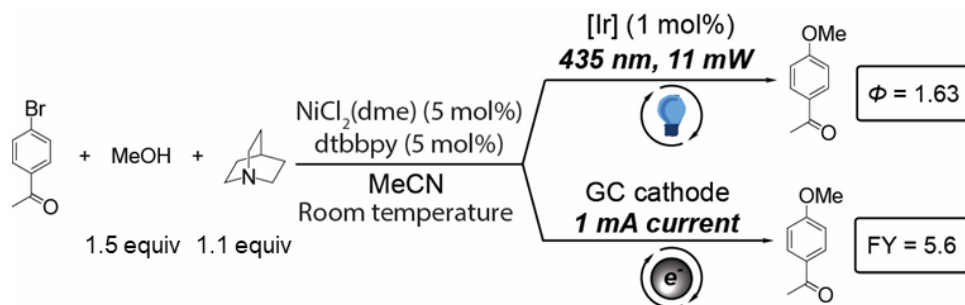


**Figure 2.2.** Quantum and faradaic yields for the redox-mediated cross-coupling reaction.

### 2.3 Transient Absorption and Electrochemical Studies on the Reaction Solution

Nanosecond transient absorption (TA) spectroscopy was used to investigate the reaction. Figure 2.3A shows the evolution of the difference spectrum obtained after laser excitation ( $\lambda_{exc} = 425$  nm) of a MeCN solution containing NiCl<sub>2</sub>(dme), dtbbpy, quinuclidine, and the Ir(III) photocatalyst [Ir(dF-CF<sub>3</sub>-ppy)<sub>2</sub>(dtbbpy)][PF<sub>6</sub>] in the absence of substrate. The Ir(III) excited state is predominantly quenched by quinuclidine as opposed to (dtbbpy)NiCl<sub>2</sub>, as verified by dynamic Stern-Volmer studies shown in Figure 2.4 (we note that the (dtbbpy)NiCl<sub>2</sub> precatalyst commonly employed in cross-coupling reactions may exist as a dimer, as shown in Figure 2.5). Thus, the TA spectrum observed at 30 ns is a superposition of contributions from a quinuclidine dimer radical cation and Ir(II) (Figures 2.6, 2.7 and 2.8).<sup>18</sup> This spectrum evolves over the course of several hundred microseconds to give a new species with 415- and 595-nm absorption features, which further transform after 5 ms to furnish a signal centered at 670 nm (Figure 2.3A). Neither species appeared when the same experiment was performed in the absence of Ni(II). Since the potential of the Ir(III/II) redox couple ( $-1.74$  V vs Fc<sup>+</sup>/Fc) is sufficient to drive the reduction of Ni(II) (Figures 2.9 and 2.10), we ascribe both signals to photochemically-generated low-valent Ni compounds. We observed that the lifetime of the signal at 670 nm decreased in the presence of 4'-bromoacetophenone (Figure 2.3B), indicating that this second species can react with aryl bromide as a potential catalytic intermediate. Furthermore, we note that this compound exhibited an increased lifetime with increasing concentrations of both quinuclidine and (dtbbpy)NiCl<sub>2</sub> in the presence of 4'-bromoacetophenone (Figure 2.11), suggesting that its reactivity towards aryl bromide is attenuated by the amine base and Ni(II).

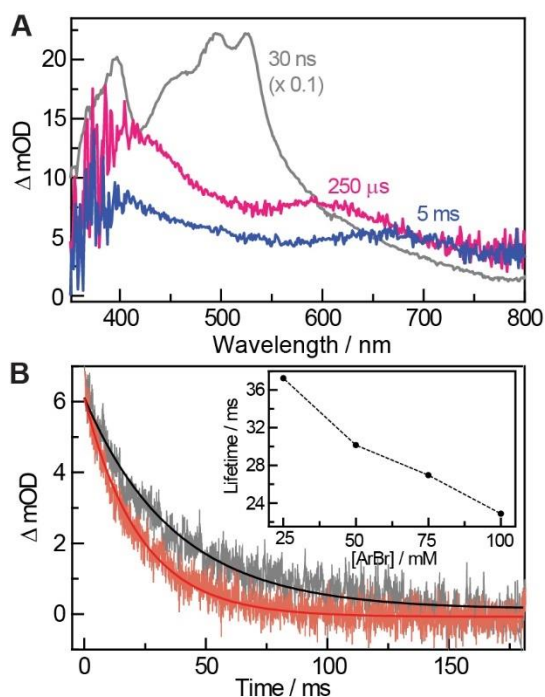


**Figure 2.3.** Transient absorption (TA) spectra of the initial reaction solution. (A) Spectrum obtained after exciting ( $\lambda_{\text{exc}} = 425 \text{ nm}$ ) a solution of 0.2 mM  $[\text{Ir}(\text{dF-CF}_3\text{-ppy})_2(\text{dtbbpy})][\text{PF}_6]$ , 5 mM  $\text{NiCl}_2(\text{dme})$ , 5 mM dtbbpy, and 50 mM quinuclidine in MeCN. (B) Single-wavelength kinetic trace monitored at 670 nm of the same solution as in A with the addition of 25 mM (— grey) and 100 mM (— orange) 4'-bromoacetophenone. Solid lines show mono-exponential fits and inset show the fitted lifetime in the presence of different concentrations of aryl bromide.

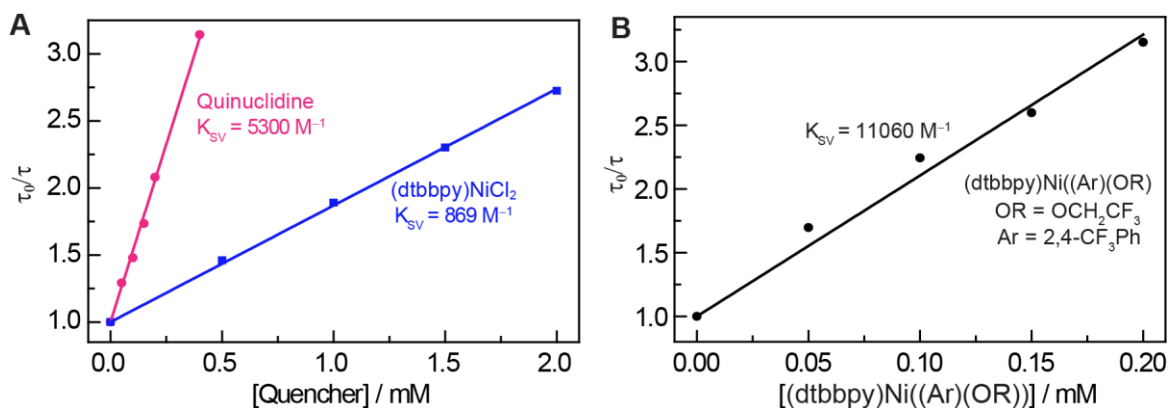


**Figure 2.4.** Dynamic Stern-Volmer quenching plots. (A) Dynamic Stern-Volmer quenching plot for the Ir(III) excited state under different concentrations of quinuclidine (— pink) and  $(\text{dtbbpy})\text{NiCl}_2$  (— blue). (B) Dynamic Stern-Volmer quenching plot for the Ir(III) excited state under different concentrations of  $(\text{dtbbpy})\text{Ni}(2,4\text{-bis}(\text{CF}_3)\text{phenyl})(\text{OCH}_2\text{CF}_3)$ .  $\tau$  and  $\tau_0$  represent the measured fluorophore lifetime in a solution with and without quencher, respectively.

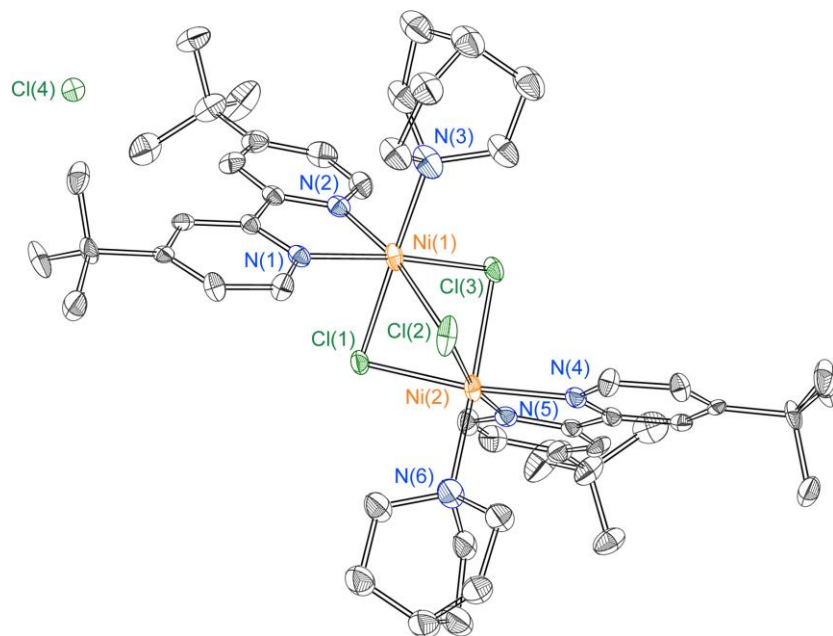


**Figure 2.5.** Crystal structure of quinuclidine-bound (dtbbpy)NiCl<sub>2</sub> as a dimeric cation. Data were collected at 100 K. Thermal ellipsoids are drawn at 50% probability and hydrogen atoms are omitted for clarity.

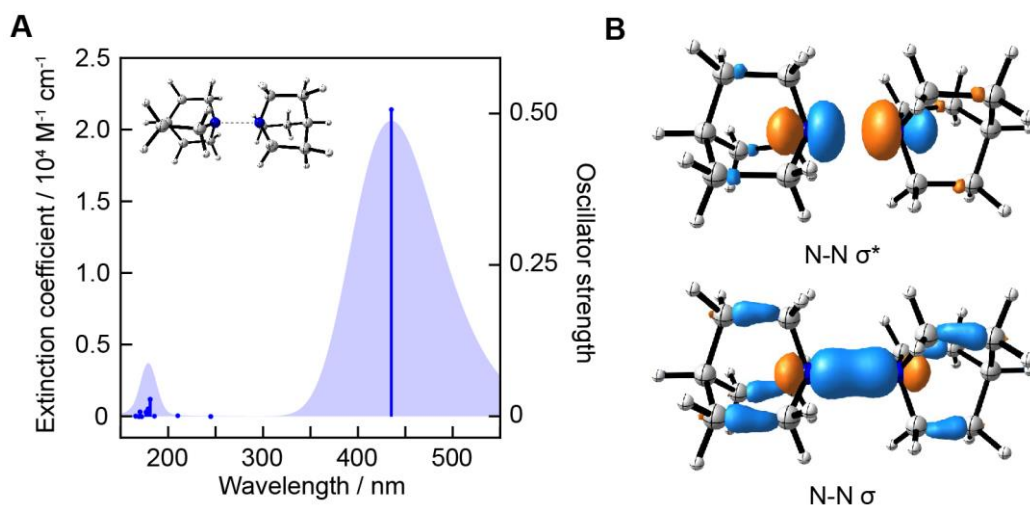


**Figure 2.6.** Computational studies of the quinuclidine dimer radical cation. (A) Simulated absorption line spectrum of the quinuclidine dimer radical cation (blue lines, right y-axis). The line spectrum has been Gaussian-broadened to 0.35 eV at half-width half height. The optimized molecular structure shows a N-N bond length of 2.308 Å and is displayed for reference. We note that the associated absorption line (435 nm) is extremely sensitive to the N-N distance, which is underestimated in our calculations by comparison to the experiment. (B) Frontier molecular orbitals associated with the lowest-energy transition.

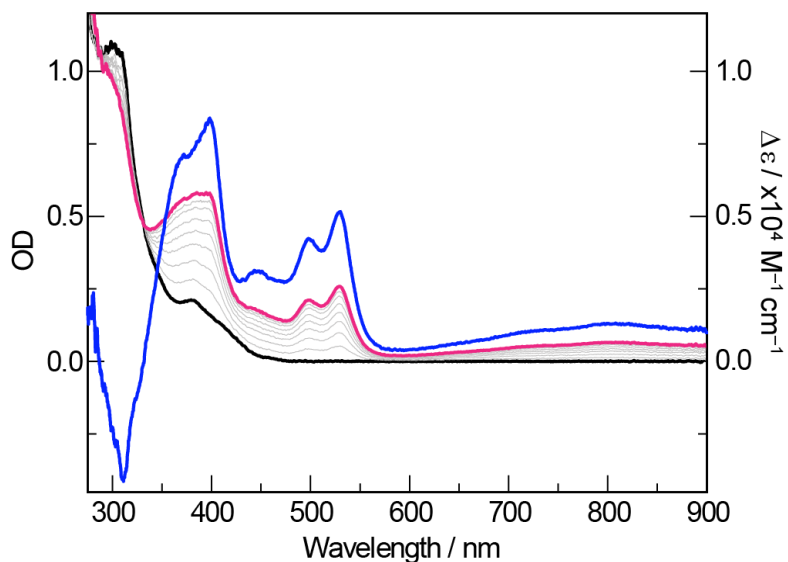


**Figure 2.7.** Spectroelectrochemistry in MeCN of  $[\text{Ir}(\text{dF-CF}_3\text{-ppy})_2(\text{dtbbpy})][\text{PF}_6]$  under a cathodic potential of  $-1.8$  V vs  $\text{Fc}^+/\text{Fc}$  showing a transition from the Ir(III) state (— black) to an Ir(II) state (— pink). The difference in extinction coefficients between the Ir(II) and Ir(III),  $\Delta\epsilon$  (— blue), is shown against the right axis.

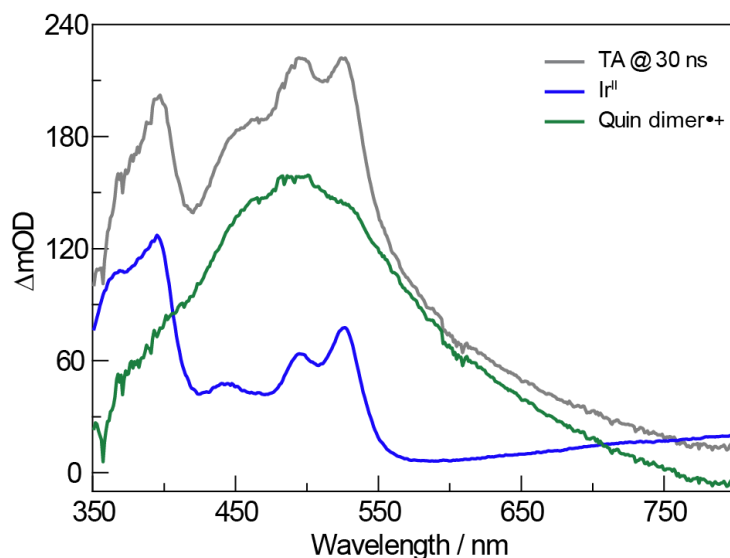


**Figure 2.8.** Deconvolution of the TA spectrum at 30 ns after photoexciting ( $\lambda_{\text{exc}} = 425$  nm) a solution of 0.2 mM  $[\text{Ir}(\text{dF-CF}_3\text{-ppy})_2(\text{dtbbpy})][\text{PF}_6]$ , 5 mM  $\text{NiCl}_2(\text{dme})$ , 5 mM dtbbpy, and 50 mM quinuclidine in MeCN. The Ir(II) spectrum (— blue) was obtained by spectroelectrochemistry. The quinuclidine dimer radical cation spectrum (— green) was obtained by subtracting the Ir(II) contribution from the TA spectrum at 30 ns with minimization of the first derivative of the resultant spectrum with respect to wavelength.



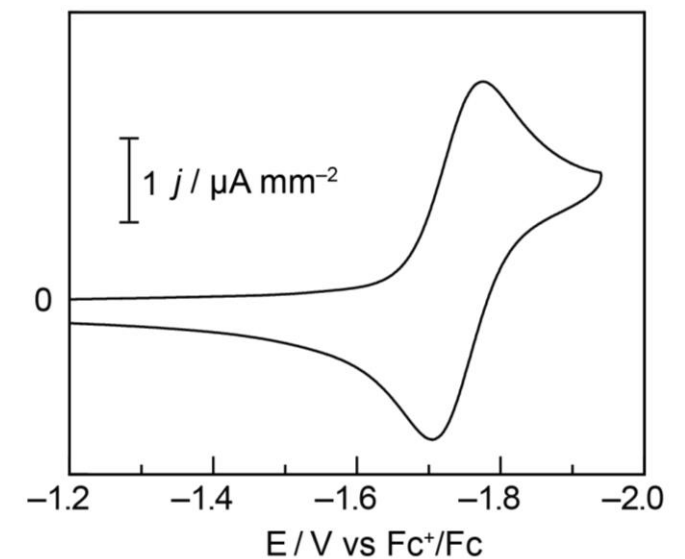


**Figure 2.9.** CV of a 1.0 mM solution in MeCN of the Ir(III) photocatalyst  $[\text{Ir}(\text{dF-CF}_3\text{-ppy})_2(\text{dtbbpy})][\text{PF}_6]$  taken with a 3.0 mm glassy carbon (GC) working electrode at  $\nu = 0.1 \text{ V s}^{-1}$ .  $E_{1/2} = -1.74 \text{ V}$ .

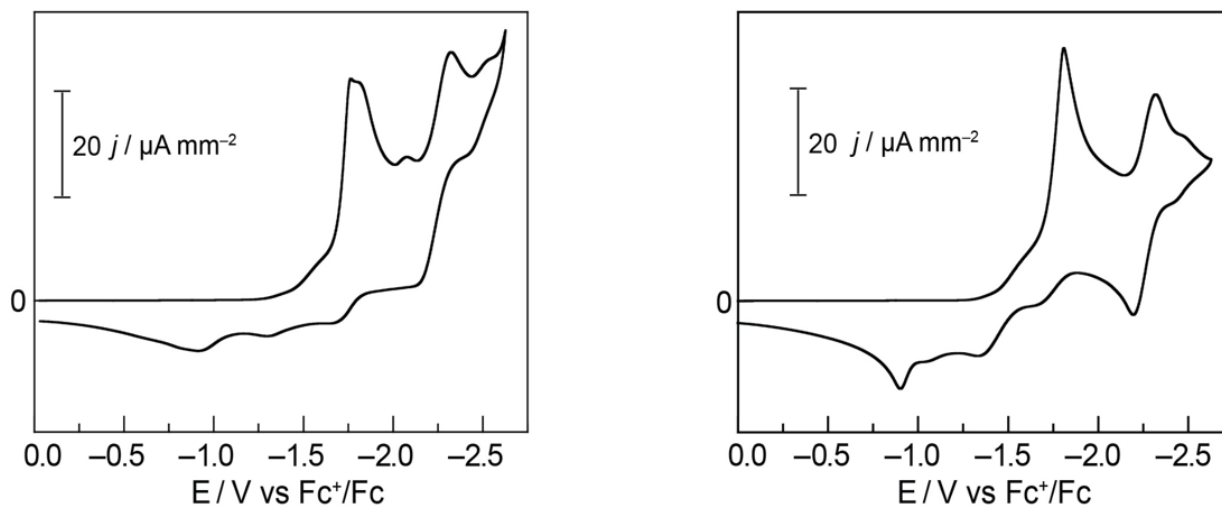


**Figure 2.10.** CVs of a MeCN solution containing 12.5 mM  $\text{NiCl}_2(\text{dme})$ , 12.5 mM dtbbpy, 275 mM quinuclidine (left) in the presence of 375 mM methanol (corresponding to initial concentrations in the photoredox reaction) and (right) in the absence of methanol. The working electrode was 3.0 mm GC and the scan rate was  $\nu = 0.1 \text{ V s}^{-1}$ .

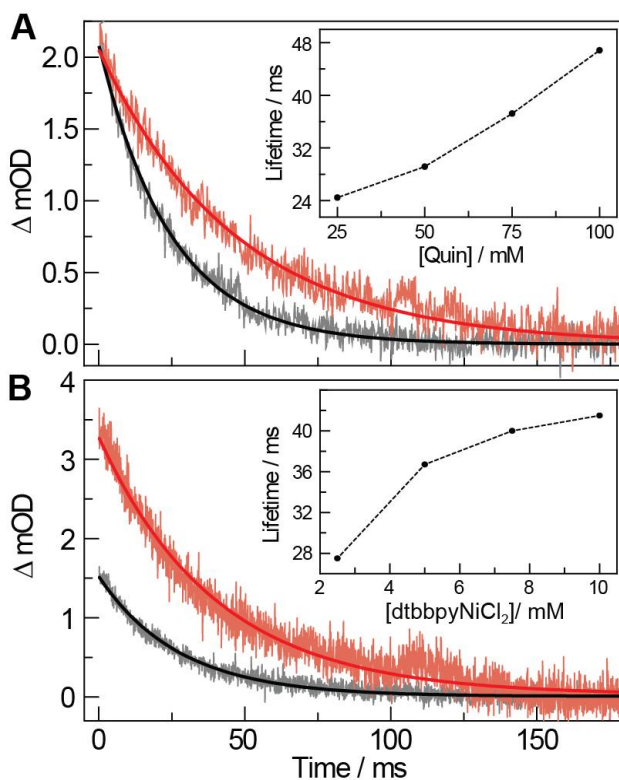


**Figure 2.11.** Single-wavelength kinetic traces ( $\lambda_{\text{exc}} = 425$  nm) monitored at 670 nm. **(A)** Kinetic trace of a solution containing 0.2 mM  $[\text{Ir}(\text{dF-CF}_3\text{-ppy})_2(\text{dtbbpy})][\text{PF}_6]$ , 5 mM  $(\text{dtbbpy})\text{NiCl}_2$ , and 100 mM 4'-bromoacetophenone with 25 mM (— grey) and 100 mM (— orange) quinuclidine. **(B)** Kinetic trace of a solution containing 0.2 mM  $[\text{Ir}(\text{dF-CF}_3\text{-ppy})_2(\text{dtbbpy})][\text{PF}_6]$ , 100 mM 4'-bromoacetophenone, and 50 mM quinuclidine with 2.5 mM (— grey) and 10 mM (— orange)  $(\text{dtbbpy})\text{NiCl}_2$ . Solid lines show mono-exponential fits and insets show the fitted lifetime in the presence of different concentrations of the additive under study.

#### 2.4 Identification and Characterization of a Paramagnetic Ni Intermediate

To determine whether this intermediate can be observed under catalytic conditions, we designed an apparatus to spectroscopically monitor the reaction while under illumination by a LED light source (Figure 2.12). By taking the difference between the spectrum obtained under irradiation and that obtained in the dark (Figure 2.13B, top), we observe the same spectroscopic feature at 670 nm seen in the TA spectra. Due to the broader spectral window of this setup, we discovered another absorption peak at  $\sim 840$  nm associated with this compound. Similarly, we were able to observe the same spectroscopic features under electrochemical conditions offered by spectroelectrochemistry of a MeCN solution of  $\text{NiCl}_2(\text{dme})$ , dtbbpy, and quinuclidine (Figure

2.13B, middle). At  $E_{\text{appl}} = -1.74$  V vs  $\text{Fc}^+/\text{Fc}$  (corresponding to the Ir(III/II) couple), we observed the growth of absorption bands characteristic of the same compound (Figure 2.14), implicating it as a common intermediate in both the electro- and photoredox reactions.

To further assess whether the intermediate was a reduction product of Ni(II), we prepared it independently from the comproportionation reaction between Ni(0) with Ni(II) in the presence of quinuclidine. Adding a MeCN solution of Ni(dtbbpy)(cod) to one with excess NiCl<sub>2</sub>(dme), dtbbpy, and quinuclidine led to the immediate formation of a dark green solution whose difference spectrum upon air exposure showed the same absorption bands centered at  $\lambda_{\text{max}} = 670$  nm and 840 nm (Figure 2.13B, bottom), as previously observed. Crystals of the intermediate, compound **1**, were grown from this solution, and single-crystal X-ray diffraction revealed the structure of a formally mixed-valent Ni(I/II) dimer (Figure 2.13A). Computational studies based on the crystal structure gave a calculated absorption spectrum (Figure 2.15) that is in qualitative agreement with the experimental spectra shown in Figure 2.13B. The frozen solution X-band EPR spectrum at 77 K in MeCN (Figure 2.13C) is characteristic of a  $S = 3/2$  species.<sup>19,20</sup> Quinuclidine and excess (dtbbpy)NiCl<sub>2</sub> were essential in forming this compound since their absence in the reaction between Ni(0) and Ni(II) led to a decomposition product (Figures 2.16 and 2.17), consistent with the increased stability observed by TA spectroscopy (Figure 2.11).

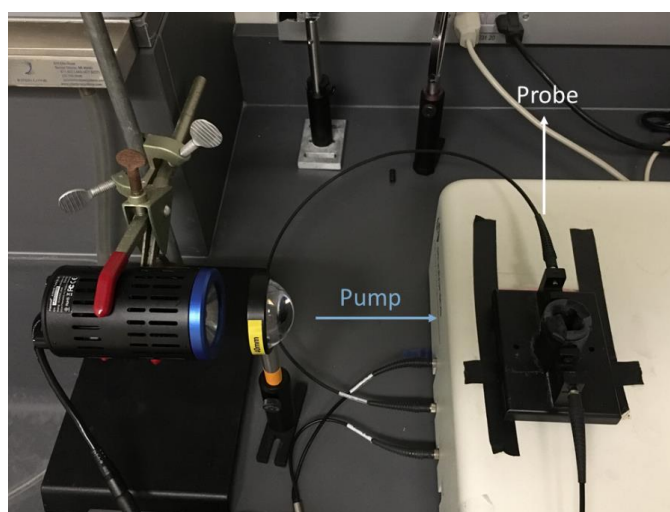


**Figure 2.12.** Apparatus used for *in situ* monitoring of the photochemical reaction.

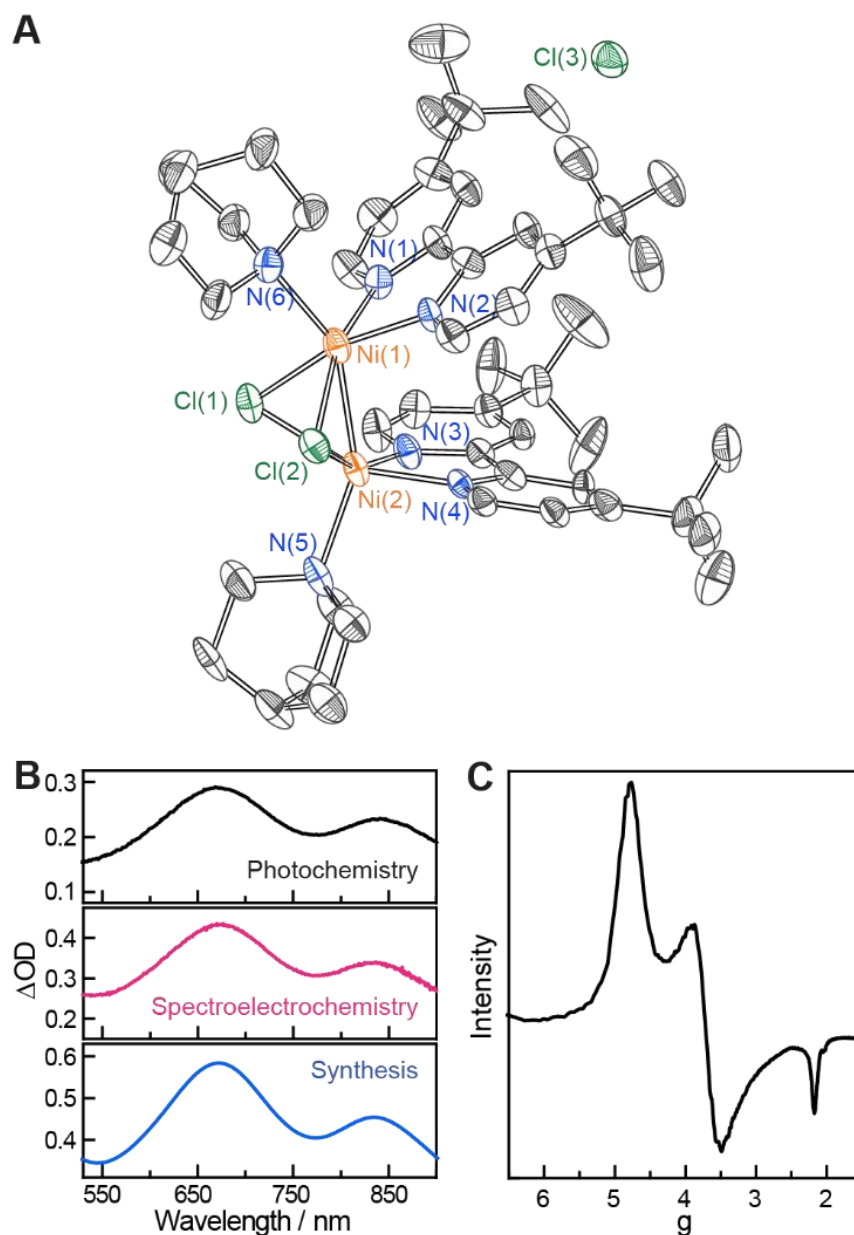


**Figure 2.13.** Characterization of a paramagnetic Ni intermediate. (A) Crystal structure of **1** collected at 100 K with thermal ellipsoids drawn at 50% probability and hydrogen atoms omitted for clarity. (B) Difference spectra observed from *in situ* monitoring of the photoredox reaction solution containing 4'-bromoacetophenone, MeOH, quinuclidine, NiCl<sub>2</sub>(dme), dtbbpy, and [Ir(dF-CF<sub>3</sub>-ppy)<sub>2</sub>(dtbbpy)](PF<sub>6</sub>) (top), from spectroelectrochemistry on a solution of NiCl<sub>2</sub>(dme), dtbbpy, and quinuclidine at -1.74 V vs Fc<sup>+</sup>/Fc (middle), and from the comproportionation of Ni(dtbbpy)(cod) with NiCl<sub>2</sub>(dme) in the presence of dtbbpy and quinuclidine (bottom). (C) X-band EPR spectrum collected at 77 K on a frozen MeCN solution of **1** prepared *via* comproportionation.

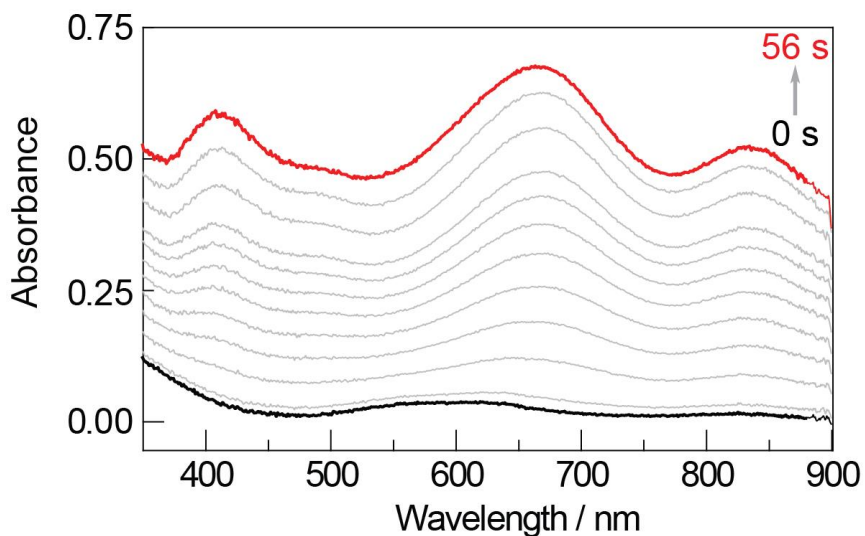


**Figure 2.14.** Spectroelectrochemistry of a MeCN solution containing 12.5 mM NiCl<sub>2</sub>(dme), 12.5 mM dtbbpy, and 275 mM quinuclidine under a cathodic potential of  $-1.74$  V vs Fc<sup>+</sup>/Fc showing a transition from the initial Ni(II) state (— black) to a state with spectroscopic features consistent with complex **1** (— red).

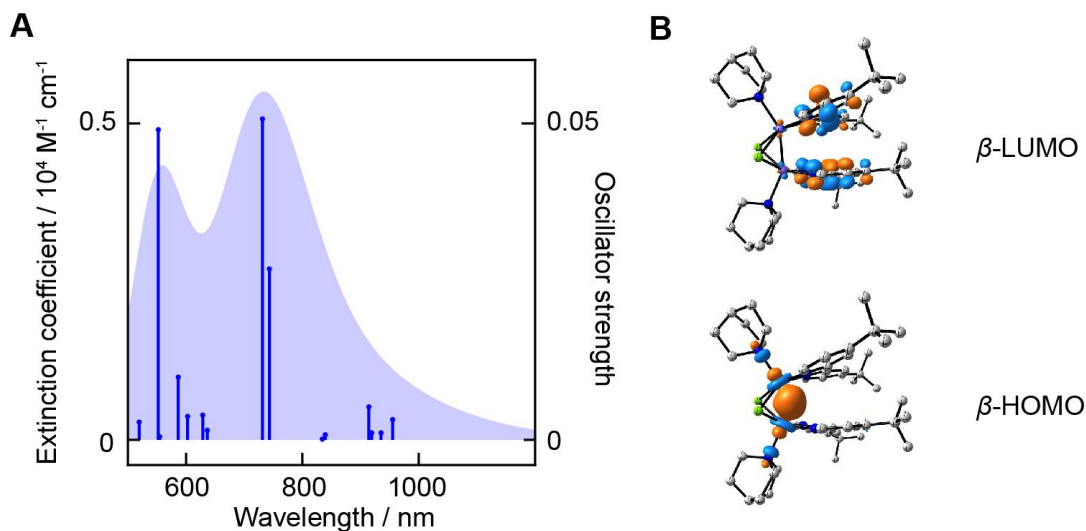


**Figure 2.15.** Computational studies of complex **1**. (A) Simulated absorption line spectrum of **1** (blue lines, right y-axis). The line spectrum has been Gaussian-broadened to 0.2 eV at half-width half height (blue shaded, left y-axis). (B) Frontier molecular orbitals associated with the strongest low-energy transition at 732 nm. The  $\beta$ -HOMO (bottom) is characterized predominantly as a  $\sigma$  orbital between the  $d_{z^2}$  orbitals of the involved Ni atoms. The  $\beta$ -LUMO (top) features  $\pi^*$  orbitals of the dtbbpy ligands, classifying the excited state as a MLCT state. Hydrogen atoms are omitted for clarity.

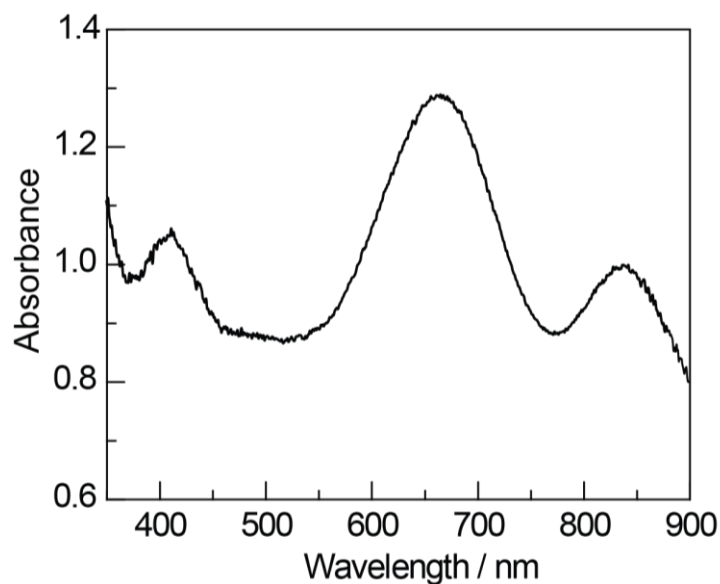


**Figure 2.16.** Spectroscopic study of the comproportionation reaction performed in the presence of quinuclidine. In the absence of quinuclidine, no discernible spectrum is observed.

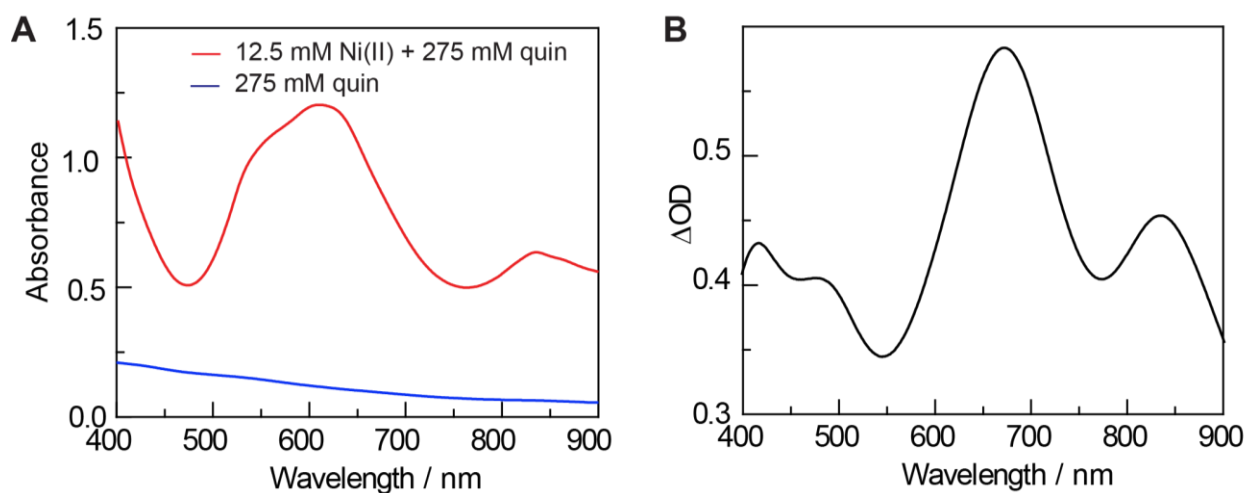


**Figure 2.17.** Stability of **1** towards dilution. (A) Dilution of Ni(I) in the presence of quinuclidine (— blue) and both (dtbbpy)NiCl<sub>2</sub> and quinuclidine (— red), demonstrating the decomposition of Ni(I) upon dilution in the absence of excess (dtbbpy)NiCl<sub>2</sub>. (B) Difference spectrum of the sample diluted in the presence of (dtbbpy)NiCl<sub>2</sub> and quinuclidine after air exposure shows that the characteristic spectroscopic features of **1** were retained under these conditions.

## 2.5 Reactivity of the Paramagnetic Ni Intermediate **1**

To establish if **1** could enter the aryl etherification catalytic cycle without photochemical activation, a MeCN solution containing 4.17 mM Ni(dtbbpy)(cod), 12.5 mM (dtbbpy)NiCl<sub>2</sub>, and 275 mM quinuclidine (corresponding to the *in situ* formation of 8.34 mM of **1** (3.3 mol% loading) based on a 2:1 stoichiometry for the production of **1** from Ni(dtbbpy)(cod)) was prepared and added dropwise to a MeCN solution containing 250 mM 4'-bromoacetophenone, 375 mM MeOH, 275 mM quinuclidine, and 12.5 mM (dtbbpy)NiCl<sub>2</sub>. Under these conditions, cross-coupled product was obtained with a turnover number (TON) of 2.1 with respect to **1** (Figure 2.18), as determined by <sup>1</sup>H NMR. This chemically induced turnover number is less than that obtained electrochemically (TON ≥ 5.8) based on the faradaic yield. We posit that the catalytic efficiency of **1** may be dependent on its concentration due to potential deleterious bimetallic pathways. The observation that (dtbbpy)Ni(Ar)(Br) is the terminal product of oxidative addition to **1** (Figure 2.19) implicates facile comproportionation between Ni(I) and Ni(III) species to form inactive Ni(II) complexes as one such pathway, consistent with our computational studies (Figure 2.20) and previous literature reports.<sup>21</sup> Accordingly, the experiment was repeated using a 0.83 mM solution of **1** (0.33 mol% loading). Under these conditions, we observed a substantially increased TON of 13.4 (Figure 2.18). A similar trend is observed if a solution of Ni(dtbbpy)(cod) is added to the substrate in place of preformed **1**. Here, the TONs are 2.0 and 3.9 at concentrations of 8.3 and 0.83 mM, respectively, suggesting that comproportionation may also be present.

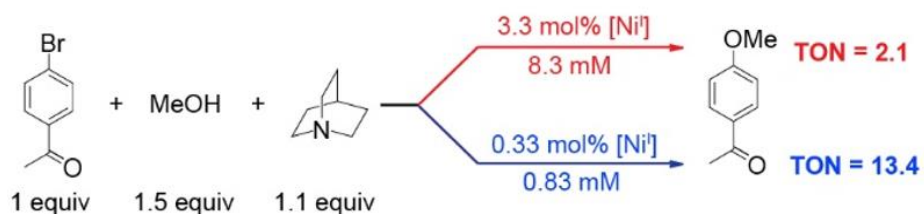


**Figure 2.18.** TON for **1** increases with decreasing concentration, implicating a potential bimetallic pathway for catalyst deactivation.

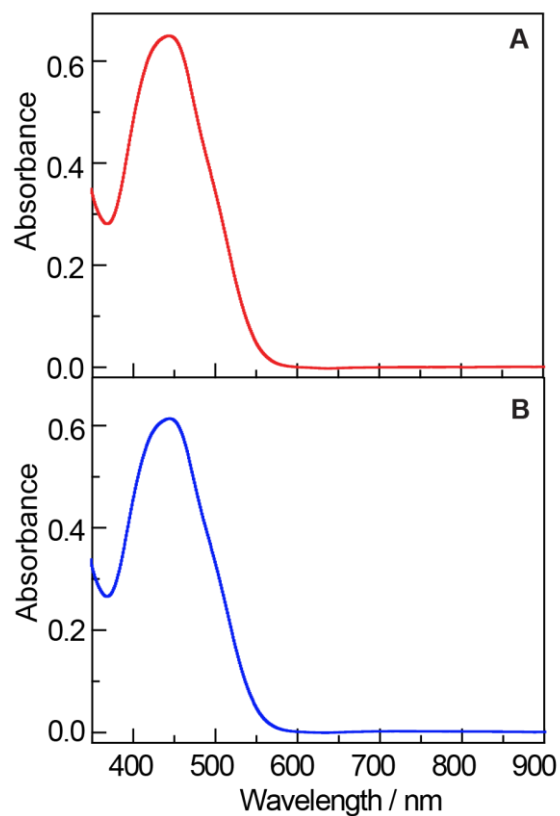


**Figure 2.19.** Spectroscopic studies of oxidative addition. **(A)** Absorption spectrum of the oxidative addition product. **(B)** Absorption spectrum of a 1 mM solution of (dtbbpy)Ni(*o*-tolyl)(Br) under similar conditions. Both spectra are background-corrected for (dtbbpy)NiCl<sub>2</sub>.

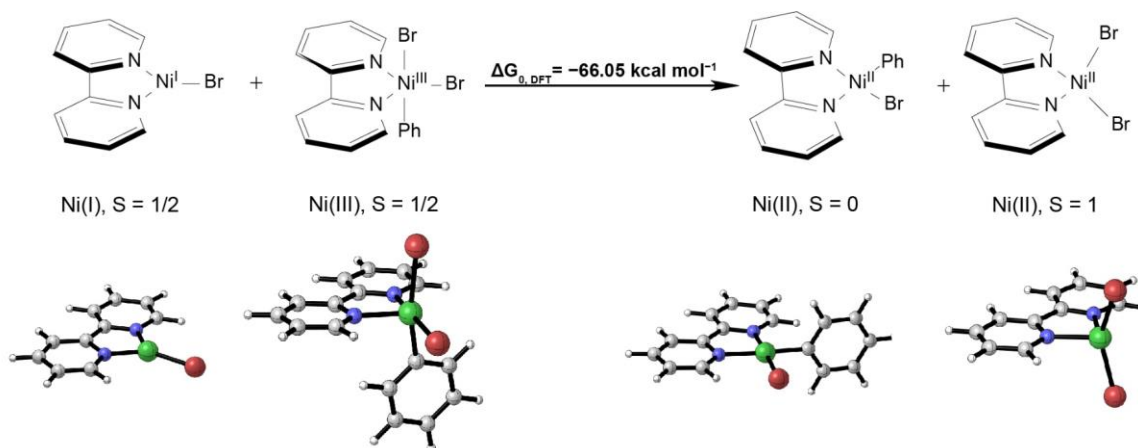


**Figure 2.20.** DFT study demonstrating that comproportionation between a monomeric Ni(I) species and the expected Ni(III) intermediate formed after oxidative addition is highly exergonic.



## 2.6 Proposed Reaction Pathway and Optimization for Energy Efficiency

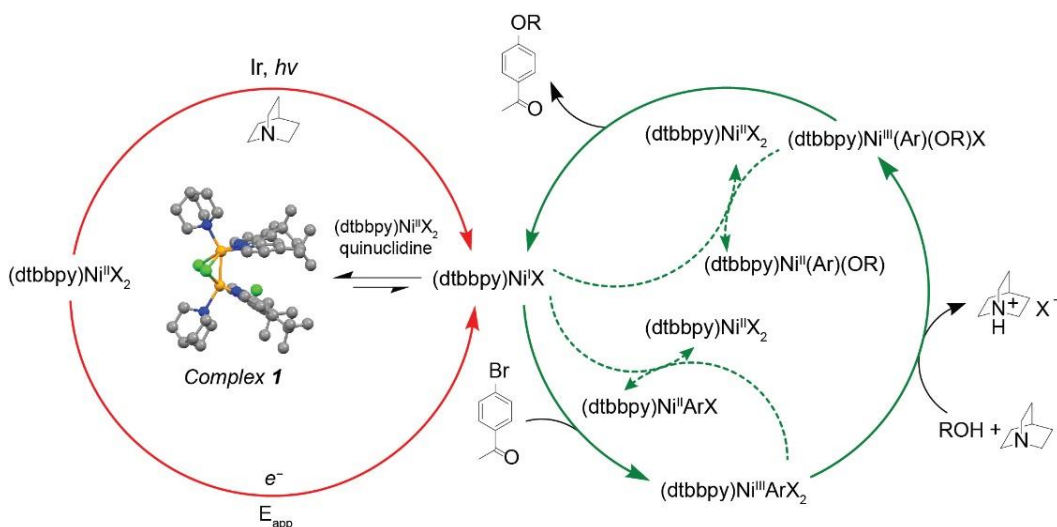


**Figure 2.21.** Proposed cycle for the redox-mediated cross-coupling reaction between alcohols and aryl bromides.

Figure 2.21 illustrates a reaction cycle consistent with our results. Reduction of the  $\text{NiX}_2$  precursor produces a putative monomeric Ni(I) intermediate that is trapped by excess Ni(II) in solution to form complex **1**. Based on the suppressed reactivity exhibited by this intermediate towards aryl bromide in the presence of quinclidine and Ni(II) (Figure 2.11), we propose that dissociation of the dimer is a prerequisite for oxidative addition, after which a sustained Ni(I/III) cycle is responsible for product formation. At high concentrations of Ni(I) or Ni(III) species, bimetallic comproportionation reactions lead to off-cycle Ni(II) complexes. Considering the ubiquity of  $(\text{dtbbpy})\text{NiX}_2$  in Ni-catalyzed photoredox platforms,<sup>14</sup> we infer that our investigation may offer insights into similar reactions.

Inspired by the discovery that high loadings of **1** led to a diminished TON, we suspected that attenuation of the Ni(I) concentration (thus attenuating comproportionation) in the photo- and electro-redox mediated methods would lead to improved energy efficiency. As shown in Figure 2.22 and Table 2.1, both the quantum and faradaic yields are substantially increased by decreasing the photon flux and current, respectively. This suggests that the reaction conditions can be tuned from a regime hampered by deleterious Ni(I/III) comproportionation into a one that stays on pathway of the productive catalytic cycle.

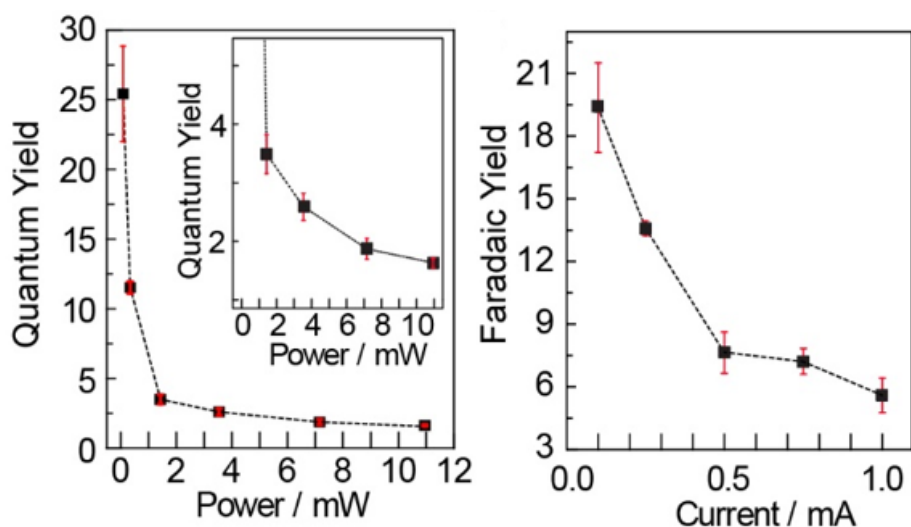


**Figure 2.22.** Energy optimization of the cross-coupling reaction. Left: power-dependence of the quantum yield for the photoredox reaction ( $\lambda_{exc} = 435$  nm). Inset shows an enlarged view of the high-power regime. Right: Current-dependence of the faradaic yield under cathodic galvanostatic electrolysis with a GC working electrode in a divided H-cell. Product yields were determined by  $^1\text{H}$  NMR relative to 1,3-benzodioxole. Error bars denote SD ( $n = 3$ ).

**Table 2.1.** Quantum and faradaic yields.

Power (mW)	% Yield of Product	Quantum Yield <sup>a</sup>
0.08	28%	$25 \pm 3$
0.34	17%	$11.5 \pm 0.4$
1.43	10%	$3.5 \pm 0.3$
3.54	10%	$2.6 \pm 0.2$
7.16	7%	$1.9 \pm 0.2$
10.95	9%	$1.63 \pm 0.08$
Current (mA)	% Yield of Product	Faradaic Yield <sup>b</sup>
0.1	14%	$19 \pm 2$
0.25	10%	$13.6 \pm 0.3$
0.5	6%	$7.6 \pm 1.0$
0.75	5%	$7.2 \pm 0.6$
1	4%	$5.6 \pm 0.8$

<sup>a</sup> quantum yield = mol product/mol photons absorbed. <sup>b</sup> faradaic yield = mol product/mol electrons passed.

## 2.7 Conclusions

Ni-catalyzed aryl etherification involves an operative self-sustained Ni(I/III) cycle in the redox-mediated reaction under both photo- and electro- redox conditions. The redox steps are only needed to rejuvenate the cycle when off-pathway reactions deplete the competent Ni(I/III) species that support the catalysis, such as the crystallographically characterized bimetallic Ni intermediate. The amine auxiliary in the catalytic cycle fulfills three roles as a: (i) as a base; (ii) as a ligand necessary for the formation of complex **1** and (iii) as a flash-quencher of the photocatalyst, all of which assist in the initiation or perpetuation of self-sustained catalytic reactivity. A bimetallic pathway leads to off-cycle Ni(II) species and we were able to leverage this understanding to simultaneously improve both the quantum and faradaic yields by factors of approximately 15 and 3, respectively. These results have ramifications for reactor design and optimization, whereby decreasing the power density can significantly increase the energy efficiency. Thus, insights into reaction pathways as described herein present effective strategies towards improving redox-mediated reactions catalyzed by transition metals, with potentially broad applications towards pharmaceutical and industrial processes.

## 2.8 Materials and Methods

**General considerations.** Commercial reagents were stored in a N<sub>2</sub>-filled glovebox and used without further purification. All liquid reagents and deuterated solvents were degassed by three cycles of freeze-pump-thaw and stored over activated 3 Å molecular sieves. 4'-bromoacetophenone, NiCl<sub>2</sub>(dme) (dme = 1,2-dimethoxyethane), dtbbpy (dtbbpy = 4,4'-di-*tert*-butyl-2,2'-dipyridyl), the iridium photocatalyst [Ir(dF-CF<sub>3</sub>-ppy)<sub>2</sub>(dtbbpy)](PF<sub>6</sub>), 1,3-benzodioxole, 2-bromotoluene, 2,4-bis(trifluoromethyl)-bromobenzene and *n*-Bu<sub>4</sub>NBF<sub>4</sub> were purchased from Sigma-Aldrich. Quinuclidine was purchased from Alfa Aesar. Ni(cod)<sub>2</sub> (cod = 1,5-cyclooctadiene) was purchased from STREM. All non-deuterated solvents were purified by the method of Grubbs and stored over activated 3 Å molecular sieves.<sup>22</sup> *n*-Bu<sub>4</sub>NBF<sub>4</sub> was dried *in vacuo* at 80 °C overnight before use. All manipulations were performed with the rigorous exclusion of air and moisture unless otherwise stated. <sup>1</sup>H NMR spectra were recorded at the Harvard University Department of

Chemistry and Chemical Biology NMR facility on an Agilent DD2 spectrometer operating at 600 MHz or a Varian Unity/Inova spectrometer operating at 500 MHz. EPR spectra were recorded on a Bruker ElexSys E500 spectrometer. The Ni(II) complexes (dtbbpy)Ni(2,4-bis(CF<sub>3</sub>)phenyl)(OCH<sub>2</sub>CF<sub>3</sub>) and (dtbbpy)Ni(*o*-tolyl)(Br) were prepared according to reported procedures.<sup>23,24</sup> Solutions of Ni(dtbbpy)(cod) were prepared *in situ* using an adapted literature procedure by adding MeCN to a vial charged with Ni(cod)<sub>2</sub> and dtbbpy (1:1 mol ratio) and stirring for 1 h at ambient temperature.<sup>25</sup> Solutions of (dtbbpy)NiCl<sub>2</sub> were prepared *in situ* by adding MeCN to a vial charged with NiCl<sub>2</sub>(dme) and dtbbpy (1:1 mol ratio), sonicating for 30 min at ambient temperature, and filtering with a 0.22 μm PTFE syringe filter.

**Quantum yield measurements.** The reaction mixtures were prepared by adding 5.5 mL of CD<sub>3</sub>CN to a 20 mL scintillation vial charged with 4'-bromoacetophenone (273.7 mg, 1.38 mmol), methanol (66.1 mg, 2.06 mmol), quinuclidine (168.2 mg, 1.51 mmol), dtbbpy (18.4 mg, 68.7 μmol), NiCl<sub>2</sub>(dme) (15.1 mg, 68.7 μmol), [Ir(dF-CF<sub>3</sub>-ppy)<sub>2</sub>(dtbbpy)][PF<sub>6</sub>] (15.4 mg, 13.7 μmol), and 1,3-benzodioxole in the glovebox. The vial was then sealed with electrical tape and the mixture was sonicated at ambient temperature for 30 min, before being passed through a 0.22 μm PTFE syringe filter. An aliquot of the solution was drawn and transferred into a 1.0 cm quartz cuvette equipped with a magnetic stir bar for each quantum yield measurement. The samples were irradiated using a 150 W Xe arc lamp (Newport 67005 arc lamp housing and 69907 power supply) under fan cooling and vigorous stirring. A 435 nm line filter was employed to generate a monochromatic beam, which was further focused with a lens (*f* = 4 cm) onto the sample. The photon flux was measured by chemical actinometry against 0.15 M potassium ferrioxalate according to a standard procedure.<sup>26</sup> Measurements of the power-dependence was carried out by placing neutral density filters before the focusing lens to attenuate the photon flux. Product yields were determined by <sup>1</sup>H NMR spectroscopy against 1,3-benzodioxole as an internal standard. Each reaction was carried out in triplicate. The quantum yields are shown in Table 2.1 along with average percent yields obtained under each condition as determined against 1,3-benzodioxole.

**Faradaic yield measurements.** The reaction mixtures were prepared by adding 16 mL of a 0.1 M *n*-Bu<sub>4</sub>NBF<sub>4</sub> electrolyte solution in MeCN to a 20 mL scintillation vial charged with 4'-bromoacetophenone (746.6 mg, 3.75 mmol), methanol (180.2 mg, 5.62 mmol), quinuclidine (458.6 mg, 4.12 mmol), dtbbpy (50.3 mg, 188 μmol), and NiCl<sub>2</sub>(dme) (41.3 mg, 188 μmol). The vial was sealed with electrical tape and sonicated at ambient temperature for 30 minutes before being passed through a 0.22 μm PTFE syringe filter. A 5.0 mL aliquot of the solution was drawn and transferred to a divided H-cell for each measurement. Cathodic galvanostatic electrolysis was performed using a glassy carbon rod working electrode (3.0 mm diameter) wrapped with PTFE tape to expose only ~1 cm of its total length to the solution. A non-aqueous Ag<sup>+</sup>/Ag reference electrode and reticulated vitreous carbon counter electrode were used. The same working electrode was used for each reaction and washed with 3 × 2 mL MeCN between electrolyses to ensure a consistent surface area. The electrolysis time was adjusted such that 0.90 C of charge was passed in each experiment. The solution was taken from the cathodic compartment at the completion of electrolysis and the solvent removed *in vacuo*. 1.0 mL of a solution containing 1,3-benzodioxole in CD<sub>3</sub>CN was added to dissolve the residue and product yield was determined by <sup>1</sup>H NMR against 1,3-benzodioxole. Each reaction was carried out in triplicate. The faradaic yields are shown in Table 2.1 along with average percent yields obtained under each condition as determined against 1,3-benzodioxole.

**Catalytic activity without photo- or electrochemical activation.** 2.0 mL of CD<sub>3</sub>CN was added to an amber vial charged with 4'-bromoacetophenone (99.5 mg, 0.5 mmol), methanol (24.0 mg, 0.75 mmol), dtbbpy (6.7 mg, 0.025 mmol), NiCl<sub>2</sub>(dme) (5.5 mg, 0.025 mmol), quinuclidine (61.1 mg, 0.55 mmol), and 1,3-benzodioxole as an internal standard. The reaction mixture was stirred for 30 min with rigorous exclusion of light and passed through a 0.22 μm PTFE syringe filter. A 1.0 mL aliquot was drawn and added to an amber vial charged with [Ir(dF-CF<sub>3</sub>-ppy)<sub>2</sub>(dtbbpy)]PF<sub>6</sub> (2.8 mg, 2.5 μmol). Both the solution containing the Ir photocatalyst and the remainder of that without were transferred to two separate J. Young NMR tubes wrapped with

aluminum foil.  $^1\text{H}$  NMR spectra taken after three days showed no product formation from either sample.

**Photochemical activity in the absence of the Ir photocatalyst.** 2.0 mL of  $\text{CD}_3\text{CN}$  was added to an amber vial charged with 4'-bromoacetophenone (99.5 mg, 0.5 mmol), methanol (24.0 mg, 0.75 mmol), dtbbpy (6.7 mg, 0.025 mmol),  $\text{NiCl}_2(\text{dme})$  (5.5 mg, 0.025 mmol), quinuclidine (61.1 mg, 0.55 mmol), and 1,3-benzodioxole as an internal standard. The reaction mixture was stirred for 30 min with rigorous exclusion of light and passed through a 0.22  $\mu\text{m}$  PTFE syringe filter. A 1.0 mL aliquot was drawn, transferred to a J. Young NMR tube, and placed before a blue LED light source with fan cooling. The product yield was measured to be 48% by  $^1\text{H}$  NMR against 1,3-benzodioxole after 24 h of irradiation.

**Photochemical activity in the absence of quinuclidine.** 3.0 mL of  $\text{CD}_3\text{CN}$  was added to an amber vial charged with 4'-bromoacetophenone (150 mg, 0.75 mmol), methanol (36 mg, 1.12 mmol), dtbbpy (10 mg, 0.038 mmol),  $\text{NiCl}_2(\text{dme})$  (8.2 mg, 0.038 mmol), and 1,3-benzodioxole as an internal standard. The reaction mixture was stirred for 30 min with rigorous exclusion of light and passed through a 0.22  $\mu\text{m}$  PTFE syringe filter. A 1.0 mL aliquot was drawn and added to a scintillation vial charged with  $\text{K}_2\text{CO}_3$  (38 mg, 0.28 mmol) and  $[\text{Ir}(\text{dF-CF}_3\text{-ppy})_2(\text{dtbbpy})][\text{PF}_6]$  (2.8 mg, 2.5  $\mu\text{mol}$ ). The vial was sealed with electrical tape and placed before a blue LED light source with fan cooling. The product yield was measured to be 37% by  $^1\text{H}$  NMR against 1,3-benzodioxole after 24 h of irradiation.

**Time-dependence of the faradaic yield.** To exclude the possibility that the trend observed in the right panel of Figure 2.22 is due to changes in electrolysis time, we decided to measure the faradaic yield under cathodic galvanostatic electrolysis at 0.5 mA for different lengths of time. The reaction mixtures were prepared by adding 16 mL of a 0.1 M  $n\text{-Bu}_4\text{NBF}_4$  electrolyte solution in MeCN to a 20 mL scintillation vial charged with 4'-bromoacetophenone (746.6 mg, 3.75 mmol), methanol (180.2 mg, 5.62 mmol), quinuclidine (458.6 mg, 4.12 mmol), dtbbpy (50.3 mg, 188  $\mu\text{mol}$ ), and  $\text{NiCl}_2(\text{dme})$  (41.3 mg, 188  $\mu\text{mol}$ ). The vial was sealed with electrical tape and sonicated at ambient temperature for 30 min before being passed through a

0.22  $\mu\text{m}$  PTFE syringe filter. A 5.0 mL aliquot of the solution was drawn and transferred to a divided H-cell for each measurement. Cathodic galvanostatic electrolysis was performed using a glassy carbon rod working electrode (3.0 mm diameter) wrapped with PTFE tape to expose only  $\sim 1$  cm of its total length to the solution. A non-aqueous  $\text{Ag}^+/\text{Ag}$  reference electrode and reticulated vitreous carbon counter electrode were used. The same working electrode was used for each reaction and washed with  $3 \times 2$  mL MeCN between electrolyses to ensure a consistent surface area. The solution was taken from the cathodic compartment at the completion of electrolysis and the solvent removed *in vacuo*. 1.0 mL of a solution containing 1,3-benzodioxole in  $\text{CD}_3\text{CN}$  was added to dissolve the residue and product yield was determined by  $^1\text{H}$  NMR against 1,3-benzodioxole. The calculated faradaic yield as a function of electrolysis time from 15 min to 90 min was invariant with a value of  $8.0 \pm 1.4\%$ .

**Dynamic Stern-Volmer measurements.** The nanosecond time-resolved emission spectroscopy setup was previously described in detail.<sup>27</sup> A Quanta-Ray Nd:YAG laser (SpectraPhysics) provides 3<sup>rd</sup> harmonic laser pulses at 355 nm with a repetition rate of 10 Hz and pulse width of  $\sim 10$  ns (FWHM). A further MOPO (SpectraPhysics) was used to provide tunable laser pulses in the visible region. Typical excitation energy was adjusted to  $\sim 1$  mJ/pulse. The dynamic Stern-Volmer quenching studies were carried out with 20  $\mu\text{M}$   $[\text{Ir}(\text{dF-CF}_3\text{-ppy})_2(\text{dtbbpy})][\text{PF}_6]$  in MeCN both in the presence and absence of quencher. All samples were prepared in a  $\text{N}_2$ -filled glovebox and sonicated for 30 min at ambient temperature before being passed through a 0.22  $\mu\text{m}$  PTFE syringe filter. Different samples were obtained by sequentially diluting a stock solution of the quencher and photocatalyst with a solution containing only the photocatalyst. Measurements were taken with vigorous magnetic stirring. The emitted light was collected by a pair of lenses and sent to a spectrometer (Triax 320) where the selected emission wavelength could be detected. Typically, the signal at 500 nm was selected and recorded by a PMT coupled to an oscilloscope (LeCroy 9384CM). The emission decays were fitted with mono-exponential functions and the lifetimes ( $\tau$ ) were extracted accordingly. The results of Stern-

Volmer dynamic quenching of the Ir(III) photocatalyst excited state by quinuclidine (— pink) and (dtbbpy)NiCl<sub>2</sub> (— blue) are shown in Figure 2.4.

**Single-wavelength kinetic studies and transient absorption spectroscopy.** All samples were prepared in a N<sub>2</sub>-filled glovebox and sonicated for 30 min at ambient temperature before being passed through a 0.22 μm PTFE syringe filter. For single-wavelength kinetic studies, samples containing different concentrations of the additive under study (quinuclidine or (dtbbpy)NiCl<sub>2</sub>) were obtained by sequential dilution of a concentrated stock solution including all compounds with a solution which excluded the additive. The samples were sparged with N<sub>2</sub> gas in a 40 mL volatile organic analyte sampling vial (Restek) during experiments and flown through a 1.0 cm flow cell (Starna) with a peristaltic pump for spectral acquisition. Single-wavelength kinetic studies for probing the stability of complex **1** are shown in Figure 2.11. The time-resolved TA spectra for a solution containing [Ir(dF-CF<sub>3</sub>-ppy)<sub>2</sub>(dtbbpy)]-[PF<sub>6</sub>] and quinuclidine in the presence of (dtbbpy)NiCl<sub>2</sub> is shown in Figure 2.8.

**Cyclic voltammetry and spectroelectrochemistry.** All electrochemical experiments were performed with a CH Instruments 760D Electrochemical Workstation (Austin, Texas) and CHI Version 10.03 software in a N<sub>2</sub>-filled glovebox. The studied compounds were dissolved in an electrolyte solution containing 0.1 M *n*-Bu<sub>4</sub>NBF<sub>4</sub> in MeCN. A three-electrode undivided cell configuration with a Pt wire counter electrode and a non-aqueous Ag<sup>+</sup>/Ag reference electrode was used for all cyclic voltammetry (CV) experiments. All working electrodes were sequentially polished on felt using diamond pastes of 3 μm and 1 μm before use. The CV of a 1 mM solution of ferrocene (Fc) was taken at the start of every experiment. Spectroelectrochemical measurements were performed using a 0.5 mm thin-layer quartz cuvette with a Pt mesh working electrode, non-aqueous Ag<sup>+</sup>/Ag reference electrode, and Pt wire counter electrode. All samples were first sonicated for 30 minutes at ambient temperature and subsequently passed through a 0.22 μm PTFE syringe filter. The UV-vis absorption spectra were recorded with OceanView 1.4.1 coupled with a light source (Ocean Optics DT-MINI-2GS) and spectrometer (Ocean Optics,



USB4000). The CV for  $[\text{Ir}(\text{dF-CF}_3\text{-ppy})_2(\text{dtbbpy})][\text{PF}_6]$  and spectroelectrochemistry for the complex's reduction are shown in Figures 2.9 and 2.7, respectively.

**In situ spectroscopic monitoring of the photoredox reaction.** We designed the apparatus shown in Figure 2.12 to probe transient intermediates that accumulate during the photochemical reaction. A focusing lens ( $f = 4 \text{ cm}$ ) was placed before a Kessil A160WE Controllable LED Aquarium Light, which was used to excite the sample placed inside the holder coupled to a S.I. Photonics Model 400 Series UV-vis spectrophotometer equipped with a deuterium light source and charge-coupled device (CCD) detector. All spectra were blank-corrected against the appropriate solvent. The sample solutions were prepared by adding 4 mL MeCN to a 20 mL scintillation vial charged with 4'-bromoacetophenone (199.0 mg, 1.0 mmol), 1-hexanol (133.2 mg, 1.5 mmol), quinuclidine (122.3 mg, 1.1 mmol), dtbbpy (13.4 mg, 50  $\mu\text{mol}$ ),  $\text{NiCl}_2(\text{dme})$  (11.0 mg, 50  $\mu\text{mol}$ ), and  $[\text{Ir}(\text{dF-CF}_3\text{-ppy})_2(\text{dtbbpy})][\text{PF}_6]$  (11.2 mg, 10  $\mu\text{mol}$ ). The vial was then sealed with electrical tape and sonicated for 30 minutes at ambient temperature, before being passed through a 0.22  $\mu\text{m}$  PTFE syringe filter. The solution was then transferred to a 1.0 cm quartz cuvette equipped with a magnetic stir bar for spectroscopic measurements.

**Comproportionation to prepare the paramagnetic Ni intermediate 1.** Comproportionation studies were carried out in a  $\text{N}_2$ -filled glovebox by the dropwise addition of 2 mL of a 300  $\mu\text{M}$  MeCN solution of  $\text{Ni}(\text{dtbbpy})(\text{cod})$  to 2 mL of one containing 5 mM of  $(\text{dtbbpy})\text{NiCl}_2$  in the presence and absence of quinuclidine (275 mM). The resulting samples were left to stir for 5 minutes before being passed through a 0.22  $\mu\text{m}$  PTFE syringe filter. Absorption spectra were collected with a 0.5 mm quartz cell using a spectrophotometer equipped with a CCD detector.

**Stability of 1 towards dilution.** A stock solution of **1** was prepared *via* the dropwise addition of 5 mL of a 12.5 mM MeCN solution of  $\text{Ni}(\text{dtbbpy})(\text{cod})$  into 5 mL of a sample containing  $\text{NiCl}_2(\text{dme})$  (13.7 mg, 62.5  $\mu\text{mol}$ ), dtbbpy (16.8 mg, 62.7  $\mu\text{mol}$ ), and quinuclidine (152.9 mg, 1.38 mmol) that had been sonicated for 30 min at ambient temperature. The resulting dark green solution was left to stir for 30 min before being passed through a 0.22  $\mu\text{m}$  PTFE syringe filter.

This solution was then diluted 10× with solutions containing only 275 mM quinuclidine (Figure 2.17A, blue trace) and 275 mM quinuclidine in the presence of 12.5 mM (dtbbpy)NiCl<sub>2</sub> (Figure 2.17A, red trace). Absorption spectra were taken with a 1.0 cm quartz cuvette on a Varian Cary 5000 UV-vis-NIR spectrophotometer.

**EPR spectroscopy.** 5 mL of a MeCN solution containing Ni(dtbbpy)(cod), prepared from Ni(cod)<sub>2</sub> (34.4 mg, 0.125 mmol) and dtbbpy (33.6 mg, 0.125 mmol), were added dropwise in a N<sub>2</sub>-filled glovebox to a 5 mL sample containing (dtbbpy)NiCl<sub>2</sub> and quinuclidine, which was prepared by adding MeCN to a vial charged with (dme)NiCl<sub>2</sub> (137.3 mg, 0.625 mmol), dtbbpy (167.8 mg, 0.625 mmol), and quinuclidine (160 mg, 1.44 mmol) and sonicating for 30 min at ambient temperature. The dark green solution obtained after addition was left to stir for 30 min, passed through a 0.22 μm PTFE syringe filter, and transferred to an EPR tube. The EPR spectrum was collected on a frozen solution at 77 K.

**Measurement of the turnover number (TON) with the Ni(I) intermediate.** 1 mL of a solution in MeCN containing 12.5 mM Ni(dtbbpy)(cod) and 275 mM quinuclidine was prepared and added dropwise to 2 mL of a sample containing 18.8 mM (dtbbpy)NiCl<sub>2</sub> and 275 mM quinuclidine to give an 8.3 mM solution of **1** assuming a 1:2 stoichiometry for the conversion of Ni(0) into **1**. The dark green solution was stirred for 30 min before being passed through a 0.22 μm PTFE syringe filter. 0.6 mL of this concentrated sample was diluted with 5 mL of a MeCN solution containing 18.8 mM (dtbbpy)NiCl<sub>2</sub> and 275 mM quinuclidine, corresponding to a 10× dilution. 0.5 mL of the 8.3 mM solution of **1** was added dropwise to 0.5 mL of a stirred solution of substrate in MeCN containing 250 mM 4'-bromoacetophenone, 375 mM methanol, 275 mM quinuclidine, and 12.5 mM (dtbbpy)NiCl<sub>2</sub>. Similarly, 5.0 mL of the 0.83 mM solution was added dropwise to 5.0 mL of an identical substrate solution. Both samples were then left to stir for 30 min at ambient temperature before the solvent was removed *in vacuo*. 1.0 mL of a solution containing 1,3-benzodioxole in CD<sub>3</sub>CN was added to dissolve the residue and product yield was determined by <sup>1</sup>H NMR against 1,3-benzodioxole. Each measurement was carried out in duplicate. The TON was found to be 2.1 at 8.3 mM and 13.4 at 0.83 mM of **1**.

**Measurement of the turnover number (TON) with Ni(0).** 0.5 mL of a solution in MeCN containing 8.3 mM Ni(dtbbpy)(cod) and 275 mM quinuclidine were prepared and added dropwise to 0.5 mL of a substrate solution containing 250 mM 4'-bromoacetophenone, 375 mM methanol, and 275 mM quinuclidine. Similarly, 5.0 mL of a solution containing 0.83 mM Ni(dtbbpy)(cod) and 275 mM quinuclidine were added dropwise to 5.0 mL of an identical substrate solution. Both samples were then left to stir at ambient temperature for 30 min before the solvent was removed *in vacuo*. 1.0 mL of a solution containing 1,3-benzodioxole in CD<sub>3</sub>CN was added to dissolve the residue and product yield was determined by <sup>1</sup>H NMR against 1,3-benzodioxole. The TON was found to be 2.0 at 8.3 mM of Ni(0) and 3.9 at 0.83 mM of Ni(0).

**Oxidative addition studies.** 0.5 mL of a MeCN solution containing 12.5 mM Ni(dtbbpy)(cod) and 275 mM quinuclidine was added dropwise to 5.8 mL of one containing 12.5 mM (dtbbpy)NiCl<sub>2</sub> and 275 mM quinuclidine. The dark green solution was left to stir for 30 min at ambient temperature before being passed through a 0.22 μm PTFE syringe filter and then added dropwise to a solution of 250 mM 2-bromotoluene. The resulting orange solution was stirred for 20 min and the absorption spectrum was taken with a 2 mm quartz cuvette on a Varian Cary 5000 UV-vis-NIR spectrophotometer (Figure 2.19A). This was compared to the spectrum of a solution containing 1.0 mM (dtbbpy)Ni(*o*-tolyl)(Br) in the presence of 250 mM 2-bromotoluene, 275 mM quinuclidine, and 12.5 mM (dtbbpy)NiCl<sub>2</sub> (Figure 2.19B). A similar spectrum is obtained in both cases, suggesting that oxidative addition to the low-valent Ni species generated from **1** forms a Ni(II) aryl species as the terminal product, consistent with a rapid comproportionation reaction between the putative monomeric Ni(I) halide and Ni(III) aryl intermediates.

**Computational studies on the quinuclidine dimer radical cation.** Quantum-mechanical calculations were carried out using density functional theory (DFT) as implemented in Gaussian 16.<sup>28</sup> Geometry optimizations (tight convergence) employed the hybrid functional ωB97XD, which accounts for dispersion and long-range interactions,<sup>29,30</sup> in combination with the polarized triple-zeta basis, def2-TZVP.<sup>31</sup> Solvation effects in MeCN were included *via* the conductor-like polarizable continuum model.<sup>32</sup> All optimized structures were verified by frequency calculations,

which served to calculate thermodynamic properties at  $T = 298.15$  K. In addition, time-dependent DFT in Gaussian 16 calculated the 30 lowest-energy vertical excitation energies at the same level of theory for the quinuclidine dimer radical cation.

**Computational studies on complex 1.** To additionally support that the crystallographic result for complex **1** is consistent with the intermediate which was spectroscopically observed, we computationally optimized the refined crystal structure in vacuum at the  $\omega$ B97XD/6-31G\* level of theory, whereby we assumed quartet multiplicity as supported by EPR. The optimized molecular structure shows a Ni-Ni bond length of 2.41 Å, slightly underestimating the crystallographic distance of 2.44 Å. Furthermore, the optimized structure differs in the angle between the two bipyridine ligands. This can be quantified by the distance between the *ipso* carbons bearing <sup>t</sup>Bu groups on both bipyridine ligands, which is found to be 4.31 Å in the computed structure, in contrast to 4.89 Å in the crystal structure.

Based on the optimized structure, we carried out time-dependent DFT calculations at the same level of theory to compute transitions to the lowest 20 excited states. The corresponding absorption spectrum of the Ni dimer (Figure 2.15A) shows visible and near-IR transitions, in agreement with the experimentally determined absorption spectrum. The most intense low-energy transition is calculated to be at 732 nm, while the experimentally observed maximum appears at 832 nm (a difference of  $1641\text{ cm}^{-1}$ , comparable to the underestimation for the quinuclidine dimer radical cation of  $2454\text{ cm}^{-1}$ ). This transition is found to result in a metal-to-ligand charge transfer (MLCT) state (Figure 2.15B), which is likely very sensitive to the Ni-Ni distance. Taking into account that the crystallographic structure displays a longer Ni-Ni bond length, we can tentatively attribute the quantitative difference in the calculated and measured absorption spectrum to an underestimation of the Ni-Ni bond length in our theory. While more theoretical work is required to fully understand the optical properties of complex **1**, our results support the assignment that the observed near-IR absorption features are due to a dimeric Ni compound.

**X-ray crystallography.** X-ray diffraction data were collected on a Bruker three-circle platform goniometer equipped with an Apex II CCD detector and Oxford Cryosystems Cryostat cooling device using  $\varphi$  and  $\omega$  scans. A fine-focus sealed tube Mo K $\alpha$  (0.71073 Å) X-ray source was used. The crystals were mounted on a cryoloop using Paratone oil. Data were integrated using SAINT and multi-scan absorption correction was applied using SADABS. The structures were solved by intrinsic phasing using SHELXT (APEX3 program suite, 2016) and refined against  $F^2$  on all data by full matrix least squares with SHELXL. All non-hydrogen atoms, including the disorder fragments, were located in the difference-Fourier maps and refined anisotropically. Hydrogen atoms were added at calculated positions and refined with a riding model. The restraints on bond lengths (SADI/SAME) and atomic displacement parameters (SIMU/RIGU) have been applied on each pair of disorder fragments as necessary.

In the case of the quinuclidine-bound (dtbbpy)NiCl<sub>2</sub> dimer, a MeCN solution was prepared with 12.5 mM (dtbbpy)NiCl<sub>2</sub> and 275 mM quinuclidine. The solution was sonicated for 15 min and then filtered through a 0.22  $\mu$ m PTFE syringe filter. Crystals suitable for X-ray diffraction were then grown by the slow evaporation of the filtrate solution in the presence of toluene at -25 °C.

In the case of compound **1**, a MeCN solution was prepared by the dropwise addition of 5 mL of a 5 mM solution of Ni(dtbbpy)(cod) to NiCl<sub>2</sub>(dme) (30.9 mg), dtbbpy (37.7 mg), and quinuclidine (153 mg) in 5 mL MeCN. This solution was then washed with 5  $\times$  5 mL pentane and quinuclidine (153 mg) was added to the MeCN fraction, from which crystals of **1** were grown at -25 °C. The structure was modelled as a two-part inversion twin.

**Table 2.2.** Crystal data for the quinuclidine-bound (dtbbpy)NiCl<sub>2</sub> dimer.

Empirical formula	C <sub>64</sub> H <sub>90</sub> Cl <sub>4</sub> N <sub>6</sub> Ni <sub>2</sub>
Formula weight	1202.63
T (K)	100(2)
$\lambda$ (Å)	0.71073
Crystal system	Orthorhombic
Space group	<i>C</i> 222 <sub>1</sub>
<i>a</i> (Å)	11.0338(8)
<i>b</i> (Å)	21.188(2)
<i>c</i> (Å)	25.9299(19)
$\alpha$ (°)	90
$\beta$ (°)	90
$\gamma$ (°)	90
<i>V</i> (Å <sup>3</sup> )	6062.0(9)
<i>Z</i>	4
$\rho_{\text{calcd}}$ (Mg/m <sup>3</sup> )	1.318
$\mu$ (mm <sup>-1</sup> )	0.842
$\theta$ range for data collection (°)	2.483 to 25.090
Index ranges	$-13 \leq h \leq 13, -25 \leq k \leq 25, -30 \leq \ell \leq 30$
Reflections collected	79611
Independent reflns ( <i>R</i> <sub>int</sub> )	5383 (0.0594)
Completeness to $\theta_{\text{max}}$	99.7%
Data/restraints/parameters	5383 / 212 / 365
GOF on <i>F</i> <sup>2</sup>	1.090
R1	0.0357
wR2	0.0831
Largest diff. peak, hole (e Å <sup>-3</sup> )	0.590, -0.424

**Table 2.3.** Crystal data for 1.

Empirical formula	C <sub>114</sub> H <sub>169</sub> Cl <sub>6</sub> N <sub>19</sub> Ni <sub>4</sub>
Formula weight	2253.17
T (K)	100(2)
$\lambda$ (Å)	0.71073
Crystal system	Orthorhombic
Space group	<i>Pca2<sub>1</sub></i>
<i>a</i> (Å)	28.293(3)
<i>b</i> (Å)	12.7260(16)
<i>c</i> (Å)	33.847(4)
$\alpha$ (°)	90
$\beta$ (°)	90
$\gamma$ (°)	90
<i>V</i> (Å <sup>3</sup> )	12187(2)
<i>Z</i>	4
$\rho_{\text{calcd}}$ (Mg/m <sup>3</sup> )	1.228
$\mu$ (mm <sup>-1</sup> )	0.792
$\theta$ range for data collection (°)	2.31 to 25.02
Index ranges	$-33 \leq h \leq 33, -15 \leq k \leq 15, -40 \leq l \leq 39$
Reflections collected	99146
Independent reflns ( <i>R</i> <sub>int</sub> )	21501 (0.0702)
Completeness to $\theta_{\text{max}}$	99.6%
Data/restraints/parameters	21501 / 1851 / 1743
GOF on <i>F</i> <sup>2</sup>	1.095
R1	0.0600
wR2	0.1421
Largest diff. peak, hole (e Å <sup>-3</sup> )	0.519, -0.531

## 2.9 Acknowledgements

Dr. Yangzhong Qin assisted with the spectroscopic work; Dr. Christoph Schnedermann assisted with the computational studies; Drs. Shao-liang Zheng, Miguel Gonzalez, and Serge Ruccolo assisted with X-ray crystallography; and Dr. Cyrille Costentin assisted with the interpretation of electrochemical data.

## 2.10 References

1. Douglas, J. J.; Sevrin, M. J.; Stephenson, C. R. Visible Light Photocatalysis: Applications and New Disconnections in the Synthesis of Pharmaceutical Agents. *J. Org. Proc. Res. Develop.* **2016**, *20*, 1134–1147.
2. Brown, D. G.; Boström, J. Analysis of Past and Present Synthetic Methodologies on Medicinal Chemistry: Where Have All the New Reactions Gone? *J. Med. Chem.* **2016**, *59*, 4443–4458.
3. Francke, R.; Little, R. D. Redox Catalysis in Organic Electrosynthesis: Basic Principles and Recent Developments. *Chem. Soc. Rev.* **2014**, *43*, 2492–2521.
4. Horn, E. J.; Rosen, B. R.; Baran, P. S. Synthetic Organic Electrochemistry: An Enabling and Innately Sustainable Method. *ACS Cent. Sci.* **2016**, *2*, 302–308.
5. Shaw, M. H.; Twilton, J.; MacMillan, D. W. C. Photoredox Catalysis in Organic Chemistry. *J. Org. Chem.* **2016**, *81*, 6898–6926.
6. Cismesia, M. A.; Yoon, T. P. Characterizing Chain Processes in Visible Light Photoredox Catalysis. *Chem. Sci.* **2015**, *6*, 5426–5434.
7. Calvo-Flores, F. G. Sustainable Chemistry Metrics. *ChemSusChem* **2009**, *2*, 905–919.
8. Jimenez-Gonzalez, C.; Constable, D. J. C.; Ponder, C. S. Evaluating the "Greenness" of Chemical Processes and Products in the Pharmaceutical Industry-A Green Metrics Primer. *Chem. Soc. Rev.* **2012**, *41*, 1485–1498.
9. Oelgemöller, M. Solar Photochemical Synthesis: From the Beginnings of Organic Photochemistry to the Solar Manufacturing of Commodity Chemicals. *Chem. Rev.* **2016**, *116*, 9664–9682.
10. Oderinde, M. S.; Varela-Alvarez, A.; Aquila, B.; Robbins, D. W.; Johannes, J. W. Effects of Molecular Oxygen, Solvent, and Light on Iridium-Photoredox/Nickel Dual-Catalyzed Cross-Coupling Reactions. *J. Org. Chem.* **2015**, *80*, 7642–7651.
11. Marchini, M.; Bergamini, G.; Cozzi Pier, G.; Ceroni, P.; Balzani, V. Photoredox Catalysis: The Need to Elucidate the Photochemical Mechanism. *Angew. Chem. Int. Ed.* **2017**, *56*, 12820–12821.
12. Studer, A.; Curran, D. P. The Electron is a Catalyst. *Nat. Chem.* **2014**, *6*, 765–773.
13. Chanon, M. Electron-Transfer-Induced Chain Reactions and Catalysis. Building Bridges between Inorganic, Organic, and Organometallic Substrates. *Acc. Chem. Res.* **1987**, *20*, 214–221.
14. Twilton, J.; Le, C.; Zhang, P.; Shaw, M. H.; Evans, R. W.; MacMillan, D. W. C. The Merger of Transition Metal and Photocatalysis. *Nat. Rev. Chem.* **2017**, *1*, 0052.
15. Shields, B. J.; Kudisch, B.; Scholes, G. D.; Doyle, A. G. Long-Lived Charge-Transfer States of Nickel(II) Aryl Halide Complexes Facilitate Bimolecular Photoinduced Electron Transfer. *J. Am. Chem. Soc.* **2018**, *140*, 3035–3039.
16. Terrett, J. A.; Cuthbertson, J. D.; Shurtleff, V. W.; MacMillan, D. W. C. Switching on Elusive Organometallic Mechanisms with Photoredox Catalysis. *Nature* **2015**, *524*, 330–334.



17. Li, C.; Kawamata, Y.; Nakamura, H.; Vantourout Julien, C.; Liu, Z.; Hou, Q.; Bao, D.; Starr Jeremy, T.; Chen, J.; Yan, M.; Baran P. S. Electrochemically Enabled, Nickel-Catalyzed Amination. *Angew. Chem. Int. Ed.* **2017**, *56*, 13088-13093.
18. Halpern, A. M.; Forsyth, D. A.; Nosowitz, M. Flash Photolysis of Saturated Amines in Acetonitrile Solution at 248 nm: Formation of Radical Cations. *J. Phys. Chem.* **1986**, *90*, 2677-2679.
19. Bill, E.; Ding, X.-Q.; Bominaar, E. L.; Trautwein, A. X.; Winkler, H.; Mandon, D.; Weiss, R.; Gold, A.; Jayaraj, K.; Hatfield, W. E.; Kirk, M. L. Evidence for Variable Metal-Radical Spin Coupling in Oxoferrylporphyrin Cation Radical Complexes. *Eur. J. Biochem.* **1990**, *188*, 665-672.
20. Kostka, K. L.; Fox, B. G.; Hendrich, M. P.; Collins, T. J.; Rickard, C. E. F.; Wright, L. J.; Munck, E. High-Valent Transition Metal Chemistry. Mossbauer and EPR Studies of High-Spin (S = 2) Iron(IV) and Intermediate-Spin (S = 3/2) Iron(III) Complexes with a Macrocyclic Tetraamido-N Ligand. *J. Am. Chem. Soc.* **1993**, *115*, 6746-6757.
21. Cloutier, J.-P.; Zargarian, D. Functionalization of the Aryl Moiety in the Pincer Complex (NCN)Ni<sup>III</sup>Br<sub>2</sub>: Insights on Ni<sup>III</sup>-Promoted Carbon-Heteroatom Coupling. *Organometallics* **2018**, *37*, 1446-1455.
22. Pangborn, A. B.; Giardello, M. A.; Grubbs, R. H.; Rosen, R. K.; Timmers, F. J. Safe and Convenient Procedure for Solvent Purification. *Organometallics* **1996**, *15*, 1518-1520.
23. Terrett, J. A.; Cuthbertson, J. D.; Shurtleff, V. W.; MacMillan, D. W. C. Switching on Elusive Organometallic Mechanisms with Photoredox Catalysis. *Nature* **2015**, *524*, 330-334.
24. Shields, B. J.; Kudisch, B.; Scholes, G. D.; Doyle, A. G. Long-Lived Charge-Transfer States of Nickel(II) Aryl Halide Complexes Facilitate Bimolecular Photoinduced Electron Transfer. *J. Am. Chem. Soc.* **2018**, *140*, 3035-3039.
25. Shields, B. J.; Doyle, A. G. Direct C(sp<sup>3</sup>)-H Cross Coupling Enabled by Catalytic Generation of Chlorine Radicals. *J. Am. Chem. Soc.* **2016**, *138*, 12719-12722.
26. C. G. Hatchard, C. A. P. A New Sensitive Chemical Actinometer - II. Potassium Ferrioxalate as a Standard Chemical Actinometer. *Proc. R. Soc. Lond. A Math. Phys. Sci.* **1956**, *235*, 518-536.
27. Holder, P. G.; Pizano, A. A.; Anderson, B. L.; Stubbe, J.; Nocera, D. G. Deciphering Radical Transport in the Large Subunit of Class I Ribonucleotide Reductase. *J. Am. Chem. Soc.* **2012**, *134*, 1172-1180.
28. Frisch, M. J.; Trucks, G. W.; Schlegel, H. B.; Scuseria, G. E.; Robb, M. A.; Cheeseman, J. R.; Scalmani, G.; Barone, V.; Petersson, G. A.; Nakatsuji, H.; Li, X.; Caricato, M.; Marenich, A. V.; Bloino, J.; Janesko, B. G.; Gomperts, R.; Mennucci, B.; Hratchian, H. P.; Ortiz, J. V.; Izmaylov, A. F.; Sonnenberg, J. L.; Williams; Ding, F.; Lipparini, F.; Egidi, F.; Goings, J.; Peng, B.; Petrone, A.; Henderson, T.; Ranasinghe, D.; Zakrzewski, V. G.; Gao, J.; Rega, N.; Zheng, G.; Liang, W.; Hada, M.; Ehara, M.; Toyota, K.; Fukuda, R.; Hasegawa, J.; Ishida, M.; Nakajima, T.; Honda, Y.; Kitao, O.; Nakai, H.; Vreven, T.; Throssell, K.; Montgomery Jr., J. A.; Peralta, J. E.; Ogliaro, F.; Bearpark, M. J.; Heyd, J. J.; Brothers, E. N.; Kudin, K. N.; Staroverov, V. N.; Keith, T. A.; Kobayashi, R.; Normand, J.; Raghavachari, K.; Rendell, A. P.; Burant, J. C.; Iyengar, S. S.; Tomasi, J.; Cossi, M.; Millam, J. M.; Klene, M.; Adamo, C.; Cammi, R.; Ochterski, J. W.; Martin, R. L.; Morokuma, K.; Farkas, O.; Foresman, J. B.; Fox, D. J. *Gaussian 16 Rev. B.01*, Wallingford, CT, 2016.

29. Chai, J.-D.; Head-Gordon, M. Long-Range Corrected Hybrid Density Functionals with Damped Atom-Atom Dispersion Corrections. *Phys. Chem. Chem. Phys.* **2008**, *10*, 6615-6620.
30. Minenkov, Y.; Singstad, Å.; Occhipinti, G.; Jensen, V. R. The Accuracy of DFT-Optimized Geometries of Functional Transition Metal Compounds: A validation study of catalysts for olefin metathesis and other reactions in the homogeneous phase. *Dalton Trans.* **2012**, *41*, 5526-5541.
31. Weigend, F.; Ahlrichs, R. Balanced Basis Sets of Split Valence, Triple Zeta Valence and Auadruple Zeta Valence Quality for H to Rn: Design and assessment of accuracy. *Phys. Chem. Chem. Phys.* **2005**, *7*, 3297-3305.
32. Barone, V.; Cossi, M. Quantum Calculation of Molecular Energies and Energy Gradients in Solution by a Conductor Solvent Model. *J. Phys. Chem. A* **1998**, *102*, 1995-2001.

*Page intentionally left blank*

## Chapter 3

# Mechanism, Optimization, and Generalization of the Photoredox Cross-Coupling Between Thiols and Aryl Halides

*Parts of this chapter have been published:*

Qin, Y.; Sun, R.; Gianoulis, N. P.; Nocera, D. G., Photoredox Nickel-Catalyzed C-S Cross-Coupling: Mechanism, Kinetics, and Generalization. *J. Am. Chem. Soc.* **2021**, *143*, 2005-2015.

### 3.1 Introduction

Photoredox generation of transition metal intermediates has emerged as a powerful strategy for promoting transformations that are otherwise difficult to access thermally.<sup>1-8</sup> A tandem approach of employing a photoredox catalyst to drive transition metal catalysis has been fruitful,<sup>9-15</sup> especially for effecting nickel-catalyzed carbon-heteroatom bond formation under mild conditions using simple and inexpensive ligands.<sup>16-25</sup> However, despite the prolific reports of new nickel photoredox methods, there have been relatively few experimental mechanistic studies due to reaction complexity.<sup>26-30</sup> The variety of potential reaction pathways in photoredox cross-coupling systems together with the accessibility of multiple oxidation states obfuscate the precise redox chemistry between the photocatalyst and the cross-coupling catalyst, and consequently, the nickel redox levels responsible for supporting catalysis. Lacking such a mechanistic understanding can impede reaction development and optimization, which often rely on time-consuming and labor-intensive trial-and-error reaction screening.

Thioethers are frequently encountered in natural bioproducts and pharmaceuticals. The potential bioactivity of thioethers in the treatment of diseases such as cancer and HIV<sup>31-35</sup> has motivated interest in developing effective methodologies for their synthesis.<sup>25, 34-43</sup> Recently, visible-light-driven photoredox nickel-catalysis has provided a new strategy to forge C-S bonds between (hetero)aryl iodides and thiols under mild conditions,<sup>25</sup> thus representing an important advance over traditional methods requiring high temperatures or strong bases.<sup>34-39</sup> Unlike other photoredox nickel-catalyzed cross-couplings between aryl bromides and alcohols, amines, or carboxylic acids,<sup>20-22</sup> where the nucleophile engages the nickel catalyst through a redox-neutral metalation-deprotonation sequence, the coupling of aryl iodides to thiols has been proposed to proceed through a 'radical' pathway via the photogeneration of thiyl radicals (Figure 3.1A),<sup>25</sup> thus circumventing the formation of free thiolate equivalents that are known to coordinatively inhibit catalysis.<sup>16, 35</sup> Conversely, computational studies have suggested an alternative 'oxidation state modulation' mechanism (Figure 3.1A) involving oxidative quenching of the excited iridium photocatalyst and the formation of a nickel thiolate from the deprotonation of coordinated thiol.<sup>44</sup> Both mechanisms invoke closed photocycles (quantum yield  $\Phi < 1$ ) requiring the

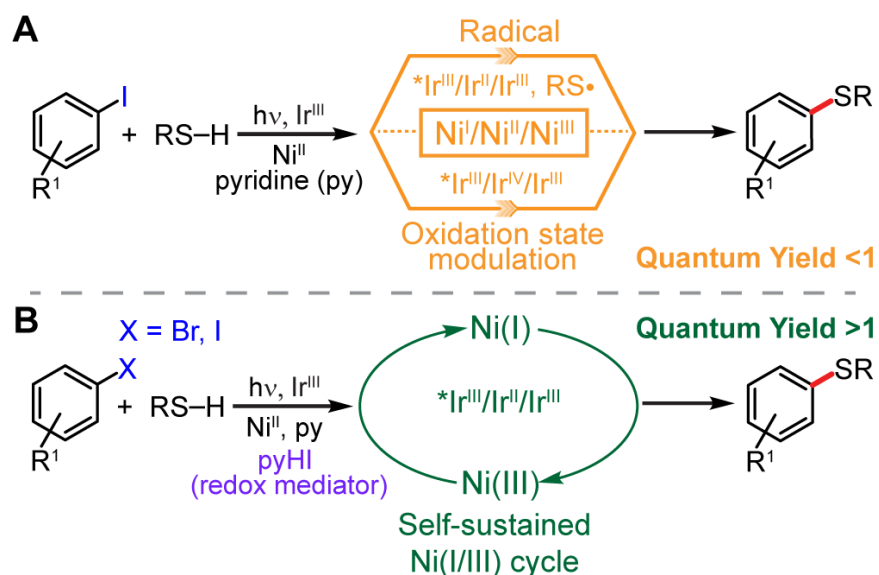


**Figure 3.1.** Mechanisms for C-S cross-coupling. (A) Proposed mechanisms for photoredox-mediated nickel-catalyzed aryl thiolation. (B) Self-sustained mechanism driven by a redox mediator as deduced from this work.

involvement of Ni(I), Ni(II), and Ni(III) intermediates for every turnover.<sup>25, 44</sup> This is in contradistinction to recent investigations of photoredox-mediated nickel-catalyzed cross-coupling of aryl bromides with alcohols,<sup>29, 45-46</sup> amines,<sup>30,45,46</sup> and carboxylic acids,<sup>45</sup> wherein  $\Phi > 1$  owing to a self-sustained Ni(I/III) dark cycle have been discovered. Whether a self-sustained Ni(I/III) cycle is also responsible for aryl thiolation warrants investigation because a thermally-sustained cycle will involve unique reaction intermediates that engender optimization strategies distinct from both of the previously proposed mechanisms (Figure 3.1A).<sup>25,44</sup>

We now report a comprehensive mechanistic study of the photoredox mediated nickel-catalyzed C-S cross-coupling (Figure 3.1B). Through a combination of time-resolved photophysical and photochemical techniques, we find that the photoredox mechanism is characterized by twelve rate constants associated with a thermally-sustained Ni(I/III) cycle with  $\Phi > 1$ . Nanosecond transient absorption spectroscopy permits the observation of the *in situ* formation and subsequent reactivity of a Ni(I) intermediate, along with a side reaction leading to thiyl radical formation. Furthermore, we identify the hitherto underappreciated, but nonetheless critical, roles of pyridinium iodide (pyHI), which is produced as a byproduct of cross-coupling.

We show that pyridinium iodide is essential in facilitating the photoredox transformation by: (i) quenching the excited photocatalyst; (ii) preventing the formation of nickel thiolate complexes that competitively absorb light; and (iii) acting as a redox mediator to efficiently generate Ni(I) from off-cycle Ni(II) species, thereby sustaining a productive Ni(I/III) catalytic cycle. By leveraging these mechanistic insights, we present a strategy to expand the substrate scope of this methodology, which has been restricted to only aryl iodides, to include aryl bromides, allowing for access to a class of electrophiles with higher availability and lower cost.

**Table 3.1.** Composition of key solutions used in kinetics studies.

Solution	Composition
S1	Ni(II) (10 mM) + py (200 mM) + thiol 2 <sup>a</sup> (150 mM)
S2	Ir(III) (150 μM) + pyHI (25 mM)
S3	S2 + py (200 mM) + thiol 2 <sup>a</sup> (150 mM)
S4	S3 + Ni(II) (10 mM)

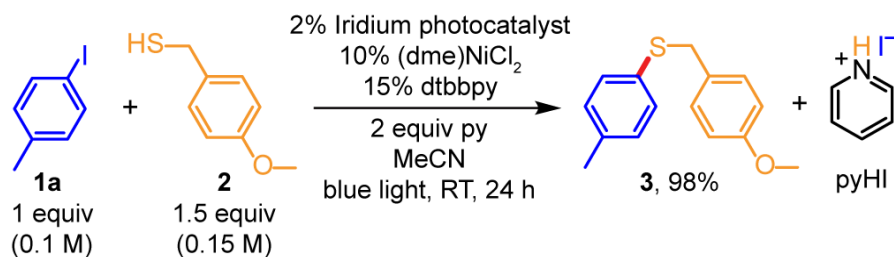
Ni(II) = (dtbbpy)NiCl<sub>2</sub>, dtbbpy = 4,4'-di-*tert*-butyl-2,2'-dipyridyl. py = pyridine. <sup>a</sup> thiol 2 = 4-methoxybenzyl mercaptan. pyHI = pyridinium iodide.

### 3.2 Quenching Studies

For convenience of presentation, Table 3.1 lists the compositions of key solutions used in this study. We undertook mechanistic investigation of the C-S cross-coupling by examining which reagents listed in Table 3.2 react with \*Ir(III) per steady-state and dynamic Stern-Volmer quenching. Pyridine does not quench \*Ir(III) (Figure 3.2). In the case of Ni(II), the steady-state  $K_{sv}$  cannot be accurately measured due to its strong and broad absorption, which overlaps with that of Ir(III) and thus requires inner-filter corrections (Figure 3.3 and see Materials and Methods). Steady-state Stern-Volmer quenching plots for reagents in Table 3.2 are shown in Figure 3.4. Ni(II) shows dynamic quenching with a rate constant of  $k_q = 7.8(3) \times 10^7 \text{ M}^{-1} \text{ s}^{-1}$ , which is ~2 orders of magnitude greater than that of any other individual component in the original reaction solution, including 4-iodotoluene (1a) and 4-methoxybenzyl mercaptan (2) (Table 3.2). Thiol compound 2 in the presence of 200 mM pyridine exhibits a quenching rate ~3 times higher than that of 2

alone. However, when concentrations of the reactants are considered, the overall contributions to the quenching of  $^*\text{Ir(III)}$  by the reactants ( $\text{Ni(II)}$ , **1a** and **2**) in the starting solution are comparable. The lifetime of  $^*\text{Ir(III)}$  in the reaction solution can be explicitly determined by monitoring the compound's emission decay at 500 nm ( $\lambda_{\text{exc}} = 430$  nm). For a fresh reaction solution, the measured lifetime was  $\tau = 450$  ns (Figure 3.5A). However, for a solution that was illuminated for 20 min under blue light, the lifetime fell below our instrumental time resolution (8 ns), indicating the *in situ* generation and accumulation of a byproduct that was an efficient quencher. In particular, the presence of an iodide substrate, thiol as a proton source (from its acid-base chemistry and PCET involvement in photoredox reactions<sup>47-49</sup>), and pyridine suggests the possibility of generating pyridinium iodide (pyHI). As shown in Table 3.2, pyHI is an exceptional quencher of  $^*\text{Ir(III)}$ ; the quenching rate constant of  $k_{\text{q,ET}} = 2.1(1) \times 10^{10} \text{ M}^{-1} \text{ s}^{-1}$  is over 2 orders of magnitude higher than that of  $\text{Ni(II)}$ . A similar quenching rate was obtained for tetrabutylammonium iodide (TBAI) (Figure 3.4D), suggesting that this unusually high quenching rate constant is due to the photooxidation of iodide ( $\text{I}^-$ ) by  $^*\text{Ir(III)}$ .

**Table 3.2.** Photoredox mediated nickel-catalyzed aryl thiolation and Stern-Volmer quenching studies.<sup>a</sup>



Reagent	$K_{\text{sv}} / \text{M}^{-1}$ (steady-state)	$K_{\text{sv}} / \text{M}^{-1}$ (dynamic)	$k_{\text{q}} / \text{M}^{-1} \text{ s}^{-1}$ (dynamic)
pyridine (py) <sup>b</sup>	-	-	-
<b>Ni(II)</b>	N.A. <sup>c</sup>	200(8)	$7.8(3) \times 10^7$
<b>1a</b>	1.5(1)	1.3(1)	$5.1(4) \times 10^5$
<b>2</b>	1.9(1)	2.4(2)	$1.1(1) \times 10^6$
<b>2 with py</b>	7.1(4)	7.6(5)	$3.4(2) \times 10^6$
pyHI	53383(3370)	54480(2243)	$2.1(1) \times 10^{10}$ <sup>d</sup>

<sup>a</sup> All reagent concentrations are referenced to a 0.1 M concentration of **1a**. <sup>b</sup> No quenching observed. <sup>c</sup> Not measured. <sup>d</sup>  $k_{\text{q,ET}}$  in kinetic modelling.



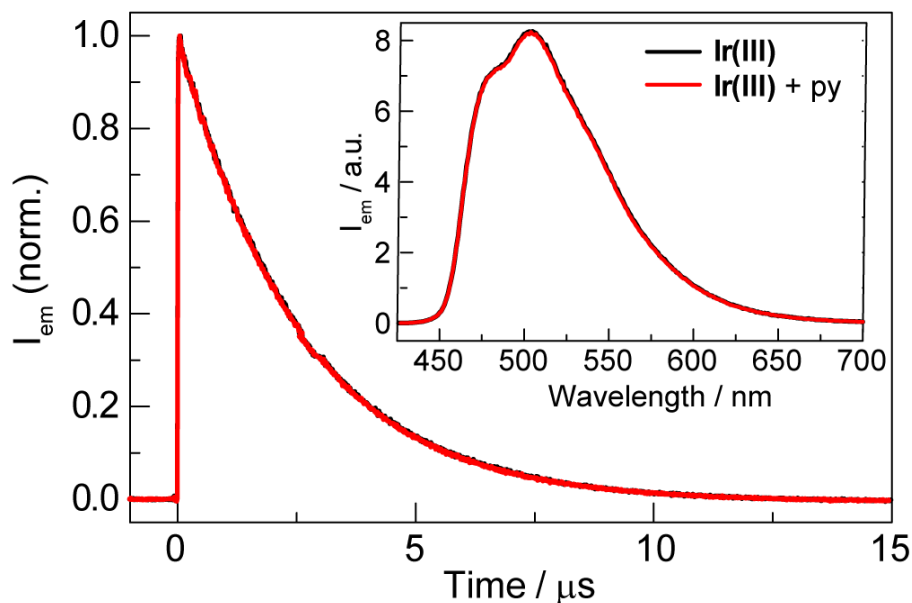


**Figure 3.2.** Emission decay and spectra of  $^*Ir(III)$ . Emission decay monitored at 500 nm for samples containing 50  $\mu M$  Ir(III) in the absence and presence of 200 mM pyridine ( $\lambda_{exc} = 355$  nm). The inset shows the corresponding steady-state emission spectra while exciting at 370 nm. The overlapped emission decays and steady-state emission spectra suggest that pyridine does not quench  $^*Ir(III)$ .

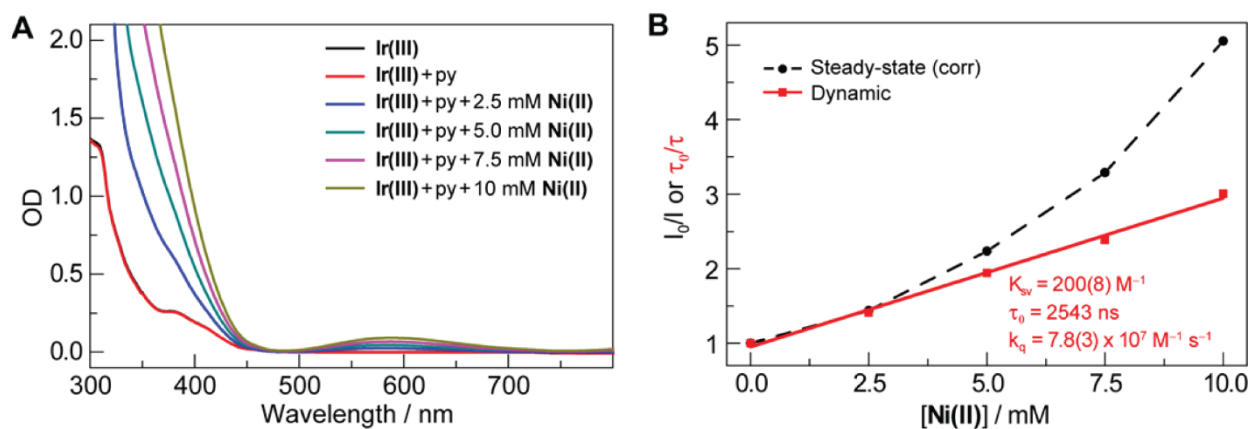


**Figure 3.3.** Stern-Volmer quenching of  $^*Ir(III)$  by Ni(II). (A) UV-vis absorption spectra of solutions containing 50  $\mu M$  Ir(III); 50  $\mu M$  Ir(III) and 200 mM pyridine; and 50  $\mu M$  Ir(III), 200 mM pyridine with various concentrations of Ni(II). The strong absorption spectrum of Ni(II) overlaps with the absorption spectrum of Ir(III), causing a significant inner filter effect. (B) Steady-state Stern-Volmer quenching plot (black) based on the corrected quenching ratio  $(I_0/I)_{corr}$  (see Materials and Methods), and dynamic Stern-Volmer quenching plot based on the emission lifetime  $\tau$ . The dynamic quenching plot was linearly fitted to extract the quenching rate constants.

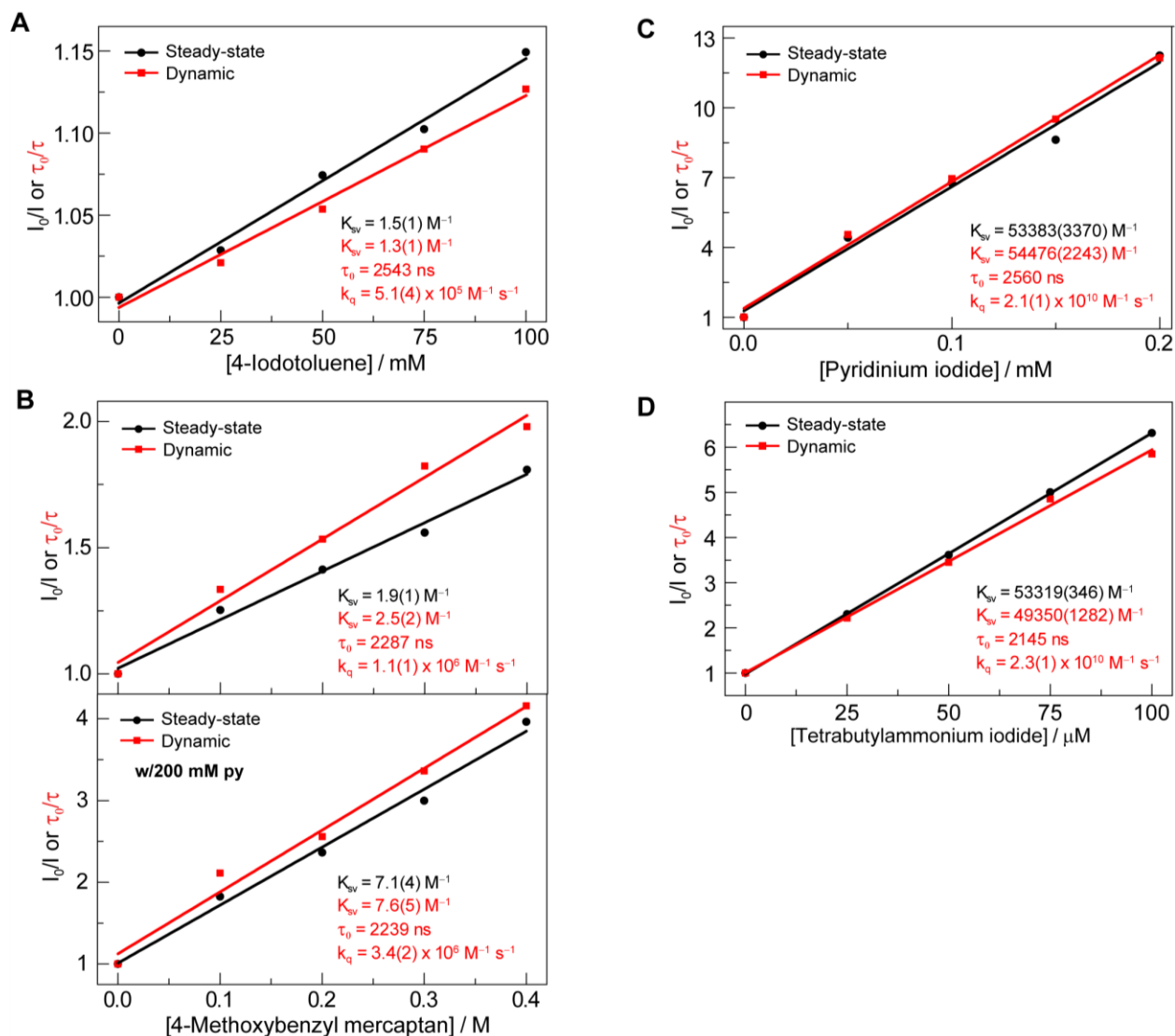


**Figure 3.4.** Stern-Volmer quenching of  $^*\text{Ir}(\text{III})$  by (A) 4-iodotoluene (1a), (B) 4-methoxybenzyl mercaptan (2) in the absence (top) and presence (bottom) of 200 mM pyridine, (C) pyridinium iodide and (D) tetrabutylammonium iodide. Steady-state (black) and dynamic (red) quenching plots match well, suggesting the absence of static quenching. Linear fitting was used to extract the quenching rate constants. The presence of pyridine in B (bottom) increases the quenching, possibly due to proton-coupled electron transfer.

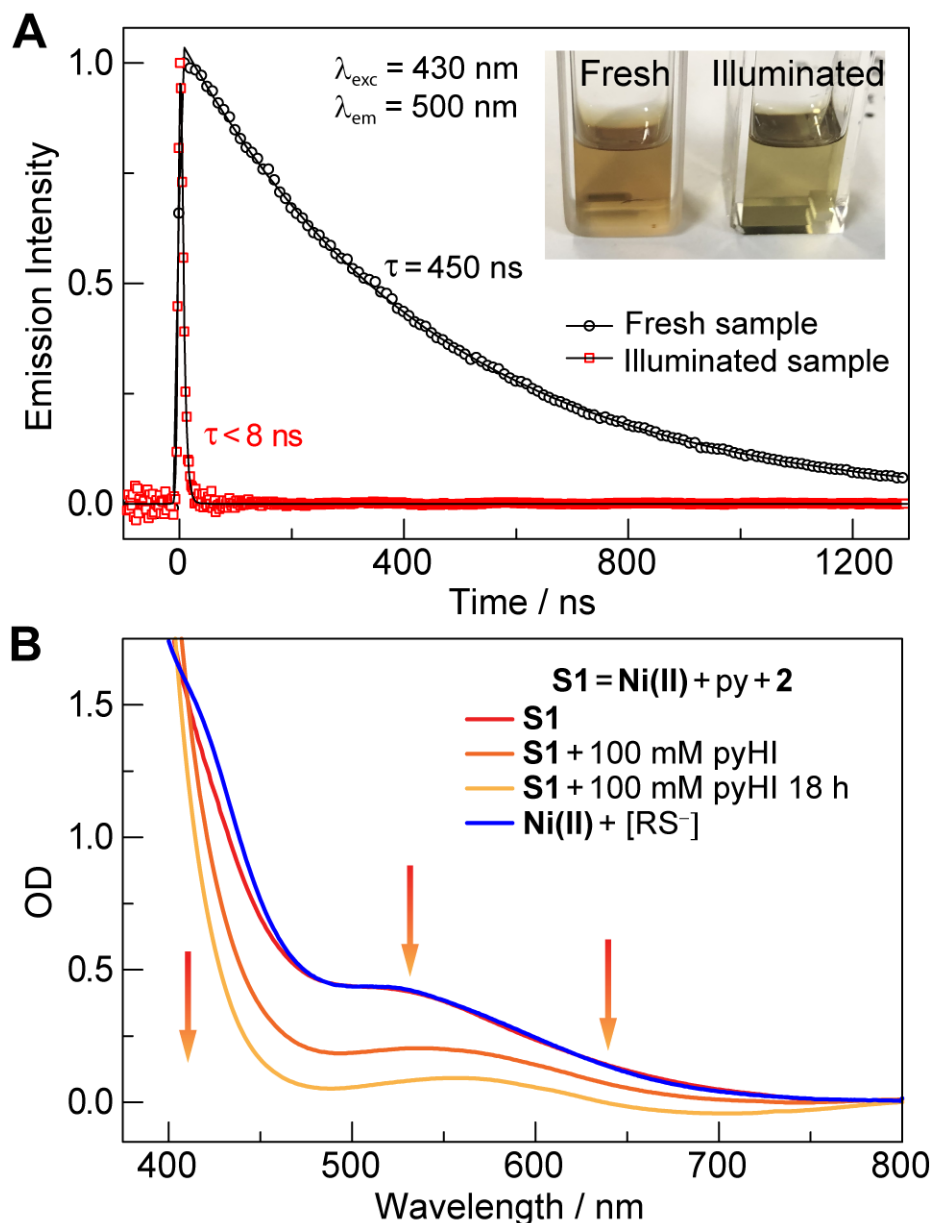


**Figure 3.5.** Spectroscopic studies on the reaction solution. (A) Time-resolved emission decay of the excited photocatalyst  $^*Ir(III)$  in a fresh and illuminated sample, the latter of which was subjected to 20 min blue light irradiation under standard reaction conditions (Table 3.2, top panel). The scatter plots and solid lines show the raw data and single-exponential fittings, respectively. The fitted lifetime  $\tau$  is significantly lower for an illuminated sample when compared to a fresh one. This change in  $^*Ir(III)$  lifetime is accompanied by a change in the color of the reaction solution, as shown in the inset. (B) UV-vis absorption spectra of solution **S1** (Table 3.1), **S1** with an additional 100 mM pyHI at 0 h and 18 h in the dark, and a solution containing Ni(II) with  $RS^-$  (potassium (4-methoxyphenyl)methanethiolate), the spectrum for which is normalized with that of **S1** at 500 nm.

### 3.3 Effect of Thiolate and pyHI on (dtbbpy)NiCl<sub>2</sub>

The initial reaction solution was orange (Figure 3.5A, inset), which we later discovered was similar to the color of solution **S1** (**S1** = 10 mM Ni(II), 200 mM pyridine and 150 mM thiol **2** in MeCN). To identify the compound responsible for the orange color, we prepared a solution of Ni(II) in the presence of potassium (4-methoxyphenyl)methanethiolate. The UV-vis absorption spectrum of this solution (Figure 3.5B, blue trace) is nearly identical to that of solution **S1** (Figure 3.5B, red trace), suggesting that the orange color is due to a nickel thiolate compound. When the complete reaction solution (Table 3.2, top) was photolyzed, the initial orange color gradually disappeared and the solution turned yellow (Figure 3.5A, inset), diagnostic of Ir(III) solutions. This result suggested protonolysis of the nickel-thiolate complex present in the initial solution. We hypothesized that the Brønsted acid pyHI is responsible for this protonolysis reaction and that this acid accumulated as the reaction progressed. Indeed, addition of 100 mM pyHI to solution **S1** prompted a color change (Figure 3.5B, red to red-orange trace) that continued to lighten in color over 18 h of storage in the dark (Figure 3.5B, orange trace). Additionally, if pyHI was added to the initial reactant solution before thiol, the orange color, indicative of the nickel-thiolate, was not observed. These results suggest that pyH<sup>+</sup> (pK<sub>a</sub> = 3.4 in DMSO)<sup>50</sup> can protonate any thiolate equivalents formed *in situ*, thereby avoiding the formation of the nickel thiolate complex, which can cause a strong inner filter effect.

### 3.4 Reaction Progress and Quantum Yield Measurements

The effect of pyHI on the C-S cross-coupling between **1a** and **2** was examined under different conditions by monitoring the product yield with time (Figure 3.6A and see Materials and Methods for details). Under reaction conditions similar to those of the published method,<sup>25</sup> where O<sub>2</sub> was present, the reaction showed an induction period in the first 20 min (Figure 3.6A, red trace) that was less prominent for an identical sample without air exposure (Figure 3.6A, black trace). However, the induction period diminished after adding 50 mM pyHI (Figure 3.6A, blue and teal traces). The sample without air exposure exhibited the highest initial photoreaction rates (Figure 3.6A, blue trace). Although the measurements (Figure 3.6A) may have large errors at the

early stages of these reactions ( $\leq 6$  min), the overall trend is clear (at times  $> 6$  min) with a measurement standard deviation of 5-15 % as shown below (Figure 3.6B).

To further quantify the reaction efficiency and gain mechanistic insight, we measured the quantum yield for the C-S cross-coupling with and without pyHI (Figure 3.6B, black and grey traces). The addition of pyHI (50 mM) results in an increase in the quantum yield by 50% (from 0.12(2) to 0.18(1)) with an incident power of 7.4 mW. The quantum yield also increases with decreasing incident power of the irradiation source; changing the incident power from 7.4 mW to 90  $\mu$ W results in a 375% increase in quantum yield (from 0.12(2) to 0.45(3) in the absence of pyHI), which is accentuated in the presence of pyHI (increase of 594%, from 0.18(1) to 1.07(11)). A quantum yield in excess of 1 ( $\Phi > 1$ ) was further corroborated by using 4'-iodoacetophenone as a substrate (Figure 3.6B, red trace). With this more electron-deficient aryl halide, the quantum yield increases from 0.28(2) at 7.4 mW to 2.04(6) at 90  $\mu$ W. Significantly, these values of  $\Phi > 1$  establish the existence of a thermally self-sustained catalytic cycle<sup>29, 45-46</sup> for product formation (*vide infra*).

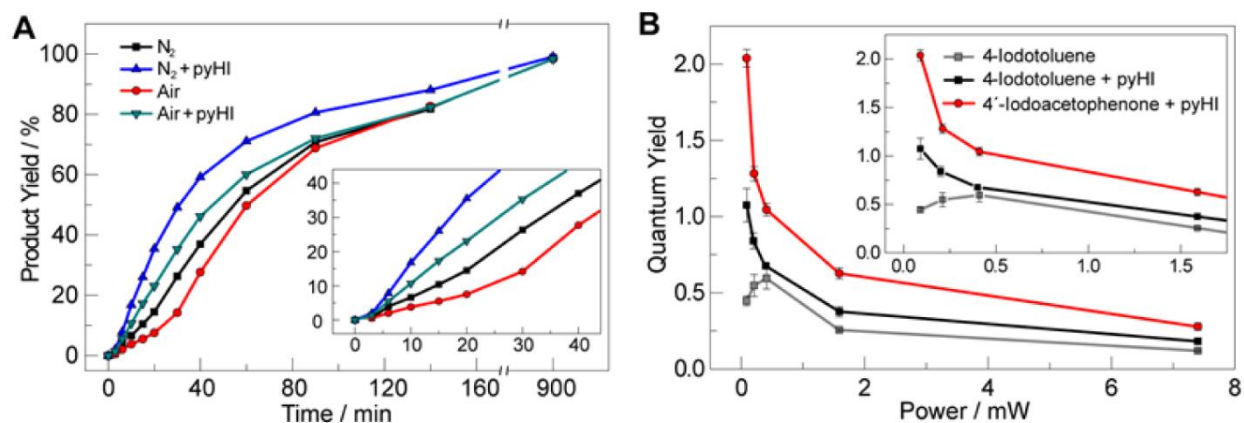


**Figure 3.6.** Chemical and quantum yields of the aryl thiolation reaction. (A) Aryl thiolation progress for a standard reaction solution with the addition of 50 mM pyHI, exposure to air, or both. (B) Power dependence of the quantum yield for aryl thiolation between 4-methoxybenzyl mercaptan and 4-iodotoluene (**1a**) or 4'-iodoacetophenone with and without additional 50 mM pyHI ( $\lambda_{\text{exc}} = 435$  nm). Lines are included to highlight the trend.

### 3.5 Transient Intermediates and Reaction Kinetics

Nanosecond TA spectroscopy was employed to interrogate the photoredox process as well as identify reaction intermediates and define the kinetics of a complete photoredox cycle. Upon addition of 25 mM pyHI or TBAI to a solution of 150  $\mu\text{M}$  **Ir(III)**, TA features at  $\sim 400$ , 525 and 720 nm were observed 30 ns after photoexcitation (Figure 3.7A). The TA spectrum consist of two components (Figure 3.7A, inset): the reduced photocatalyst, **Ir(II)**, and  $\text{I}_2\cdot^-$ . The spectrum of **Ir(II)** (maxima at 400 and 525 nm) has been previously determined by spectroelectrochemistry.<sup>29</sup> Subtraction of the **Ir(II)** spectrum from the TA spectrum recorded at 30 ns yields the blue trace (Materials and Methods for details), which matches that of  $\text{I}_2\cdot^-$  (maxima at 395 and 720 nm).<sup>51</sup> These results confirm that  $\text{I}^-$  quenches  $^*\text{Ir(III)}$  by electron transfer to form **Ir(II)** and  $\text{I}\cdot$ , the latter of which reacts facilyly with  $\text{I}^-$ .<sup>51</sup> Based on the Stern-Volmer quenching study (Table 3.2), the electron transfer rate between  $^*\text{Ir(III)}$  and  $\text{I}^-$  is  $k_{\text{q,ET}} = 2.1(1) \times 10^{10} \text{ M}^{-1} \text{ s}^{-1}$ .

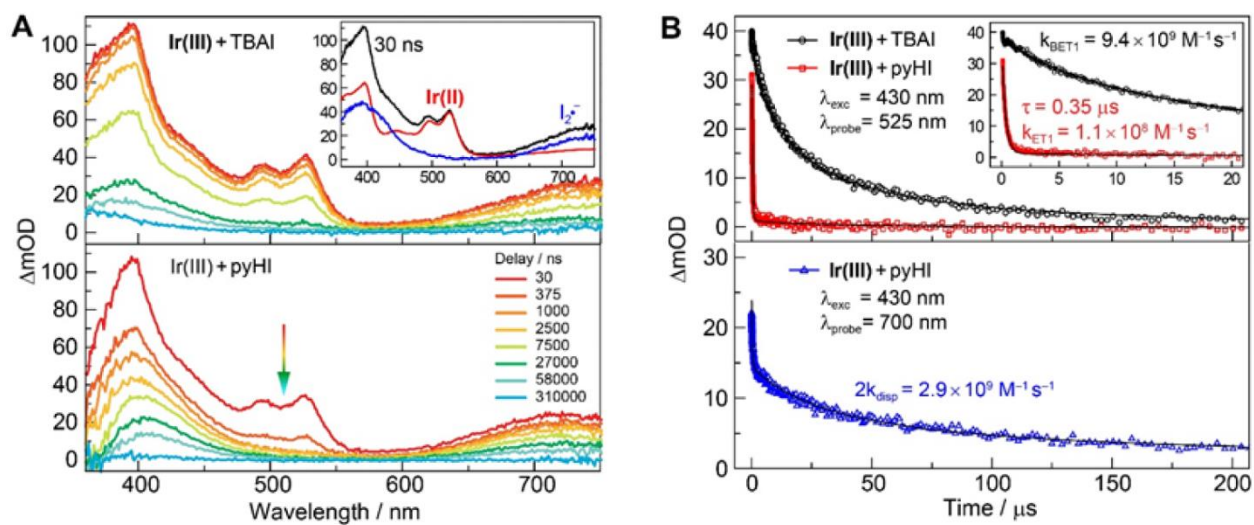


**Figure 3.7.** Transient absorption studies on the quenching of  $^*\text{Ir(III)}$ . (A) TA spectra of a solution containing 150  $\mu\text{M}$  **Ir(III)** and 25 mM TBAI or pyHI ( $\lambda_{\text{exc}} = 430 \text{ nm}$ ). The inset shows that the corresponding TA spectrum at 30 ns can be deconvolved into contributions from **Ir(II)** (red) and  $\text{I}_2\cdot^-$  (blue). The delay times listed in the bottom panel also apply to the top panel. (B) The TA kinetic traces probed at 525 nm and 700 nm predominantly show the decay of **Ir(II)** and  $\text{I}_2\cdot^-$ , respectively. The scatter plots and the solid lines show the raw data and model fittings, respectively (see Materials and Methods for details).

In addition to the role of iodide, we also investigated the role of pyH<sup>+</sup>. The TA spectrum for solution **S2** (**S2** = 150 μM **Ir(III)** + 25 mM pyHI) shows clear distinctions in time evolution for **Ir(II)** as compared to when pyHI was replaced with TBAI (Figure 3.7A). For the solution with TBAI, the TA features at 525 nm (predominantly **Ir(II)**) and 720 nm (predominantly I<sub>2</sub><sup>·-</sup>) both decay at a similar rate, suggesting a clean back electron transfer reaction between I<sub>2</sub><sup>·-</sup> and **Ir(II)** to form 2I<sup>-</sup> and **Ir(III)**. However, with pyHI, the TA feature at 525 nm (**Ir(II)**) decays much faster than that at 720 nm (I<sub>2</sub><sup>·-</sup>), suggesting that the disappearance of **Ir(II)** is predominantly due to the reaction between **Ir(II)** and pyH<sup>+</sup> to form **Ir(III)** and pyH<sup>·</sup>. Similarly, in the presence of 1-methylpyridinium iodide, a faster decay of **Ir(II)** was also observed (Figure 3.8), ruling out the possibility that the reaction between **Ir(II)** and pyH<sup>+</sup> required a proton. By monitoring the decay of **Ir(II)** at 525 nm with TBAI as the quencher, we extracted a rate constant for the back electron transfer reaction between I<sub>2</sub><sup>·-</sup> and **Ir(II)** (Figure 3.7B, black curve and Materials and Methods for details) of  $k_{\text{BET1}} = 9.4(2) \times 10^9 \text{ M}^{-1} \text{ s}^{-1}$ , consistent with an appreciable driving force ( $E_{1/2}(\text{Ir(III/II)}) = -1.74 \text{ V}^{29}$  and  $E_{1/2}(\text{I}_2 \cdot^- / \text{I}^-) < 0.30 \text{ V}^{52}$  vs Fc<sup>0</sup>/Fc). For the case of pyHI (Figure 3.7B, red curve), and accounting for  $k_{\text{BET1}}$  (see Materials and Methods for details), an electron transfer rate constant of  $k_{\text{ET1}} = 1.14(3) \times 10^8 \text{ M}^{-1} \text{ s}^{-1}$  is extracted for the reaction between pyH<sup>+</sup> and **Ir(II)**, which is also thermodynamically favored ( $E^\circ \approx -1.7 \text{ V}$  vs Fc<sup>0</sup>/Fc for the pyH<sup>+</sup>/pyH<sup>·</sup> couple,<sup>53-54</sup> where 0.4 V was subtracted to convert reference potential from SCE to Fc<sup>0</sup>/Fc). Note, despite  $k_{\text{BET1}}$  being nearly two orders of magnitude larger than  $k_{\text{ET1}}$ , we observed faster reaction of **Ir(II)** with pyH<sup>+</sup> than with I<sub>2</sub><sup>·-</sup> due to the higher concentration of pyH<sup>+</sup> (25 mM pyH<sup>+</sup> versus less than 10 μM I<sub>2</sub><sup>·-</sup>). Additionally, I<sub>2</sub><sup>·-</sup>, monitored at 700 nm (Figure 3.7B, blue curve), decays more slowly for the solution containing pyHI versus one containing TBAI due to the fast disappearance of **Ir(II)** in the former, which attenuates the back reaction between I<sub>2</sub><sup>·-</sup> and **Ir(II)**. Since I<sub>2</sub><sup>·-</sup> is known to disproportionate, we attribute the slower decay at 700 nm to the disproportionation of I<sub>2</sub><sup>·-</sup> to form I<sub>3</sub><sup>-</sup> and I<sup>-</sup>, for which we extracted a rate constant of  $2k_{\text{disp}} = 2.9(1) \times 10^9 \text{ M}^{-1} \text{ s}^{-1}$  (see Materials and Methods for details), consistent with reported rate constants.<sup>51, 55</sup>

With the reaction and kinetics for solution **S2** as a reference, the kinetics of **S2** solutions

containing more components of the C-S cross-coupling reaction were examined. The addition of 150 mM thiol **2** to solution **S2** resulted in little change to the TA spectra and kinetics (Figures 3.9 and 3.10). However, the addition of both 200 mM pyridine and 150 mM **2** to solution **S2**, resulting in solution **S3** (= **S2** + 150 mM **2** + 200 mM py), accelerates the decay of  $I_2 \cdot^-$  (Figure 3.11). We posit that the faster decay may result from proton-coupled electron transfer (PCET) between compound **2** and  $I_2 \cdot^-$  in the presence of pyridine as a base to form thiyl radical  $2 \cdot$ ,  $2I^-$  and  $pyH^+$ , which may occur in either a concerted or a stepwise fashion.<sup>56-57</sup> To assess this contention, we chose to replace **2** in **S3** with thiophenol (PhSH) because the PhS· radical exhibits absorption in the visible region, allowing us to observe the radical product if PCET does indeed occur. The inset of Figure 3.11 shows the difference of TA spectra measured at 6.3 μs between solutions of **S2** + 150 mM PhSH in the absence and presence of 200 mM pyridine (Figures 3.10A and 3.10B, respectively); subtracting the spectrum without pyridine from that with pyridine furnishes a spectral profile (Figure 3.11 inset, grey trace and Figure 3.10C) with a band maximum at 450 nm, which is similar to the absorption profile of the PhS· radical (Figure 3.11 inset, red trace) as obtained independently by photolyzing a solution of 6 mM diphenyl disulfide (PhSSPh) with laser pulses at 355 nm. The PCET rate constants for thiol oxidation were derived to be  $k_{PCET} = 2.6(1) \times 10^5 M^{-1} s^{-1}$  for thiol **2** and  $k_{PCET} = 3.6(1) \times 10^5 M^{-1} s^{-1}$  for PhSH (see Materials and Methods). The observation of the thiyl radicals by TA is consistent with their presence in C-S cross-coupling, as ascertained from radical trapping studies.<sup>25</sup>



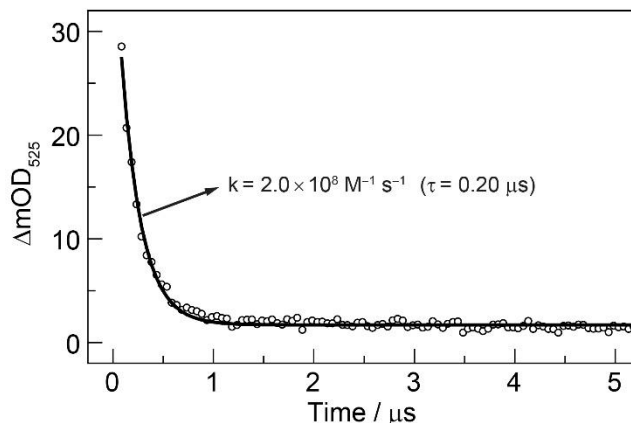


**Figure 3.8.** Reaction between **Ir(II)** and 1-methylpyridinium iodide. TA kinetic trace measured at 525 nm for a MeCN solution containing 150  $\mu\text{M}$  **Ir(III)** and 25 mM 1-methylpyridinium iodide. The fast decay with a time constant of  $\tau = 0.200(4) \mu\text{s}$  is due to the reaction between **Ir(II)** and 1-methylpyridinium, and the rate constant is extracted to be  $k = 2.00(4) \times 10^8 \text{ M}^{-1} \text{ s}^{-1}$  based on a single exponential fit (solid line).

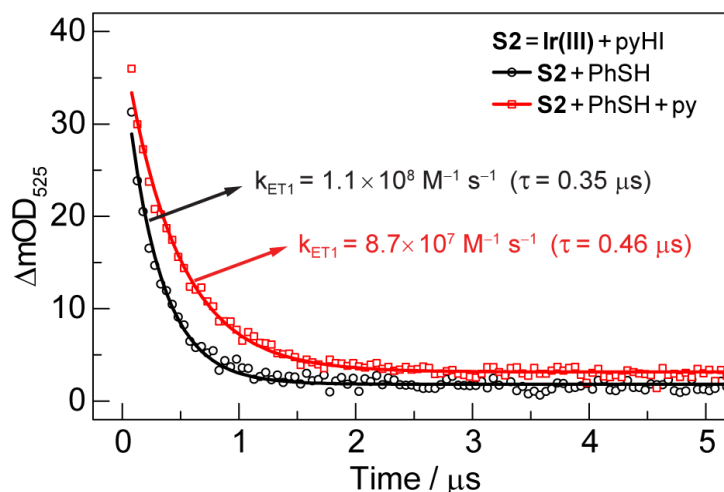


**Figure 3.9.** Reaction between **Ir(II)** and pyHI. TA kinetic trace measured at 525 nm for a MeCN solution containing 150  $\mu\text{M}$  **Ir(III)**, 25 mM pyHI and 150 mM thiophenol in the absence (black plots) or presence (red plots) of 200 mM pyridine. The initial fast decays are due to the reaction between **Ir(II)** and  $\text{pyH}^+$ , for which the rate constant was extracted based on single-exponential fitting. In the absence of pyridine, the decay time is  $0.35(1) \mu\text{s}$  corresponding to  $k_{\text{ET1}} = 1.14(3) \times 10^8 \text{ M}^{-1} \text{ s}^{-1}$ . In the presence of 200 mM pyridine, the decay time is  $0.46(1) \mu\text{s}$  corresponding to  $k_{\text{ET1}} = 8.7(2) \times 10^7 \text{ M}^{-1} \text{ s}^{-1}$ .

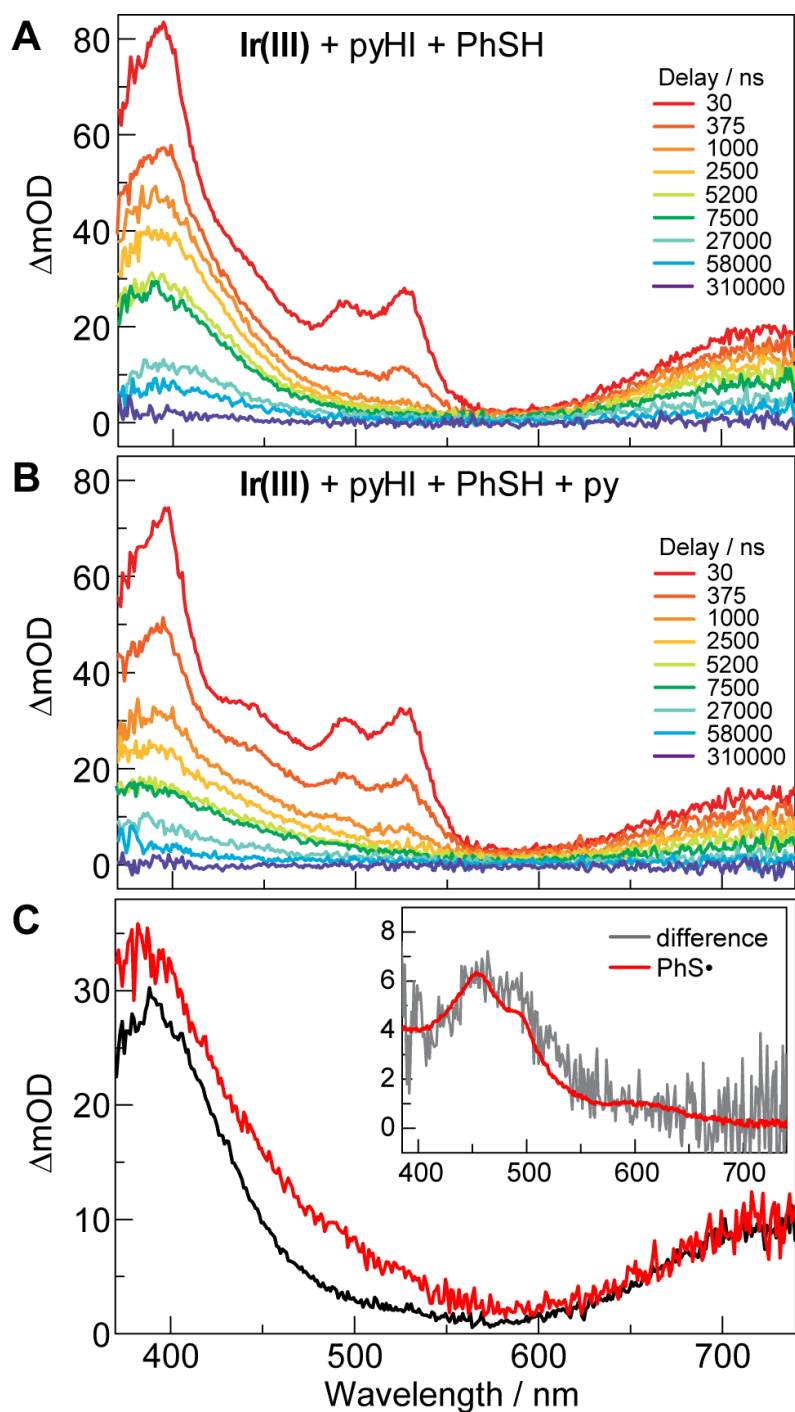


**Figure 3.10.** Formation of thiyl radical. TA spectra of MeCN solutions containing 150  $\mu M$  **Ir(III)**, 25 mM pyHI and 150 mM thiophenol in the absence (A) or presence (B) of 200 mM py ( $\lambda_{exc} = 430$  nm). (C) The TA spectra at 6.3  $\mu s$  for solutions in A and B were aligned at 700 nm to show a difference due to the thiophenoxy radical. The inset shows the difference TA spectrum (grey), which matches the absorption spectrum of thiophenoxy radical (red) obtained independently by photo-exciting a diphenyl disulfide solution (6 mM) in MeCN at  $\lambda_{exc} = 355$  nm.

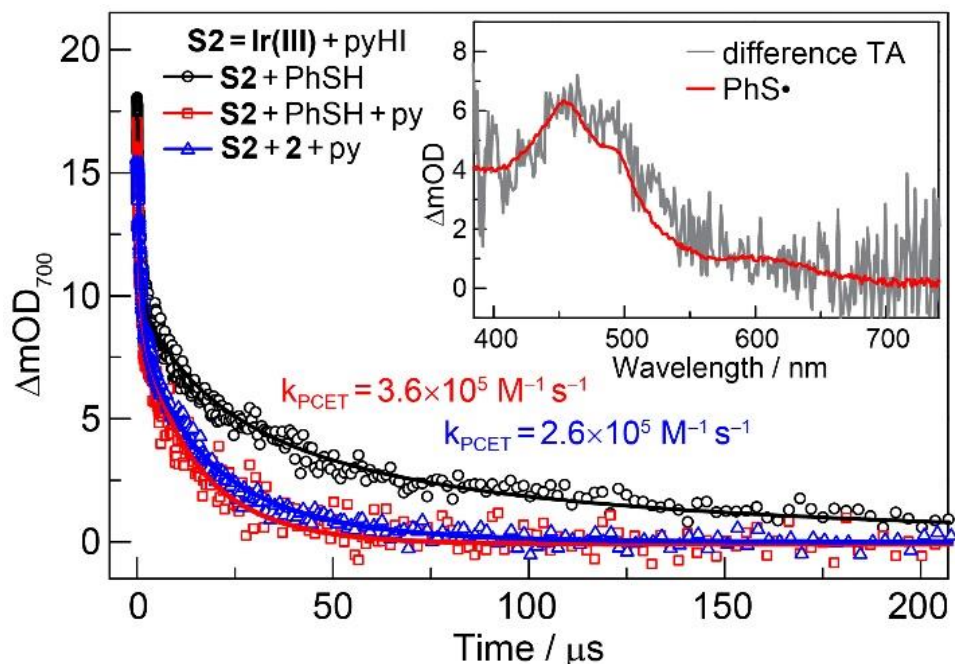


**Figure 3.11.** TA kinetic trace probed at 700 nm for solution **S2** (150  $\mu\text{M}$  **Ir(III)**) and 25 mM pyHI) with 150 mM thiophenol, 150 mM thiophenol in the presence of 200 mM pyridine, and 150 mM 4-methoxybenzyl mercaptan in the presence of 200 mM pyridine ( $\lambda_{\text{exc}} = 430$  nm). The faster decay for solutions containing pyridine is due to PCET between  $\text{I}_2 \cdot^-$  and thiol with pyridine as a base. The scatter plots and solid lines show the raw data and model fittings, respectively (see Materials and Methods for details). The inset shows the difference TA spectrum at 6.3  $\mu\text{s}$  (grey) for solutions of **S2** with 150 mM thiophenol in the absence and presence of 200 mM pyridine; this difference spectrum matches the TA spectrum of thiophenoxy radical (red) obtained independently from directly exciting diphenyl disulfide at  $\lambda_{\text{exc}} = 355$  nm.

We next interrogated the role of Ni in the photoredox cycle by adding 10 mM **Ni(II)** to **S3** (**S4** = **S3** + 10 mM **Ni(II)**). The measured TA spectra for solution **S4** is shown in Figure 3.12A. Subtracting the TA spectrum of solution **S3** at 7.5  $\mu\text{s}$  from that of **S4** yielded the difference TA spectrum (Figure 3.12B), which clearly shows two absorption features with maxima at 425 and 600 nm. These spectral features have been observed previously in photoredox aryl etherification<sup>29</sup> and arise from a **Ni(I)** intermediate. To further assess our assignment of the absorption bands in Figure 3.12B to a **Ni(I)** intermediate, we monitored the comproportionation between **Ni(0)** [**Ni(0)** = (dtbbpy)Ni(cod)] and **Ni(II)** (see Materials and Methods). Electron paramagnetic resonance (EPR) measurement of the comproportionation product supported the presence of a new **Ni(I)** species

(Figure 3.13A). Furthermore, the comproportionation solution showed an absorption spectrum (Figure 3.13B) distinct from that of **Ni(0)** or **Ni(II)** (Figure 3.13C), with an absorption band in the 600 nm region. Exposure of the same solution to air led to the disappearance of the 600 nm band to give the **Ni(II)** absorption spectrum. To assess whether the **Ni(I)** species formed by the comproportionation reaction accounts for the TA difference spectrum shown in Figure 3.12B, the difference absorption spectrum for comproportionated solutions before and after air exposure (i.e., **Ni(I)** spectrum - **Ni(II)** spectrum) was computed (Figure 3.13D) and found to be similar to the difference TA spectrum shown in Figure 3.12B (red curve), thus supporting the formation of **Ni(I)** under photoredox conditions.

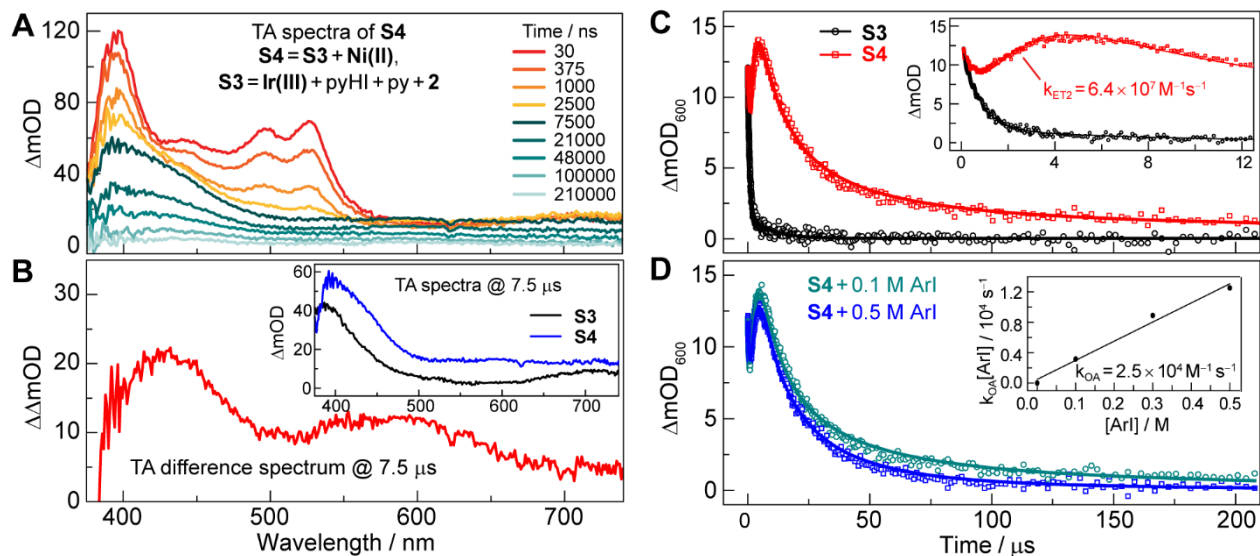


**Figure 3.12.** TA spectra of reaction solutions with the inclusion of Ni. (A) TA spectra ( $\lambda_{\text{exc}} = 430$  nm) of solution **S4** (150  $\mu\text{M}$  **Ir(III)**, 25 mM pyHI, 200 mM pyridine, 150 mM 4-methoxybenzyl mercaptan, and 10 mM **Ni(II)**). (B) The difference TA spectrum at 7.5  $\mu\text{s}$  for solution **S3** and **S4** (parent spectra shown in the inset), revealing the presence of a putative **Ni(I)** intermediate. (C) TA kinetic trace measured at 600 nm for solution **S3** (black) and **S4** (red). The additional rising feature on the red curve suggests the formation of **Ni(I)** with a time constant of 1.56  $\mu\text{s}$ . (D) TA kinetic trace measured at 600 nm for solution **S4** with 0.1 and 0.5 M 4-iodotoluene, **1a**. The faster decay for solutions with higher concentrations of aryl iodide implies the oxidative addition of aryl iodide to the **Ni(I)**. The scatter plots and solid lines show the raw data and model fittings, respectively (see Materials and Methods for details). The inset shows the linear fit to extract the oxidative addition rate constant  $k_{\text{OA}}$  of 4-iodotoluene, **1a**.

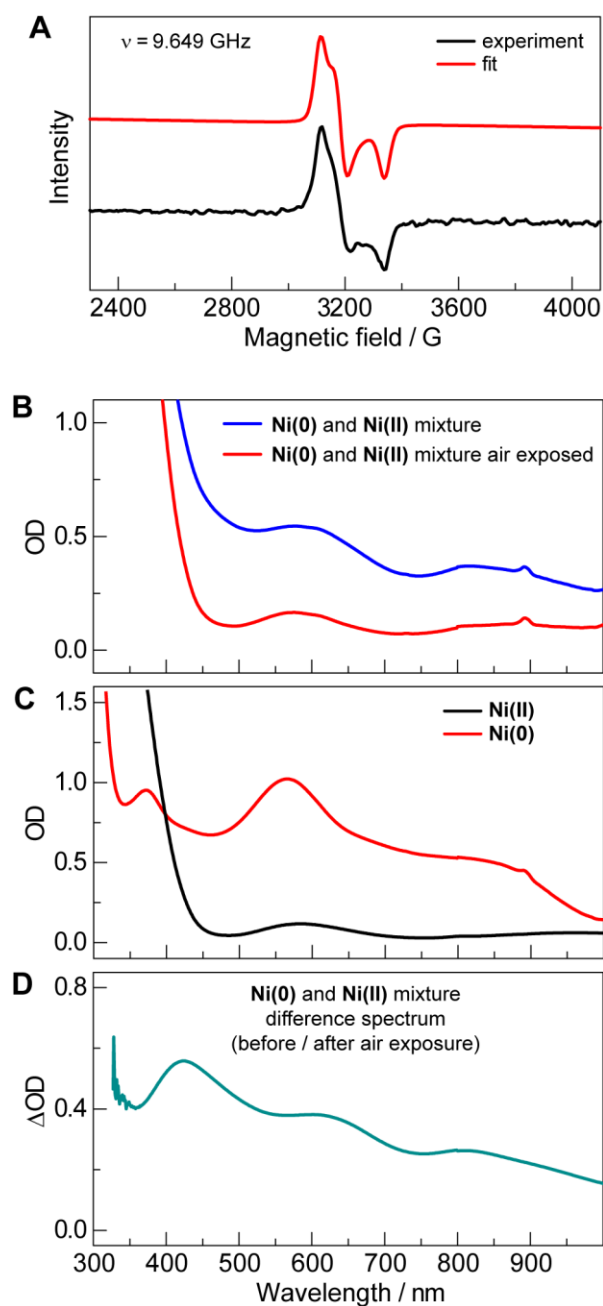


**Figure 3.13. Ni(I)** made from comproportionation between **Ni(0)** and **Ni(II)**. (A) The EPR spectrum (black curve) for a comproportionation solution in the presence of 200 mM py (see Materials and Methods). The simulated EPR spectrum was obtained using  $g_1 = 2.20$ ,  $g_2 = 2.15$ ,  $g_3 = 2.05$  and  $S = 1/2$ . (B) The UV-vis absorption spectrum of a comproportionation solution in the presence of 200 mM pyridine (see Materials and Methods). The spectrum of the same solution after exposure to air shows diminished absorption. (C) The UV-vis absorption spectrum of **Ni(II)** and **Ni(0)** in the presence of 200 mM pyridine (see Materials and Methods). (D) The difference spectrum of the two raw spectra shown in B.

Accordingly, the kinetics of the **Ni(I)** intermediate, for which the 600 nm band offered a direct signature, were defined. Figure 3.12C shows the decay kinetics for the 600-nm signal of solution **S4**. A slight decay in signal over 0.5  $\mu\text{s}$  is followed by a rise over 5  $\mu\text{s}$  and then a subsequent slow decay lasting several hundreds of microseconds (Figure 3.12C, red trace). This evolution of the signal contrasts the immediate drop in signal at 600 nm observed for solution **S3** (Figure 3.12C, black trace) where no nickel complex was present. An additional control experiment on a similar solution without thiol **2** but with the **Ni(II)** complex (**S4** - 150 mM **2**) also showed a decay-rise-decay feature, suggesting that the formation of **Ni(I)** species is not due to thiol **2** (Figure 3.14D, black trace). Significantly, the initial fast decay and slow rise indicate that the formation of **Ni(I)** occurs through the action of an intermediate that is not **Ir(II)**, as its formation is slower than the disappearance of **Ir(II)**. This result establishes that **Ni(I)** is not generated from the direct reduction of **Ni(II)** by **Ir(II)**. As noted in Figure 3.7A,  $\text{pyH}\cdot$  is present during the photoredox transformation and thus may act as a reductant for **Ni(II)**. Consistent with this contention, the rate constant for the reaction between  $\text{pyH}\cdot$  and **Ni(II)** was determined to be  $k_{\text{ET2}} = 6.4(5) \times 10^7 \text{ M}^{-1} \text{ s}^{-1}$  whether in the presence or absence of thiol. From modelling (Materials and Methods) the slow decay over 5 to 200  $\mu\text{s}$ ,  $k_{\text{BET2}} = 8.5(4) \times 10^9 \text{ M}^{-1} \text{ s}^{-1}$ , is ascribed to the back reaction between **Ni(I)** and  $\text{I}_2\cdot^-$  to form **Ni(II)** and  $2\text{I}^-$ .

Given the reported reduction potential for **Ir(II)** ( $E_{1/2} = -1.74 \text{ V vs Fc}^+/\text{Fc}$ ),<sup>29</sup> it should be able to directly reduce **Ni(II)** in the absence of  $\text{pyH}^+$ . To test this hypothesis, we obtained the TA spectrum of a solution containing 150  $\mu\text{M}$  **Ir(III)**, 25 mM TBAI, 200 mM py, and 10 mM **Ni(II)**. We monitored the absorption maximum of **Ir(II)** at 525 nm, which was generated immediately following the initial quenching and then decayed slowly due to the back reaction (Figures 3.14A and 3.14B, red curves). Monitoring **Ni(I)** at 600 nm, a decay-and-rise feature was not observed on a short time scale ( $< 5 \mu\text{s}$ ) (Figure 3.14D, red trace). However, an additional TA feature appeared on a longer time scale ( $>50 \mu\text{s}$ ) after **Ir(II)** and  $\text{I}_2\cdot^-$  had decayed significantly (shown by the comparison of the red curves in Figures 3.14C and 3.14D). This additional TA feature is likely due to the reaction between **Ir(II)** and **Ni(II)** in the presence of pyridine to form **Ir(III)** and **Ni(I)**,

the rate constant of which was extracted to be  $k_{\text{ET3}} = 2.5(5) \times 10^6 \text{ M}^{-1} \text{ s}^{-1}$  (Figure 3.15 and see Materials and Methods).

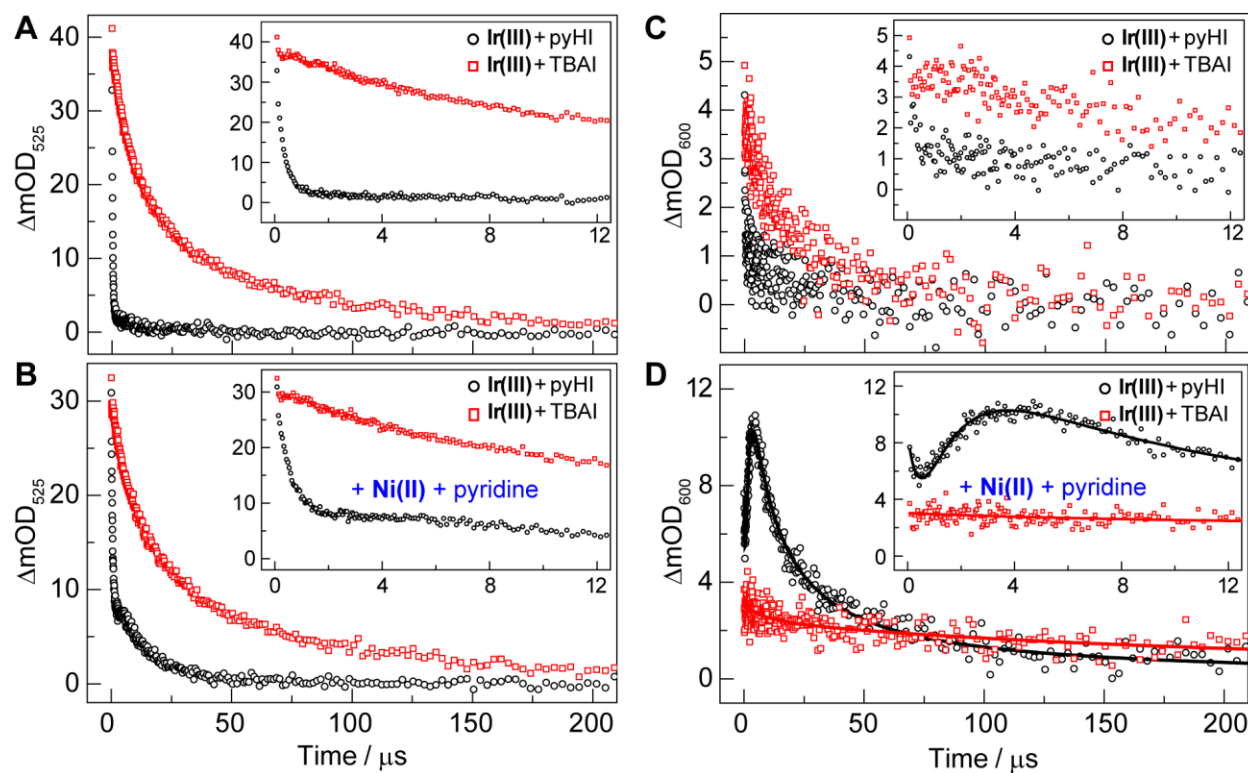


**Figure 3.14.** Decay of **Ir(II)** and formation of **Ni(I)** mediated by pyHI. TA kinetic traces at 525 nm for MeCN solutions containing  $150 \mu\text{M}$  **Ir(III)** and  $25 \text{ mM}$  pyHI or TBAI in the absence (A) or presence (B) of  $10 \text{ mM}$  **Ni(II)** and  $200 \text{ mM}$  py. TA kinetic traces at 600 nm for MeCN solutions containing  $150 \mu\text{M}$  **Ir(III)** and  $25 \text{ mM}$  pyHI or TBAI in the absence (C) or presence (D) of  $10 \text{ mM}$  **Ni(II)** and  $200 \text{ mM}$  py. Model fitting (black line in D) suggests a rate constant of  $k_{\text{BET2}} = 8.5(4) \times 10^9 \text{ M}^{-1} \text{ s}^{-1}$  for the back reaction between **Ni(I)** and  $\text{I}_2 \cdot^-$  (see Materials and Methods). The fitting details for the red line in D are provided in Figure 3.15.

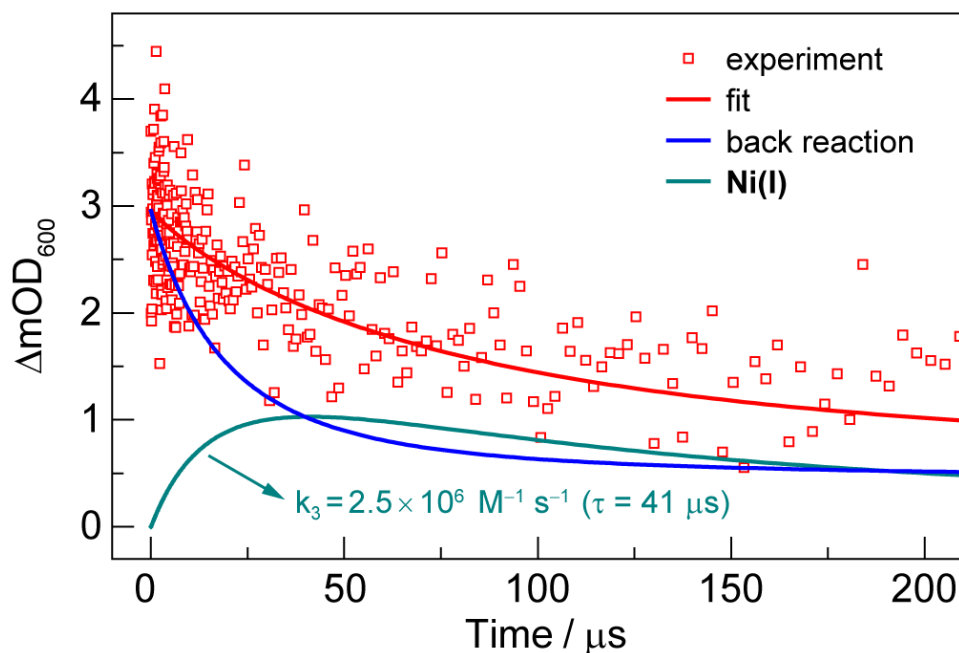


**Figure 3.15.** Direct reduction of **Ni(II)** by **Ir(II)** in the presence of pyridine. The TA signal at 600 nm for a solution containing 150  $\mu\text{M}$  **Ir(III)**, 25 mM TBAI, 10 mM **Ni(II)** and 200 mM py was fitted with a custom model (red trace, see Materials and Methods for fitting details). The signal consists of two components including a back reaction component (blue trace) due to the reaction between **Ir(II)** and  $\text{I}_2\cdot^-$  with a known rate constant of  $k_{\text{BET1}} = 9.4 \times 10^9 \text{ M}^{-1} \text{ s}^{-1}$ , and fitted component **Ni(I)** (dark cyan trace) showing a formation time of 41(8)  $\mu\text{s}$  with a corresponding rate constant of  $k_{\text{ET3}} = 2.5(5) \times 10^6 \text{ M}^{-1} \text{ s}^{-1}$ .

The rate constant for the direct reduction of **Ni(II)** by **Ir(II)** in the presence of pyridine is much smaller than that of the  $\text{pyH}\cdot$  mediated process. However, in the absence of pyridine, **Ir(II)** can effectively reduce **Ni(II)** directly to form **Ni(I)** with a rate constant of  $k_{\text{ET4}} = 3.0(4) \times 10^7 \text{ M}^{-1} \text{ s}^{-1}$  (Figure 3.16 and Materials and Methods for details). These results suggest that pyridine makes **Ni(II)** less amenable towards reduction. Indeed, the absorption spectrum of **Ni(II)** showed clear differences with and without 200 mM pyridine (Figure 3.17A). We further carried out cyclic voltammetry (CV) measurements on **Ni(II)** in the absence and presence of 200 mM pyridine. Despite the irreversibility of the reduction wave, its onset shifted cathodically by  $\sim 200$  mV when pyridine was present (Figure 3.17B), consistent with the smaller reduction rate ( $k_{\text{ET3}}$ ) observed for **Ni(II)** in the presence of pyridine.



With the formation pathways of **Ni(I)** determined, we further probed its oxidative addition (OA) reactivity<sup>58</sup> with 4-iodotoluene (**1a**) by monitoring the TA kinetics of **Ni(I)** at 600 nm. The **Ni(I)** decay became faster when the concentration of **1a** was increased from 0 M to 0.5 M (Figures 3.12C and 3.12D). Specifically, with 0.5 M **1a**, the signal drops to nearly zero after 100  $\mu\text{s}$ . With fitting (see Materials and Methods), we extract the apparent OA rate constant,  $k_{\text{OA}}[\text{ArI}]$ , as a function of the aryl iodide concentration (Figure 3.12D, inset), where the slope of the linear fit furnishes a bimolecular OA rate constant of  $k_{\text{OA}} = 2.5(2) \times 10^4 \text{ M}^{-1} \text{ s}^{-1}$ . We emphasize that the obtained rate ( $k_{\text{OA}}$ ) may offer an upper limit for the OA if other unknown reactions exist between **Ni(I)** and ArI. Given the quantitative product yield and high quantum yields observed (Figure 3.6), we believe that OA is likely the major reaction here. The observed  $k_{\text{OA}}$  is also consistent with previously reported values,<sup>59</sup> despite the differences in ligand environment. Due to the absence of any salient signals in the TA spectrum, we were unable to measure the rates of ligand exchange or reductive elimination at **Ni(III)** following OA.

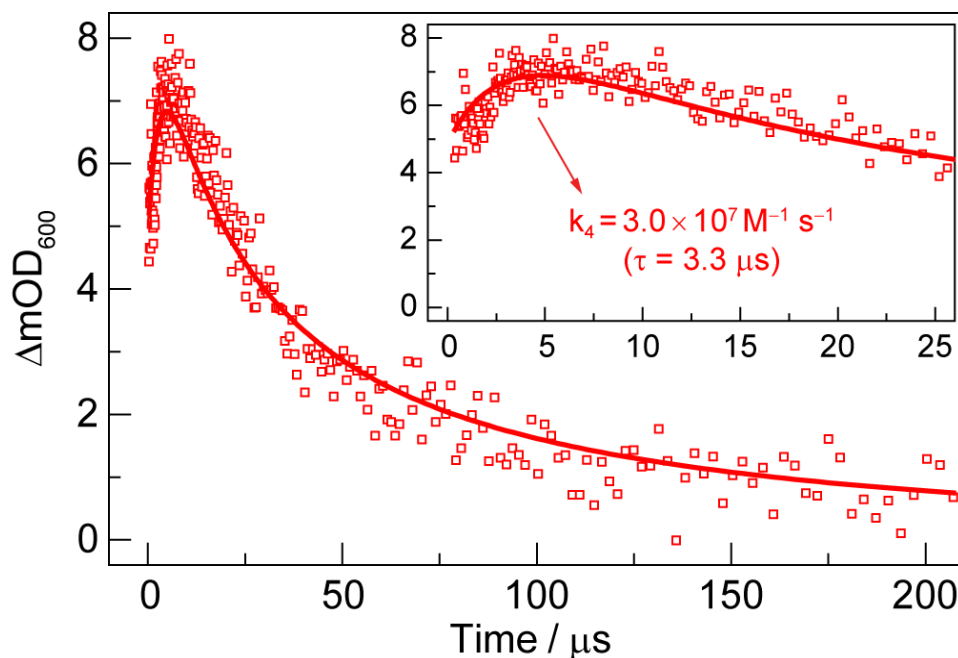


**Figure 3.16.** Direct reduction of **Ni(II)** by **Ir(II)** in the absence of pyridine. The TA signal at 600 nm for a solution containing 150  $\mu\text{M}$  **Ir(III)**, 25 mM TBAI and 10 mM **Ni(II)** was fitted with a custom model (red trace, see Materials and Methods for fitting details). The fitted formation of **Ni(I)** shows a formation time of 3.3(4)  $\mu\text{s}$  and a rate constant of  $k_{\text{ET4}} = 3.0(4) \times 10^7 \text{ M}^{-1} \text{ s}^{-1}$ .

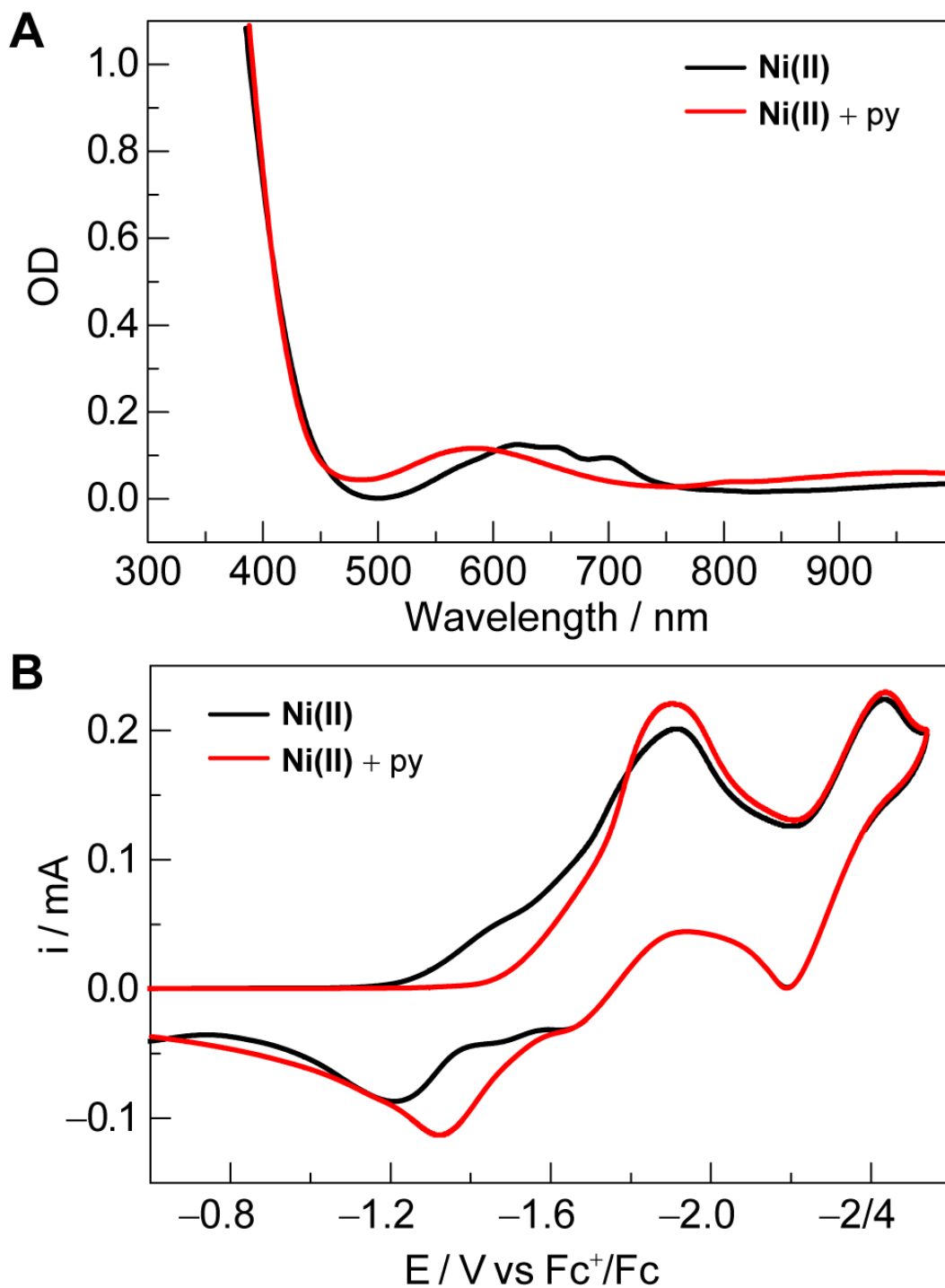
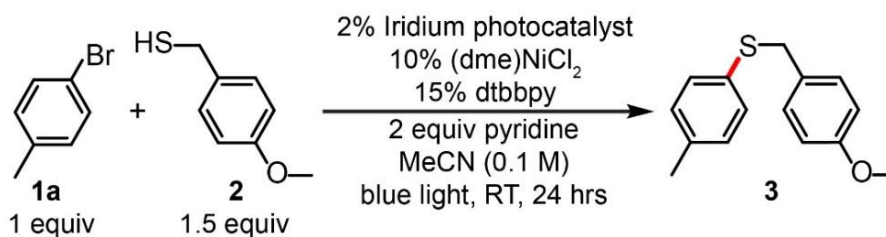


**Figure 3.17.** Ni(II) interaction with pyridine. (A) The UV-vis absorption spectra for Ni(II) in the absence (black curve) and presence (red curve) of 200 mM pyridine. (B) The CV for 10 mM Ni(II) in the absence (black curve) and presence (red curve) of 200 mM py (See Materials and Methods). The onset of reduction shifted cathodically by ~200 mV for the solution with pyridine when compared to that without.

### 3.6 Reaction Optimization and Generalization

In line with previous observations,<sup>25</sup> we found that the substrate scope for the C-S cross-coupling reaction was limited to aryl iodides (Table 3.3) under the conditions shown in Table 3.2. Guided by our mechanistic insights, which show the important, but previously unidentified, roles of pyridinium and iodide in the photoredox cycle, we found that the addition of pyHI and a slightly elevated temperature of 55 °C enables the C-S cross-coupling between 4-bromotoluene (**1b**) and thiol **2** (Table 3.4, top). Similarly, high yields were also obtained when TBAI was added since pyH<sup>+</sup> is able to be generated *in situ* (Table 3.4). Finally, multiple aryl bromides and thiols were tested (Table 3.4, bottom). The optimized strategy applied well to aryl bromides with electron withdrawing groups (**4-8**), electron donating groups (**1b**, **9**), and aryl heterocycles (**10-12**). Aryl thiols (**13-15**) and alkyl thiols (**2**, **16-18**) also worked well. Moreover, the amino acid cysteine (**18**) showed a high yield, indicating potential applicability in biosystems. Therefore, the generality of our optimization strategy was confirmed.

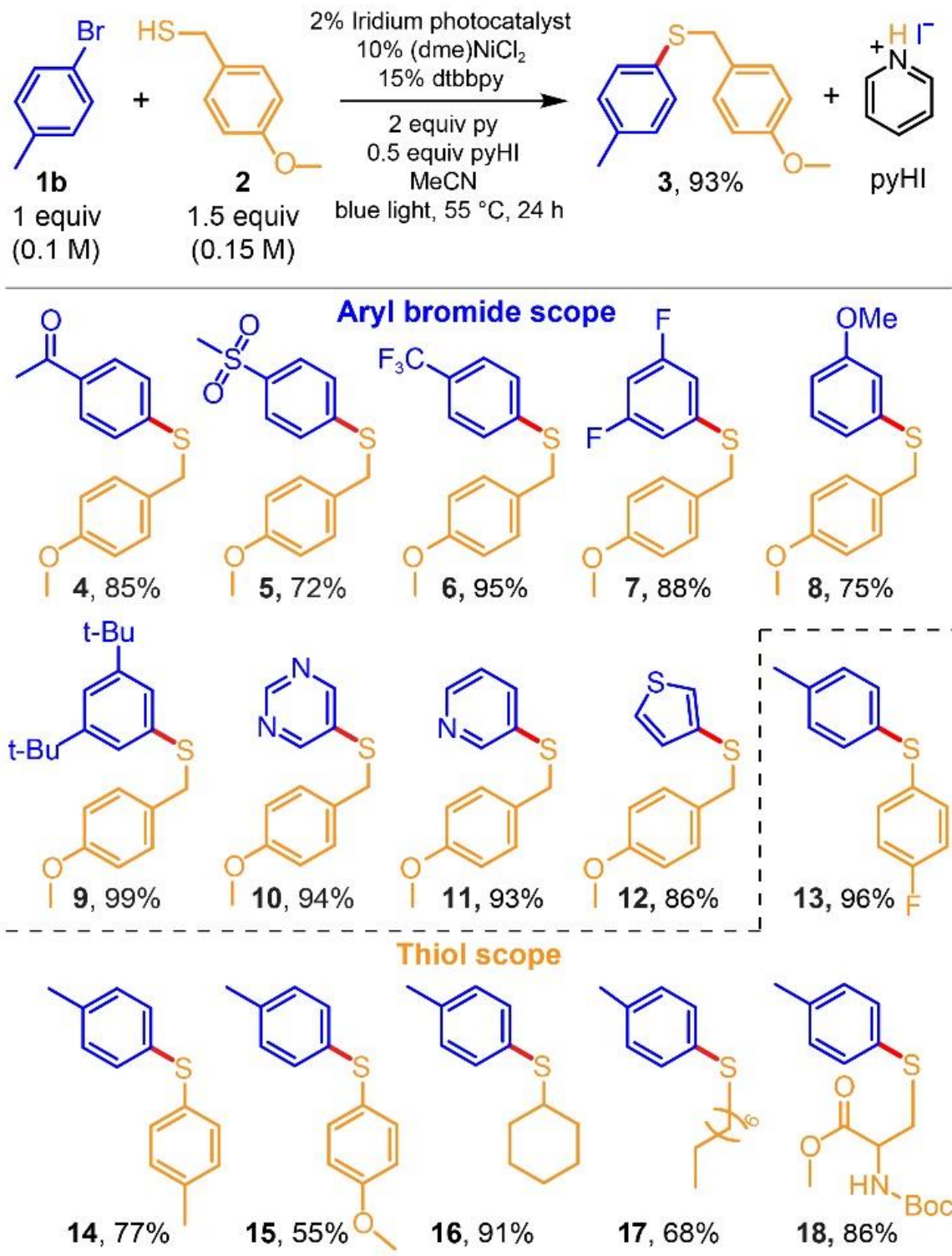
**Table 3.3.** Optimization for the cross-coupling between thiol and aryl bromide.



Entry	Change from standard conditions	Yield (%) <sup>a</sup>
1	no change	0 <sup>b</sup>
2	55 °C	0
3	add 50 mM TBAI	45
4	add 50 mM PyHI	49
5	add 50 mM TBAI, 55 °C	91
6	add 50 mM PyHI, 55 °C	93

<sup>a</sup>Yield was determined by <sup>1</sup>H NMR with respect to the internal standard (1,3-benzodioxole). <sup>b</sup>Yield of 0 indicates that no product was detected within the instrument detection sensitivity.

**Table 3.4.** Photoredox mediated nickel-catalyzed aryl thiolation using aryl bromide. Top panel shows the reaction used in photochemical kinetics studies with the bromo analogue of **1a**; bottom panel shows generalization to a range of substrates.



### 3.7 Discussion

Figure 3.18 summarizes the elementary reactions, reaction intermediates, and critical rate constants for a comprehensive description of the photoredox nickel-catalyzed cross-coupling between aryl halides and thiols. The productive reaction pathway consists of the following steps: (i) photoexcitation of **Ir(III)** to generate **\*Ir(III)**; (ii) reductive quenching of **\*Ir(III)** by  $I^-$  to generate **Ir(II)** and  $I\cdot$  (Figure 3.18, red cycle); (iii) reduction of  $pyH^+$  by **Ir(II)** to generate a pyridyl radical  $pyH\cdot$  and **Ir(III)**; (iv) reduction of the **Ni(II)** precatalyst by  $pyH\cdot$  to form a **Ni(I)** species (Figure 3.18, blue cycle); (v) oxidative addition of aryl halide to **Ni(I)** to form a putative **Ni(III)** aryl halide complex and (vi) ligand exchange on **Ni(III)** and subsequent reductive elimination to release product and reform **Ni(I)** (Figure 3.18, green cycle). In addition to the major pathway of generating **Ni(I)** from step (iv), a minor pathway was also identified that (vii) generates **Ni(I)** from the direct reaction between **Ir(II)** and **Ni(II)**.

The important role of the reactivity of downstream products originating from photogenerated  $I\cdot$  is shown in the orange cycle of Figure 3.18. Following the initial quenching,  $I\cdot$  complexes with  $I^-$  to form  $I_2\cdot^-$ ,<sup>51</sup> which reacts with **Ir(II)** or **Ni(I)** via back electron transfer, leading to the deactivation of these two key intermediates. Alternatively,  $I_2\cdot^-$  may oxidize thiol in the presence of pyridine via PCET to generate a thiyl radical and  $pyH^+$ , both of which eventually undergoes back reaction with **Ni(I)** in what is likely a multi-step process involving electron and proton transfer (Figure 3.18, purple cycle). Additionally,  $I_2\cdot^-$  can also disproportionate to  $I^-$  and  $I_3^-$  (Figure 3.7B), the latter of which can also oxidize **Ni(I)**. However, under actual reaction conditions, this disproportionation becomes negligible given the fast back electron transfer and PCET reactions.

The mechanism we have elucidated herein highlights the importance of accessing and perpetuating a thermally-sustained and productive Ni(I/III) cycle, which is evidenced by the larger-than-one quantum yields observed at low powers (Figure 3.6B). Due to the bimolecular nature of all the back-electron transfer reactions, the overall energy efficiency will decrease due to higher concentrations of the intermediates being generated at higher excitation powers. This

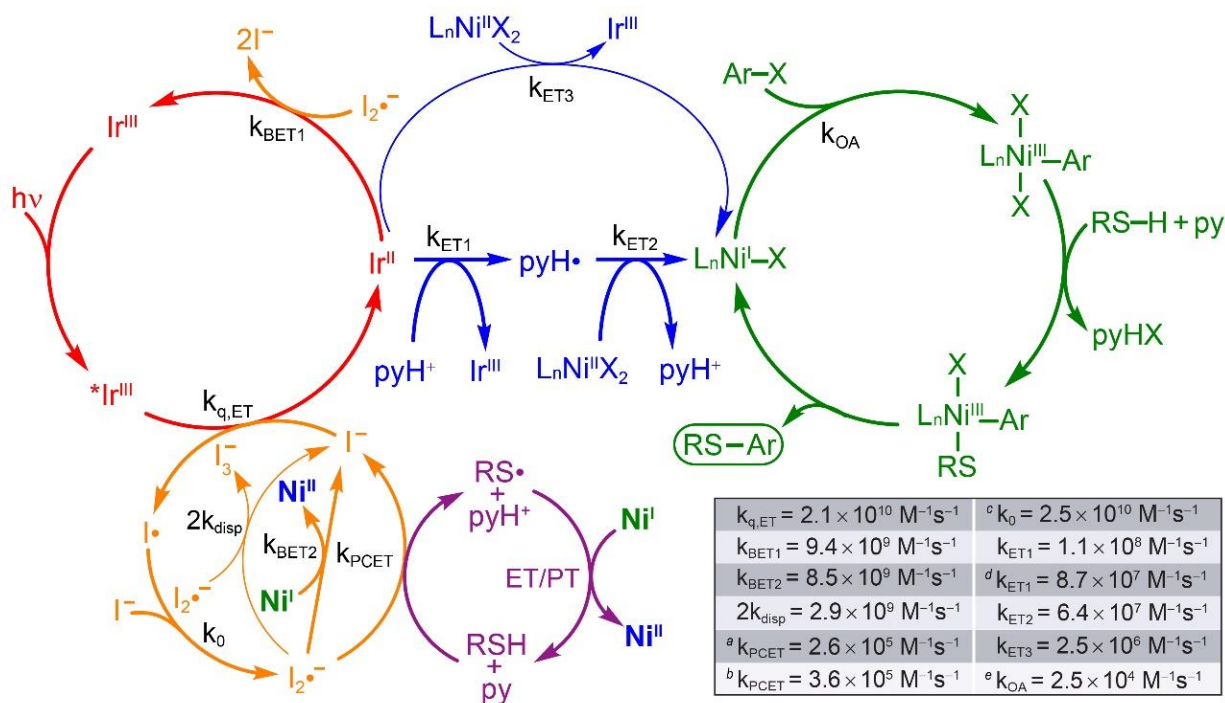


**Figure 3.18.** Complete reaction mechanism and key rate constants for photoredox mediated nickel-catalyzed aryl thiolation. <sup>a</sup> PCET reaction between  $I_2 \cdot^-$  and compound **2**. <sup>b</sup> PCET reaction between  $I_2 \cdot^-$  and thiophenol. <sup>c</sup> Rate was reported by ref 53. <sup>d</sup> For the reaction with 200 mM pyridine. <sup>e</sup> Oxidative addition of 4-iodotoluene.  $Ni^{II} = L_n Ni^{II} X_2$ ;  $Ni^I = L_n Ni^I X$ . ET = electron transfer; PT = proton transfer.

was indeed observed, as the quantum yield increased significantly as the power of the excitation source was diminished (Figure 3.6B). Such an observation is in line with our previous results for photoredox aryl etherification, where the Ni(I/III) cycle is enhanced as the deactivation of the on-cycle nickel intermediates is attenuated at lower powers.<sup>29</sup> However, the photoredox aryl etherification and the C-S cross-coupling reaction reported here access the on-cycle **Ni(I)** catalyst in distinct ways. The direct reduction pathway, which is predominant in aryl etherification, becomes inefficient for generating **Ni(I)** in C-S cross-coupling due to the retarded reaction ( $k_{ET3}$ ) between **Ir(II)** and **Ni(II)** as compared to the competing back reaction ( $k_{BET1}$ ) between **Ir(II)** and  $I_2 \cdot^-$  (Figures 3.7 and 3.15). The  $pyH^+$  that is formed *in situ* provides an efficient pathway to transport electrons from **Ir(II)** to **Ni(II)** through  $pyH^+/pyH\cdot$  mediators to form **Ni(I)**, and hence sustain the productive Ni(I/III) cycle (Figure 3.18). Although  $pyH^+$  has often been used as a redox mediator in

CO<sub>2</sub> reduction<sup>53-54, 60-61</sup> and, recently, in nickel-catalyzed aryl amination with catalytic amounts of Zn metal as a reductant,<sup>62</sup> our discovery reveals an underappreciated role of pyH<sup>+</sup> as a viable mediator in photoredox chemistry.

The mechanism in Figure 3.18 differs from the previously reported ‘radical’ and ‘oxidation state modulation’ mechanisms<sup>25,44</sup> (Figure 3.1A) in critical ways. These mechanisms propose the production of Ni(I) by reduction of Ni(II) for each turnover in the cycle. This restricts the quantum yield to be  $\Phi \leq 1$ , which is inconsistent with our measurements (Figure 3.6B). Additionally, these two previously proposed mechanisms invoked a reductive quenching of \*Ir(III) by thiol to generate Ir(II) and thiyl radical cation,<sup>25</sup> or, alternatively, oxidative quenching of \*Ir(III) by Ni(II) to generate Ni(I) and Ir(IV) (Figure 3.1A).<sup>44</sup> Based on the relative  $k_q$  values in Table 3.2, we found that the initial step subsequent to photoexcitation of Ir(III) predominantly involves the reductive quenching of \*Ir(III) by I<sup>-</sup> to generate Ir(II) and I<sup>·</sup>. The rapid sequestration of I<sup>·</sup> by I<sup>-</sup> to generate I<sub>2</sub><sup>·-</sup> with a rate constant close to the diffusional limit ( $k_0$ )<sup>51</sup> carries the benefit of suppressing the back-electron transfer between I<sup>·</sup> and Ir(II), which is propagated to the self-sustaining Ni(I/III) catalytic cycle (Figure 3.18, green cycle) via pyridinium redox mediation (Figure 3.18, blue cycle). Moreover, the thiyl radical in the ‘radical’ mechanism, whose presence was inferred from reported trapping experiments<sup>25</sup> and corroborated by our TA studies (Figure 3.11), was previously proposed to be generated by direct quenching of \*Ir(III) and on-cycle with nickel cross-coupling catalysis (Figure 3.1A, top path).<sup>25</sup> In contrast, we discovered that the radical may be generated by its PCET reaction with I<sub>2</sub><sup>·-</sup> (Figure 3.11) and, most importantly, is not required for the nickel cross-coupling catalytic cycle (Figure 3.18).

### 3.8 Conclusions

Combining Stern-Volmer quenching studies, quantum yield measurements and nanosecond TA spectroscopy, we have identified the productive reaction pathways along with critical reaction intermediates and rate constants for photoredox nickel-catalyzed cross-coupling between thiols and aryl halides. We have found that a self-sustained Ni(I/III) cycle is operative for product formation, in contrast to previously proposed closed photocycles involving Ni(I), Ni(II),

and Ni(III) states. In addition to identifying the productive cycle, we also determined that pyHI formed *in situ* serves three crucial roles in facilitating the cross-coupling reaction: (1) I<sup>-</sup> serves as an effective quencher for \*Ir(III) to form I· and the highly reducing Ir(II); (2) pyH<sup>+</sup> serves as an electron shuttle between Ir(II) and Ni(II) to form Ir(III) and Ni(I) through the intermediacy of pyH·; and (3) pyH<sup>+</sup> prevents formation of nickel thiolate complexes, which would interfere with the light absorption of Ir(III) via an inner filter effect. Knowledge of these reaction pathways and the roles of pyHI allowed us to optimize the reaction efficiency and expand the substrate scope from aryl iodides to include aryl bromides, thus broadening the applicability of photoredox C-S cross-coupling chemistry. The broader deployment of redox mediators such as I<sup>-</sup>/I<sub>2</sub>·<sup>-</sup> and pyH<sup>+</sup>/pyH· may merit further investigation and can provide a general strategy for future photoredox methods development. In summary, this study demonstrates an example of how mechanistic understanding of complex photoredox systems can inform the optimization and development of photoredox reaction methodologies.

### 3.9 Materials and Methods

**General considerations.** All samples were prepared in a nitrogen-filled glovebox with commercial reagents and anhydrous acetonitrile stored over activated 3 Å molecular sieves. Ir(III) (= [Ir(dF-CF<sub>3</sub>-ppy)<sub>2</sub>(dtbbpy)][PF<sub>6</sub>]) and dtbbpy= 4,4'-di-*tert*-butyl-2,2'-dipyridyl) was purchased from Strem Chemicals and used as received. Ni(II) (= (dtbbpy)NiCl<sub>2</sub>) was prepared *in situ* from (dme)NiCl<sub>2</sub> and dtbbpy, both of which were purchased from Sigma-Aldrich and used as received. Thiols were obtained from Oakwood Chemical. 1-Methylpyridinium iodide was prepared from a metathesis reaction between 1-methylpyridinium chloride and sodium iodide in acetonitrile. Typically, reaction solutions were stored in a 20-mL glass vial and sealed with electric tape. The photocatalytic reactions were carried out on solutions as reported previously<sup>25</sup> except that, rather than purging the head space with nitrogen, all samples described herein were prepared in a glovebox. Additionally, in place of a 34 W blue LED excitation source, solutions were illuminated with a Kessil A160WE Tuna Blue light source at a short distance (Figure 3.19A), and constantly agitated with a magnetic stirrer and cooled with a fan. For reactions at 55 °C, a hot plate equipped



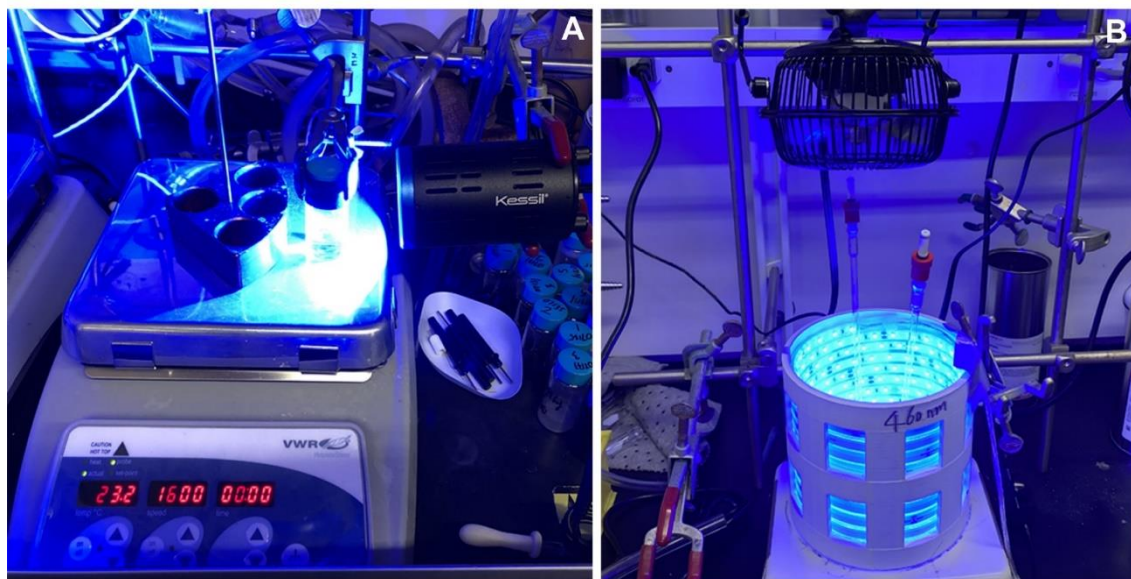


**Figure 3.19.** Blue-light-driven photoredox setups. (A) Reactions running in 20-mL glass vials were excited with a Kessil lamp (A160WE). (B) Reactions running in J. Young NMR tubes were excited with a blue LED strip light arranged in a cylindrical configuration.

with a thermocouple was used. UV-vis spectra were measured with a Cary 5000 spectrophotometer (Agilent) and blank-corrected against the solvent. NMR spectra were recorded on an Agilent DD2 spectrometer (600 MHz) or a Varian/Inova spectrometer (500 MHz). The product yields were obtained based on the  $^1\text{H}$  NMR spectra referenced to pre-quantified 1,3-benzodioxole as the internal standard.

**Stern-Volmer quenching studies.** Steady-state emission spectra were obtained using a fluorimeter (Photon Technology International, Model QM4). Steady-state Stern-Volmer quenching studies were carried out by measuring the steady-state emission intensity ( $I$ ) at 500 nm and exciting the photocatalyst **Ir(III)** at 370 nm. The dynamic Stern-Volmer quenching studies were carried out by exciting solutions at 430 nm and measuring the lifetime ( $\tau$ ) of the photocatalyst excited state,  $^*\text{Ir(III)}$ , at 500 nm using the laser setup described below. The quenching ratio ( $I_0/I$  or  $\tau_0/\tau$ ) and the Stern-Volmer constant ( $K_{sv}$ ) were determined by the relation,

$$I_0/I \text{ or } \tau_0/\tau = 1 + K_{sv} [\text{quencher}]$$

where  $I_0$  and  $\tau_0$  are the emission intensity and lifetime in the absence of quencher, respectively.

The quenching rate ( $k_q$ ) is given by  $k_q = K_{sv}/\tau_0$ . Depending on the experimental conditions and the presence of adventitious oxygen in the sample, the measured  $\tau_0$  varies marginally (see Figure 3.4).

**Reaction progress and quantum yield measurements.** Reaction solutions were prepared with acetonitrile- $d_3$  and stored in J. Young NMR tubes (1 mL each) in a  $N_2$ -filled glovebox. For samples exposed to air, the screw cap of the NMR tube was opened for ~5 sec and then closed, and the solution was mixed by turning the NMR tube over repeatedly. This procedure was repeated two more times. All NMR tubes were placed in a 3-D printed NMR tube holder which was located at the center of the cylindrically-arranged 24 W blue LED strip lights (Figure 3.19B) to ensure that each sample receives the same amount of illumination. A fan was mounted at the top of the apparatus to cool the samples. The product yields were obtained at different times based on the  $^1H$  NMR spectra. For quantum yield measurements, the output from a 150 W Xe arc lamp (Newport 67005 arc lamp housing and 69907 universal arc lamp power supply) was passed through a 435 nm band pass filter (FWHM = 10 nm) and a lens ( $f = 40$  mm) was used to focus the light onto the reaction solution contained within a 1-cm cuvette. The power reaching the sample was attenuated by neutral density filters and measured with an Ophir ORION/PD power meter equipped with a PD-300-ROHS head sensor. The photon flux was calibrated against a potassium ferrioxalate standard based on a published procedure.<sup>63</sup> Each quantum yield measurement was performed in triplicate.

**Time-resolved emission and transient absorption spectroscopy.** A Quanta-Ray Nd:YAG laser (SpectraPhysics) produced laser pulses at 355 nm at a repetition rate of 10 Hz and a time width of 8 ns. The 355 nm laser pulses were either directly used or passed to a MOPO (SpectraPhysics) to produce laser pulses at 430 nm for sample excitation. A 75 W xenon-arc lamp (PTI, Model A1010) was used to generate white probe light for transient absorption (TA) measurements. Both excitation and probe beams were focused and overlapped onto the sample, which was typically contained in a 1-cm cuvette. The emission of the photocatalyst and the transmitted probe light were directed to a Triax 320 spectrometer and the signal was detected with a photomultiplier tube (PMT) (Hamamatsu) coupled to a 1 GHz oscilloscope (LeCroy, Model

9384CM) or a CCD camera (Andor Technology). Further details of the laser spectroscopic setup can be found elsewhere.<sup>64</sup>

**Steady-state quenching.** As seen in Figure 3.3, due to the inner filter effect caused by **Ni(II)**, the excitation light is competitively absorbed by **Ni(II)** against the photocatalyst **Ir(III)**. Therefore, the quenching ratio  $I_0/I$ , based on the measured steady-state emission intensity ( $I$  at 500 nm) of the excited photocatalyst, **\*Ir(III)**, needs to be corrected. The corrected quenching ratio  $(I_0/I)_{\text{corr}}$  was calculated based on<sup>1</sup>

$$(I_0/I)_{\text{corr}} = (I_0/I) \frac{\text{Abs}(\text{Ir})}{\text{Abs}(\text{Ir}) + \text{Abs}(\text{Ni})} \frac{1 - 10^{-(\text{Abs}(\text{Ir}) + \text{Abs}(\text{Ni}))}}{1 - 10^{-\text{Abs}(\text{Ir})}}$$

where  $\text{Abs}(\text{Ir})$  and  $\text{Abs}(\text{Ni})$  are the optical densities (OD) of **Ir(III)** and **Ni(II)**, respectively, at the excitation wavelength ( $\lambda_{\text{exc}} = 370$  nm). The quenching plot (Figure 3.3B, black curve) exhibits weak static quenching after this correction. We note that correction is more accurate when the inner-filter absorption is weak,<sup>1</sup> which is not the case for Figure 3.3A.

**Spectrum deconvolution.** As seen in the inset of Figure 3.7A, the transient absorption (TA) spectrum at 30 ns, after photoexciting a MeCN solution containing 150  $\mu\text{M}$  **Ir(III)** and 25 mM TBAI, consists of contributions from both **Ir(II)** and  $\text{I}_2 \cdot^-$ . The spectrum of **Ir(II)** has been previously determined by spectroelectrochemistry.<sup>2</sup> The spectrum for  $\text{I}_2 \cdot^-$  shows a negligible absorption in the region from 540 to 580 nm.<sup>3</sup> Therefore, we can determine the **Ir(II)** contribution by normalizing the total TA spectrum at 30 ns with the spectrum of **Ir(II)** in the 530-550 nm spectral region. The difference shown by the blue curve in the inset of Figure 3.7A matches well with the previously reported spectrum of  $\text{I}_2 \cdot^-$ .<sup>3</sup>

**Fitting models.** All kinetic trace data before 100 ns were truncated due to scattering or residual emission. All data beyond 100 ns were fitted with either a single-exponential decay or kinetic models. In the following rate equations, square brackets indicate the concentration of the corresponding chemical species at time  $t$  (e.g.,  $[\text{Ir(II)}]$  is concentration of complex **Ir(II)** at time  $t$ ).

**Back reaction between Ir(II) and  $I_2 \cdot^-$ .** In the presence of 25 mM I<sup>-</sup>, \*Ir(III) was effectively quenched within our instrument resolution (8 ns) to form Ir(II) and I $\cdot$ . The latter then associates with I<sup>-</sup> to form  $I_2 \cdot^-$  with a reported rate constant of  $k_0 = 2.5(4) \times 10^{10} \text{ M}^{-1} \text{ s}^{-1}$ ,<sup>3</sup> which suggests that  $I_2 \cdot^-$  forms quickly within our instrument resolution given the presence of 25 mM I<sup>-</sup>. Therefore, as shown in Figure 3.7A, we observed the TA spectrum of Ir(II) and  $I_2 \cdot^-$  immediately after laser excitation at 430 nm. In the presence of TBAI, the TA spectra show similar decay patterns at 525 nm and 720 nm suggesting a clean back reaction between Ir(II) and  $I_2 \cdot^-$ , and hence we can numerically fit the TA trace at 525 nm to extract the back reaction rate  $k_{\text{BET1}}$  based on the following rate equations:

$$\begin{aligned}\frac{d[\text{Ir(II)}]}{dt} &= -k_{\text{BET1}}[\text{Ir(II)}][I_2 \cdot^-] \\ \frac{d[I_2 \cdot^-]}{dt} &= -k_{\text{BET1}}[\text{Ir(II)}][I_2 \cdot^-] \\ S &= \Delta\epsilon_{\text{Ir(II)}}[\text{Ir(II)}] + \Delta\epsilon_{I_2 \cdot^-}[I_2 \cdot^-]\end{aligned}$$

The total TA signal S at 525 nm consists of two contributions from Ir(II) and  $I_2 \cdot^-$ .  $\Delta\epsilon_{\text{Ir(II)}}$  and  $\Delta\epsilon_{I_2 \cdot^-}$  are the difference extinction coefficients for Ir(II) and  $I_2 \cdot^-$ , respectively. They were fixed to  $5100 \text{ M}^{-1} \text{ cm}^{-1}$  and  $300 \text{ M}^{-1} \text{ cm}^{-1}$ , respectively, at 525 nm based on previous literature.<sup>2,3</sup> Finally,  $k_{\text{BET1}}$  was extracted to be  $k_{\text{BET1}} = 9.4(2) \times 10^9 \text{ M}^{-1} \text{ s}^{-1}$  as shown in Figure 3.7B.

**Reaction between Ir(II) and pyH<sup>+</sup>, and disproportionation of  $I_2 \cdot^-$ .** Similar to the case with TBAI, in the presence of pyHI as the quencher, Ir(II) and  $I_2 \cdot^-$  immediately form after excitation. However, Ir(II) quickly disappears due to its reaction with pyH<sup>+</sup> to form Ir(III) and pyH $\cdot$  (see Figure 3.7) with a rate of  $k_{\text{ET1}}$ . Hence, the leftover  $I_2 \cdot^-$  lives longer and eventually decays through disproportionation to form  $I_3^-$  and I<sup>-</sup> with a rate of  $2k_{\text{disp}}$ . We model these processes with the following rate equations:

$$\frac{d[\text{Ir(II)}]}{dt} = -k_{\text{BET1}}[\text{Ir(II)}][I_2 \cdot^-] - k_{\text{ET1}}[\text{pyH}^+][\text{Ir(II)}]$$

$$\frac{d[I_2^{\bullet-}]}{dt} = -k_{\text{BET1}}[\text{Ir(II)}][I_2^{\bullet-}] - 2k_{\text{disp}}[I_2^{\bullet-}]^2$$

$$S = \Delta\varepsilon_{\text{Ir(II)}}[\text{Ir(II)}] + \Delta\varepsilon_{I_2^{\bullet-}}[I_2^{\bullet-}]$$

The total TA signal  $S$  consists of two contributions from **Ir(II)** and  $I_2^{\bullet-}$ .  $\Delta\varepsilon_{\text{Ir(II)}}$  and  $\Delta\varepsilon_{I_2^{\bullet-}}$  are the difference extinction coefficients for **Ir(II)** and  $I_2^{\bullet-}$ , respectively. With  $k_{\text{BET1}}$  determined from the previous step and known values for  $\Delta\varepsilon_{\text{Ir(II)}}$  and  $\Delta\varepsilon_{I_2^{\bullet-}}$  ( $5100 \text{ M}^{-1} \text{ cm}^{-1}$  and  $300 \text{ M}^{-1} \text{ cm}^{-1}$ , respectively),<sup>2,3</sup> we fitted the TA trace at 525 nm (Figure 3.7B, red trace) and extracted  $k_{\text{ET1}} = 1.14(3) \times 10^8 \text{ M}^{-1} \text{ s}^{-1}$ . Similarly, we fitted the TA trace at 700 nm (Figure 3.7B, blue trace) with a fixed  $k_{\text{BET1}}$  and known values for  $\Delta\varepsilon_{\text{Ir(II)}}$  and  $\Delta\varepsilon_{I_2^{\bullet-}} = 950 \text{ M}^{-1} \text{ cm}^{-1}$  and  $1500 \text{ M}^{-1} \text{ cm}^{-1}$ , respectively),<sup>2,3</sup> and obtained that  $2k_{\text{disp}} = 2.9(1) \times 10^9 \text{ M}^{-1} \text{ s}^{-1}$ , which is consistent with the reported literature value.<sup>3</sup>

**Proton-coupled electron transfer from  $I_2^{\bullet-}$  to thiol.** As demonstrated in Figure 3.11,  $I_2^{\bullet-}$  decays faster for a solution (containing  $150 \mu\text{M Ir(III)}$ ,  $25 \text{ mM pyHI}$  and  $150 \text{ mM thiols}$ ) with  $200 \text{ mM pyridine}$  than one without. This indicates a proton-coupled electron transfer (PCET) from thiol to  $I_2^{\bullet-}$  in the presence of pyridine to form thiyl radical and  $\text{pyH}^+$ . We model these processes with the following rate equations:

$$\frac{d[\text{Ir(II)}]}{dt} = -k_{\text{BET1}}[\text{Ir(II)}][I_2^{\bullet-}] - k_{\text{ET1}}[\text{pyH}^+][\text{Ir(II)}]$$

$$\frac{d[I_2^{\bullet-}]}{dt} = -k_{\text{BET1}}[\text{Ir(II)}][I_2^{\bullet-}] - 2k_{\text{disp}}[I_2^{\bullet-}]^2 - k_{\text{PCET}}[\text{Thiol}][I_2^{\bullet-}]$$

$$S = \Delta\varepsilon_{\text{Ir(II)}}[\text{Ir(II)}] + \Delta\varepsilon_{I_2^{\bullet-}}[I_2^{\bullet-}]$$

The total TA signal  $S$  at 700 nm consists of two contributions from **Ir(II)** and  $I_2^{\bullet-}$ .  $\Delta\varepsilon_{\text{Ir(II)}}$  and  $\Delta\varepsilon_{I_2^{\bullet-}}$  are the difference extinction coefficients for **Ir(II)** and  $I_2^{\bullet-}$ , respectively. Note,  $k_{\text{ET1}}$  slightly decreases in the presence of  $200 \text{ mM pyridine}$  (Figure 3.9). With known values for  $k_{\text{BET1}}$ ,  $k_{\text{ET1}}$ ,  $2k_{\text{disp}}$ ,  $\Delta\varepsilon_{\text{Ir(II)}}$  and  $\Delta\varepsilon_{I_2^{\bullet-}}$ , we fitted the TA trace at 700 nm (Figure 3.11, blue and red traces) and extracted  $k_{\text{PCET}} = 2.6(1) \times 10^5 \text{ M}^{-1} \text{ s}^{-1}$  for 4-methoxybenzyl mercaptan (**2**) and  $k_{\text{PCET}} = 3.6(1) \times 10^5 \text{ M}^{-1} \text{ s}^{-1}$  for thiophenol (PhSH).

**Ni(I) formation and oxidative addition.** In a solution containing 150  $\mu\text{M}$  **Ir(III)**, 25 mM pyHI, 200 mM pyridine, 150 mM thiol compound 2 and 10 mM **Ni(II)**, we observed a new transient species, which we assigned to **Ni(I)**. This **Ni(I)** was generated by  $\text{pyH}\cdot$  with a rate constant of  $k_{\text{ET2}}$  following the reaction between **Ir(II)** and  $\text{pyH}^+$ , indicated by the rising feature in Figure 3.12C (red curve). The slow decay in a few hundred microseconds was attributed to the back reaction between **Ni(I)** and  $\text{I}_2\cdot^-$  with a rate constant of  $k_{\text{BET2}}$ . **Ni(I)** can also react with aryl iodide (**1a**) through oxidative addition with a rate of  $k_{\text{OA}}[\text{ArI}]$  and a rate constant of  $k_{\text{OA}}$ . Because  $\text{I}_2\cdot^-$  has many decay pathways, we intend to simplify the PCET, disproportionation and other possible unknown processes with one pseudo-first-order decay with a rate constant of  $k_5$ . We can then write the rate equations as the following:

$$\begin{aligned}\frac{d[\text{Ir(II)}]}{dt} &= -k_{\text{BET1}}[\text{Ir(II)}][\text{I}_2\cdot^-] - k_{\text{ET1}}[\text{pyH}^+][\text{Ir(II)}] \\ \frac{d[\text{pyH}\cdot]}{dt} &= k_{\text{ET1}}[\text{pyH}^+][\text{Ir(II)}] - k_{\text{ET2}}[\text{Ni(II)}][\text{pyH}\cdot] \\ \frac{d[\text{Ni(I)}]}{dt} &= k_{\text{ET2}}[\text{Ni(II)}][\text{pyH}\cdot] - k_{\text{BET2}}[\text{Ni(I)}][\text{I}_2\cdot^-] - k_{\text{OA}}[\text{ArI}][\text{Ni(I)}] \\ \frac{d[\text{I}_2\cdot^-]}{dt} &= -k_{\text{BET1}}[\text{Ir(II)}][\text{I}_2\cdot^-] - k_{\text{BET2}}[\text{Ni(I)}][\text{I}_2\cdot^-] - k_5[\text{I}_2\cdot^-] \\ S &= \Delta\varepsilon_{\text{Ir(II)}}[\text{Ir(II)}] + \Delta\varepsilon_{\text{I}_2\cdot^-}[\text{I}_2\cdot^-] + \Delta\varepsilon_{\text{Ni(I)}}[\text{Ni(I)}]\end{aligned}$$

The total TA signal  $S$  at 600 nm consists of three contributions from **Ir(II)**,  $\text{I}_2\cdot^-$  and **Ni(I)**.  $\Delta\varepsilon_{\text{Ir(II)}}$ ,  $\Delta\varepsilon_{\text{I}_2\cdot^-}$  and  $\Delta\varepsilon_{\text{Ni(I)}}$  are the difference extinction coefficients for **Ir(II)**,  $\text{I}_2\cdot^-$  and **Ni(I)** respectively. With  $k_{\text{BET1}}$  and  $k_{\text{ET1}}$  determined previously, and known values for  $\Delta\varepsilon_{\text{Ir(II)}}$  and  $\Delta\varepsilon_{\text{I}_2\cdot^-}$  ( $430 \text{ M}^{-1} \text{ cm}^{-1}$  and  $230 \text{ M}^{-1} \text{ cm}^{-1}$ , respectively),<sup>2,3</sup> we first fitted the TA trace at 600 nm (Figure 3.12C, red curve) in the absence of aryl iodide by setting  $[\text{ArI}]$  to 0 (Figure 3.12C, red curve). In this case, we were trying to fit  $k_{\text{ET2}}$ ,  $k_{\text{BET2}}$ ,  $k_5$ , and  $\Delta\varepsilon_{\text{Ni(I)}}$  from one TA trace, which could introduce a large degree of uncertainty. Fortunately,  $\Delta\varepsilon_{\text{Ni(I)}}$  is an insensitive parameter and  $k_{\text{ET2}}$  describes a fast process, so we could extract  $k_{\text{ET2}}$  with reasonable precision. We did not expect to determine  $k_{\text{BET2}}$  and  $k_5$  accurately in this case, but rather set these parameters free to get the best fitting of the

curve for determining the oxidative addition rate in the following step. From this, we obtained  $\Delta\varepsilon_{\text{Ni(I)}} = 1000 \text{ M}^{-1} \text{ cm}^{-1}$ ,  $k_{\text{ET2}} = 6.4(5) \times 10^7 \text{ M}^{-1} \text{ s}^{-1}$ ,  $k_{\text{BET2}} = 6.3(8) \times 10^9 \text{ M}^{-1} \text{ s}^{-1}$ ,  $k_5 = 3.0(2) \times 10^3 \text{ s}^{-1}$ .

To extract the apparent oxidative addition rate  $k_{\text{OA}}[\text{ArI}]$ , we fix all the values obtained from the previous fitting without aryl iodide, and then set  $k_{\text{OA}}[\text{ArI}]$ , as one parameter, free to fit the curves for solutions with known concentration of aryl iodide (Figure 3.12D, blue or cyan traces). In short, we were fitting the oxidative addition (the difference between the blue or cyan trace in Figure 3.12D and the red trace in Figure 3.12C) with just one parameter  $k_{\text{OA}}$ . We measured the apparent oxidative addition rate  $k_{\text{OA}}[\text{ArI}]$  under three different concentrations of 4-iodotoluene (Figure 3.12D, inset), to finally extract an oxidative addition rate constant of  $k_{\text{OA}} = 2.5(2) \times 10^4 \text{ M}^{-1} \text{ s}^{-1}$ , which is consistent with reported value in the literature.<sup>4</sup>

For the solution in the absence of thiol and aryl iodide, a similar decay-rise-decay TA feature was observed at 600 nm (Figure 3.14D, black trace). We can use the same model to fit the trace by setting  $k_{\text{OA}}$  and  $k_5$  to 0, to indicate the absence of the corresponding reactions. With known values for  $k_{\text{BET1}}$ ,  $k_{\text{ET1}}$ ,  $\Delta\varepsilon_{\text{Ir(II)}}$ ,  $\Delta\varepsilon_{\text{I}_2^{\bullet-}}$ ,  $\Delta\varepsilon_{\text{Ni(I)}}$ , we fitted the TA trace as shown in Figure 3.14D (black line). We obtained  $k_{\text{ET2}} = 6.8(3) \times 10^7 \text{ M}^{-1} \text{ s}^{-1}$ , which is in the error range of the value fitted from the previous section ( $k_{\text{ET2}} = 6.4(5) \times 10^7 \text{ M}^{-1} \text{ s}^{-1}$ ). Meanwhile, we also obtained  $k_{\text{BET2}} = 8.5(4) \times 10^9 \text{ M}^{-1} \text{ s}^{-1}$  for the back-electron transfer between **Ni(I)** and  $\text{I}_2^{\bullet-}$ . Note this is slightly larger than the previously fitted value ( $k_{\text{BET2}} = 6.3(8) \times 10^9 \text{ M}^{-1} \text{ s}^{-1}$ ). We believe that this value is more accurate considering the absence of the PCET reaction for thiols in this case.

**Ni(I) formation from direct reduction of Ni(II) by Ir(II).** For a solution containing 150  $\mu\text{M}$  **Ir(III)**, 25 mM TBAI, 10 mM **Ni(II)** and 200 mM pyridine, we observed a new species form slowly over tens of microseconds (Figure 3.15, red trace), which we assigned to **Ni(I)** formed through direct reduction of **Ni(II)** by **Ir(II)** with a rate constant of  $k_{\text{ET3}}$ . Similar to the previous section, the slow decay over a few hundred microseconds was presumably attributed to the back reaction between **Ni(I)** and  $\text{I}_2^{\bullet-}$  with a rate constant of  $k_{\text{BET2}}$ . Then, we can write the following rate equations:

$$\frac{d[\text{Ir(II)}]}{dt} = -k_{\text{BET1}}[\text{Ir(II)}][\text{I}_2^{\bullet-}] - k_{\text{ET3}}[\text{Ni(II)}][\text{Ir(II)}]$$

$$\frac{d[I_2^{\bullet-}]}{dt} = -k_{\text{BET1}}[\text{Ir(II)}][I_2^{\bullet-}] - k_{\text{BET2}}[\text{Ni(I)}][I_2^{\bullet-}]$$

$$\frac{d[\text{Ni(I)}]}{dt} = k_{\text{ET3}}[\text{Ni(II)}][\text{Ir(II)}] - k_{\text{BET2}}[\text{Ni(I)}][I_2^{\bullet-}]$$

$$S = \Delta\varepsilon_{\text{Ir(II)}}[\text{Ir(II)}] + \Delta\varepsilon_{I_2^{\bullet-}}[I_2^{\bullet-}] + \Delta\varepsilon_{\text{Ni(I)}}[\text{Ni(I)}]$$

The total TA signal  $S$  at 600 nm consists of three contributions from **Ir(II)**,  $I_2^{\bullet-}$ , **Ni(I)**.  $\Delta\varepsilon_{\text{Ir(II)}}$ ,  $\Delta\varepsilon_{I_2^{\bullet-}}$  and  $\Delta\varepsilon_{\text{Ni(I)}}$  are the difference extinction coefficients for **Ir(II)**,  $I_2^{\bullet-}$  and **Ni(I)**, respectively, which are known to be  $430 \text{ M}^{-1} \text{ cm}^{-1}$ ,  $230 \text{ M}^{-1} \text{ cm}^{-1}$  and  $1000 \text{ M}^{-1} \text{ cm}^{-1}$ .  $k_{\text{BET1}}$  and  $k_{\text{BET2}}$  were also known from previous fitting. Therefore, we effectively fit one parameter which is  $k_{\text{ET3}}$ . By fitting the TA trace at 600 nm (Figure 3.15), we extracted  $k_{\text{ET3}} = 2.5(5) \times 10^6 \text{ M}^{-1} \text{ s}^{-1}$ , corresponding to a formation time of  $\tau = 41(8) \mu\text{s}$ .

For the same solution in the absence of pyridine (containing  $150 \mu\text{M}$  **Ir(III)**,  $25 \text{ mM}$  TBAI and  $10 \text{ mM}$  **Ni(II)**), the same fitting model was used except that  $k_{\text{ET3}}$  and  $k_{\text{BET2}}$  were replaced by  $k_{\text{ET4}}$  and  $k_{\text{BET3}}$ , representing the same reactions, but in the absence of pyridine. The fitting results were shown in Figure 3.16, and we extracted  $k_{\text{ET4}} = 3.0(4) \times 10^7 \text{ M}^{-1} \text{ s}^{-1}$  and  $k_{\text{BET3}} = 5.8(3) \times 10^9 \text{ M}^{-1} \text{ s}^{-1}$ .

**Decay of Ir(II) and formation of Ni(I) mediated by pyHI.** Due to the dominant absorption of **Ir(II)** at 525 nm and **Ni(I)** at 600 nm (inset of Figure 3.7A, and Figure 3.12B), we chose to measure their reaction kinetics at those two respective wavelengths. With TBAI as the quencher, the TA traces at 525 nm (Figures 3.14A and B, red traces) follow a similar trend and decay slowly due to the back reaction between **Ir(II)** and  $I_2^{\bullet-}$ , regardless of the presence of  $10 \text{ mM}$  **Ni(II)** and  $200 \text{ mM}$  pyridine. This suggests that **Ir(II)** does not efficiently react with **Ni(II)** when pyridine is present. Conversely, with pyHI as the quencher (Figures 3.14A and B, black traces), **Ir(II)** quickly reacts with  $\text{pyH}^+$  as shown by the initial fast drop of the TA signal. An additional feature due to **Ni(I)** was observed for the solution with  $10 \text{ mM}$  **Ni(II)** and  $200 \text{ mM}$  pyridine (Figure 3.14B, black trace). This is better demonstrated by the TA traces at 600 nm (Figure 3.14D, black trace). The decay-rise-decay feature in Figure 3.14D is similar to what is observed in Figure 3.12C, suggesting that the formation of **Ni(I)** is not related to the thiol. Interestingly, with TBAI as the quencher, the TA trace at 600 nm exhibits a long-lasting signal with a minor decay for a solution with  $10 \text{ mM}$



**Ni(II)** and 200 mM pyridine (Figure 3.14D, red trace), in contrast to the case without **Ni(II)** and pyridine (Figure 3.14C, red trace). This likely suggests that **Ir(II)** can react with **Ni(II)** to form **Ni(I)** and **Ir(III)**, but on a much longer time scale. Therefore, we propose that **Ni(I)** is generated through the reduction of **Ni(II)** by either  $\text{pyH}\cdot$  or **Ir(II)**, with the former being more efficient.

**UV-vis Study with (dtbbpy)NiCl<sub>2</sub> in the presence of thiolate.** A 50-mL glass bottle was charged with (dme)NiCl<sub>2</sub> (43.9 mg, 0.200 mmol) and dtbbpy (80.5 mg, 0.300 mmol). MeCN (20 mL) was then added and the reaction mixture was stirred for 30 min at room temperature to form **Ni(II)**. A 5 mL aliquot was drawn and added to a 20-mL scintillation vial charged with potassium (4-methoxyphenyl)methanethiolate (4.8 mg, 0.025 mmol), which was prepared from the corresponding thiol and potassium *tert*-butoxide, and the reaction mixture was stirred at room temperature for 2 h. The mixture was then filtered using a 0.2- $\mu\text{m}$  PTFE syringe filter and diluted 10 times with MeCN. A UV-vis spectrum was recorded on the resulting solution.

**Preparation of Ni compounds and UV-vis absorption.** The 10 mM **Ni(0)** [**Ni(0)** = (dtbbpy)Ni(cod)] solution was prepared by adding dtbbpy (17.7 mg, 0.0660 mmol), Ni(cod)<sub>2</sub> (16.5 mg, 0.0600 mmol), and pyridine (94.9 mg, 1.20 mmol) to a 20-mL glass vial. The mixture was dissolved in 6 mL MeCN and stirred for 1 h, following which the solution was filtered through a 0.2- $\mu\text{m}$  PTFE filter. The 10 mM **Ni(II)** [**Ni(II)** = (dtbbpy)NiCl<sub>2</sub>] solution was prepared by adding dtbbpy (24.3 mg, 0.0900 mmol), (dme)NiCl<sub>2</sub> (13.2 mg, 0.0600 mmol) and pyridine (94.9 mg, 1.20 mmol) to a 20-mL glass vial. The mixture was dissolved in 6 mL MeCN and stirred for 1 h, following which the solution was filtered through a 0.2- $\mu\text{m}$  PTFE filter. The **Ni(0)** solution was further diluted 40 $\times$  with a MeCN solution containing 200 mM pyridine before the UV-vis spectrum was taken. A solution mixture of **Ni(0)** and **Ni(II)** was made by adding 0.1 mL of the **Ni(0)** solution to 2 mL of the **Ni(II)** solution. Because the resulting solution was still strongly colored, we further diluted the mixed solution 4 $\times$  with the **Ni(II)** solution for the UV-vis absorption measurement. All operations were performed in a N<sub>2</sub>-filled glovebox, and the final solution was stored in an air-tight 1-cm path-length cuvette. For samples exposed to air, we briefly opened the cuvette for  $\sim$ 5 sec and gently shook the cuvette. This process was repeated two more times to fully expose the

sample to air.

**EPR of Ni(0) and Ni(II) Mixture.** 5 mL of MeCN was added to Ni(cod)<sub>2</sub> (13.8 mg, 0.0500 mmol) and dtbbpy (13.4 mg, 0.0500 mmol), and stirred for 2.5 h at room temperature to provide a solution of (dtbbpy)Ni(cod) (**Solution I**). **Solution II** was prepared by adding 5 mL of MeCN to (dme)NiCl<sub>2</sub> (11.0 mg, 0.0500 mmol), dtbbpy (20.1 mg, 0.0750 mmol), and pyridine (79.0 mg, 1.00 mmol) and stirring for 2.5 h at room temperature. A 0.5 mL aliquot of **Solution I** was added then added to **Solution II**, and an EPR spectrum was collected on the resulting sample at 77 K.

**Electrochemistry.** Cyclic voltammetry (CV) measurements were performed with a model 760D electrochemical workstation and software (CH Instruments). Glassy carbon, Ag<sup>+</sup>/Ag, and Pt wire were used as the working, reference, and counter electrodes, respectively. All CVs were referenced to the ferrocenium/ferrocene (Fc<sup>+</sup>/Fc) couple. The **Ni(II)** solution used was as described earlier in the Materials and Methods (Preparation of Ni Compounds and UV-vis Absorption), except that pyridine was omitted and 100 mM TBAPF<sub>6</sub> was added as electrolyte.

### 3.10 Acknowledgements

Dr. Yangzhong Qin performed the acquisition and modelling of spectroscopic data in addition to assisting with reactivity studies. Mr. Nikolas P. Gianoulis assisted with sample preparation and measurements.

### 3.11 References

1. Twilton, J.; Le, C.; Zhang, P.; Shaw, M. H.; Evans, R. W.; MacMillan, D. W. C., The Merger of Transition Metal and Photocatalysis. *Nat. Rev. Chem.* **2017**, *1*, 0052.
2. Tellis, J. C.; Kelly, C. B.; Primer, D. N.; Jouffroy, M.; Patel, N. R.; Molander, G. A., Single-Electron Transmetalation via Photoredox/Nickel Dual Catalysis: Unlocking a New Paradigm for  $sp^3$ - $sp^2$  Cross-Coupling. *Acc. Chem. Res.* **2016**, *49*, 1429-1439.
3. Ghosh, I.; Marzo, L.; Das, A.; Shaikh, R.; Konig, B., Visible Light Mediated Photoredox Catalytic Arylation Reactions. *Acc. Chem. Res.* **2016**, *49*, 1566-1577.
4. Levin, M. D.; Kim, S.; Toste, F. D., Photoredox Catalysis Unlocks Single-Electron Elementary Steps in Transition Metal Catalyzed Cross-Coupling. *ACS Cent. Sci.* **2016**, *2*, 293-301.
5. Diccianni, J. B.; Diao, T. N., Mechanisms of Nickel-Catalyzed Cross-Coupling Reactions. *Trends Chem.* **2019**, *1*, 830-844.
6. Hossain, A.; Bhattacharyya, A.; Reiser, O., Copper's Rapid Ascent in Visible-Light Photoredox Catalysis. *Science* **2019**, *364*, eaav9713.
7. McAtee, R. C.; McClain, E. J.; Stephenson, C. R. J., Illuminating Photoredox Catalysis. *Trends Chem.* **2019**, *1*, 111-125.
8. Hockin, B. M.; Li, C. F.; Robertson, N.; Zysman-Colman, E., Photoredox Catalysts Based on Earth-Abundant Metal Complexes. *Catal. Sci. Technol.* **2019**, *9*, 889-915.
9. Tlahuext-Aca, A.; Hopkinson, M. N.; Daniliuc, C. G.; Glorius, F., Oxidative Addition to Gold(I) by Photoredox Catalysis: Straightforward Access to Diverse (C,N)-Cyclometalated Gold(III) Complexes. *Chem. Eur. J.* **2016**, *22*, 11587-11592.
10. Reed, N. L.; Herman, M. I.; Miltchev, V. P.; Yoon, T. P., Photocatalytic Oxyamination of Alkenes: Copper(II) Salts as Terminal Oxidants in Photoredox Catalysis. *Org. Lett.* **2018**, *20*, 7345-7350.
11. Ackerman, L. K. G.; Alvarado, J. I. M.; Doyle, A. G., Direct C-C Bond Formation from Alkanes Using Ni-Photoredox Catalysis. *J. Am. Chem. Soc.* **2018**, *140*, 14059-14063.
12. Shimomaki, K.; Murata, K.; Martin, R.; Iwasawa, N., Visible-Light-Driven Carboxylation of Aryl Halides by the Combined Use of Palladium and Photoredox Catalysts. *J. Am. Chem. Soc.* **2017**, *139*, 9467-9470.
13. Yoo, W. J.; Tsukamoto, T.; Kobayashi, S., Visible-Light-Mediated Chan-Lam Coupling Reactions of Aryl Boronic Acids and Aniline Derivatives. *Angew. Chem. Int. Ed.* **2015**, *54*, 6587-6590.
14. He, J.; Chen, C. Y.; Fu, G. C.; Peters, J. C., Visible-Light-Induced, Copper-Catalyzed Three-Component Coupling of Alkyl Halides, Olefins, and Trifluoromethylthiolate To Generate Trifluoromethyl Thioethers. *ACS Catal.* **2018**, *8*, 11741-11748.
15. Zhang, G. T.; Liu, C.; Yi, H.; Meng, Q. Y.; Bian, C. L.; Chen, H.; Jian, J. X.; Wu, L. Z.; Lei, A. W., External Oxidant-Free Oxidative Cross-Coupling: A Photoredox Cobalt-Catalyzed Aromatic C-H Thiolation for Constructing C-S Bonds. *J. Am. Chem. Soc.* **2015**, *137*, 9273-9280.

16. Hartwig, J. F., Carbon-Heteroatom Bond Formation Catalysed by Organometallic Complexes. *Nature* **2008**, *455*, 314-322.
17. Park, B. Y.; Pirnot, M. T.; Buchwald, S. L., Visible Light-Mediated (Hetero)aryl Amination Using Ni(II) Salts and Photoredox Catalysis in Flow: A Synthesis of Tetracaine. *J. Org. Chem.* **2020**, *85*, 3234-3244.
18. Lim, C. H.; Kudisch, M.; Liu, B.; Miyake, G. M., C-N Cross-Coupling via Photoexcitation of Nickel-Amine Complexes. *J. Am. Chem. Soc.* **2018**, *140*, 7667-7673.
19. Key, R. J.; Vannucci, A. K., Nickel Dual Photoredox Catalysis for the Synthesis of Aryl Amines. *Organometallics* **2018**, *37*, 1468-1472.
20. Corcoran, E. B.; Pirnot, M. T.; Lin, S. S.; Dreher, S. D.; DiRocco, D. A.; Davies, I. W.; Buchwald, S. L.; MacMillan, D. W. C., Aryl Amination Using Ligand-Free Ni(II) Salts and Photoredox Catalysis. *Science* **2016**, *353*, 279-283.
21. Terrett, J. A.; Cuthbertson, J. D.; Shurtleff, V. W.; MacMillan, D. W. C., Switching on Elusive Organometallic Mechanisms with Photoredox Catalysis. *Nature* **2015**, *524*, 330-334.
22. Welin, E. R.; Le, C.; Arias-Rotondo, D. M.; McCusker, J. K.; MacMillan, D. W. C., Photosensitized, Energy Transfer-Mediated Organometallic Catalysis Through Electronically Excited Nickel(II). *Science* **2017**, *355*, 380-384.
23. Kim, T.; McCarver, S. J.; Lee, C.; MacMillan, D. W. C., Sulfonamidation of Aryl and Heteroaryl Halides through Photosensitized Nickel Catalysis. *Angew. Chem. Int. Ed.* **2018**, *57*, 3488-3492.
24. Jouffroy, M.; Kelly, C. B.; Molander, G. A., Thioetherification via Photoredox/Nickel Dual Catalysis. *Org. Lett.* **2016**, *18*, 876-879.
25. Oderinde, M. S.; Frenette, M.; Robbins, D. W.; Aquila, B.; Johannes, J. W., Photoredox Mediated Nickel Catalyzed Cross-Coupling of Thiols With Aryl and Heteroaryl Iodides via Thiyl Radicals. *J. Am. Chem. Soc.* **2016**, *138*, 1760-1763.
26. Shields, B. J.; Kudisch, B.; Scholes, G. D.; Doyle, A. G., Long-Lived Charge-Transfer States of Nickel(II) Aryl Halide Complexes Facilitate Bimolecular Photoinduced Electron Transfer. *J. Am. Chem. Soc.* **2018**, *140*, 3035-3039.
27. Ting, S. I.; Garakyaraghi, S.; Taliaferro, C. M.; Shields, B. J.; Scholes, G. D.; Castellano, F. N.; Doyle, A. G., (3d-d Excited States of Ni(II) Complexes Relevant to Photoredox Catalysis: Spectroscopic Identification and Mechanistic Implications. *J. Am. Chem. Soc.* **2020**, *142*, 5800-5810.
28. Yin, H. L.; Fu, G. C., Mechanistic Investigation of Enantioconvergent Kumada Reactions of Racemic  $\alpha$ -Bromoketones Catalyzed by a Nickel/Bis(oxazoline) Complex. *J. Am. Chem. Soc.* **2019**, *141*, 15433-15440.
29. Sun, R.; Qin, Y.; Ruccolo, S.; Schnedermann, C.; Costentin, C.; Nocera, D. G., Elucidation of a Redox-Mediated Reaction Cycle for Nickel-Catalyzed Cross Coupling. *J. Am. Chem. Soc.* **2019**, *141*, 89-93.

30. Till, N. A.; Tian, L.; Dong, Z.; Scholes, G. D.; MacMillan, D. W. C., Mechanistic Analysis of Metallaphotoredox C-N Coupling: Photocatalysis Initiates and Perpetuates Ni(I)/Ni(III) Coupling Activity. *J. Am. Chem. Soc.* **2020**, *142*, 15830-15841.
31. Jarrett, J. T., The Biosynthesis of Thiol- and Thioether-containing Cofactors and Secondary Metabolites Catalyzed by Radical S-Adenosylmethionine Enzymes. *J. Biol. Chem.* **2015**, *290*, 3972-3979.
32. Ilardi, E. A.; Vitaku, E.; Njardarson, J. T., Data-Mining for Sulfur and Fluorine: An evaluation of pharmaceuticals to reveal opportunities for drug design and discovery. *J. Med. Chem.* **2014**, *57*, 2832-2842.
33. Scott, K. A.; Njardarson, J. T., Analysis of US FDA-Approved Drugs Containing Sulfur Atoms. *Top. Curr. Chem.* **2018**, *376*.
34. Feng, M. H.; Tang, B. Q.; Liang, S. H.; Jiang, X. F., Sulfur Containing Scaffolds in Drugs: Synthesis and application in medicinal chemistry. *Curr. Top. Med. Chem.* **2016**, *16*, 1200-1216.
35. Eichman, C. C.; Stambuli, J. P., Transition Metal Catalyzed Synthesis of Aryl Sulfides. *Molecules* **2011**, *16*, 590-608.
36. Fernandez-Rodriguez, M. A.; Shen, Q. L.; Hartwig, J. F., A General and Long-Lived Catalyst for the Palladium-Catalyzed Coupling of Aryl Halides with Thiols. *J. Am. Chem. Soc.* **2006**, *128*, 2180-2181.
37. Murata, M.; Buchwald, S. L., A General and Efficient Method for the Palladium-Catalyzed Cross-Coupling of Thiols and Secondary Phosphines. *Tetrahedron* **2004**, *60*, 7397-7403.
38. Ke, F.; Qu, Y. Y.; Jiang, Z. Q.; Li, Z. K.; Wu, D.; Zhou, X. G., An Efficient Copper-Catalyzed Carbon-Sulfur Bond Formation Protocol in Water. *Org. Lett.* **2011**, *13*, 454-457.
39. Qiao, Z. J.; Wei, J. P.; Jiang, X. F., Direct Cross-Coupling Access to Diverse Aromatic Sulfide: Palladium-Catalyzed Double C-S Bond Construction Using Na<sub>2</sub>S<sub>2</sub>O<sub>3</sub> as a Sulfurating Reagent. *Org. Lett.* **2014**, *16*, 1212-1215.
40. Wang, X.; Cuny, G. D.; Noel, T., A Mild, One-Pot Stadler-Ziegler Synthesis of Arylsulfides Facilitated by Photoredox Catalysis in Batch and Continuous-Flow. *Angew. Chem. Int. Ed.* **2013**, *52*, 7860-7864.
41. Liu, B.; Lim, C. H.; Miyake, G. M., Visible-Light-Promoted C-S Cross-Coupling via Intermolecular Charge Transfer. *J. Am. Chem. Soc.* **2017**, *139*, 13616-13619.
42. Jiang, M.; Li, H. F.; Yang, H. J.; Fu, H., Room-Temperature Arylation of Thiols: Breakthrough with aryl chlorides. *Angew. Chem. Int. Ed.* **2017**, *56*, 874-879.
43. Sikari, R.; Sinha, S.; Das, S.; Saha, A.; Chakraborty, G.; Mondal, R.; Paul, N. D., Achieving Nickel Catalyzed C-S Cross-Coupling under Mild Conditions Using Metal Ligand Cooperativity. *J. Org. Chem.* **2019**, *84*, 4072-4085.
44. Ren, H.; Li, G. F.; Zhu, B.; Lv, X. D.; Yao, L. S.; Wang, X. L.; Su, Z. M.; Guan, W., How Does Iridium(III) Photocatalyst Regulate Nickel(II) Catalyst in Metallaphotoredox-Catalyzed C-S Cross-Coupling? Theoretical and Experimental Insights. *ACS Catal.* **2019**, *9*, 3858-3865.

45. Sun, R.; Qin, Y.; Nocera, D. G., General Paradigm in Photoredox Ni-Catalyzed Cross-Coupling Allows for Light-Free Access to Reactivity. *Angew. Chem. Int. Ed.* **2020**, *59*, 2-9.
46. Qin, Y. Z.; Martindale, B. C. M.; Sun, R.; Rieth, A. J.; Nocera, D. G., Solar-Driven Tandem Photoredox Nickel-Catalysed Cross-Coupling Using Modified Carbon Nitride. *Chem. Sci* **2020**, *11*, 7456-7461.
47. Miller, D. C.; Choi, G. J.; Orbe, H. S.; Knowles, R. R., Catalytic Olefin Hydroamidation Enabled by Proton-Coupled Electron Transfer. *J. Am. Chem. Soc.* **2015**, *137*, 13492-13495.
48. Qiu, G. Q.; Knowles, R. R., Understanding Chemoselectivity in Proton-Coupled Electron Transfer: A Kinetic Study of Amide and Thiol Activation. *J. Am. Chem. Soc.* **2019**, *141*, 16574-16578.
49. Rucolo, S.; Qin, Y. Z.; Schnedermann, C.; Nocera, D. G., General Strategy for Improving the Quantum Efficiency of Photoredox Hydroamidation Catalysis. *J. Am. Chem. Soc.* **2018**, *140*, 14926-14937.
50. Kolthoff, I. M.; Chantooni, M. K.; Bhowmik, S., Dissociation Constants of Uncharged and Monovalent Cation Acids in Dimethyl Sulfoxide. *J. Am. Chem. Soc.* **1968**, *90*, 23-28.
51. Gardner, J. M.; Abrahamsson, M.; Farnum, B. H.; Meyer, G. J., Visible Light Generation of Iodine Atoms and I-I Bonds: Sensitized I<sup>-</sup> Oxidation and I<sub>3</sub><sup>-</sup> Photodissociation. *J. Am. Chem. Soc.* **2009**, *131*, 16206-16214.
52. Wang, X. G.; Stanbury, D. M., Oxidation of Iodide by a Series of Fe(III) Complexes in Acetonitrile. *Inorg. Chem.* **2006**, *45*, 3415-3423.
53. Keith, J. A.; Carter, E. A., Theoretical Insights into Pyridinium-Based Photoelectrocatalytic Reduction of CO<sub>2</sub>. *J. Am. Chem. Soc.* **2012**, *134*, 7580-7583.
54. Lim, C. H.; Holder, A. M.; Hynes, J. T.; Musgrave, C. B., Reduction of CO<sub>2</sub> to Methanol Catalyzed by a Biomimetic Organo-Hydride Produced from Pyridine. *J. Am. Chem. Soc.* **2014**, *136*, 16081-16095.
55. Elliot, A. J., A Pulse-Radiolysis Study of the Reaction of OH with I<sub>2</sub> and the Decay of I<sub>2</sub><sup>-</sup>. *Can. J. Chem.* **1992**, *70*, 1658-1661.
56. Cukier, R. I.; Nocera, D. G., Proton-Coupled Electron Transfer. *Annu. Rev. Phys. Chem.* **1998**, *49*, 337-369.
57. Reece, S. Y.; Nocera, D. G., Proton-Coupled Electron Transfer in Biology: Results From Synergistic Studies in Natural and Model Systems. *Annu. Rev. Biochem* **2009**, *78*, 673-699.
58. Tsou, T. T.; Kochi, J. K., Mechanism of Oxidative Addition - Reaction of Nickel(0) Complexes with Aromatic Halides. *J. Am. Chem. Soc.* **1979**, *101*, 6319-6332.
59. Amatore, C.; Jutand, A., Rates and Mechanisms of Electron-Transfer Nickel-Catalyzed Homocoupling and Carboxylation Reactions - an Electrochemical Approach. *Acta Chem. Scand.* **1990**, *44*, 755-764.
60. Cole, E. B.; Lakkaraju, P. S.; Rampulla, D. M.; Morris, A. J.; Abelev, E.; Bocarsly, A. B., Using a One-Electron Shuttle for the Multielectron Reduction of CO<sub>2</sub> to Methanol: Kinetic, Mechanistic, and Structural Insights. *J. Am. Chem. Soc.* **2010**, *132*, 11539-11551.

61. Lebegue, E.; Agullo, J.; Belanger, D., Electrochemical Behavior of Pyridinium and N-Methyl Pyridinium Cations in Aqueous Electrolytes for CO<sub>2</sub> Reduction. *ChemSusChem* **2018**, *11*, 219-228.
62. Han, D. Y.; Li, S. S.; Xia, S. Q.; Su, M. C.; Jin, J., Nickel-Catalyzed Amination of (Hetero)aryl Halides Facilitated by a Catalytic Pyridinium Additive. *Chem. Eur. J.* **2020**, *26*, 12349-12354.
63. Hatchard, C. G.; Parker, C. A., A New Sensitive Chemical Actinometer -II. Potassium Ferrioxalate as a Standard Chemical Actinometer. *Proc. R. Soc. London, Ser. A* **1956**, *235*, 518-536.
64. Holder, P. G.; Pizano, A. A.; Anderson, B. L.; Stubbe, J.; Nocera, D. G., Deciphering Radical Transport in the Large Subunit of Class I Ribonucleotide Reductase. *J. Am. Chem. Soc.* **2012**, *134*, 1172-1180.

## Chapter 4

# Mechanism-Informed, Light-Free Access to Photoredox-Like Reactivity in Ni-Catalyzed Carbon-Heteroatom Cross-Coupling Reactions

*Parts of this chapter have been published:*

Sun, R.; Qin, Y.; Nocera, D. G., General Paradigm in Photoredox Ni-Catalyzed Cross-Coupling Allows for Light-Free Access to Reactivity. *Angew. Chem. Int. Ed.* **2020**, *59*, 9527-9533.



## 4.1 Introduction

Transition metal catalyzed cross-coupling of aryl halides with nucleophiles is a powerful strategy employed in the construction of the  $sp^2$  carbon-heteroatom bonds that are ubiquitous in pharmaceutical and natural products.<sup>1-5</sup> Although Pd-catalyzed cross-coupling reactions constitute an established field, there has been interest in developing Ni-catalyzed systems due to the broader range of accessible electrophiles and innately more sustainable qualities of Ni as an earth-abundant metal.<sup>6-11</sup> Traditionally, the development of these methodologies emphasizes the design of elaborate and specialized ligands (Figure 4.1A) to make the stereoelectronic properties of the metal center amenable towards the elementary steps that constitute a cross-coupling cycle.<sup>12-15</sup> However, recent developments in photoredox catalysis (Figure 4.1B) have demonstrated that these transformations can be effected using simple commercially available ligands under exceptionally mild conditions through the synergistic action of a photocycle and a transition metal cross-coupling cycle.<sup>16</sup> Several seminal studies have demonstrated that the amination,<sup>17</sup> etherification,<sup>18</sup> and esterification<sup>19</sup> of aryl bromides can be realized under Ni photoredox catalysis using either no exogenous ligand (amination) or simple bipyridyl ligands (etherification and esterification), whereby an Ir(III) photocatalyst has been proposed to generate Ni(II) excited state or Ni(III) intermediates that are necessary for the kinetically challenging reductive elimination of carbon-heteroatom bonds. The interest ignited by these discoveries has led to an immense and ever-growing body of photochemical literature that report the recapitulation of this Ni-catalyzed carbon-heteroatom cross-coupling reactivity across a myriad of different photocatalyst combinations.<sup>20-32</sup>

Notwithstanding the high chemical efficiency achievable under photoredox cross-coupling, the sustainability of these methodologies has been comparatively underemphasized. In particular, the energy cost of the high energy photons employed (typically blue, violet, or near-UV) in photoredox chemistry has often been overlooked, despite the importance of Energy Intensity, defined as energy consumption per unit mass of product, as a metric in quantifying the sustainability of chemical processes.<sup>33-34</sup> Furthermore, the majority of photocatalysts used are

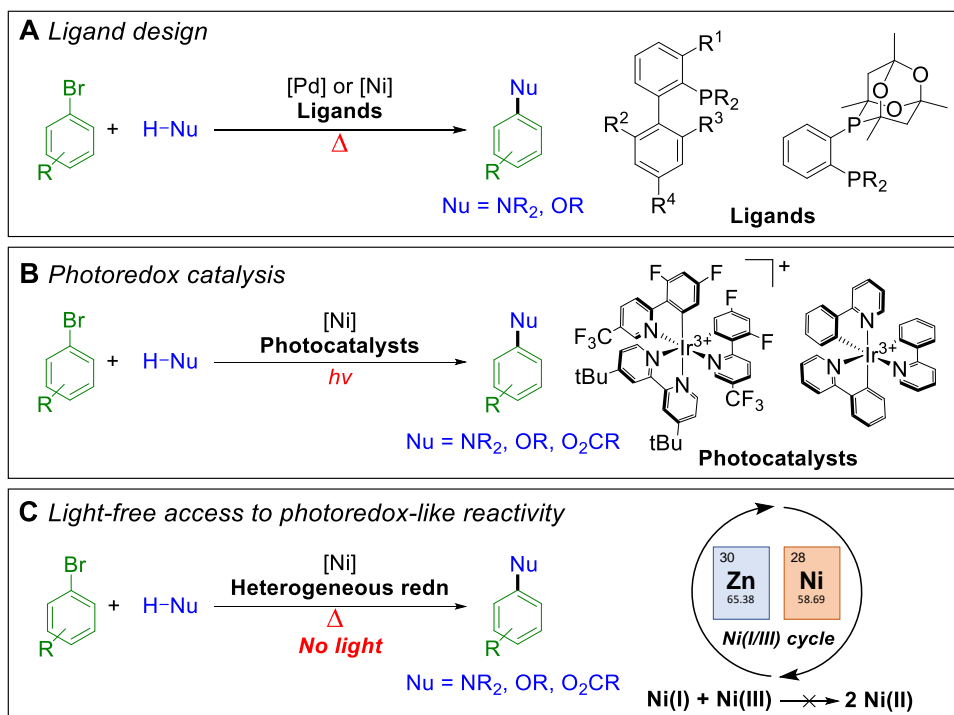


**Figure 4.1.** Strategies for carbon-heteroatom cross-coupling: (A) traditional thermal catalysis, ligand-controlled reactivity; (B) redox catalysis, oxidation state-controlled reactivity; (C) this work, light-free access to photoredox-like oxidation state-controlled reactivity.

based on precious metals such as iridium and ruthenium, and the reaction mechanisms, an understanding of which is critical for rational optimization towards more energy efficient and sustainable methodologies, remain largely undefined. Previous work by our group demonstrated that, in contrast to the closed photocycles commonly proposed for photoredox cross-coupling reactions (Figure 4.2, A and B),<sup>17-19, 21-23, 35-37</sup> a Ni(I/III) cycle (Figure 4.2, C) may be operative in the reaction between aryl bromides and alcohols to form *O*-aryl ethers, where the photon only served to resuscitate the cycle once the catalytically active Ni(I) or Ni(III) species are depleted to form inactive Ni(II) complexes via a highly exergonic comproportionation reaction, akin to what had been proposed for the related electrochemical amination of aryl bromides.<sup>38-39</sup> Given the various mechanistic possibilities proposed for photoredox Ni cross-coupling,<sup>35-37</sup> it was unclear if similar dark cycles were operative in other reactions. A productive dark cycle has important ramifications for methodology development and optimization, as it implies that the necessity of

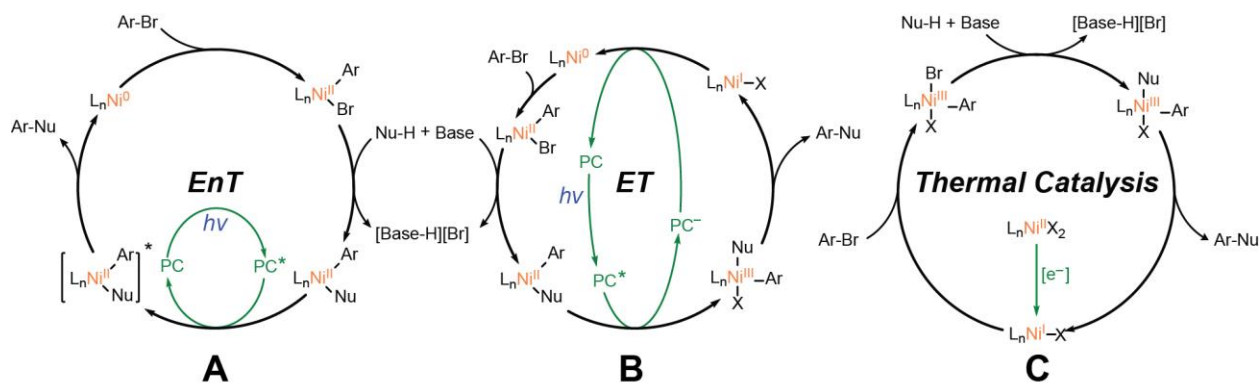


**Figure 4.2.** Mechanisms invoked in photoredox Ni-catalyzed cross-coupling: (A) energy transfer-mediated catalysis; (B) oxidation state modulation; (C) thermally-sustained Ni(I/III) cycle. PC = photocatalyst. EnT = energy transfer. ET = electron transfer.

both continuous energy input and precious metal photocatalysts can be entirely obviated while preserving all the advantages of photoredox cross-coupling systems (i.e., exceptionally mild conditions using inexpensive and readily accessible ligands under Ni catalysis). Despite numerous examples of Ni(I/III) cross-coupling cycles,<sup>40-43</sup> the propensity of Ni to undergo one-electron redox processes has made elucidation of reaction mechanisms challenging in many cases,<sup>44</sup> and the factors that dictate whether a reaction occurs through a Ni(0/II) or a Ni(I/III) cycle are not fully understood. Hence, a general strategy for selectively engaging the Ni(I/III) redox couple under thermal catalysis has remained largely elusive.

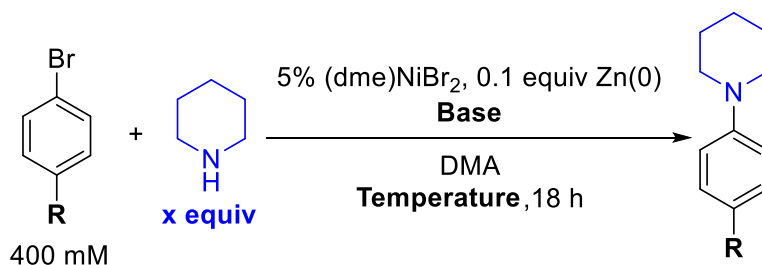
Herein, we demonstrate that photoinitiated, thermally sustained reactivity may constitute a general paradigm in photoredox nickel cross-coupling by showing that the amination, etherification, and esterification of aryl bromides are all accessible under strictly thermal conditions. To this end, we show that photoredox-like reactivity can be recapitulated in the complete absence of a photon source by replacing the Ir photocatalyst and light with a substoichiometric amount of an earth-abundant heterogeneous reductant. Although the combination of a mild heterogeneous reductant and NiX<sub>2</sub> precatalysts has been previously utilized in reductive coupling reactions and as a convenient substitute for sensitive Ni(0) catalysts,<sup>45-48</sup> we demonstrate that the biphasic nature of the reduction process can allow for selective access to a Ni(I/III) cycle by ensuring that the active Ni(I) and Ni(III) intermediates are

maintained at sufficiently low concentrations to mitigate comproportionation. Using this approach, a variety of heteroatomic nucleophiles (amines, alcohols, and carboxylic acids) can be successfully cross-coupled with aryl bromides in the absence of light or precious metal photocatalysts under conditions that otherwise bear resemblance to the parent photoredox systems.

#### 4.2 Development of Light-Free Analogues of Photoredox-Mediated Cross-Coupling Reactions

We began our investigation by studying the photoredox-mediated ligand-free amination of aryl bromides, for which we measured a quantum yield of  $\Phi = 2.7 \pm 0.1$  (see Materials and Methods for details). This confirms the presence of a dark cycle, in contrast to the closed Ni(0/II/III/I) cycle previously proposed for this reaction.<sup>17</sup> Thus, we hypothesized that Zn(0), a commonly employed reductant in Ni cross-coupling catalysis, could replace the combination of photocatalyst and light due to the heterogeneity of the reduction process leading to the slow formation of Ni(I) equivalents, thereby disfavoring comproportionation.

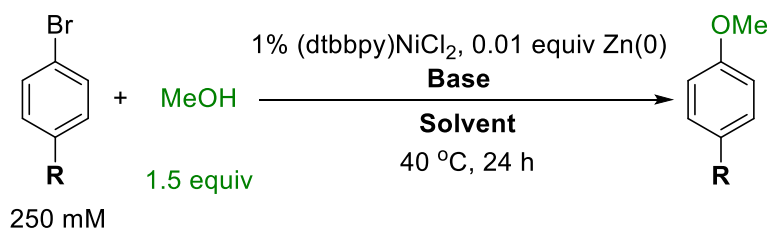
As shown in Table 4.1, a substoichiometric amount of Zn(0) metal in combination with (dme)NiBr<sub>2</sub> (dme = 1,2-dimethoxyethane) furnished the expected aniline product in the cross-coupling between 4-bromobenzotrifluoride and piperidine in the presence of triethylamine at room temperature without exogenous ligand (Entry 1), thereby recapitulating the reactivity observed under photoredox conditions. Upon further optimization, 1,4-diazabicyclo[2.2.2]octane (DABCO) was found to be a more effective base (Entry 2) and elevated temperatures were deleterious (Entries 3-5). For more electron rich arenes (e.g. 4-bromotoluene), quinuclidine was found to be superior to DABCO in furnishing cross-coupled product (Entries 6 and 7), consistent with its higher basicity facilitating the requisite deprotonation of amine.<sup>49</sup> It is noteworthy that the superior performance of DABCO and quinuclidine under this light-free protocol parallels their status as the most effective bases in previously reported photoredox-mediated ligand-free amination reactions, consistent with the existence of a common productive dark cycle as we propose.

**Table 4.1.** Optimization of light-free amination.

Entry	R group	Piperidine equiv	Base (equiv)	T (°C)	Ar-NR <sub>2</sub> Yield (%)
1	CF <sub>3</sub>	1.5	NEt <sub>3</sub> (1.5)	RT	73 <sup>a</sup>
2	CF <sub>3</sub>	1.5	DABCO (1.5)	RT	91 <sup>a</sup>
3	CF <sub>3</sub>	1.5	DABCO (0.1) + NEt <sub>3</sub> (1.5)	RT	88 <sup>a</sup>
4	CF <sub>3</sub>	1.5	DABCO (0.1) + NEt <sub>3</sub> (1.5)	40	72 <sup>a</sup>
5	CF <sub>3</sub>	1.5	DABCO (0.1) + NEt <sub>3</sub> (1.5)	60	53 <sup>a</sup>
6	CH <sub>3</sub>	2.0	DABCO (1.8)	RT	27 <sup>b</sup>
7	CH <sub>3</sub>	2.0	Quin. (1.8)	RT	56 <sup>b</sup>

<sup>a</sup> Yields determined by <sup>19</sup>F NMR. <sup>b</sup> Yields determined by <sup>1</sup>H NMR. DMA = *N,N*-dimethylacetamide. DABCO = 1,4-diazabicyclo[2.2.2]octane. Quin. = quinuclidine.

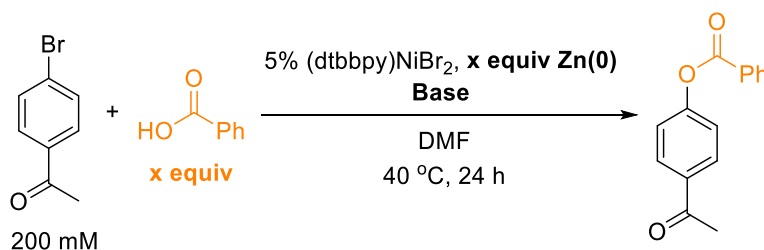
Given the similarity of conditions employed across Ni photoredox cross-coupling methodologies,<sup>17-19, 50</sup> we hypothesized that this strategy of using a heterogeneous reducing agent to thermally access and sustain a Ni(I/III) cycle may be generalized to other nucleophiles. As shown in Entry 1 of Table 4.2, we obtained the expected cross-coupled product in the reaction between methanol and 4'-bromoacetophenone using only 0.01 equivalents of Zn(0) and 1 mol% (dtbbpy)NiCl<sub>2</sub> (dtbbpy = 4,4'-di-*tert*-butyl-2,2'-dipyridyl) prepared *in situ* from (dme)NiCl<sub>2</sub> and dtbbpy. This result further lends credence to the productive Ni(I/III) cycle invoked in our previous mechanistic study.<sup>38</sup>

**Table 4.2.** Optimization of light-free etherification.

Entry	R group	Base (equiv)	Solvent	Ar-OR Yield (%) <sup>a</sup>
1	Ac	NEt <sub>3</sub> (3.0)	MeCN	87
2	Ac	DBU (1.1)	THF	95
3	Ac	Quin. (0.1) + K <sub>3</sub> PO <sub>4</sub> (3.0)	THF	N.D.
4	CH <sub>3</sub>	DBU (1.1)	THF	14
5	CH <sub>3</sub>	MTBD (1.1)	THF	37
6	CH <sub>3</sub>	MTBD (2.0)	THF	5

<sup>a</sup> Yields determined by <sup>1</sup>H NMR. Ac = acetyl. DBU = 1,8-diazabicyclo[5.4.0]undec-7-ene. MTBD = 7-methyl-1,5,7-triazabicyclo[4.4.0]dec-5-ene. N.D. = not detected.

Upon further optimization, we discovered that switching to THF in combination with the stronger amidine base, 1,8-diazabicyclo[5.4.0]undec-7-ene (DBU), led to a higher yield (Entry 2). Inorganic bases such as K<sub>3</sub>PO<sub>4</sub> were ineffective (Entry 3), possibly due to slow proton transfer kinetics or the precipitation of halides required to stabilize *in situ* generated Ni(I) species. For less active aryl bromides, the use of 7-methyl-1,5,7-triazabicyclo[4.4.0]dec-5-ene (MTBD) in place of DBU resulted in superior yields (Entries 4 and 5), whereas increasing the base concentration had a deleterious effect (Entry 6), consistent with the coordinative inhibition of catalytic intermediates by amine bases previously observed for related Pd-catalyzed systems.<sup>51</sup> We next targeted cross-coupling carboxylic acids with aryl bromides to generate the respective *O*-aryl esters. As shown in Entry 1 of Table 4.3, we observed the formation of the desired ester in the reaction between 4'-bromoacetophenone and benzoic acid in the presence of (dtbbpy)NiBr<sub>2</sub> and Zn(0) metal. Reaction optimization revealed HN(<sup>t</sup>Bu)(<sup>i</sup>Pr) to be the most effective base (Entries 2

**Table 4.3.** Optimization of light-free esterification.

Entry	BzOH equiv	Base (equiv)	Zn(0) equiv	Ar-O <sub>2</sub> CR Yield (%) <sup>a</sup>
1	2.0	Quin. (2.0)	0.1	46
2	2.0	NEt <sub>3</sub> (2.0)	0.1	54
3	2.0	HN( <sup>t</sup> Bu)( <sup>i</sup> Pr) (2.0)	0.1	64
4	2.0	HN( <sup>t</sup> Bu)( <sup>i</sup> Pr) (2.0)	0.5	82
5	3.0	HN( <sup>t</sup> Bu)( <sup>i</sup> Pr) (3.0)	0.5	61
6	2.0 as [TBA][OBz]	None	0.5	75

<sup>a</sup> Yields determined by <sup>1</sup>H NMR. TBA = tetrabutylammonium. OBz = benzoate

and 3) and, in contrast to amination and etherification, a higher Zn(0) loading was found to be necessary for efficient cross-coupling (Entry 4). Increasing the amount of acid and base beyond two equivalents did not increase the yield (Entry 5). The use of tetrabutylammonium benzoate in place of benzoic acid and base gave a comparable yield (Entry 6), suggesting that the active nucleophile engaging with the nickel catalyst may be carboxylate rather than carboxylic acid.

The success of aryl esterification is noteworthy given the diminished nucleophilicity of carboxylates relative to other heteroatomic cross-coupling substrates, as demonstrated by the requirement for super-stoichiometric amounts of silver salts in a reported Pd-catalyzed methodology for the esterification of aryl iodides,<sup>52</sup> and a scarcity of examples for the direct cross-coupling of carboxylic acids with aryl bromides under thermal nickel catalysis. Moreover, reports of this transformation under photochemical conditions unanimously invoke photosensitization pathways that necessitate access to a Ni(II) excited state as a precondition for reductive elimination,<sup>19, 23, 26, 31</sup> whereas our reactions in the absence of light preclude any

possibility of excited state formation. These results suggest a Ni(I/III) pathway as an alternative, and hitherto unexplored, mechanistic strategy for achieving this transformation.

### 4.3 Control Experiments and Mechanistic Insights

Next, we performed a series of control experiments to assess our contention that the dominant productive pathways in all three transformations involve a Ni(I/III) cycle. The necessity of both nickel and Zn(0) was demonstrated by the absence of product formation when either was excluded under the A conditions in Figure 4.3 (see Materials and Methods). Furthermore, the yields were greatly diminished when the combination of Ni(II) and Zn(0) was replaced with a Ni(0) source under analogous conditions (Figure 4.3, B), suggesting that the Ni(II) aryl species which form after oxidative addition of the aryl bromide are incapable of undergoing the requisite carbon-heteroatom reductive elimination. Control experiments wherein COD was added to the reactions under the A conditions of Figure 4.3 showed that the difference in reactivity between the A and B conditions of Figure 4.3 is not entirely attributable to the presence of COD (see Materials and Methods). This is consistent with a Ni(I/III) mechanism being the dominant productive pathway as suggested by our previous mechanistic study and literature precedent proposing the necessity of Ni(III) for reductive elimination.<sup>21, 35-36, 38, 41, 53</sup> The background reactivity observed in these control experiments with Ni(0) sources may be attributed to the generation of Ni(I) equivalents during oxidative addition of aryl bromide to Ni(0) as previously proposed.<sup>54-57</sup> We also discovered that Ni(0) in combination with Zn(0) gave higher yields than Ni(0) alone (Figure 4.3, C), suggesting that inactive Ni(II) aryl complexes may be reductively resurrected to re-enter the Ni(I/III) cycle. This may indicate that Zn(0) can further reduce Ni(II) aryl complexes to form Ni(I) aryl species that undergo subsequent oxidative addition to give on-cycle Ni(III) intermediates, in a manner analogous to what has been proposed for Ni-catalyzed reductive coupling.<sup>44</sup>

We were able to establish further parallels between the reactivity reported herein and that under the previously studied photochemical conditions. For example, we observed the formation of a previously characterized Ni(I)-Ni(II) dimer upon treatment of a solution containing Ni(II)



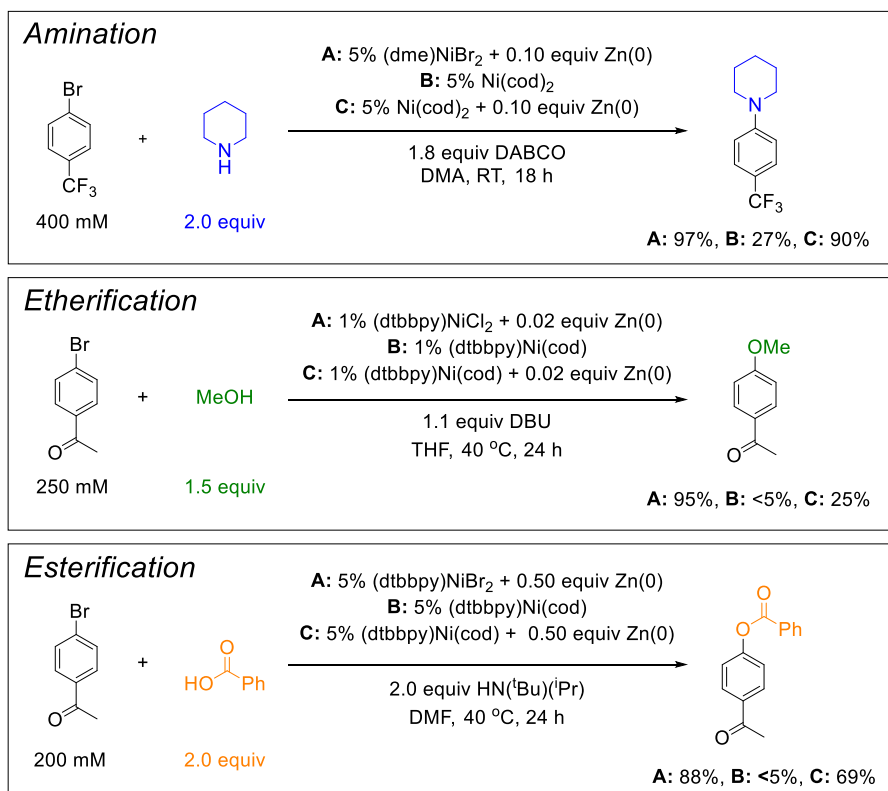


**Figure 4.3.** Effects of nickel source on yields for the three cross-coupling reactions. Yields were determined by <sup>19</sup>F NMR for amination and <sup>1</sup>H NMR for etherification and esterification. COD = 1,5-cyclooctadiene.

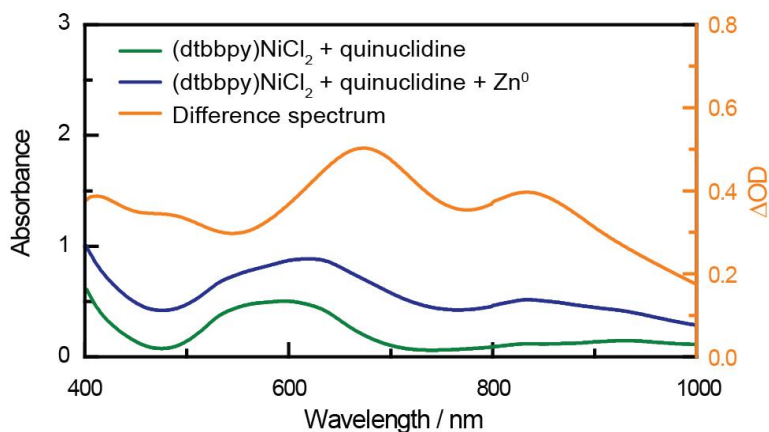


**Figure 4.4.** Absorption spectrum of a MeCN solution containing 12.5 mM (dtbbpy)NiCl<sub>2</sub> and 250 mM quinuclidine (— green, left axis), 12.5 mM (dtbbpy)NiCl<sub>2</sub> and 250 mM quinuclidine stirred with Zn(0) (— blue, left axis), and the difference spectrum between the two samples (— orange, right axis). Note the peaks *circa* 670 and 840 nm corresponding to the Ni(I)-Ni(II) dimer in the difference spectrum.

precatalyst with Zn(0) (see Figure 4.4),<sup>38</sup> suggesting that Zn(0) serves a role analogous to the Ir photocatalyst in the related photoredox reaction by providing access to Ni(I) equivalents necessary for catalysis. Furthermore, similar to the photoredox reaction, there is evidence to suggest the existence of deleterious bimetallic pathways leading to the formation of off-cycle intermediates since we observed a decrease in reaction yield with increasing nickel loading under certain conditions (see Figure 4.5).

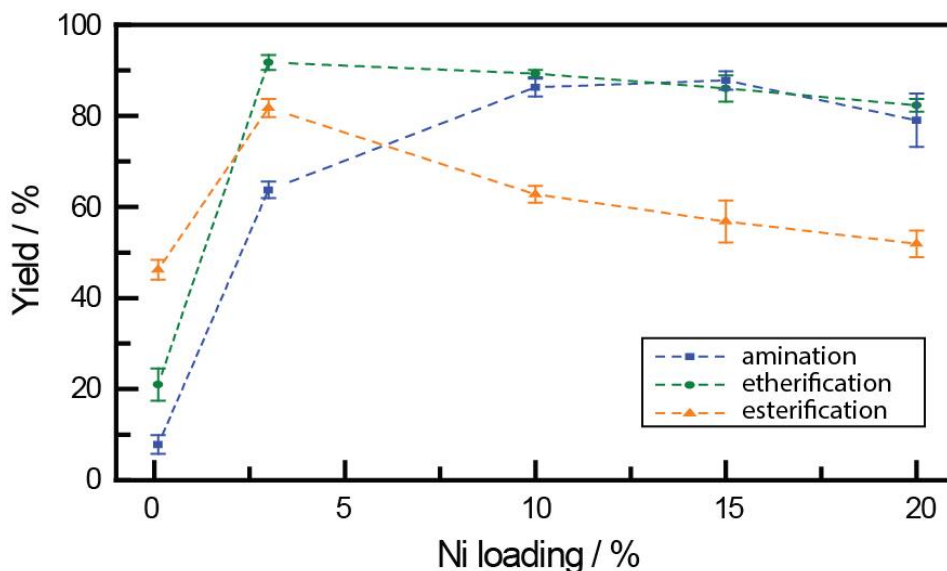


**Figure 4.5.** Reaction yield as a function of nickel loading. Catalyst loading was calculated with respect to aryl bromide. Error bars denote SD ( $n = 3$ ).

#### 4.4 Generality of the Light-Free Reactions

In order to verify the generality of our conclusions across multiple substrates, we investigated the scope to which photoredox-like reactivity could be recapitulated without light, as shown in Figure 4.6. For amination, anilines (**8-10**) and cyclic secondary amines (**1-5**) such as piperidine, which is the most ubiquitous heterocyclic moiety in FDA-approved pharmaceuticals, can all be effectively cross-coupled.<sup>58</sup> Notably, pyrrolidine was not required as an additive for the cross-coupling of anilines, in contrast to the photoredox-mediated reaction where it serves an indispensable role.<sup>17</sup> More challenging substrates such as cyclic primary amines (**6**) or acyclic

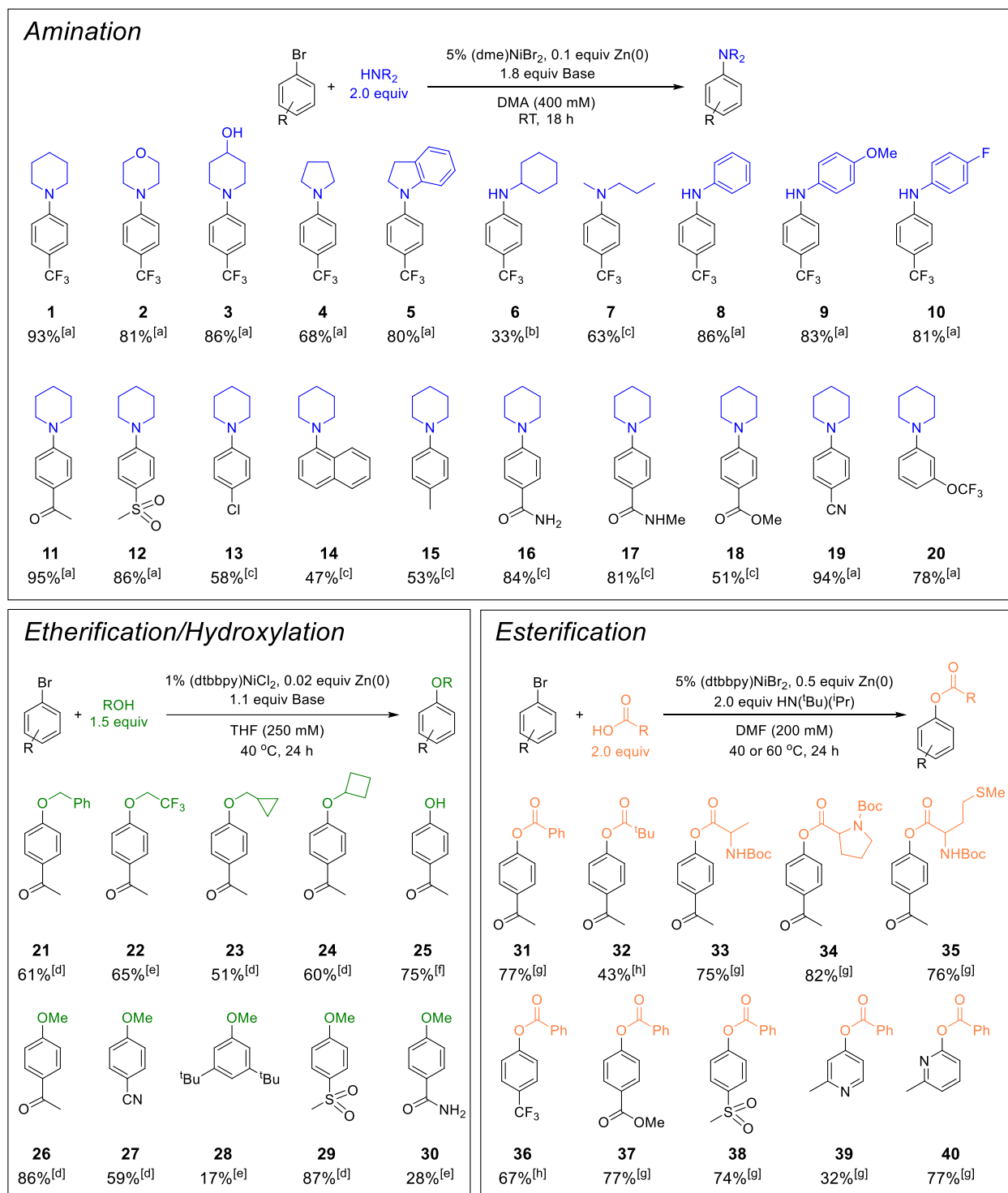


**Figure 4.6.** Demonstration of the generality of light-free reactivity. [a] DABCO used as the base. [b] Quinuclidine used as the base and DMSO used as the solvent. [c] Quinuclidine used as the base. [d] DBU used as the base. [e] MTBD used as the base. [f] See Materials and Methods for details. [g] Reaction performed at 40 °C. [h] Reaction performed at 60 °C. *Boc* = *tert*-butyloxycarbonyl.

secondary amines (**7**) can be successfully cross-coupled using quinuclidine as the base. Furthermore, high chemoselectivity for C-N coupling was observed in the presence of alcoholic functionality (**3**). The yield was found to be highly sensitive towards the coordinating abilities of the amine, with attempts to couple linear primary alkyl amines and heterocyclic aryl bromides being unsuccessful, consistent with their greater binding affinity resulting in the formation of coordinatively saturated Ni(I) species that are unable to dissociate a sufficient number of ligands to undergo concerted oxidative addition.<sup>59</sup> This supposition is supported by the observation that a sterically hindered primary amine (cyclohexylamine) could be successfully coupled (**6**). Given the evidence for mechanistic substrate dependence in Ni cross-coupling reactions,<sup>60</sup> the inefficiency of these recalcitrant coupling partners under our light-free conditions may imply that the extent to which photochemical resuscitation of inactive Ni(II) complexes contributes to the overall observed reactivity could be similarly substrate dependent. With respect to the aryl bromide, the highest yields were obtained with those possessing electron deficient substituents such as ketone (**11**), sulfone (**12**), nitrile (**19**), and trifluoromethyl ether (**20**) functionality. Protic moieties such as those found in amides were well-tolerated (**16** and **17**), and C-N bond formation occurred preferentially at the bromide-functionalized carbon with high fidelity when carbon-chlorine bonds were present on the arene (**13**). Arenes without electron withdrawing groups could also be cross-coupled, albeit in lower yields (**14** and **15**). For etherification, sterically unencumbered primary alcohols (**21-23**) were found to be the most active substrates, consistent with the photoredox system. Notably, weakly nucleophilic alcohols such as 2,2,2-trifluoroethanol could be coupled in moderate yield (**22**). However, secondary alcohols more sterically hindered than cyclobutanol (**24**) were ineffective under our conditions. We discovered that cross-coupling with water proceeds well under conditions analogous to those for esterification (see Materials and Methods), allowing us to obtain **25** in 75% yield. Electron deficient arenes were found to be the most reactive with various polar groups being well-tolerated (**26**, **27**, and **29**). The inclusion of amide functionality significantly diminishes the yield (**30**), possibly due to coordinative inhibition of the nickel catalyst. Regarding esterification, *Boc*-protected amino acids and benzoic

acid were very efficiently coupled (**31**, **33–35**), and sterically hindered pivalic acid gave product in moderate yield (**32**). Aryl bromide reactivity was consistent with that observed for etherification and amination, where electron poor arenes proved to be efficient substrates (**36–38**). However, in contrast to the two previous reactions, derivatives of heterocyclic amines were also accessible (**39** and **40**). Taken together, the breadth of products for which we could successfully recapitulate photoredox-like reactivity in the absence of light establishes the generality of a Ni(I/III) cycle as a productive pathway in photoredox-mediated Ni cross-coupling catalysis.

#### 4.5 Conclusions

We demonstrate that a thermally sustained Ni(I/III) cycle may constitute a general productive mechanism in Ni-catalyzed photoredox-mediated cross-coupling. Our results show that Ni-catalyzed amination, etherification, and esterification of aryl bromides can all be realized across a wide range of substrates *without light* under conditions which otherwise bear resemblance to the parent photochemical methodologies. To this end, one may wish to re-evaluate the growing body of literature that invokes energy transfer as the mechanism for catalysis.<sup>19, 23, 25, 26, 31, 50</sup> As we show here, only a small amount of Ni(I) can initiate self-sustained Ni(I)/Ni(III) thermal catalysis. We suspect that in many of the cycles ascribing catalysis to energy transfer there may well be the production of small amounts of Ni(I) through photoreduction,

Whereas various methodologies exist for the amination and etherification of aryl bromides, our esterification protocol described herein is especially notable given the scarcity of direct Ni-catalyzed cross-coupling between carboxylic acids and aryl bromides under light-free conditions. Critical to this dark reactivity is the ability to selectively engage and sustain a Ni(I/III) catalytic cycle while attenuating deactivation of the catalyst to inactive Ni(II) complexes through bimetallic pathways. This may be achieved through the slow formation of Ni(I) equivalents from NiX<sub>2</sub> precursors with substoichiometric amounts of an earth-abundant heterogeneous reducing agent, thereby allowing us to access photoredox-like cross-coupling reactivity with its intrinsic

advantages while obviating the need for continuous irradiation using high-energy photons or precious metal photocatalysts.

#### 4.6 Materials and Methods

**General considerations.** Reagents were purchased from commercial suppliers, stored in a nitrogen-filled glovebox, and used without further purification with the exception of anilines that showed significant discoloration, which were purified by vacuum distillation. Zinc powder was purchased from Sigma-Aldrich and activated by treatment with dilute HCl according to a standard procedure.<sup>61</sup> All liquid reagents and deuterated solvents were degassed by three cycles of freeze-pump-thaw and stored over activated 3 Å molecular sieves for at least 12 h before use. All non-deuterated solvents were purified by the method of Grubbs and stored over activated 3 Å molecular sieves.<sup>62</sup> All manipulations were performed with the rigorous exclusion of air and moisture unless otherwise stated. <sup>1</sup>H, <sup>13</sup>C, and <sup>19</sup>F NMR spectra were recorded at the Harvard University Department of Chemistry and Chemical Biology NMR facility on an Agilent DD2 spectrometer operating at 600 MHz, a Varian Unity/Inova spectrometer operating at 500 MHz, or a Varian Mercury spectrometer operating at 400 MHz. Chemical shifts for <sup>1</sup>H and <sup>13</sup>C NMR spectra were referenced to residual solvent signals. Chemical shifts for <sup>19</sup>F NMR spectra were referenced to a 50:50 CFCl<sub>3</sub>:CDCl<sub>3</sub> solution. Mass spectrometry was performed at the Harvard University FAS Small Molecule Mass Spectrometry Facility on an Agilent 6220 ESI-TOF spectrometer in positive mode. UV-vis-NIR spectroscopy was performed using a 1.0 cm quartz cuvette (Starna Cells) on a Varian Cary 5000 spectrophotometer. dme = 1,2-dimethoxyethane. dtbbpy = 4,4'-di-*tert*-butyl-2,2'-dipyridyl. DMA = *N,N*-dimethylacetamide. COD = 1,5-cyclooctadiene.

**Quantum yield measurement for amination.** 2.0 mL of a 1.0 mM solution of [Ir(dF-CF<sub>3</sub>-ppy)<sub>2</sub>(dtbbpy)]PF<sub>6</sub> (2.2 mg, 2.0 μmol) was prepared in DMA. Next, a 20 mL scintillation vial was charged with 4-bromobenzotrifluoride (337 mg, 1.50 mmol), pyrrolidine (160 mg, 2.25 mmol), (dme)NiBr<sub>2</sub> (11.6 mg, 37.5 μmol), DABCO (303 mg, 2.70 mmol), 1,3-benzodioxole (18 mg, 0.15 mmol) and 0.3 mL of the 1 mM photocatalyst solution. DMA (6 mL) was then added and the solution was wrapped with aluminum foil, stirred for 30 min on a magnetic stirrer, and filtered

with a 0.22  $\mu\text{m}$  PTFE syringe filter. The resultant solution was stored in a scintillation vial wrapped with aluminum foil. For each quantum yield measurement, a 1.5 mL aliquot of this solution was placed in a 1 cm quartz cuvette and illuminated using monochromic light provided by a 150 W Xe arc lamp (Newport 67005 arc lamp housing and 69907 power supply) with a 350 nm band-pass filter (Thorlabs FB350-10). The power was attenuated with neutral density filters and measured by an Ophir ORION/PD power meter and PD-300-ROHS head sensor. The photon flux was further calibrated using ferrioxalate actinometry.<sup>63</sup> The reactions were performed in triplicate and yields were determined by  $^1\text{H}$  NMR.

**Light-free amination protocol.** In a nitrogen-filled glovebox, 2.0 mL of DMA was added to a 20 mL scintillation vial charged with aryl halide (0.80 mmol, 1.0 equiv), amine (1.6 mmol, 2.0 equiv), base (1.44 mmol, 1.80 equiv), (dme)NiBr<sub>2</sub> (0.04 mmol, 0.05 equiv), and zinc powder (0.08 mmol, 0.10 equiv). The vial was then sealed with electrical tape and vigorously stirred at room temperature for 18 h. The reaction mixture was then diluted with DCM and loaded onto a chromatography column for purification.

**Light-free etherification protocol.** In a nitrogen-filled glovebox, 4.0 mL of THF was added to a 20 mL scintillation vial charged with aryl halide (1.00 mmol, 1.00 equiv), alcohol (1.50 mmol, 1.50 equiv), base (1.10 mmol, 1.10 equiv), (dme)NiCl<sub>2</sub> (0.01 mmol, 0.01 equiv), dtbbpy (0.01 mmol, 0.01 equiv), and zinc powder (0.02 mmol, 0.02 equiv). The vial was then sealed with electrical tape and vigorously stirred at 40 °C for 24 h. The reaction mixture was then diluted with DCM and loaded onto a chromatography column for purification.

**Light-free esterification protocol.** In a nitrogen-filled glovebox, 2.0 mL of DMF was added to a 20 mL scintillation vial charged with aryl halide (0.40 mmol, 1.0 equiv), carboxylic acid (0.80 mmol, 2.0 equiv), *N*-*tert*-butylisopropylamine (0.80 mmol, 2.0 equiv), NiBr<sub>2</sub>-diglyme (0.02 mmol, 0.05 equiv), dtbbpy (0.02 mmol, 0.05 equiv), and zinc powder (0.20 mmol, 0.50 equiv). The vial was then sealed with electrical tape and vigorously stirred at 40 °C for 24 h. The reaction mixture was then diluted with DCM and loaded onto a chromatography column for purification. In cases

where phenol corresponding to the aryl halide was observed as an impurity, the eluted fractions from the column were combined, concentrated, and washed with saturated aqueous  $\text{Na}_2\text{CO}_3$ .

**Spectroscopic verification of Nickel(I) formation.** In a nitrogen-filled glovebox, 6 mL of MeCN was added to a 20 mL scintillation vial charged with  $(\text{dme})\text{NiCl}_2$  (16.5 mg, 0.08 mmol), dtbbpy (20.1 mg, 0.08 mmol), and quinuclidine (166.8 mg, 1.50 mmol). This mixture was stirred for 15 min and a 4 mL aliquot was drawn, to which zinc powder (1.3 mg, 0.02 mmol) was added. Both the remaining stock solution (sample A) and reaction mixture containing zinc (sample B) were left to stir at room temperature for 6 h, before being filtered using 0.22  $\mu\text{m}$  PTFE syringe filters. A UV-vis-NIR spectrum was collected on sample A (Figure 4.4 green trace), after which it was brought back into the glovebox. A 0.4 mL aliquot of sample B was then diluted with 1.8 mL of sample A and a UV-vis-NIR spectrum was collected on the resulting solution (Figure 4.4, blue trace).

**Control reaction with omission of Ni or Zn.** The general cross-coupling procedures were followed for all control experiments with the omission of the relevant catalyst component. All other parameters were as specified under the 'A' conditions of Figure 4.3. Table 4.4 summarizes these results. Residual aryl bromide was quantified by  $^{19}\text{F}$  NMR against 1-fluoronaphthalene for amination, by  $^1\text{H}$  NMR against 1,3-benzodioxole for etherification, and by  $^1\text{H}$  NMR against 1,4-dimethoxybenzene for esterification. No cross-coupled product was observed in any sample.

**Effect of COD on reactions with Ni(II).** In order to probe the possibility that the differences in reactivity observed between Ni(0) and Ni(II) sources was due to the presence of COD in the former, the reactions shown under the 'A' conditions in Figure 4.3 were performed with the addition of COD (2.0 equiv relative to Ni). The following yields were obtained by NMR spectroscopy ( $^{19}\text{F}$  for amination,  $^1\text{H}$  for etherification and esterification): 91% for amination, 96% for etherification, and 83% for esterification.



**Table 4.4.** Summary of control reactions without Ni or Zn.

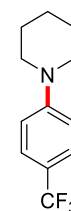
Reaction	Omitted component	Ar-Br remaining (%)
Amination	Zn(0)	> 95%
	(dme)NiBr <sub>2</sub>	> 95%
Etherification	Zn(0)	> 95%
	(dme)NiCl <sub>2</sub>	> 95%
Esterification	Zn(0)	> 95%
	NiBr <sub>2</sub> ·diglyme	84%

**Effect of Ni loading on reaction efficiency.** In these measurements, 4-bromobenzotrifluoride was used as the aryl bromide in all cases with pyrrolidine as the nucleophilic coupling partner for amination, methanol for etherification, and benzoic acid for esterification. In the case of amination and esterification, reaction conditions were as specified in the corresponding SI entries for those substrates with the catalyst loading adjusted accordingly. In the case of etherification, the reaction was performed using the standard etherification conditions with DBU as the base and 0.1 equiv Zn(0). Reaction solutions were prepared from dilution of a catalyst stock solution to reach the appropriate Ni loading. All yields were determined by <sup>19</sup>F NMR spectroscopy.

#### 4.7 Product Characterization

##### 1-(4-(Trifluoromethyl)phenyl)piperidine (1)

The light-free amination protocol was followed using 4-bromobenzotrifluoride as the aryl halide, piperidine as the amine, and DABCO as the base. The product was purified by column chromatography on silica gel using a gradient of 5–15% EtOAc/hexanes to give a colorless oil (170 mg, 92.7%). NMR spectra matched those previously reported.<sup>29</sup>



<sup>1</sup>H NMR (500 MHz, CDCl<sub>3</sub>): δ 7.45 (d, *J* = 8.7 Hz, 2H), 6.91 (d, *J* = 8.7 Hz, 2H), 3.27 (t, *J* = 5.4 Hz, 4H), 1.71–1.59 (m, 6H).

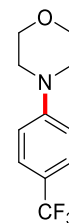
<sup>13</sup>C{<sup>1</sup>H} NMR (126 MHz, CDCl<sub>3</sub>): δ 153.9, 126.4 (q, *J*<sub>C-F</sub> = 3.7 Hz), 125.0 (q, *J*<sub>C-F</sub> = 270.3 Hz), 119.6 (q, *J*<sub>C-F</sub> = 32.8 Hz), 114.7, 49.4, 25.6, 24.4.

$^{19}\text{F}$  NMR (470 MHz,  $\text{CDCl}_3$ ):  $\delta$  -61.2 (s, 3F).

HRMS (ESI)  $m/z$ : calculated for  $[\text{M}+\text{H}]^+$  230.1151, found 230.1155.

#### 4-(4-(Trifluoromethyl)phenyl)morpholine (2)

The light-free amination protocol was followed using 4-bromobenzotrifluoride as the aryl halide, morpholine as the amine, and DABCO as the base. The product was purified by column chromatography on silica gel using a gradient of 5–15% EtOAc/hexanes to give a white solid (150 mg, 81.1%). NMR spectra matched those previously reported.<sup>29</sup>



$^1\text{H}$  NMR (500 MHz,  $\text{CDCl}_3$ ):  $\delta$  7.50 (d,  $J$  = 8.5 Hz, 2H), 6.92 (d,  $J$  = 8.5 Hz, 2H), 3.86 (t,  $J$  = 4.9 Hz, 4H), 3.24 (t,  $J$  = 4.9 Hz, 4H).

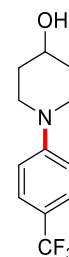
$^{13}\text{C}\{^1\text{H}\}$  NMR (126 MHz,  $\text{CDCl}_3$ ):  $\delta$  153.4, 126.6 (q,  $J_{\text{C-F}}$  = 3.8 Hz), 124.8 (q,  $J_{\text{C-F}}$  = 270.6 Hz), 121.2 (q,  $J_{\text{C-F}}$  = 32.3 Hz), 114.5, 66.8, 48.3.

$^{19}\text{F}$  NMR (470 MHz,  $\text{CDCl}_3$ ):  $\delta$  -61.5 (s, 3F).

HRMS (ESI)  $m/z$ : calculated for  $[\text{M}+\text{H}]^+$  232.0944, found 232.0979.

#### 1-(4-(Trifluoromethyl)phenyl)piperidin-4-ol (3)

The light-free amination protocol was followed using 4-bromobenzotrifluoride as the aryl halide, piperidin-4-ol as the amine, and DABCO as the base. The product was purified by column chromatography on silica gel using a gradient of 0–100% EtOAc/hexanes to give a white solid (168 mg, 85.6%). NMR spectra matched those previously reported.<sup>29</sup>



$^1\text{H}$  NMR (500 MHz,  $\text{CDCl}_3$ ):  $\delta$  7.46 (d,  $J$  = 8.6 Hz, 2H), 6.93 (d,  $J$  = 8.6 Hz, 2H), 3.91 (tt,  $J$  = 8.4, 4.1 Hz, 1H), 3.70–3.61 (m, 2H), 3.04 (ddd,  $J$  = 12.9, 9.6, 3.2 Hz, 2H), 2.05–1.94 (m, 2H), 1.70–1.61 (m, 2H), 1.51 (d,  $J$  = 4.2 Hz, 1H).

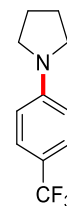
$^{13}\text{C}\{^1\text{H}\}$  NMR (126 MHz,  $\text{CDCl}_3$ ):  $\delta$  153.2, 126.6 (q,  $J_{\text{C-F}}$  = 3.8 Hz), 124.9 (q,  $J_{\text{C-F}}$  = 270.5 Hz), 120.2 (q,  $J_{\text{C-F}}$  = 32.7 Hz), 114.9, 67.7, 46.1, 33.8.

$^{19}\text{F}$  NMR (470 MHz,  $\text{CDCl}_3$ ):  $\delta$  -61.3 (s, 3F).

HRMS (ESI)  $m/z$ : calculated for  $[\text{M}+\text{H}]^+$  246.1100, found 246.1085.

#### 1-(4-(Trifluoromethyl)phenyl)pyrrolidine (4)

The light-free amination protocol was followed using 4-bromobenzotrifluoride as the aryl halide, pyrrolidine as the amine, and DABCO as the base. The product was purified by column chromatography on silica gel using a gradient of 5-15% EtOAc/hexanes to give a beige solid (117 mg, 68.0%). NMR spectra matched those previously reported.<sup>29</sup>



<sup>1</sup>H NMR (500 MHz, CDCl<sub>3</sub>): δ 7.43 (d, *J* = 8.7 Hz, 2H), 6.54 (d, *J* = 8.7 Hz, 2H), 3.61–3.13 (m, 4H), 2.49–1.74 (m, 4H).

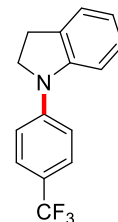
<sup>13</sup>C{<sup>1</sup>H} NMR (126 MHz, CDCl<sub>3</sub>): δ 149.9, 126.5 (q, *J*<sub>CF</sub> = 3.9 Hz), 125.5 (q, *J*<sub>CF</sub> = 270.0 Hz), 116.8 (q, *J*<sub>CF</sub> = 32.6 Hz), 111.0, 47.7, 25.6.

<sup>19</sup>F NMR (376 MHz, CDCl<sub>3</sub>): δ -60.6 (s, 3F).

HRMS (ESI) *m/z*: calculated [M+H]<sup>+</sup> 216.0995, found 216.1007.

#### 1-(4-(Trifluoromethyl)phenyl)indoline (5)

The light-free amination protocol was followed using 4-bromobenzotrifluoride as the aryl halide, indoline as the amine, and DABCO as the base. The product was purified by column chromatography on silica gel using a gradient of 5-15% EtOAc/hexanes to give a white solid (169 mg, 80.2%). NMR spectra matched those previously reported.<sup>17</sup>



<sup>1</sup>H NMR (500 MHz, CDCl<sub>3</sub>): δ 7.55 (d, *J* = 8.5 Hz, 2H), 7.31–7.17 (m, 4H), 7.11 (t, *J* = 7.7 Hz, 1H), 6.82 (t, *J* = 7.4 Hz, 1H), 3.99 (t, *J* = 8.4 Hz, 2H), 3.16 (t, *J* = 8.4 Hz, 2H).

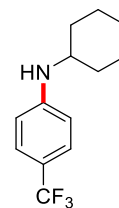
<sup>13</sup>C{<sup>1</sup>H} NMR (126 MHz, CDCl<sub>3</sub>): δ 146.8, 145.7, 131.9, 127.3, 126.5 (q, *J*<sub>CF</sub> = 3.7 Hz), 125.5, 124.8 (q, *J*<sub>CF</sub> = 270.8 Hz), 121.7 (q, *J*<sub>CF</sub> = 32.7 Hz), 120.3, 116.1, 109.2, 52.0, 28.2.

<sup>19</sup>F NMR (470 MHz, CDCl<sub>3</sub>): δ -61.5 (s, 3F).

HRMS (ESI) *m/z*: calculated for [M+H]<sup>+</sup> 264.0995, found 264.1022.

### ***N*-Cyclohexyl-4-(trifluoromethyl)aniline (6)**

The light-free amination protocol was adapted using 4-bromobenzotrifluoride as the aryl halide, cyclohexylamine as the amine, and quinuclidine as the base in DMSO. The product was purified by column chromatography on silica gel using a gradient of 0-15% EtOAc/hexanes to give a white solid (64 mg, 33%). NMR spectra matched those previously reported.<sup>29</sup>



<sup>1</sup>H NMR (500 MHz, CDCl<sub>3</sub>): δ 7.37 (d, *J* = 8.2 Hz, 2H), 6.57 (d, *J* = 8.2 Hz, 2H), 3.88 (d, *J* = 8.3 Hz, 1H), 3.51-3.25 (m, 1H), 2.05 (dd, *J* = 12.9, 2.6 Hz, 2H), 1.83-1.71 (m, 2H), 1.70-1.57 (m, 1H), 1.45-1.33 (m, 2H), 1.29-1.11 (m, 3H).

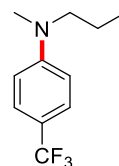
<sup>13</sup>C{<sup>1</sup>H} NMR (126 MHz, CDCl<sub>3</sub>): δ 149.9, 126.8 (q, *J*<sub>C-F</sub> = 3.7 Hz), 125.2 (q, *J*<sub>C-F</sub> = 270.2 Hz), 118.2 (q, *J*<sub>C-F</sub> = 32.6 Hz), 112.1, 51.5, 33.3, 25.9, 25.0.

<sup>19</sup>F NMR (470 MHz, CDCl<sub>3</sub>): δ -60.8 (s, 3F).

HRMS (ESI) *m/z*: calculated for [M+H]<sup>+</sup> 244.1308, found 244.1343.

### ***N*-Methyl-*N*-propyl-4-(trifluoromethyl)aniline (7)**

The light-free amination protocol was followed using 4-bromobenzotrifluoride as the aryl halide, *N*-methylpropan-1-amine as the amine, and quinuclidine as the base. The product was purified by column chromatography on silica gel using a gradient of 0-15% EtOAc/pentane to give a pale-yellow oil (109 mg, 62.7%).



<sup>1</sup>H NMR (500 MHz, CDCl<sub>3</sub>): δ 7.43 (d, *J* = 9.0 Hz, 2H), 6.66 (d, *J* = 9.0 Hz, 2H), 3.32 (t, *J* = 7.5 Hz, 2H), 2.98 (s, 3H), 1.66-1.56 (m, 2H), 0.93 (t, *J* = 7.4 Hz, 3H).

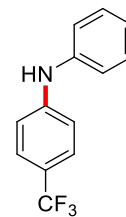
<sup>13</sup>C{<sup>1</sup>H} NMR (126 MHz, CDCl<sub>3</sub>): δ 151.4, 126.5 (q, *J*<sub>C-F</sub> = 3.8 Hz), 125.4 (q, *J*<sub>C-F</sub> = 270.0 Hz), 117.0 (q, *J*<sub>C-F</sub> = 32.6 Hz), 110.9, 54.3, 38.5, 20.1, 11.6.

<sup>19</sup>F NMR (470 MHz, CDCl<sub>3</sub>): δ -60.8 (s, 3F).

HRMS (ESI) *m/z*: calculated for [M+H]<sup>+</sup> 218.1151, found 218.1152.

#### **N-Phenyl-4-(trifluoromethyl)aniline (8)**

The light-free amination protocol was followed using 4-bromobenzotrifluoride as the aryl halide, aniline as the amine, and DABCO as the base. The product was purified by column chromatography on silica gel using a gradient of 25–75% EtOAc/hexanes to give a white solid (163 mg, 85.9%). NMR spectra matched those previously reported.<sup>29</sup>



<sup>1</sup>H NMR (500 MHz, CDCl<sub>3</sub>): δ 7.47 (d, *J* = 8.5 Hz, 2H), 7.33 (t, *J* = 8.0 Hz, 2H), 7.15 (d, *J* = 7.5 Hz, 2H), 7.08–7.02 (m, 3H), 5.91 (s, 1H).

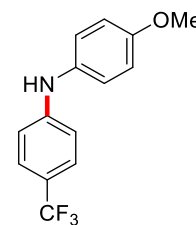
<sup>13</sup>C{<sup>1</sup>H} NMR (126 MHz, CDCl<sub>3</sub>): δ 146.9, 141.3, 129.7, 126.8 (q, *J*<sub>CF</sub> = 3.8 Hz), 124.7 (q, *J*<sub>CF</sub> = 270.8 Hz), 123.1, 121.8 (q, *J*<sub>CF</sub> = 32.8 Hz), 120.2, 115.5.

<sup>19</sup>F NMR (470 MHz, CDCl<sub>3</sub>): δ -61.5 (s, 3F).

HRMS (ESI) *m/z*: calculated for [M+H]<sup>+</sup> 238.0838, found 238.0839.

#### **4-Methoxy-N-(4-(trifluoromethyl)phenyl)aniline (9)**

The light-free amination protocol was followed using 4-bromobenzotrifluoride as the aryl halide, 4-methoxyaniline as the amine, and DABCO as the base. The product was purified by column chromatography on silica gel using a gradient of 25–75% EtOAc/hexanes to give a dark solid (177 mg, 82.8%). NMR spectra matched those previously reported.<sup>64</sup>



<sup>1</sup>H NMR (500 MHz, CDCl<sub>3</sub>): δ 7.43 (d, *J* = 8.8 Hz, 2H), 7.13 (d, *J* = 8.9 Hz, 2H), 6.92 (d, *J* = 8.9 Hz, 2H), 6.86 (d, *J* = 8.8 Hz, 2H), 5.73 (s, 1H), 3.83 (s, 3H).

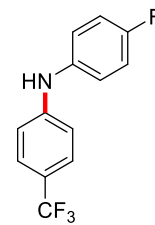
<sup>13</sup>C{<sup>1</sup>H} NMR (126 MHz, CDCl<sub>3</sub>): δ 156.6, 148.7, 133.8, 126.8 (q, *J*<sub>CF</sub> = 3.7 Hz), 124.9 (q, *J*<sub>CF</sub> = 270.5 Hz), 124.4, 120.6 (q, *J*<sub>CF</sub> = 32.7 Hz), 115.0, 113.9, 55.7.

<sup>19</sup>F NMR (470 MHz, CDCl<sub>3</sub>): δ -61.2 (s, 3F).

HRMS (ESI) *m/z*: calculated for [M+H]<sup>+</sup> 268.0944, found 268.0939.

#### 4-Fluoro-*N*-(4-(trifluoromethyl)phenyl)aniline (10)

The light-free amination protocol was followed using 4-bromobenzotrifluoride as the aryl halide, 4-fluoroaniline as the amine, and DABCO as the base. The product was purified by column chromatography on silica gel using a gradient of 25–75% EtOAc/hexanes to give a white solid (165 mg, 80.8%). NMR spectra matched those previously reported.<sup>29</sup>



<sup>1</sup>H NMR (500 MHz, CDCl<sub>3</sub>): δ 7.45 (d, *J* = 8.6 Hz, 2H), 7.20–7.10 (m, 2H), 7.09–7.00 (m, 2H), 6.93 (d, *J* = 8.5 Hz, 2H), 5.79 (s, 1H).

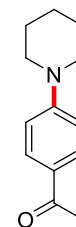
<sup>13</sup>C{<sup>1</sup>H} NMR (126 MHz, CDCl<sub>3</sub>): δ 159.3 (d, *J*<sub>C-F</sub> = 242.6 Hz), 147.6, 137.1 (d, *J*<sub>C-F</sub> = 2.7 Hz), 126.9 (q, *J*<sub>C-F</sub> = 3.8 Hz), 124.8 (q, *J*<sub>C-F</sub> = 270.7 Hz), 123.2 (d, *J*<sub>C-F</sub> = 8.1 Hz), 121.5 (q, *J*<sub>C-F</sub> = 32.7 Hz), 116.4 (d, *J*<sub>C-F</sub> = 22.5 Hz), 114.7.

<sup>19</sup>F NMR (470 MHz, CDCl<sub>3</sub>): δ -61.5 (s, 3F), -119.2 (m, 1F).

HRMS (ESI) *m/z*: calculated for [M+H]<sup>+</sup> 256.0744, found 256.0747.

#### 1-(4-(Piperidin-1-yl)phenyl)ethan-1-one (11)

The light-free amination protocol was followed using 4'-bromoacetophenone as the aryl halide, piperidine as the amine, and DABCO as the base. The product was purified by column chromatography on silica gel using a gradient of 10–35% EtOAc/hexanes to give a white solid (154 mg, 94.7%). NMR spectra matched those previously reported.<sup>65</sup>



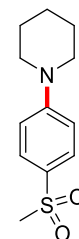
<sup>1</sup>H NMR (500 MHz, CDCl<sub>3</sub>): δ 7.85 (d, *J* = 9.1 Hz, 2H), 6.84 (d, *J* = 9.1 Hz, 2H), 3.35 (t, *J* = 5.2 Hz, 4H), 2.50 (s, 3H), 1.69–1.61 (m, 6H).

<sup>13</sup>C{<sup>1</sup>H} NMR (126 MHz, CDCl<sub>3</sub>): δ 196.4, 154.5, 130.6, 126.8, 113.3, 48.7, 26.2, 25.5, 24.5.

HRMS (ESI) *m/z*: calculated for [M+H]<sup>+</sup> 204.1383, found 204.1398.

#### 1-(4-(Methylsulfonyl)phenyl)piperidine (12)

The light-free amination protocol was followed using 1-bromo-4-(methylsulfonyl)benzene as the aryl halide, piperidine as the amine, and DABCO as the base. The product was purified by column chromatography on silica gel using a gradient of 0–40%



EtOAc/hexanes to give a white solid (164 mg, 85.6%). NMR spectra matched those previously reported.<sup>66</sup>

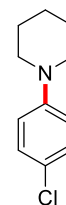
<sup>1</sup>H NMR (500 MHz, CDCl<sub>3</sub>): δ 7.72 (d, *J* = 8.9 Hz, 2H), 6.90 (d, *J* = 9.0 Hz, 2H), 3.36 (t, *J* = 4.7 Hz, 4H), 3.00 (s, 3H), 1.70–1.64 (m, 6H).

<sup>13</sup>C{<sup>1</sup>H} NMR (126 MHz, CDCl<sub>3</sub>): δ 154.6, 129.2, 127.4, 113.8, 48.7, 45.1, 25.3, 24.4.

HRMS (ESI) *m/z*: calculated for [M+H]<sup>+</sup> 240.1053, found 240.1059.

### 1-(4-Chlorophenyl)piperidine (13)

The light-free amination protocol was followed using 1-bromo-4-chlorobenzene as the aryl halide, piperidine as the amine, and quinuclidine as the base. The product was purified by column chromatography on silica gel using DCM as the eluent to give a white solid (91 mg, 58%). NMR spectra matched those previously reported.<sup>65</sup>



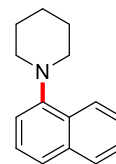
<sup>1</sup>H NMR (500 MHz, CDCl<sub>3</sub>): δ 7.18 (d, *J* = 9.3 Hz, 2H), 6.84 (d, *J* = 9.3 Hz, 2H), 3.11 (t, *J* = 5.5 Hz, 4H), 1.73–1.66 (m, 4H), 1.61–1.53 (m, 2H).

<sup>13</sup>C{<sup>1</sup>H} NMR (126 MHz, CDCl<sub>3</sub>): δ 150.9, 128.9, 124.0, 117.8, 50.8, 25.8, 24.3.

HRMS (ESI) *m/z*: calculated for [M+H]<sup>+</sup> 196.0888, found 196.0894.

### 1-(Naphthalen-1-yl)piperidine (14)

The light-free amination protocol was followed using 1-bromonaphthalene as the aryl halide, piperidine as the amine, and quinuclidine as the base. The product was purified by column chromatography on silica gel using DCM as the eluent to give a yellow oil (80 mg, 47%). NMR spectra matched those previously reported.<sup>65</sup>



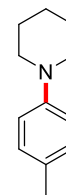
<sup>1</sup>H NMR (500 MHz, CDCl<sub>3</sub>): δ 8.22–8.18 (m, 1H), 7.81 (dd, *J* = 7.1, 2.3 Hz, 1H), 7.52 (d, *J* = 8.2 Hz, 1H), 7.49–7.43 (m, 2H), 7.39 (t, *J* = 7.8 Hz, 1H), 7.06 (dd, *J* = 7.4, 0.8 Hz, 1H), 3.06 (s, br, 4H), 1.85 (quint, *J* = 5.6 Hz, 4H), 1.67 (s, br, 2H).

<sup>13</sup>C{<sup>1</sup>H} NMR (126 MHz, CDCl<sub>3</sub>): δ 151.2, 134.9, 129.3, 128.4, 126.0, 125.8, 125.3, 124.0, 123.0, 114.6, 54.8, 26.8, 24.8.

HRMS (ESI) *m/z*: calculated for [M+H]<sup>+</sup> 212.1434, found 212.1436.

### 1-(*p*-Tolyl)piperidine (15)

The light-free amination protocol was followed using 1-bromo-4-methylbenzene as the aryl halide, piperidine as the amine, and quinuclidine as the base. The product was purified by column chromatography on silica gel using a gradient of 0–15% EtOAc/pentane to give a yellow oil (74 mg, 53%). NMR spectra matched those previously reported.<sup>65</sup>



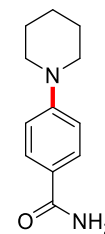
<sup>1</sup>H NMR (500 MHz, CDCl<sub>3</sub>): δ 7.07 (d, *J* = 8.2 Hz, 2H), 6.88 (d, *J* = 8.2 Hz, 2H), 3.10 (t, *J* = 5.6 Hz, 4H), 2.27 (s, 3H), 1.77–1.67 (m, 4H), 1.59 (quint, *J* = 5.9 Hz, 2H).

<sup>13</sup>C{<sup>1</sup>H} NMR (126 MHz, CDCl<sub>3</sub>): δ 150.4, 129.6, 128.8, 117.1, 51.4, 26.1, 24.4, 20.6.

HRMS (ESI) *m/z*: calculated for [M+H]<sup>+</sup> 176.1434, found 176.1456.

### 4-(Piperidin-1-yl)benzamide (16)

The light-free amination protocol was followed using 4-bromobenzamide as the aryl halide, piperidine as the amine, and quinuclidine as the base. The product was purified by column chromatography on silica gel using a gradient of 0–10% MeOH/DCM to give a white solid (138 mg, 84.4%). <sup>1</sup>H NMR spectrum matched that previously reported.<sup>67</sup>



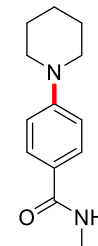
<sup>1</sup>H NMR (500 MHz, (CD<sub>3</sub>)<sub>2</sub>SO): δ 7.72 (d, *J* = 8.6 Hz, 2H), 7.67 (s, 1H), 6.98 (s, 1H), 6.90 (d, *J* = 8.8 Hz, 2H), 3.26 (t, *J* = 5.2 Hz, 4H), 1.64–1.48 (m, 6H).

<sup>13</sup>C{<sup>1</sup>H} NMR (126 MHz, (CD<sub>3</sub>)<sub>2</sub>SO): δ 167.7, 153.0, 128.9, 122.7, 113.5, 48.3, 24.9, 24.0.

HRMS (ESI) *m/z*: calculated for [M+H]<sup>+</sup> 205.1335, found 205.1340.

### *N*-Methyl-4-(piperidin-1-yl)benzamide (17)

The light-free amination protocol was followed using 4-bromo-*N*-methylbenzamide as the aryl halide, piperidine as the amine, and quinuclidine as the base. The product was purified by column chromatography on silica gel using a gradient of 25–100% EtOAc/hexanes to give a white solid (141 mg, 80.7%).



<sup>1</sup>H NMR (500 MHz, (CD<sub>3</sub>)<sub>2</sub>SO): δ 8.10 (q, *J* = 4.6 Hz, 1H), 7.68 (d, *J* = 8.7 Hz, 2H), 6.91 (d, *J* = 8.7 Hz, 2H), 3.25 (t, *J* = 4.8 Hz, 4H), 2.73 (d, *J* = 4.5 Hz, 3H), 1.60–1.54 (m, 6H).

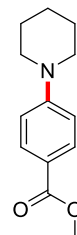
<sup>13</sup>C{<sup>1</sup>H} NMR (126 MHz, (CD<sub>3</sub>)<sub>2</sub>SO): δ 166.4, 152.9, 128.3, 123.1, 113.6, 48.3, 26.1, 25.0, 23.9.



HRMS (ESI)  $m/z$ : calculated for  $[M+H]^+$  219.1492, found 219.1491.

#### Methyl 4-(piperidin-1-yl)benzoate (18)

The light-free amination protocol was followed using methyl 4-bromobenzoate as the aryl halide, piperidine as the amine, and quinuclidine as the base. The product was purified by column chromatography on silica gel using a gradient of 0–15% EtOAc/hexanes to give a white solid (90 mg, 51%).  $^1\text{H}$  NMR spectrum matched that previously reported.<sup>68</sup>



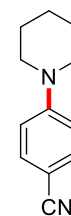
$^1\text{H}$  NMR (500 MHz,  $\text{CDCl}_3$ ):  $\delta$  7.89 (d,  $J = 8.9$  Hz, 2H), 6.85 (d,  $J = 8.9$  Hz, 2H), 3.85 (s, 3H), 3.33 (t,  $J = 5.2$  Hz, 4H), 1.71–1.58 (m, 6H).

$^{13}\text{C}\{^1\text{H}\}$  NMR (126 MHz,  $\text{CDCl}_3$ ):  $\delta$  167.3, 154.6, 131.3, 118.8, 113.7, 51.6, 48.9, 25.5, 24.5.

HRMS (ESI)  $m/z$ : calculated for  $[M+H]^+$  220.1332, found 220.1348.

#### 4-(Piperidin-1-yl)benzotrile (19)

The light-free amination protocol was followed using 4-bromobenzotrile as the aryl halide, piperidine as the amine, and DABCO as the base. The product was purified by column chromatography on silica gel using a gradient of 0–30% EtOAc/hexanes to give a white solid (140 mg, 94.0%). NMR spectra matched those previously reported.<sup>69</sup>



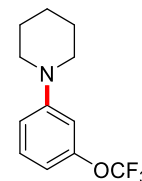
$^1\text{H}$  NMR (500 MHz,  $\text{CDCl}_3$ ):  $\delta$  7.46 (d,  $J = 8.8$  Hz, 2H), 6.83 (d,  $J = 8.9$  Hz, 2H), 3.33 (t,  $J = 5.2$  Hz, 4H), 1.70–1.61 (m, 6H).

$^{13}\text{C}\{^1\text{H}\}$  NMR (126 MHz,  $\text{CDCl}_3$ ):  $\delta$  153.7, 133.6, 120.5, 114.2, 99.0, 48.6, 25.4, 24.4.

HRMS (ESI)  $m/z$ : calculated for  $[M+H]^+$  187.1230, found 187.1231.

#### 1-(3-(Trifluoromethoxy)phenyl)piperidine (20)

The light-free amination protocol was followed using 1-bromo-3-(trifluoromethoxy)benzene as the aryl halide, piperidine as the amine, and DABCO as the base. The product was purified by column chromatography on silica gel using DCM as the eluent to give a colorless oil (152 mg, 77.5%).



$^1\text{H NMR}$  (500 MHz,  $\text{CDCl}_3$ ):  $\delta$  7.24–7.19 (m, 1H), 6.84–6.79 (m, 1H), 6.73–6.70 (m, 1H), 6.66–6.61 (m, 1H), 3.18 (t,  $J = 5.8$  Hz, 4H), 1.74–1.65 (m, 4H), 1.59 (quint, 5.8 Hz, 2H).

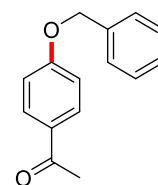
$^{13}\text{C}\{^1\text{H}\}$  NMR (126 MHz,  $\text{CDCl}_3$ ):  $\delta$  153.5, 150.5, 130.0, 120.7 (q,  $J_{\text{C-F}} = 256.3$  Hz), 114.2, 110.6, 108.6, 50.1, 25.7, 24.4.

$^{19}\text{F NMR}$  (470 MHz,  $\text{CDCl}_3$ ):  $\delta$  -57.5 (s, 3F).

HRMS (ESI)  $m/z$ : calculated for  $[\text{M}+\text{H}]^+$  246.1100, found 246.1101.

### 1-(4-(Benzyloxy)phenyl)ethan-1-one (21)

The light-free etherification protocol was followed using 4'-bromoacetophenone as the aryl halide, benzyl alcohol as the alcohol, and DBU as the base. The product was purified by column chromatography on silica gel using a gradient of 0–15% EtOAc/hexanes to give a white solid (139 mg, 61.4%). NMR spectra matched those previously reported.<sup>18</sup>



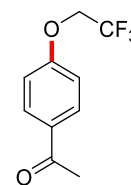
$^1\text{H NMR}$  (500 MHz,  $\text{CDCl}_3$ ):  $\delta$  7.94 (d,  $J = 8.9$  Hz, 2H), 7.45–7.38 (m, 4H), 7.37–7.32 (m, 1H), 7.01 (d,  $J = 8.9$  Hz, 2H), 5.14 (s, 2H), 2.56 (s, 3H).

$^{13}\text{C}\{^1\text{H}\}$  NMR (126 MHz,  $\text{CDCl}_3$ ):  $\delta$  196.8, 162.7, 136.3, 130.7, 130.6, 128.8, 128.3, 127.6, 114.6, 70.2, 26.5.

HRMS (ESI)  $m/z$ : calculated for  $[\text{M}+\text{H}]^+$  227.1067, found 227.1066.

### 1-(4-(2,2,2-Trifluoroethoxy)phenyl)ethan-1-one (22)

The light-free etherification protocol was followed using 4'-bromoacetophenone as the aryl halide, 2,2,2-trifluoroethanol as the alcohol, and MTBD as the base. The product was purified by column chromatography on silica gel using a gradient of 0–15% EtOAc/hexanes to give a white solid (142 mg, 65.1%). NMR spectra matched those previously reported.<sup>18</sup>



$^1\text{H NMR}$  (500 MHz,  $\text{CDCl}_3$ ):  $\delta$  7.97 (d,  $J = 8.8$  Hz, 2H), 6.99 (d,  $J = 8.8$  Hz, 2H), 4.42 (q,  $J = 7.9$  Hz, 2H), 2.58 (s, 3H).

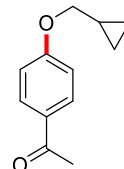
$^{13}\text{C}\{^1\text{H}\}$  NMR (126 MHz,  $\text{CDCl}_3$ ):  $\delta$  196.7, 160.9, 132.0, 130.8, 123.2 (q,  $J_{\text{C-F}} = 278.1$  Hz), 114.6, 65.7 (q,  $J_{\text{C-F}} = 36.2$  Hz), 26.5.

$^{19}\text{F}$  NMR (470 MHz,  $\text{CDCl}_3$ ):  $\delta$  -73.9 (t,  $J = 8.0$  Hz).

HRMS (ESI)  $m/z$ : calculated for  $[\text{M}+\text{H}]^+$  219.0627, found 219.0623.

### 1-(4-(Cyclopropylmethoxy)phenyl)ethan-1-one (23)

The light-free etherification protocol was followed using 4'-bromoacetophenone as the aryl halide, cyclopropylmethanol as the alcohol, and DBU as the base. The product was purified by column chromatography on silica gel using a gradient of 0-15% EtOAc/hexanes to give a white solid (97 mg, 51%). NMR spectra matched those previously reported.<sup>18</sup>



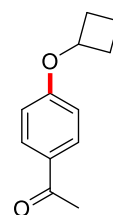
$^1\text{H}$  NMR (500 MHz,  $\text{CDCl}_3$ ):  $\delta$  7.92 (d,  $J = 8.8$  Hz, 2H), 6.92 (d,  $J = 8.8$  Hz, 2H), 3.87 (d,  $J = 7.0$  Hz, 2H), 2.55 (s, 3H), 1.34-1.24 (m, 1H), 0.73-0.62 (m, 2H), 0.40-0.34 (m, 2H).

$^{13}\text{C}\{^1\text{H}\}$  NMR (126 MHz,  $\text{CDCl}_3$ ):  $\delta$  196.9, 163.1, 130.7, 130.4, 114.3, 73.1, 26.5, 10.2, 3.4.

HRMS (ESI)  $m/z$ : calculated for  $[\text{M}+\text{H}]^+$  191.1067, found 191.1066.

### 1-(4-Cyclobutoxyphenyl)ethan-1-one (24)

The light-free etherification protocol was followed using 4'-bromoacetophenone as the aryl halide, cyclobutanol as the alcohol, and DBU as the base. The product was purified by column chromatography on silica gel using a gradient of 50-100% DCM/hexanes to give a white solid (114 mg, 59.9%).



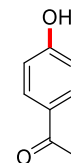
$^1\text{H}$  NMR (500 MHz,  $\text{CDCl}_3$ ):  $\delta$  7.91 (d,  $J = 8.9$  Hz, 2H), 6.83 (d,  $J = 8.8$  Hz, 2H), 4.75-4.66 (m, 1H), 2.54 (s, 3H), 2.52-2.43 (m, 2H), 2.24-2.13 (m, 2H), 1.93-1.84 (m, 1H), 1.78-1.65 (m, 1H).

$^{13}\text{C}\{^1\text{H}\}$  NMR (126 MHz,  $\text{CDCl}_3$ ):  $\delta$  196.9, 161.7, 130.7, 130.3, 114.8, 71.9, 30.6, 26.5, 13.4.

HRMS (ESI)  $m/z$ : calculated for  $[\text{M}+\text{H}]^+$  191.1067, found 191.076.

### 1-(4-Hydroxyphenyl)ethan-1-one (25)

In a nitrogen-filled glovebox, 2.0 mL of DMF was added to a 20 mL scintillation vial charged with 4'-bromoacetophenone (0.40 mmol, 1.00 equiv), water (4.00 mmol, 10.0 equiv), *N*-*tert*-butylisopropylamine (0.80 mmol, 2.00 equiv), NiBr<sub>2</sub>·diglyme (0.02 mmol, 0.05 equiv), dtbbpy (0.02 mmol, 0.05 equiv), and zinc powder (0.20 mmol, 0.50 equiv). The vial was sealed with electrical tape and vigorously stirred at 40 °C for 24 h. The reaction mixture was then diluted with DCM, syringe filtered, and purified *via* column chromatography on silica gel (25-100% EtOAc/hexanes) to give a white solid (41 mg, 75%). NMR spectra matched those previously reported.<sup>18</sup>



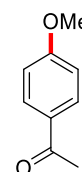
<sup>1</sup>H NMR (500 MHz, CDCl<sub>3</sub>): δ 7.92 (d, *J* = 8.7 Hz, 2H), 6.91 (d, *J* = 8.8 Hz, 2H), 6.10 (s, 1H), 2.57 (s, 3H).

<sup>13</sup>C{<sup>1</sup>H} NMR (126 MHz, CDCl<sub>3</sub>): δ 198.4, 161.2, 131.3, 130.0, 115.6, 26.5.

HRMS (ESI) *m/z*: calculated for [M+H]<sup>+</sup> 137.0597, found 137.0618.

### 1-(4-Methoxyphenyl)ethan-1-one (26)

The light-free etherification protocol was followed using 4'-bromoacetophenone as the aryl halide, methanol as the alcohol, and DBU as the base. The product was purified by column chromatography on silica gel using a gradient of 0-15% EtOAc/pentane to give a white solid (129 mg, 85.9%). NMR spectra matched those previously reported.<sup>18</sup>



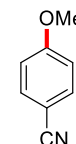
<sup>1</sup>H NMR (500 MHz, CDCl<sub>3</sub>): δ 7.94 (d, *J* = 8.4 Hz, 2H), 6.93 (d, *J* = 8.6 Hz, 2H), 3.87 (s, 3H), 2.56 (s, 3H).

<sup>13</sup>C{<sup>1</sup>H} NMR (126 MHz, CDCl<sub>3</sub>): δ 196.8, 163.6, 130.7, 130.4, 113.8, 55.5, 26.4.

HRMS (ESI) *m/z*: calculated for [M+H]<sup>+</sup> 151.0754, found 151.0756.

### 4-Methoxybenzotrile (27)

The light-free etherification protocol was followed using 4-bromobenzotrile as the aryl halide, methanol as the alcohol, and DBU as the base. The product was purified by column



chromatography on silica gel using a gradient of 0-15% EtOAc/hexanes to give a white solid (79 mg, 59%). NMR spectra matched those previously reported.<sup>22</sup>

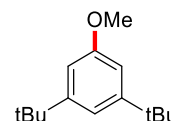
<sup>1</sup>H NMR (500 MHz, CDCl<sub>3</sub>): δ 7.59 (d, *J* = 8.9 Hz, 2H), 6.95 (d, *J* = 8.9 Hz, 2H), 3.86 (s, 3H).

<sup>13</sup>C{<sup>1</sup>H} NMR (126 MHz, CDCl<sub>3</sub>): δ 163.0, 134.1, 119.3, 114.9, 104.1, 55.7.

HRMS (ESI) *m/z*: calculated for [M+H]<sup>+</sup> 134.0600, found 134.0594.

### 1,3-Di-*tert*-butyl-5-methoxybenzene (28)

The light-free etherification protocol was followed using 1-bromo-3,5-di-*tert*-butylbenzene as the aryl halide, methanol as the alcohol, and MTBD as the base.



The product was purified by column chromatography on silica gel using a gradient of 0-10% EtOAc/hexanes to give a colorless oil (38 mg, 17%).

<sup>1</sup>H NMR (600 MHz, CDCl<sub>3</sub>): δ 7.03 (t, *J* = 1.6 Hz, 1H), 6.77 (d, *J* = 2.3 Hz, 2H), 3.82 (s, 3H), 1.32 (s, 18H).

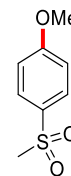
<sup>13</sup>C{<sup>1</sup>H} NMR (126 MHz, CDCl<sub>3</sub>): δ 159.2, 152.4, 115.1, 108.4, 55.3, 35.1, 31.6.

HRMS (ESI) *m/z*: calculated for [M+H]<sup>+</sup> 221.1900, found 221.1905.

### 1-Methoxy-4-(methylsulfonyl)benzene (29)

The light-free etherification protocol was followed using 1-bromo-4-(methylsulfonyl)benzene as the aryl halide, methanol as the alcohol, and DBU as the base.

The product was purified by column chromatography on silica gel using a gradient of 25-100% EtOAc/hexanes to give a white solid (162 mg, 87%). NMR spectra matched those previously reported.<sup>22</sup>



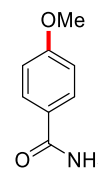
<sup>1</sup>H NMR (500 MHz, CDCl<sub>3</sub>): δ 7.87 (d, *J* = 8.9 Hz, 2H), 7.02 (d, *J* = 8.9 Hz, 2H), 3.89 (s, 3H), 3.03 (s, 3H).

<sup>13</sup>C{<sup>1</sup>H} NMR (126 MHz, CDCl<sub>3</sub>): δ 163.8, 132.4, 129.6, 114.6, 55.8, 45.0.

HRMS (ESI) *m/z*: calculated for [M+H]<sup>+</sup> 187.0423, found 187.0429.

#### 4-Methoxybenzamide (30)

The light-free etherification protocol was followed using 4-bromobenzamide as the aryl halide, methanol as the alcohol, and MTBD as the base. The product was purified by column chromatography on silica gel using a gradient of 0–100% EtOAc/hexanes to give a white solid (43 mg, 28%). NMR spectra matched those previously reported.<sup>70</sup>



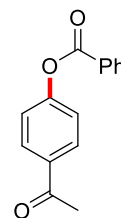
<sup>1</sup>H NMR (500 MHz, (CD<sub>3</sub>)<sub>2</sub>SO): δ 7.88–7.79 (m, 3H), 7.18 (s, 1H), 6.97 (d, *J* = 8.8 Hz, 2H), 3.80 (s, 3H).

<sup>13</sup>C{<sup>1</sup>H} NMR (126 MHz, (CD<sub>3</sub>)<sub>2</sub>SO): δ 167.4, 161.5, 129.3, 126.5, 113.4, 55.3.

HRMS (ESI) *m/z*: calculated for [M+H]<sup>+</sup> 152.0706, found 152.0556.

#### 4-Acetylphenyl benzoate (31)

The light-free esterification protocol was followed using 4'-bromoacetophenone as the aryl halide and benzoic acid as the acid. The product was purified by column chromatography on silica gel using a gradient of 0–40% EtOAc/hexanes to give a white solid (74 mg, 77%). NMR spectra matched those previously reported.<sup>19</sup>



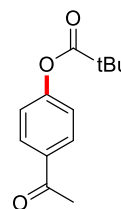
<sup>1</sup>H NMR (500 MHz, CDCl<sub>3</sub>): δ 8.21 (dd, *J* = 8.3, 1.7 Hz, 2H), 8.06 (d, *J* = 8.7 Hz, 2H), 7.67 (t, *J* = 7.5 Hz, 1H), 7.53 (t, *J* = 7.8 Hz, 2H), 7.34 (d, *J* = 8.7 Hz, 2H), 2.63 (s, 3H).

<sup>13</sup>C{<sup>1</sup>H} NMR (126 MHz, CDCl<sub>3</sub>): δ 197.0, 164.8, 154.8, 135.0, 134.1, 130.4, 130.2, 129.2, 128.8, 122.1, 26.8.

HRMS (ESI) *m/z*: calculated for [M+H]<sup>+</sup> 241.0859, found 241.0875.

#### 4-Acetylphenyl pivalate (32)

The light-free esterification protocol was adapted using 4'-bromoacetophenone as the aryl halide and pivalic acid as the acid with the reaction mixture heated to 60°C. The product was purified by column chromatography on silica gel using a gradient of 0–40% EtOAc/hexanes to give a white solid (38 mg, 43%). NMR spectra matched those previously reported.<sup>71</sup>



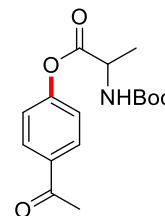
<sup>1</sup>H NMR (500 MHz, CDCl<sub>3</sub>): δ 7.99 (d, *J* = 8.7 Hz, 2H), 7.16 (d, *J* = 8.8 Hz, 2H), 2.60 (s, 3H), 1.37 (s, 9H).

$^{13}\text{C}\{^1\text{H}\}$  NMR (126 MHz,  $\text{CDCl}_3$ ):  $\delta$  197.0, 176.7, 155.1, 134.7, 130.0, 121.9, 39.4, 27.2, 26.8.

HRMS (ESI)  $m/z$ : calculated for  $[\text{M}+\text{H}]^+$  221.1172, found 221.1180.

#### 4-Acetylphenyl (*tert*-butoxycarbonyl)alaninate (33)

The light-free esterification protocol was followed using 4'-bromoacetophenone as the aryl halide and *N*-(*tert*-butoxycarbonyl)-*L*-alanine as the acid. The product was purified by column chromatography on silica gel using a gradient of 0–40% EtOAc/hexanes to give a white solid (92 mg, 75%).



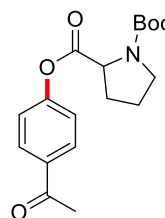
$^1\text{H}$  NMR (500 MHz,  $\text{CDCl}_3$ ):  $\delta$  8.00 (d,  $J$  = 8.8 Hz, 2H), 7.21 (d,  $J$  = 8.8 Hz, 2H), 5.05 (d,  $J$  = 7.8 Hz, 1H), 4.60–4.50 (m, 1H), 2.60 (s, 3H), 1.56 (d,  $J$  = 7.3 Hz, 3H), 1.46 (s, 9H).

$^{13}\text{C}\{^1\text{H}\}$  NMR (126 MHz,  $\text{CDCl}_3$ ):  $\delta$  196.9, 171.7, 155.3, 154.3, 135.1, 130.1, 121.7, 80.4, 49.6, 28.4, 26.7, 18.4.

HRMS (ESI)  $m/z$ : calculated for  $[\text{M}+\text{Na}]^+$  330.1312, found 330.1354.

#### 4-Acetylphenyl (*tert*-butoxycarbonyl)prolinate (34)

The light-free esterification protocol was followed using 4'-bromoacetophenone as the aryl halide and *N*-(*tert*-butoxycarbonyl)-*L*-proline as the acid. The product was purified by column chromatography on silica gel using a gradient of 0–40% EtOAc/hexanes, after which the eluted fractions were concentrated and washed with saturated  $\text{Na}_2\text{CO}_3$  and dried using  $\text{Na}_2\text{SO}_4$ . The solvent was then removed *in vacuo* to give a white solid (110 mg, 82.5%). NMR spectra showed a mixture of two rotamers (denoted by superscripts).



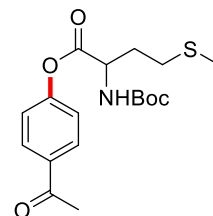
$^1\text{H}$  NMR (500 MHz,  $\text{CDCl}_3$ ):  $\delta$  8.01<sup>1</sup> (d,  $J$  = 8.6 Hz, 1.1H), 7.98<sup>2</sup> (d,  $J$  = 8.6 Hz, 0.9H), 7.22<sup>2</sup> (d,  $J$  = 8.6 Hz, 0.9H), 7.20<sup>1</sup> (d,  $J$  = 8.6 Hz, 1.1H), 4.52<sup>2</sup> (dd,  $J$  = 8.6, 4.4 Hz, 0.4H), 4.46<sup>1</sup> (dd,  $J$  = 8.7, 4.4 Hz, 0.6H), 3.67–3.39 (m, 2.0H), 2.60<sup>1</sup> (s, 1.6H), 2.59<sup>2</sup> (s, 1.3H), 2.45–2.29 (m, 1.0H), 2.23–2.11 (m, 1.0H), 2.11–2.01 (m, 1.0H), 2.01–1.90 (m, 1.0H), 1.48<sup>2</sup> (s, 3.9H), 1.45<sup>1</sup> (s, 5.1H).

$^{13}\text{C}\{^1\text{H}\}$  NMR (126 MHz,  $\text{CDCl}_3$ ):  $\delta$  197.0<sup>2</sup>, 196.8<sup>1</sup>, 171.3<sup>2</sup>, 171.2<sup>1</sup>, 154.7<sup>1</sup>, 154.6<sup>2</sup>, 154.4<sup>1</sup>, 153.7<sup>2</sup>, 135.0<sup>1</sup>, 134.8<sup>2</sup>, 130.1<sup>1</sup>, 130.0<sup>2</sup>, 121.8<sup>2</sup>, 121.4<sup>1</sup>, 80.4<sup>1</sup>, 80.2<sup>2</sup>, 59.3<sup>1</sup>, 59.2<sup>2</sup>, 48.8<sup>2</sup>, 46.6<sup>1</sup>, 31.2<sup>1</sup>, 30.1<sup>2</sup>, 28.5, 26.7, 24.7<sup>2</sup>, 23.9<sup>1</sup>.

HRMS (ESI)  $m/z$ : calculated for  $[\text{M}+\text{Na}]^+$  356.1468, found 356.1479.

#### 4-Acetylphenyl (*tert*-butoxycarbonyl)methioninate (35)

The light-free esterification protocol was followed using 4'-bromoacetophenone as the aryl halide and *N*-(*tert*-butoxycarbonyl)-*L*-methionine as the acid. The product was purified by column chromatography on silica gel using a gradient of 0–40% EtOAc/hexanes to give a white solid (111 mg, 75.5%).



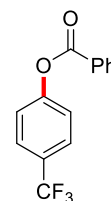
$^1\text{H}$  NMR (500 MHz,  $\text{CDCl}_3$ ):  $\delta$  7.99 (d,  $J$  = 8.8 Hz, 2H), 7.21 (d,  $J$  = 8.8 Hz, 2H), 5.23 (d,  $J$  = 8.4 Hz, 1H), 4.73–4.48 (m, 1H), 2.70–2.61 (m, 2H), 2.59 (s, 3H), 2.36–2.24 (m, 1H), 2.16–2.05 (m, 4H), 1.45 (s, 9H).

$^{13}\text{C}\{^1\text{H}\}$  NMR (126 MHz,  $\text{CDCl}_3$ ):  $\delta$  196.9, 170.8, 155.5, 154.2, 135.1, 130.1, 121.6, 80.5, 53.1, 31.7, 30.2, 28.4, 26.7, 15.7.

HRMS (ESI)  $m/z$ : calculated for  $[\text{M}+\text{Na}]^+$  390.1346, found 390.1334.

#### 4-(Trifluoromethyl)phenyl benzoate (36)

The light-free esterification protocol was followed using 4-bromobenzotrifluoride as the aryl halide and benzoic acid as the acid with the reaction heated to 60 °C. The product was purified by column chromatography on silica gel using a gradient of 0–40% EtOAc/hexanes to give a white solid (71 mg, 67%). NMR spectra matched those previously reported.<sup>19</sup>



$^1\text{H}$  NMR (600 MHz,  $\text{CDCl}_3$ ):  $\delta$  8.21 (dd,  $J$  = 8.3, 1.2 Hz, 2H), 7.71 (d,  $J$  = 8.7 Hz, 2H), 7.67 (t,  $J$  = 7.5 Hz, 1H), 7.54 (t,  $J$  = 7.7 Hz, 2H), 7.36 (d,  $J$  = 8.7 Hz, 2H).

$^{13}\text{C}\{^1\text{H}\}$  NMR (126 MHz,  $\text{CDCl}_3$ ):  $\delta$  164.8, 153.6, 134.1, 130.4, 129.1, 128.8, 128.3 (q,  $J_{\text{C-F}}$  = 33.0 Hz), 127.0, 124.0 (q,  $J_{\text{C-F}}$  = 272.1 Hz), 122.4.

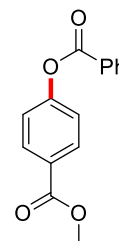


$^{19}\text{F}$  NMR (470 MHz,  $\text{CDCl}_3$ ): -62.2 (s, 3F).

HRMS (ESI)  $m/z$ : calculated for  $[\text{M}+\text{H}]^+$  267.0627, found 267.0608.

#### Methyl 4-(benzyloxy)benzoate (37)

The light-free esterification protocol was followed using methyl 4-bromobenzoate as the aryl halide and benzoic acid as the acid. The product was purified by column chromatography on silica gel using a gradient of 0–80% EtOAc/hexanes to give a white solid (79 mg, 77%). NMR spectra matched those previously reported.<sup>19</sup>



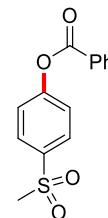
$^1\text{H}$  NMR (500 MHz,  $\text{CDCl}_3$ ):  $\delta$  8.20 (dd,  $J = 8.1, 0.9$  Hz, 2H), 8.13 (d,  $J = 8.8$  Hz, 2H), 7.66 (t,  $J = 7.5$  Hz, 1H), 7.52 (t,  $J = 7.8$  Hz, 2H), 7.31 (d,  $J = 8.8$  Hz, 2H), 3.93 (s, 3H).

$^{13}\text{C}\{^1\text{H}\}$  NMR (126 MHz,  $\text{CDCl}_3$ ):  $\delta$  166.5, 164.8, 154.8, 134.0, 131.4, 130.4, 129.2, 128.8, 127.9, 52.3.

HRMS (ESI)  $m/z$ : calculated for  $[\text{M}+\text{H}]^+$  257.0808, found 257.0806.

#### 4-(Methylsulfonyl)phenyl benzoate (38)

The light-free esterification protocol was followed using 1-bromo-4-(methylsulfonyl)benzene as the aryl halide and benzoic acid as the acid. The product was purified by column chromatography on silica gel using a gradient of 0–80% EtOAc/hexanes to give a white solid (82 mg, 74%).



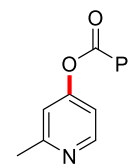
$^1\text{H}$  NMR (600 MHz,  $\text{CDCl}_3$ ):  $\delta$  8.20 (dd,  $J = 8.2, 1.1$  Hz, 2H), 8.03 (d,  $J = 8.8$  Hz, 2H), 7.68 (t,  $J = 7.4$  Hz, 1H), 7.54 (t,  $J = 7.8$  Hz, 2H), 7.45 (d,  $J = 8.7$  Hz, 2H), 3.09 (s, 3H).

$^{13}\text{C}\{^1\text{H}\}$  NMR (126 MHz,  $\text{CDCl}_3$ ):  $\delta$  164.6, 155.2, 138.1, 134.3, 130.5, 129.4, 128.9, 128.8, 123.0, 44.8.

HRMS (ESI)  $m/z$ : calculated for  $[\text{M}+\text{H}]^+$  277.0529, found 277.0539.

#### 2-Methylpyridin-4-yl benzoate (39)

The light-free esterification protocol was adapted using 4-bromo-2-methylpyridine as the aryl halide and benzoic acid as the acid. Aqueous LiBr and  $\text{Na}_2\text{CO}_3$  were added to the crude reaction mixture in DMF at the completion of the reaction, and the



resulting suspension was extracted with EtOAc. The organic fractions were dried over Na<sub>2</sub>SO<sub>4</sub> and the solvent was removed *in vacuo*. The residue was dissolved in DCM and purified by column chromatography on silica gel using a gradient of 0–60% EtOAc/hexanes to give a colorless oil (27 mg, 32%). NMR spectra matched those previously reported.<sup>19</sup>

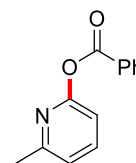
<sup>1</sup>H NMR (500 MHz, CDCl<sub>3</sub>): δ 8.56 (d, *J* = 5.5 Hz, 1H), 8.18 (dd, *J* = 8.3, 1.2 Hz, 2H), 7.66 (t, *J* = 7.5 Hz, 1H), 7.53 (t, *J* = 7.8 Hz, 2H), 7.11 (d, *J* = 2.7 Hz, 1H), 7.06 (dd, *J* = 5.7, 2.6 Hz, 1H), 2.61 (s, 3H).

<sup>13</sup>C{<sup>1</sup>H} NMR (126 MHz, CDCl<sub>3</sub>): δ 164.1, 160.8, 158.3, 150.8, 134.2, 130.4, 129.0, 128.9, 116.6, 114.4, 24.6.

HRMS (ESI) *m/z*: calculated for [M+H]<sup>+</sup> 214.0863, found 214.0874.

#### 6-Methylpyridin-2-yl benzoate (40)

The light-free esterification protocol was adapted using 2-bromo-6-methylpyridine as the aryl halide and benzoic acid as the acid. Aqueous LiBr and Na<sub>2</sub>CO<sub>3</sub> were added to the crude reaction mixture in DMF at the completion of the reaction, and the



resulting suspension was extracted with EtOAc. The organic fractions were dried over Na<sub>2</sub>SO<sub>4</sub> and the solvent was removed *in vacuo*. The residue was dissolved in DCM and purified by column chromatography on silica gel using a gradient of 0–40% EtOAc/hexanes to give a colorless oil (66 mg, 77%).

<sup>1</sup>H NMR (500 MHz, CDCl<sub>3</sub>): δ 8.23 (dd, *J* = 8.3, 1.2 Hz, 2H), 7.72 (t, *J* = 7.8 Hz, 1H), 7.63 (t, *J* = 7.4 Hz, 1H), 7.50 (t, *J* = 7.8 Hz, 2H), 7.12 (d, *J* = 7.5 Hz, 1H), 7.00 (d, *J* = 8.1 Hz, 1H), 2.57 (s, 3H).

<sup>13</sup>C{<sup>1</sup>H} NMR (126 MHz, CDCl<sub>3</sub>): δ 165.1, 158.4, 157.6, 139.8, 133.9, 130.5, 129.3, 128.6, 121.7, 113.5, 24.2.

HRMS (ESI) *m/z*: calculated for [M+H]<sup>+</sup> 214.0863, found 214.0871.

## 4.8 NMR Spectra

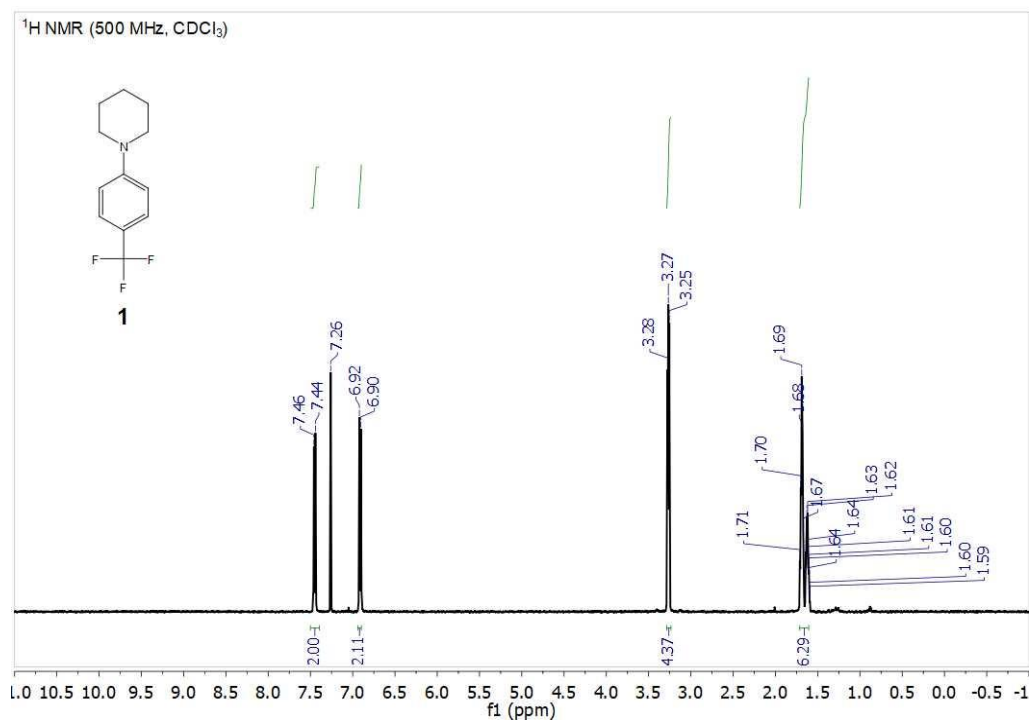


Figure 4.7. <sup>1</sup>H NMR spectrum of (**1**).

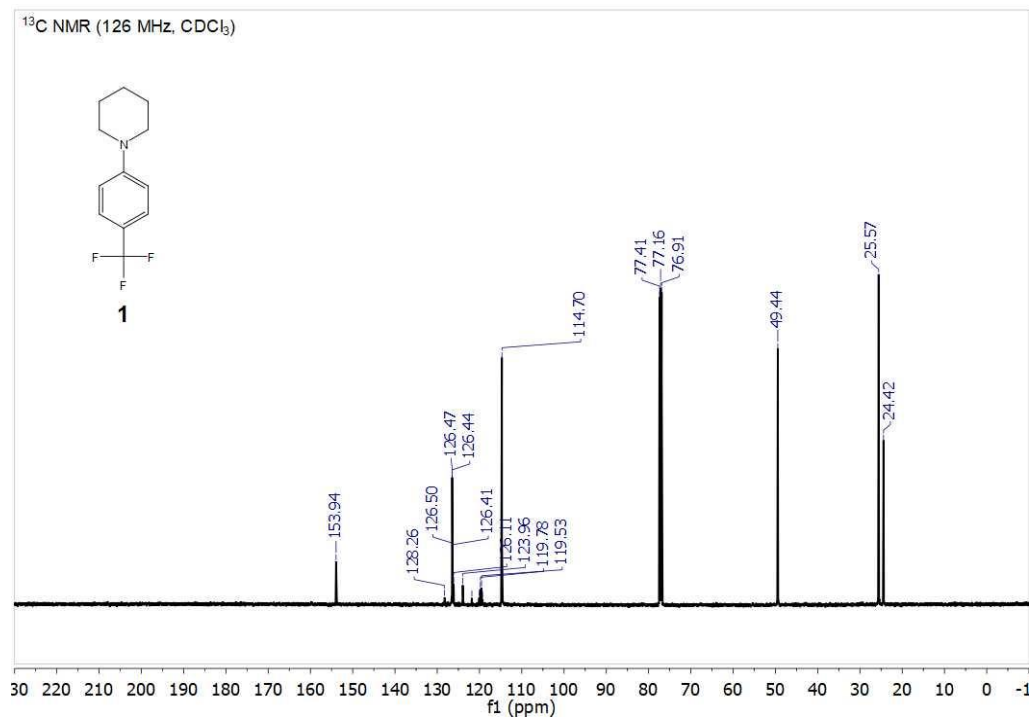


Figure 4.8. <sup>13</sup>C NMR spectrum of (**1**).

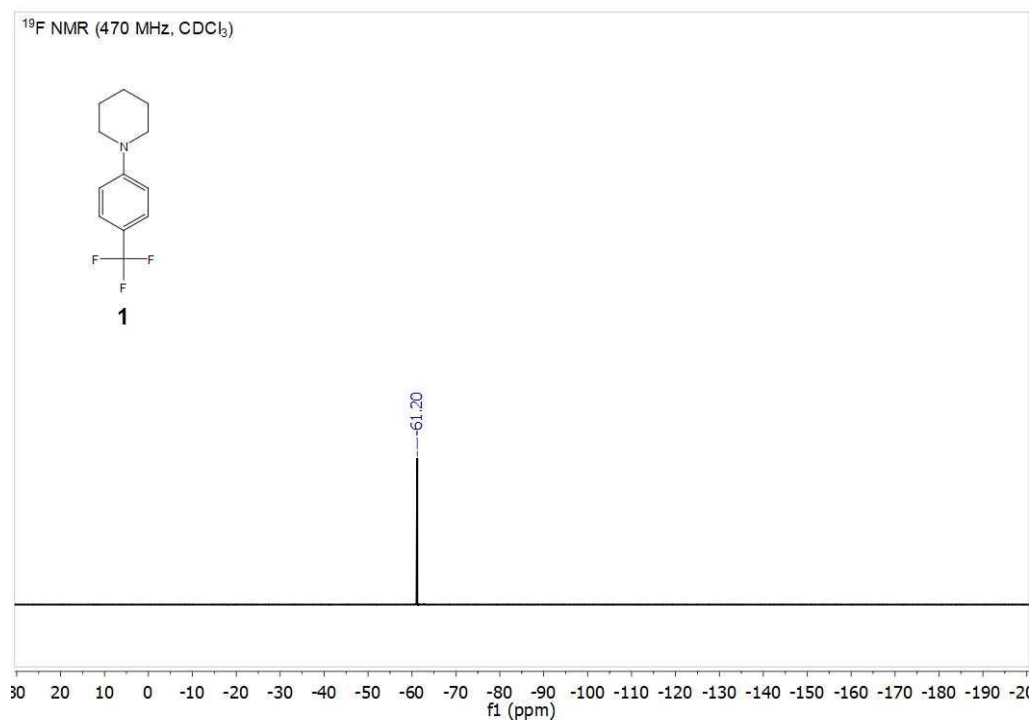


Figure 4.9. <sup>19</sup>F NMR spectrum of (1).

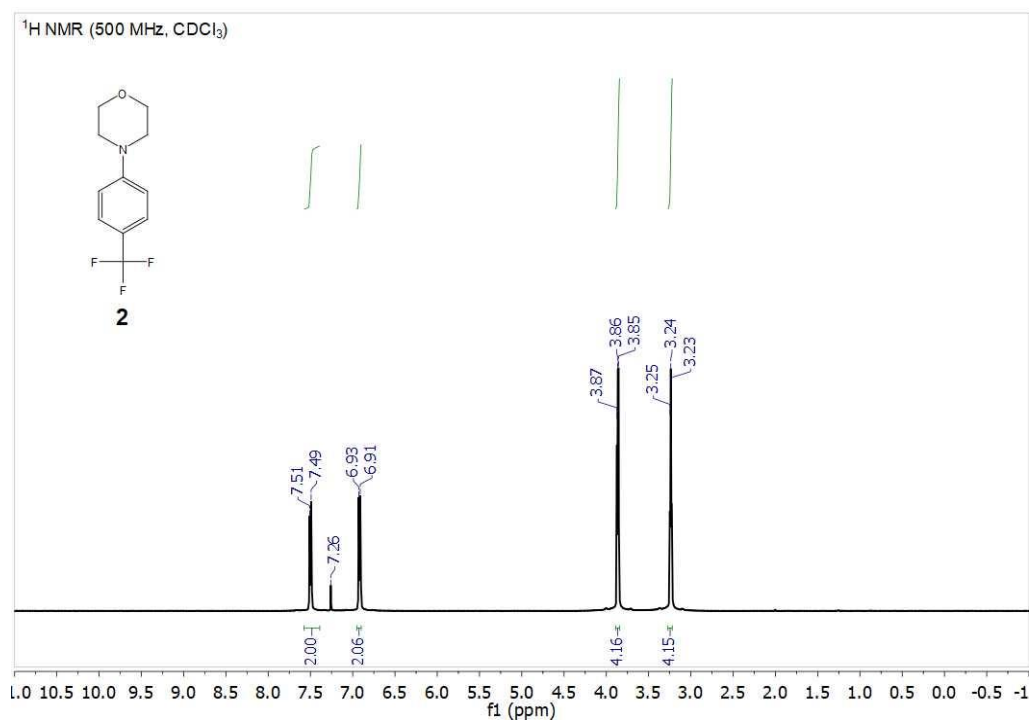


Figure 4.10. <sup>1</sup>H NMR spectrum of (2).

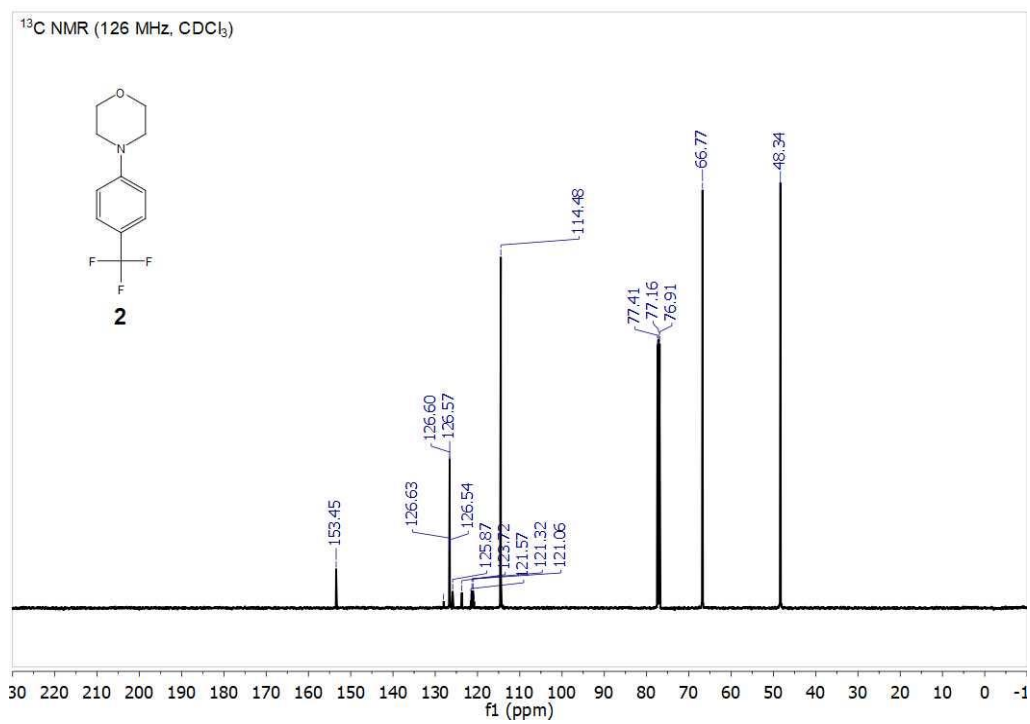


Figure 4.11. <sup>13</sup>C NMR spectrum of (2).

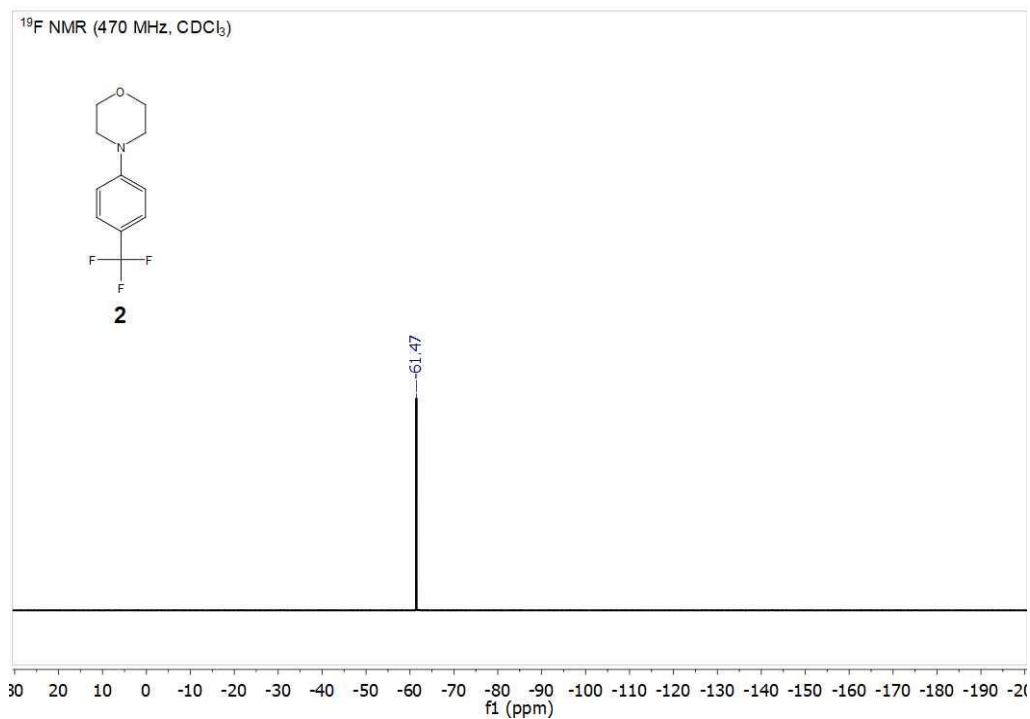


Figure 4.12. <sup>19</sup>F NMR spectrum of (2).

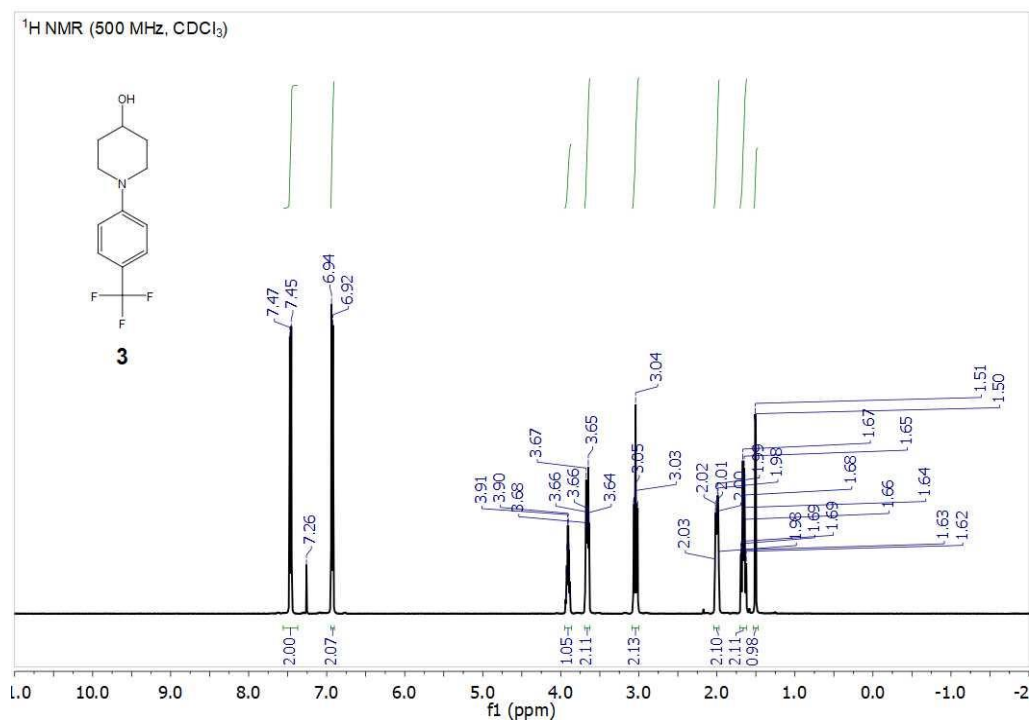


Figure 4.13. <sup>1</sup>H NMR spectrum of (**3**).

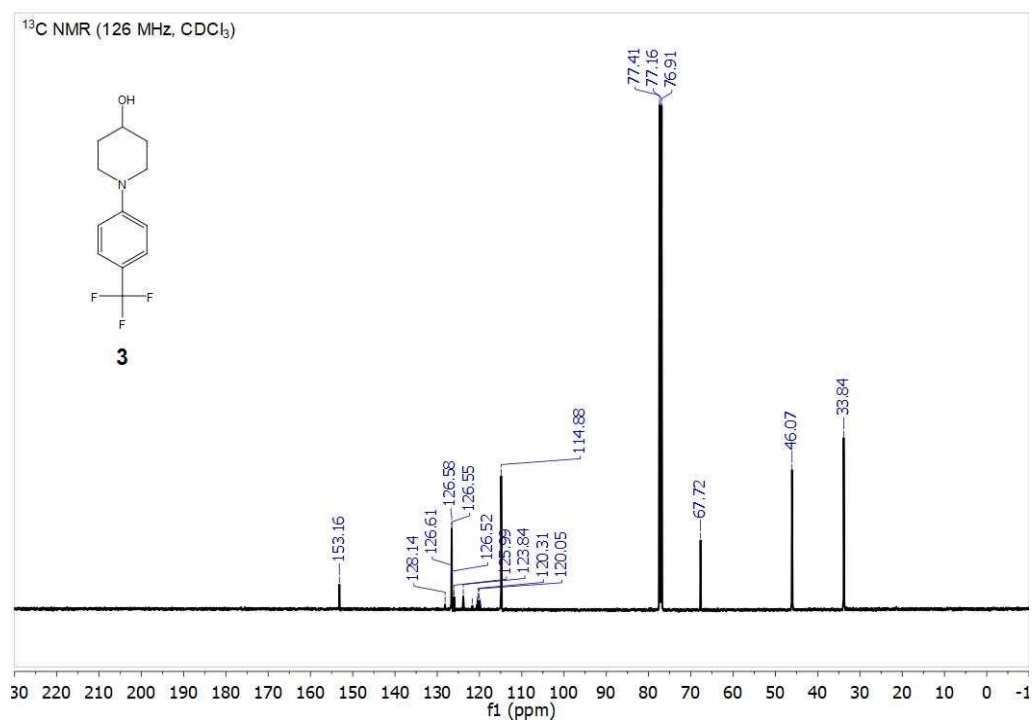


Figure 4.14. <sup>13</sup>C NMR spectrum of (**3**).

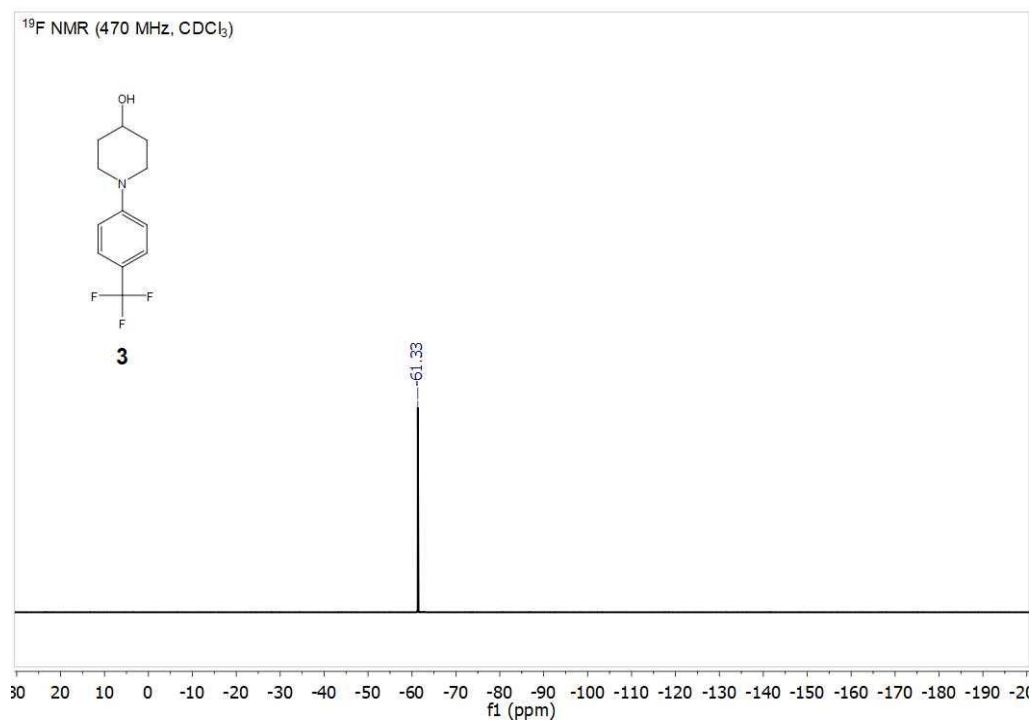


Figure 4.15. <sup>19</sup>F NMR spectrum of (3).

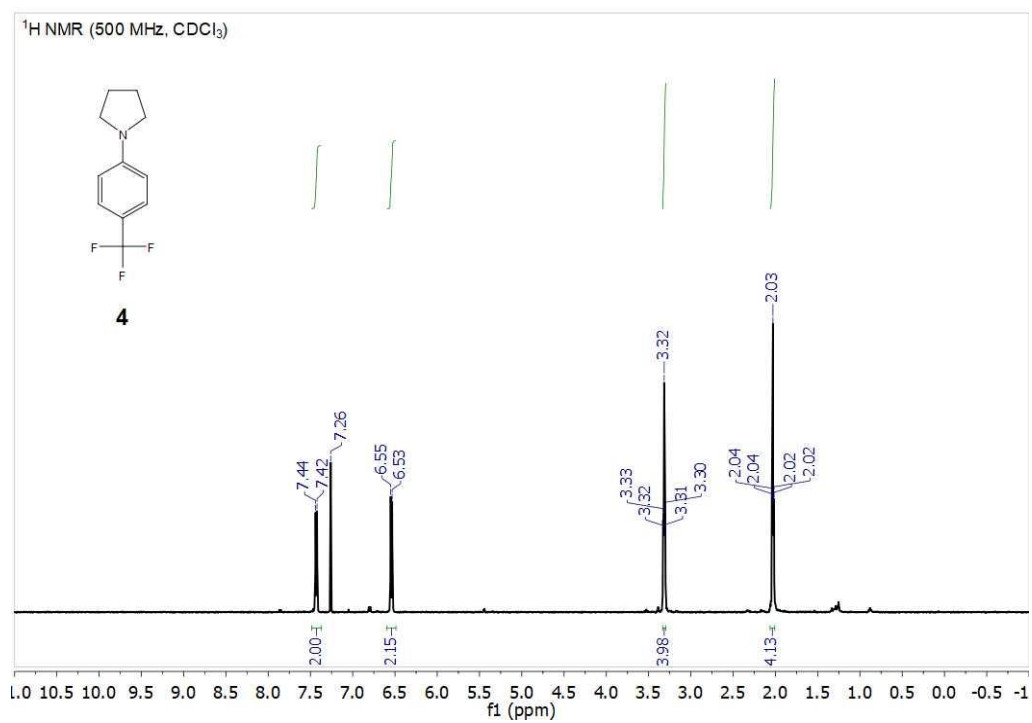


Figure 4.16. <sup>1</sup>H NMR spectrum of (4).

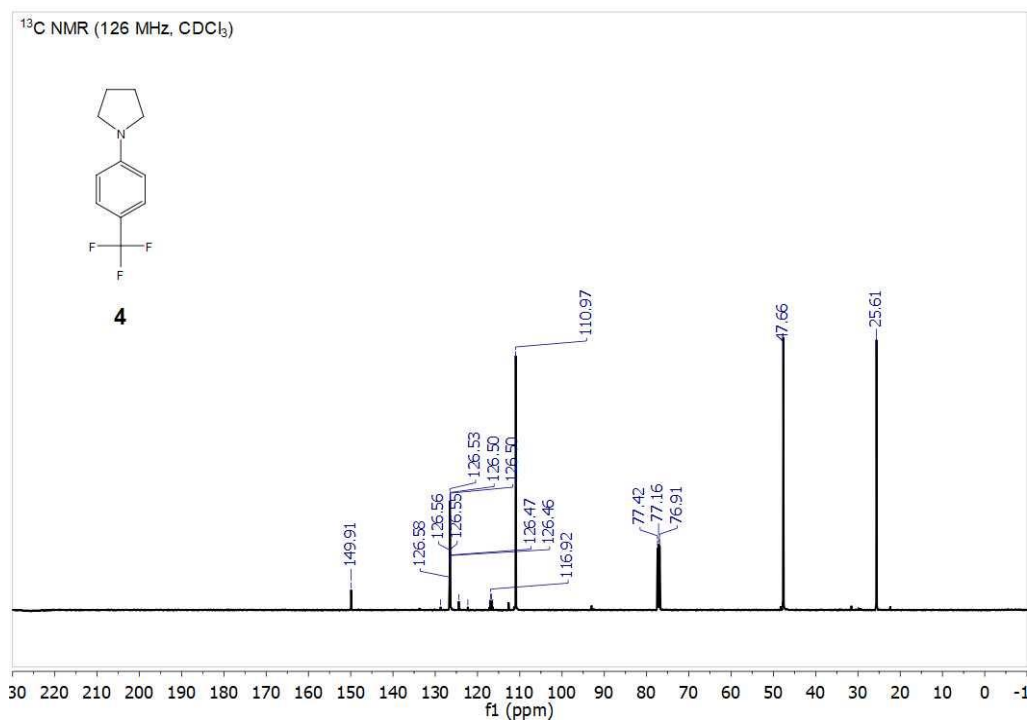


Figure 4.17. <sup>13</sup>C NMR spectrum of (4).

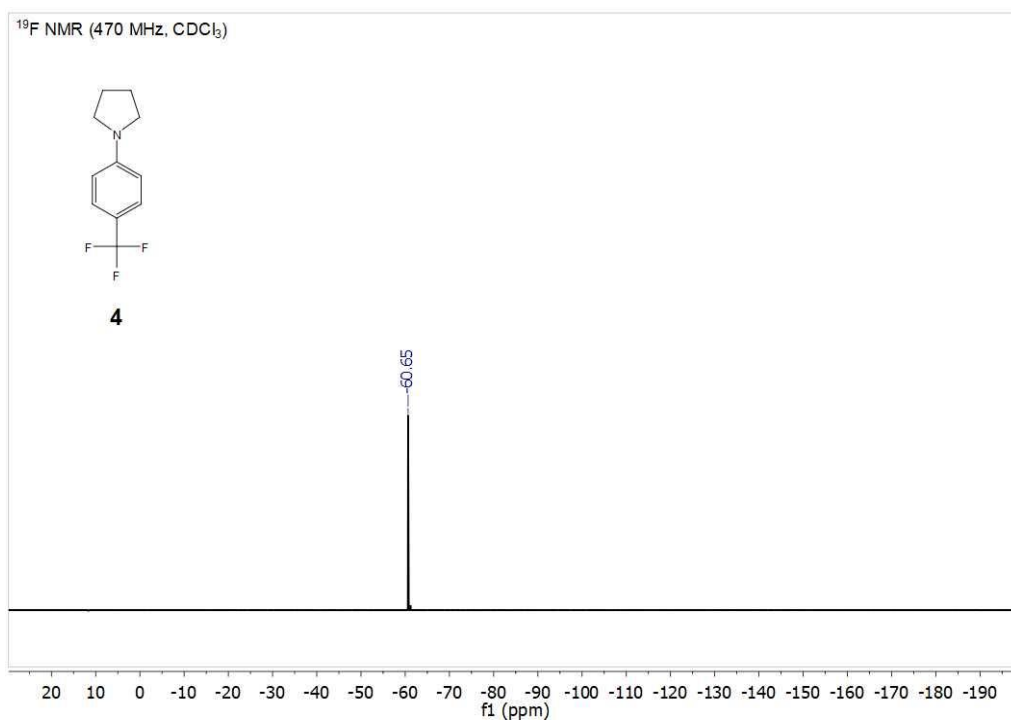


Figure 4.18. <sup>19</sup>F NMR spectrum of (4).



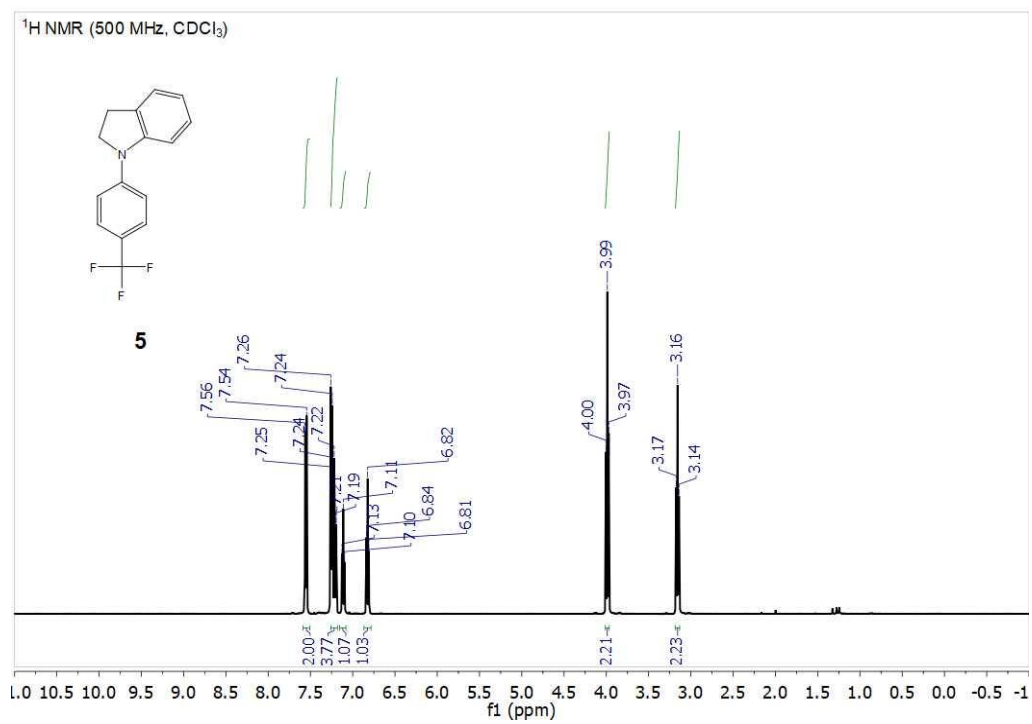


Figure 4.19. <sup>1</sup>H NMR spectrum of (5).

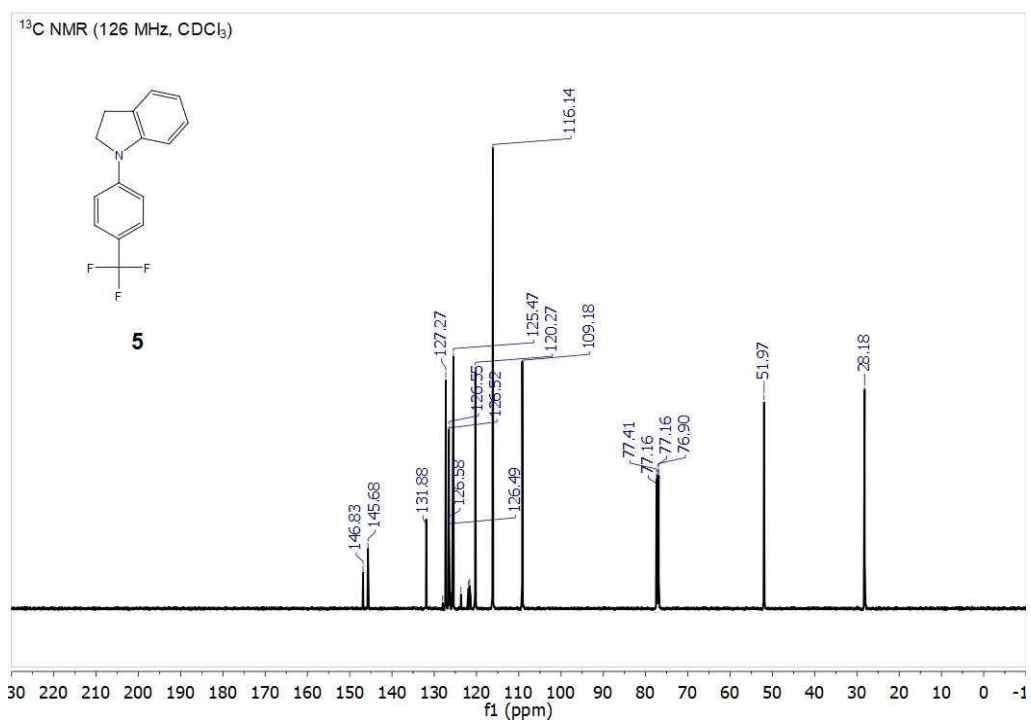


Figure 4.20. <sup>13</sup>C NMR spectrum of (5).

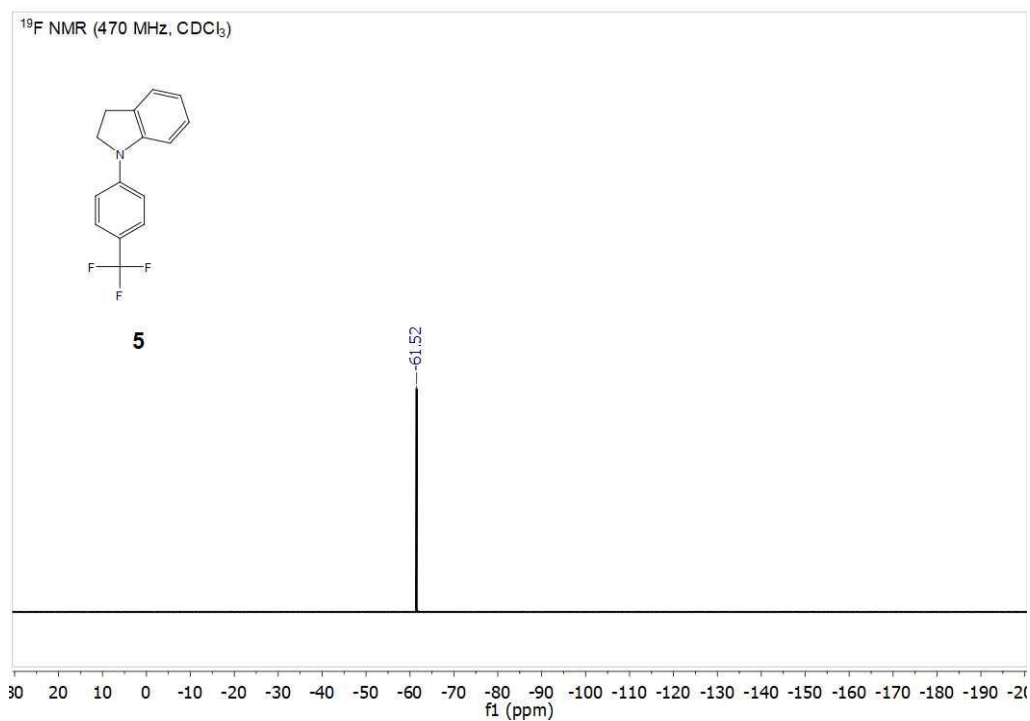


Figure 4.21. <sup>19</sup>F NMR spectrum of (5).

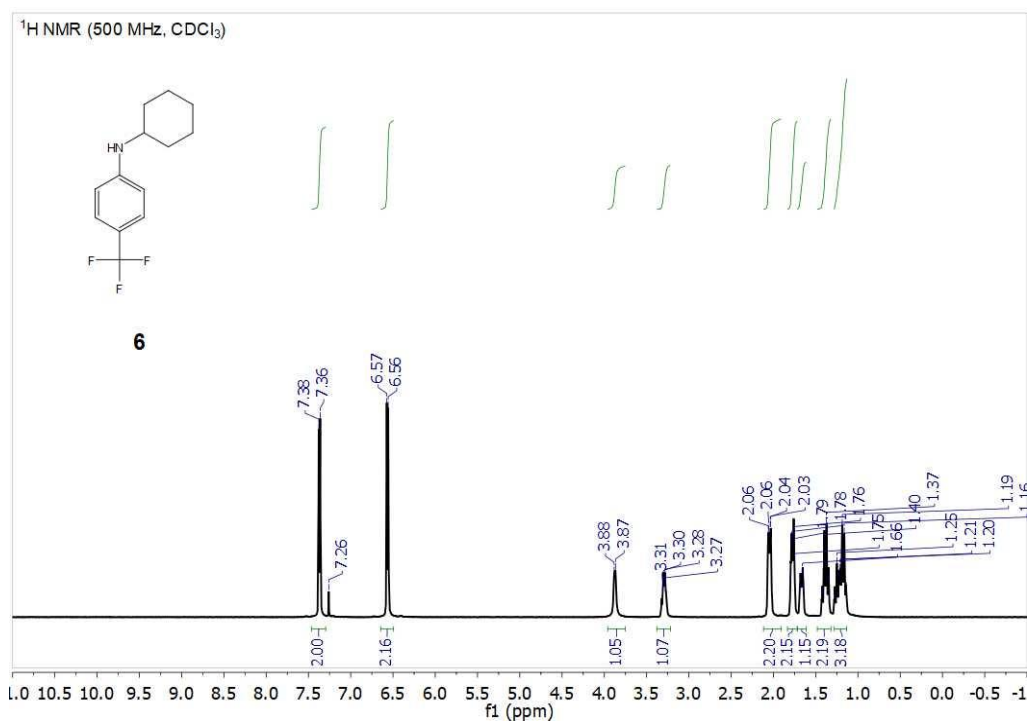


Figure 4.22. <sup>1</sup>H NMR spectrum of (6).

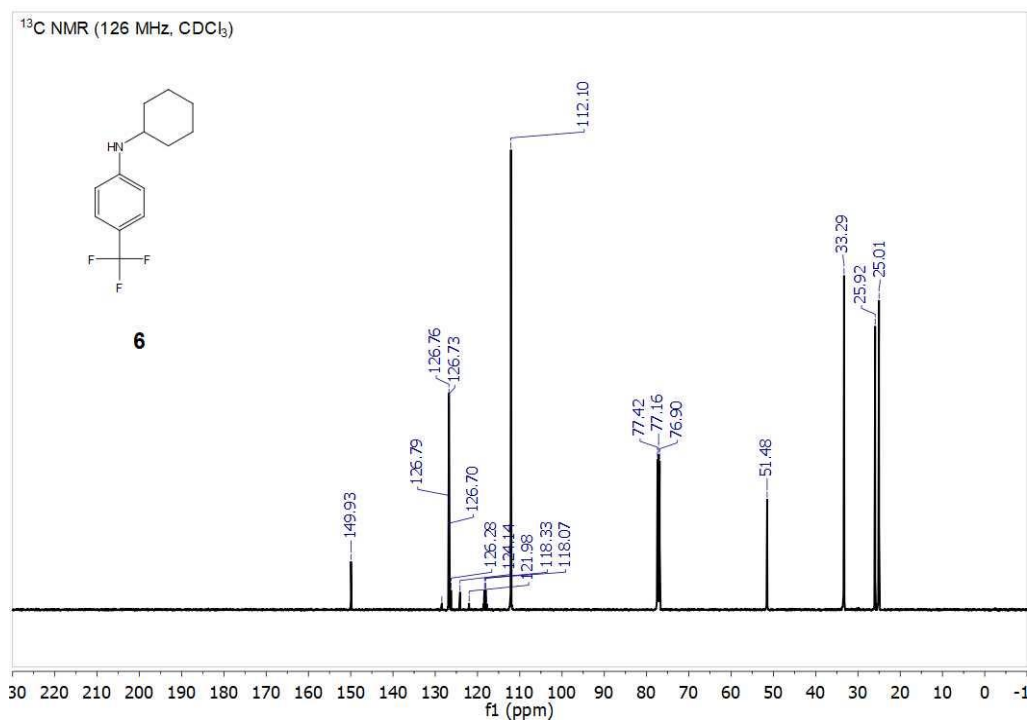


Figure 4.23. <sup>13</sup>C NMR spectrum of (**6**).

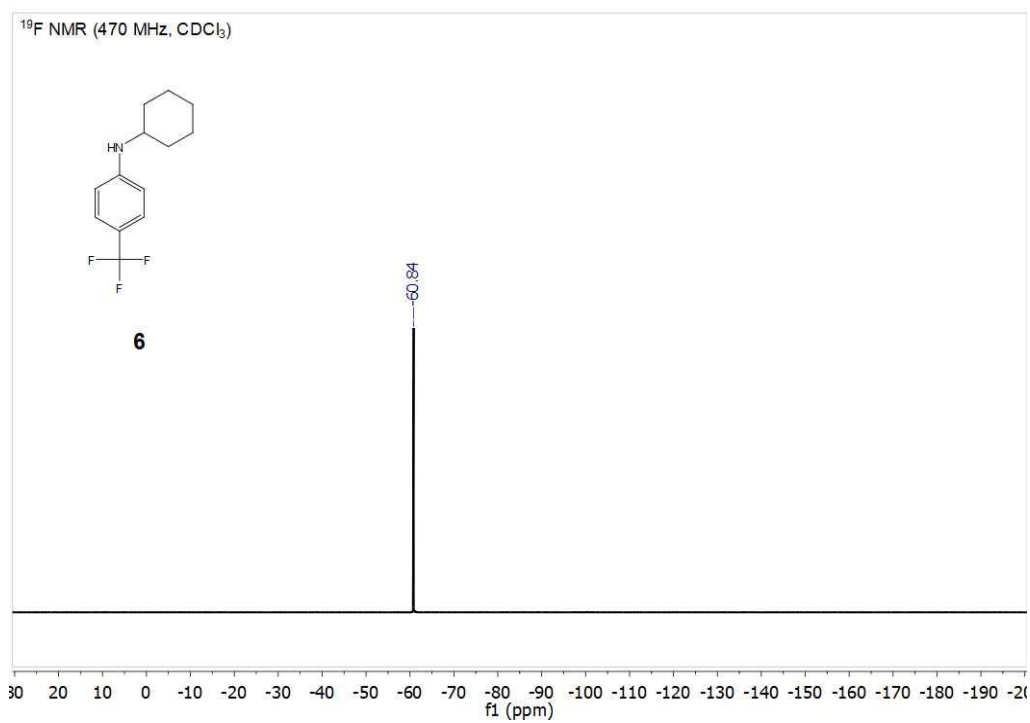


Figure 4.24. <sup>19</sup>F NMR spectrum of (**6**).

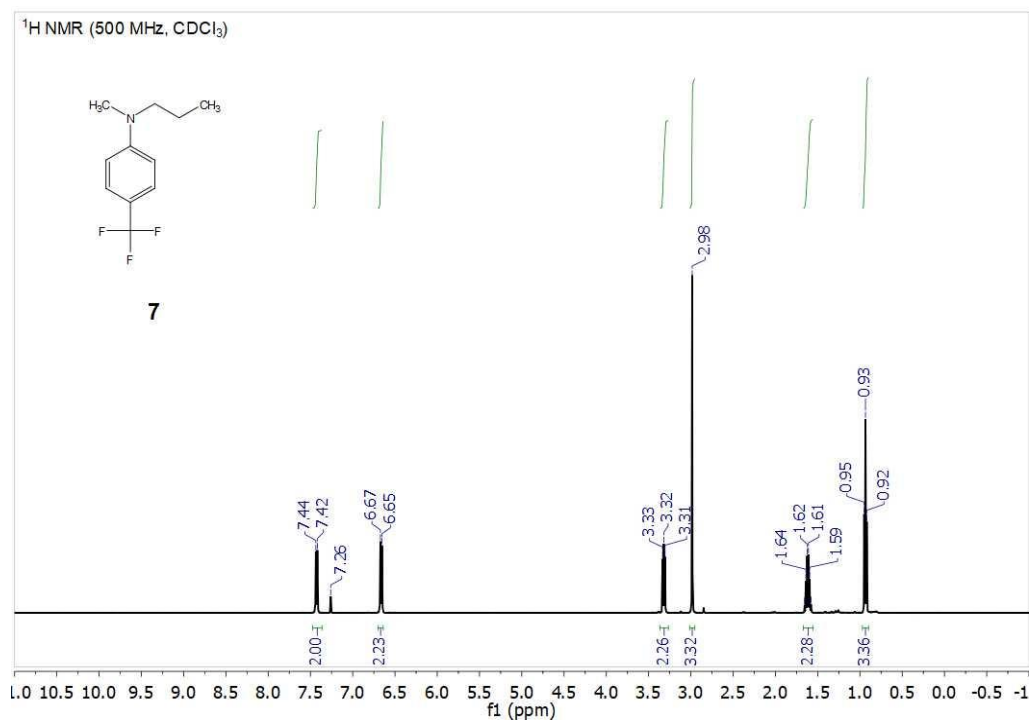


Figure 4.25. <sup>1</sup>H NMR spectrum of (7).

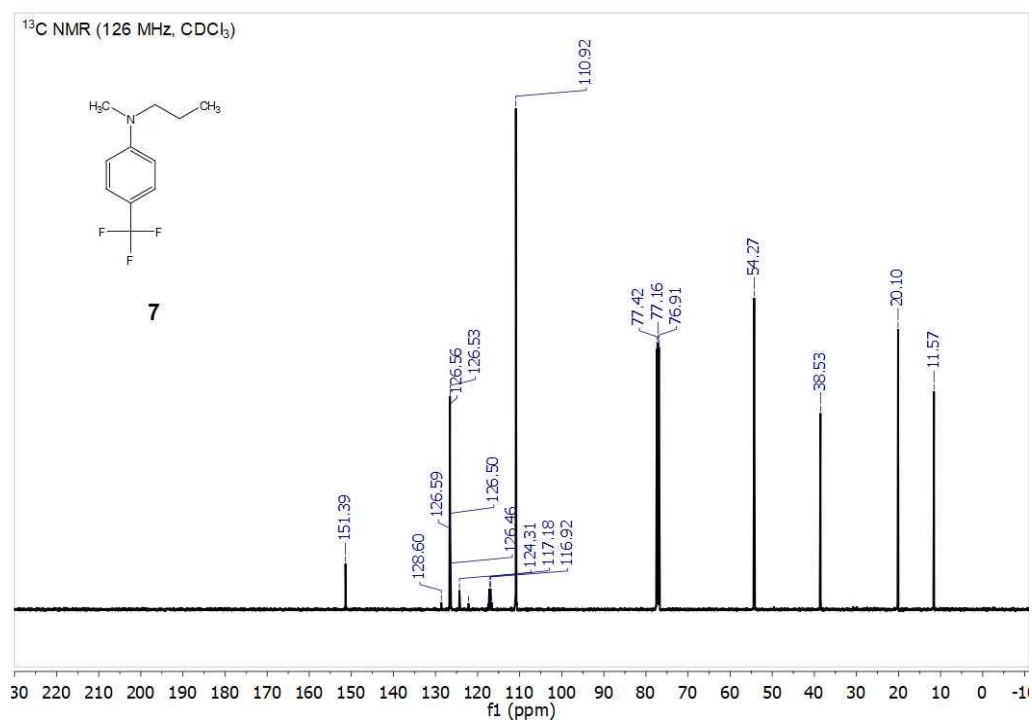


Figure 4.26. <sup>13</sup>C NMR spectrum of (7).

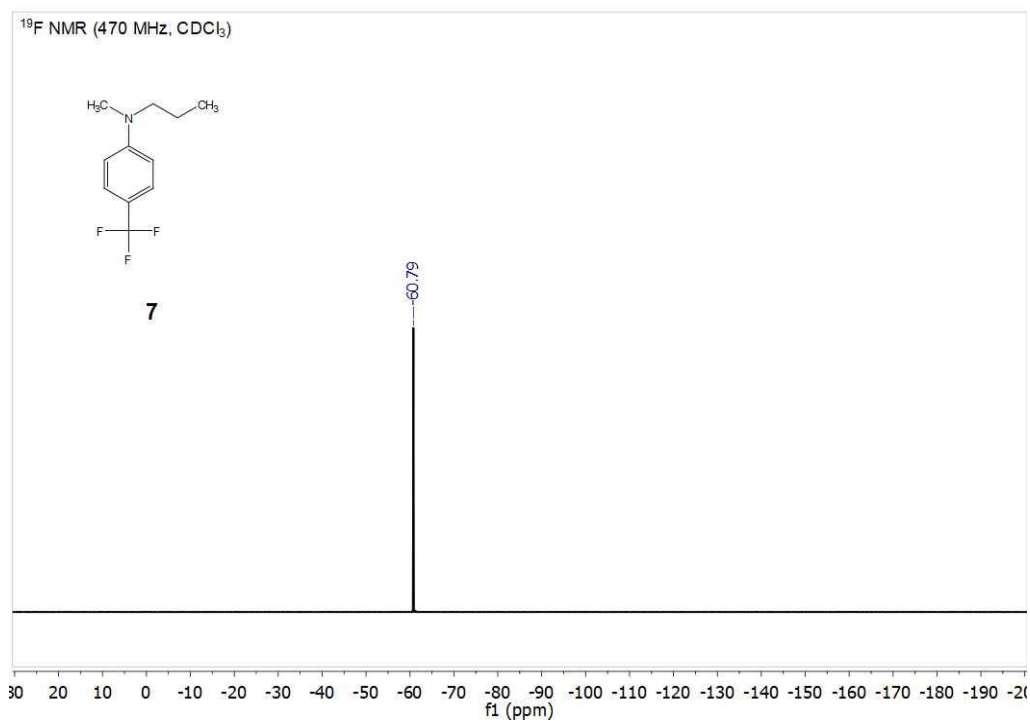


Figure 4.27. <sup>19</sup>F NMR spectrum of (7).

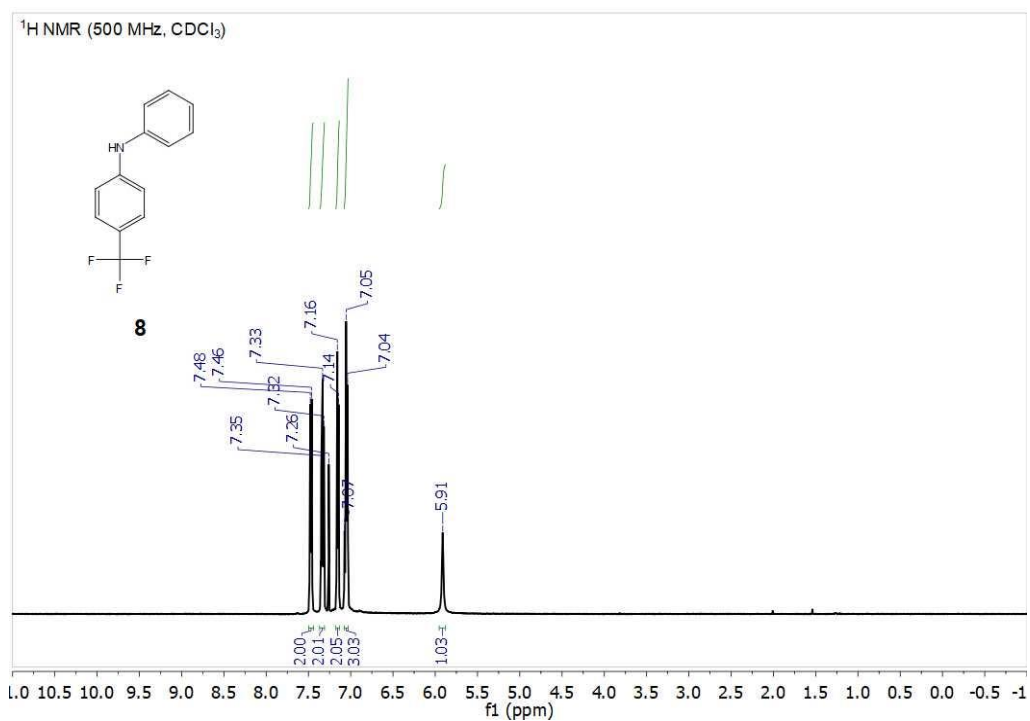


Figure 4.28. <sup>1</sup>H NMR spectrum of (8).

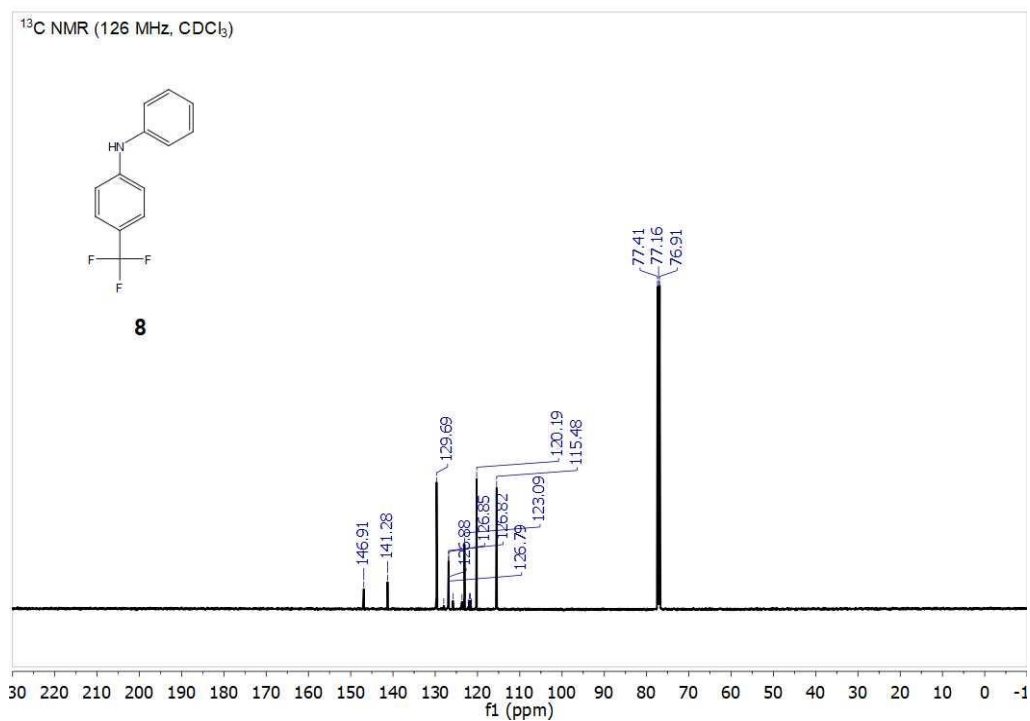


Figure 4.29. <sup>13</sup>C NMR spectrum of (**8**).

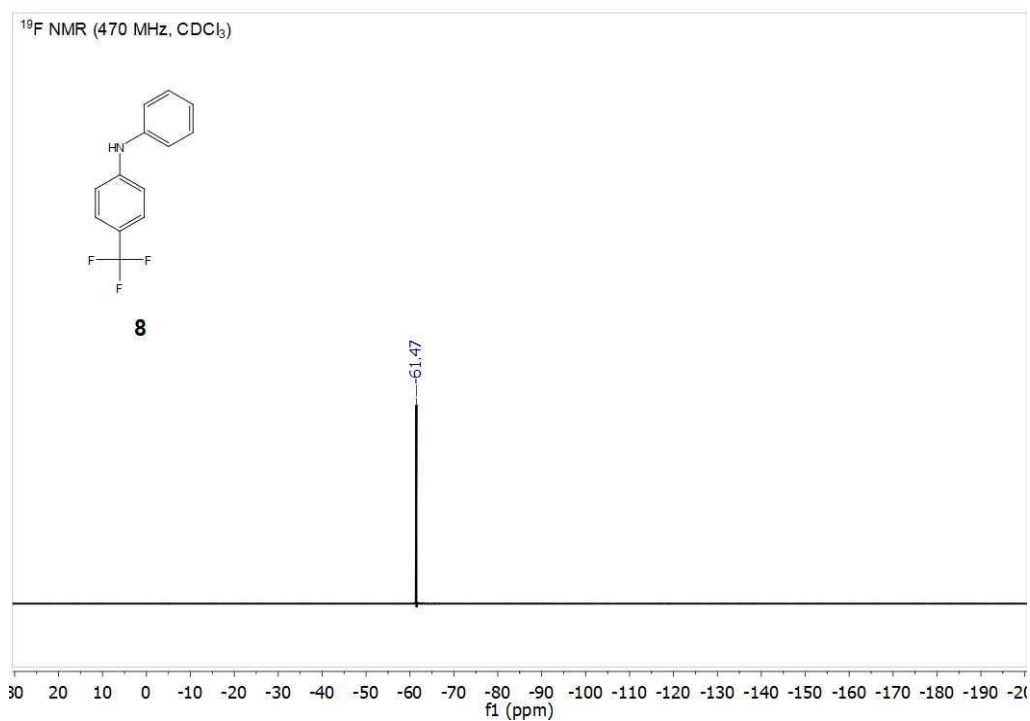


Figure 4.30. <sup>19</sup>F NMR spectrum of (**8**).

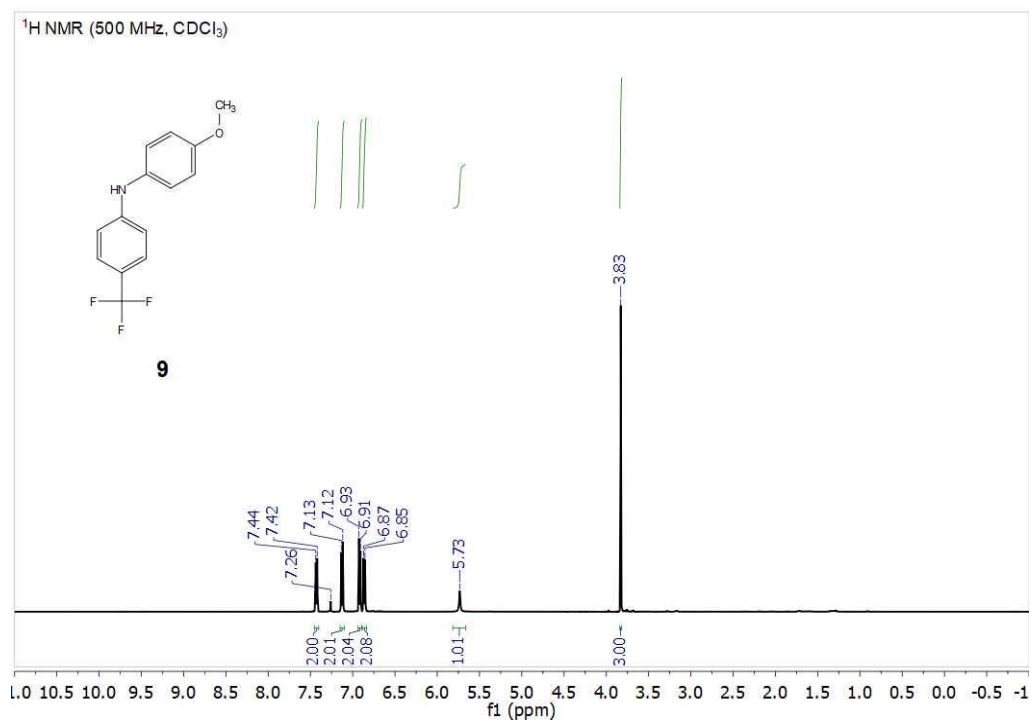


Figure 4.31. <sup>1</sup>H NMR spectrum of (9).

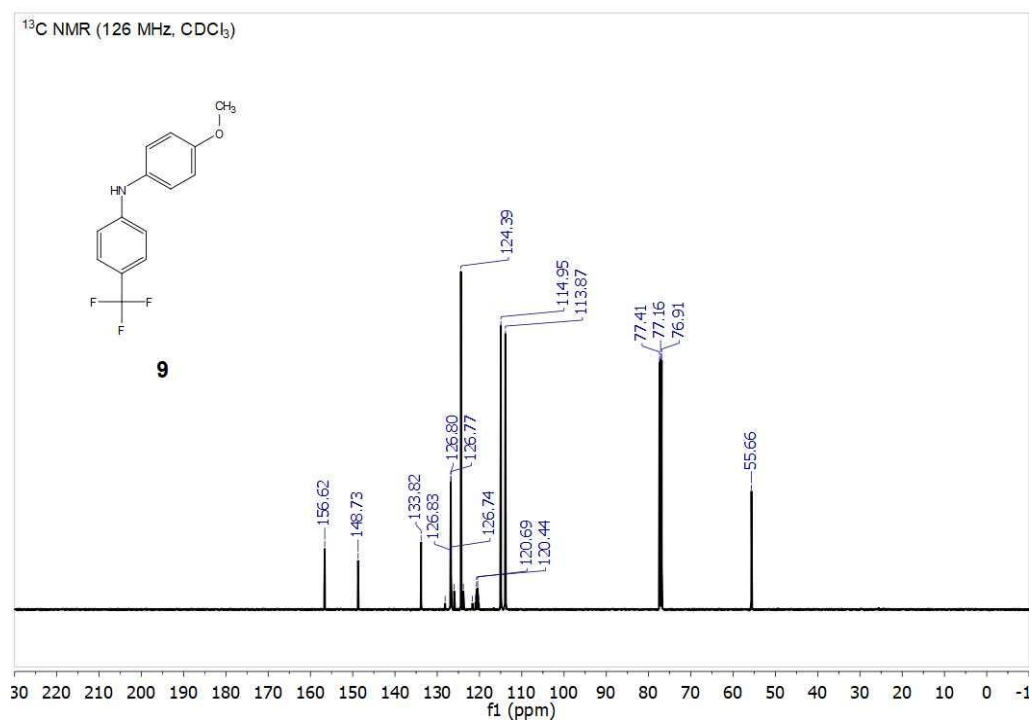


Figure 4.32. <sup>13</sup>C NMR spectrum of (9).

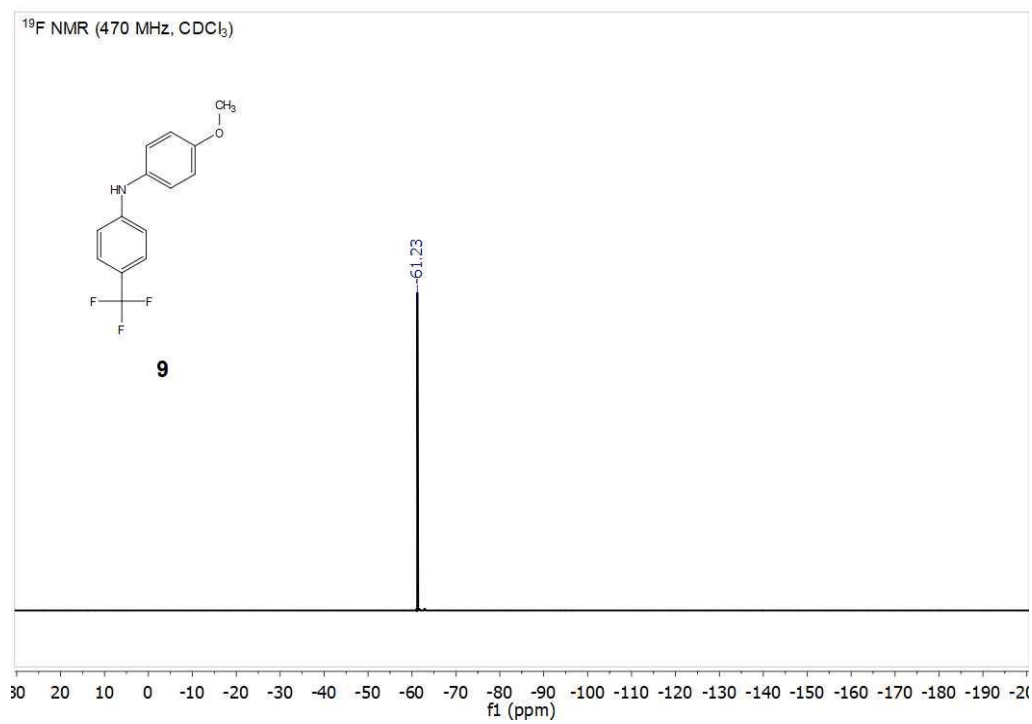


Figure 4.33. <sup>19</sup>F NMR spectrum of (9).

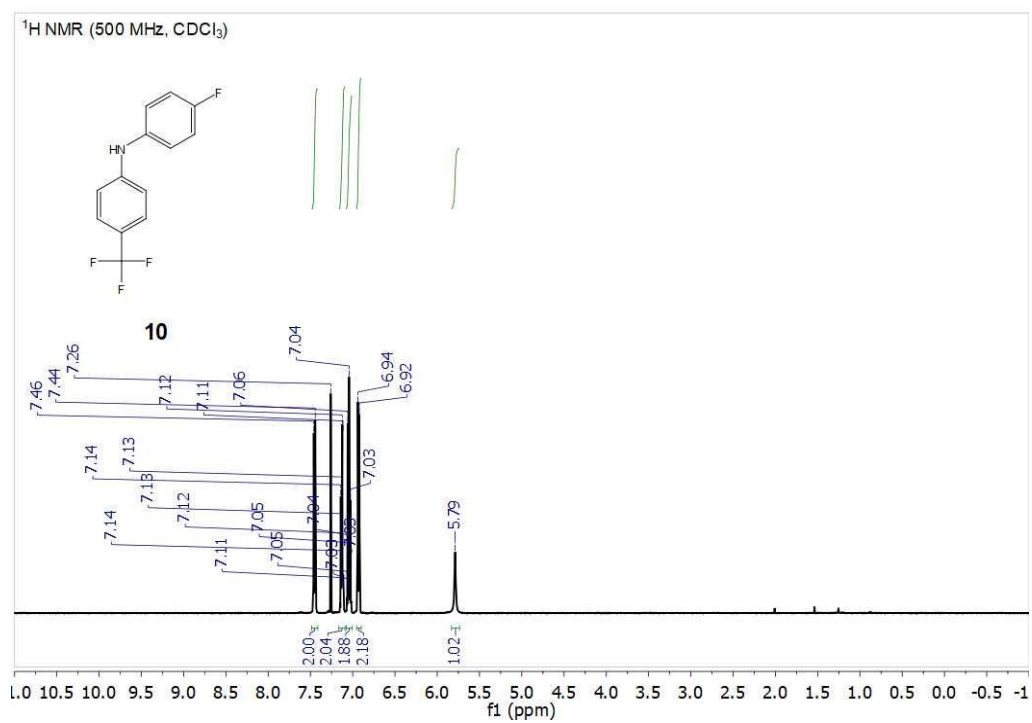


Figure 4.34. <sup>1</sup>H NMR spectrum of (10).



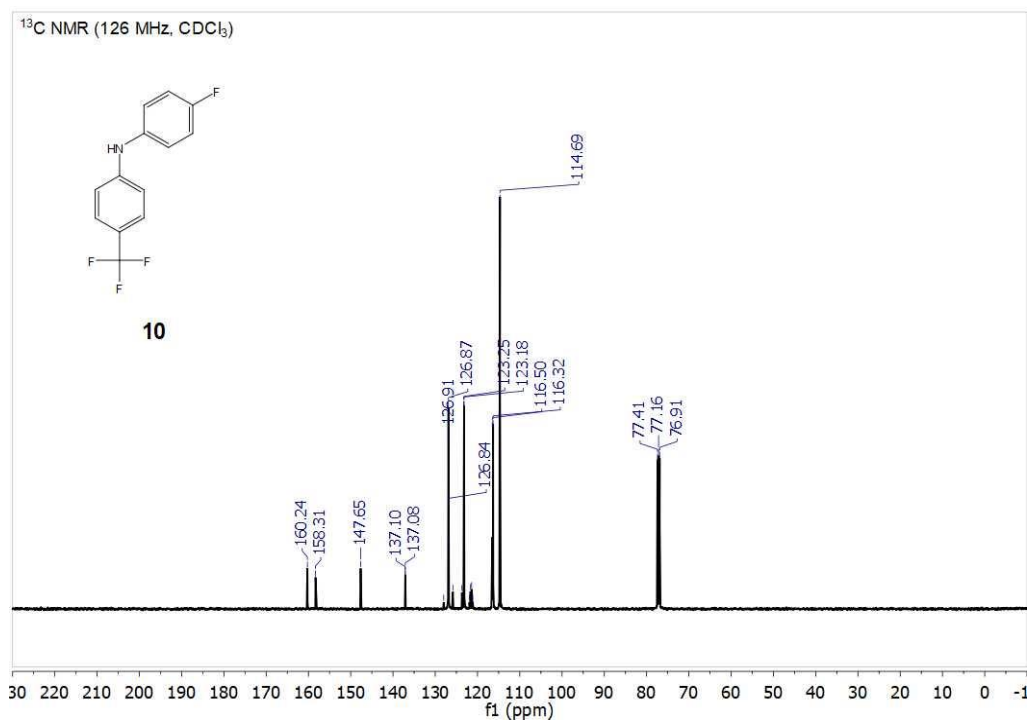


Figure 4.35. <sup>13</sup>C NMR spectrum of (10).

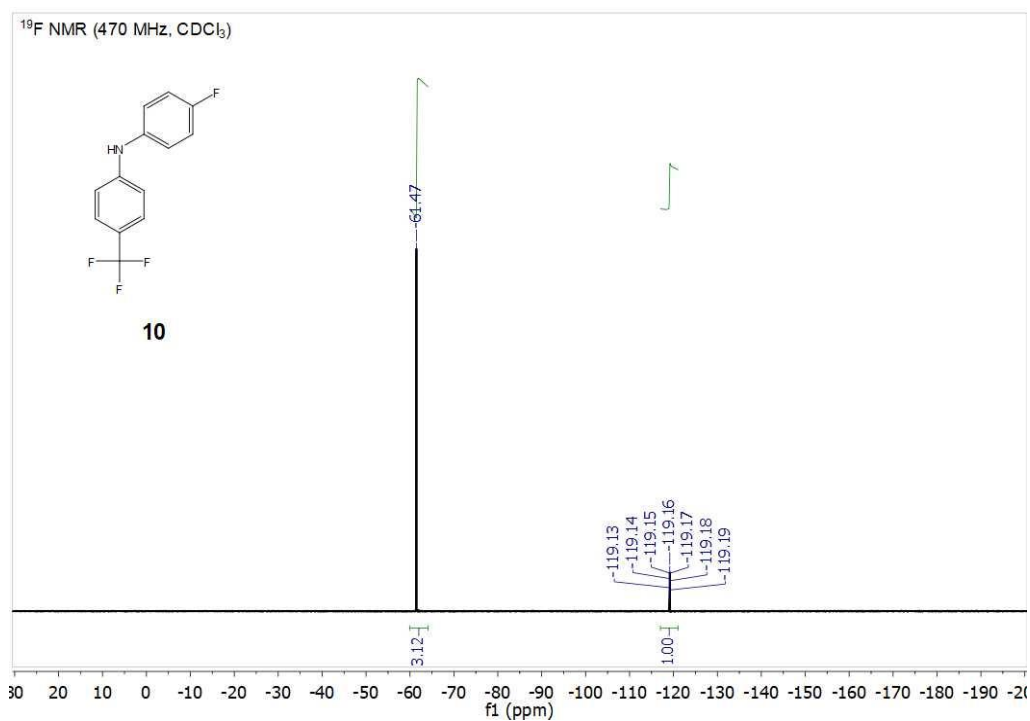


Figure 4.36. <sup>19</sup>F NMR spectrum of (10).

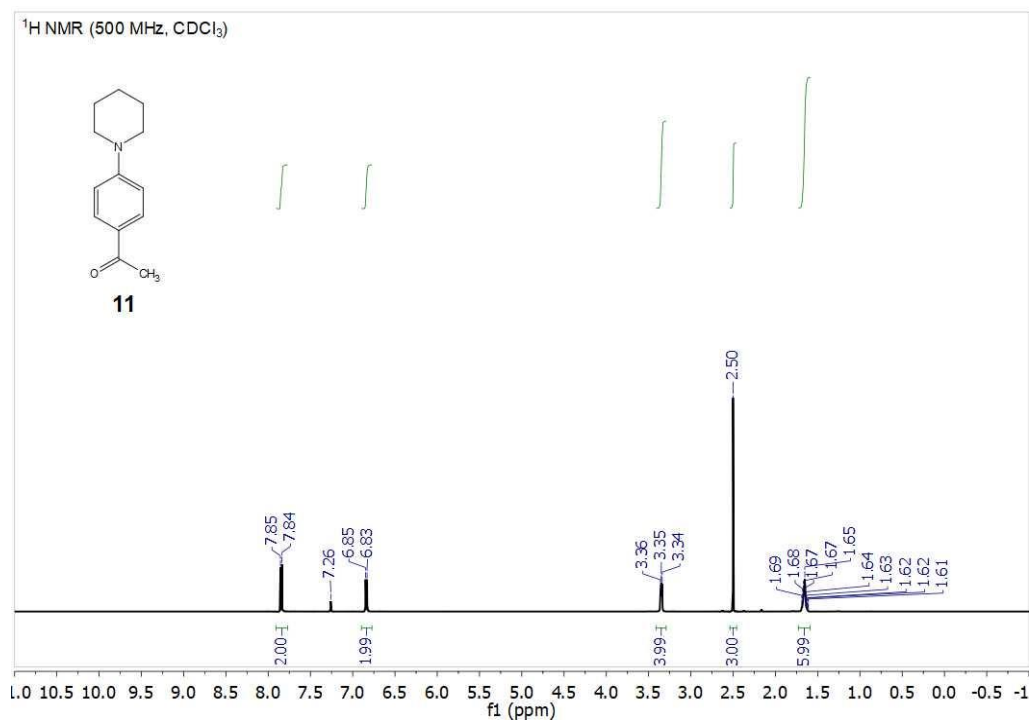


Figure 4.37. <sup>1</sup>H NMR spectrum of (11).

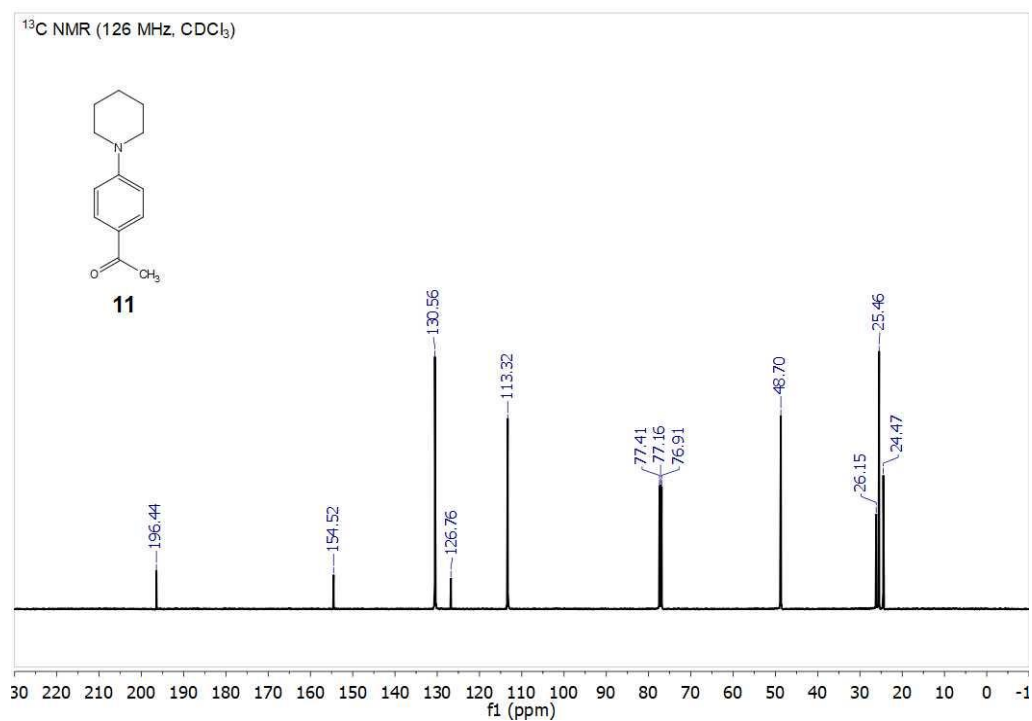


Figure 4.38. <sup>13</sup>C NMR spectrum of (11).

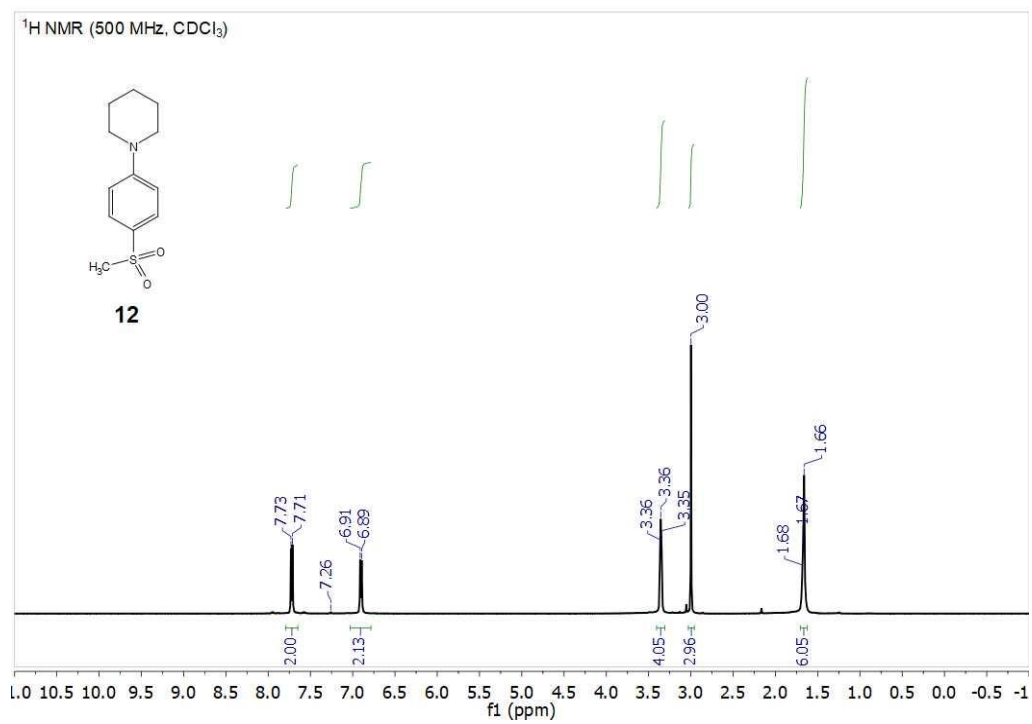


Figure 4.39. <sup>1</sup>H NMR spectrum of (12).

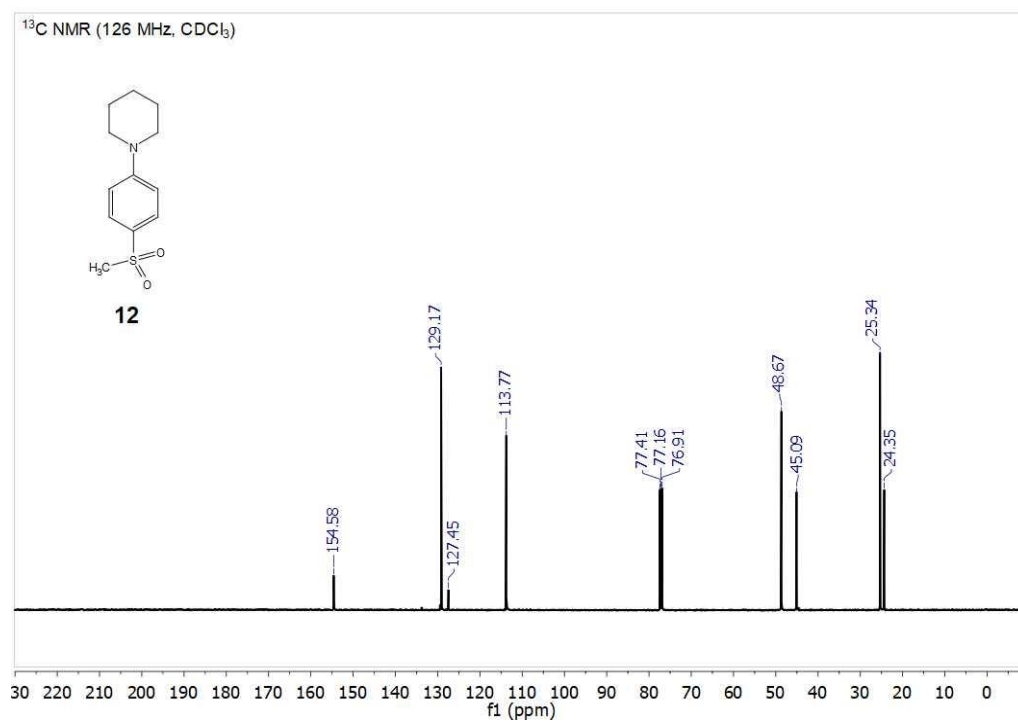


Figure 4.40. <sup>13</sup>C NMR spectrum of (12).

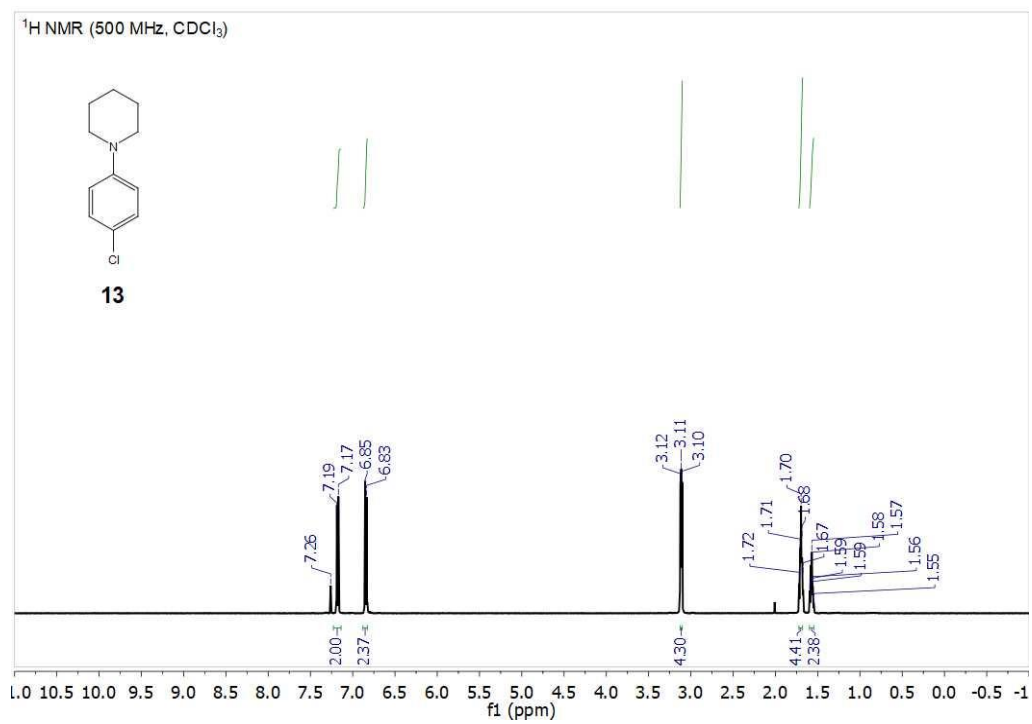


Figure 4.41. <sup>1</sup>H NMR spectrum of (13).

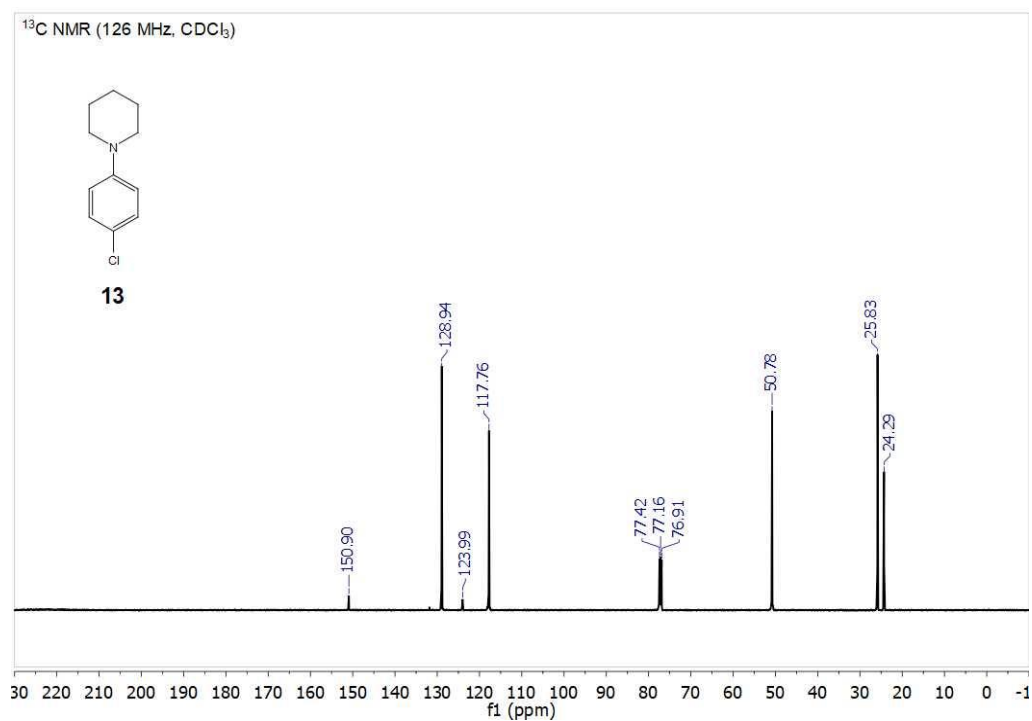


Figure 4.42. <sup>13</sup>C NMR spectrum of (13).

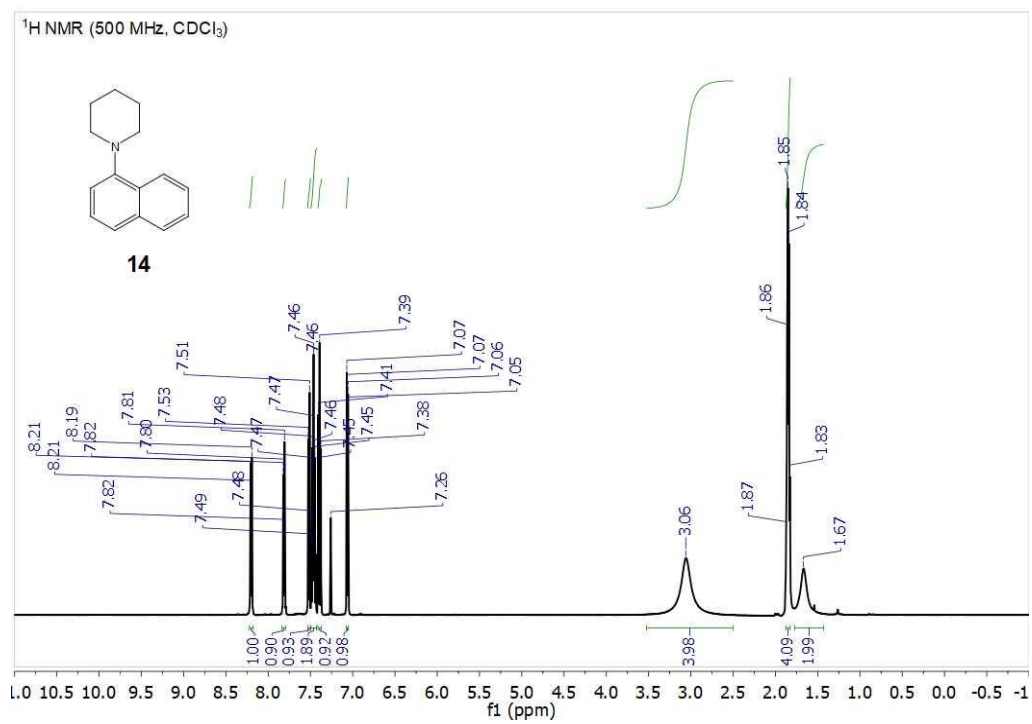


Figure 4.43. <sup>1</sup>H NMR spectrum of (14).

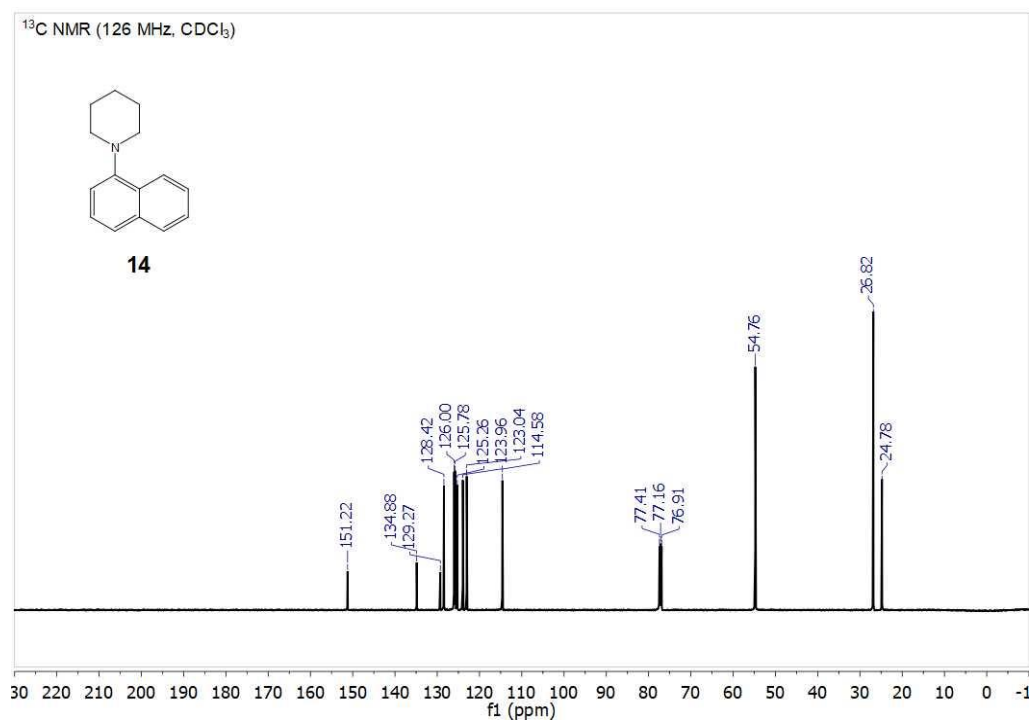


Figure 4.44. <sup>13</sup>C NMR spectrum of (14).

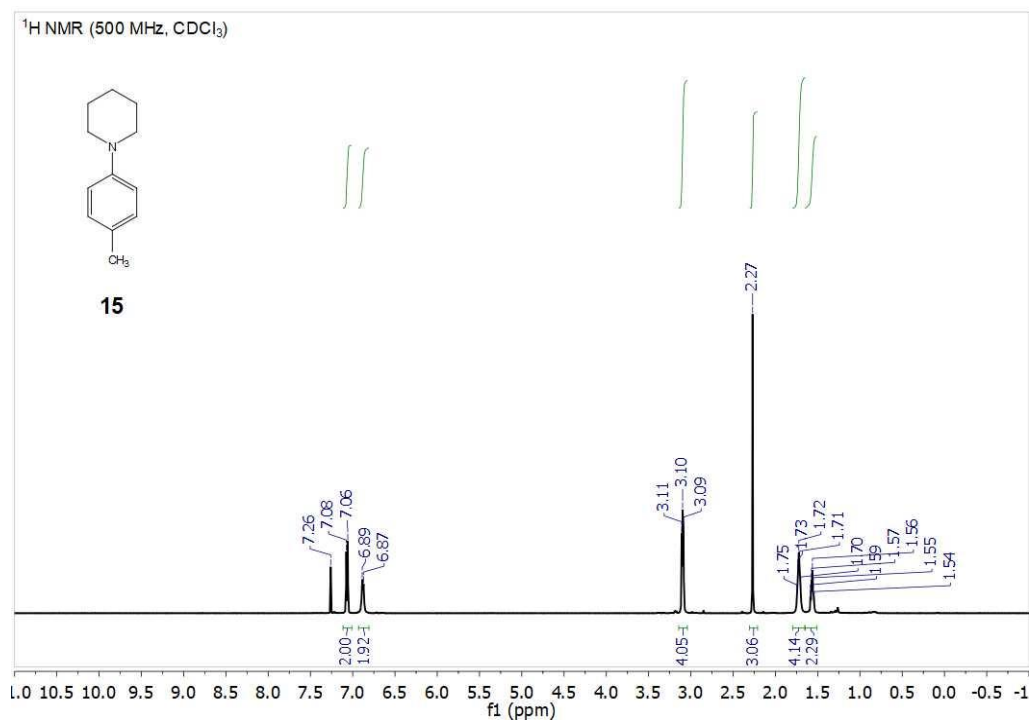


Figure 4.45. <sup>1</sup>H NMR spectrum of (15).

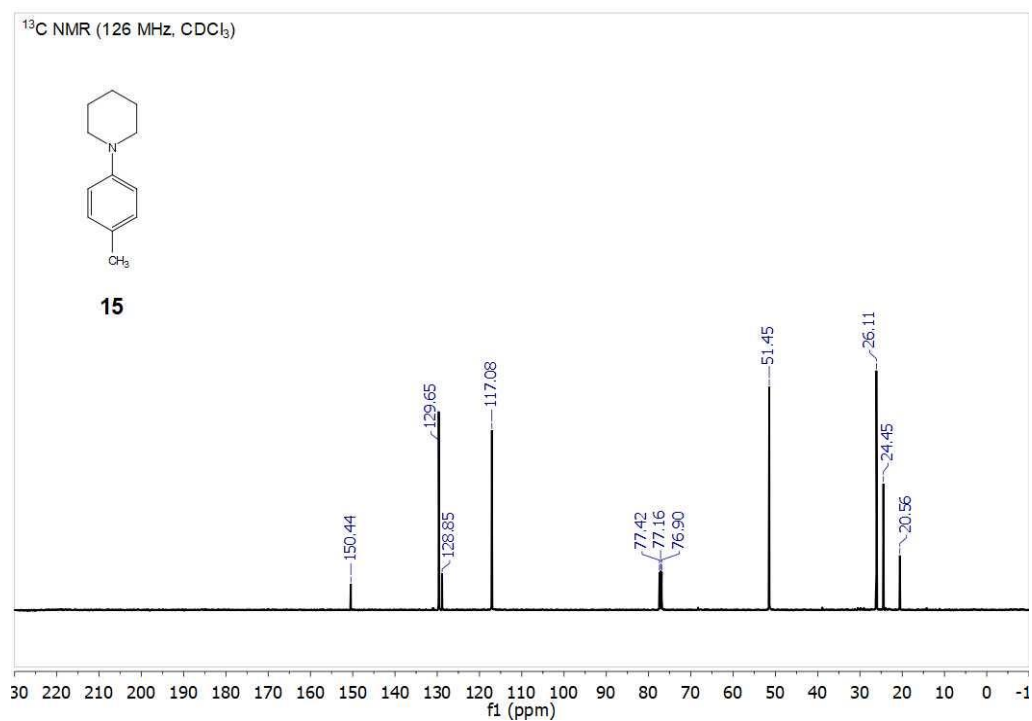


Figure 4.46. <sup>13</sup>C NMR spectrum of (15).

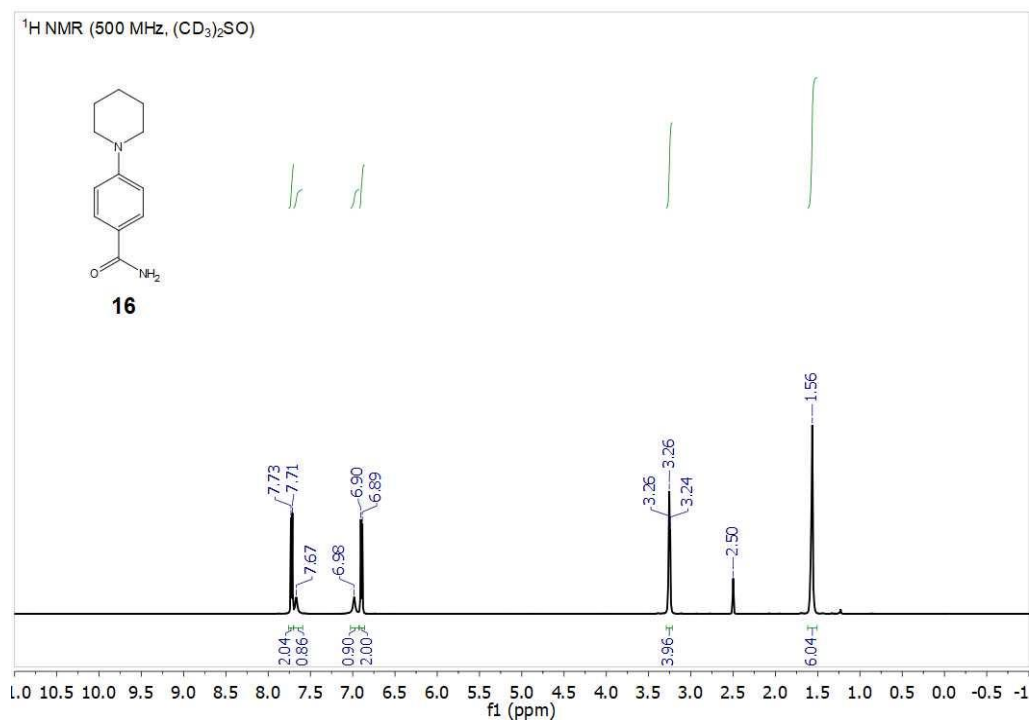


Figure 4.47. <sup>1</sup>H NMR spectrum of (16).

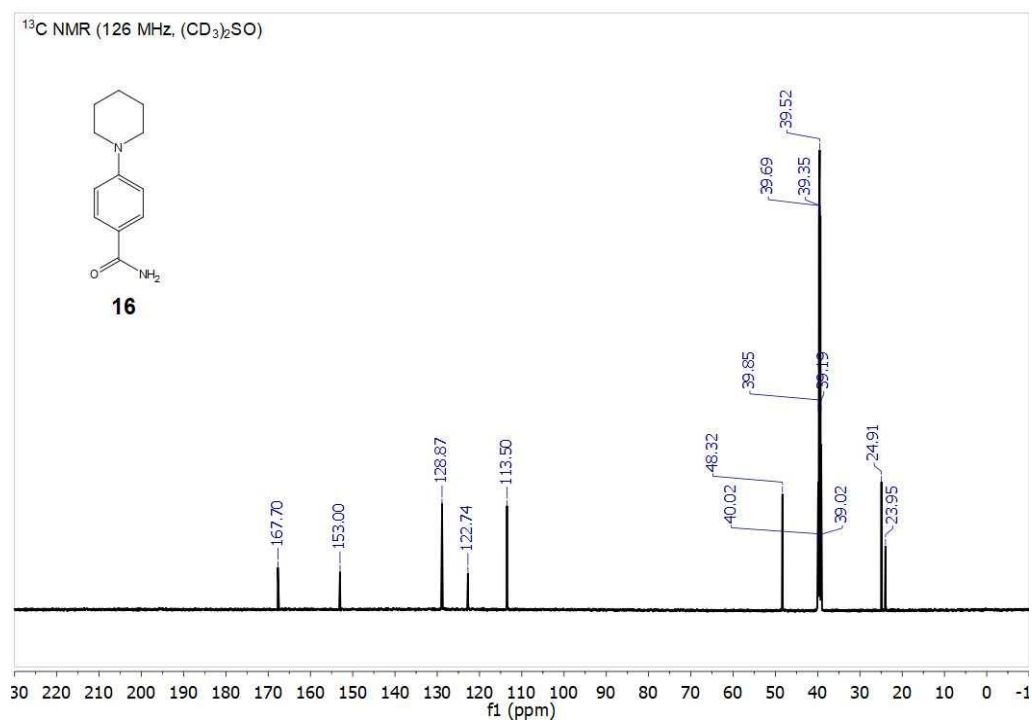


Figure 4.48. <sup>13</sup>C NMR spectrum of (16).

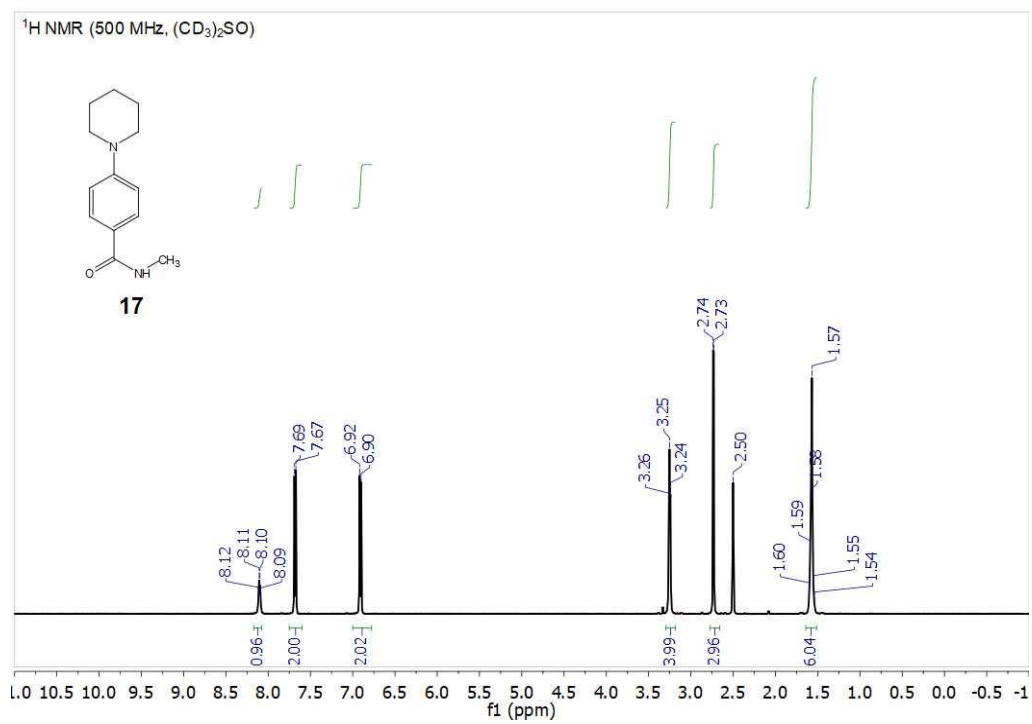


Figure 4.49. <sup>1</sup>H NMR spectrum of (17).

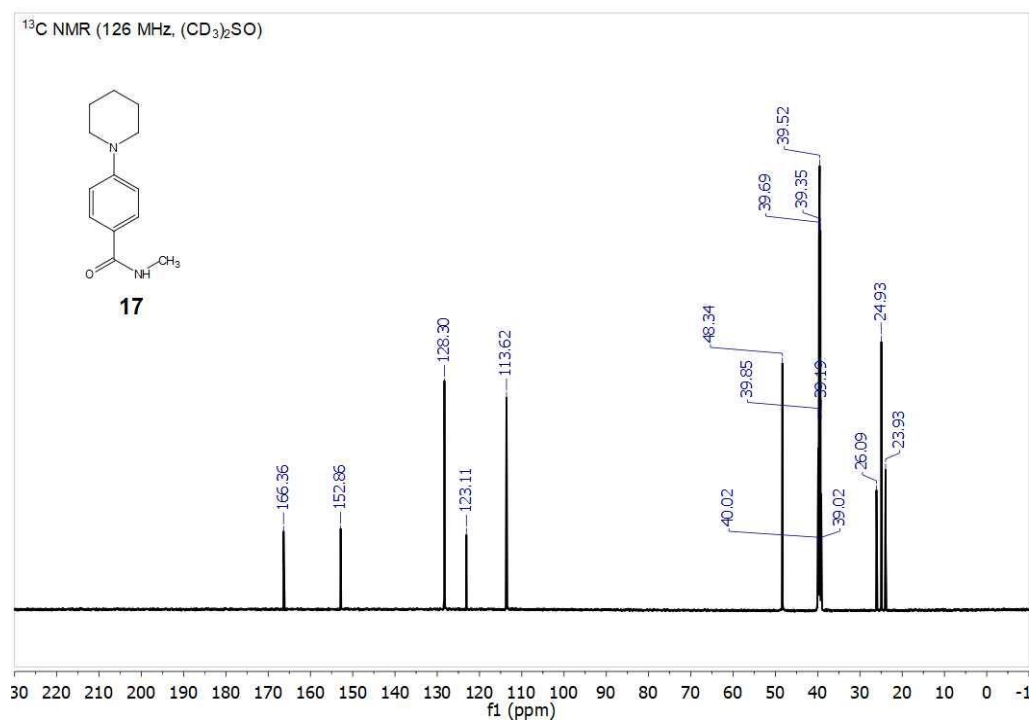


Figure 4.50. <sup>13</sup>C NMR spectrum of (17).



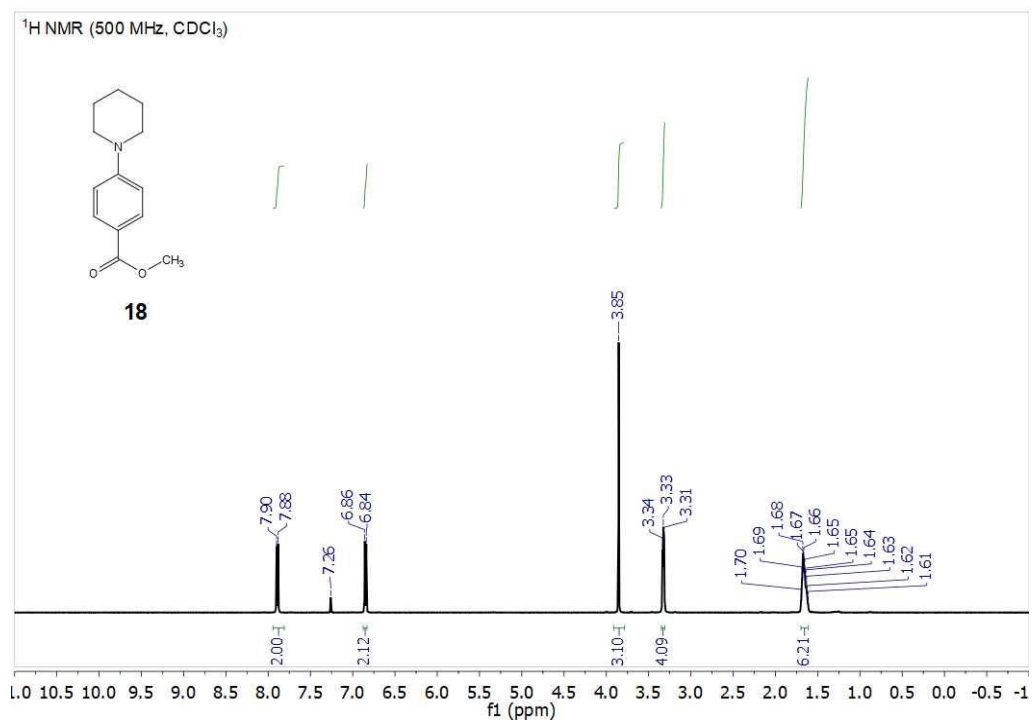


Figure 4.51. <sup>1</sup>H NMR spectrum of (**18**).

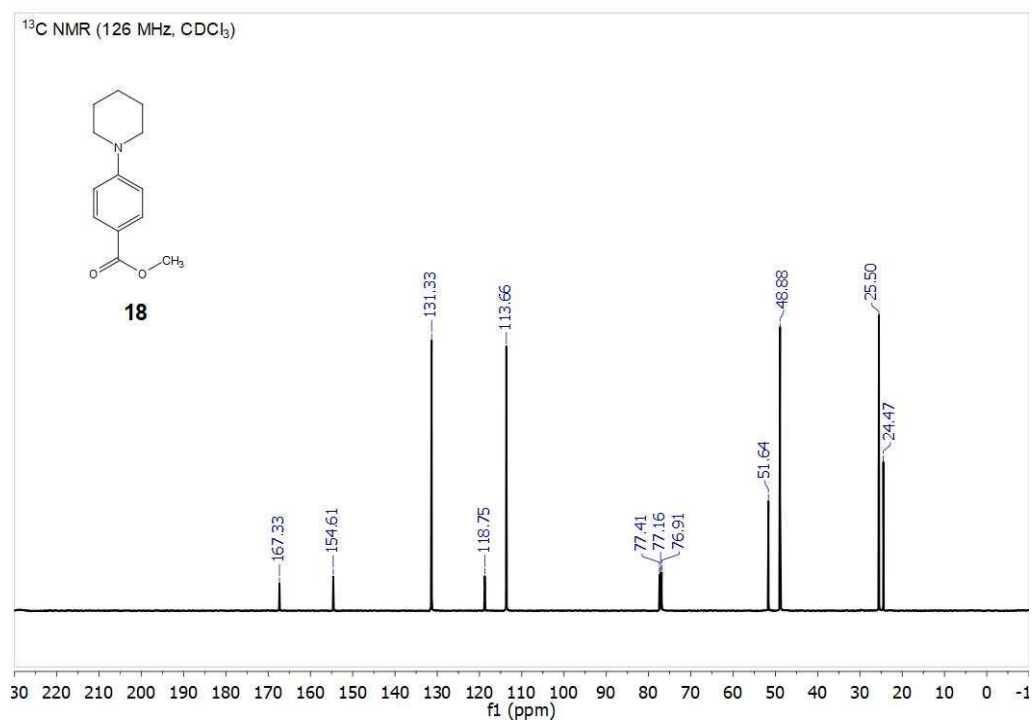


Figure 4.52. <sup>13</sup>C NMR spectrum of (**18**).

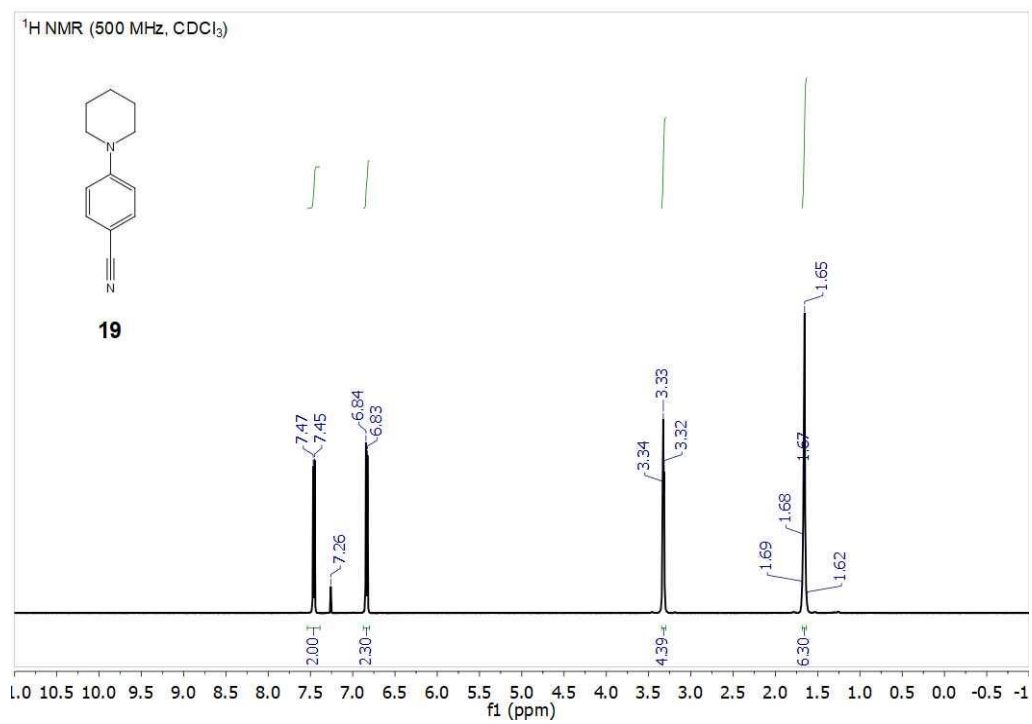


Figure 4.53. <sup>1</sup>H NMR spectrum of (19).

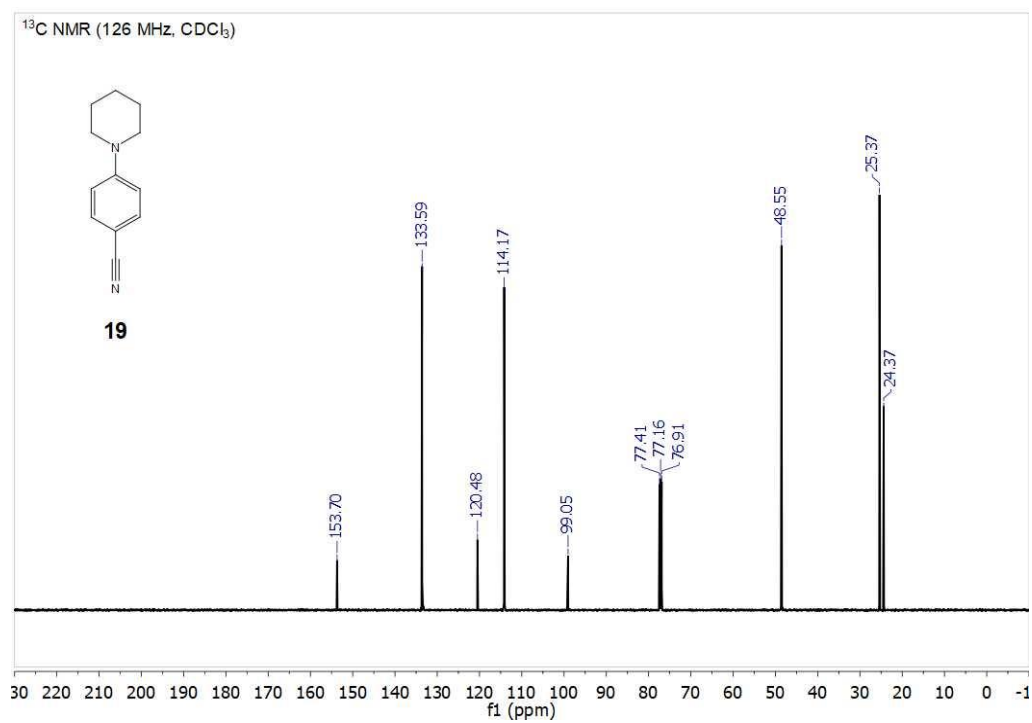


Figure 4.54. <sup>13</sup>C NMR spectrum of (19).

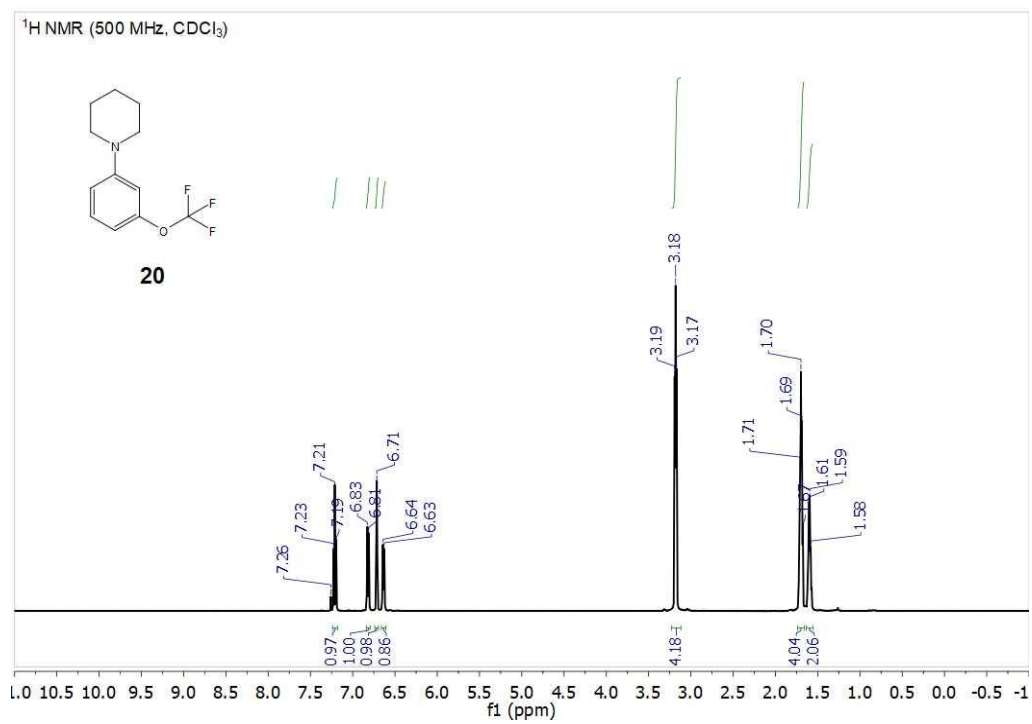


Figure 4.55. <sup>1</sup>H NMR spectrum of (20).

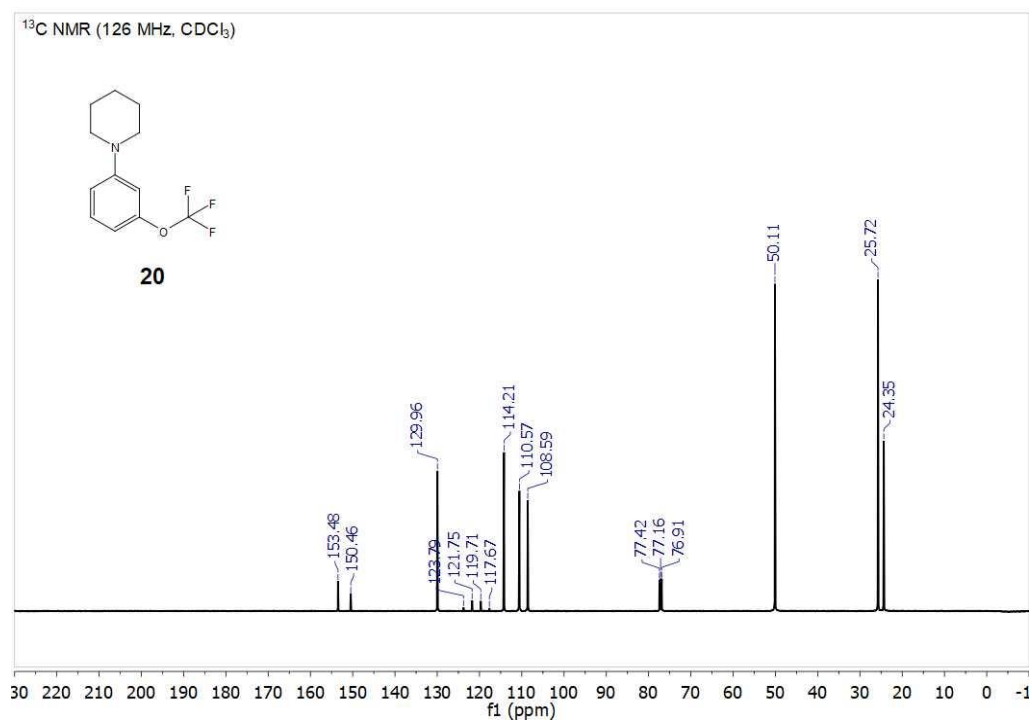


Figure 4.56. <sup>13</sup>C NMR spectrum of (20).

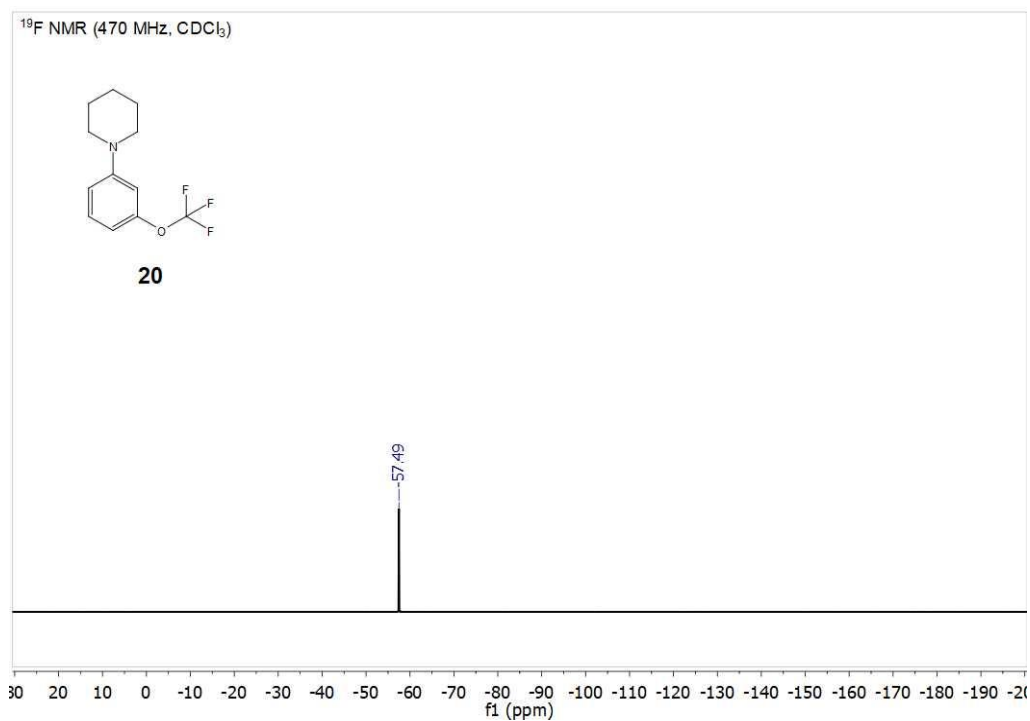


Figure 4.57. <sup>19</sup>F NMR spectrum of (**20**).

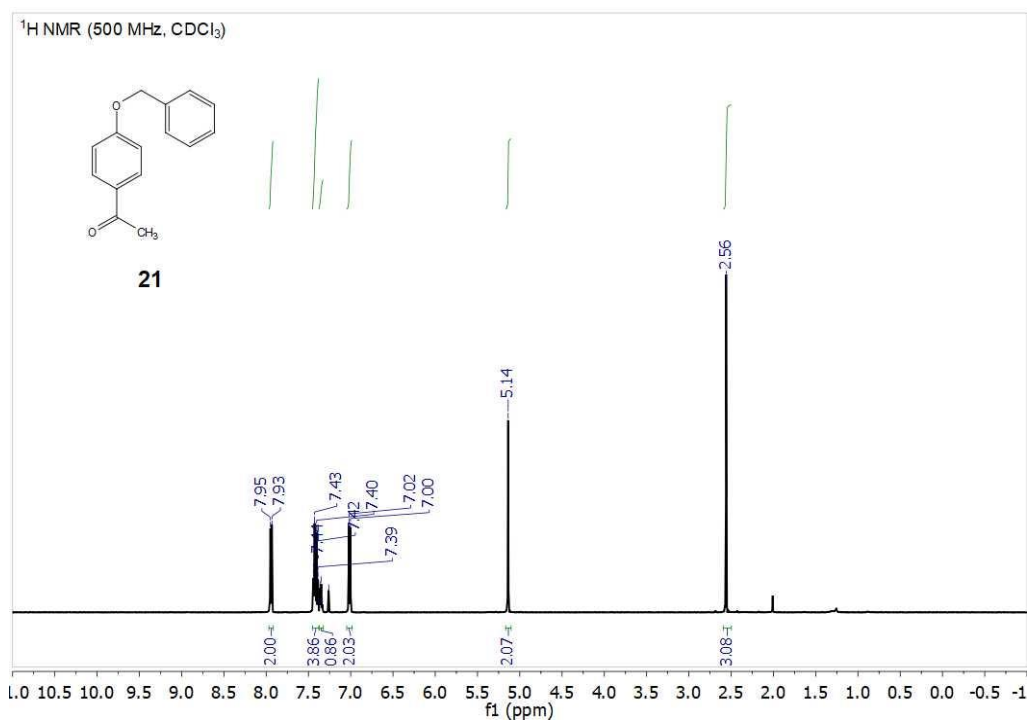


Figure 4.58. <sup>1</sup>H NMR spectrum of (**21**).

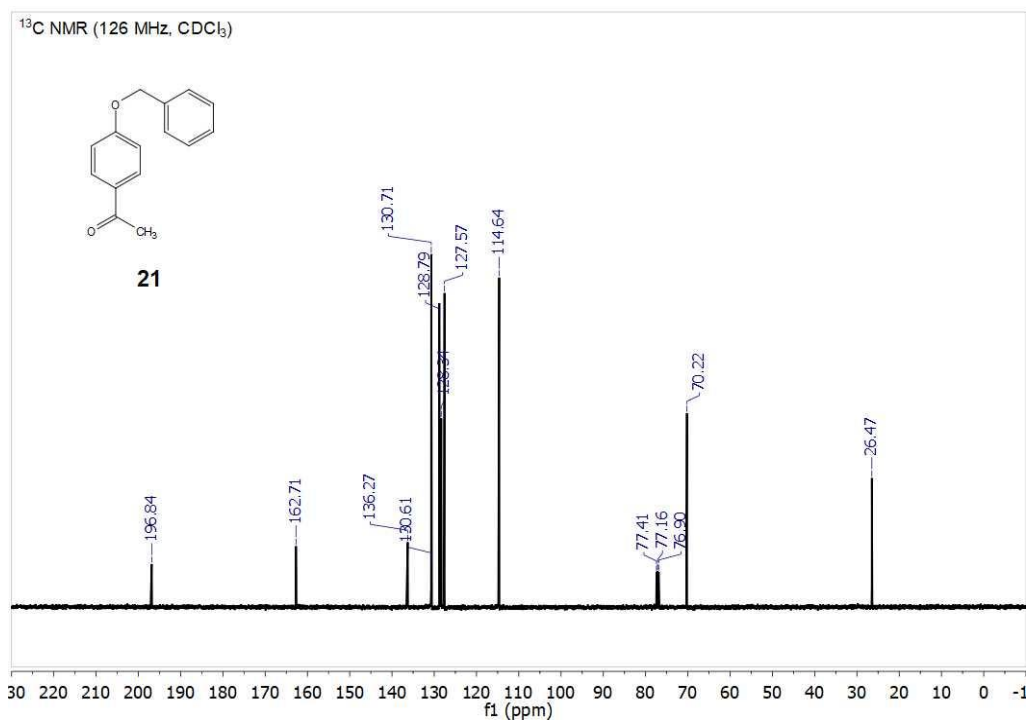


Figure 4.59. <sup>13</sup>C NMR spectrum of (21).

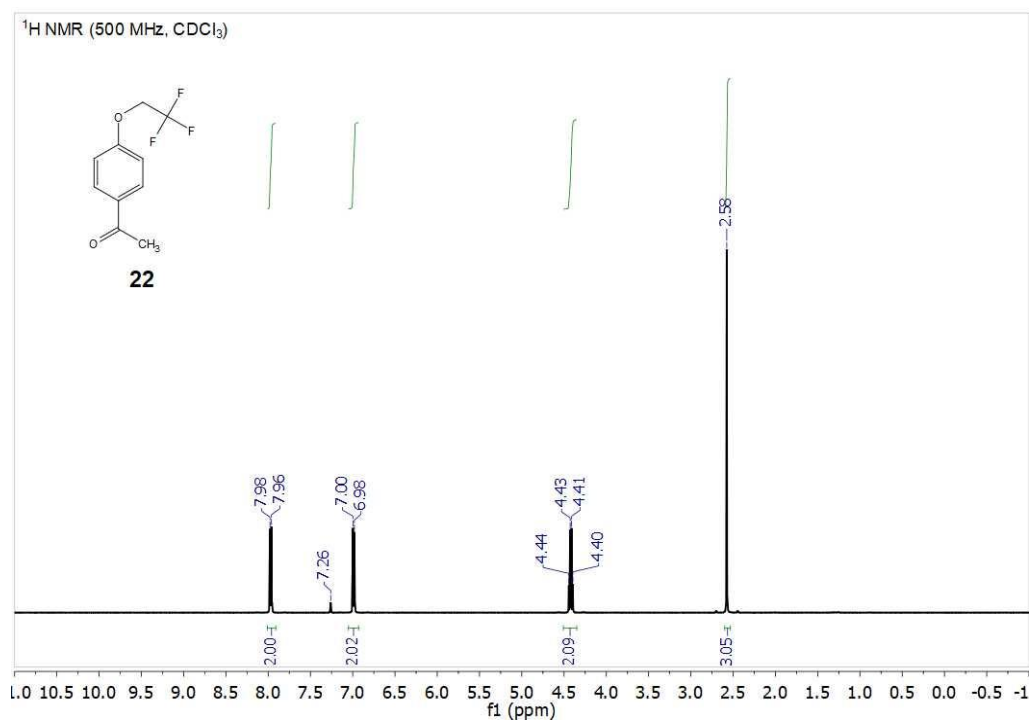


Figure 4.60. <sup>1</sup>H NMR spectrum of (22).

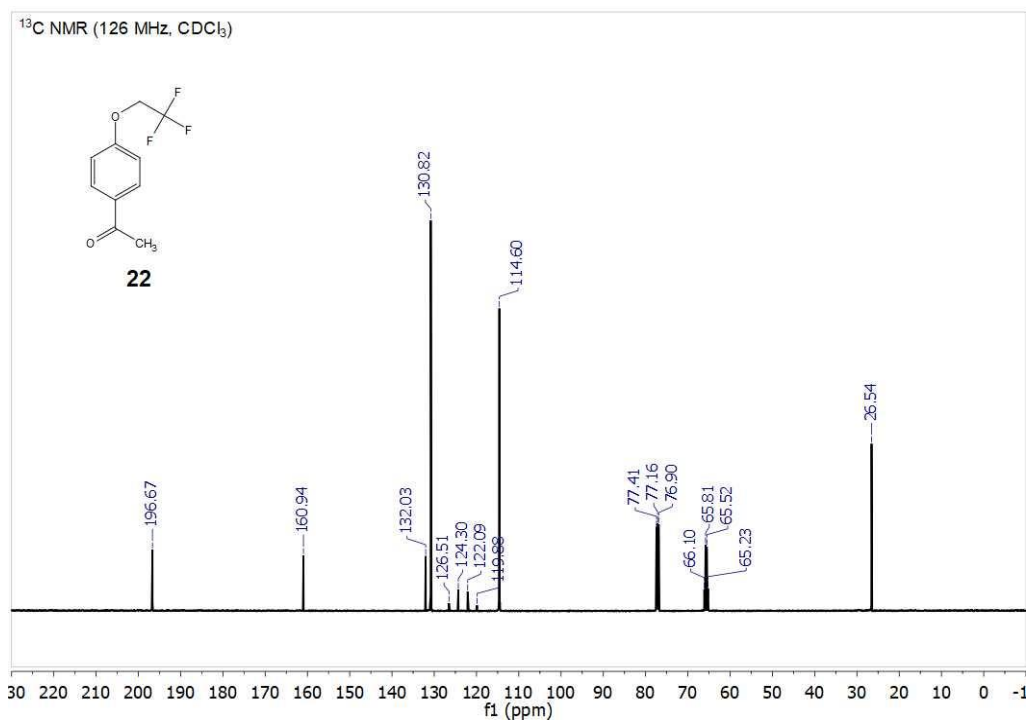


Figure 4.61. <sup>13</sup>C NMR spectrum of (22).

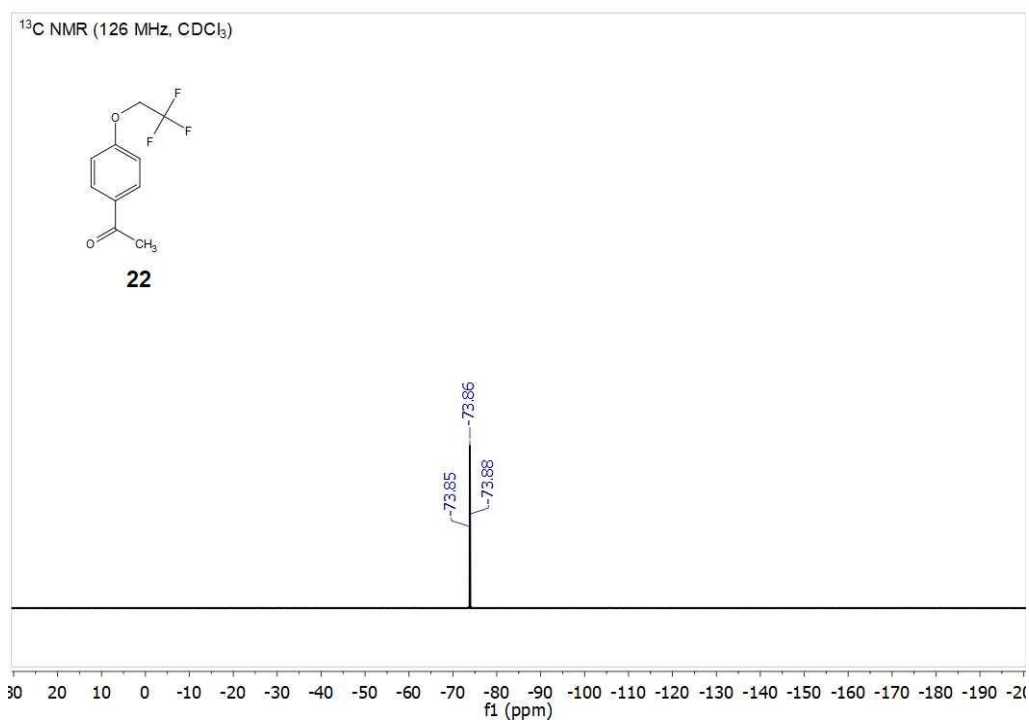


Figure 4.62. <sup>19</sup>F NMR spectrum of (22).

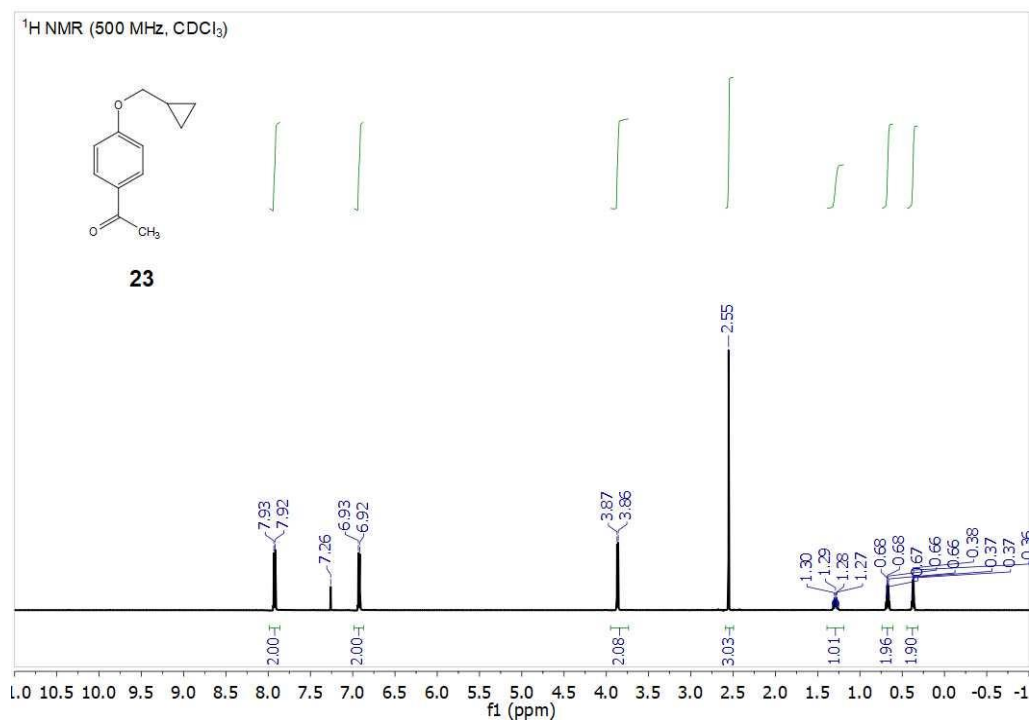


Figure 4.63. <sup>1</sup>H NMR spectrum of (23).

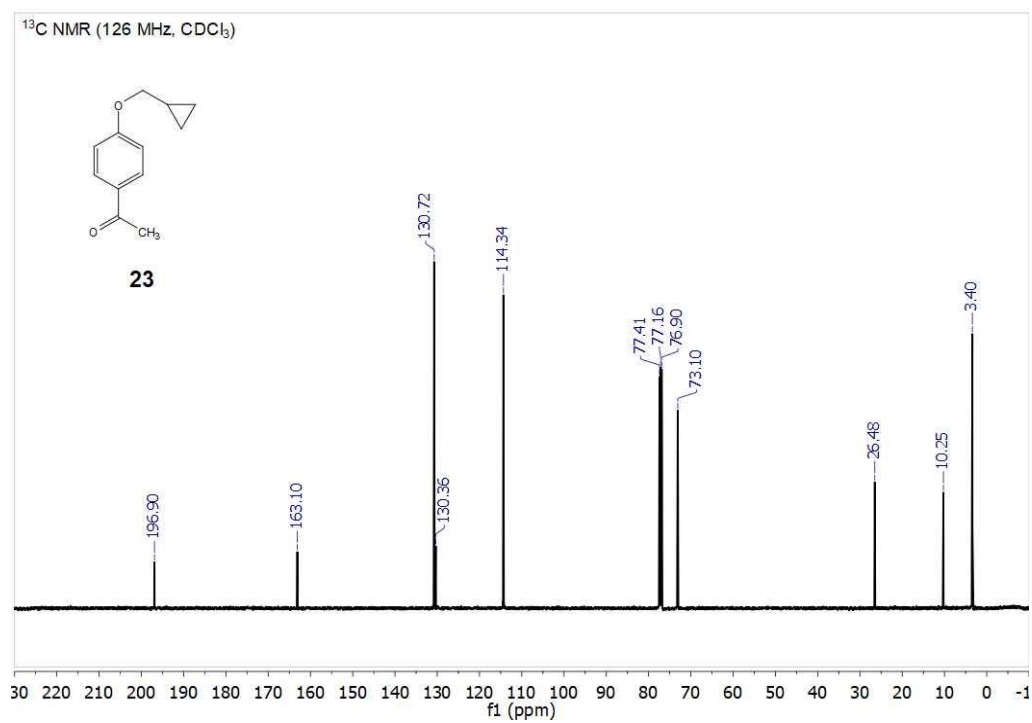


Figure 4.64. <sup>13</sup>C NMR spectrum of (23).

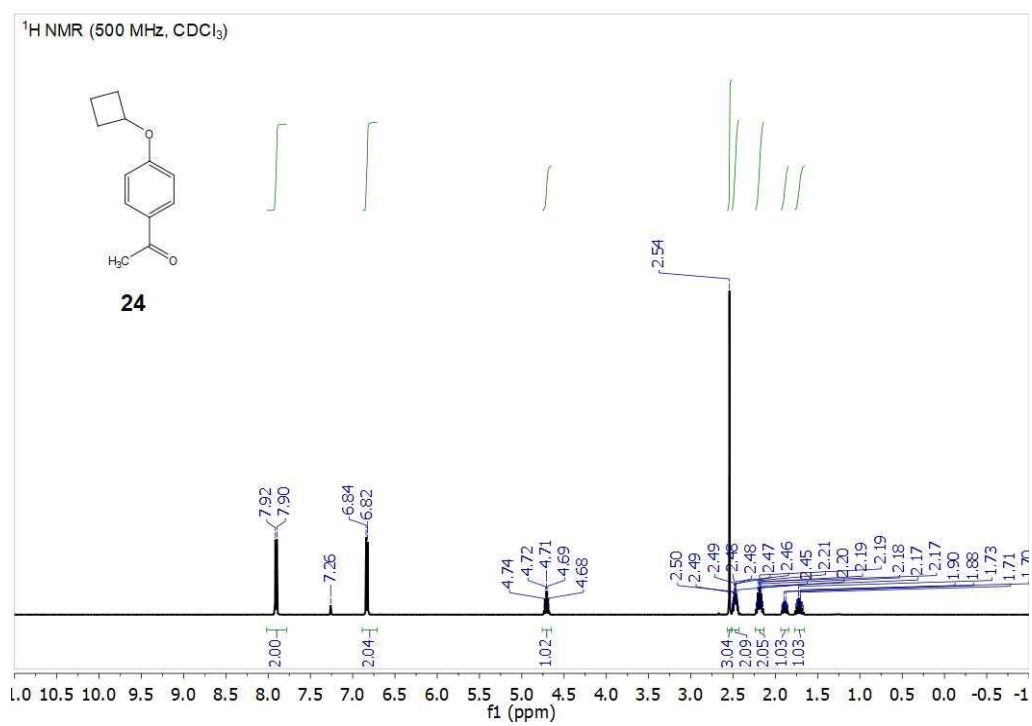


Figure 4.65. <sup>1</sup>H NMR spectrum of (**24**).

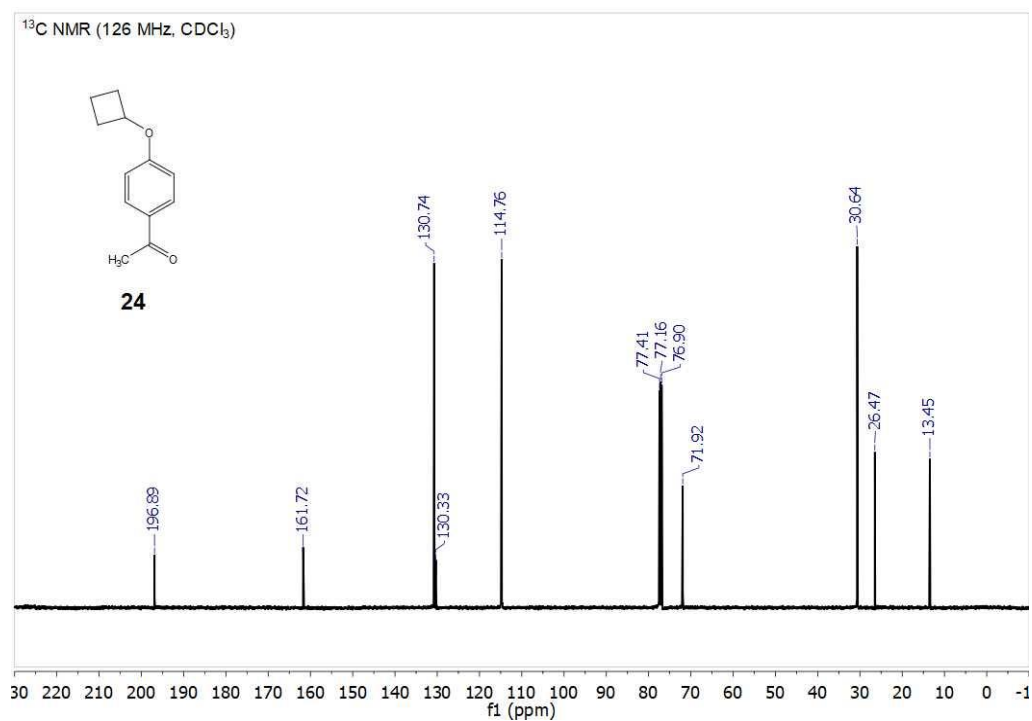


Figure 4.66. <sup>13</sup>C NMR spectrum of (**24**).



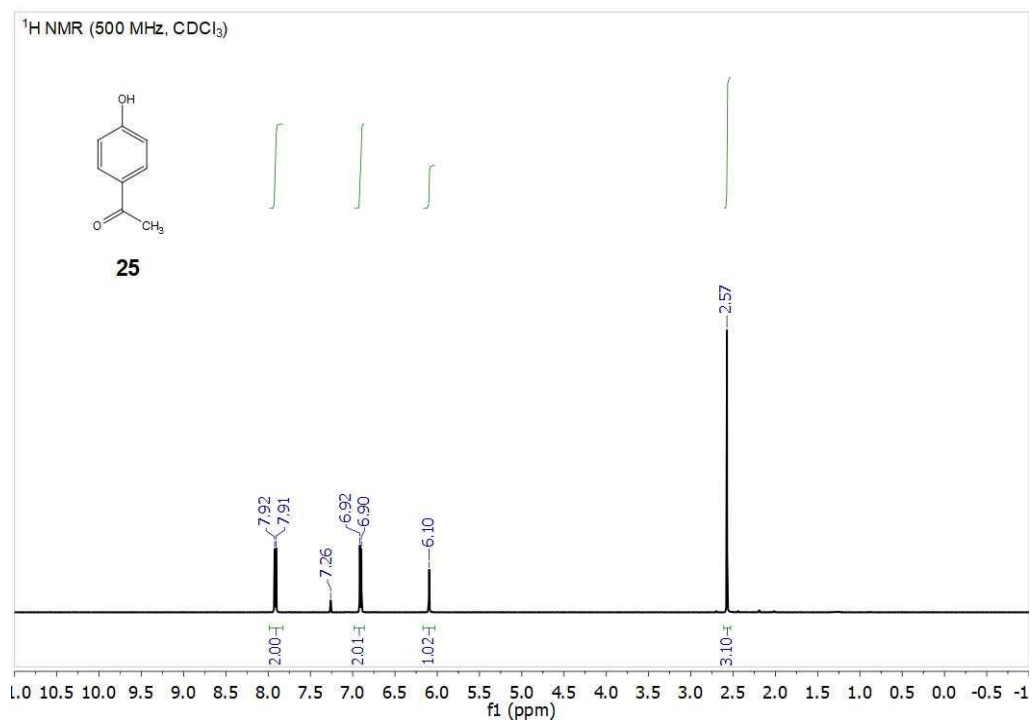


Figure 4.67. <sup>1</sup>H NMR spectrum of (25).

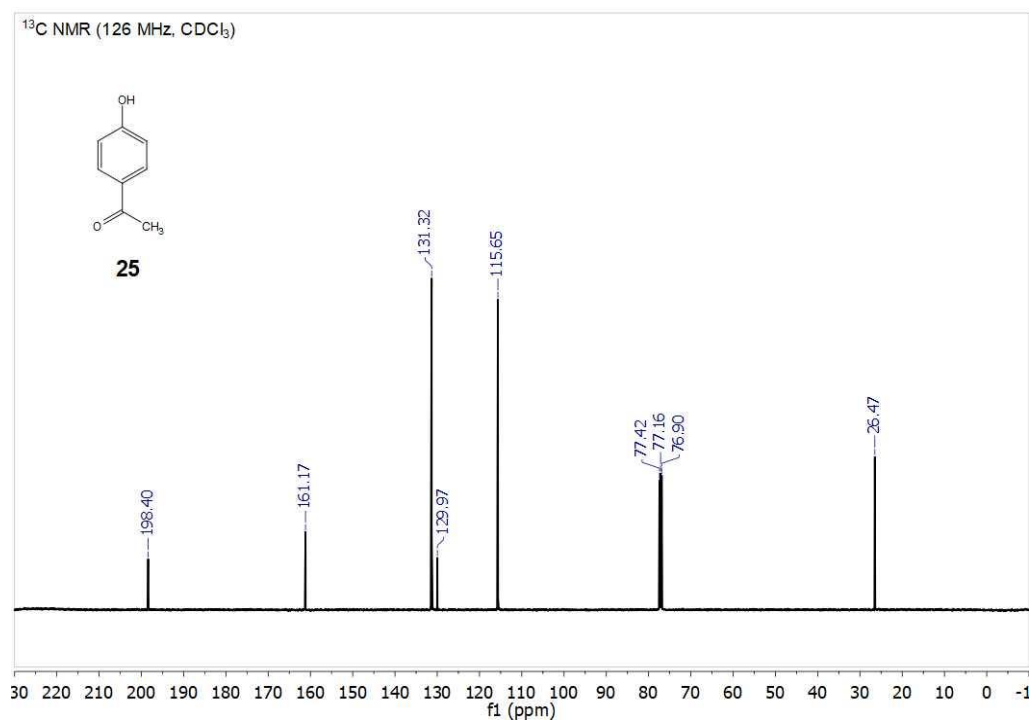


Figure 4.68. <sup>13</sup>C NMR spectrum of (25).

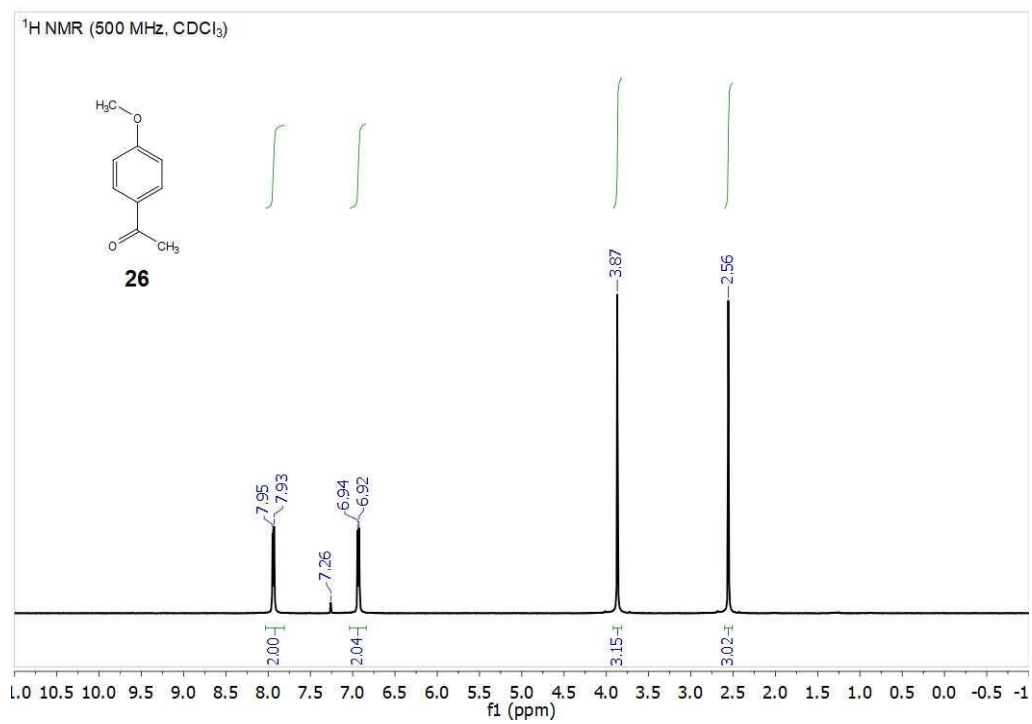


Figure 4.69. <sup>1</sup>H NMR spectrum of (26).

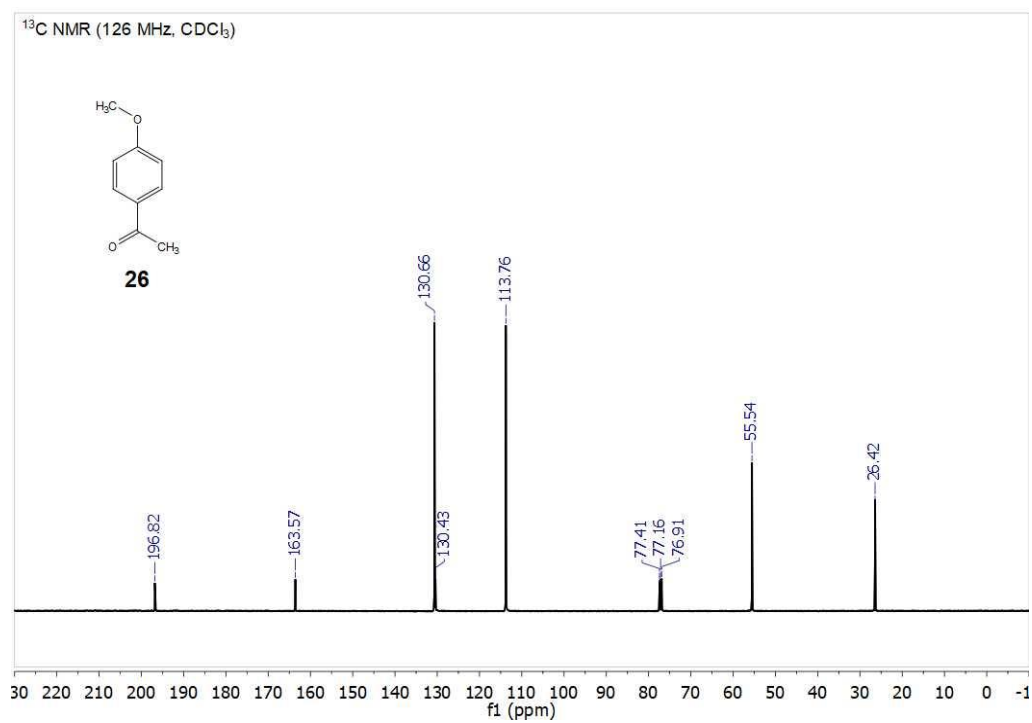


Figure 4.70. <sup>13</sup>C NMR spectrum of (26).

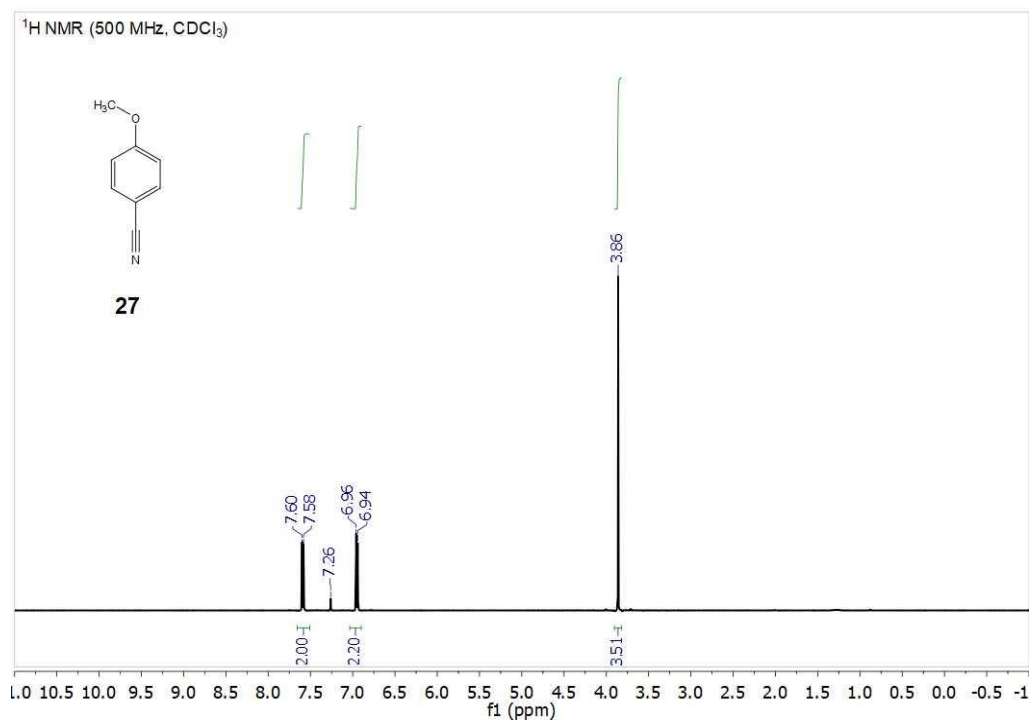


Figure 4.71. <sup>1</sup>H NMR spectrum of (27).

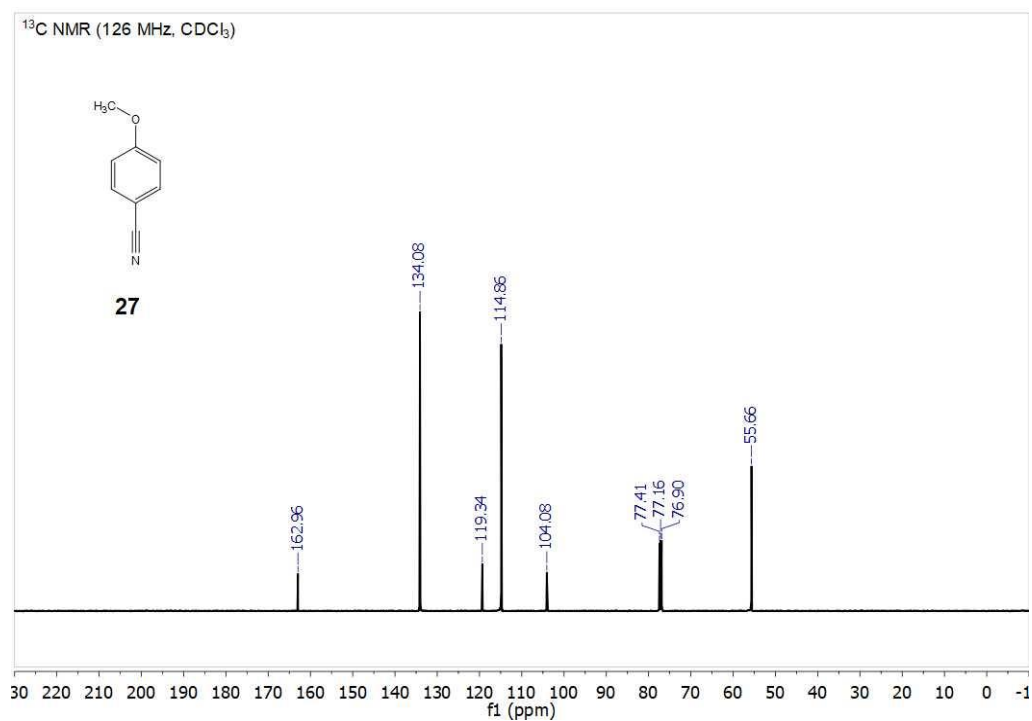


Figure 4.72. <sup>13</sup>C NMR spectrum of (27).

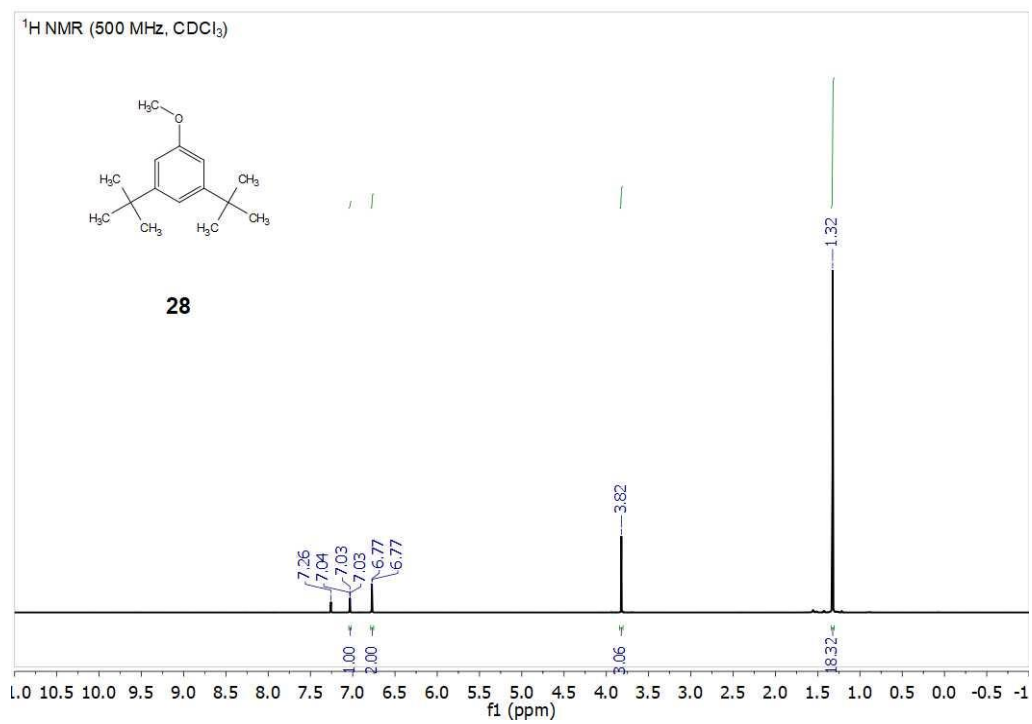


Figure 4.73. <sup>1</sup>H NMR spectrum of (28).

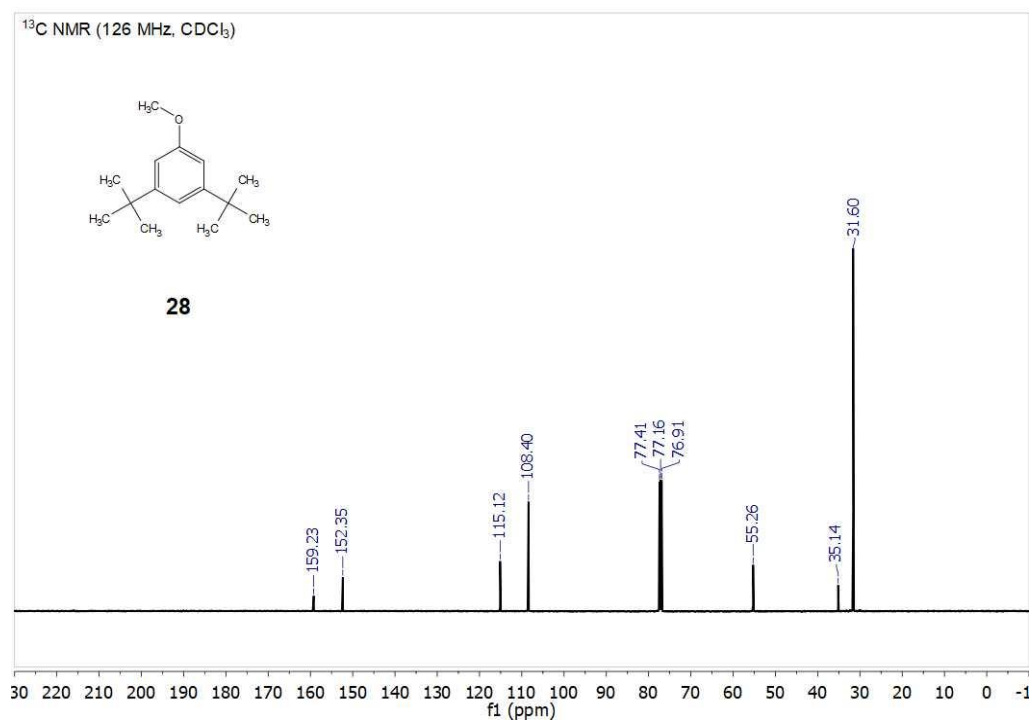


Figure 4.74. <sup>13</sup>C NMR spectrum of (28).

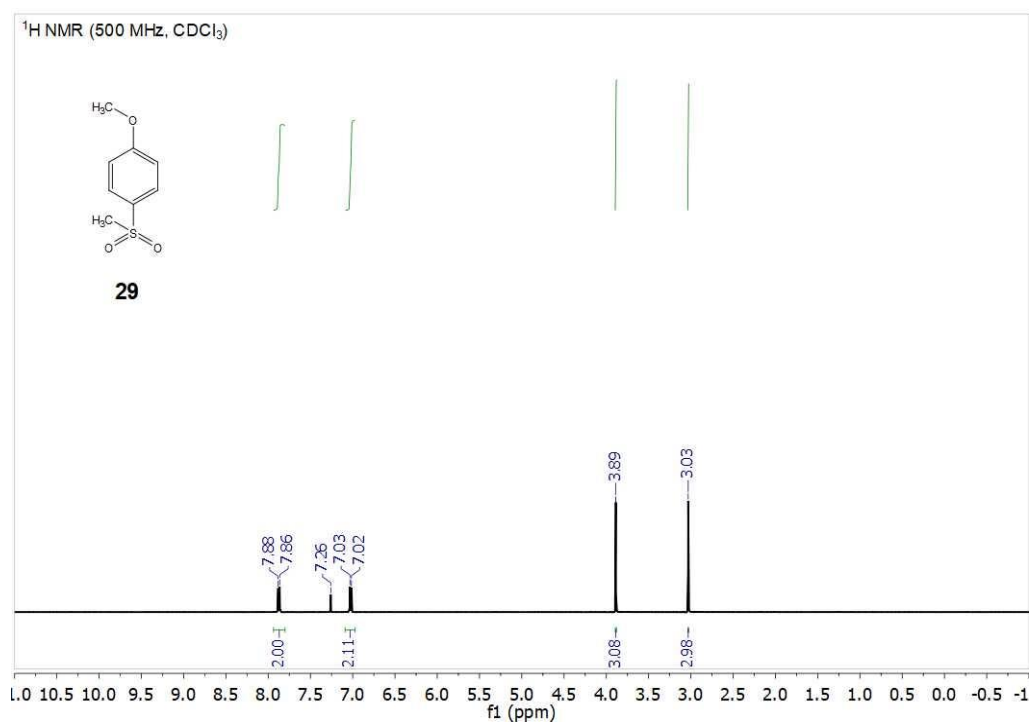


Figure 4.75. <sup>1</sup>H NMR spectrum of (29).

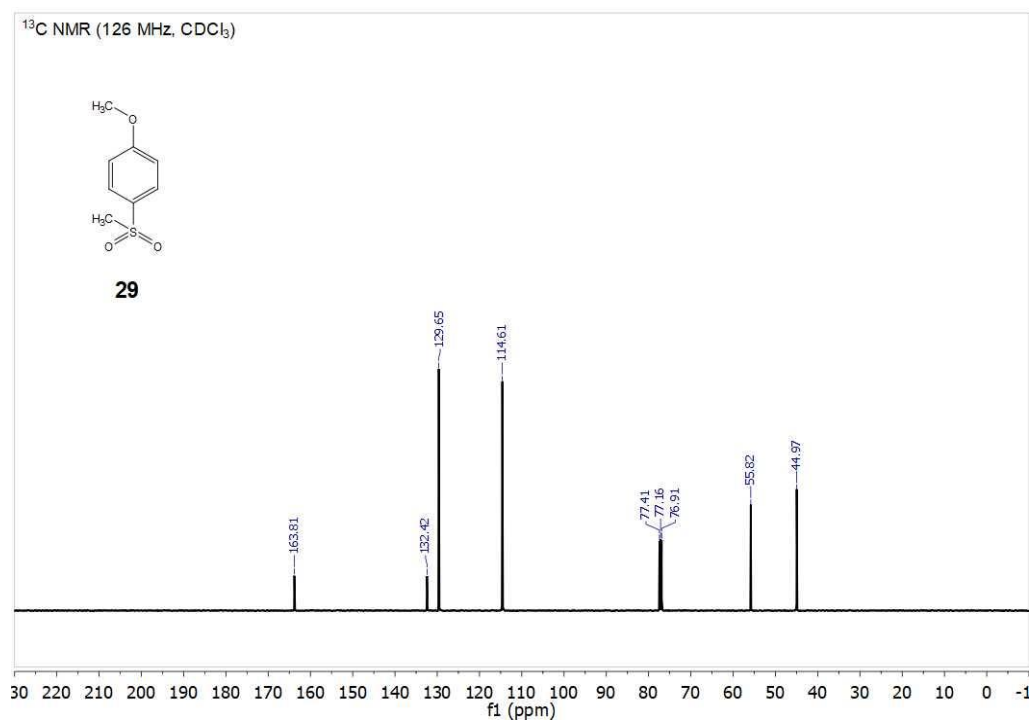


Figure 4.76. <sup>13</sup>C NMR spectrum of (29).

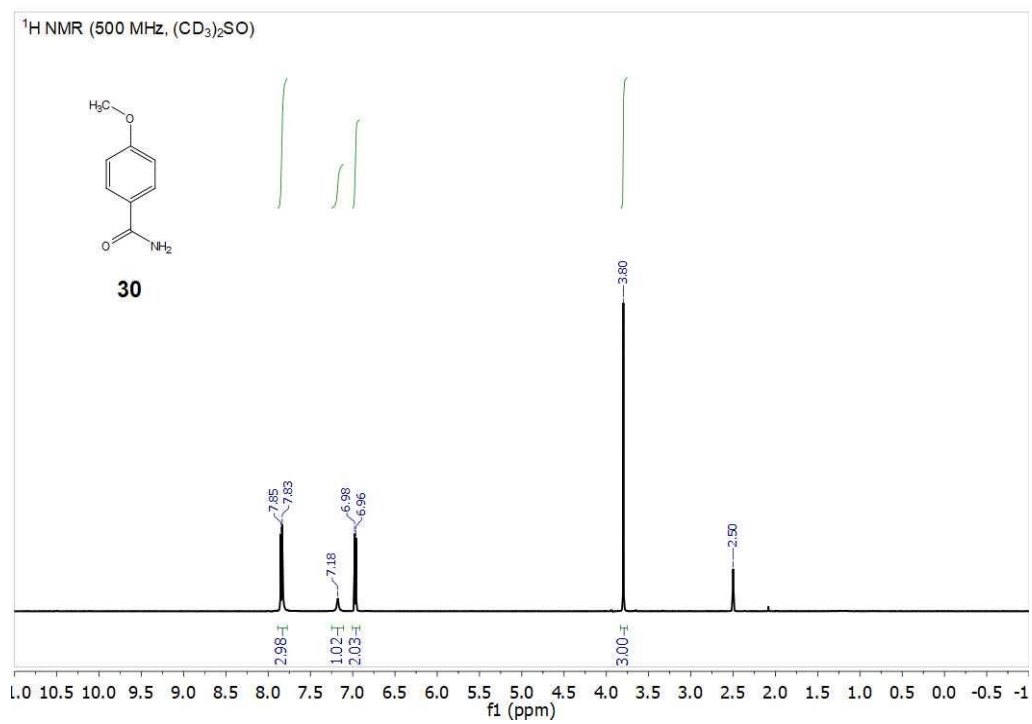


Figure 4.77. <sup>1</sup>H NMR spectrum of (30).

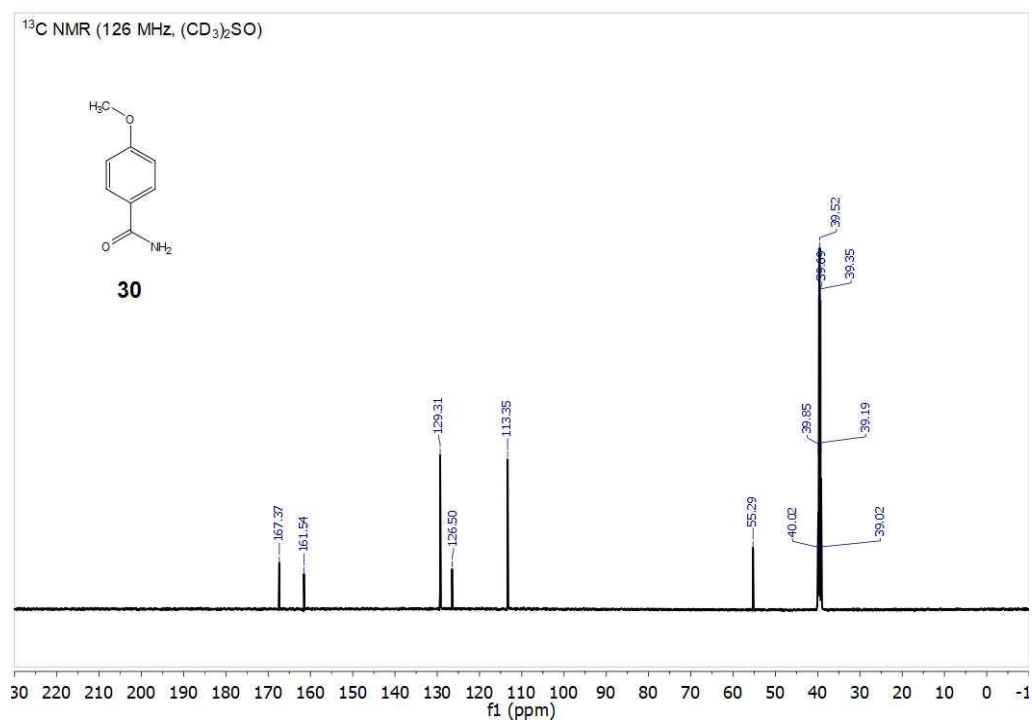


Figure 4.78. <sup>13</sup>C NMR spectrum of (30).

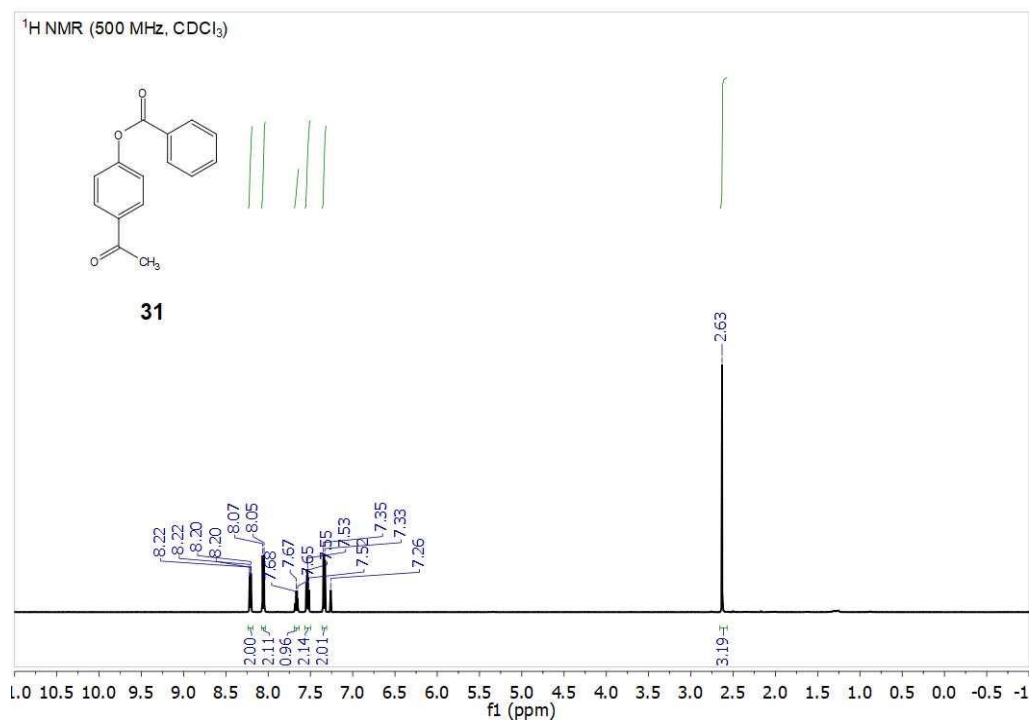


Figure 4.79. <sup>1</sup>H NMR spectrum of (31).

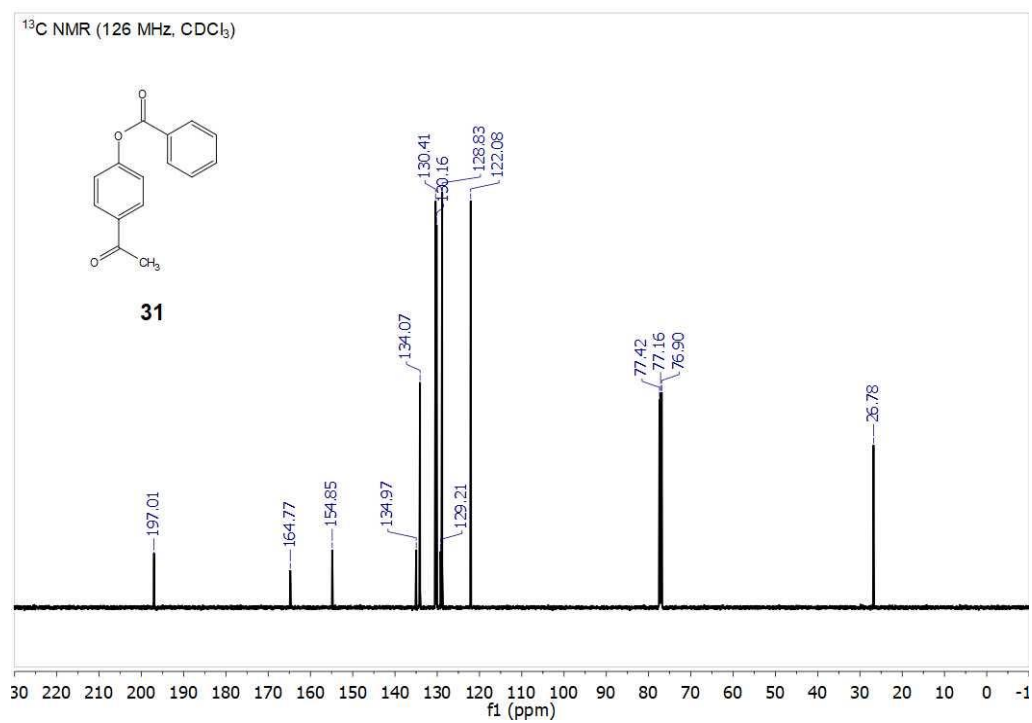


Figure 4.80. <sup>13</sup>C NMR spectrum of (31).

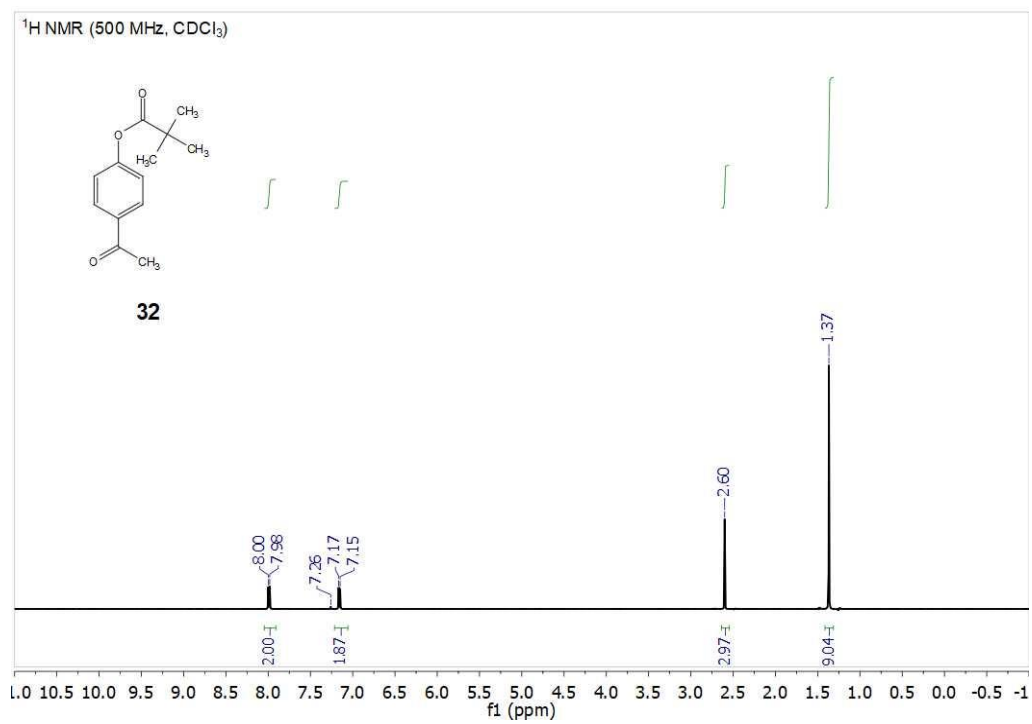


Figure 4.81. <sup>1</sup>H NMR spectrum of (32).

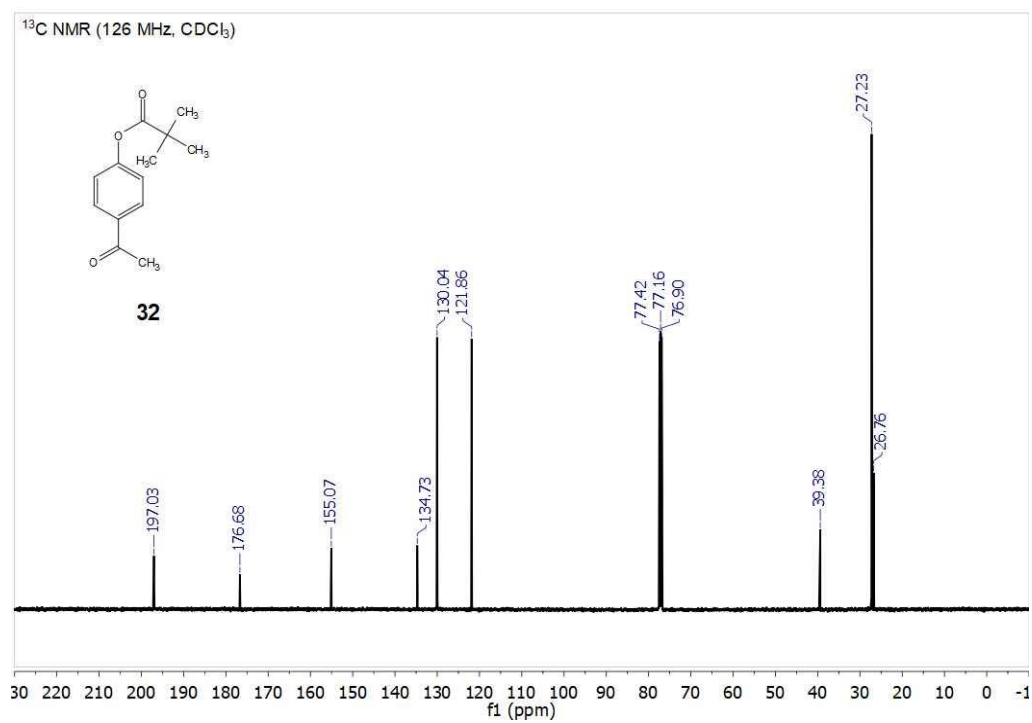


Figure 4.82. <sup>13</sup>C NMR spectrum of (32).



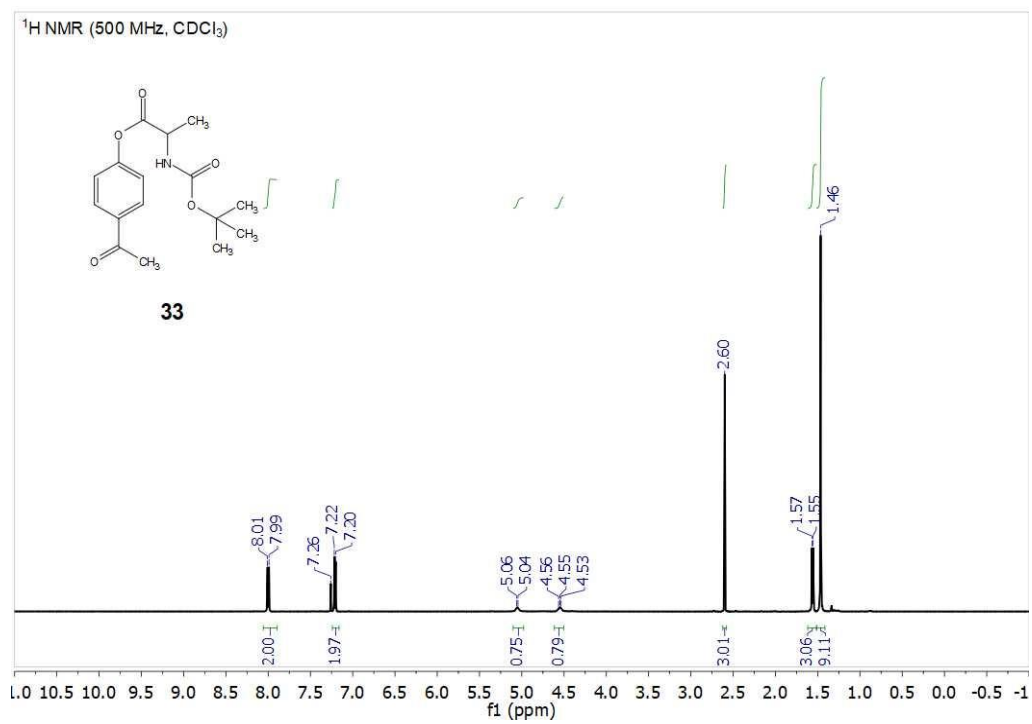


Figure 4.83. <sup>1</sup>H NMR spectrum of (33).

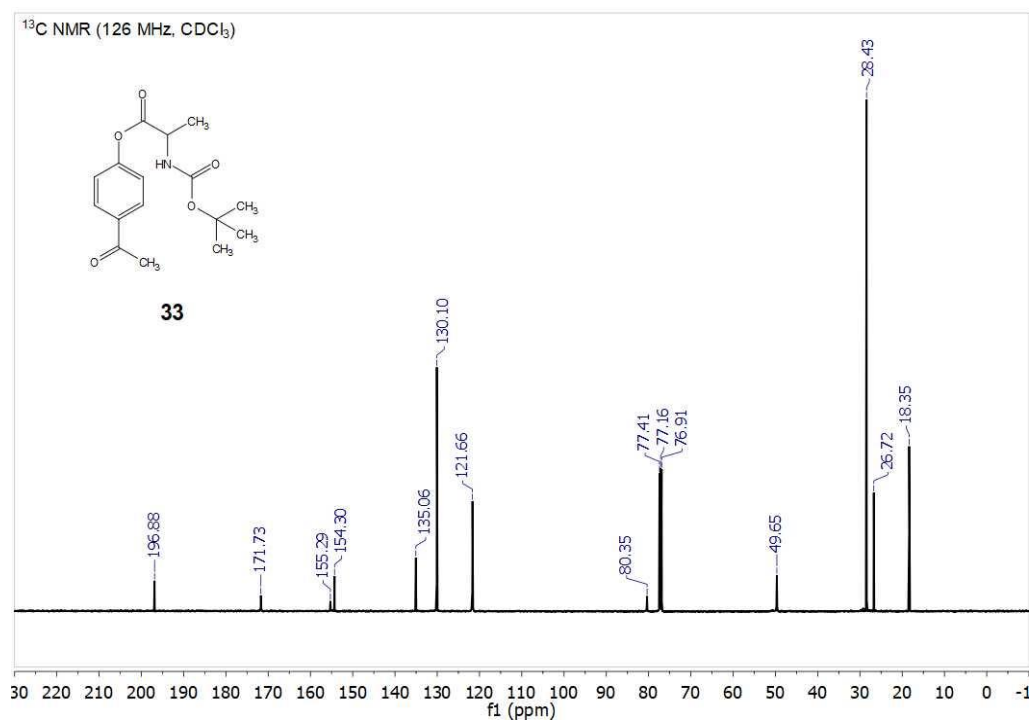


Figure 4.84. <sup>13</sup>C NMR spectrum of (33).

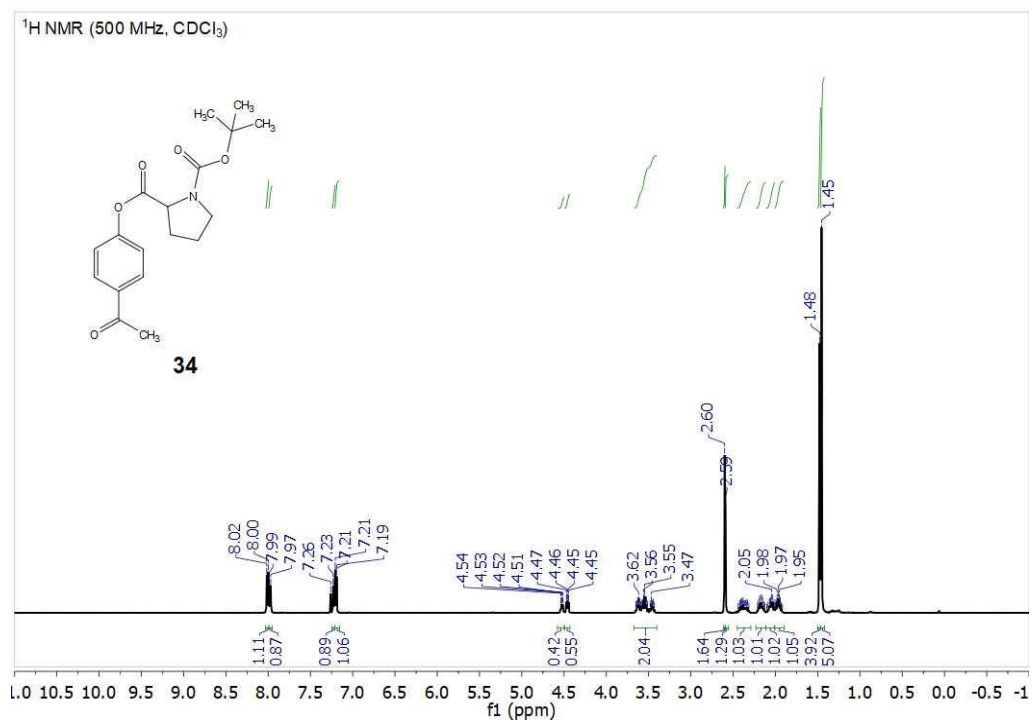


Figure 4.85. <sup>1</sup>H NMR spectrum of (**34**).

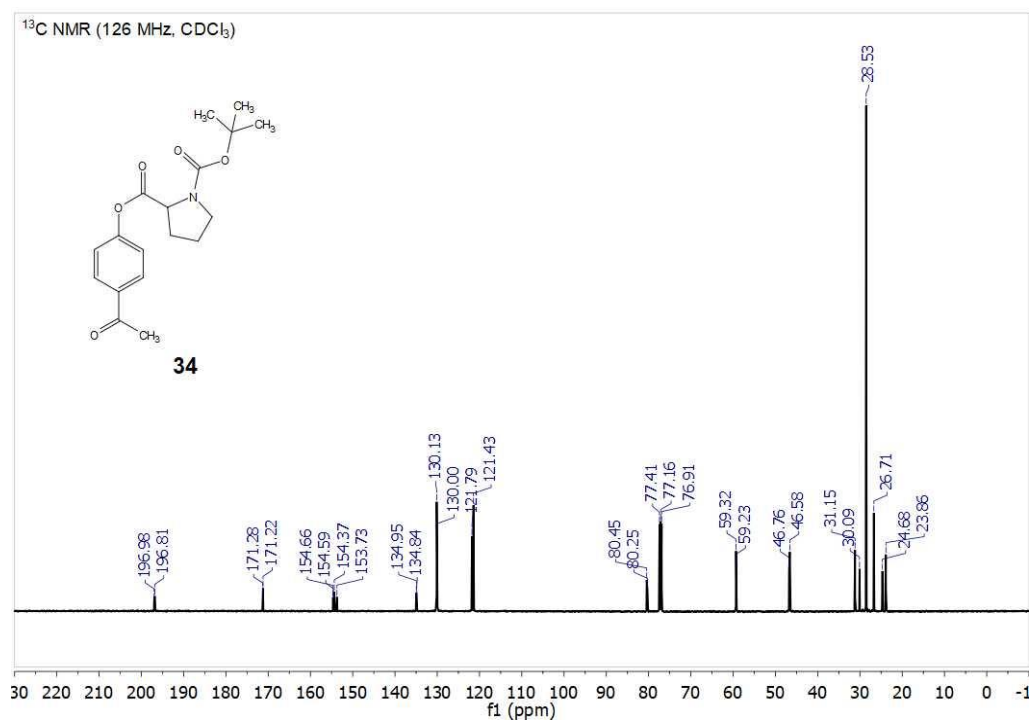


Figure 4.86. <sup>13</sup>C NMR spectrum of (**34**).

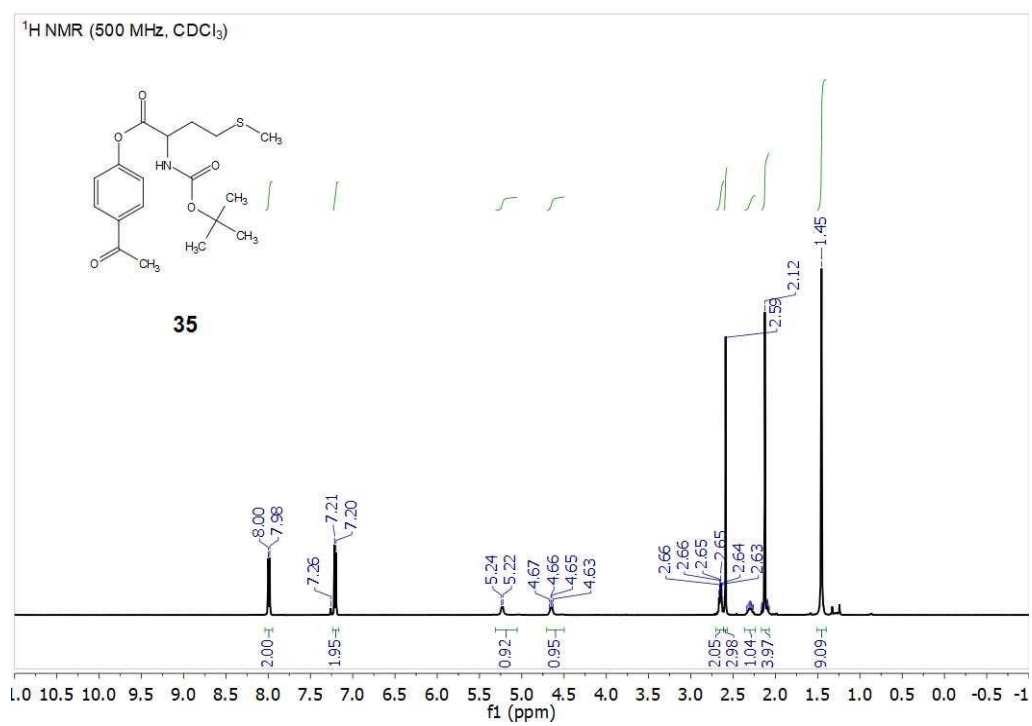


Figure 4.87. <sup>1</sup>H NMR spectrum of (35).

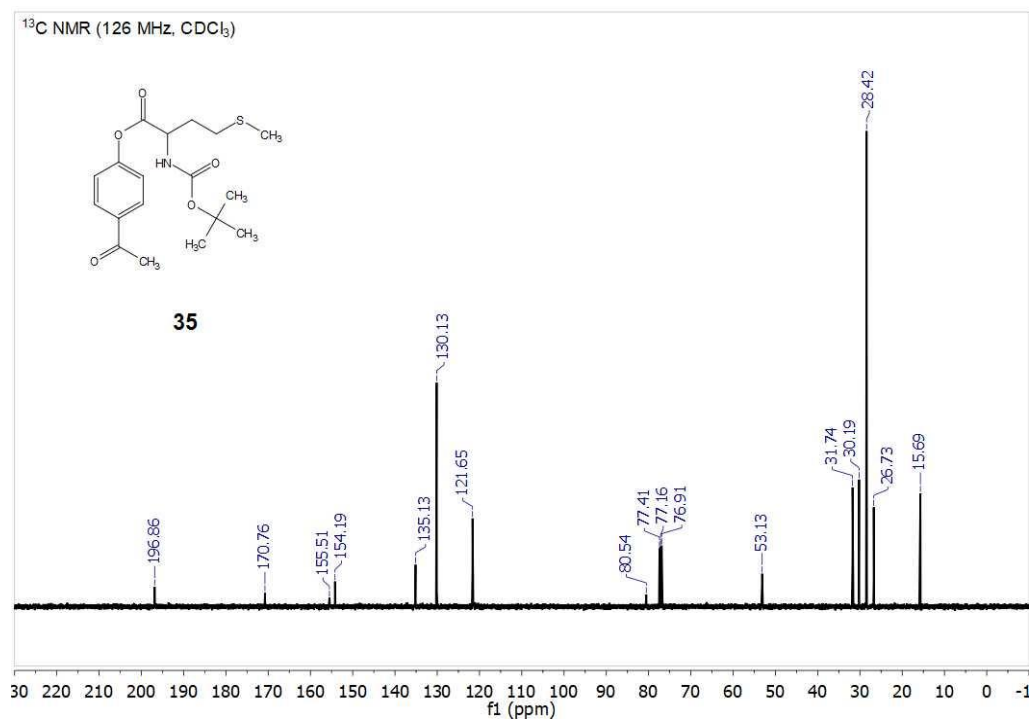


Figure 4.88. <sup>13</sup>C NMR spectrum of (35).

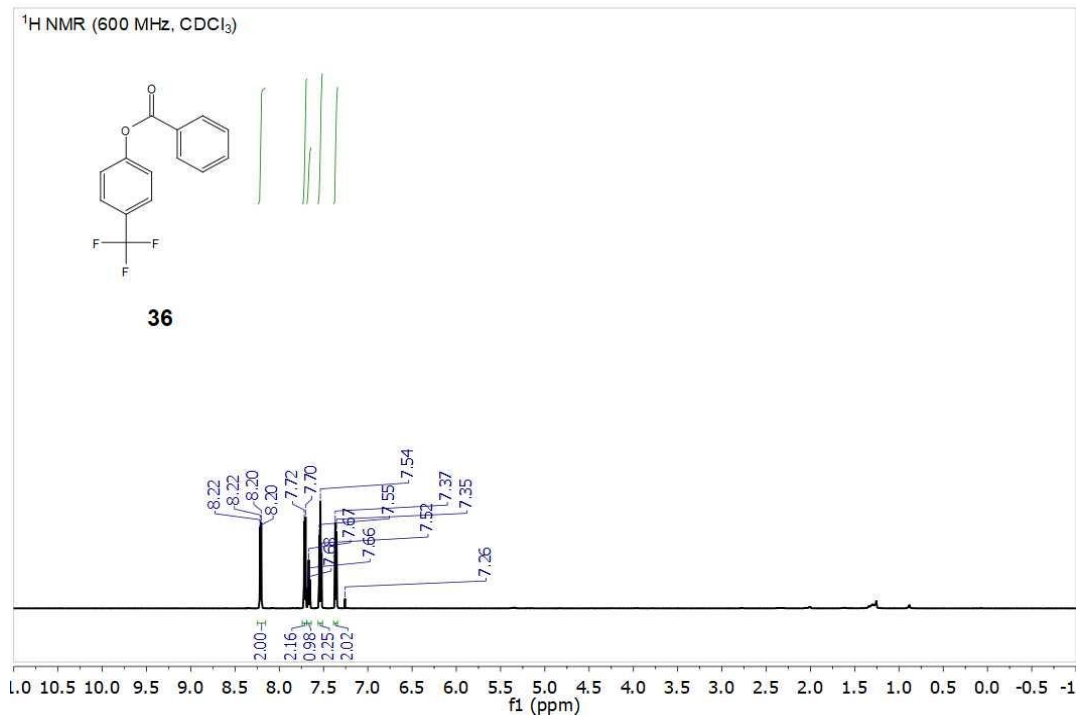


Figure 4.89. <sup>1</sup>H NMR spectrum of (36).

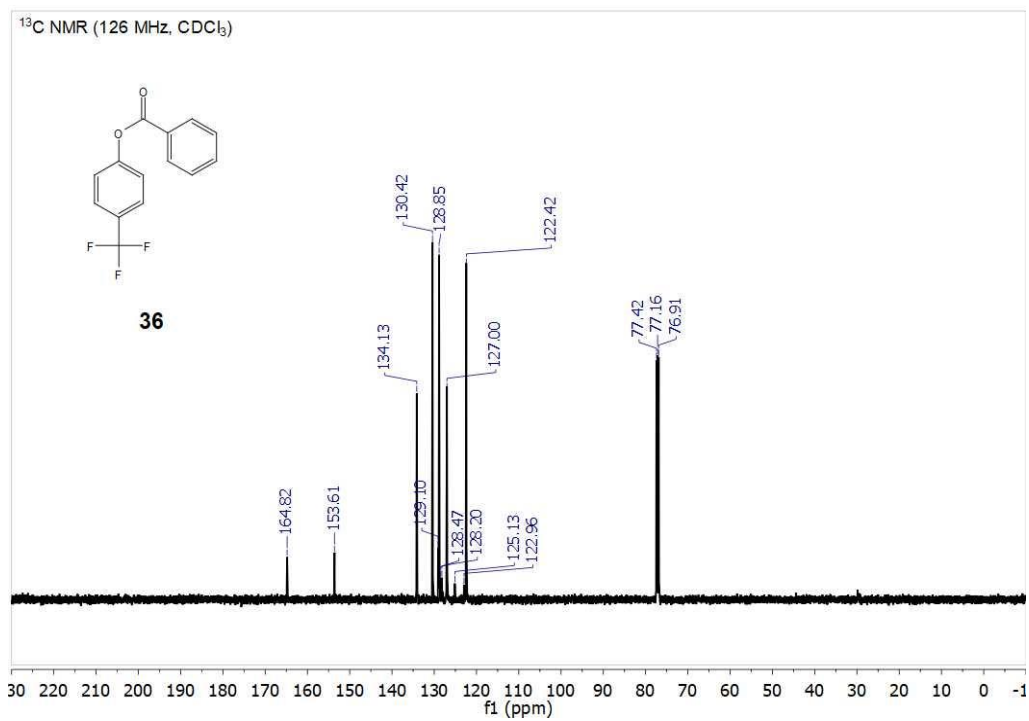


Figure 4.90. <sup>13</sup>C NMR spectrum of (36).

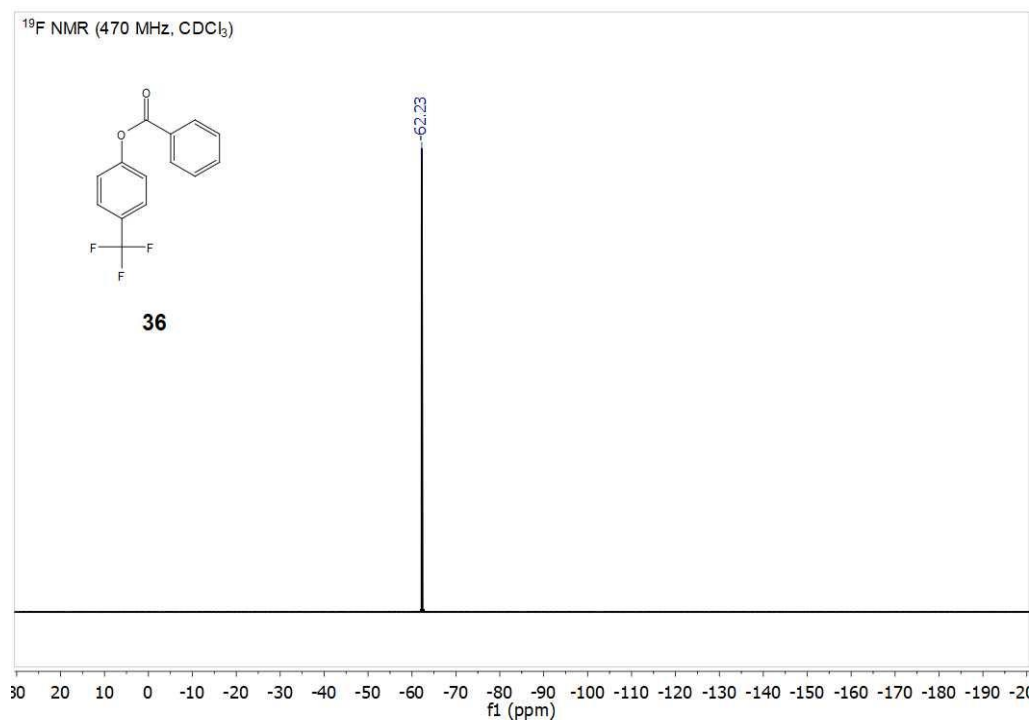


Figure 4.91. <sup>19</sup>F NMR spectrum of (36).

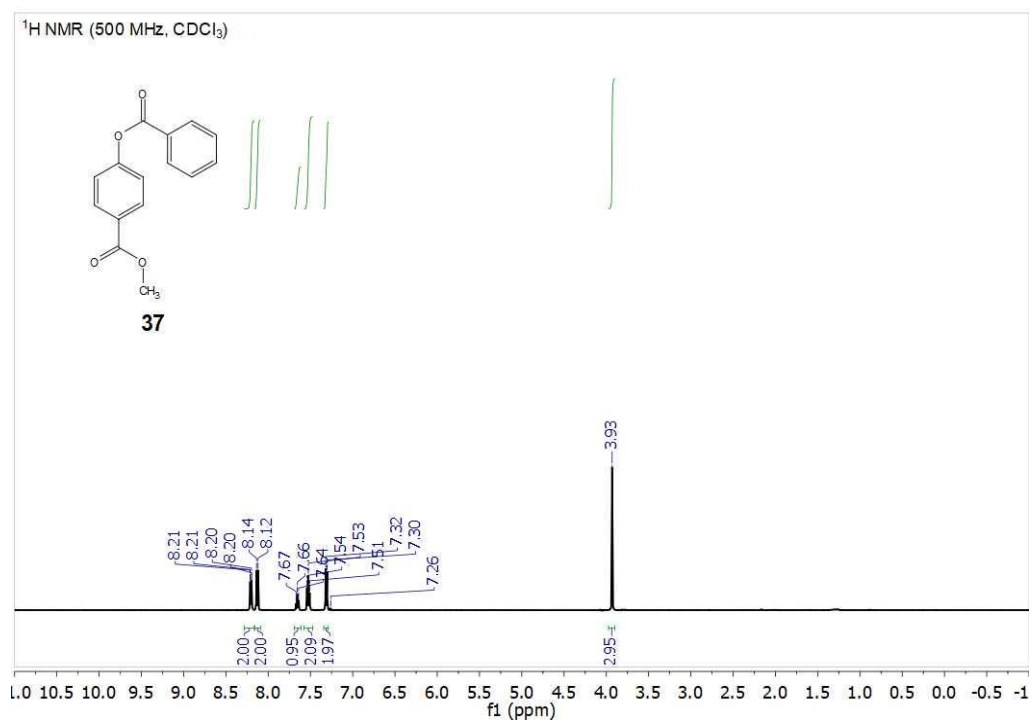


Figure 4.92. <sup>1</sup>H NMR spectrum of (37).

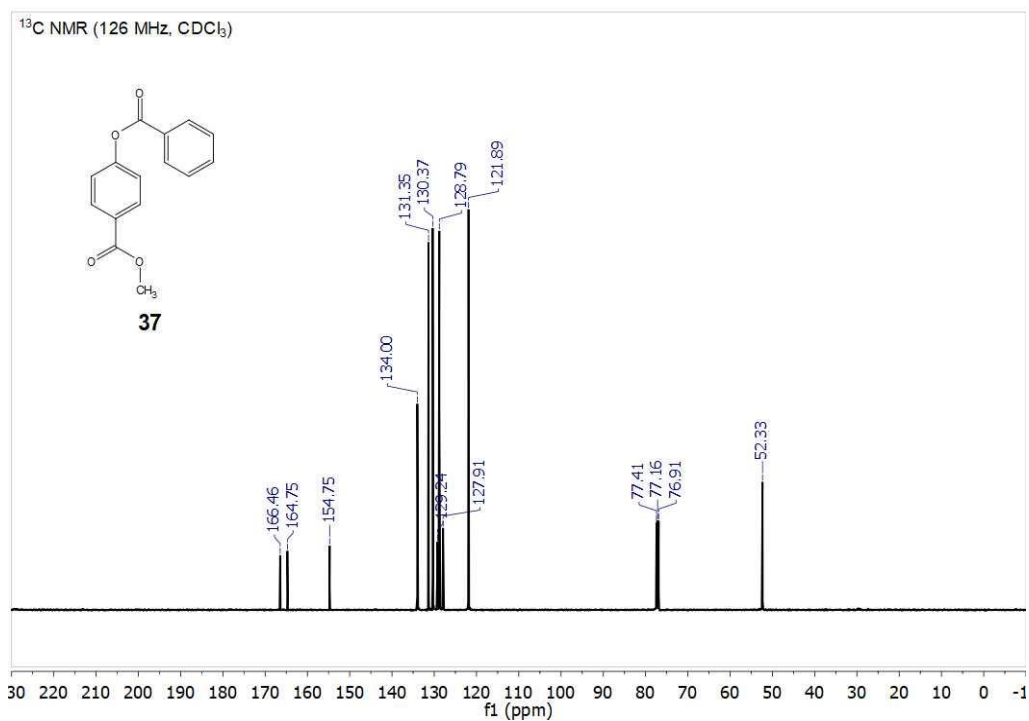


Figure 4.93. <sup>13</sup>C NMR spectrum of (37).

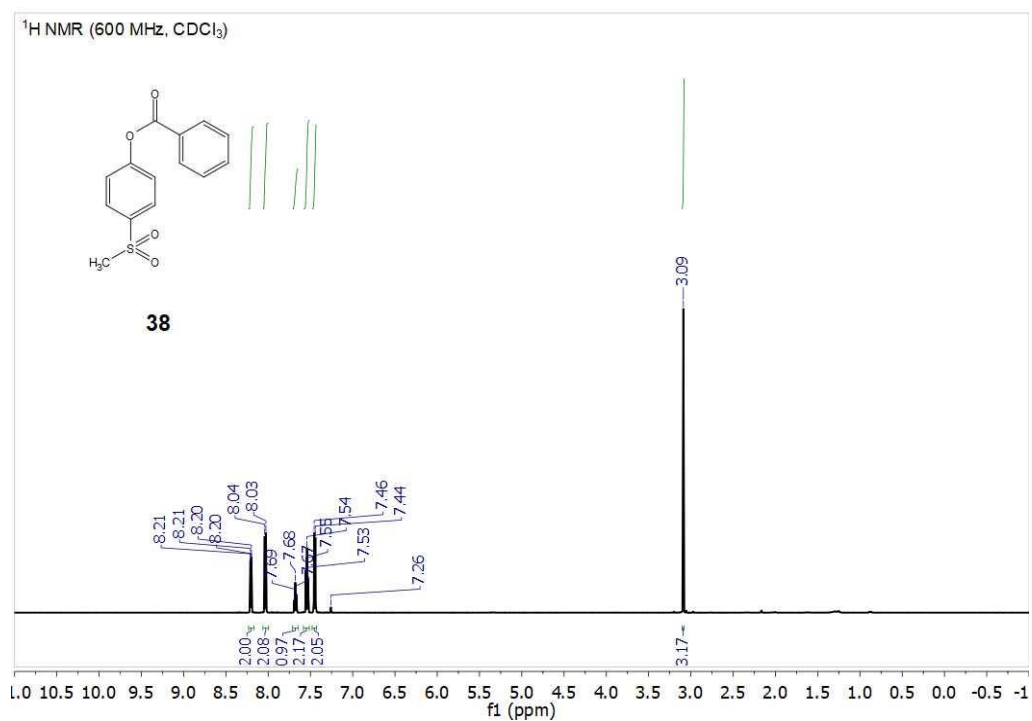


Figure 4.94. <sup>1</sup>H NMR spectrum of (38).

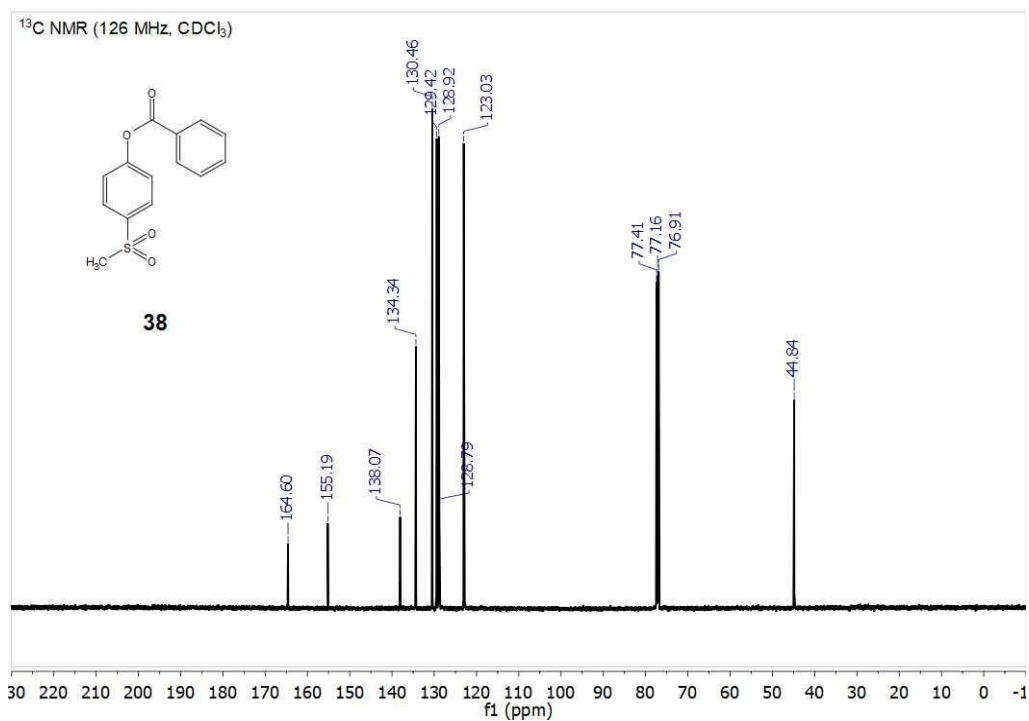


Figure 4.95. <sup>13</sup>C NMR spectrum of (**38**).

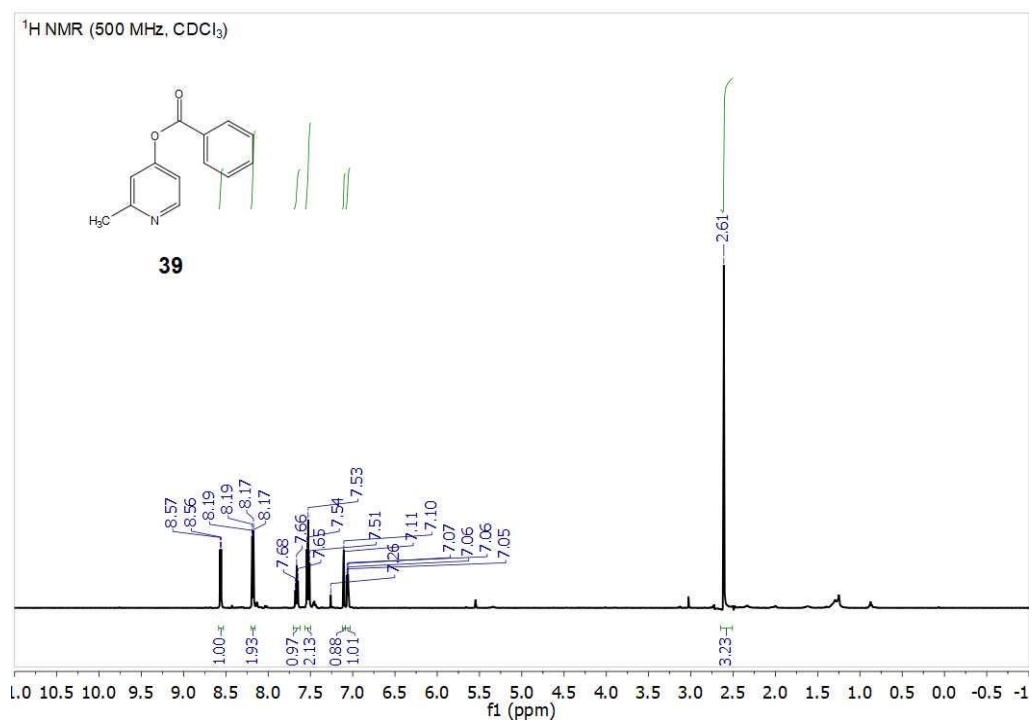


Figure 4.96. <sup>1</sup>H NMR spectrum of (**39**).





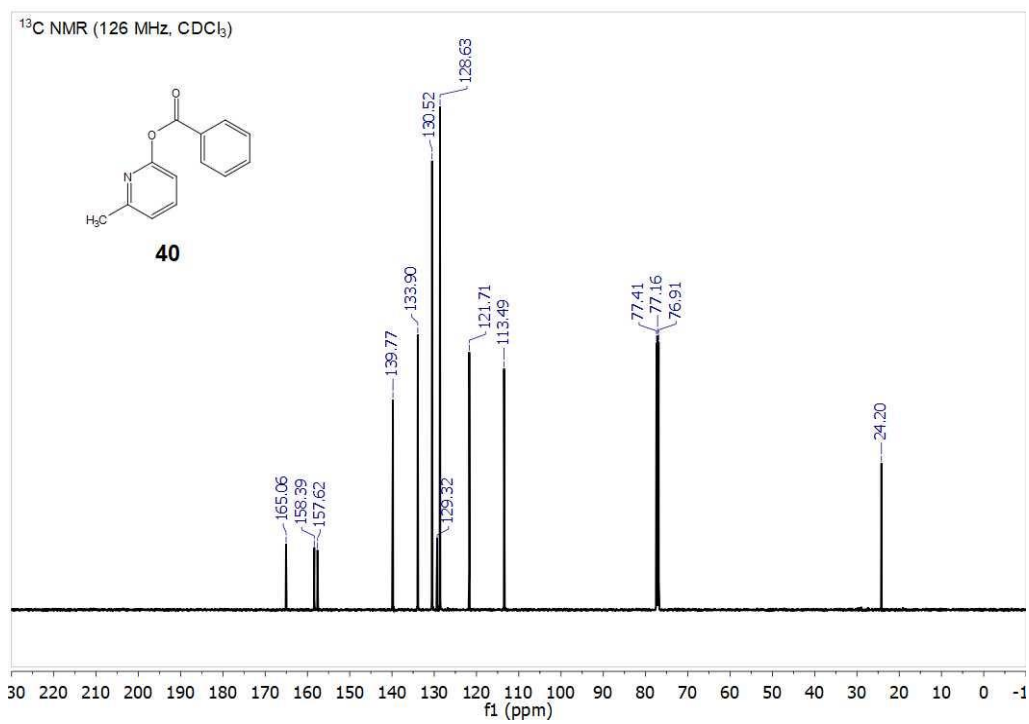


Figure 4.99. <sup>13</sup>C NMR spectrum of (**40**).

#### 4.9 Acknowledgements

Dr. Yangzhong Qin assisted with the quantum yield measurements.

#### 4.10 References

1. Ruiz-Castillo, P.; Buchwald, S. L., Applications of Palladium-Catalyzed C-N Cross-Coupling Reactions. *Chem. Rev.* **2016**, *116*, 12564-12649.
2. Hartwig, J. F., Carbon-Heteroatom Bond Formation Catalysed by Organometallic Complexes. *Nature* **2008**, *455*, 314-322.
3. Huang, Y.-B.; Yang, C.-T.; Yi, J.; Deng, X.-J.; Fu, Y.; Liu, L., Cu-Catalyzed Carbon-Heteroatom Coupling Reactions under Mild Conditions Promoted by Resin-Bound Organic Ionic Bases. *J. Org. Chem.* **2011**, *76*, 800-810.
4. Xu, J.; Liu, R. Y.; Yeung, C. S.; Buchwald, S. L., Monophosphine Ligands Promote Pd-Catalyzed C-S Cross-Coupling Reactions at Room Temperature with Soluble Bases. *ACS Catal.* **2019**, 6461-6466.
5. Shields, J. D.; Gray, E. E.; Doyle, A. G., A Modular, Air-Stable Nickel Precatalyst. *Org. Lett.* **2015**, *17*, 2166-2169.
6. Arika, Z. T.; Maekawa, Y.; Nambo, M.; Crudden, C. M., Preparation of Quaternary Centers via Nickel-Catalyzed Suzuki-Miyaura Cross-Coupling of Tertiary Sulfones. *J. Am. Chem. Soc.* **2018**, *140*, 78-81.
7. Tasker, S. Z.; Standley, E. A.; Jamison, T. F., Recent Advances in Homogeneous Nickel Catalysis. *Nature* **2014**, *509*, 299.
8. Dudnik, A. S.; Fu, G. C., Nickel-Catalyzed Coupling Reactions of Alkyl Electrophiles, Including Unactivated Tertiary Halides, to Generate Carbon-Boron Bonds. *J. Am. Chem. Soc.* **2012**, *134*, 10693-10697.
9. Igarashi, T.; Haito, A.; Chatani, N.; Tobisu, M., Nickel-Catalyzed Reductive Cleavage of Carbon-Oxygen Bonds in Anisole Derivatives using Diisopropylaminoborane. *ACS Catal.* **2018**, *8*, 7475-7483.
10. Schirmer, T. E.; Wimmer, A.; Weinzierl, F. W. C.; König, B., Photo-Nickel Dual Catalytic Benzoylation of Aryl Bromides. *Chem. Commun.* **2019**, 55, 10796-10799.
11. Sahoo, B.; Bellotti, P.; Juliá-Hernández, F.; Meng, Q.-Y.; Crespi, S.; König, B.; Martin, R., Site-Selective, Remote sp<sup>3</sup> C-H Carboxylation Enabled by the Merger of Photoredox and Nickel Catalysis. *Chem. Eur. J.* **2019**, *25*, 9001-9005.
12. Ingoglia, B. T.; Wagen, C. C.; Buchwald, S. L., Biaryl Monophosphine Ligands in Palladium-Catalyzed C-N Coupling: An Updated User's Guide. *Tetrahedron* **2019**, 4199-4211.
13. MacQueen, P. M.; Tassone, J. P.; Diaz, C.; Stradiotto, M., Exploiting Ancillary Ligation to Enable Nickel-Catalyzed C-O Cross-Couplings of Aryl Electrophiles with Aliphatic Alcohols. *J. Am. Chem. Soc.* **2018**, *140*, 5023-5027.
14. Clark, J. S. K.; Ferguson, M. J.; McDonald, R.; Stradiotto, M., Pd<sup>2</sup>-DalPhos Enables the Nickel-Catalyzed C-N Cross-Coupling of Primary Heteroarylamines and (Hetero)aryl Chlorides. *Angew. Chem. Int. Ed.* **2019**, *58*, 6391-6395.

15. Tassone, J. P.; England, E. V.; MacQueen, P. M.; Ferguson, M. J.; Stradiotto, M., PhPAd-DalPhos: Ligand-Enabled, Nickel-Catalyzed Cross-Coupling of (Hetero)aryl Electrophiles with Bulky Primary Alkylamines. *Angew. Chem. Int. Ed.* **2019**, *58*, 2485-2489.
16. Twilton, J.; Le, C.; Zhang, P.; Shaw, M. H.; Evans, R. W.; MacMillan, D. W. C., The Merger of Transition Metal and Photocatalysis. *Nat. Rev. Chem.* **2017**, *1*, 0052.
17. Corcoran, E. B.; Pirnot, M. T.; Lin, S.; Dreher, S. D.; DiRocco, D. A.; Davies, I. W.; Buchwald, S. L.; MacMillan, D. W. C., Aryl Amination Using Ligand-Free Ni(II) Salts and Photoredox Catalysis. *Science* **2016**, *353*, 279-283.
18. Terrett, J. A.; Cuthbertson, J. D.; Shurtleff, V. W.; MacMillan, D. W. C., Switching on Elusive Organometallic Mechanisms with Photoredox Catalysis. *Nature* **2015**, *524*, 330-334.
19. Welin, E. R.; Le, C.; Arias-Rotondo, D. M.; McCusker, J. K.; MacMillan, D. W. C., Photosensitized, Energy Transfer-Mediated Organometallic Catalysis Through Electronically Excited Nickel(II). *Science* **2017**, *355*, 380-385.
20. Du, Y.; Pearson, R. M.; Lim, C.-H.; Sartor, S. M.; Ryan, M. D.; Yang, H.; Damrauer, N. H.; Miyake, G. M., Strongly Reducing, Visible-Light Organic Photoredox Catalysts as Sustainable Alternatives to Precious Metals. *Chem. Eur. J.* **2017**, *23*, 10962-10968.
21. Key, R. J.; Vannucci, A. K., Nickel Dual Photoredox Catalysis for the Synthesis of Aryl Amines. *Organometallics* **2018**, *37*, 1468-1472.
22. Liu, Y.-Y.; Liang, D.; Lu, L.-Q.; Xiao, W.-J., Practical Heterogeneous Photoredox/Nickel Dual Catalysis for C-N and C-O Coupling Reactions. *Chem. Commun.* **2019**, *55*, 4853-4856.
23. Zhu, D.-L.; Li, H.-X.; Xu, Z.-M.; Li, H.-Y.; Young, D. J.; Lang, J.-P., Visible Light Driven, Nickel-Catalyzed Aryl Esterification Using a Triplet Photosensitiser Thioxanthen-9-one. *Org. Chem. Front.* **2019**, *6*, 2353-2359.
24. Oderinde, M. S.; Jones, N. H.; Juneau, A.; Frenette, M.; Aquila, B.; Tentarelli, S.; Robbins, D. W.; Johannes, J. W., Highly Chemoselective Iridium Photoredox and Nickel Catalysis for the Cross-Coupling of Primary Aryl Amines with Aryl Halides. *Angew. Chem. Int. Ed.* **2016**, *55*, 13219-13223.
25. Zhu, X.; Lin, Y.; San Martin, J.; Sun, Y.; Zhu, D.; Yan, Y., Lead Halide Perovskites for Photocatalytic Organic Synthesis. *Nat. Commun.* **2019**, *10*, 2843.
26. Pieber, B.; Malik, J. A.; Cavedon, C.; Gisbertz, S.; Savateev, A.; Cruz, D.; Heil, T.; Zhang, G.; Seeberger, P. H., Semi-Heterogeneous Dual Nickel/Photocatalysis using Carbon Nitrides: Esterification of Carboxylic Acids with Aryl Halides. *Angew. Chem. Int. Ed.* **2019**, *58*, 9575-9580.
27. Yang, L.; Huang, Z.; Li, G.; Zhang, W.; Cao, R.; Wang, C.; Xiao, J.; Xue, D., Synthesis of Phenols: Organophotoredox/Nickel Dual Catalytic Hydroxylation of Aryl Halides with Water. *Angew. Chem. Int. Ed.* **2018**, *57*, 1968-1972.
28. Cavedon, C.; Madani, A.; Seeberger, P. H.; Pieber, B., Semiheterogeneous Dual Nickel/Photocatalytic (Thio)etherification Using Carbon Nitrides. *Org. Lett.* **2019**, *21*, 5331-5334.

29. Lim, C.-H.; Kudisch, M.; Liu, B.; Miyake, G. M., C-N Cross-Coupling via Photoexcitation of Nickel-Amine Complexes. *J. Am. Chem. Soc.* **2018**, *140*, 7667-7673.
30. Lan, G.; Quan, Y.; Wang, M.; Nash, G. T.; You, E.; Song, Y.; Veroneau, S. S.; Jiang, X.; Lin, W., Metal-Organic Layers as Multifunctional Two-Dimensional Nanomaterials for Enhanced Photoredox Catalysis. *J. Am. Chem. Soc.* **2019**, *141*, 15767-15772.
31. Lu, J.; Pattengale, B.; Liu, Q.; Yang, S.; Shi, W.; Li, S.; Huang, J.; Zhang, J., Donor-Acceptor Fluorophores for Energy-Transfer-Mediated Photocatalysis. *J. Am. Chem. Soc.* **2018**, *140*, 13719-13725.
32. Zhu, Y.-Y.; Lan, G.; Fan, Y.; Veroneau, S. S.; Song, Y.; Micheroni, D.; Lin, W., Merging Photoredox and Organometallic Catalysts in a Metal-Organic Framework Significantly Boosts Photocatalytic Activities. *Angew. Chem.* **2018**, *130*, 14286-14290.
33. Calvo-Flores, F. G., Sustainable Chemistry Metrics. *ChemSusChem* **2009**, *2*, 905-919.
34. Ruccolo, S.; Qin, Y.; Schnedermann, C.; Nocera, D. G., General Strategy for Improving the Quantum Efficiency of Photoredox Hydroamidation Catalysis. *J. Am. Chem. Soc.* **2018**, *140*, 14926-14937.
35. Zhu, B.; Yan, L.-K.; Geng, Y.; Ren, H.; Guan, W.; Su, Z.-M., IrIII/NiII-Metallaphotoredox Catalysis: The Oxidation State Modulation Mechanism Versus the Radical Mechanism. *Chem. Commun.* **2018**, *54*, 5968-5971.
36. Qi, Z.-H.; Ma, J., Dual Role of a Photocatalyst: Generation of Ni(0) Catalyst and Promotion of Catalytic C-N Bond Formation. *ACS Catalysis* **2018**, *8*, 1456-1463.
37. Ren, H.; Li, G.-F.; Zhu, B.; Lv, X.-D.; Yao, L.-S.; Wang, X.-L.; Su, Z.-M.; Guan, W., How Does Iridium(III) Photocatalyst Regulate Nickel(II) Catalyst in Metallaphotoredox-Catalyzed C-S Cross-Coupling? Theoretical and Experimental Insights. *ACS Catalysis* **2019**, *9*, 3858-3865.
38. Sun, R.; Qin, Y.; Ruccolo, S.; Schnedermann, C.; Costentin, C.; Nocera, D. G., Elucidation of a Redox-Mediated Reaction Cycle for Nickel-Catalyzed Cross Coupling. *J. Am. Chem. Soc.* **2019**, *141*, 89-93.
39. Kawamata, Y.; Vantourout, J. C.; Hickey, D. P.; Bai, P.; Chen, L.; Hou, Q.; Qiao, W.; Barman, K.; Edwards, M. A.; Garrido-Castro, A. F.; deGruyter, J. N.; Nakamura, H.; Knouse, K.; Qin, C.; Clay, K. J.; Bao, D.; Li, C.; Starr, J. T.; Garcia-Irizarry, C.; Sach, N.; White, H. S.; Neurock, M.; Minter, S. D.; Baran, P. S., Electrochemically Driven, Ni-Catalyzed Aryl Amination: Scope, Mechanism, and Applications. *J. Am. Chem. Soc.* **2019**, *141*, 6392-6402.
40. Tsou, T. T.; Kochi, J. K., Mechanism of Biaryl Synthesis with Nickel Complexes. *J. Am. Chem. Soc.* **1979**, *101*, 7547-7560.
41. Inatomi, T.; Fukahori, Y.; Yamada, Y.; Ishikawa, R.; Kanegawa, S.; Koga, Y.; Matsubara, K., Ni(I)-Ni(III) Cycle in Buchwald-Hartwig Amination of Aryl Bromide Mediated by NHC-Ligated Ni(I) Complexes. *Catal. Sci. Technol.* **2019**, *9*, 1784-1793.
42. Jones, G. D.; Martin, J. L.; McFarland, C.; Allen, O. R.; Hall, R. E.; Haley, A. D.; Brandon, R. J.; Konovalova, T.; Desrochers, P. J.; Pulay, P.; Vicic, D. A., Ligand Redox Effects in the Synthesis, Electronic Structure, and Reactivity of an Alkyl-Alkyl Cross-Coupling Catalyst. *J. Am. Chem. Soc.* **2006**, *128*, 13175-13183.

43. Diccianni, J. B.; Diao, T., Mechanisms of Nickel-Catalyzed Cross-Coupling Reactions. *Trends Chem.*
44. Lin, Q.; Diao, T., Mechanism of Ni-Catalyzed Reductive 1,2-Dicarbonylfunctionalization of Alkenes. *J. Am. Chem. Soc.* **2019**.
45. Wang, X.; Ma, G.; Peng, Y.; Pitsch, C. E.; Moll, B. J.; Ly, T. D.; Wang, X.; Gong, H., Ni-Catalyzed Reductive Coupling of Electron-Rich Aryl Iodides with Tertiary Alkyl Halides. *J. Am. Chem. Soc.* **2018**, *140*, 14490-14497.
46. Sheng, J.; Ni, H.-Q.; Zhang, H.-R.; Zhang, K.-F.; Wang, Y.-N.; Wang, X.-S., Nickel-Catalyzed Reductive Cross-Coupling of Aryl Halides with Monofluoroalkyl Halides for Late-Stage Monofluoroalkylation. *Angew. Chem. Int. Ed.* **2018**, *57*, 7634-7639.
47. Biswas, S.; Weix, D. J., Mechanism and Selectivity in Nickel-Catalyzed Cross-Electrophile Coupling of Aryl Halides with Alkyl Halides. *J. Am. Chem. Soc.* **2013**, *135*, 16192-16197.
48. Richmond, E.; Moran, J., Recent Advances in Nickel Catalysis Enabled by Stoichiometric Metallic Reducing Agents. *Synthesis* **2018**, *50*, 499-513.
49. Aggarwal, V. K.; Emme, I.; Fulford, S. Y., Correlation between pK<sub>a</sub> and Reactivity of Quinuclidine-Based Catalysts in the Baylis–Hillman Reaction: Discovery of Quinuclidine as Optimum Catalyst Leading to Substantial Enhancement of Scope. *J. Org. Chem.* **2003**, *68*, 692-700.
50. Kim, T.; McCarver, S. J.; Lee, C.; MacMillan, D. W. C., Sulfonamidation of Aryl and Heteroaryl Halides through Photosensitized Nickel Catalysis. *Angew. Chem. Int. Ed.* **2018**, *57*, 3488-3492.
51. Dennis, J. M.; White, N. A.; Liu, R. Y.; Buchwald, S. L., Pd-Catalyzed C–N Coupling Reactions Facilitated by Organic Bases: Mechanistic Investigation Leads to Enhanced Reactivity in the Arylation of Weakly Binding Amines. *ACS Catal.* **2019**, *9*, 3822-3830.
52. Kitano, H.; Ito, H.; Itami, K., Palladium-Catalyzed Esterification of Carboxylic Acids with Aryl Iodides. *Org. Lett.* **2018**, *20*, 2428-2432.
53. Cloutier, J.-P.; Zargarian, D., Functionalization of the Aryl Moiety in the Pincer Complex (NCN)Ni<sup>III</sup>Br<sub>2</sub>: Insights on Ni<sup>III</sup>-Promoted Carbon–Heteroatom Coupling. *Organometallics* **2018**, *37*, 1446-1455.
54. Shields, B. J.; Kudisch, B.; Scholes, G. D.; Doyle, A. G., Long-Lived Charge-Transfer States of Nickel(II) Aryl Halide Complexes Facilitate Bimolecular Photoinduced Electron Transfer. *J. Am. Chem. Soc.* **2018**, *140*, 3035-3039.
55. Tsou, T. T.; Kochi, J. K., Mechanism of Oxidative Addition. Reaction of Nickel(0) Complexes with Aromatic Halides. *J. Am. Chem. Soc.* **1979**, *101*, 6319-6332.
56. Nelson, D. J.; Maseras, F., Steric Effects Determine the Mechanisms of Reactions between bis(N-heterocyclic carbene)-Nickel(0) Complexes and Aryl Halides. *Chem. Commun.* **2018**, *54*, 10646-10649.
57. Funes-Ardoiz, I.; Nelson, D. J.; Maseras, F., Halide Abstraction Competes with Oxidative Addition in the Reactions of Aryl Halides with [Ni(PMe<sub>n</sub>Ph<sub>(3-n)</sub>)<sub>4</sub>]. *Chem. Eur. J.* **2017**, *23*, 16728-16733.

58. Vitaku, E.; Smith, D. T.; Njardarson, J. T., Analysis of the Structural Diversity, Substitution Patterns, and Frequency of Nitrogen Heterocycles among U.S. FDA Approved Pharmaceuticals. *J. Med. Chem.* **2014**, *57*, 10257-10274.
59. Nakamura, Y.; Maruya, K.-i.; Mizoroki, T., A Study of the Ligand Exchange of Bromo(o-tolyl)bis(triphenylphosphine)nickel(II) with Amine by Means of <sup>31</sup>P- and <sup>13</sup>C-NMR Spectroscopy. *Bull. Chem. Soc. Jpn.* **1980**, *53*, 3089-3092.
60. Lavoie, C. M.; McDonald, R.; Johnson, E. R.; Stradiotto, M., Bisphosphine-Ligated Nickel Precatalysts in C(sp<sup>2</sup>)-N Cross-Couplings of Aryl Chlorides: A Comparison of Nickel(I) and Nickel(II). *Adv. Synth. Catal.* **2017**, *359*, 2972-2980.
61. Smith, C. R., Activated Zinc Dust. *Synlett* **2009**, *2009*, 1522-1523.
62. Pangborn, A. B.; Giardello, M. A.; Grubbs, R. H.; Rosen, R. K.; Timmers, F. J., Safe and Convenient Procedure for Solvent Purification. *Organometallics* **1996**, *15*, 1518-1520.
63. Hatchard, C. G.; Parker, C. A.; Bowen, E. J., A New Sensitive Chemical Actinometer - II. Potassium Ferrioxalate as a Standard Chemical Actinometer. *Proc. R. Soc. Lond. A Math. Phys. Sci.* **1956**, *235*, 518-536.
64. Zhu, X.; Zhang, Q.; Su, W., Solvent-Free N-Arylation of Amines with Arylboronic Acids under Ball Milling Conditions. *RSC Adv.* **2014**, *4*, 22775-22778.
65. Shu, X.-Z.; Xia, X.-F.; Yang, Y.-F.; Ji, K.-G.; Liu, X.-Y.; Liang, Y.-M., Selective Functionalization of sp<sup>3</sup> C-H Bonds Adjacent to Nitrogen Using (Diacetoxyiodo)benzene (DIB). *J. Org. Chem.* **2009**, *74*, 7464-7469.
66. Johnson, T. C.; Elbert, Bryony L.; Farley, A. J. M.; Gorman, T. W.; Genicot, C.; Lallemand, B.; Pasau, P.; Flasz, J.; Castro, J. L.; MacCoss, M.; Dixon, D. J.; Paton, R. S.; Schofield, C. J.; Smith, M. D.; Willis, M. C., Direct Sulfonylation of Anilines Mediated by Visible Light. *Chem. Sci.* **2018**, *9*, 629-633.
67. Lakshminarayana, N.; Prasad, Y. R.; Gharat, L.; Thomas, A.; Narayanan, S.; Raghuram, A.; Srinivasan, C. V.; Gopalan, B., Synthesis and Evaluation of Some Novel Dibenzo[b,d]furan Carboxylic Acids as Potential Anti-Diabetic Agents. *Eur. J. Med. Chem.* **2010**, *45*, 3709-3718.
68. Van Baelen, G.; Maes, B. U. W., Study of the Microwave-Assisted Hydrolysis of Nitriles and Esters and the Implementation of this System in Rapid Microwave-Assisted Pd-Catalyzed Amination. *Tetrahedron* **2008**, *64*, 5604-5619.
69. Geukens, I.; Fransaer, J.; De Vos, D. E., Aromatic Amination of Aryl Chlorides Catalyzed by Ni Nanoparticles in Aliphatic Phosphonium-Based Ionic Liquids. *ChemCatChem* **2011**, *3*, 1431-1434.
70. Wang, J. Y.; Strom, A. E.; Hartwig, J. F., Mechanistic Studies of Palladium-Catalyzed Aminocarbonylation of Aryl Chlorides with Carbon Monoxide and Ammonia. *J. Am. Chem. Soc.* **2018**, *140*, 7979-7993.
71. Guo, L.; Hsiao, C.-C.; Yue, H.; Liu, X.; Rueping, M., Nickel-Catalyzed Csp<sup>2</sup>-Csp<sup>3</sup> Cross-Coupling via C-O Bond Activation. *ACS Catal.* **2016**, *6*, 4438-4442.

*Page intentionally left blank*

## Chapter 5

# **Selective Activation of N-H Bonds by Photoexcited Ketones through Unidirectional Proton-Coupled Electron Transfer**



## 5.1 Introduction

Leveraging proton-coupled electron transfer (PCET) in organic photoredox chemistry has led to a powerful strategy for the selective generation of heteroatom-centered radicals in organic molecules with C-H bonds whose bond dissociation energies (BDEs) are much lower than those of the corresponding acidic X-H bonds (e.g., ~100 kcal/mol for an amide N-H bond<sup>1</sup> vs ~83 kcal/mol for an allylic C-H bond<sup>2</sup>).<sup>3-6</sup> The energetic electrophilic heteroatom-derived radicals can undergo subsequent reactions such as addition to olefins to generate anti-Markovnikov products, in contrast to the Markovnikov regioselectivity typically seen under thermal catalysis.<sup>1,7,8</sup> The photoredox hydroamidation reaction is an exemplar of such reactivity,<sup>1</sup> where an Ir photocatalyst in combination with a phosphate base allows for the selective generation of an amidyl radical that then undergoes addition to an olefin. The lactam compounds furnished through this method are important motifs in many pharmaceutical compounds.<sup>9</sup>

For coordinatively saturated photoreagents (PC\*) such as Ir and Ru polypyridyl and cyclometallated complexes, the PCET activation of the amide substrate necessarily occurs by a bidirectional mechanism (Figure 5.1), where the electron is accepted by PC\* in an outer-sphere reaction and the proton is accepted by the exogenous base. Alternatively, PCET may occur by a unidirectional mechanism when the proton and electron are transferred to the same acceptor PC<sub>B</sub>\* (Figure 5.1).<sup>10-13</sup> The unidirectional PCET mechanism is prevalent for photocatalysts that offer sustainable alternatives<sup>14-17</sup> to the criticality, carbon footprint, and toxicity of precious metal photocatalysts.<sup>18-23</sup> Additionally, unidirectional PCET, which is bimolecular, also offers the advantage of decreased molecularity compared to trimolecular bidirectional PCET. Thus, unidirectional PCET rates are inherently higher than bidirectional ones, leading to more energy efficient methods. Although bidirectional PCET systems may benefit from ground state pre-association (e.g., hydrogen bonding or ion pairing) to give an essentially bimolecular reaction, this can be disrupted by polar/hydrogen-bonding solvents or charged species in solution, thus limiting versatility.

Examples of the application of unidirectional PCET in organic chemistry include photogenerated halogen radicals from earth abundant metal complexes, which have been

identified as key intermediates in the PCET activation of C(sp<sup>3</sup>)-H bonds for alkylation,<sup>24-27</sup> alkenylation,<sup>28</sup> arylation,<sup>29-31</sup> acylation,<sup>26,32</sup> and amination<sup>33,34</sup> reactions. Similarly, polyoxometallates such as the decatungstate anion, have also been used to effect the functionalization of alkanes through C-H abstraction.<sup>35</sup> However, the activation of substrates by these compounds is predominantly dictated by thermodynamic bond strengths with contributions from steric and polarity effects, leading to an inferior control of selectivity compared to that seen in bidirectional PCET systems. Indeed, the chemoselective activation of stronger substrate bonds by unidirectional PCET photocatalysts remains a significant challenge that has yet to be surmounted.<sup>36,37</sup>

Photoreagents that promote hydrogen atom transfer (HAT) inherently activate substrates by unidirectional PCET. A conspicuous HAT photochemistry is the Norrish Type II reaction of triplet excited states of ketones.<sup>38,39</sup> Beyond the longstanding use of photoexcited ketones in establishing radical-chain polymerization reactions,<sup>40-43</sup> they have emerged in photoredox methodologies.<sup>44,45</sup> However, this reactivity has been mainly limited to abstraction of thermodynamically activated C-H bonds adjacent to aryl or heteroatomic functionality, in contrast to the exquisite chemoselectivity for strong X-H bonds seen in bidirectional PCET systems. Here, we report a hitherto underappreciated property of triplet state ketones — inherent HAT selectivity for stronger, acidic X-H bonds over weaker C-H ones (Figure 5.1). Mechanistic studies establish that such chemoselectivity is a result of a concerted asynchronous unidirectional PCET process and demonstrate that camphorquinone (CQ) — an inexpensive, non-toxic, and blue-light absorbing 1,2-diketone commonly used as a polymerization photoinitiator<sup>46</sup> — can selectively effect intramolecular hydroamidation reactions efficiently.

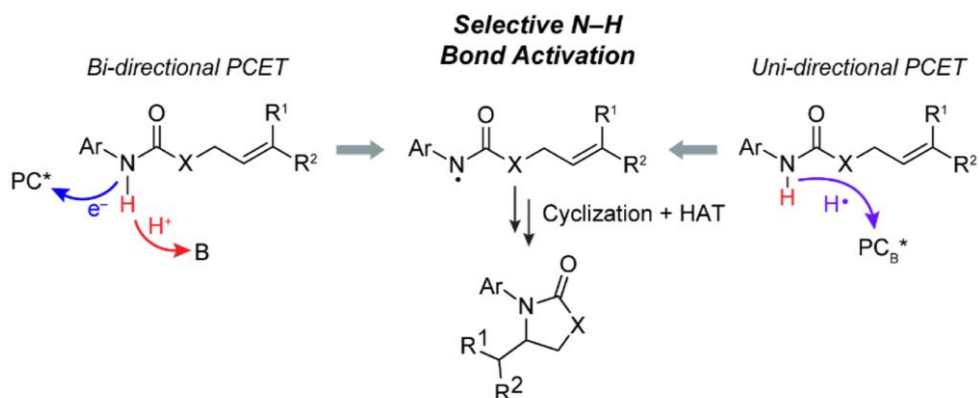


**Figure 5.1.** Photoredox intramolecular hydroamidation reaction promoted by bidirectional and unidirectional PCET. The bidirectional PCET occurs by an outer-sphere electron transfer to a photoexcited acceptor ( $PC^*$ ) followed by proton transfer to an exogenous base. Unidirectional PCET occurs when the photoredox reagent,  $PC_B^*$ , is the electron and proton acceptor such as the triplet excited state of ketones (this work).

## 5.2 Transient Absorption Studies of Amidyl Radical Formation

Transient absorption (TA) spectroscopy permits the reaction between amide **1** and CQ to be directly examined. We focused on this initial quenching step responsible for amidyl radical formation because the subsequent steps leading to cycloamidation (i.e., cyclization and subsequent HAT to furnish the lactam) occur independently of the photocatalyst.<sup>47</sup> Figure 5.2 shows the transient absorption spectra for solutions containing CQ (5 mM) alone and those containing CQ with amides **1** and **5** (10 mM). The spectrum of CQ in Figure 5.2A shows the relaxation of the  $^*CQ$  excited state, while the spectra for CQ in the presence of **5** and **1** in Figures 5.2B and 5.2C, respectively, show initial absorbance dominated by the excited state of CQ at 200 ns (black traces), followed by a gradual evolution to a spectrum containing features at 430 nm and 310 nm (blue trace for **5** and red trace for **1**). The peak at 430 nm is ascribed to the amidyl radical<sup>47</sup> while the 310 nm feature is tentatively assigned to  $CQ-H\cdot$  due to its resemblance to the spectrum of  $CQ\cdot^-$  obtained by spectroelectrochemistry (Figure 5.3B). Figure 5.4 shows the TA kinetic trace at 430 nm for samples containing CQ and amide substrate **5**, which is identical to substrate **1** with the exception of an olefin moiety. Substrate **5** is strategic because it is unable to undergo cyclization upon amidyl radical formation, thus allowing for the kinetics of forward and

back HAT reactions to be measured without interference from other chemical processes. From kinetic modelling (see Materials and Methods), we extract an HAT rate constant of  $k_{\text{FH}} = 2.9 \times 10^7 \text{ M}^{-1} \text{ s}^{-1}$  and a back reaction rate constant of  $k_{\text{BH}} = 8.3 \times 10^9 \text{ M}^{-1} \text{ s}^{-1}$ , where the latter is similar to the back-electron-transfer rate constant measured for the Ir/base-catalyzed system ( $k_{\text{BET}} = 7.9 \times 10^9 \text{ M}^{-1} \text{ s}^{-1}$ ).<sup>47</sup>

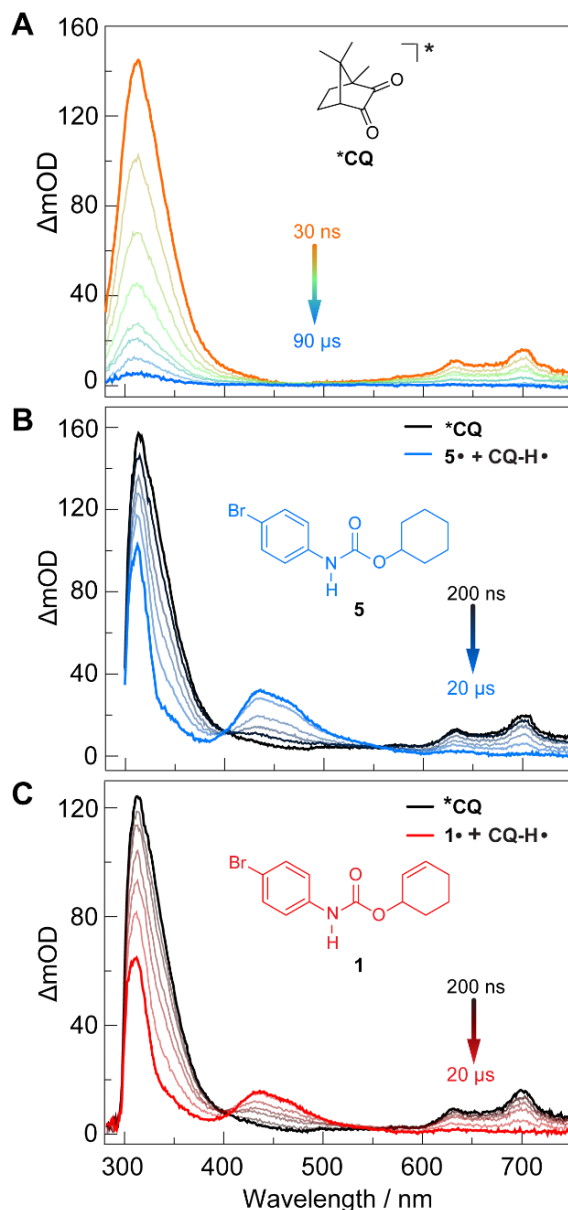


**Figure 5.2.** TA spectra of DCM solutions containing CQ (5 mM) and amide substrates (10 mM) in DCM. **A:** for a solution of CQ alone. **B:** for a solution of CQ with amide 5 as the substrate. **C:** for a solution of CQ with amide 1 as the substrate.  $\lambda_{\text{exc}} = 460 \text{ nm}$ .

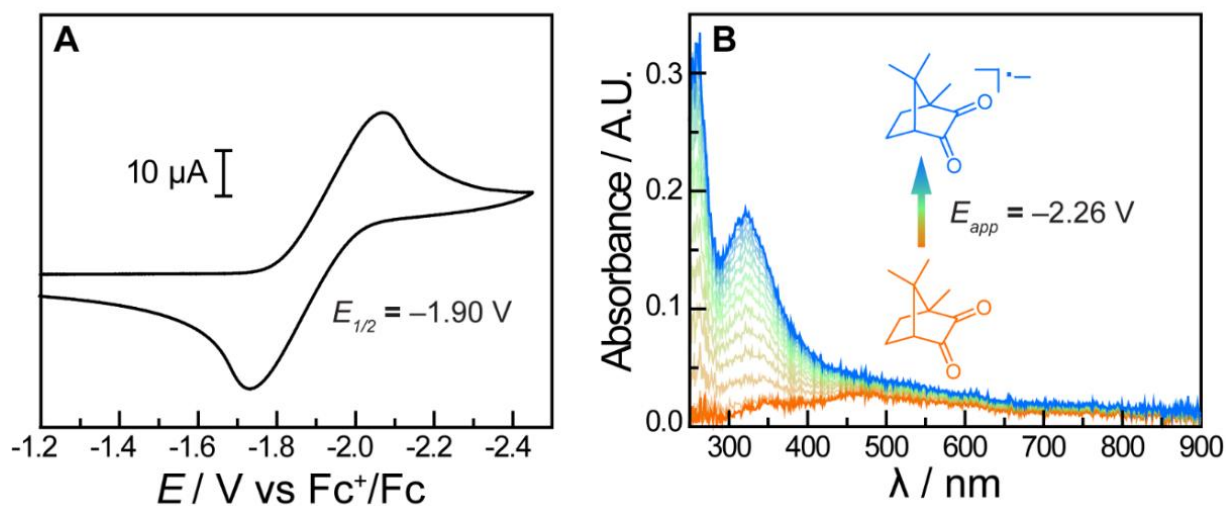


**Figure 5.3.** Electrochemical studies on CQ. (A) Cyclic voltammogram of 2 mM CQ in DCM with 0.1 M [TBA][PF<sub>6</sub>] as the supporting electrolyte. (B) Spectroelectrochemistry on 2 mM CQ in DCM with 0.1 M [TBA][PF<sub>6</sub>] as the supporting electrolyte in a 0.5 mm pathlength cell using a Pt mesh working electrode.

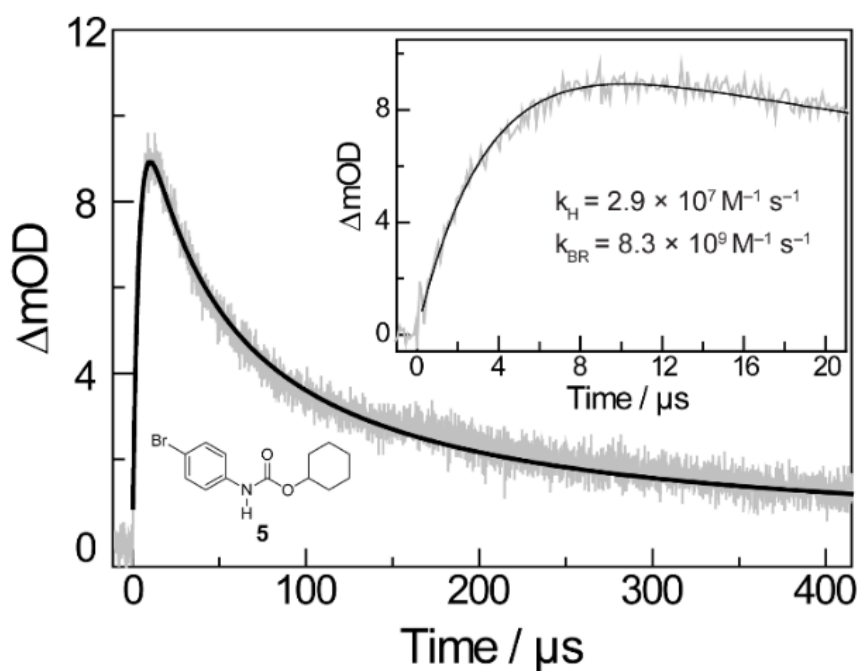


**Figure 5.4.** Kinetic trace monitored at 430 nm of a DCM solution containing 5 mM CQ, and 10 mM amide substrate 5. Insets show a magnified view at shorter timescales along with extracted rate constants.  $\lambda_{\text{exc}} = 460 \text{ nm}$ .

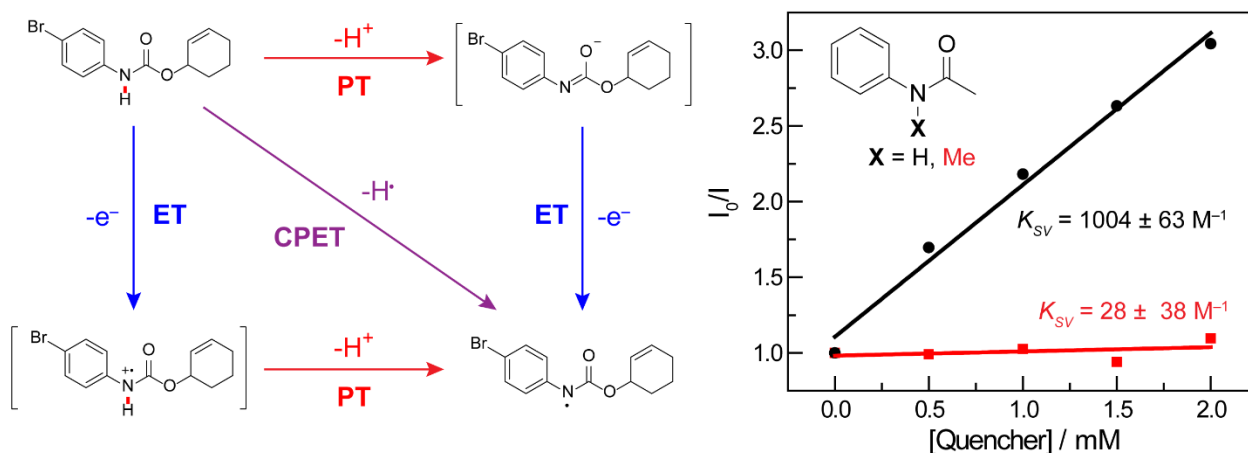
### 5.3 Mechanism of the PCET Process

The processes that lead to the formal transfer of a hydrogen atom can be described using a 'square-scheme,' (Figure 5.5 left panel), where the edges correspond to fully stepwise mechanisms with sequential proton transfer (PT) and electron transfer (ET) steps and the diagonal corresponds to a concerted proton-electron transfer (CPET).<sup>48</sup> We note for CPET, the electron and proton may move together synchronously (diagonal pathway) or may move asynchronously (zig-zag pathway).<sup>7</sup> The distinguishing feature of the ET/PT or PT/ET edge pathways from CPET pathways (synchronous or asynchronous) is that the latter is characterized by a single transition state anywhere within the square. In order to delineate which pathway is operative in the generation of amidyl radicals by \*CQ, we first note that \*CQ has an oxidation potential of 0.33 V vs Fc<sup>+</sup>/Fc, based on the cyclic voltammogram of E(CQ/CQ<sup>•-</sup>) = -1.90 V vs Fc<sup>+</sup>/Fc shown in Figure 5.3A and the previously reported emission excited state energy of 2.23 eV for CQ at 77 K.<sup>49</sup> As \*CQ is a far weaker photooxidant for outer-sphere ET than the Ir catalyst (oxidation potential of 0.85 V),<sup>47</sup> which itself is not quenched by the amide substrate in the absence of base,<sup>1</sup> a stepwise ET-PT pathway for amidyl radical formation is unfeasible based on the redox potential of \*CQ. This is further corroborated by a comparison of the Stern-Volmer constants ( $K_{SV}$ ) for acetanilide and *N*-methylacetanilide, where the latter is expected to have a similar or lower oxidation potential for outer-sphere ET when compared to the former; however, only the former possesses a proton which can engage in a PCET process. As shown in the right panel of Figure 5.5, the Stern-Volmer constant for *N*-methylacetanilide [ $K_{SV} = 28(38) \text{ M}^{-1}$ ] is two orders of magnitude lower than for acetanilide [ $K_{SV} = 1004(63) \text{ M}^{-1}$ ], which suggests that the quenching does not proceed by an ET/PT mechanism.

In order to differentiate between the PT-ET and CPET mechanisms, we investigated the relative quenching of \*CQ by a series of Ph-XH compounds and their X-methylated derivatives. Since all the Ph-XH substrates show irreversible oxidation waves, we used the gas-phase ionization energies (IEs) of these compounds as a measure of their oxidation potential as has been previously discussed for asynchronous CPET pathways.<sup>50</sup> Table 5.1 lists the calculated

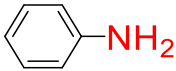
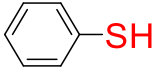
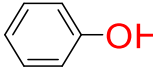
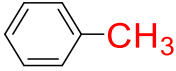
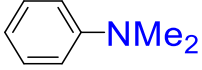
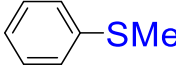
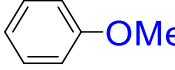
quenching rate constants ( $k_q$ ) for these compounds (Figure 5.6) along with their ionization energies (IEs), X-H BDEs, and  $pK_a$  values in DMSO. If a PT-ET mechanism were operative, a correlation between  $k_q$  and  $pK_a$  is expected since the quenching would be governed by proton transfer. However, this is not the case. We observe that the  $k_q$  values correlate with IEs. Moreover, when we compare the quenching rates for phenol [ $k_q = 3.18 (0.14) \times 10^9 \text{ M}^{-1} \text{ s}^{-1}$ ] and phenol-d<sub>6</sub> [ $k_q = 2.07 (0.13) \times 10^9 \text{ M}^{-1} \text{ s}^{-1}$ ] in DCM, we find a kinetic isotope effect (KIE) of  $k_H/k_D = 1.54 (0.06)$ , implying a PCET quenching process. To confirm that the quenching of <sup>\*</sup>CQ by Ph-XH substrates leads to X-H bond homolysis, we employed TA spectroscopy to study the reaction between CQ (10 mM) and phenol (20 mM) in DCM. Under these conditions, we observed the clear formation of phenoxy radical with features at ~380 and ~400 nm (Figure 5.7).<sup>51</sup>

Taken together, these results are most consistent with a concerted asynchronous CPET mechanism whose transition state is predominantly ET in character, but does not involve the generation of distinct, oxidized intermediates preceding proton transfer. This mechanism explains the chemoselectivity for amide N-H bond activation over allylic C-H bonds, since the IEs for the former are much lower than those for the latter (e.g., 8.2 eV for 4'-fluoroacetanilide vs 8.9–9.1 eV for cyclohexene).<sup>52</sup>



**Figure 5.5.** Mechanisms of amidyl radical generation. **Left:** A square scheme illustrating the possible pathways for PCET. **Right:** Stern-Volmer plot for the quenching of CQ (1 mM) by acetanilide (— black) and *N*-methylacetanilide (— red) in DCM.

**Table 5.1.** Correlation of the quenching rate ( $k_q$ ) of  $^*CQ$  in DCM with different thermodynamic parameters of the quenchers.

	Ionization Energy (eV) <sup>52</sup>	$k_q$ ( $M^{-1} s^{-1}$ ) <sup>a</sup>	X-H BDE (kcal/mol) <sup>53</sup>	$pK_a$ in DMSO <sup>54</sup>
	7.7	$1.12 (0.08) \times 10^{11}$	90 (Gas phase)	31
	8.3	$3.11 (0.14) \times 10^9$	84 (TR-PAC)	10
	8.5	$3.18 (0.14) \times 10^9$	88 (Gas phase)	18
	8.8	<i>Not observed</i>	90 (Gas phase)	43
	7.1	$2.75 (0.11) \times 10^{10}$	—	—
	7.9	$4.51 (0.29) \times 10^7$	—	—
	8.2	$5.75 (0.39) \times 10^4$	—	—

<sup>a</sup> Calculated from the Stern-Volmer constant ( $K_{SV}$ ) using a value of  $\tau = 30.6 (0.1) \mu s$  for the lifetime of the CQ triplet state, as determined from time-resolved emission spectroscopy (see Figure 5.6 for Stern-Volmer plots).



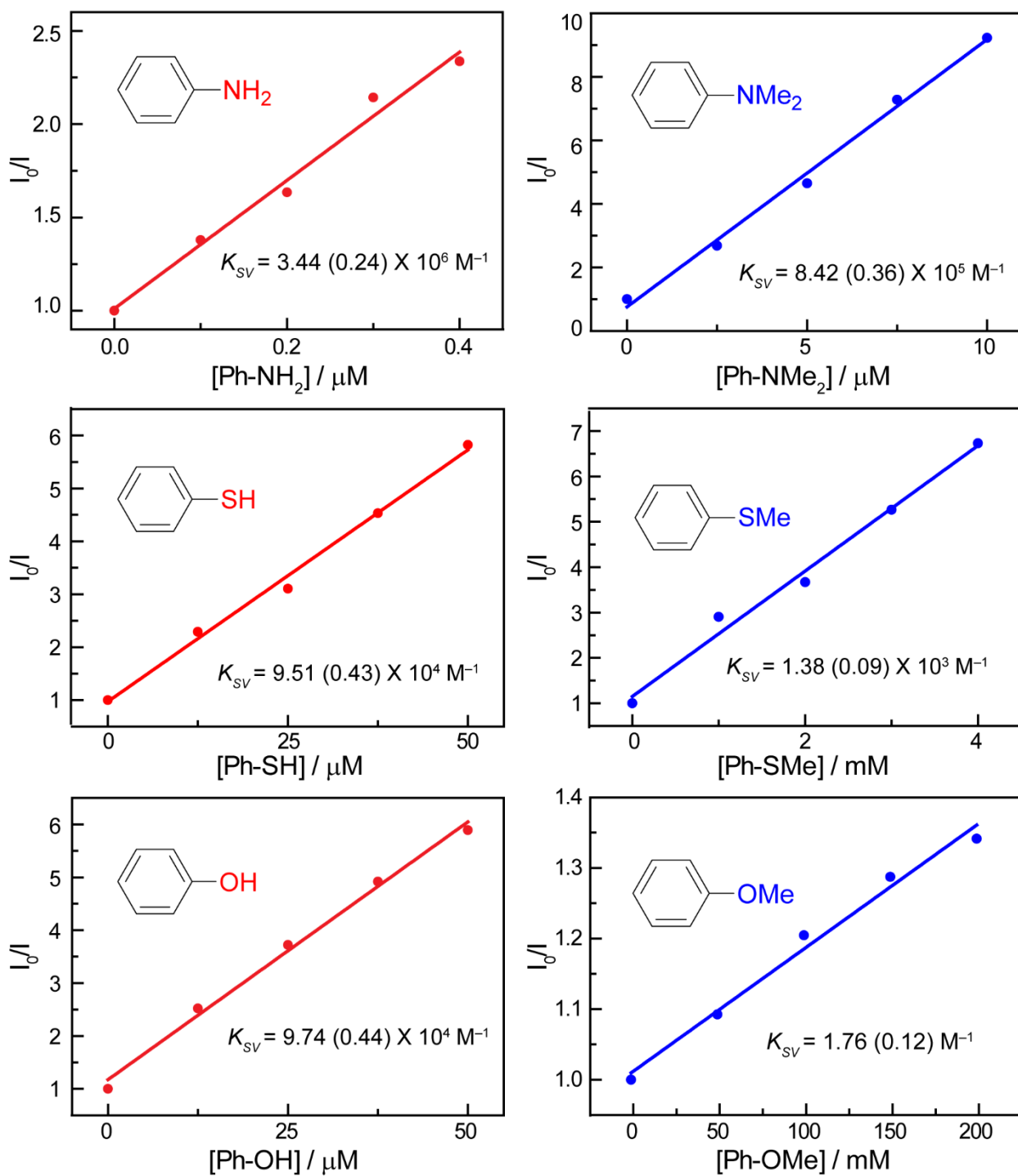


**Figure 5.6.** Stern-Volmer plots for different quenchers reacting with 1 mM CQ in DCM.  $\lambda_{exc} = 450$  nm.

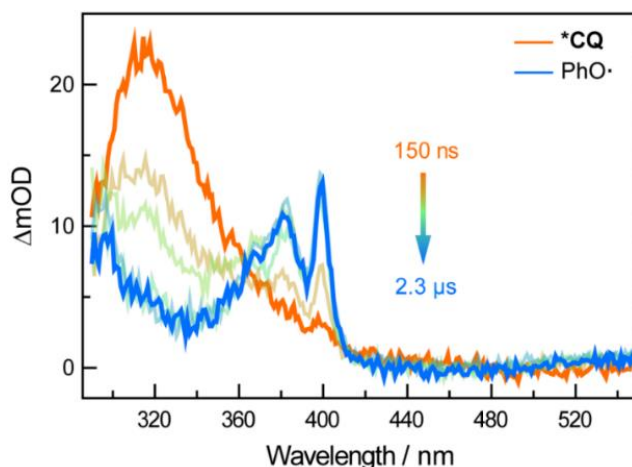


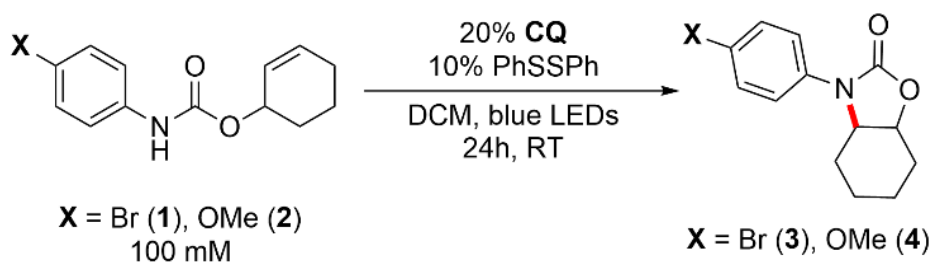
**Figure 5.7.** TA spectra of a DCM solution containing CQ (10 mM) and phenol (20 mM) showing the evolution from an initial spectrum dominated by  $^*\text{CQ}$  (— orange trace) to one dominated by  $\text{PhO}\cdot$  (— blue trace).  $\lambda_{\text{exc}} = 460 \text{ nm}$ .

#### 5.4 Intramolecular Hydroamidation with Camphorquinone

To demonstrate the synthetic utility of these insights, we sought to establish whether CQ itself can serve as a competent photocatalyst in intramolecular hydroamidation reactions in the absence of an exogenous base. As shown in Entry 1 of Table 5.2, cyclized product **3** can be formed from **1** in a 94% yield after 24 h of blue LED irradiation using 20% CQ and 10% phenyl disulfide (PhSSPh). The omission of disulfide (Entry 2) or its replacement with thiol (Entry 3) led to significantly diminished yields, consistent with previous observations under Ir-catalyzed conditions.<sup>47,55</sup> Attenuated yield was also observed for the methoxy-substituted substrate **2** (Entry 4), which has been shown to undergo cyclization at a rate that is three orders of magnitude slower upon amidyl radical formation when compared to **1**.<sup>47</sup> However, by switching from PhSSPh to 2,4,6-triisopropylphenyl disulfide [(TripS)<sub>2</sub>] with substrate **2**, we observed significantly improved yields (Entry 5). This may be due to the fact that the TripS $\cdot$  radical formed *in situ* has a reduced propensity towards off-cycle disulfide formation when compared to its phenyl congener. Finally, we investigated the performance of CQ-mediated hydroamidation in acetonitrile (MeCN), a highly polar solvent. The original method using an outer-sphere Ir photooxidant and a phosphate base necessitated a trimolecular reaction requiring the coalescence of  $^*\text{Ir}$ , base, and amide substrate in order for PCET to occur. This is aided by ion pairing between the cationic Ir photooxidant and

anionic phosphate base in DCM,<sup>47</sup> which can be disrupted by a highly polar solvent. Since **CQ** is a neutral species which does not rely on ion pairing effects for its PCET activity, we posited that it could deliver superior yields in MeCN. Indeed, as shown in Entries 6 and 7, the use of **CQ** results in a yield that was ~3× higher than that with the Ir/base system; switching from PhSSPh to (TripS)<sub>2</sub> further resulted in a substantial increase in the yield to 43% (Entry 8).

**Table 5.2.** Optimization of the **CQ**-mediated intramolecular cycloamidation of alkenes.



Entry	X Group	Differences from standard conditions listed above	Yield (%) <sup>a</sup>
1	Br	None	94
2	Br	No PhSSPh	9
3	Br	PhSH instead of PhSSPh	45
4	OMe	None	32
5	OMe	(TripS) <sub>2</sub> in place of PhSSPh	51
6	Br	MeCN in place of DCM	14
7	Br	Knowles' conditions, <sup>b</sup> MeCN in place of DCM	<5
8	Br	(TripS) <sub>2</sub> in place of PhSSPh, MeCN in place of DCM	43

<sup>a</sup> Yield determined by <sup>1</sup>H NMR spectroscopy. <sup>b</sup> Same conditions as the published procedure, ref 1, with 10% PhSSPh in place of 20% PhSH for consistency with **CQ**-mediated conditions. Trip = 2,4,6-triisopropylphenyl.

To verify that the cycloamidation catalysis is attributable to CQ and not an impurity or *in situ* generated species, we measured the yield of cyclized product **4** from methoxy-substituted substrate **2**. The amount of CQ remaining as a function of reaction time was ascertained by  $^1\text{H}$  NMR spectroscopy under the conditions shown in Table 5.2. As seen in Figure 5.8 (red traces), no increase in product yield was observed (dashed line) after CQ was completely consumed at  $\sim 10$  h (solid line) when  $(\text{TriPS})_2$  was used as the disulfide. With PhSSPh as the disulfide, a much slower reaction was observed (black traces), consistent with the lower yield shown in Table 5.2.

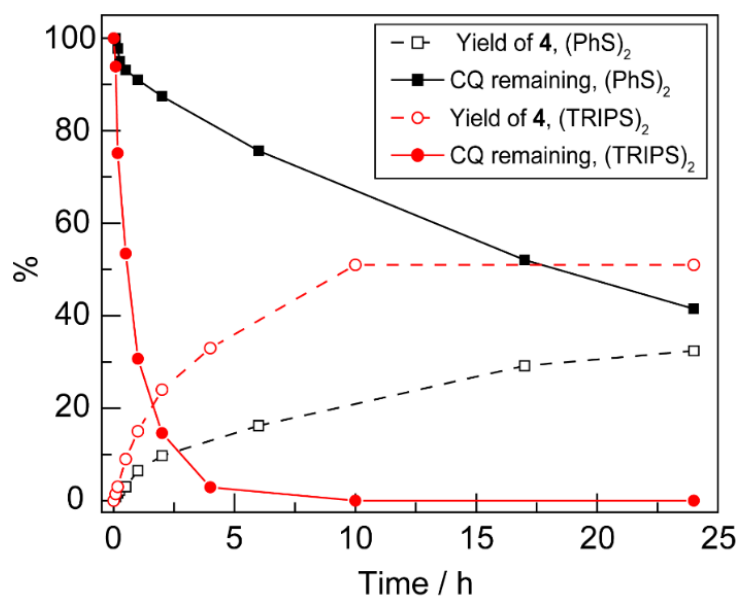


**Figure 5.8.** Time traces for the yield of cyclized product **4** (dashed lines) and % remaining of CQ (solid lines). Black traces are for the reaction performed with PhSSPh and red traces are with  $(\text{TRIPS})_2$ . The conditions for the reactions were as described in the Materials and Methods section.

Given the ubiquity of ketones as photoinitiators through their HAT chemistry, we sought to establish whether the selective generation of amidyl radicals via activation of the amide N-H bond in the presence of weak C-H bonds might be a general phenomenon. To this end, we used the cycloamidation reaction as an assay for amidyl radical generation. Although CQ remained the highest yielding ketone among those examined, a wide range of mono- and diketones gave significant yields of the cyclized product **2** (Figure 5.9), as determined by  $^1\text{H}$  NMR spectroscopy. Surprisingly, several commonly employed photoinitiators, which have been extensively studied

for their propensity to readily undergo C-H abstraction, such as diacetyl<sup>56-58</sup> (**11**) and acetophenone<sup>59-61</sup> (**14**) gave significant yields of product, with the balance of the reaction being accounted for by unreacted starting material. These results demonstrate that chemoselectivity in hydroamidation photoredox transformations promoted by the HAT chemistry of triplet ketones is not limited to CQ.

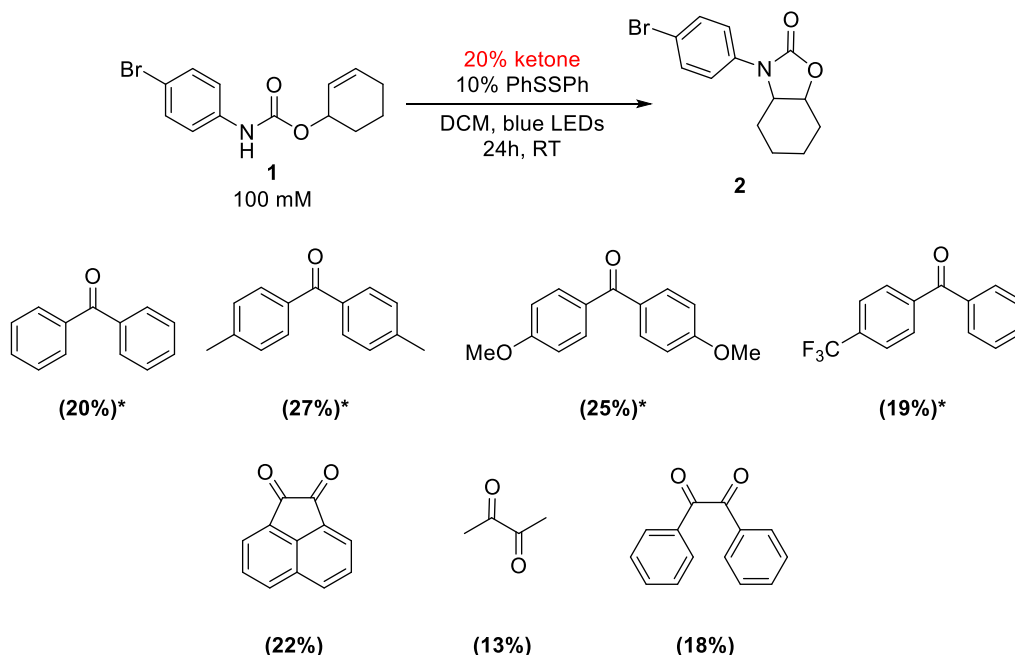


**Figure 5.9.** Photoredox intramolecular cycloamidation using various ketones as the photocatalyst. Yields as determined by <sup>1</sup>H NMR spectroscopy are denoted in parentheses. \*For ketones which absorbed poorly in the visible region, a 370 nm LED light source (Kessil) was used in place of the standard blue LEDs.

To confirm the generality of the CQ-catalyzed hydroamidation reaction, we tested multiple substrates under the optimized conditions in Table 5.2. As shown in Figure 5.10, a variety of alkene-bearing amides undergo hydroamidation under CQ photocatalysis. For more challenging substrates, (TripS)<sub>2</sub> may be used in place of PhSSPh to improve the yield. Of note, Lewis acidic functionality, such as the pinacolboranyl (Bpin) moiety, was well-tolerated.

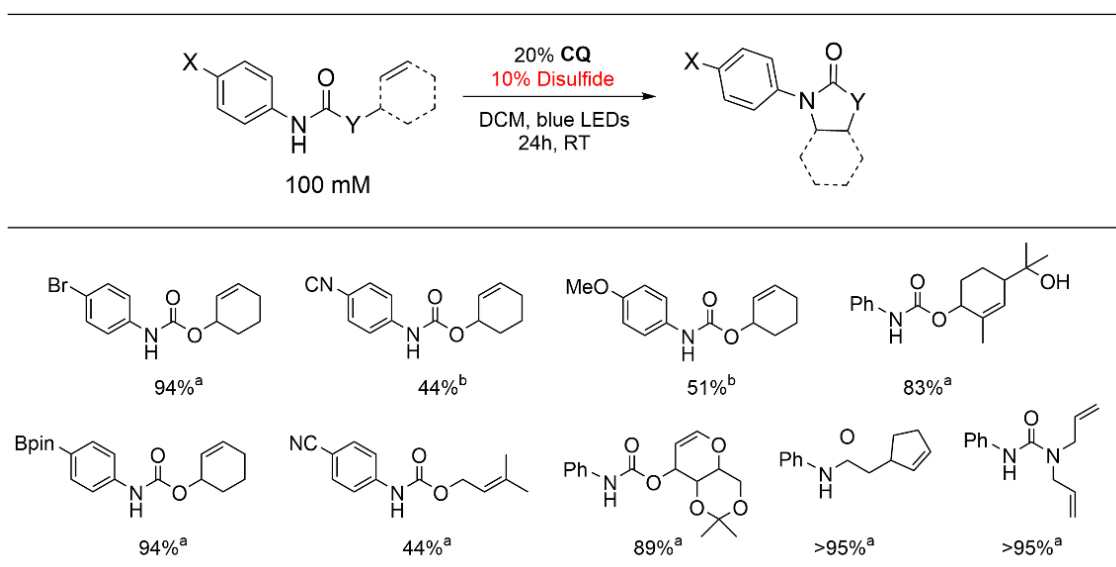


**Figure 5.10.** Scope of the CQ-mediated intramolecular alkene hydroamidation reaction. <sup>a</sup> PhSSPh used as the disulfide. <sup>b</sup> (TripS)<sub>2</sub> used as the disulfide. Yields determined by <sup>1</sup>H NMR spectroscopy using 1,4-bis(trifluoromethyl)benzene or 1,3,5-tris(trifluoromethyl)benzene as an internal standard.

## 5.5 Conclusions

In conclusion, the excited states of ketones exhibit a surprising selectivity for selective amide N-H activation over weaker C-H bonds, as confirmed through Stern-Volmer and transient absorption experiments. This selectivity results from asynchronous CPET, where the reactivity is largely dictated by the ionization energy of the functional group. This mechanism may be exploited to catalyze the intramolecular hydroamidation of alkenes under photoredox conditions with camphorquinone, an inexpensive and non-toxic diketone, leading to a greener reaction.

## 5.6 Materials and Methods

**General considerations.** All manipulations were performed with the rigorous exclusion of air and moisture unless otherwise stated. Commercial reagents were stored in a N<sub>2</sub>-filled glovebox and used without further purification. All liquid reagents and deuterated solvents were degassed by three cycles of freeze-pump-thaw and stored over activated 3Å molecular sieves prior to use. All non-deuterated solvents were purified by the method of Grubbs and stored over activated 3Å molecular sieves.<sup>62</sup> Camphorquinone and tributylmethylammonium dibutyl

phosphate were purchased from Sigma Aldrich. The Ir photooxidant, (2,2'-bipyridine)bis[3,5-difluoro-2-[5-trifluoromethyl-2-pyridinyl-kN)phenyl-kC]iridium(III) hexafluorophosphate, was purchased from Strem Chemicals. All amide substrates were either purchased or prepared as previously described.<sup>1</sup> <sup>1</sup>H NMR spectra were recorded at the Laukien-Purcell Instrumentation Center in the Department of Chemistry and Chemical Biology at Harvard University on an Agilent DD2 spectrometer operating at 600 MHz, a Varian Unity/Inova spectrometer operating at 500 MHz, or a JEOL ECZ400S spectrometer operating at 400 MHz.

**General procedure for the CQ-mediated intramolecular hydroamidation.** A mixture of CQ (100  $\mu$ L of a stock solution of 0.100 g CQ in 3 mL  $\text{CD}_2\text{Cl}_2$ ; 0.02 mmol, 20 mol%), disulfide (0.01 mmol, 10 mol%), 1,4-bis(trifluoromethyl)benzene or 1,3,5-tris(trifluoromethyl)benzene as an internal standard, and amide substrate (0.1 mmol) was diluted with 0.88 mL  $\text{CD}_2\text{Cl}_2$  to give a final concentration of 100 mM substrate. The reaction solution was transferred to a J-Young NMR tube, which was taken to the spectrometer to establish the starting ratio of substrate to internal standard. Then, the reaction was irradiated using a Kessil A160WE Tuna Blue LED lamp under fan cooling. After 24 h, the reaction yield was determined by <sup>1</sup>H NMR spectroscopy.

**Single-Wavelength kinetic studies and transient absorption spectroscopy.** The nanosecond transient absorption (TA) spectroscopy setup was described previously in detail.<sup>63</sup> A Quanta-Ray Nd:YAG laser (SpectraPhysics) provides 3rd harmonic laser pulses at 355 nm with a repetition rate of 10 Hz and pulse width of  $\sim$ 10 ns (FWHM). A further MOPO (SpectraPhysics) was used to provide tunable laser pulses in the visible region. Typical excitation energy was adjusted to  $\sim$ 4 mJ/pulse @460 nm. Solutions were prepared in the glovebox and flown through a 1.0 cm flow cell (Starna) with a peristaltic pump for spectral acquisition. To extract the rate constants for HAT ( $k_H$ ) and back reaction ( $k_{BR}$ ), we use the following rate equation to model the TA trace:

$$\frac{d[5 \bullet]}{dt} = k_H[5] - k_{BR}[5 \bullet][\text{CQH} \bullet]$$

As shown in Figure 2A and 2B, the signal at 430 nm is due to the amidyl radical exclusively,<sup>47</sup> therefore, the signal can be written as  $S_{430nm} = \epsilon[5]$ , where  $\epsilon = 4100 M^{-1} cm^{-1}$  is the extinction coefficient of the amidyl radical at 430 nm, determined from previous studies.<sup>47</sup>

**Cyclic voltammetry and spectroelectrochemistry.** All electrochemical experiments were performed with a CH Instruments 760D Electrochemical Workstation (Austin, Texas) and CHI Version 10.03 software in a N<sub>2</sub>-filled glovebox. CQ was dissolved in an electrolyte solution containing 0.1 M n-Bu<sub>4</sub>NBF<sub>4</sub> in DCM. A three-electrode undivided cell configuration with a glassy carbon working electrode, Pt wire counter electrode, and non-aqueous Ag/Ag<sup>+</sup> reference electrode was used for all cyclic voltammetry (CV) experiments. Working electrodes were sequentially polished on felt using diamond pastes of 3 μm and 1 μm before use. Ferrocene (Fc) was added to each sample at the end of each measurement. Spectroelectrochemical measurements were performed using a 0.5 mm thin-layer quartz cuvette with a Pt mesh working electrode, non-aqueous Ag/Ag<sup>+</sup> reference electrode, and Pt wire counter electrode. The UV-vis absorption spectra were recorded with OceanView 1.4.1 coupled with a light source (Ocean Optics DT-MINI-2GS) and spectrometer (Ocean Optics, USB4000).

**Steady-State Stern-Volmer studies.** Fluorometry was performed on a QM4 fluorometer (Photon Technology International). Different samples were obtained by sequentially diluting a stock solution of the quencher and photocatalyst with a solution containing only the photocatalyst and transferred into 1 cm quartz cuvettes (Starna) for measurement. Steady-state quenching studies were performed by using the peak phosphorescence intensity with excitation at 450 nm. Samples were exposed to air after the measurements to fully quench the phosphorescence. The resulting fluorescence spectrum was subtracted from the total emission spectra to obtain the phosphorescence-only spectra.

## 5.7 Acknowledgements

Dr. Yangzhong Qin contributed to the spectroscopic studies. Dr. Serge Ruccolo and Mr. Nathaniel Hibbert contributed to the reactivity and electrochemistry studies.



## 5.8 References

1. Miller, D. C.; Choi, G. J.; Orbe, H. S.; Knowles, R. R. Catalytic Olefin Hydroamidation Enabled by Proton-Coupled Electron Transfer. *J. Am. Chem. Soc.* **2015**, *137*, 13492–13495.
2. Khursan, S. L.; Mikhailov, D. A.; Yanborisov, V. M.; Borisov, D. I. AM1 Calculations of Bond Dissociation Energies. Allylic and Benzylic C–H Bonds. *React. Kinet. Catal. Lett.* **1997**, *61*, 91–95.
3. Murray, P. R. D.; Cox, J. H.; Chiappini, N. D.; Roos, C. B.; McLoughlin, E. A.; Hejna, B. G.; Nguyen, S. T.; Ripberger, H. H.; Ganley, J. M.; Tsui, E.; Shin, N. Y.; Koronkiewicz, B.; Qiu, G.; Knowles, R. R. Photochemical and Electrochemical Applications of Proton-Coupled Electron Transfer in Organic Synthesis. *Chem. Rev.* **2021**. DOI: 10.1021/acs.chemrev.1c00374.
4. Zhu, Q.; Graff, D. E.; Knowles, R. R. Intermolecular Anti-Markovnikov Hydroamination of Unactivated Alkenes with Sulfonamides Enabled by Proton-Coupled Electron Transfer. *J. Am. Chem. Soc.* **2018**, *140*, 741–747.
5. Choi, G. J.; Zhu, Q.; Miller, D. C.; Gu, C. J.; Knowles, R. R. Catalytic Alkylation of Remote C–H Bonds Enabled by Proton-Coupled Electron Transfer. *Nature* **2016**, *539*, 268–271.
6. Ota, E.; Wang, H.; Frye, N. L.; Knowles, R. R. A Redox Strategy for Light-Driven, Out-of-Equilibrium Isomerizations and Application to Catalytic C–C Bond Cleavage Reactions. *J. Am. Chem. Soc.* **2019**, *141*, 1457–1462.
7. Margrey, K. A.; Nicewicz, D. A. A General Approach to Catalytic Alkene Anti-Markovnikov Hydrofunctionalization Reactions via Acridinium Photoredox Catalysis. *Acc. Chem. Res.* **2016**, *49*, 1997–2006.
8. Miller, D. C.; Ganley, J. M.; Musacchio, A. J.; Sherwood, T. C.; Ewing, W. R.; Knowles, R. R. Anti-Markovnikov Hydroamination of Unactivated Alkenes with Primary Alkyl Amines. *J. Am. Chem. Soc.* **2019**, *141*, 16590–16594.
9. Kim, T.; McCarver, S. J.; Lee, C.; MacMillan, D. W. C. Sulfonamidation of Aryl and Heteroaryl Halides through Photosensitized Nickel Catalysis. *Angew. Chem. Int. Ed.* **2018**, *57*, 3488–3492.
10. Cukier, R. I.; Nocera, D. G. Proton-Coupled Electron Transfer. *Annu. Rev. Phys. Chem.* **1998**, *49*, 337–369.
11. Reece, S. Y.; Nocera, D. G. Proton-Coupled Electron Transfer in Biology: Results from Synergistic Studies in Natural and Model Systems. *Annu. Rev. Biochem.* **2009**, *78*, 673–699.
12. Chang, C. J.; Brown, J. D. K.; Chang, M. C. Y.; Baker, E. A.; Nocera, D. G. Electron Transfer in Hydrogen-Bonded Donor-Acceptor Supramolecules, In *Electron Transfer in Chemistry*, V. Balzani, Ed., Wiley-VCH: Weinheim, Germany, 2001, vol. 3, Ch. 2.4, pp 409–461.
13. Darcy, J. W.; Koronkiewicz, B.; Parada, G. A.; Mayer, J. M. A Continuum of Proton-Coupled Electron Transfer Reactivity. *Acc. Chem. Res.* **2018**, *51*, 2391–2399.
14. Du, Y.; Pearson, R. M.; Lim, C.-H.; Sartor, S. M.; Ryan, M. D.; Yang, H.; Damrauer, N. H.; Miyake, G. M. Strongly Reducing, Visible-Light Organic Photoredox Catalysts as Sustainable Alternatives to Precious Metals. *Chem. Eur. J.* **2017**, *23*, 10962–10968.

15. Pieber, B.; Malik, J. A.; Cavedon, C.; Gisbertz, S.; Savateev, A.; Cruz, D.; Heil, T.; Zhang, G.; Seeberger, P. H. Semi-Heterogeneous Dual Nickel/Photocatalysis Using Carbon Nitrides: Esterification of Carboxylic Acids with Aryl Halides. *Angew. Chem. Int. Ed.* **2019**, *58*, 9575–9580.
16. Qin, Y. Z.; Martindale, B. C. M.; Sun, R.; Rieth, A. J.; Nocera, D. G. Solar-Driven Tandem Photoredox Nickel-Catalysed Cross-Coupling Using Modified Carbon Nitride. *Chem. Sci.* **2020**, *11*, 7456–7461.
17. Abderrazak, Y.; Bhattacharyya, A.; Reiser, O. Visible-Light-Induced Homolysis of Earth-Abundant Metal-Substrate Complexes: A Complementary Activation Strategy in Photoredox Catalysis. *Angew. Chem. Int. Ed.* **2021**, *60*, 21100–21115.
18. Corcoran, E. B.; Pirnot, M. T.; Lin, S. S.; Dreher, S. D.; DiRocco, D. A.; Davies, I. W.; Buchwald, S. L.; MacMillan, D. W. C. Aryl Amination Using Ligand-Free Ni(II) Salts and Photoredox Catalysis. *Science* **2016**, *353*, 279–283.
19. Sahoo, B.; Bellotti, P.; Juliá-Hernández, F.; Meng, Q.-Y.; Crespi, S.; König, B.; Martin, R. Site-Selective, Remote sp<sup>3</sup> C–H Carboxylation Enabled by the Merger of Photoredox and Nickel Catalysis. *Chem. Eur. J.* **2019**, *25*, 9001–9005.
20. Shin Nick, Y.; Ryss Jonathan, M.; Zhang, X.; Miller Scott, J.; Knowles R., R. Light-Driven Deracemization Enabled by Excited-State Electron Transfer. *Science* **2019**, *366*, 364–369.
21. Zhu, Q.; Gentry, E. C.; Knowles, R. R. Catalytic Carbocation Generation Enabled by the Mesolytic Cleavage of Alkoxyamine Radical Cations. *Angew. Chem. Int. Ed.* **2016**, *55*, 9969–9973.
22. Liang, Y.; Zhang, X.; MacMillan, D. W. C. Decarboxylative sp<sup>3</sup> C–N Coupling via Dual Copper and Photoredox Catalysis. *Nature* **2018**, *559*, 83–88.
23. Hunt, A. J.; Farmer, T. J.; Clark, J. H. Elemental Sustainability and the Importance of Scarce Element Recovery. In *Element Recovery and Sustainability*, The Royal Society of Chemistry: London, 2013; pp 1–28.
24. Treacy, S. M. R.; Rovis, T. Copper Catalyzed C(sp<sup>3</sup>)-H Bond Alkylation via Photoinduced Ligand-to-Metal Charge Transfer. *J. Am. Chem. Soc.* **2021**, *143*, 2729–2735.
25. Kang, Y. C.; Treacy, S. M.; Rovis, T. Iron-Catalyzed Photoinduced LMCT: A 1° C–H Abstraction Enables Skeletal Rearrangements and C(sp<sup>3</sup>)-H Alkylation. *ACS Catal.* **2021**, *11*, 7442–7449.
26. Rohe, S.; Morris, A. O.; McCallum, T.; Barriault, L. Hydrogen Atom Transfer Reactions via Photoredox Catalyzed Chlorine Atom Generation. *Angew. Chem. Int. Ed.* **2018**, *57*, 15664–15669.
27. Deng, H.-P.; Zhou, Q.; Wu, J. Microtubing-Reactor-Assisted Aliphatic C–H Functionalization with HCl as a Hydrogen-Atom-Transfer Catalyst Precursor in Conjunction with an Organic Photoredox Catalyst. *Angew. Chem. Int. Ed.* **2018**, *57*, 12661–12665.
28. Deng, H.-P.; Fan, X.-Z.; Chen, Z.-H.; Xu, Q.-H.; Wu, J. Photoinduced Nickel-Catalyzed Chemo- and Regioselective Hydroalkylation of Internal Alkynes with Ether and Amide  $\alpha$ -Hetero C(sp<sup>3</sup>)H Bonds. *J. Am. Chem. Soc.* **2017**, *139*, 13579–13584.

29. Shields, B. J.; Doyle, A. G. Direct C(sp<sup>3</sup>)-H Cross Coupling Enabled by Catalytic Generation of Chlorine Radicals. *J. Am. Chem. Soc.* **2016**, *138*, 12719–12722.
30. Zidan, M.; Morris, A. O.; McCallum, T.; Barriault, L. The Alkylation and Reduction of Heteroarenes with Alcohols Using Photoredox Catalyzed Hydrogen Atom Transfer via Chlorine Atom Generation. *Eur. J. Org. Chem.* **2020**, *10*, 1453–1458.
31. Nielsen, M. K.; Shields, B. J.; Liu, J.; Williams, M. J.; Zacuto, M. J.; Doyle, A. G. Mild, Redox-Neutral Formylation of Aryl Chlorides through the Photocatalytic Generation of Chlorine Radicals. *Angew. Chem. Int. Ed.* **2017**, *56*, 7191–7194.
32. Ackerman, L. K. G.; Alvarado, J. I. M.; Doyle, A. G. Direct C-C Bond Formation from Alkanes using Ni-Photoredox Catalysis. *J. Am. Chem. Soc.* **2018**, *140*, 14059–14063.
33. Yang, Q.; Wang, Y.-H. Qiao, Y.; Gau, M.; Carroll, P. J.; Walsh, P. J.; Schelter, E. J. Photocatalytic C-H Activation and the Subtle Role of Chlorine Radical Complexation in Reactivity. *Science* **2021**, *372*, 847–852.
34. Hu, A.; Guo, J.-J.; Pan, H.; Zuo, Z. Selective Functionalization of Methane, Ethane, and Higher Alkanes by Cerium Photocatalysis. *Science* **2018**, *361*, 668–672.
35. Ravelli, D.; Fagnoni, M.; Fukuyama, T.; Nishikawa, T.; Ryu, I. Site-Selective C-H Functionalization by Decatungstate Anion Photocatalysis: Synergistic Control by Polar and Steric Effects Expands the Reaction Scope. *ACS Catal.* **2018**, *8*, 701–713.
36. Holmberg-Douglas, N.; Nicewicz, D. A. Photoredox-Catalyzed C-H Functionalization Reactions. *Chem. Rev.* [Online early access]. DOI: 10.1021/acs.chemrev.1c00311. Published Online: Sept. 29, 2021. <https://pubs.acs.org/doi/abs/10.1021/acs.chemrev.1c00311> (accessed Jan. 2, 2022).
37. Kariofillis, S. K.; Doyle, A. G. Synthetic and Mechanistic Implications of Chlorine Photoelimination in Nickel/Photoredox C(sp<sup>3</sup>)-H Cross-Coupling. *Acc. Chem. Res.* **2021**, *54*, 988–1000.
38. Turro, N. J. *Modern Molecular Photochemistry*, University Science Books: Sausalito CA, 1991.
39. Walling, C.; Gibian, M. J. Hydrogen Abstraction Reactions by the Triplet States of Ketones. *J. Am. Chem. Soc.* **1965**, *87*, 3361–3364.
40. Xu, Y.; Noirbent, G.; Brunel, D.; Liu, F.; Gimes, D.; Sun, K.; Zhang, Y.; Liu, S.; Morlet-Savary, F.; Xiao, P.; Dumur, F.; Lalevée, J. Ketone Derivatives as Photoinitiators for Both Radical and Cationic Photopolymerizations under Visible LED and Application in 3D Printing. *Eur. Polym. J.* **2020**, *132*, 109737.
41. Dadashi-Silab, S.; Doran, S.; Yagci, Y. Photoinduced Electron Transfer Reactions for Macromolecular Syntheses. *Chem. Rev.* **2016**, *116*, 10212–10275.
42. Block, H.; Ledwith, A.; Taylor, A. R. Polymerization of Methyl Methacrylate Photosensitized by Benzophenones. *Polymer* **1971**, *12*, 271–288.
43. Amirzadeh, G.; Schnabel, W. On the Photoinitiation of Free Radical Polymerization—Laser Flash Photolysis Investigations on Thioxanthone Derivatives. *Makromol. Chem.* **1981**, *182*, 2821–2835.

44. Tripathi, C. B.; Ohtani, T.; Corbett, M. T.; Ooi, T. Photoredox Ketone Catalysis for the Direct C-H Imidation and Acyloxylation of Arenes. *Chem. Sci.* **2017**, *8*, 5622–5627.
45. Mateos, J.; Cuadros, S.; Vega-Peñaloza, A.; Dell'Amico, L. Unlocking the Synthetic Potential of Light-Excited Aryl Ketones: Applications in Direct Photochemistry and Photoredox Catalysis. *Synlett.* **2021**, Article No. st-2021-a0053-a.
46. Kowalska, A.; Sokolowski, J.; Bociong, K. The Photoinitiators Used in Resin Based Dental Composite—A Review and Future Perspectives. *Polymers* **2021**, *13*, 470.
47. Rucolo, S.; Qin, Y.; Schnedermann, C.; Nocera, D. G. General Strategy for Improving the Quantum Efficiency of Photoredox Hydroamidation Catalysis. *J. Am. Chem. Soc.* **2018**, *140*, 14926–14937.
48. Mayer, J. M.; Rhile, I. J. Thermodynamics and Kinetics of Proton-Coupled Electron Transfer: Stepwise vs. Concerted Pathways. *Biochim. Biophys. Acta Bioenerg.* **2004**, *1655*, 51–58.
49. Larson, D. B.; Arnett, J. F.; Wahlborg, A.; McGlynn, S. P. Emission Characteristics of Camphorquinone. *J. Am. Chem. Soc.* **1974**, *96*, 6507–6508.
50. Hodgkiss, J. M.; Rosenthal, J.; Nocera, D. G. The Relation Between Hydrogen Atom Transfer and Proton-Coupled Electron Transfer in Model Systems. In *Handbook of Hydrogen Transfer. Physical and Chemical Aspects of Hydrogen Transfer*; J. T. Hynes, J. P. Klinman, H.-H. Limbach, R. L. Schowen, Eds; Wiley-VCH: Weinheim, Germany, 2006; Vol. II, Part IV, Ch. 17, pp 503–562.
51. Land, E. J.; Ebert, M. Pulse Radiolysis Studies of Aqueous Phenol. Water Elimination from Dihydroxycyclohexadienyl Radicals to Form Phenoxyl. *Trans. Faraday Soc.* **1967**, *63*, 1181–1190.
52. Lias, S. G.; Bartmess, J. E.; Liebman, J. F.; Holmes, J. L.; Levin, R. D.; Mallard, W. G., NIST Chemistry WebBook, NIST Standard Reference Database Number 69. Linstrom, P. J.; Mallard, W. G., Eds. National Institute of Standards and Technology: Gaithersburg MD, 20899.
53. Luo, Y.-R., *Handbook of Bond Dissociation Energies in Organic Compounds*. CRC press: 2002.
54. Bordwell, F. G., Equilibrium Acidities in Dimethyl Sulfoxide Solution. *Acc. Chem. Res.* **1988**, *21*, 456–463.
55. Berg, N.; Bergwinkl, S.; Nuernberger, P.; Horinek, D.; Gschwind, R. M. Extended Hydrogen Bond Networks for Effective Proton-Coupled Electron Transfer (PCET) Reactions: The Unexpected Role of Thiophenol and Its Acidic Channel in Photocatalytic Hydroamidations. *J. Am. Chem. Soc.* **2021**, *143*, 724–735.
56. Huang, C.-Y.; Li, J.; Liu, W.; Li, C.-J. Diacetyl as a “Traceless” Visible Light Photosensitizer in Metal-Free Cross-Dehydrogenative Coupling Reactions. *Chem. Sci.* **2019**, *10*, 5018–5024.
57. Proctor, R. S. J.; Chuentragool, P.; Colgan, A. C.; Phipps, R. J. Hydrogen Atom Transfer-Driven Enantioselective Minisci Reaction of Amides. *J. Am. Chem. Soc.* **2021**, *143*, 4928–4934.
58. Dantas, J. A.; Echemendía, R.; Santos, M. S.; Paixão, M. W.; Ferreira, M. A. B.; Corrêa, A. G. Green Approach for Visible-Light-Induced Direct Functionalization of 2-Methylquinolines. *J. Org. Chem.* **2020**, *85*, 11663–11678.

59. Campbell, M. W.; Yuan, M.; Polites, V. C.; Gutierrez, O.; Molander, G. A. Photochemical C-H Activation Enables Nickel-Catalyzed Olefin Dicarbofunctionalization. *J. Am. Chem. Soc.* **2021**, *143*, 3901–3910.
60. Han, L.; Xia, J.-B.; You, L.; Chen, C. Ketone-Catalyzed Photochemical C(sp<sup>3</sup>)-H Chlorination. *Tetrahedron* **2017**, *73*, 3696–3701.
61. Capaldo, L.; Ravelli, D. Hydrogen Atom Transfer (HAT): A Versatile Strategy for Substrate Activation in Photocatalyzed Organic Synthesis. *Eur. J. Org. Chem.* **2017**, 2017, 2056–2071.
62. Pangborn, A. B.; Giardello, M. A.; Grubbs, R. H.; Rosen, R. K.; Timmers, F. J., Safe and Convenient Procedure for Solvent Purification. *Organometallics* **1996**, *15*, 1518-1520.
63. Holder, P. G.; Pizano, A. A.; Anderson, B. L.; Stubbe, J.; Nocera, D. G., Deciphering Radical Transport in the Large Subunit of Class I Ribonucleotide Reductase. *J. Am. Chem. Soc.* **2012**, *134*, 1172-1180.

## **Chapter 6**

### **Properties and Reactivity of Tetradehydrocorrins**

## 6.1 Introduction

Macrocyclic compounds featuring a tetrapyrrole moiety are ubiquitous in biological systems and vital for life. Synthetic tetrapyrrolic compounds and their metallated derivatives have found a multitude of applications in catalysis<sup>1,2</sup> energy conversion,<sup>3,4</sup> bioimaging,<sup>5,6</sup> and medicine.<sup>7</sup> Among these, the most widely studied are those featuring the porphyrin and corrole macrocycles (Figure 6.1). The breadth of accessible states of hydrogenation spanning from the fully oxidized form (i.e., porphyrin and corrole) to  $6e^-$  and  $6H^+$  (porphyrinogen from porphyrin) or  $8e^-$  and  $8H^+$  fully reduced forms (corrin from corrole) encompasses a rich variety of macrocycles with distinct chemical properties, biological functions, and applications. Although hydrogenated porphyrins in intermediate states of reduction (e.g., chlorins, bacteriochlorins, and isobacteriochlorins) have been extensively studied,<sup>8,9</sup> the analogous corrole-derived compounds remain virtually unexplored.<sup>10-14</sup> For instance, despite the extensive body of literature on the redox and photochemical properties of bacteriochlorins and isobacteriochlorins ( $4e^-$  and  $4H^+$  reduced forms of porphyrin, Figure 6.1), including the essential roles of bacteriochlorins in photosynthesis,<sup>15-17</sup> the analogous  $4e^-$  and  $4H^+$  reduced forms of corrole (e.g., tetrahydrocorrin or TDC) have scarcely been examined (Figure 6.2). This chemical space is interesting from a bioinorganic perspective as at the reductive terminus lies cobalamin.

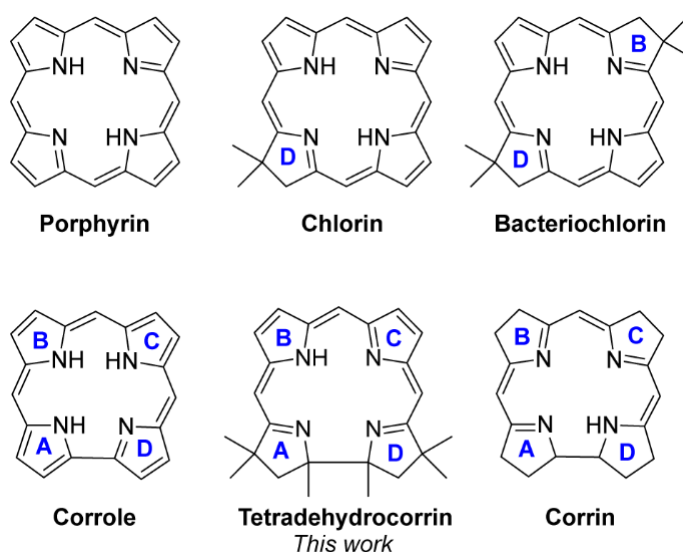


**Figure 6.1.** Structures of various tetrapyrrolic macrocycles.

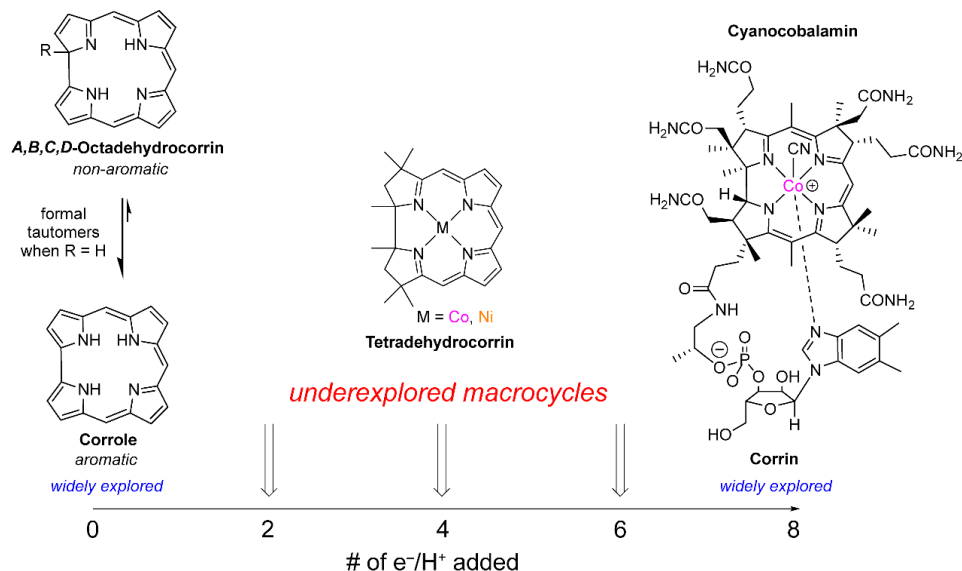


**Figure 6.2.** Corrole and its derivatives in various states of hydrogenation.

The nomenclature of dehydrogenated corrinoids is unsettled in the literature. For example, tetradehydrocorrins (TDCs) have been characterized as didehydrocorrins due to the presence of two additional double bonds.<sup>18</sup> Nonetheless, TDC and corroles are 4e<sup>-</sup>, 4H<sup>+</sup> and 8e<sup>-</sup>, 8H<sup>+</sup> oxidized forms of corrin, respectively (Figure 6.2).<sup>19-21</sup> Although there have been previous reports on the synthesis and reactivity of compounds that have been called ‘tetradehydrocorrins’,<sup>18,20,22-25</sup> those compounds are better characterized as octadehydrocorrins in accordance with nomenclature convention,<sup>19</sup> and will be referred to as such herein.

Although the syntheses of variously substituted free-base and metallated porphyrins have been extensively studied,<sup>26-28</sup> synthetic routes to hydroporphyrins are under active investigation<sup>8</sup> due to the structural challenges associated with these fascinating molecules. Similarly new methods dominate the synthesis of variously substituted free-base and metallated chlorins<sup>29-34</sup> and corroles,<sup>35-47</sup> with interest in TDCs only recently beginning to emerge.<sup>11,12</sup> A key feature of the structure of corrins is the presence of a gem-dialkyl group in each reduced ring, stabilizing the highly reduced macrocycle. Similar stabilizing features are essential in synthetic dehydrocorrins. Hence, long-established routes to porphyrins and corroles are generally inapplicable for the preparation of stable, hydrogenated macrocycles. In this study, we introduce a streamlined synthetic route to nickel and cobalt TDC compounds, and characterize their structural features,



spectroscopic properties, and oxidation-reduction chemistry across three redox states ( $[\text{M-TDC}]^+$ ,  $([\text{M-TDC}]^-)$ , and  $[\text{M-TDC}]^0$ ) of the TDC macrocycle.

## 6.2 Syntheses of $[\text{M-TDC}]^+$ Complexes and Crystal Structure of $[\text{Ni-TDC}]^+$

As part of a de novo route to gem-dimethyl-substituted bacteriochlorins that relies on the self-condensation of a 1-(dimethoxymethyl)dihydrodipyrin, a *B,D*-TDC was found as a byproduct.<sup>25</sup> The *B,D*-TDC contained a single dimethoxymethyl group at the A-D ring junction and was found to rearrange to form the bacteriochlorin upon treatment with mild acid.<sup>48</sup> Several routes to *B,D*-TDCs bearing a hydrolytically stable substituent at the AD ring junction were developed, but each route required the lengthy synthesis of two distinct dihydrodipyrins.<sup>15,16</sup> An improved strategy to gain access to *B,C*-TDC macrocycles by condensation of a dihydrodipyrin and an aldehyde was developed, but the multistep route<sup>24,49,50</sup> to such dihydrodipyrins has relied on extensive chromatography, again limiting access to the *B,C*-TDC. To gain broad access to *B,C*-TDCs, the route to the precursor dihydrodipyrin **1** (Figure 6.3) was refined and streamlined (see Figure 6.4). Key improvements include modifications of conditions to increase the yield of individual steps (particularly the reductive cyclization to give **1**), consolidation of several steps without intermediate purification, and overall diminished reliance on chromatography, which together enabled synthesis on larger scale (up to 2-g batches of dihydrodipyrin **1**). With **1** in hand, a  $\text{Ga}(\text{OTf})_3$ -templated condensation reaction with *p*-tolualdehyde, followed by metalation with the corresponding metal acetate, aerobic oxidation, and washing with aqueous  $\text{KNO}_3$  or brine furnished the respective TDC complexes (Figure 6.3).

The structure of the TDC macrocycle was provided by the Ni(II) complex, as Co gave inferior crystals. The  $^1\text{H}$  NMR spectrum of  $[\text{Ni-TDC}]^+$  suggests a low-spin diamagnetic compound. Crystals suitable for X-ray diffraction were grown from the slow evaporation of a concentrated DCM solution in the presence of hexanes at 4 °C. The crystal structure, shown in Figure 6.5, confirms the assignment of the complex as  $[\text{Ni-TDC}]^+$ . The coordination geometry about the Ni atom is square planar, consistent with a low-spin  $d^8$  metal. The vicinal dimethyl groups on the macrocycle are revealed to adopt a *trans* configuration.

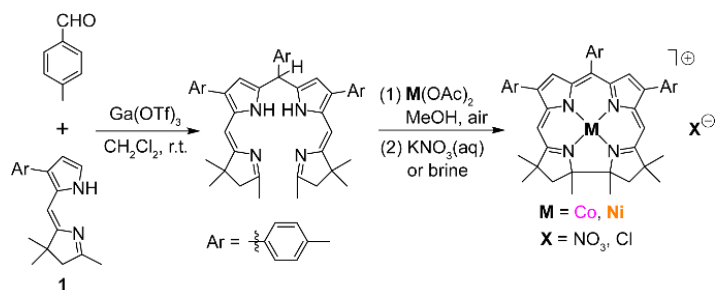


**Figure 6.3.** Synthetic scheme for the preparation of metallated TDCs.

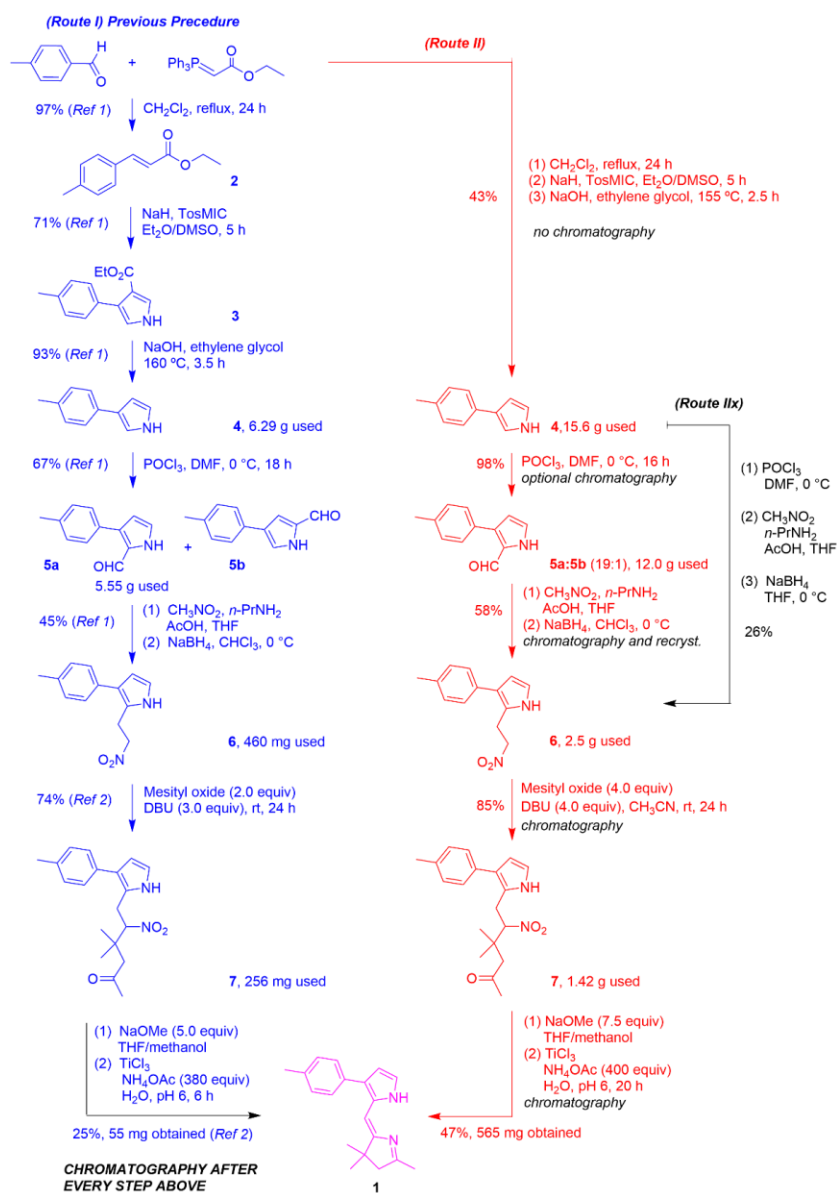


**Figure 6.4.** Refined routes to *p*Tol-DHDP-Me (1). The prior route is shown in blue, the new route in red.

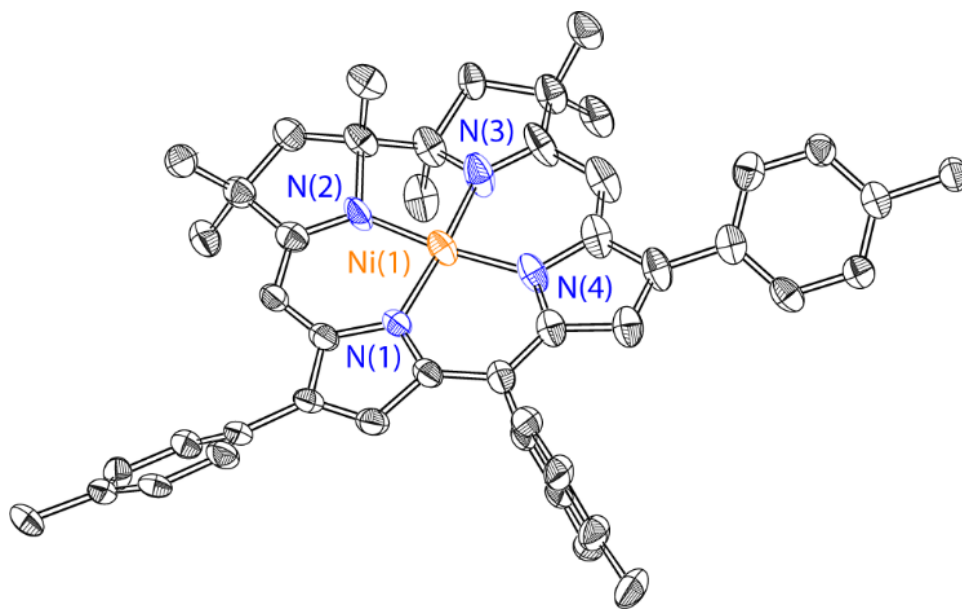


**Figure 6.5.** Crystal structure of  $[\text{Ni-TDC}]^+$  with hydrogen atoms, counter-ion, and solvent molecules omitted for clarity.

Interestingly, the  $[\text{M-TDC}]^+$  compounds were stable to oxygen. For example, given that the binding of  $\text{O}_2$  to  $\text{Co(II)}$  compounds is well-known,<sup>51</sup> the lack of  $[\text{Co(II)-TDC}]^+$  reactivity is noteworthy. Moreover, even the reduced  $\text{Co(I)}$  form,  $[\text{Co-TDC}]$ , did not undergo aerobic oxidation under ambient conditions. Indeed, attempts to synthesize a formal  $\text{Co(II)}$  superoxide compound were unsuccessful, as treatment of an acetate salt of  $[\text{Co-TDC}]^+$  in MeCN with excess  $\text{KO}_2$  and 18-crown-6 led to the immediate formation of a reduced  $[\text{Co-TDC}]$  (Figure 6.6), implying that the parent  $\text{Co(II)}$  complex undergoes simple one-electron reduction by superoxide without oxygen coordination. This stability of  $[\text{Co-TDC}]$  is redolent of that previously reported for a  $\text{Co(I)}$  octa-dehydrocorrins, which also exhibited unusual stability towards oxidation.<sup>25</sup>

### 6.3 Oxidation-Reduction Chemistry of $[\text{M-TDC}]^+$ Complexes

The cyclic voltammograms (CVs) of  $[\text{Co-TDC}]^+$  and  $[\text{Ni-TDC}]^+$  both show two reversible cathodic waves in acetonitrile under a  $\text{N}_2$ -atmosphere (Figure 6.7). For  $[\text{Co-TDC}]^+$ , the half-wave potentials measured against  $\text{Fc}^+/\text{Fc}$  for the formal  $\text{Co(II/I)}$  and  $\text{Co(I/0)}$  redox couples are  $-0.46$  V and  $-1.56$  V, respectively. The corresponding  $\text{Ni(II/I)}$  and  $\text{Ni(I/0)}$  potentials are  $-0.70$  V and  $-1.43$  V, respectively. This  $\Delta E_{1/2} = 0.24$  V difference in redox potentials between the  $\text{Co(II/I)}$  and  $\text{Ni(II/I)}$

couples is redolent of that for Co- and Ni- tetraarylporphyrins ( $\Delta E_{1/2} = 0.27$  V), where the one-electron reduction of the Co derivative was found to be predominantly metal-centered while that of the Ni derivative contained significant  $\pi$ -anion character.<sup>52</sup> Thus, we posit that a similar trend may exist for the TDC ligand platform, where  $[\text{Ni-TDC}]^+$  exhibits ligand-centered reactions upon reduction. To assess this contention, the reduced compounds were independently prepared and spectroscopically examined. The doubly reduced  $[\text{Ni-TDC}]^-$  complex was obtained by bulk electrolysis of  $[\text{Ni-TDC}]^+$  at  $E_{\text{appl}} = -1.7$  V. The singly reduced  $[\text{Ni-TDC}]$  complex was afforded by comproportionation of  $[\text{Ni-TDC}]^+$  and  $[\text{Ni-TDC}]^-$  in a 1:1 ratio. The EPR spectrum of the formally reduced Ni(I) complex,  $[\text{Ni-TDC}]$ , was measured on comproportionated solutions frozen to 3 K (Figure 6.8). The spectrum was simulated with an isotropic signal of  $g = 2.02$ , supporting the contention that this compound is best characterized as Ni(II) with a ligand-based TDC anion radical. This finding is similar to the electronic structure of mono-reduced Ni(II) porphyrins at room temperature<sup>52,53</sup> where the reduction of the metal center lies to more negative potentials than macrocyclic ring reduction.

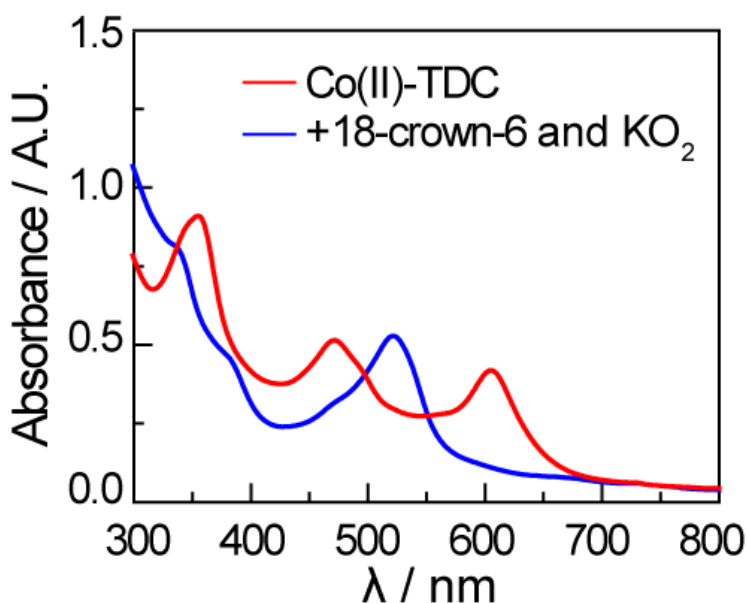


**Figure 6.6.** UV-vis spectra of  $[\text{Co-TDC}]^+$  as the acetate salt in MeCN before (— blue) and after (— red) treatment with excess  $\text{KO}_2$  and 18-crown-6. No appreciable spectroscopic changes were observed in the sample treated with 18-crown-6 and  $\text{KO}_2$  upon air exposure.

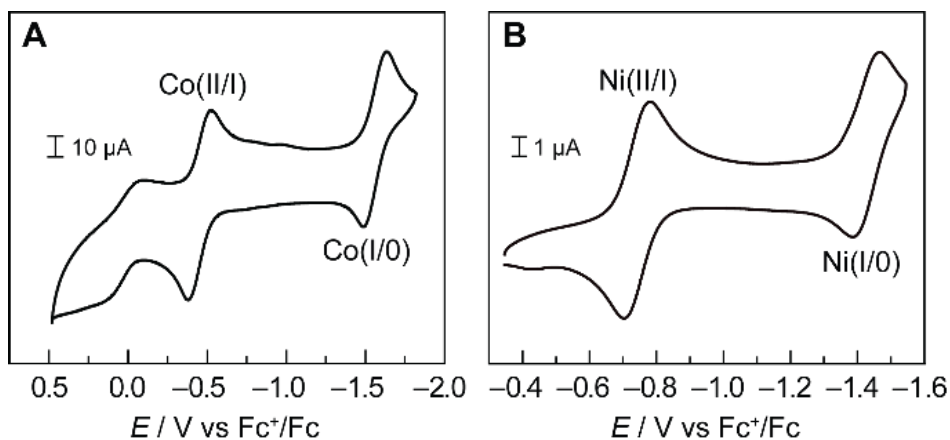


**Figure 6.7.** CVs of [Co-TDC]<sup>+</sup> (A) and [Ni-TDC]<sup>+</sup> (B) using a glassy carbon working electrode in MeCN with 0.1 M *n*-Bu<sub>4</sub>NPF<sub>6</sub> as the supporting electrolyte.  $\nu = 0.1$  V/s.  $E_{1/2}[\text{Co(II/I)}] = -0.46$  V,  $E_{1/2}[\text{Co(I/0)}] = -1.56$  V.  $E_{1/2}[\text{Ni(II/I)}] = -0.70$  V,  $E_{1/2}[\text{Ni(I/0)}] = -1.43$  V.

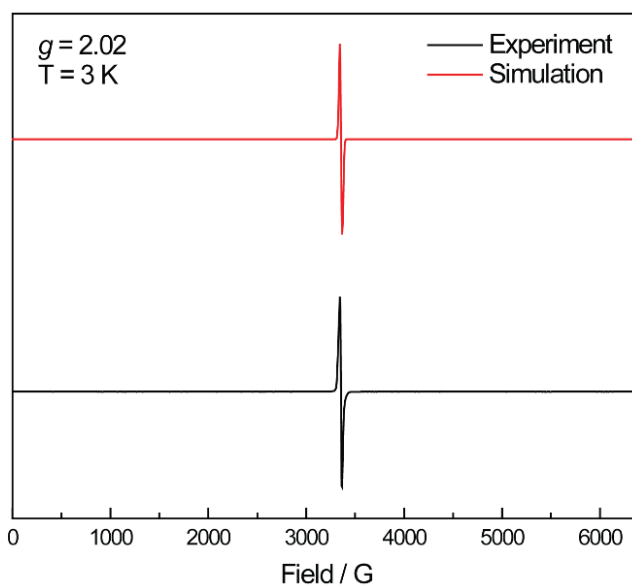


**Figure 6.8.** EPR spectrum of [Ni-TDC] collected at 3 K. Simulated with an isotropic signal at  $g = 2.02$ .

The three different redox states of the metal TDC complexes display unique absorption features that are captured by spectroelectrochemistry (Figure 6.9). The spectra of the [M-TDC]<sup>+</sup> bear resemblance to those reported for the respective M(II)-octahydrocorrin compounds collected in DCM (M = Co) and in pH 7 aqueous buffer (M = Ni).<sup>22,49</sup> These absorption profiles proved useful in monitoring the reaction chemistry of the TDC compounds.

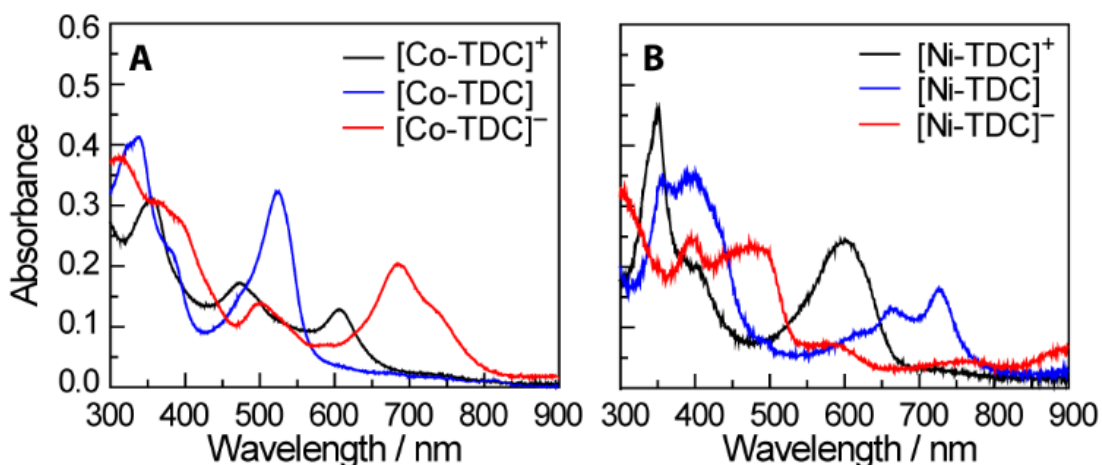


**Figure 6.9.** Reductive spectroelectrochemistry of  $[M\text{-TDC}]^+$  complexes in MeCN containing 0.1 M  $n\text{-Bu}_4\text{NPF}_6$ . (A) UV-vis-NIR spectra of  $[\text{Co-TDC}]^+$  showing the cationic (— black), singly reduced (— blue,  $E_{\text{appl}} = -0.7$  V), and doubly reduced (— red,  $E_{\text{appl}} = -1.7$  V) redox states. (B) UV-vis-NIR spectra of  $[\text{Ni-TDC}]^+$  showing the cationic (— black), singly reduced (— blue,  $E_{\text{appl}} = -1.0$  V), and doubly reduced (— red,  $E_{\text{appl}} = -1.7$  V) redox states.

The reduction of the TDC ring suggests redox noninnocence regarding the reactivity of highly reduced nickel TDC complexes. Such redox noninnocence of the ligand has been shown to play a prominent role in the hydrogen evolution reaction (HER).<sup>52,54</sup> Accordingly, the reduction chemistry and subsequent proton reactivity of Ni-TDC complexes were investigated chemically and electrochemically.

The reductive electrochemistry of  $[\text{Ni-TDC}]^+$  was investigated in acidic media. Figure 6.10A shows the cyclic voltammograms of  $[\text{Ni-TDC}]^+$  upon cathodic scans in the presence of benzoic acid (BzOH). The peak current ( $i_{pc}$ ) and potential ( $E_{pc}$ ) of the first cathodic wave remains unchanged and is consistent with simple one-electron reduction of  $[\text{Ni-TDC}]^+$  to  $[\text{Ni-TDC}]$ . The insensitivity of  $i_{pc}$  to BzOH addition suggests the acid is too weak ( $\text{p}K_a = 21.5$  in acetonitrile<sup>55</sup>) to protonate  $[\text{Ni-TDC}]$ . Conversely, the reversible feature of the second cathodic process becomes irreversible in the presence of BzOH and  $E_{pc}$  shifts anodically with increasing concentrations of BzOH; a corresponding re-oxidation wave appears at  $-0.4$  V. That  $i_{pc}$  does not increase with BzOH, together with the insensitivity of the first cathodic wave to BzOH addition and an anodic shift of the second wave, indicates that reaction with weak acid is involved only upon the second reduction.

With the much stronger trifluoroacetic acid (TFA,  $pK_a = 12.65$  in acetonitrile<sup>56</sup>), the current of the first wave increases with increasing concentration of acid (Figure 6.10B), eventually reaching a value of  $i_{pc}$  that is double of what was observed in the absence of acid. The increase is indicative of a two-electron reduction when a strong acid is present. We note that to more negative potentials the cyclic voltammogram becomes overwhelmed by background current associated with the hydrogen evolution reaction on the glassy carbon working electrode.<sup>57</sup>

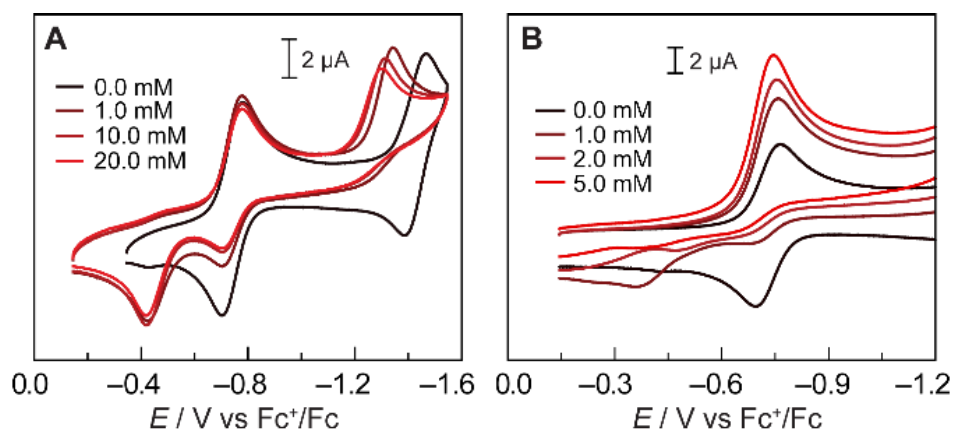


**Figure 6.10.** CVs of 1 mM  $[\text{Ni-TDC}]^+$  in the presence of acid using a glassy carbon working electrode in MeCN with 0.1 M  $n\text{-Bu}_4\text{NPF}_6$  as the supporting electrolyte.  $\nu = 0.1$  V/s. (A) With added benzoic acid (BzOH). (B) with added trifluoroacetic acid (TFA).

The nature of the reductive electrochemistry shown in Figure 6.10 is revealed by chemical reduction studies in conjunction with spectroelectrochemical measurements of  $[\text{Ni-TDC}]^+$  in the presence of BzOH and TFA. The addition of two electrons and a proton to  $[\text{Ni-TDC}]^+$  effectively amounts to a hydride addition. Accordingly, the reductive chemistry of  $[\text{Ni-TDC}]^+$  was examined with  $\text{LiBH}_4$  as a chemical reductant. Treating a MeCN solution of  $[\text{Ni-TDC}]^+$  with excess  $\text{LiBH}_4$  leads to the immediate formation of a compound with a distinct UV-vis feature with maxima at 568 and 600 nm (Figure 6.11A, blue trace). This spectrum evolves over the course of 10 min to eventually give spectroscopic features (Figure 6.11A, red trace) consistent with that of  $[\text{Ni-TDC}]^-$  obtained from spectroelectrochemistry (Figure 6.9B, red trace). Addition of excess TFA to a solution of  $[\text{Ni-TDC}]^+ + \text{LiBH}_4$  results in the appearance of a final product with an absorption maximum of 553 nm (Figure 6.11B). High-resolution mass spectrometry (HRMS) on this

hydrogenated product shows a peak at  $m/z = 715.3330$  (Figure 6.12), consistent with the value required for  $[\text{Ni-TDC-H}_2]^+$  ( $m/z = 715.3305$ ).

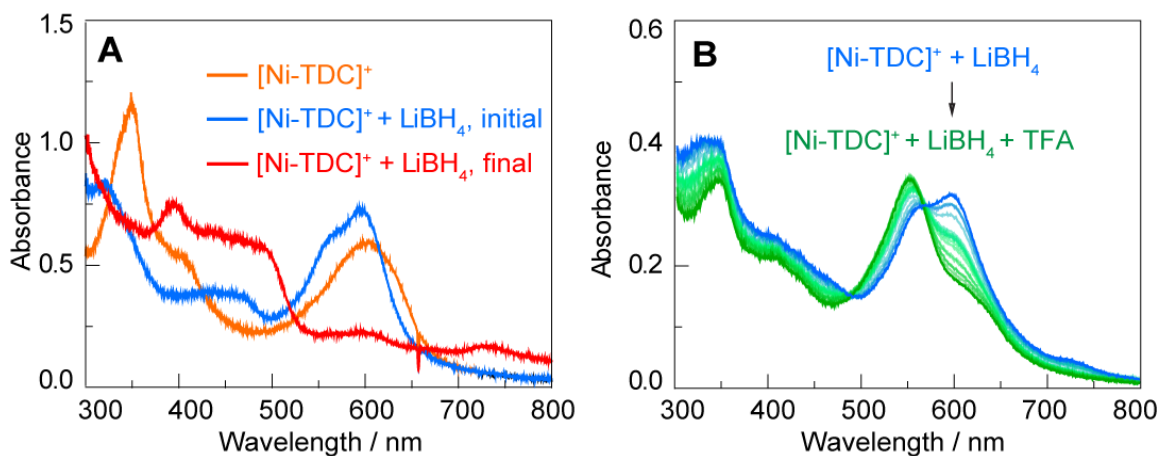


**Figure 6.11.** Chemical reduction of  $[\text{Ni-TDC}]^+$  with  $\text{LiBH}_4$ . (A) Initial spectrum of  $[\text{Ni-TDC}]^+$  (— orange), immediately after addition of excess  $\text{LiBH}_4$  (— blue), 10 min after addition of  $\text{LiBH}_4$  (— red). (B) Treatment of the  $\text{LiBH}_4$ -derived intermediate with excess trifluoroacetic acid (TFA) showing the initial (— blue) and final (— green) spectra.

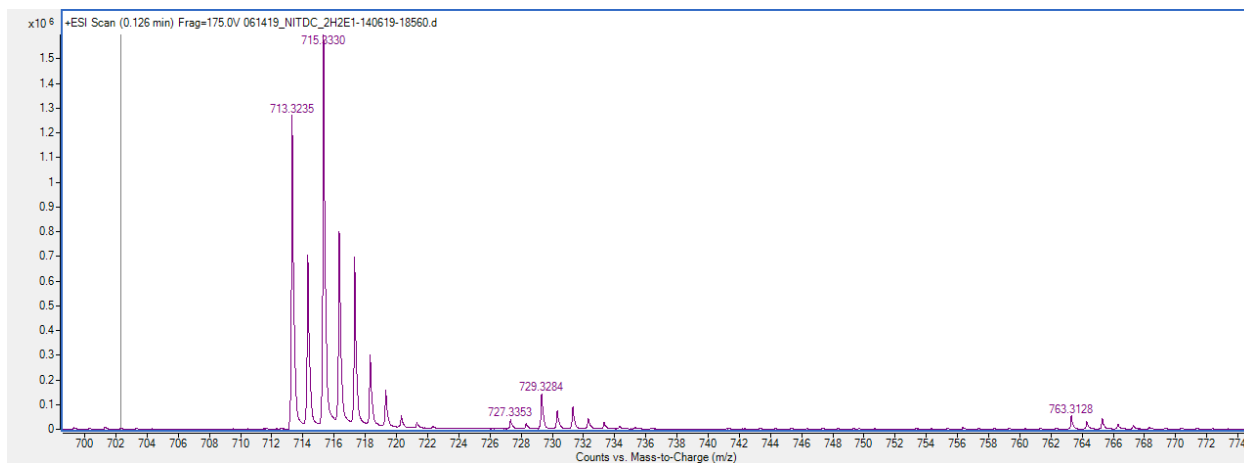


**Figure 6.12.** HRMS (ESI, positive mode) of the putative  $[\text{Ni-TDC-H}]$  intermediate after treatment with TFA. The peak at  $715.3330$  is consistent with the formation of  $[\text{Ni-TDC-H}_2]^+$ .

The reduction chemistry of Figure 6.11 is captured by spectroelectrochemistry of  $[\text{Ni-TDC}]^+$  in acidic acetonitrile. The terminal product obtained when  $[\text{Ni-TDC}]^+$  is reduced under a potential of  $E_{\text{appl}} = -1.5$  V vs  $\text{Fc}^+/\text{Fc}$  in the presence of  $\text{BzOH}$  (Figure 6.13A, — blue trace) is consonant with the product obtained from the reduction of  $[\text{Ni-TDC}]^+ + \text{LiBH}_4$  (Figure 6.11A, —



blue trace). In the presence of TFA and  $E_{appl} = -0.8$  V vs  $Fc^+/Fc$ , the spectroelectrochemical absorption spectrum (Figure 6.13B, — green trace) is that of  $[Ni-TDC]^+ + LiBH_4 + TFA$  (Figure 6.11B, — green trace). Moreover, we were also able to spectroelectrochemically confirm the lack of reactivity for  $[Ni-TDC]$  with BzOH observed by CV in Figure 6.10A. As seen in Figure 6.14, the spectrum obtained when  $[Ni-TDC]^+$  was electrolyzed at  $E_{appl} = -0.8$  V vs  $Fc^+/Fc$  in the presence of BzOH is unchanged from that of  $[Ni-TDC]$  shown in Figure 6.9B.

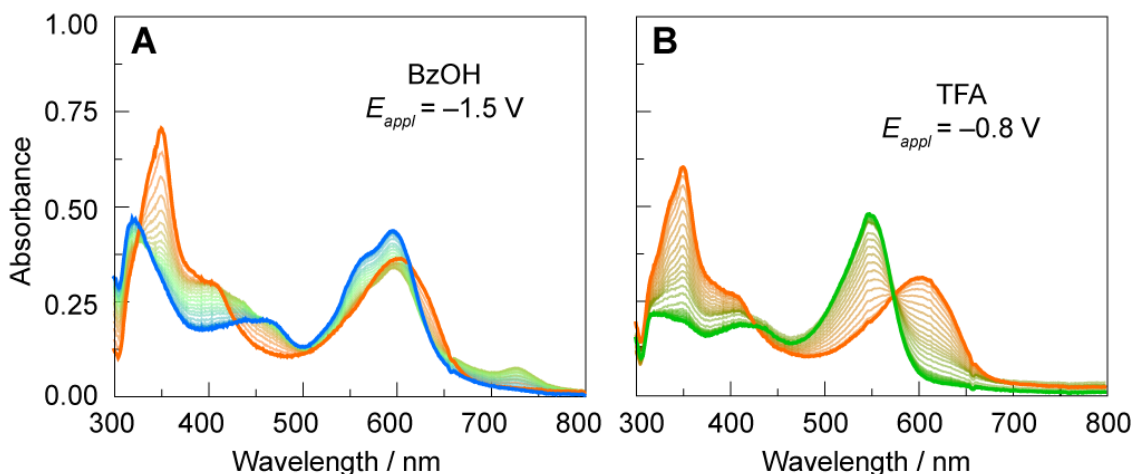


**Figure 6.13.** Reductive spectroelectrochemistry of 1mM  $[Ni-TDC]^+$  in MeCN containing 0.1 M  $n-Bu_4NPF_6$  (— orange) and final spectra under an applied potential ( $E_{appl}$ ) of (A) -1.5 V with excess benzoic acid (BzOH) (— blue) and (B) -0.8 V with excess trifluoroacetic acid (TFA) (— green).

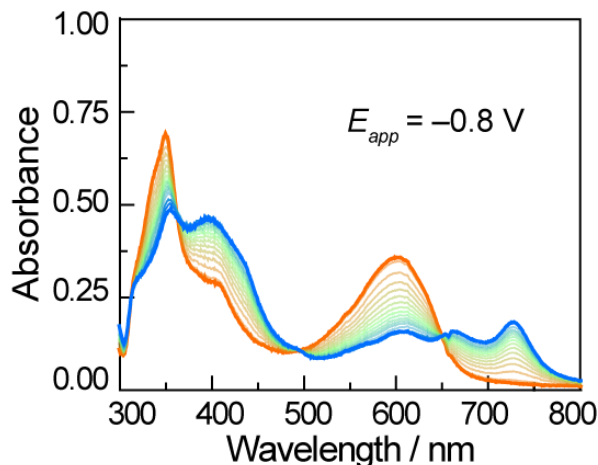


**Figure 6.14.** Reductive spectroelectrochemistry of 1 mM  $[Ni-TDC]^+$  with excess BzOH in MeCN containing 0.1 M  $n-Bu_4NPF_6$  showing the initial (— orange) and final (— blue) spectra under an applied potential of -0.8 V vs  $Fc^+/Fc$ .

The reaction scheme in Figure 6.15 is consistent with the results of the chemical and spectroelectrochemical reduction chemistry. Treatment of  $[\text{Ni-TDC}]^+$  with  $\text{LiBH}_4$  leads to the formation of the intermediate  $[\text{Ni-TDC-H}]$  via hydride addition, whose spectrum is shown in the blue traces in Figures 6.11A and 6.13A. Further reaction of  $[\text{Ni-TDC-H}]$  with  $\text{LiBH}_4$ , which may function as a base, leads to deprotonation of the former, resulting in the formation of  $[\text{Ni-TDC}]^-$  (red pathway). Whereas  $\text{BzOH}$  is too weak an acid to react with  $[\text{Ni-TDC-H}]$ ,  $\text{TFA}$  leads to protonation of the latter (green pathway), yielding  $[\text{Ni-TDC-H}_2]^+$  as characterized by the absorption spectrum shown by the green traces in Figures 6.11B and 6.13B.

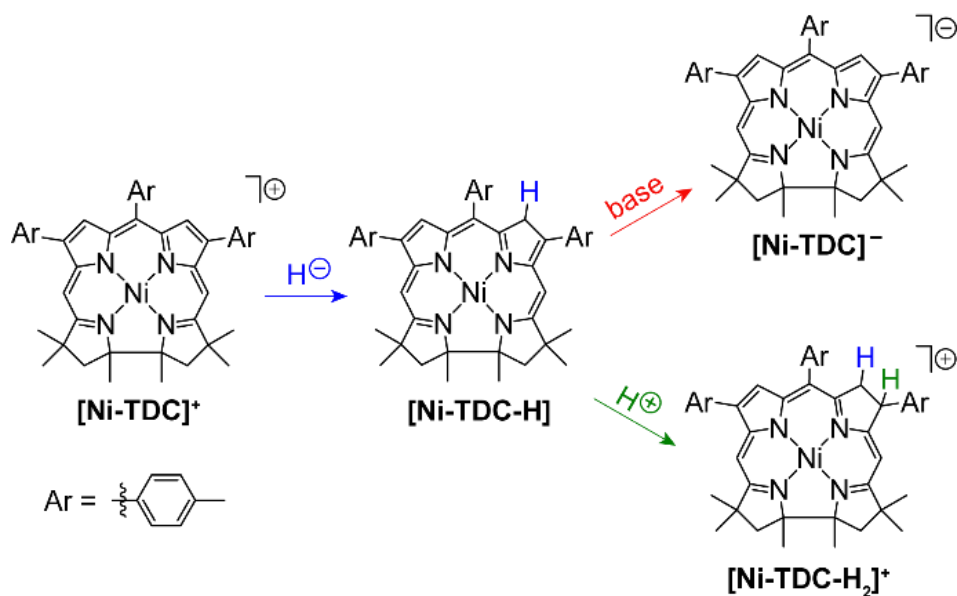


**Figure 6.15.** A mechanism for the chemical reduction of  $[\text{Ni-TDC}]^+$  by  $\text{LiBH}_4$  and subsequent reaction with acid. Note that only one of the possible isomers is shown for  $[\text{Ni-TDC-H}]$  and  $[\text{Ni-TDC-H}_2]^+$ .

The CV data in Figure 6.10 are illuminated by chemical reduction and spectroelectrochemical spectra of Figures 6.11 and 6.13. In the presence of  $\text{BzOH}$ , the insensitivity of the first cathodic wave to  $\text{BzOH}$  addition, together with the anodic shift in  $E_{pc}$  without a concomitant increase in  $i_{pc}$  for the second cathodic wave implies an overall EEC process, where two electrons and one proton (formally, a hydride) are added to  $[\text{Ni-TDC}]^+$  to form  $[\text{Ni-TDC-H}]$ . This is supported by a comparison between the spectroelectrochemical data in Figure 6.13A

(— blue trace) with the UV-vis spectrum shown in Figure 8A (— blue trace). In Figure 6.13A, the electrode was poised at  $-1.5$  V (corresponding to the second cathodic wave in Figure 6.10A), and the terminal product obtained from this electrolysis matches that formed from chemical addition of a hydride to  $[\text{Ni-TDC}]^+$ . Owing to the much higher acidity of TFA in comparison to BzOH, protonation occurs after the first reduction in the presence of the former. The observation that  $i_{pc}$  of the first cathodic wave increases with increasing concentrations of TFA, eventually leading to an  $i_{pc}$  value double of that observed in the absence of TFA, implies either an ECE (2 electron, 1 proton reduction) or an ECEC (2 electron, 2 proton reduction) process. Spectroelectrochemical and chemical reduction experiments allow us to differentiate between these two mechanisms. Under a potential of  $E_{appl} = -0.8$  V (corresponding to the first cathodic wave in Figure 6.10B), the terminal product obtained has a spectrum (Figure 6.13B, — green trace) distinct from those of  $[\text{Ni-TDC-H}]$  (Figures 6.11A and 6.13A, — blue traces). Instead, the spectrum matches that obtained from the reaction of  $[\text{Ni-TDC}]^+$  with  $\text{LiBH}_4$  followed by TFA (Figure 6.11B, — green trace), corresponding to overall addition of two electrons and two protons. This implies that the process corresponding to the cathodic wave in Figure 6.10B is an ECEC reaction leading to the overall formation of  $[\text{Ni-TDC-H}_2]^+$ .

#### 6.4 Computational Studies of Ni-TDC Derivatives

The redox properties of the various redox levels of Ni-TDC were supported by computational investigation of the frontier molecular orbitals (FMOs). The relaxed geometries of the three redox levels of Ni-TDC compounds and associated frontier molecular orbitals (FMOs) were determined from density functional theory (DFT, see Materials and Methods for detailed information). In agreement with the crystal structure of  $[\text{Ni-TDC}]^+$ , computations predicted a quasi  $D_{4h}$  Ni environment (Figure 6.16). At room temperature (thermally available energy of  $\sim 25$  meV), the HOMO and HOMO-1 orbitals are energetically degenerate with an energy difference of  $169\text{ cm}^{-1}$  and represent a combination of the metal  $d_{z^2}$  orbital and significant  $\pi$ -character from the conjugated fragment of the TDC ligand. We note that only the HOMO-2, which lies  $1073\text{ cm}^{-1}$  below the HOMO, is entirely localized on the metal  $d_{z^2}$  orbital. The LUMO is dominated by  $\pi$ -

bonding character of the conjugated ligand with minor contributions from the metal  $d_{xz}$  and  $d_{yz}$  orbitals (Figure 6.17). Based on these FMOs, one-electron reduction of  $[\text{Ni-TDC}]^+$  to  $[\text{Ni-TDC}]$  leads to partial filling of the ligand-centered LUMO, consistent with the EPR spectrum of  $[\text{Ni-TDC}]$  (Figure 6.8). Subsequent one-electron reduction to  $[\text{Ni-TDC}]^-$  adds an electron to this same LUMO to result in the closed-shell species. The corresponding FMOs, visualized along the reduction series in Figure 6.18, emphasize that the redox reactivity of Ni-TDC proceeds with strong participation of the conjugated segment of the TDC ligand. These calculations corroborate our experimental findings on predominantly ligand-mediated reduction activity as proposed in Figure 6.15.

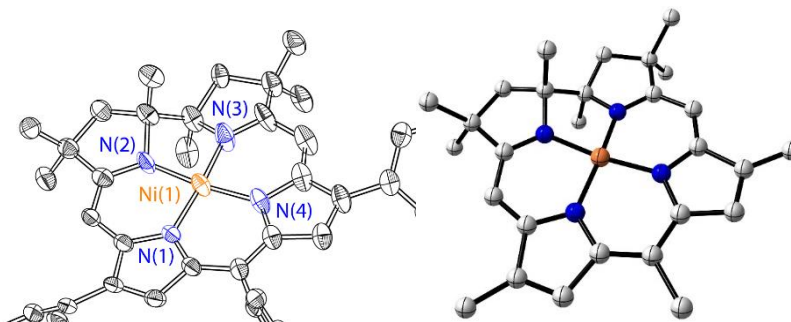


**Figure 6.16.** Comparison of crystallographic and computed structure of  $[\text{Ni-TDC}]^+$ . Crystal structure is cropped to be more directly comparable to the calculated structure. Hydrogen atoms are omitted for clarity.

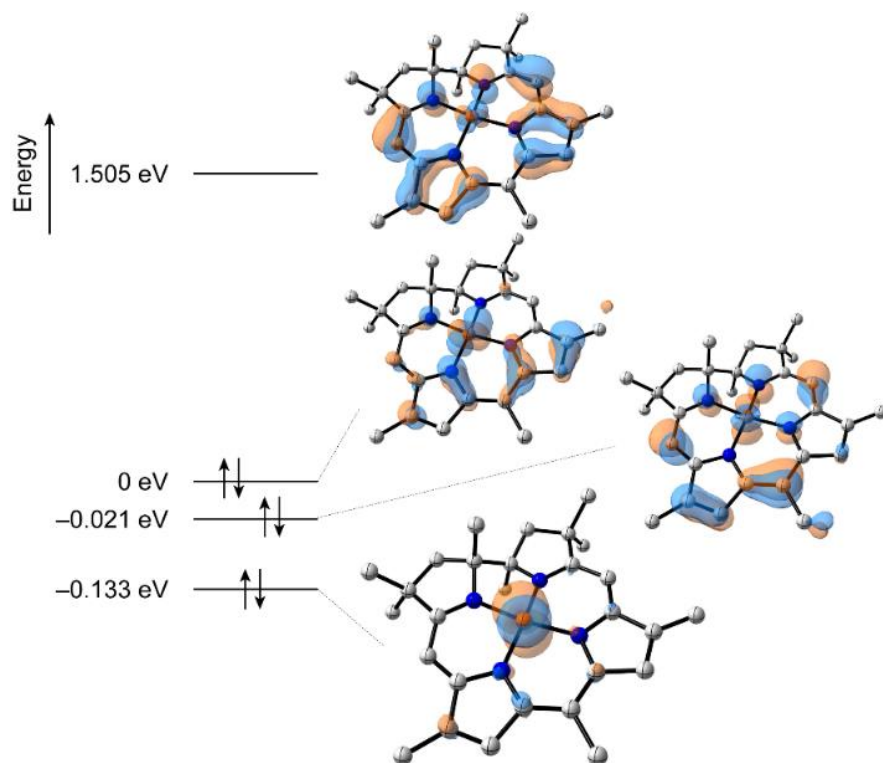


**Figure 6.17.** Frontier orbitals and relative energies of  $[\text{Ni-TDC}]^+$ .

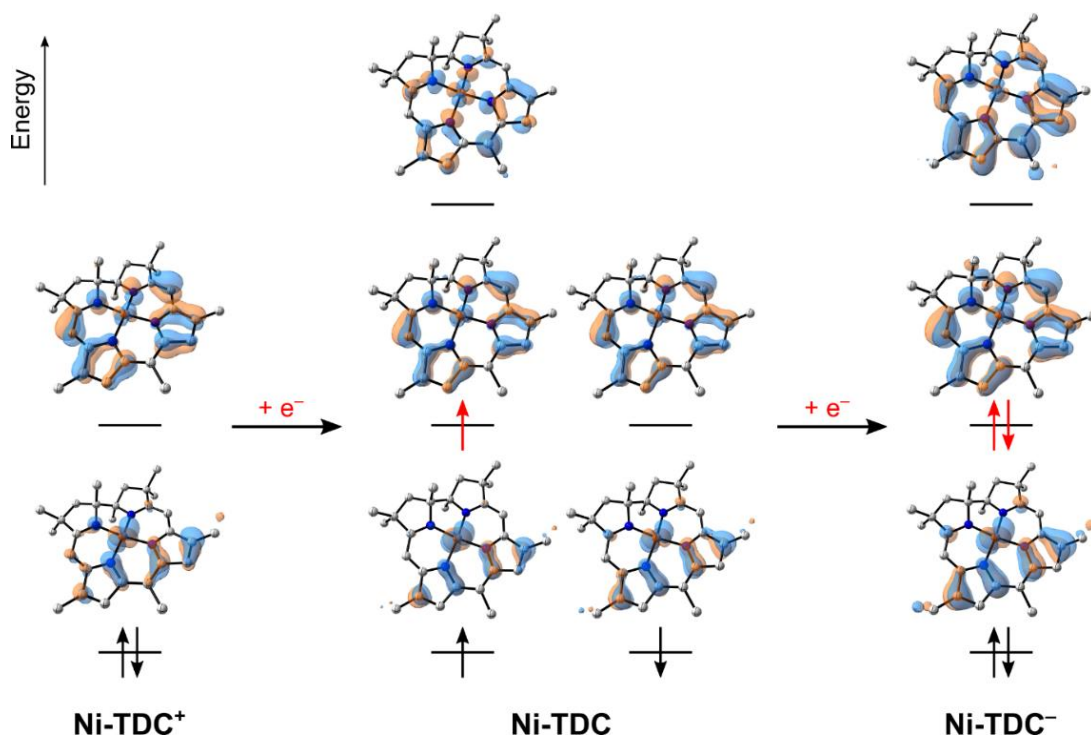


**Figure 6.18.** Frontier orbital evolution along the reduction series of  $[\text{Ni-TDC}]^+$ . Energies are not to scale.

## 6.5 Femtosecond Transient Absorption Spectroscopy of Ni-TDC Compounds

Time-resolved transient absorption (TA) spectra of Ni-TDC compounds in different redox states is shown in Figures 6.19A, 6.19C, 6.19E and 6.20. On the short time scale of one picosecond, clear decay and/or rise features are observed for  $[\text{Ni-TDC}]^+$  and  $[\text{Ni-TDC}]^-$ , indicating ultrafast vibronic cooling and solvation. Conversely, any fast decay for  $[\text{Ni-TDC}]$  is largely absent (Figure 6.20B). On the slower timescale of up to 3 nanoseconds, the TA spectra show multiphasic decay (Table S1); for  $[\text{Ni-TDC}]^+$ , the TA spectra show excited-state absorption (ESA) at  $\sim 525$  nm and ground-state bleaching (GSB) at  $\sim 620$  nm (Figure 6.19A), in addition to a minor ESA and GSB at 690 nm and 730 nm, respectively. After 40 ps, the ESA decays completely and a GSB remains showing no decay up to 250 ps. To better quantify the dynamics of the  $[\text{Ni-TDC}]^+$  excited state, two traces at 525 nm and 620 nm, corresponding to the ESA and GSB, respectively, were fitted by multi-exponential decay. The ESA trace at 525 nm shows a fast rise with a time constant of  $\tau = 0.41$  ps followed by a decay with a time constant of  $\tau = 9.4$  ps. Similarly, the GSB trace at 620 nm exhibits fast decay ( $\tau = 0.30$  ps) and slow rise ( $\tau = 13.4$  ps), consistent with the ESA trace. Interestingly, the GSB shows significant contribution (39%) from a long-lived component that does not decay within 250 ps, in contrast to the negligible long-lived components present in the ESA (Table 6.1). Similar to  $[\text{Ni-TDC}]^+$ ,  $[\text{Ni-TDC}]$  also shows ESA and GSB features in the TA spectra (Figure 6.20C). The dynamic traces show matching time constants of 0.21 ps and 6.1 ps for the ESA at 550 nm, and 0.27 ps and 6.5 ps for the GSB at 725 nm. Negligible long-lived components were observed for both the ESA and the GSB beyond 250 ps, suggesting a complete decay of the excited state back to the ground state for  $[\text{Ni-TDC}]$ .

For  $[\text{Ni-TDC}]^-$ , the TA spectra show GSB at 490 nm and broadband ESA beyond from 520 nm to 750 nm (Figure 6.19E), distinct from the spectra of  $[\text{Ni-TDC}]$  and  $[\text{Ni-TDC}]^+$  (Figure 6.19A and C), which typically exhibit major ESA on the blue side and GSB on the red side. These spectral features correlate well with the ground-state UV-vis absorption, where  $[\text{Ni-TDC}]^-$  shows weaker absorption than  $[\text{Ni-TDC}]$  and  $[\text{Ni-TDC}]^+$  from 525 to 800 nm. The kinetic traces for  $[\text{Ni-TDC}]^-$  suggest rather slow dynamics. Specifically, the ESA at 550 nm has one rising component ( $\tau = 0.34$

ps) and two decay components ( $\tau = 3.3$  and 1094 ps) while the GSB at 490 nm has two fast decay components ( $\tau = 0.84$  and 6.5 ps) and one rising component ( $\tau = 1200$  ps). Similar to  $[\text{Ni-TDC}]^+$ , the GSB for  $[\text{Ni-TDC}]^-$  also exhibits an additional long-lived component beyond 2.8 ns which accounts for 38.3% of the total rise amplitude (see Table 6.1). Note that for all the long dynamic components beyond our probe window, we fit them with a fixed time constant of 20 ns, while the actual time may vary. The fs-TA studies suggest that the excited state of  $[\text{Ni-TDC}]$  relaxes completely to the ground state with a time constant of  $\sim 6$  ps, significantly shorter than that of  $[\text{Ni-TDC}]^+$  and  $[\text{Ni-TDC}]^-$  with time constants of  $\sim 11$  ps and  $\sim 1150$  ps, respectively. This is consistent with the fast internal conversion rates of excited-state doublets.<sup>58-62</sup> More importantly, both  $[\text{Ni-TDC}]^+$  and  $[\text{Ni-TDC}]^-$  exhibit a significant long-lived component as shown by the constant GSB beyond our probe time window. These results suggest that  $[\text{Ni-TDC}]$  possesses the highest photostability, and  $[\text{Ni-TDC}]^+$  and  $[\text{Ni-TDC}]^-$  may be able to access a long-lived photo-induced state that could be potentially used for photochemistry.

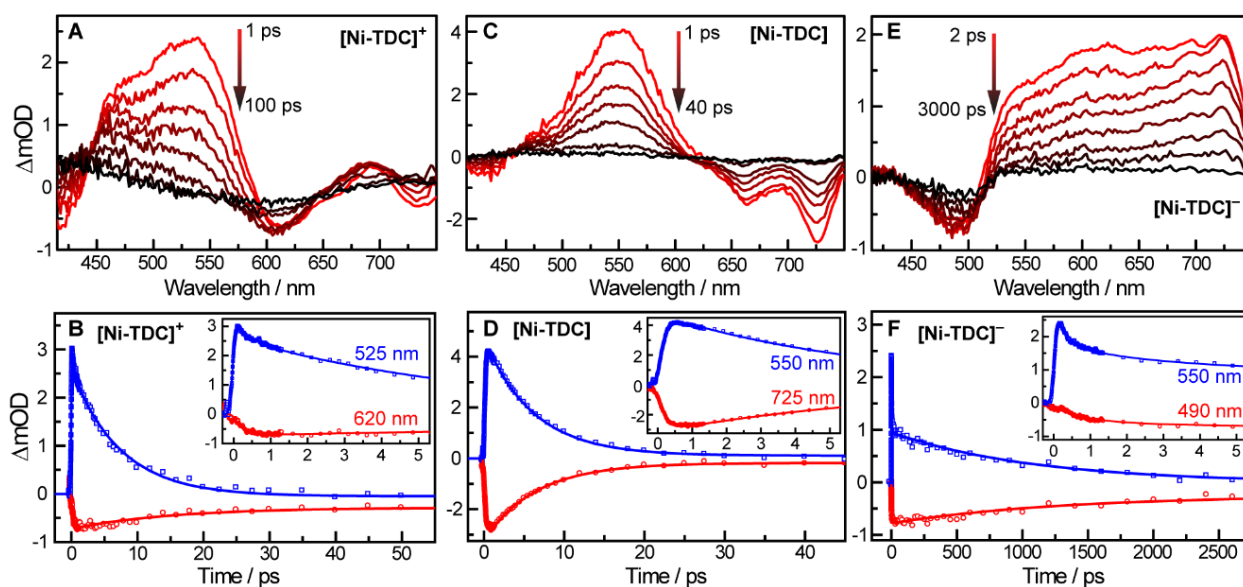


**Figure 6.19.** TA spectra and dynamic traces of Ni-TDC compounds in THF. The TA spectral evolution and dynamic traces are shown for  $[\text{Ni-TDC}]^+$  (A and B),  $[\text{Ni-TDC}]$  (C and D), and  $[\text{Ni-TDC}]^-$  (E and F).  $\lambda_{\text{exc}} = 400$  nm.

**Table 6.1.** Fitting parameters for TA kinetic traces.

	[Ni-TDC] <sup>-</sup>		[Ni-TDC]		[Ni-TDC] <sup>+</sup>	
	490 nm (-)	550 nm (+)	725 nm (-)	550 nm (+)	620 nm (-)	525 nm (+)
<b>A<sub>1</sub> (%)</b>	75.4	37.8	97.3	-84.9	80.7	18.7
<b>A<sub>2</sub> (%)</b>	27.4	28.2	-94.5	97.8	-61.1	81.3
<b>A<sub>3</sub> (%)</b>	-61.7	34.1	-5.5	2.2	-38.9	-1.5
<b>A<sub>4</sub> (%)</b>	-38.3	-	-	-	-	-
<b>τ<sub>1</sub> (ps)</b>	0.84	0.34	0.27	0.21	0.30	0.41
<b>τ<sub>2</sub> (ps)</b>	6.5	3.3	6.5	6.1	13.4	9.4
<b>τ<sub>3</sub> (ps)</b>	1200	1094	20000	20000	20000	20000
<b>τ<sub>4</sub> (ps)</b>	20000	-	-	-	-	-



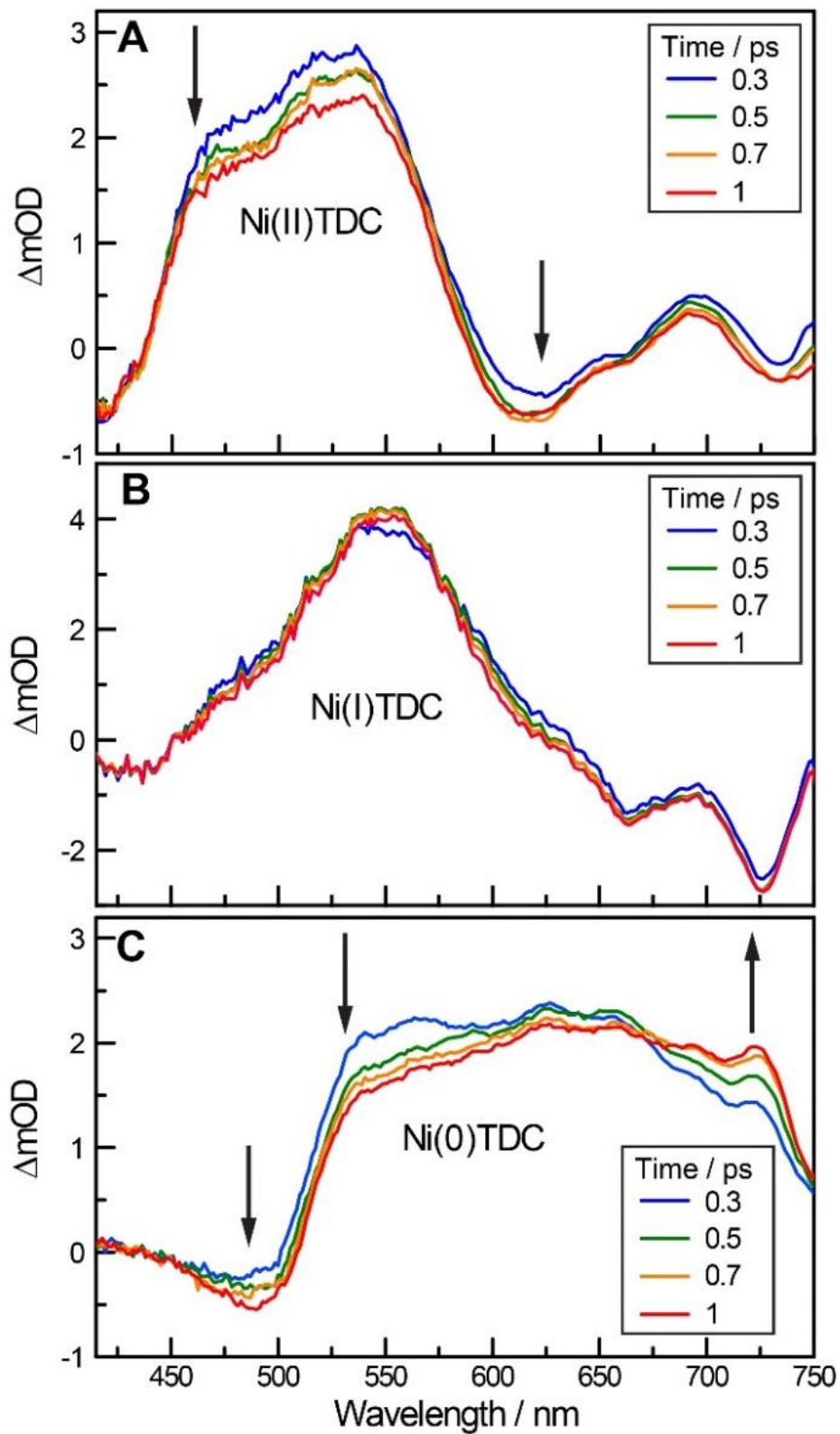


Figure 6.20. Ultrafast TA spectral evolution for  $[\text{Ni-TDC}]^+$  (A),  $[\text{Ni-TDC}]$  (B) and  $[\text{Ni-TDC}]^-$  (C).

## 6.6 Conclusions

The metalated derivatives of a readily accessible tetrapyrrolic macrocycle, TDC, occupy a chemical midpoint between metalated corroles and corrins. The Ni(II) derivative, **[Ni-TDC]<sup>+</sup>**, affords structural characterization of the TDC macrocycle. Under anaerobic conditions in the absence of acid, the CVs of both **[Co-TDC]<sup>+</sup>** and **[Ni-TDC]<sup>+</sup>** exhibit two reversible one-electron reduction waves, implying that the **[M-TDC]** and **[M-TDC]<sup>-</sup>** compounds are stable, as confirmed by chemical reductant studies. EPR spectroscopy and DFT calculations suggest that the one-electron reduction of **[Ni-TDC]<sup>+</sup>** to form **[Ni-TDC]** is predominantly ligand centered. In the presence of BzOH, the first cathodic reduction of **[Ni-TDC]<sup>+</sup>** is unaffected, whereas the second cathodic reduction furnishes a new species, **[Ni-TDC-H]**, through the formal addition of hydride, as corroborated by the chemical reduction of **[Ni-TDC]<sup>+</sup>** with LiBH<sub>4</sub>. **[Ni-TDC-H]** can be protonated by TFA to form **[Ni-TDC-H<sub>2</sub>]<sup>+</sup>**, the latter of which can also be furnished through the direct electroreduction of **[Ni-TDC]<sup>+</sup>** in the presence of excess TFA. This susceptibility of the TDC macrocycle towards hydrogenation is redolent of other Ni tetrapyrrole complexes, which are known to undergo ring reduction under HER conditions.<sup>52,54</sup> However, the TDC ligand platform is distinguished from other commonly studied tetrapyrroles by exceptional ability in stabilizing low-valent metals, as evidenced by the air-stability of the formally Co(I) compound **[Co-TDC]**.

## 6.7 Materials and Methods

**General considerations.** Acetonitrile was purified and dried through a neutral alumina column under argon. The supporting electrolyte, *n*-Bu<sub>4</sub>NPF<sub>6</sub>, was purchased from Sigma Aldrich (>99%), recrystallized from a water-ethanol mixture, and dried. Molecular sieves (3 Å, beads) were heated (>140 °C) under vacuum for 2 days prior to use. THF used in all reactions was freshly distilled from Na/benzophenone ketyl unless noted. CHCl<sub>3</sub> was stabilized with ethanol. All commercially available compounds were used as received. <sup>1</sup>H NMR and <sup>13</sup>C NMR spectra were collected at room temperature in CDCl<sub>3</sub> unless noted otherwise.

**Synthesis of 7,8,12,13-tetradehydro-1,3,3,17, 17,19-hexamethyl-7,10,13-tri-*p*-tolylcorrinato-cobalt(II) nitrate [Co-TDC]<sup>+</sup>.** Dihydrodipyrin **1** (106 mg, 0.38 mmol) and *p*-

tolualdehyde (23  $\mu$ L, 0.19 mmol) in  $\text{CH}_2\text{Cl}_2$  (19.0 mL) were treated with  $\text{Ga}(\text{OTf})_3$  (290 mg, 0.57 mmol) at room temperature under argon and stirred for 20 h. The reaction mixture was washed with brine, dried ( $\text{Na}_2\text{SO}_4$ ), and concentrated. The residue was dissolved in methanol (24 mL), treated with  $\text{Co}(\text{OAc})_2 \cdot 4\text{H}_2\text{O}$  (142 mg, 0.57 mmol) immediately, stirred at room temperature for 15 h, and exposed to air. The reaction mixture was then filtered. The filtrate was concentrated, and the resulting residue was dissolved in  $\text{CH}_2\text{Cl}_2$ . The organic phase was washed with brine, dried ( $\text{Na}_2\text{SO}_4$ ) and concentrated. Chromatography [alumina,  $\text{CH}_2\text{Cl}_2$ ; then  $\text{CH}_2\text{Cl}_2/\text{MeOH}$  (10:1)] afforded a green-brown solid. The resulting solid was dissolved in methanol (1.0 mL) and treated with a solution of  $\text{KNO}_3$  (0.20 g, 2.0 mmol) in water (1.5 mL). The precipitate was collected by filtration and recrystallized from chloroform/hexanes to give a brown solid (33 mg, 22% from **1**). UV-Vis ( $\text{CH}_2\text{Cl}_2$ ), nm (relative absorbance): 350 (3.3), 508 (2.0), 581 (br) (1.0). HRMS (ESI)  $m/z$ : requires 714.3127 for  $[\text{M}^+]$  ( $\text{M} = \text{C}_{46}\text{H}_{47}\text{CoN}_4$ ), found 714.3140, LD-MS: found 715.4.

**Synthesis of 7,8,12,13-tetradehydro-1,3,3,17, 17,19-hexamethyl-7,10,13-tri-*p*-tolyl-corrinatonicel(II) chloride  $[\text{Ni-TDC}]^+$ .** Dihydrodipyrin **1** (106.0 mg, 0.38 mmol) and *p*-tolualdehyde (23  $\mu$ L, 0.19 mmol) in  $\text{CH}_2\text{Cl}_2$  (19.0 mL) were treated with  $\text{Ga}(\text{OTf})_3$  (290.0 mg, 0.57 mmol) at room temperature under argon and stirred for 20 h. The reaction mixture was washed with brine, dried ( $\text{Na}_2\text{SO}_4$ ) and concentrated. The residue was dissolved in methanol (24 mL), treated with  $\text{Ni}(\text{OAc})_2 \cdot 4\text{H}_2\text{O}$  (142.0 mg, 0.57 mmol) immediately, stirred at room temperature for 1 h, and exposed to air. The reaction mixture was then filtered. The filtrate was concentrated, and the resulting residue was dissolved in  $\text{CH}_2\text{Cl}_2$ . The organic phase was washed with brine, dried ( $\text{Na}_2\text{SO}_4$ ) and concentrated. Chromatography [alumina,  $\text{CH}_2\text{Cl}_2$ ; then  $\text{CH}_2\text{Cl}_2/\text{MeOH}$  (10:1)] afforded a blue solid. The resulted solid was dissolved in  $\text{CH}_2\text{Cl}_2$ , the organic phase was washed with brine (5 times), dried, and concentrated. The resulting solid was recrystallized from  $\text{CH}_2\text{Cl}_2$ /hexanes to give a blue solid (70 mg, 46% from **1**). Crystals suitable for X-ray diffraction were grown by the slow evaporation of a DCM solution in the presence of hexanes at 4  $^\circ\text{C}$ .  $^1\text{H}$  NMR (500 MHz):  $\delta$  1.56 (s, 12H, overlaps with  $\text{H}_2\text{O}$ ), 1.62 (s, 6H), 2.459 (s, 6H), 2.465 (d,  $J = 12.8$  Hz, 2H), 2.50 (s, 3H), 2.67 (d,  $J = 13.6$  Hz, 2H), 6.91 (s, 2H), 7.29 (s, 2H), 7.35 (d,  $J = 7.9$  Hz, 6H), 7.40 (d,  $J = 7.5$  Hz, 2H), 7.43

(d,  $J = 7.9$  Hz, 4H). HRMS (ESI)  $m/z$ : requires 713.31487 for  $[M^+]$  ( $M = C_{46}H_{47}NiN_4$ ), found 713.3140.

**Reduction of  $[Ni-TDC]^+$  with bulk electrolysis.** A MeCN solution of  $[Ni-TDC]^+$  in 0.1 M  $n-Bu_4NPF_6$  was prepared. Electrolysis was performed at  $E_{appl} = -1.7$  V vs  $Fc^+/Fc$  in a  $N_2$ -filled glovebox using an H-cell equipped with a carbon foam working electrode, zinc metal counter electrode, and  $Ag^+/Ag$  reference electrode. Aliquots of the reaction solution were removed periodically and monitored by UV-vis-NIR absorption spectroscopy in the glovebox until the absorption spectrum matched that of the doubly reduced  $[Ni-TDC]^-$  obtained by spectroelectrochemistry.

**Reduction of  $[Ni-TDC]^+$  with  $LiBH_4$ .** In a 1.0 cm pathlength quartz cuvette, excess  $LiBH_4$  was added to a solution of  $[Ni-TDC]^+$  in dry acetonitrile in a  $N_2$ -atmosphere glovebox. UV-vis-NIR spectra were collected on the resulting sample immediately and 10 min after  $LiBH_4$  addition. In experiments studying the protonation of the putative  $[Ni-TDC-H]$  intermediate, excess TFA was immediately added to the  $[Ni-TDC]^+$  solution subsequent to addition of  $LiBH_4$  and the UV-vis-NIR spectral evolution of the resulting solution was monitored. Electrospray ionization mass spectrometry (ESI-MS) data are reported for the molecular ion or protonated molecular ion.

**Reduction of  $[Co-TDC]^+$  with  $KO_2$ .** In a  $N_2$ -filled glovebox 2 mg of  $[Co-TDC]^+$  (as the acetate salt) was dissolved in 20 mL of MeCN. To this solution, excess  $KO_2$  and 18-crown-6 were added, and the resulting pink mixture was immediately filtered with a 0.22  $\mu m$  PTFE syringe filter. The filtrate was then diluted 8-fold with MeCN and a UV-vis spectrum was collected.

**Electrochemistry.** All potentials are reported vs. the  $Fc^+/Fc$  redox couple. Thin-layer spectroelectrochemistry data were recorded in a  $N_2$ -filled glovebox on an Ocean Optics spectrometer with a 0.5 mm path length quartz cell, a Pt mesh working electrode, a Pt wire counter electrode, and a non-aqueous  $Ag^+/Ag$  reference electrode, all of which were purchased from BioAnalytical Systems. UV-vis-NIR spectra were recorded at room temperature in quartz cuvettes on either a Varian Cary 5000 UV-vis-NIR spectrometer or an Ocean Optics spectrometer. Cyclic voltammograms (CVs) were collected using a CH Instruments potentiostat. Tetradehydrocorrins were dissolved in a solution containing  $n-Bu_4NPF_6$  (0.1 M) as supporting electrolyte. A three-electrode cell configuration was used with a Pt wire counter electrode, a non-

aqueous  $\text{Ag}^+/\text{Ag}$  reference electrode, and a glassy carbon working electrode that was meticulously polished before each measurement. The polishing procedure was performed on felt using different diamond pastes of different sizes (15, 6, 3, and 1  $\mu\text{m}$ ). The electrode was briefly sonicated in ethanol and dried under a stream of compressed air before use. The working electrodes were repolished with 1  $\mu\text{m}$  diamond paste in between CV measurements. Ohmic drop was compensated for using the positive feedback compensation implemented in the instrument.

**EPR spectroscopy.** The **[Ni-TDC]** sample for EPR was prepared from the comproportionation of **[Ni-TDC]<sup>+</sup>** and **[Ni-TDC]<sup>-</sup>** solutions in 0.1 M  $[\text{n-Bu}_4\text{N}][\text{PF}_6]$  in MeCN, where the latter was prepared via bulk electrolysis as described above. A stock solution of **[Ni-TDC]<sup>+</sup>** was prepared in 0.1 M  $[\text{n-Bu}_4\text{N}][\text{PF}_6]$  in MeCN and an aliquot was taken and electrolyzed to form **[Ni-TDC]<sup>-</sup>**. The remaining **[Ni-TDC]<sup>+</sup>** solution was then titrated into the solution of **[Ni-TDC]<sup>-</sup>** until the characteristic absorption feature of the latter at  $\sim 490$  nm disappeared as observed by UV-vis spectroscopy. EPR spectra of **[Ni-TDC]** were collected on a Bruker ElexSys E500 spectrometer.

**Femtosecond transient absorption spectroscopy.** A Ti:Sapphire laser (Libra HE, Coherent) generates fundamental 1 kHz pulses at 800 nm ( $\sim 50$  fs) and a power of 3 W. An OPerA SOLO (Coherent) is seeded with 2 W of 800 nm fundamental to provide pump pulses in the UV-vis-IR region. The pump pulses were aligned to a 1.7 m translation stage (Aerotech ATS62150, U100 controller) equipped with a hollow retro-reflector (Newport), following which an ultrabroadband polarizer and  $\lambda/2$  waveplate (Thorlabs) were used to produce linearly polarized pulses at magic angle with respect to the probe pulses. For the probe and reference pulses, broadband white light pulses were generated by focusing a small fraction ( $\sim 1$  mW) of the 800 nm fundamental ( $f = 100$  mm, Thorlabs) into a 5 mm thick calcium fluoride plate ( $\text{CaF}_2$ ) that was constantly moved linearly to avoid thermal damage. The generated white light beam was collimated reflectively ( $f = 50$  mm, Thorlabs) and aligned onto a 15 mm translation stage (PhysikInstrumente, M-111.DG, Mercury DC controller). The residual fundamental was removed by a notch filter (EK SMA, VEI6053). The filtered white light was then passed to a neutral density filter (Thorlabs, NDUV04B), from which the reflected and transmitted pulses were generated and

serve as probe and reference, respectively. The pump and probe beams were overlapped onto the sample stored in a 1 mm sealed quartz cuvette. The final probe and reference beams were detected by two linear array CCD cameras. The final instrumental response time is ~150 fs determined by measuring the FWHM of the scattering light around the excitation wavelength at 400 nm. The short translation stage was typically used to take data in a few picoseconds with a time step of 10–30 fs and the long stage was used for measurements from 2 to 3000 ps with a varying time step. The Ni-TDC compounds were dissolved in THF solution and further diluted to achieve an OD ~0.4–0.8 at 400 nm for TA spectroscopic study. All the sample preparations were performed in a N<sub>2</sub>-filled glove box.

**Transient absorption data analysis.** The single wavelength dynamic trace shows either excited state absorption (ESA, positive signal) or ground state bleaching (GSB, negative signal). Each trace was fitted with multiple exponentials convoluted with the instrument response function (IRF), a gaussian function with FWHM=150 fs, described in the following formula:

$$S = IRF \otimes \sum_{i=1}^4 A_i e^{\frac{t}{\tau_i}} A_i$$

For the ESA, the initial rise was fitted with negative amplitude and the following decay was fitted with positive amplitude. Conversely, for the GSB, the initial decrease of the signal was fitted with positive amplitude and the following increase of the signal was fitted with negative amplitude.

**X-ray crystallography.** Crystals of [Ni-TDC]<sup>+</sup> were grown by the slow evaporation of a DCM solution in the presence of hexanes at 4°C. X-ray diffraction data were collected on a Bruker three-circle platform goniometer equipped with an Apex II CCD detector and Oxford Cryosystems Cryostat cooling device using  $\varphi$  and  $\omega$  scans. A fine-focus sealed tube Mo K $\alpha$  (0.71073 Å) X-ray source was used. The crystal was mounted on a cryoloop using Paratone oil. Data were integrated using SAINT and multi-scan absorption correction was applied using SADABS. The structure was solved by intrinsic phasing using SHELXT (APEX3 program suite, 2016) and refined against F<sup>2</sup> on all data by full matrix least squares with SHELXL. All non-hydrogen atoms, including the disorder fragments, were located in the difference-Fourier maps and refined anisotropically. Hydrogen

atoms were added at calculated positions and refined with a riding model. The restraints on bond lengths (SADI/SAME) and atomic displacement parameters (SIMU/RIGU) have been applied on each pair of disorder fragments as necessary.

**Table 6.2.** Crystal data and structure refinement for [Ni-TDC]<sup>+</sup>.

Empirical formula	C <sub>46</sub> H <sub>50.5</sub> ClN <sub>4</sub> NiO <sub>1.8</sub>
Formula weight	781.56
T (K)	100(2)
$\lambda$ (Å)	0.71073
Crystal system	Triclinic
Space group	$P\bar{1}$
$a$ (Å)	11.169(3)
$b$ (Å)	13.332(5)
$c$ (Å)	16.156(6)
$\alpha$ (°)	90.924(7)
$\beta$ (°)	107.172(7)
$\gamma$ (°)	113.381(6)
$V$ (Å <sup>3</sup> )	2070.6(13)
$Z$	2
$\rho_{\text{calcd}}$ (Mg/m <sup>3</sup> )	1.254
$\mu$ (mm <sup>-1</sup> )	0.574
$\theta$ range for data collection (°)	1.951 to 25.143
Index ranges	$-13 \leq h \leq 13, -15 \leq k \leq 15, -19 \leq l \leq 19$
Reflections collected	25219
Independent reflns ( $R_{\text{int}}$ )	7199 (0.0916)
Completeness to $\theta_{\text{max}}$	97.0%
Data/restraints/parameters	7199 / 1021 / 734
GOF on $F^2$	1.043
$R_1$	0.0746
$wR_2$	0.2253
Largest diff. peak, hole (e Å <sup>-3</sup> )	1.382, -0.502

**Computational studies.** DFT calculations in Gaussian 16<sup>63</sup> were carried out at the UBP86/def2-TZVP level of theory in combination with the conductor-like polarizable continuum

model (C-PCM) to implicitly account for solvation in MeCN and frequency calculations confirmed optimized structures. The functional is well suited to describe Ni-containing macrocycles, as shown by previous computational reports on chlorins and porphyrins, while the use of a balanced polarized triple-zeta basis set ensures good energetic and geometric convergence as well as an adequate description of the conjugated macrocycle.<sup>50,58</sup>

Geometry optimizations started from the experimentally derived crystal structure of [Ni-TDC]<sup>+</sup> (singlet, +1 charge, trans vicinal dimethyl groups) whereby phenyl groups were replaced with methyl groups for computational tractability. The optimised structure features a nearly D<sub>4h</sub> Ni environment and is in good agreement with the crystal structure (Figure SDF1). Geometry optimisation for the other oxidation states were conducted by sequentially adding or removing 1 electron and optimising the resulting structure. For the formally Ni(II) and Ni(0) compounds, singlet states were computed, while Ni(I) was computed as doublet. Spin contamination did not occur, and triplet states were not considered in this study.

## 6.8 NMR Spectra

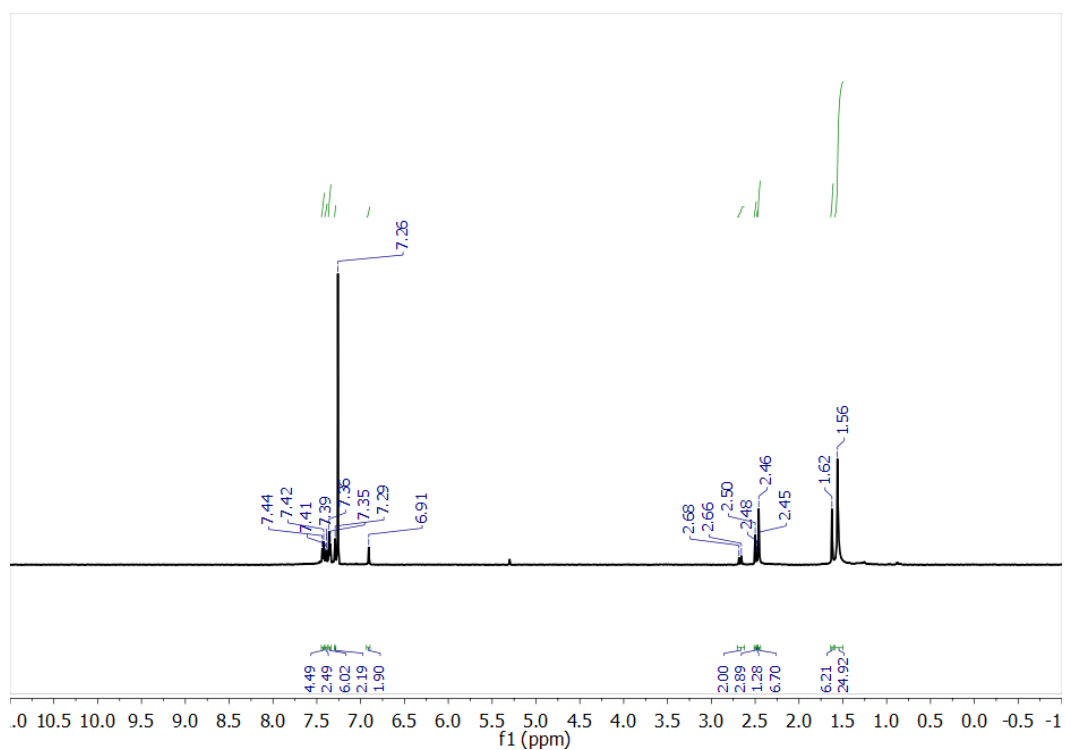


Figure 6.21. <sup>1</sup>H NMR spectrum of [Ni-TDC]<sup>+</sup> taken in CDCl<sub>3</sub>.



## 6.9 Acknowledgements

Sijia Liu (Lindsey Group) and Dr. Mengran Liu prepared the TDC complexes. Drs. Andrew Maher and Mengran Liu assisted with the spectroelectrochemistry. Dr. Yangzhong Qin performed the transient absorption measurements. Dr. Christoph Schnedermann assisted with the computational studies. Dr. Shao-Liang Zheng assisted with X-ray crystallography.

## 6.10 References

1. Silva, R. C.; Silva, L. O.; Bartolomeu, A. A.; Brocksom, T. J.; Oliveira, K. T. Recent Applications of Porphyrins as Photocatalysts in Organic Synthesis: Batch and Continuous Flow Approaches. *Beil. J. Org. Chem.* **2020**, *16*, 917–955.
2. Rybicka-Jasińska, K.; Shan, W.; Zawada, K.; Kadish, K. M.; Gryko, D. Porphyrins as Photoredox Catalysts: Experimental and Theoretical Studies. *J. Am. Chem. Soc.* **2016**, *138*, 15451–15458.
3. Gust, D.; Moore, T. A.; Moore, A. L. Solar Fuels via Artificial Photosynthesis. *Acc. Chem. Res.* **2009**, *42*, 1890–1898.
4. Walter, M. G.; Rudine, A. B.; Wamser, C. C. Porphyrins and Phthalocyanines in Solar Photovoltaic Cells. *J. Porph. Phthalocyanines* **2010**, *14*, 759–792.
5. Imran, M.; Ramzan, M.; Qureshi, A. K.; Khan, M. A.; Tariq, M. Emerging Applications of Porphyrins and Metalloporphyrins in Biomedicine and Diagnostic Magnetic Resonance Imaging. *Biosensors* **2018**, *8*, 95.
6. Ptaszek, M. Porphyrins and Hydroporphyrins for In Vivo Bioimaging, In *Applications of Porphyrinoids as Functional Materials*, Lang, H.; Rueffer, T., Eds., RSC Publishing: 2021, Ch 10.
7. Dolmans, D. E. J. G. J.; Fukumura, D.; Jain, R. K. Photodynamic Therapy for Cancer. *Nat. Rev. Cancer* **2003**, *3*, 380–387.
8. Taniguchi, M.; Lindsey, J. S. Synthetic Chlorins, Possible Surrogates for Chlorophylls, Prepared by Derivatization of Porphyrins. *Chem. Rev.* **2017**, *117*, 344–535.
9. Pucelik, B.; Sułek, A.; Dąbrowski, J. M. Bacteriochlorins and Their Metal Complexes as NIR-Absorbing Photosensitizers: Properties, Mechanisms, and Applications. *Coord. Chem. Rev.* **2020**, *416*, 213340.
10. Montforts, F.-P. (A→D) Ring Closure to the Nickel(II)-B,C,D-Hexadecahydrocorrinato. *Angew. Chem. Int. Ed. Engl.* **1982**, *21*, 214–215.
11. Zhang, S.; Nagarjuna Reddy, M.; Mass, O.; Kim, H.-J.; Hu, G.; Lindsey, J. S. Synthesis of Tailored Hydrodipyrins and Their Examination in Directed Routes to Bacteriochlorins and Tetradecahydrocorrins. *New J. Chem.* **2017**, *41*, 11170–11189.
12. Deans, R. M.; Mass, O.; Diers, J. R.; Bocian, D. F.; Lindsey, J. S. Serendipitous Synthetic Entrée to Tetradecahydro Analogues of Cobalamins. *New J. Chem.* **2013**, *37*, 3964–3975.
13. Johnson, A. W. Synthesis of Corrins and Related Macrocycles Based on Pyrrolic Intermediates. *Philos. Trans. R. Soc. Lond. B Biol. Sci.* **1976**, *273*, 319–326.
14. Miyazaki, Y.; Oohora, K.; Hayashi, T. Methane Generation via Intraprotein C–S Bond Cleavage in Cytochrome b562 Reconstituted with Nickel Didehydrocorrin. *J. Organomet. Chem.* **2019**, *901*, 120945.
15. Guberman-Pfeffer, M. J.; Greco, J. A.; Samankumara, L. P.; Zeller, M.; Birge, R. R.; Gascón, J. A.; Brückner, C. Bacteriochlorins with a Twist: Discovery of a Unique Mechanism to Red-Shift the Optical Spectra of Bacteriochlorins. *J. Am. Chem. Soc.* **2017**, *139*, 548–560.

16. Taniguchi, M.; Cramer, D. L.; Bhise, A. D.; Kee, H. L.; Bocian, D. F.; Holten, D.; Lindsey, J. S. Accessing the Near-Infrared Spectral Region with Stable, Synthetic, Wavelength-Tunable Bacteriochlorins. *New J. Chem.* **2008**, *32*, 947-958.
17. Peters, M. K.; Röhricht, F.; Näther, C.; Herges, R. One-Pot Approach to Chlorins, Isobacteriochlorins, Bacteriochlorins, and Pyrrocorphins. *Org. Lett.* **2018**, *20*, 7879-7883.
18. Morita, Y.; Oohora, K.; Sawada, A.; Kamachi, T.; Yoshizawa, K.; Hayashi, T. Redox Potentials of Cobalt Corrinoids with Axial Ligands Correlate with Heterolytic Co-C Bond Dissociation Energies. *Inorg. Chem.* **2017**, *56*, 1950-1955.
19. Nomenclature of Corrinoids, *Pure Appl. Chem.* **1976**, *48*, 495-502.
20. Genokhova, N. S.; Melent'eva, T. A.; Berezovskii, V. M. Synthesis of Corroles and Octadecahydrocorrins. *Russ. Chem. Rev.* **1980**, *49*, 1056-1067.
21. Kim, H.-J.; Lindsey, J. S. De Novo Synthesis of Stable Tetrahydroporphyrinic Macrocycles: Bacteriochlorins and a Tetradecahydrocorrin. *J. Org. Chem.* **2005**, *70*, 5475-5486.
22. Ogawa, A.; Oohora, K.; Hayashi, T. Synthesis and Characterization of *meso*-Substituted Cobalt Tetradecahydrocorrin and Evaluation of Its Electrocatalytic Behavior toward CO<sub>2</sub> Reduction and H<sub>2</sub> Evolution. *Inorg. Chem.* **2018**, *57*, 14644-14652.
23. Morita, Y.; Oohora, K.; Mizohata, E.; Sawada, A.; Kamachi, T.; Yoshizawa, K.; Inoue, T.; Hayashi, T., Crystal Structures and Coordination Behavior of Aqua- and Cyano-Co(III) Tetradecahydrocorrins in the Heme Pocket of Myoglobin. *Inorg. Chem.* **2016**, *55*, 1287-1295.
24. Liu, C.-J.; Thompson, A.; Dolphin, D. Synthesis, Structure and Properties of 1,19-Disubstituted Tetradecahydrocorrin Cobalt Complexes. *J. Inorg. Biochem.* **2001**, *83*, 133-138
25. Hush, N. S.; Woolsey, I. S. Reduced Species of Cobalt and Nickel Complexes Analogous to Vitamin B<sub>12</sub>. *J. Am. Chem. Soc.* **1972**, *94*, 4107-4114.
26. Dolphin, D. Structure and Synthesis, Part A-B. *The Porphyrins*, edited by David Dolphin, New York: Academic Press, 1978, Vol.1-2.
27. Lindsey, J. S. Synthesis of *meso*-Substituted Porphyrins. In *The Porphyrin Handbook*; Kadish, K. M., Smith, K. M., Guilard, R., Eds.; Academic Press: San Diego, CA, 2000; Vol. 1, pp 45-118.
28. Lindsey, J. S. The Synthesis of *meso*-Substituted Porphyrins. In *Metalloporphyrins; Catalyzed Oxidations*; Montanari, F., Casella, L., Eds.; Kluwer Academic Publishers, Dordrecht, The Netherlands. 1994; pp 49-86.
29. Liu, M.; Dogutan, D. K.; Nocera, D. G. Synthesis of Hangman Chlorins. *J. Org. Chem.* **2020**, *85*, 5065-5072.
30. Maher, A. G.; Passard, G.; Dogutan, D. K.; Halbach, R. L.; Anderson, B. L.; Gagliardi, C. J.; Taniguchi, M.; Lindsey, J. S.; Nocera, D. G. Hydrogen Evolution Catalysis by a Sparsely Substituted Cobalt Chlorin. *ACS Catal.* **2017**, *7*, 3597-3606.
31. Banerjee, S.; Phadte, A. A.  $\beta$ -*meso*-Annulated *meso*-Tetraarylchlorins: A Study of the Effect of Ring Fusion on Chlorin Conformation and Optical Spectra. *ChemistrySelect* **2020**, *5*, 11127-11144.

32. Wang, P.; Lindsey, J. S. Riley Oxidation of Heterocyclic Intermediates on Paths to Hydroporphyrins—A Review. *Molecules* **2020**, *25*, 1858.
33. Battersby, A. R. Tetrapyrroles: The Pigments of Life. *Nat. Prod. Rep.* **2000**, *17*, 507-526.
34. Montforts, F.-P.; Glasenapp-Breiling, M., Chapter 1 The Synthesis of Chlorins, Bacteriochlorins, Isobacteriochlorins and Higher Reduced Porphyrins. In *Prog. Heterocycl. Chem.*, Gribble, G. W.; Gilchrist, T. L., Eds. Elsevier: 1998; Vol. 10, pp 1-24.
35. Dogutan, D. K.; Bediako, D. K.; Graham, D. J.; Lemon, C. M.; Nocera, D. G. Proton-Coupled Electron Transfer Chemistry of Hangman Macrocycles: Hydrogen and Oxygen Evolution Reactions. *J. Porphyr. Phthalocyanines* **2015**, *19*, 1-8.
36. Graham, D. J.; Dogutan, D. K.; Schwalbe, M.; Nocera, D. G. Hangman Effect on Hydrogen Peroxide Dismutation by Fe(III) Corroles. *Chem. Commun.* **2012**, *48*, 4175-4177.
37. Lemon, C. M.; Dogutan, D. K.; Nocera, D. G., Porphyrin and Corrole Platforms for Water Oxidation, Oxygen Reduction, and Peroxide Dismutation. In *Handbook of Porphyrin Science*, World Scientific Publishing Company: 2012; Vol. Volume 21, pp 1-143.
38. Dogutan, D. K.; McGuire, R.; Nocera, D. G. Electrocatalytic Water Oxidation by Cobalt(III) Hangman  $\beta$ -Octafluoro Corroles. *J. Am. Chem. Soc.* **2011**, *133*, 9178-9180.
39. Dogutan, D. K.; Stoian, S. A.; McGuire, R.; Schwalbe, M.; Teets, T. S.; Nocera, D. G. Hangman Corroles: Efficient Synthesis and Oxygen Reaction Chemistry. *J. Am. Chem. Soc.* **2011**, *133*, 131-140.
40. Schwalbe, M.; Dogutan, D. K.; Stoian, S. A.; Teets, T. S.; Nocera, D. G. Xanthene-Modified and Hangman Iron Corroles. *Inorg. Chem.* **2011**, *50*, 1368-1377.
41. Araújo, A. R. L.; Tomé, A. C.; Santos, C. I. M.; Faustino, M. A. F.; Neves, M. G. P. M. S.; Simões, M. M. Q.; Moura, N. M. M.; Abu-Orabi, S. T.; Cavaleiro, J. A. S. Azides and Porphyrinoids: Synthetic Approaches and Applications. Part 1—Azides, Porphyrins and Corroles. *Molecules* **2020**, *25*, 1662.
42. Mondal, S.; Naik, P. K.; Adha, J. K.; Kar, S. Synthesis, Characterization, and Reactivities of High Valent Metal-Corrole (M = Cr, Mn, and Fe) Complexes. *Coord. Chem. Rev.* **2019**, *400*, 213043.
43. Ganguly, S.; Ghosh, A. Seven Clues to Ligand Noninnocence: The Metallocorrole Paradigm. *Acc. Chem. Res.* **2019**, *52*, 2003-2014.
44. Lei, H.; Li, X.; Meng, J.; Zheng, H.; Zhang, W.; Cao, R. Structure Effects of Metal Corroles on Energy-Related Small Molecule Activation Reactions. *ACS Catal.* **2019**, *9*, 4320-4344.
45. Ghosh, A. Electronic Structure of Corrole Derivatives: Insights from Molecular Structures, Spectroscopy, Electrochemistry, and Quantum Chemical Calculations. *Chem. Rev.* **2017**, *117*, 3798-3881.
46. Orłowski, R.; Gryko, D.; Gryko, D. T. Synthesis of Corroles and Their Heteroanalogs. *Chem. Rev.* **2017**, *117*, 3102-3137.
47. Teo, R. D.; Hwang, J. Y.; Termini, J.; Gross, Z.; Gray, H. B. Fighting Cancer with Corroles. *Chem. Rev.* **2017**, *117*, 2711-2729.

48. Aravindu, K.; Krayner, M.; Kim, H.-J.; Lindsey, J. S. Facile Synthesis of a B,D-Tetradehydrocorrin and Rearrangement to Bacteriochlorins. *New J. Chem.* **2011**, *35*, 1376-1384.
49. Krayner, M.; Ptaszek, M.; Kim, H.-J.; Meneely, K. R.; Fan, D.; Secor, K.; Lindsey, J. S. Expanded Scope of Synthetic Bacteriochlorins via Improved Acid Catalysis Conditions and Diverse Dihydrodipyrin-Acetals. *J. Org. Chem.* **2010**, *75*, 1016-1039.
50. Zhang, S.; Kim, H.-J.; Tang, Q.; Yang, E.; Bocian, D. F.; Holten, D.; Lindsey, J. S. Synthesis and Photophysical Characteristics of 2,3,12,13-Tetraalkylbacteriochlorins. *New J. Chem.* **2016**, *40*, 5942-5956.
51. Niederhoffer, E. C.; Timmons, J. H.; Martell, A. E. Thermodynamics of Oxygen Binding in Natural and Synthetic Dioxygen Complexes. *Chem. Rev.* **1984**, *84*, 137-203.
52. Maher, A. G.; Liu, M.; Nocera, D. G. Ligand Noninnocence in Nickel Porphyrins: Nickel Isobacteriochlorin Formation under Hydrogen Evolution Conditions. *Inorg. Chem.* **2019**, *58*, 7958-7968.
53. Kadish, K. M.; Franzen, M. M.; Han, B. C.; Araullo-McAdams, C.; Sazou, D. Factors Determining the Site of Electroreduction in Nickel Metalloporphyrins. Spectral Characterization of Nickel(I) Porphyrins, Nickel(II) Porphyrin  $\pi$ -anion radicals, and Nickel(II) Porphyrin  $\pi$ -Anion Radicals with Some Nickel(I) Character. *J. Am. Chem. Soc.* **1991**, *113*, 512-517.
54. Solis, B. H.; Maher, A. G.; Dogutan, D. K.; Nocera, D. G.; Hammes-Schiffer, S. Nickel Phlorin Intermediate Formed by Proton-Coupled Electron Transfer in Hydrogen Evolution Mechanism. *Proc. Natl. Acad. Sci. U. S. A.* **2016**, *113*, 485-492.
55. Kütt, A.; Tshepelevitsh, S.; Saame, J.; Lökov, M.; Kaljurand, I.; Selberg, S.; Leito, I. Strengths of Acids in Acetonitrile. *Eur. J. Org. Chem.* **2021**, *2021*, 1407-1419.
56. Muckerman, J. T.; Skone, J. H.; Ning, M.; Wasada-Tsutsui, Y. Toward the Accurate Calculation of  $pK_a$  Values in Water and Acetonitrile. *Biochim. Biophys. Acta, Bioenerg.* **2013**, *1827*, 882-891.
57. McCarthy, B. D.; Martin, D. J.; Rountree, E. S.; Ullman, A. C.; Dempsey, J. L. Electrochemical Reduction of Brønsted Acids by Glassy Carbon in Acetonitrile—Implications for Electrocatalytic Hydrogen Evolution. *Inorg. Chem.* **2014**, *53*, 8350-8361.
58. Rieth, A. J.; Gonzalez, M. I.; Kudisch, B.; Nava, M.; Nocera, D. G. How Radical are 'Radical' Photocatalysts? A Closed-Shell Meisenheimer Complex is Identified as a Super-Reducing Photoreagent. *J. Am. Chem. Soc.* **2021**, *143*, 14352-14359.
59. Zinchenko Kristina, S.; Ardana-Lamas, F.; Seidu, I.; Neville Simon, P.; van der Veen, J.; Lanfaloni Valentina, U.; Schuurman Michael, S.; Wörner Hans, J., Sub-7-Femtosecond Conical-Intersection Dynamics Probed at the Carbon K-edge. *Science* **2021**, *371*, 489-494.
60. Gumy, J. C.; Vauthey, E. Investigation of the Excited-State Dynamics of Radical Ions in the Condensed Phase Using the Picosecond Transient Grating Technique. *J. Phys. Chem. A* **1997**, *101*, 8575-8580.

61. Gosztola, D.; Niemczyk, M. P.; Sevc, W.; Lukas, A. S.; Wasielewski, M. R. Excited Doublet States of Electrochemically Generated Aromatic Imide and Diimide Radical Anions. *J. Phys. Chem. A* **2000**, *104*, 6545-6551.
62. Fujitsuka, M.; Kim, S. S.; Lu, C.; Toji, S.; Majima, T. Intermolecular and Intramolecular Electron Transfer Processes from Excited Naphthalene Diimide Radical Anions. *J. Phys. Chem. B* **2015**, *119*, 7275-7282.
63. Frisch, M. J.; Trucks, G. W.; Schlegel, H. B.; Scuseria, G. E.; Robb, M. A.; Cheeseman, J. R.; Scalmani, G.; Barone, V.; Petersson, G. A.; Nakatsuji, H.; Li, X.; Caricato, M.; Marenich, A. V.; Bloino, J.; Janesko, B. G.; Gomperts, R.; Mennucci, B.; Hratchian, H. P.; Ortiz, J. V.; Izmaylov, A. F.; Sonnenberg, J. L.; Williams; Ding, F.; Lipparini, F.; Egidi, F.; Goings, J.; Peng, B.; Petrone, A.; Henderson, T.; Ranasinghe, D.; Zakrzewski, V. G.; Gao, J.; Rega, N.; Zheng, G.; Liang, W.; Hada, M.; Ehara, M.; Toyota, K.; Fukuda, R.; Hasegawa, J.; Ishida, M.; Nakajima, T.; Honda, Y.; Kitao, O.; Nakai, H.; Vreven, T.; Throssell, K.; Montgomery Jr., J. A.; Peralta, J. E.; Ogliaro, F.; Bearpark, M. J.; Heyd, J. J.; Brothers, E. N.; Kudin, K. N.; Staroverov, V. N.; Keith, T. A.; Kobayashi, R.; Normand, J.; Raghavachari, K.; Rendell, A. P.; Burant, J. C.; Iyengar, S. S.; Tomasi, J.; Cossi, M.; Millam, J. M.; Klene, M.; Adamo, C.; Cammi, R.; Ochterski, J. W.; Martin, R. L.; Morokuma, K.; Farkas, O.; Foresman, J. B.; Fox, D. J. *Gaussian 16 Rev. B.01*, Wallingford, CT, 2016.

*Page intentionally left blank*

## Chapter 7

### **Synthesis of an Elusive Dearomatized Tetrapyrrole: The Chlorinphlorin**



## 7.1 Introduction

Hydrogenation of unsaturated compounds is a common transformation in chemistry and biology, but the reaction typically occurs by different mechanisms. Whereas chemical hydrogenation usually relies on H<sub>2</sub> as the reductant, nature uses enzymes to form saturated bonds with electrons provided from a redox cofactor and protons from pre-positioned donors. For instance, in anoxygenic photosynthetic bacteria, bio-hydrogenation of chlorophyll to bacteriochlorophyll is performed by a chlorophyllide oxidoreductase (COR) with two electrons provided by a reduced ferredoxin and two protons by peptidyl residues proximate to the active site.<sup>1</sup> Similarly, hydrogenation by the dark-operative protochlorophyllide oxidoreductase (DPOR), which reduces protochlorophyllide (a heme-derivative) to form a direct precursor of chlorophyll *a* in a light-independent route, is accomplished with electrons from a Fe<sub>4</sub>S<sub>4</sub> cluster coupled to proton transfers from intramolecular propionic acid and a nearby aspartate.<sup>2</sup>

The chemical reduction of unsaturated olefin bonds by proton-coupled electron transfer (PCET) occurs at high potential and is a kinetically cumbersome transformation<sup>3</sup> that is avoided when H<sub>2</sub> is the reductant. However, in biological reductions, the different sources of the electron and proton imposes that the hydrogenation of the olefin bond occurs by PCET. Multi-site PCET hydrogenations of the unsaturated bonds of biological macrocycles can give rise to unusual macrocyclic cores that are not accessible by direct reduction. Such PCET reactivity is generally derived from redox non-innocence of ligands.<sup>4</sup> Hydrogenation of an olefin moiety involving the methine carbon in a porphyrin ring gives rise to phlorins, which are an initial intermediate in the formation of chlorins (hydrogenation of one C<sub>β</sub>-C<sub>β</sub> bond) (Figure 7.1) and are also found as intermediates in porphyrin catalysis of the hydrogen evolution reaction.<sup>5,6</sup> In macrocyclic cores that are reduced beyond porphyrins, the phlorin is more enigmatic. Whereas the methine positions next to the pyrroline ring of a chlorin have higher electron density and thus are susceptible to electrophilic attack, the chlorinphlorin has nevertheless been elusive (Figure 7.1). The only reports of chlorinphlorin describe its generation from electrochemical<sup>7,8</sup> or photochemical<sup>9,10</sup> reduction of a chlorophyll-derived parent molecule. The oddity of chlorinphlorin<sup>11</sup> has resulted in its inadequate characterization, which has been restricted to a

single, broad absorption trace<sup>11</sup> and <sup>1</sup>H NMR spectra.<sup>7,9</sup> In addition to the fundamental interest in the formation of a chlorinphlorin from PCET reduction of the chlorin macrocycle, the hydrogenation of the chlorin macrocycle is intriguing because the chemistry of reduced chlorins is the keystone to the biosynthesis of bacteriochlorophylls.<sup>12,13</sup> Accordingly, an understanding of the multi-site PCET hydrogenation of chlorin to chlorinphlorin is intriguing and, more generally, provides insight into the reduction of unsaturated carbon-carbon bonds by PCET in biology. Here, we report the the formation of a chlorinphlorin from a chlorin through PCET under spectroelectrochemical conditions in the presence of exogenous acid. Furthermore, we demonstrate the chemical synthesis and structural characterization of this elusive tetrapyrrole.

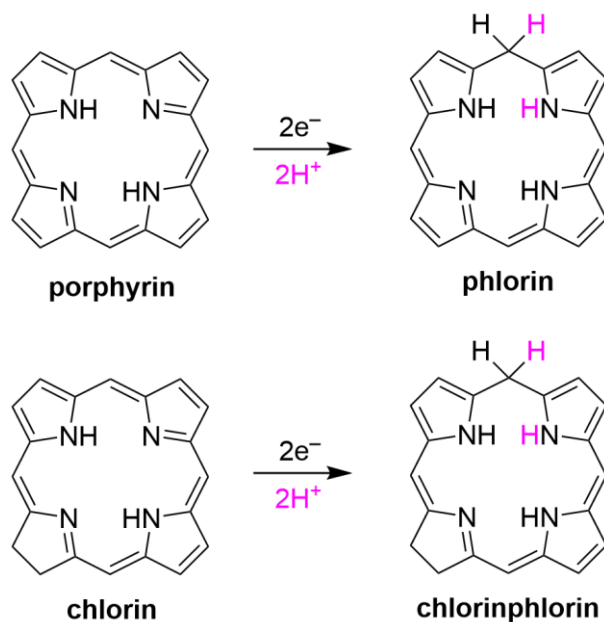


**Figure 7.1.** Reduction of tetrapyrrole macrocyclic rings to produce phlorins.

## 7.2 Synthesis and Structure of *meso*-Tetraphenylchlorinphlorin

Given previous reports claiming the generation of a chlorinphlorin through the electrochemical reduction of a chlorin in the presence of a Brønsted acid,<sup>7</sup> the reduction of *meso*-tetraphenylchlorin in the presence of benzoic acid (BA) in DCM was investigated by spectroelectrochemistry. As shown in Figure 7.2, when a DCM solution containing 15 mM *meso*-tetraphenylchlorin and 100 mM BA is subjected to an applied potential of  $E_{app} = -1.78$  V vs  $Fc^+/Fc$ ,

the Soret band disappears with a concomitant growth of a broad feature centered at ~540 nm, where the latter feature is reminiscent of a previously reported UV-vis spectrum for a putative chlorinphlorin.<sup>11</sup> To unequivocally confirm the formation of a chlorinphlorin, we sought to chemically reduce chlorin in the presence of acid and structurally characterize the resulting compound. A protonation-reduction sequence was achieved by reduction of *meso*-tetraphenylchlorin with cobaltocene subsequent to protonation using tosylic acid monohydrate. The reduction product was then isolated by preparatory thin-layer chromatography (TLC). The UV-vis absorption spectrum of this chemically prepared species (Figure 7.2B) matches the spectroelectrochemical spectrum (Figure 7.2A). This compound was then crystallized and the structure is shown in Figure 7.3. To the best of our knowledge, this represents the first example of a crystallographically characterized chlorinphlorin. The structure is distinguished by the tetrahedral geometry of the C(11) methine carbon.

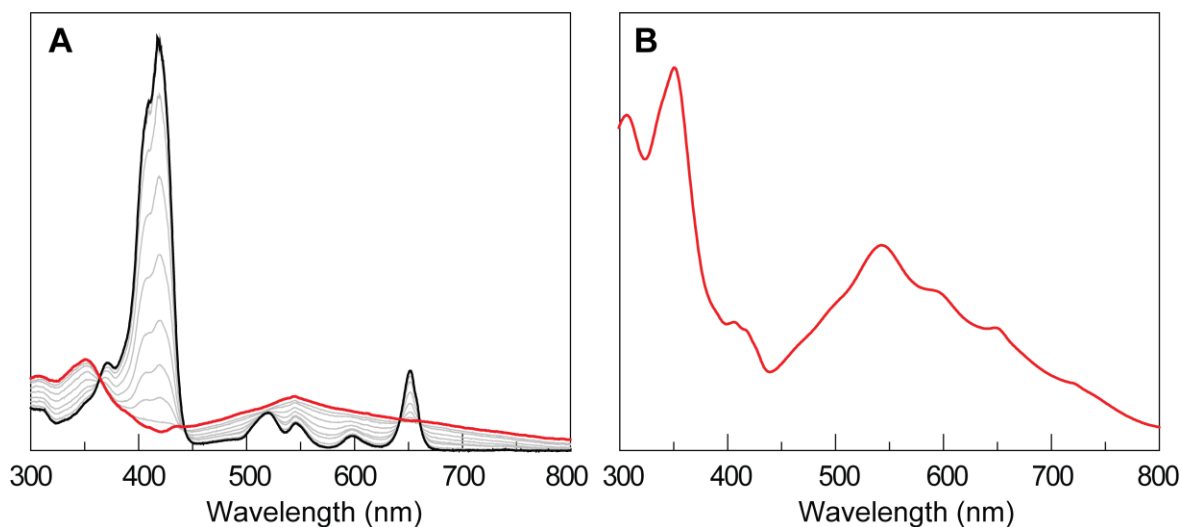


**Figure 7.2.** UV-vis characterization of chlorinphlorin. (A) Thin-layer UV-vis spectroelectrochemistry in a N<sub>2</sub>-filled glovebox on a solution of 15 mM *meso*-tetraphenylchlorin and 100 mM benzoic acid in CD<sub>2</sub>Cl<sub>2</sub> with *n*-Bu<sub>4</sub>NPF<sub>6</sub> (0.1 M) as an electrolyte under an applied potential of -1.78 V vs Fc<sup>+</sup>/Fc. The black and red traces show the initial and final spectra, respectively. (B) UV-vis spectrum of the isolated *meso*-tetraphenylchlorinphlorin product from chemical reduction in DCM.

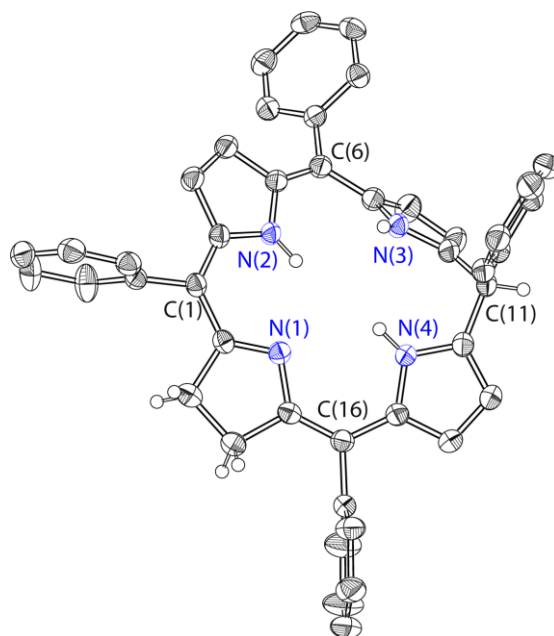


**Figure 7.3.** Crystal structure of the synthesized chlorinphlorin. A hydrogen-bonded pyridine molecule and all non-oxidizable hydrogen atoms bound to carbon have been omitted for clarity. Thermal ellipsoids are drawn at 50% probability.

### 7.3 Conclusions

The electrochemical reduction of a free-base chlorin by PCET furnishes a reduced macrocycle as revealed by spectroelectrochemistry. This elusive reduction product was unequivocally established as a chlorinphlorin by its independent chemical preparation and X-ray structural characterization.

### 7.4 Materials and Methods

**General considerations.** All non-deuterated solvents were purified by the method of Grubbs and stored over activated 3 Å molecular sieves.<sup>1</sup> Deuterated solvents were degassed by three cycles of freeze-pump-thaw and stored over activated 3 Å molecular sieves. The supporting electrolyte, *n*-Bu<sub>4</sub>NPF<sub>6</sub>, was purchased from Sigma Aldrich (> 99%), recrystallized from a water-ethanol mixture, and dried. *meso*-Tetraphenylchlorin was purchased from TCI America and used as received. Thin-layer spectroelectrochemistry data were recorded in a N<sub>2</sub>-filled glovebox on an Ocean Optics spectrometer with a 0.5 mm path length quartz cell, a Pt mesh working electrode,

a Pt wire counter electrode, and a non-aqueous Ag<sup>+</sup>/Ag reference electrode. NMR spectra were recorded at the Laukien-Purcell Instrumentation Center in the Department of Chemistry and Chemical Biology at Harvard University on a JEOL ECZ400S spectrometer operating at 400 MHz.

**Synthesis of *meso*-tetraphenylchlorinphlorin.** In a N<sub>2</sub>-filled glovebox, *meso*-tetraphenylchlorin (30.0 mg, 0.0486 mmol) was dissolved in 5 mL of DCM and tosylic acid monohydrate (9.2 mg, 0.049 mmol) was added as a solid. The reaction mixture was stirred for 2 h at room temperature and cobaltocene (9.2 mg, 0.049 mmol) was subsequently added dropwise as a solution in DCM (~2 mL). The resulting violet solution was stirred for 15 min. This procedure was repeated with a second equivalent of tosylic acid monohydrate (9.2 mg, 0.049 mmol) and cobaltocene (9.2 mg, 0.049 mmol). The solvent was then concentrated *in vacuo* and the product was purified under a N<sub>2</sub> atmosphere by preparatory thin-layer chromatography on silica with DCM as the mobile phase. The titular compound was isolated as a violet powder (23 mg, 77%). Crystals for X-ray crystallography were grown by vapor diffusion of hexanes into a pyridine solution of the compound. <sup>1</sup>H and <sup>13</sup>C NMR spectra are shown in Figure S10. <sup>1</sup>H NMR (400 MHz, CD<sub>2</sub>Cl<sub>2</sub>): δ 7.63 (dd, *J* = 7.8, 1.7 Hz, 2H), 7.50-7.33 (m, 13H), 7.30 (br, 1H), 7.20-7.09 (m, 3H), 7.00 (d, *J* = 5.2 Hz, 2H), 6.90 (d, *J* = 7.9 Hz, 2H), 6.62 (t, *J* = 2.6 Hz, 1H), 6.60-6.54 (m, 3H), 6.51 (t, *J* = 3.1 Hz, 1H), 6.29 (s, 1H), 6.01 (t, *J* = 2.8 Hz, 1H) 2.84-2.55 (m, 4H). <sup>13</sup>C NMR (101 MHz, CD<sub>2</sub>Cl<sub>2</sub>): δ 152.1, 151.4, 142.6, 141.4, 140.6, 140.3, 135.8, 134.1, 133.0, 132.5, 131.3, 131.2, 129.2, 128.81, 128.78, 128.6, 128.3, 127.61, 127.60, 127.3, 126.5, 125.4, 124.3, 120.9, 119.7, 116.5, 115.4, 112.0, 111.0, 109.3, 106.4, 44.6, 36.4, 30.4. HRMS (ESI) *m/z*: calculated for [M+H]<sup>+</sup> 619.2856, found 619.2843.

**X-ray crystallography details.** X-ray diffraction data were collected at the Advanced Photon Source at the Argonne National Laboratory on a Huber three-circle goniometer with free  $\kappa$  using a Pilatus 1M CdTe Pixel Array Detector and an Oxford Cryosystems cryostat operating at 100 K. A synchrotron X-ray source with a wavelength of 0.41328 Å was used. The crystal was mounted on a cryoloop using Paratone oil. Data were integrated using SAINT and multi-scan absorption correction was applied using SADABS. The structure was solved by intrinsic phasing using SHELXT (APEX3 program suite, 2016) and refined against F<sup>2</sup> on all data by full matrix least

squares with SHELXL. All atoms were located in the difference-Fourier maps and all non-hydrogen atoms were refined anisotropically. The crystal structure with the difference-Fourier map (green) used to locate hydrogen atoms bound to pyrrolic nitrogen atoms is shown in Figure 7.4. Crystal data and structure refinement for *meso*-tetraphenylchlorinphlorin are listed in Table 7.1.

**Table 7.1.** Crystal data and structure refinement for *meso*-tetraphenylchlorinphlorin.

Empirical formula	C <sub>49</sub> H <sub>39</sub> N <sub>5</sub>
Formula weight	697.85
T (K)	100
$\lambda$ (Å)	0.41328
Crystal system	Monoclinic
Space group	<i>P2<sub>1</sub>/n</i>
<i>a</i> (Å)	16.617(4)
<i>b</i> (Å)	11.878(2)
<i>c</i> (Å)	20.263(7)
$\alpha$ (°)	90
$\beta$ (°)	110.077(7)
$\gamma$ (°)	90
<i>V</i> (Å <sup>3</sup> )	3731.9(17)
<i>Z</i>	4
$\rho_{\text{calcd}}$ (Mg/m <sup>3</sup> )	1.242
$\mu$ (mm <sup>-1</sup> )	0.034
$\theta$ range for data collection (°)	2.29 to 14.15
Index ranges	-19 ≤ <i>h</i> ≤ 19, -14 ≤ <i>k</i> ≤ 12, -24 ≤ <i>l</i> ≤ 24
Reflections collected	6673
<i>R</i> <sub>int</sub>	0.0694
Completeness to $\theta_{\text{max}}$	99.4%
Data/restraints/parameters	6673 / 0 / 644
GOF on <i>F</i> <sup>2</sup>	1.055
<i>R</i> <sub>1</sub>	0.0537
w <i>R</i> <sub>2</sub>	0.1394
Largest diff. peak, hole (e Å <sup>-3</sup> )	0.324, -0.258

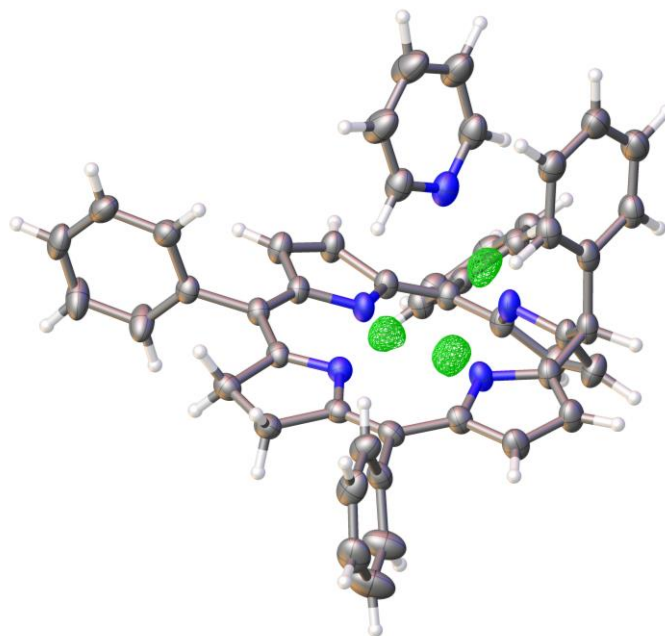


**Figure 7.4.** Crystal structure with the difference-Fourier map (green) used to locate hydrogen atoms bound to pyrrolic nitrogen atoms.

## 7.5 NMR Spectra

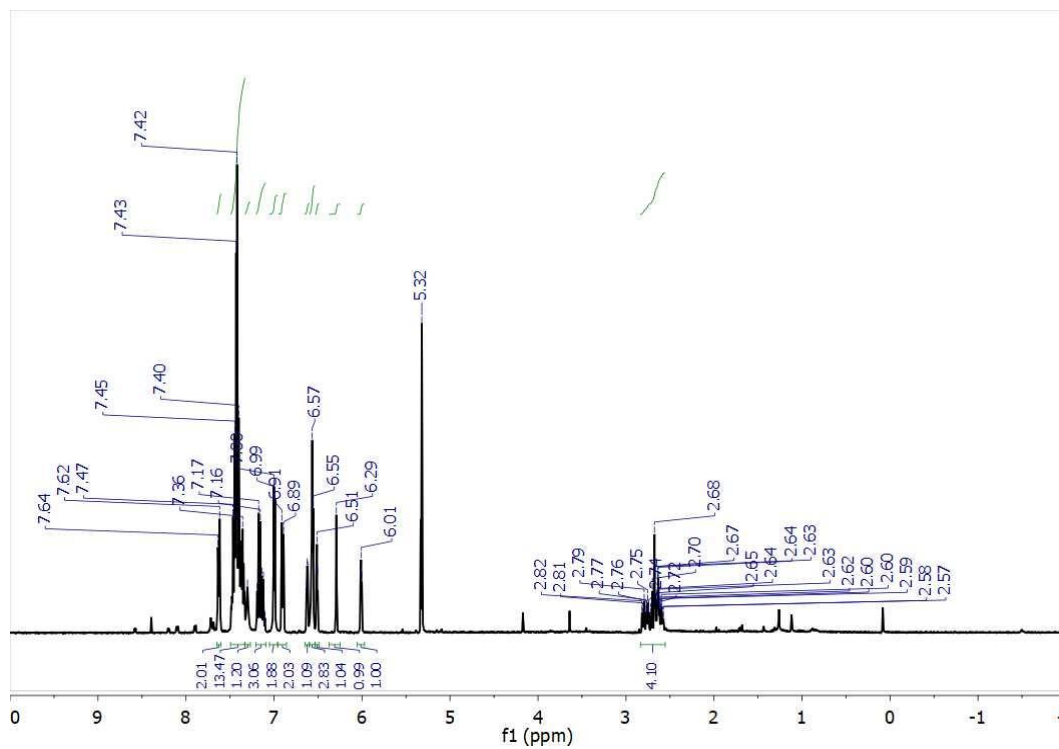


**Figure 7.5.**  $^1\text{H}$  NMR (400 MHz,  $\text{CD}_2\text{Cl}_2$ ) of *meso*-tetraphenylchlorinphlorin.

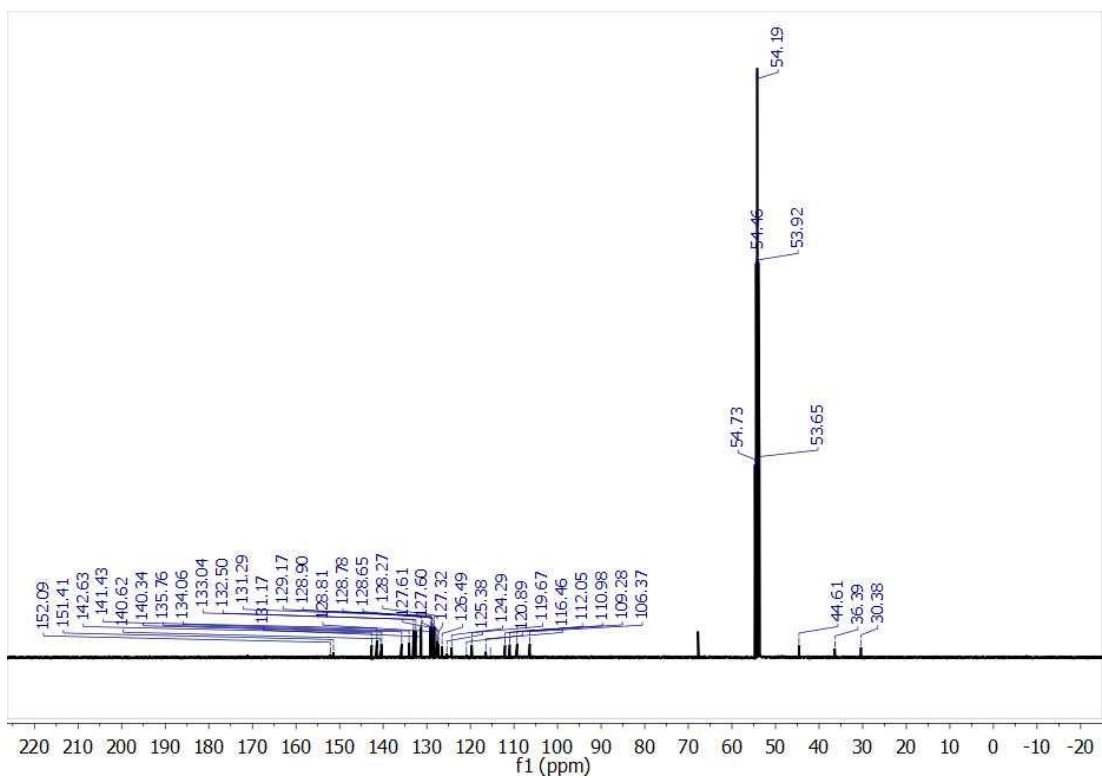


**Figure 7.6.**  $^{13}\text{C}$  NMR (101 MHz,  $\text{CD}_2\text{Cl}_2$ ) of *meso*-tetraphenylchlorinphlorin.

## 7.6 Acknowledgements

Dr. Shao-Liang Zheng assisted with X-ray crystallography.



## 7.7 References

1. Tamiaki, H.; Teramura, M.; Tsukatani, Y. Reduction Processes in Biosynthesis of Chlorophyll Molecules: Chemical Implication of Enzymatically Regio- and Stereoselective Hydrogenations in the Late Stages of Their Biosynthetic Pathway. *Bull. Chem. Soc. Jpn.* **2015**, *89*, 161–173.
2. Muraki, N.; Nomata, J.; Ebata, K.; Mizoguchi, T.; Shiba, T.; Tamiaki, H.; Kurisu, G.; Fujita, Y. X-ray Crystal Structure of the Light-Independent Protochlorophyllide Reductase. *Nature* **2010**, *465*, 110–114.
3. Derosa, J.; Garrido-Barros, P.; Peters, J. C. Electrocatalytic Reduction of C–C  $\pi$  Bonds via a Cobaltocene-Derived Concerted Proton-Electron Transfer Mediator: Fumarate Hydrogenation as a Model Study. *J. Am. Chem. Soc.* **2021**, *143*, 9303–9307.
4. Costentin, C.; Savéant, J. M.; Tard, C. Ligand “Noninnocence” in Coordination Complexes vs. Kinetic, Mechanistic, and Selectivity Issues in Electrochemical Catalysis. *Proc. Natl. Acad. Sci. U.S.A.* **2018**, *115*, 9104–9109.
5. Solis, B. H.; Maher, A. G.; Dogutan, D. K.; Nocera, D. G.; Hammes-Schiffer, S. Nickel Phlorin Intermediate Formed by Proton-Coupled Electron Transfer in Hydrogen Evolution Mechanism. *Proc. Natl. Acad. Sci. U.S.A.* **2016**, *113*, 485–492.
6. Maher, A. G.; Liu, M.; Nocera, D. G. Ligand Non-Innocence in Nickel Porphyrins: Nickel Isobacteriochlorin Formation under Hydrogen Evolution Conditions. *Inorg. Chem.* **2019**, *58*, 7958–7968.
7. Inhoffen, H. H.; Jäger, P.; Mählich, R.; Mengler, C. D. Zur Weiteren Kenntnis des Chlorophylls und des Hämins, XII. Elektrochemische reduktionen an porphyrinen und chlorinen, IV, *Justus Liebigs Ann. Chem.* **1967**, *704*, 188–207.
8. Inhoffen, H. H.; Jäger, P.; Mählich, R. Further Knowledge of Chlorophyll and of Hemin. 32. Partial Synthesis of Rhodin-G7-Trimethyl Ester from Chlorin-E6-Trimethyl Ester and at Same Time Completion of Harvard Synthesis of Chlorophyll A to Chlorophyll B. *Justus Liebigs Ann. Chem.* **1971**, 749, 109.
9. Suboch, V. P.; Shul’ga, A. M.; Sevchenko, A. N.; Zhuravlev, A. G.; Gurinovich, G. P.; Glazkov, Y. V. Structure of Products of Chlorin Photoreduction Reaction. *Dokl. Akad. Nauk SSSR* **1972**, *204*, 404.
10. Krasnovskii, A. A. Obratimoe fotokhimicheskoe vosstanovlenie khlorofilla askorbinovoi kislotoi, *Dokl. Acad. Nauk. SSSR* **1948**, *60*, 421–424.
11. Scheer, H.; Inhoffen, H. H. Hydroporphyrins: Reactivity, Spectroscopy, and Hydroporphyrin Analogues. In *The Porphyrins*, Dolphin, D., Ed., Academic Press: 1978, pp 45–90.
12. Taniguchi, M.; Ptaszek, M.; McDowell, B. E.; Boyle, P. D.; Lindsey, J. S. Sparsely Substituted Chlorins as Core Constructs in Chlorophyll Analogue Chemistry. Part 3: Spectral and Structural Properties. *Tetrahedron* **2007**, *63*, 3850–3863.
13. Taniguchi, M.; Lindsey, J. S. Synthetic Chlorins, Possible Surrogates for Chlorophylls, Prepared by Derivatization of Porphyrins. *Chem. Rev.* **2017**, *117*, 344–535.

14. Pangborn, A. B.; Giardello, M. A.; Grubbs, R. H.; Rosen, R. K.; Timmers, F. J. Safe and Convenient Procedure for Solvent Purification. *Organometallics* **1996**, *15*, 1518-1520.